School of Optometry and Vision Sciences

An *in vivo* investigation of optic nerve head microstructure in primary open angle glaucoma

Ryan Lee Bartlett

A thesis submitted to Cardiff University for the degree of Doctor of Philosophy

October 2020

Declaration

Statement 1

This thesis is being submitted in partial fulfilment of the requirements for the degree of PhD.

Statement 2

This work has not been submitted in substance for any other degree or award at this or any other university or place of learning, nor is it being submitted concurrently in candidature for any other degree or award.

Statement 3

I hereby give consent for my thesis, if accepted, to be available in the University's Open Access repository and for inter-library loan, and for the title and summary to be made available to outside organisations.

Declaration

This thesis is the result of my own independent work, except where otherwise stated, and the views expressed are my own. Other sources are acknowledged by explicit references.

Copyright

All images, where applicable, had permission for use in this thesis. Copyright permits are shown in Appendix V.

Acknowledgments

Firstly, an immense thank you to Dr Julie Albon and Prof Rachel North. Their help, guidance, and expert advice throughout this PhD has been of epic proportions and is hugely appreciated. Thank you to Prof James Morgan for allowing and helping with participant recruitment. Thank you to Nick White for his expert advice and support in imaging and signal analysis, whose friendship is fondly missed. Additional thanks to Dr J R Fergusson for training in OCT image acquisition, and for ensuring the research OCT device was in good working order.

Thank you to Health and Care Research Wales, Welsh Government for funding this work, and thank you to the participants who took part in this study.

I would like to acknowledge thanks for additional datasets acquired by Dr B E Frost in a College of Optometrists study awarded to Dr Julie Albon.

Thank you to Dr A Pozarickij for his genuine bonhomie, and several pointers on how to use/grapple with R statistical software.

Thank you to my family; Bethan, Mum, and Dad for your continued support and encouragement, and for offering me a place for write-up. Thank you to Brooke and Llywelyn for keeping me on my toes.

Finally, Rebecca, sincerely thank you. Without you, and your unconditional friendship and support, none of this would have been possible.

Summary

Glaucoma remains the leading cause of irreversible blindness in the world. Since retinal ganglion cell (RGC) axonal degeneration precedes permanent vision loss, identification of ONH parameters affected in the earliest stages of primary open angle glaucoma (POAG) is critical to ensure early diagnosis.

This cross-sectional study used enhanced-depth imaging optical coherence tomography (EDI-OCT; 1040/70nm) to acquire 10° and 20° scans centred on the ONH (glaucomatous; n=128 or healthy controls; n=60). Regional measures of prelamina and LC depth and thickness, nerve fibre layer thickness at ONH border (bNFL) and peripapillary (pNFL), neuroretinal minimum rim width; (MRW) and area; (MRA) were analysed. This is the first study to quantify volumetric parameters including optic cup, prelamina and LC volume, and also Bruch's membrane opening (BMO) surface area. Furthermore, LC connective tissue alignment was probed regionally and depth-wise within the LC. Statistical modelling was performed to identify ONH parameters that best contributed to characterisation of ONHs in the earliest stages of POAG.

Regional measures of prelamina depth and thickness, and LC thickness were able to differentiate between control eyes and preperimetric (PG), and early glaucoma (EG) (P<0.05). Additionally, EG LC volume was significantly less than in controls (P<0.05). Significant associations of these parameters with loss of VF sensitivity (VF Mean deviation [MD]) were identified. Border and pNFL thickness, MRW (but not MRA) significantly differed between controls and PG and EG (P<0.05); and decreased with VF MD. Lamina cribrosa connective tissue alignment altered in a region and depth specific manner between PG LC and controls, or EG LCs (P<0.05), providing an original *in vivo* indicator of disease.

In conclusion, *in vivo* ONH and NFL parameters are able to discriminate between healthy ONHs and early POAG ONHs; providing a group index with potential as a novel biomarker for early diagnosis, critical to personalised clinical decision making.

Table of contents

List of figures

Chapter 1: Introduction

Chapter 2: Methods

Chapter 3: Evaluation of ONH depth and thickness parameters in Glaucoma

Chapter 4: Volumetric measures of ONH parameters in Glaucoma

Chapter 5: Analysis of lamina cribrosa microstructural parameters in Glaucoma

Chapter 6: Statistical modelling to determine ONH factors that characterise disease stage in Glaucoma

Chapter 7: Discussion

Appendix I

Appendix III

Appendix IV

List of tables

Chapter 2: Methods

Chapter 3: Evaluation of ONH depth and thickness parameters in Glaucoma

Chapter 4: Volumetric measures of ONH parameters in Glaucoma

Chapter 5: Analysis of lamina cribrosa microstructural parameters in Glaucoma

Chapter 6: Statistical modelling to determine ONH factors that characterise disease stage in Glaucoma

Chapter 7: Discussion

Appendix II

Appendix III

Appendix IV

Abbreviations

A	angle of scan
ACD	anterior chamber depth
APON	acquired pit of the optic nerve
AxL	axial length
BM	Bruch's membrane
BMO	Bruch's membrane opening
bNFL	border nerve fibre layer
C	control
CCT	central corneal thickness
D	dioptres
dB	decibels
EDI	enhanced depth imaging
EG	early glaucoma
FD-OCT	Fourier domain optical coherence tomography
G	glaucoma
I	inferior
IN	inferior-nasal
IOP	intraocular pressure
IT	inferior-temporal
LC	lamina cribrosa
MAG	moderate-advanced glaucoma
MD	Mean Deviation
mm	millimetres
mmHg	millimetres of mercury
MRA	minimum rim area
MRW	minimum rim width
MS	mean spherical refractive error
n	number
N	nasal
NFL	nerve fibre layer

NICE	National Institute for Health and Care Excellence
nm	nanometres
NRR	neuroretinal rim
NTG	normal tension glaucoma
OCT	optical coherence tomography
ONH	optic nerve head
P	axial eye length – 1.82mm
PG	preperimetric glaucoma
pNFL	peripapillary nerve fibre layer
POAG	primary open angle glaucoma
PreL	prelamina
RGC	retinal ganglion cell
S	superior
SD-OCT	spectral domain optical coherence tomography
SN	superior-nasal
SS-OCT	swept source optical coherence tomography
ST	superior-temporal
T	temporal
TD-OCT	time domain optical coherence tomography
VF	visual field
µm	micrometres
2D	two dimensional
3D	three dimensional

I. Chapter 1: Introduction

Glaucoma is the leading cause of irreversible blindness worldwide and is estimated to affect around 60 million people with approximately 10% being bilaterally blind (Resnikoff et al., 2004; Quigley and Broman, 2006; Quigley, 2011; Tham et al., 2014; Bourne et al., 2016; Flaxman et al., 2017). In England and Wales, glaucoma remains a leading cause of visual impairment certification (Bunce, Xing and Wormald, 2010; Rahman et al., 2020). In the UK, around 10% of blind and partially sighted registrations are attributed to glaucoma (Bunce and Wormald, 2008).

Glaucoma is a multifactorial disease whereby various combinations of vascular (Hayreh, 1969; Flammer and Orgul, 1998) and mechanical (Minckler, Bunt and Johanson, 1977; Gaasterland, Tanishima and Kuwabara, 1978) mechanisms have been suggested as important contributors to retinal ganglion cell (RGC) death (Quigley, Dunkelberger and Green, 1989; Quigley, 1999; Almasieh et al., 2012), and axonal dysfunction (Quigley et al., 1987; Furuyoshi et al., 2000), reviewed by Burgoyne (2011); Downs, Roberts and Sigal (2011); Davis et al. (2016).

The lamina cribrosa (LC) has been proposed as a primary site of RGC axonal injury in glaucoma (Minckler, 1981; Quigley et al., 1981; Quigley et al., 1983), reviewed by Burgoyne (2011); Downs et al. (2011); Downs and Girkin (2017). The LC is positioned deep within the optic nerve head (ONH) and provides important structural and nutritional support to traversing RGC axons (Dandona et al., 1990; Elkington et al., 1990). Compression, posterior displacement and rearrangement of the LC connective tissue beams have been associated with RGC axon loss in POAG and a decrease in visual function (Quigley, Addicks and Green, 1982; Quigley et al., 1983; Fontana et al., 1998; Furlanetto et al., 2013; Tan et al., 2019).

Careful clinical evaluation of the appearance of the ONH and retinal nerve fibre layer (RNFL), along with consideration of visual field (VF) function are important aspects in glaucoma disease assessment (Caprioli, 1989; Budde and Jonas, 1999; Jonas et al., 2017). The optic disc is the anterior portion of the ONH that is viewed through the pupil of the eye in clinical inspection. The ONH in human eyes is typically vertically oval in shape. In a Caucasian

population, Quigley et al. (1990) reported a mean vertical ONH diameter of 1.88mm, and horizontally 1.70mm. In normal eyes the optic disc area is approximately 2.4mm^2 (Sihota et al., 2005), and generally there is no significant difference in optic disc area between males and females (Hermann et al., 2004).

Where RGC axons converge on the optic disc, this results in a central depression within the optic disc; termed the 'optic cup'. The cup to disc ratio is a clinical measure made along the vertical meridian of the ONH to represent the diameter of the optic cup in relation to the diameter of the optic disc (Coleman, 1999; Keltner et al., 2006; Tatham et al., 2013). In normal eyes, Jonas, Gusek and Naumann (1988b) reported an average vertical cup-disc ratio of 0.34. An inter-eye asymmetry in cup-disc ratio of 0.2 or more can be indicative of glaucoma development (Wang et al., 2010), and even relatively small changes in cup-disc ratio may be associated with large losses of RGC axons, particularly in eyes with large cup to disc ratio (Tatham et al., 2013). A larger cup to disc ratio has been reported in Afro-Caribbean patients, compared to Caucasian (Girkin et al., 2003); whereby Beck, Servais and Hayreh (1987) report 0.35 and 0.24 respectively.

Since cup-disc ratio is considered an important clinical parameter in the evaluation of the ONH, it is important to acknowledge its variability with respect to disc size. For instance, a large cup-disc ratio in a large ONH may not be indicative of glaucoma disease (Garway-Heath et al., 1998). The cup-disc ratio staging system suffers from drawbacks since it does not account for disc size, and that focal loss of the NRR is not adequately identified (Henderer, 2006; Spaeth et al., 2006). The disc damage likelihood scale is based on the appearance of optic disc NRR corrected for disc diameter, and has been reported to be more reproducible than the cup-disc ratio system in estimating the amount of disc damage in glaucoma participants (Spaeth et al., 2002).

Approximately one million RGC axons leave each retina through the scleral canal at the ONH (Anderson and Hoyt, 1969; Jonas et al., 1990), with a physiological age-related decrease in number of axons by ~0.3% each year (Harwerth, Wheat and Rangaswamy, 2008). Jonas et al. (1992) reported an average annual loss of ~4000 nerve fibres. Within the ONH, the RGC axons form bundles and demonstrate a high degree of spatial order. The inner layer of the retina is

the retinal nerve fibre layer which is composed of the RGC axons (Jonas et al., 2017). The nerve fibre layer (NFL) increases in thickness from the periphery of the retina towards the optic disc. As nerve fibres course towards the ONH, fibres from the nasal, superior and inferior retina follow a direct route, along with fibres from the nasal side of the fovea. Fibres temporal to the fovea take arcuate paths to enter the ONH at its upper and lower edges, hence damage to the NFL within these areas can lead to an arcuate VF defect seen in glaucoma disease (Quigley et al., 1989; Coleman, 1999).

I.1 Structure of the optic nerve head

Within the ONH, it is the LC that provides mechanical support for RGC axon fascicles (bundles of several thousand axons) as they pass through the scleral canal. If the ONH were to be sectioned longitudinally, it can be divided into three distinct regions; the prelamina, the LC, and the postlaminar optic nerve, see Figure 1.1.

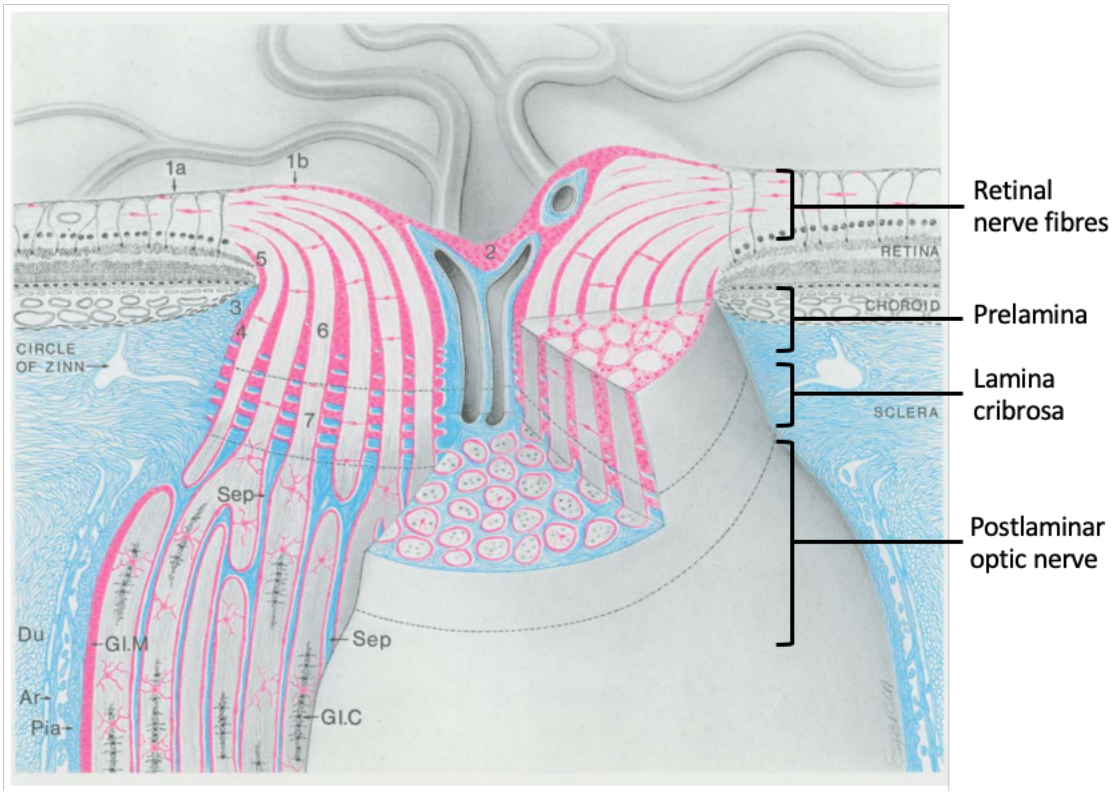

Figure 1.1: Schematic drawing of human ONH, where blue indicates connective tissue and pink indicates astrocytes. Adapted from Anderson and Hoyt (1969). Copyright permit shown in Appendix V.

I.1.1 Prelamina

The prelamina is the region of the ONH that is routinely examined in ophthalmic assessment and is composed of RGC axon bundles, capillaries, and astrocytes (Hernandez, Igoe and Neufeld, 1986; Ye and Hernandez, 1995). The prelamina is covered by a thin layer of astrocytes, the internal limiting membrane of Elschnig, which separates the ONH from the vitreous and is continuous with the internal limiting membrane of the retina (Hogan, Alvarado and Weddell, 1971). Here, axon bundles are arranged into columns. Glial tissue is positioned between ONH axons and the choroid (layer of Jacoby) and extends forwards to separate ONH axons from the outer retinal layers (Anderson, Hoyt and Hogan, 1967; Anderson and Hoyt, 1969).

I.1.2 Lamina cribrosa

The lamina cribrosa (LC) is a thin sieve-like meshwork structure located at the level of the sclera and is composed of 10-11 cribriform plates (Quigley and Addicks, 1981; Quigley et al., 1983). These LC sheets are a network of collagen fibrils and elastic fibres that allow separation of RGC axons into bundles (Radius and Gonzales, 1981; Hernandez et al., 1989) that traverse axially through the LC pores. The LC connective tissue beams are primarily composed of collagen type I, III, IV, V and elastic fibres; with collagen fibrils interspersed with elastic fibres comprising the core of the LC beams (Hernandez et al., 1986; Morrison et al., 1990; Albon et al., 1995; Albon et al., 2000a). Astrocytes surround the LC pores and form glial columns between the connective tissue and the axon bundles (Morrison et al., 1990; Oyama, Abe and Ushiki, 2006). Experimental studies have demonstrated posterior bowing of the LC after intraocular pressure (IOP) elevation in a model of ocular hypertension using human (Yan et al., 1994) and monkey eyes (Bellezza et al., 2003; Yang et al., 2011b).

To exit the eye, RGC axon bundles pass through the LC pores formed by the LC connective tissue beams. There is considerable variation in size of the 200-400 LC pores that transmit axon bundles; with the diameter of pores varying from 10µm to greater than 100µm (Quigley and Addicks, 1981). Using scanning laser ophthalmoscopy, Ivers et al. (2011) reported an average pore area of 1713 ± 1413 μm^2 in the normal human LC *in vivo*. The anterior LC contains larger pores than the posterior LC, with more pores found at the posterior LC surface since pores divide with increased axial depth, and aid in the organisation of RGC axon bundles

(Quigley and Addicks, 1981; Ogden et al., 1988).Within the LC, regional variation in structure has been shown, with the superior and inferior ONH poles containing less connective tissue and glial elements than the nasal and temporal ONH regions, and typically, the largest pores are found in the superior and inferior LC regions (Quigley and Addicks, 1981; Radius and Gonzales, 1981); see Figure 1.2. This regional difference in LC structure is proposed to contribute to an increased vulnerability to ONH damage in glaucoma disease whereby the LC offers less structural support to RGC axons, and an increased susceptibility to axonal damage (Quigley et al., 1981).

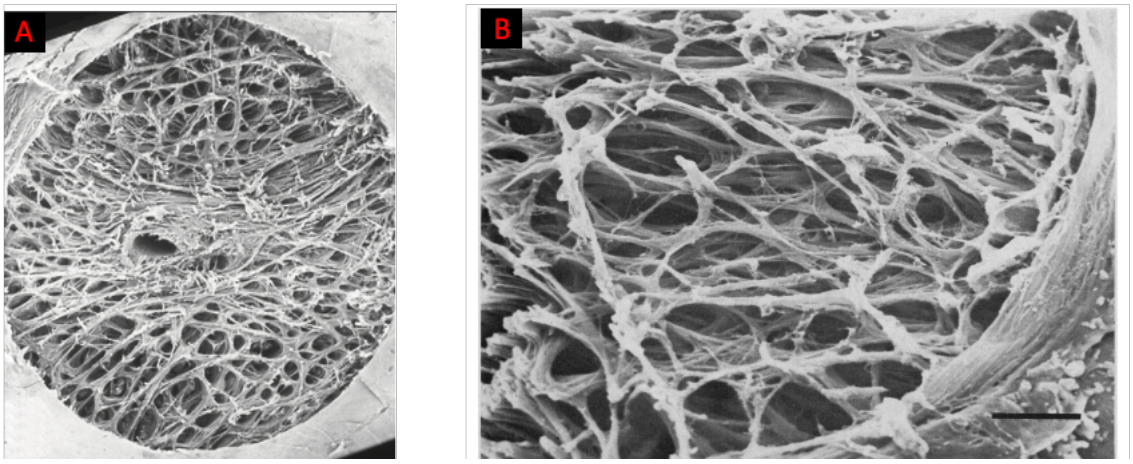

Figure 1.2: Scanning electron microscopy image of human LC indicating larger LC pores and less connective tissue in the superior and inferior poles compared to the nasal-temporal regions (A). Successive LC sheets are thinner and sparser in the inferior pole (B), leading to selectively more loss of RGC axons in the superior and inferior LC regions. Image A from Quigley (2011). Image B from Quigley and Addicks (1981). Copyright permits shown in Appendix V.

I.1.3 Postlaminar optic nerve

As optic nerve (ON) axons enter the postlaminar region, they become myelinated and the optic nerve diameter increases from ~1.5mm at prelamina and LC levels, to ~3.0mm in the postlaminar region (Fujita, Imagawa and Uehara, 2000). Myelination of axons does not normally extend into the LC and retina, however, Tarabishy, Alexandrou and Traboulsi (2007) reported that myelinated retinal nerve fibres are developmental anomalies and are present in approximately 1% of all eyes. Bundles of myelinated nerve axons are segregated by connective tissue septae oriented in the same axis of the ON and continuous with that of the LC. In the postlaminar region, meningeal sheaths surround the optic nerve with a thin pia

mater, a middle arachnoid mater and a thick outer collagenous dura mater (Fujita et al., 2000; Oyama et al., 2006). The LC containing elastic fibres are considered to be compliant to mechanical force affected by elevated IOP (Oyama et al., 2006); where an increased outward migration of the LC insertion into the pia mater has been reported in an ocular hypertension model using *ex vivo* human eyes (Sigal et al., 2010).

I.2 Glaucoma

Glaucoma is an optic neuropathy characterised by progressive and irreversible damage to RGC axons and ultimately has a detrimental effect on vision (Quigley, 1999; Balaratnasingam et al., 2007). The disease results in a distinctive appearance to the optic disc and VF loss (Weinreb and Khaw, 2004). The characteristic excavated optic disc appearance in glaucoma results from stretching and compression, and alterations within the connective tissue of the lamina cribrosa (Quigley et al., 1983; Downs et al., 2011; Downs and Girkin, 2017); Figure 1.3.

Glaucoma represents a group of chronically progressive disorders that effect the optic nerve (Davis et al., 2016; Schuster et al., 2020). Data from population-based surveys indicate that roughly one in forty adults over the age of 40 has glaucoma with reduced visual function, with prevalence increasing from 2% in adults over 40 years of age, to 7% in adults over 75 years of age, reaching 10% in persons over 90 years old (Quigley, 2011; Schuster et al., 2020). Vision loss from glaucoma is permanent, and the disease is usually asymptomatic until a late stage when visual problems arise (Quigley, 2011; Jonas et al., 2017). Additionally, it is reported that only 10% to 50% of people with glaucoma are aware they have the disease (Rotchford et al., 2003; Leite, Sakata and Medeiros, 2011; Budenz et al., 2013) Therefore, the ability to diagnose glaucoma early and detect its progression is essential as appropriate treatment can slow disease progression and preserve visual function (Kotowski et al., 2012; Weinreb, Aung and Medeiros, 2014; Karaskiewicz et al., 2017).

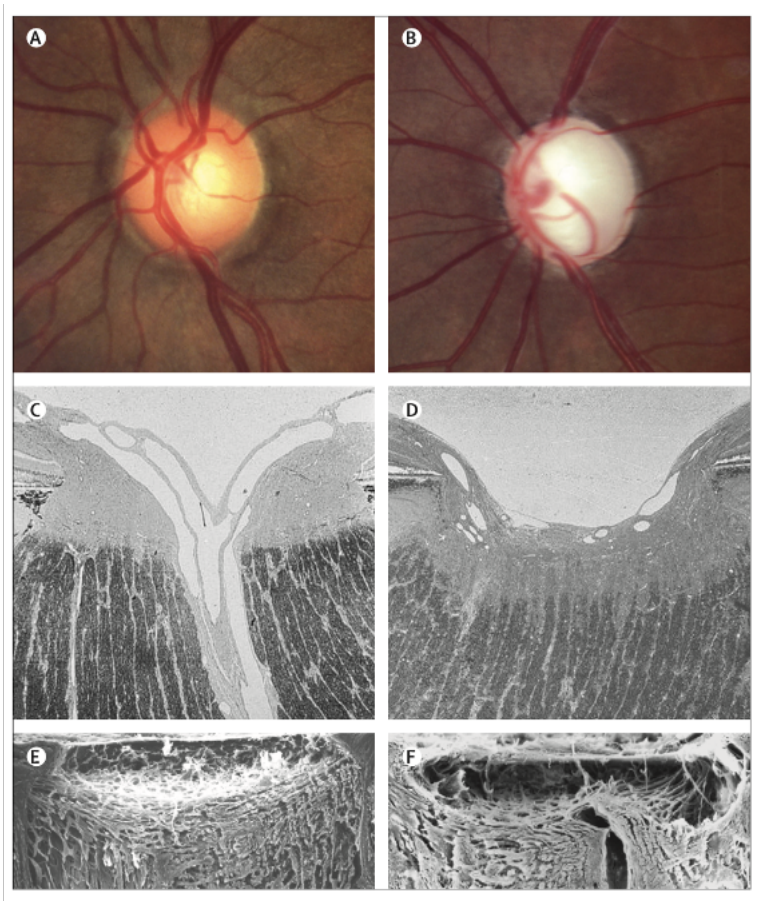

Figure 1.3: Comparison of healthy (left) and glaucomatous (right) appearance to ONH. In participants without glaucoma the optic cup is a small central pale area (a), whereas in glaucoma there is expansion and excavation of the optic cup and loss of the neuroretinal rim (b). The histological appearance of a healthy ONH (c) changes in glaucoma with loss of prelamina tissue and deepening of the optic cup (d). The connective tissue in the healthy ONH (e) alters in glaucoma where there is deformation and backward bowing of the LC (f). From Quigley (2011). Copyright permit shown in Appendix V.

Currently, there is no gold standard criteria for the detection and monitoring of structural damage in the continuum of glaucoma (Grewal and Tanna, 2013; Schuster et al., 2020). In the UK, examination of the ONH and fundus is mandatory in all optometric eye examinations performed by community-based optometrists (Myint et al., 2011). At present, according to NICE (2017) guidelines for all UK-based optometrists, detection of glaucoma is primarily based upon a triad of clinical measures; appearance of the ONH, measurement of intraocular pressure (IOP), and visual field examination (Anderson, 2006; Jonas et al., 2017). Regarding optic disc assessment, the ratio of the diameter of the cup to the disc is used to assess the volume of neuroretinal rim tissue. As nerve fibres die in glaucoma cases, the outer rim of disc tissue becomes thinner, causing the cup to enlarge (Jonas et al., 1988b; Jonas, Gusek and

Naumann, 1988c). However, within the 'normal' population there is large variation in the size of the optic disc and cup (Caprioli and Miller, 1987; Jonas et al., 1988a). To encompass the number of axons leaving the eye, larger optic discs would display thinner NRR and a larger cup than smaller optic discs (Quigley et al., 1990; Gardiner et al., 2014). Therefore, a large cup-disc ratio in a large ONH is not necessarily an indicator of glaucoma (Garway-Heath et al., 1998). Optic disc cupping is widely variable in the population where Jonas et al. (1988b) reported a range of 0.00-0.87 for the cup-disc ratio in a study of normal eyes. The loss of nerve fibres in other optic atrophies such as ischaemic optic neuropathy and toxic amblyopia causes the surface of the disc to subside and become pale, whereas the unique feature of glaucomatous atrophy is the deeply excavated appearance of the ONH (Quigley et al., 1982; Jonas et al., 2017).

At present there is no known cure for glaucoma, and vision loss from glaucoma cannot be recovered. Current treatments for glaucoma are based on lowering IOP to slow the rate of disease progression and preserve the patient's quality of vision (Gordon et al., 2002; Heijl et al., 2002; Kass et al., 2002; Leske et al., 2003). However, it has been reported that despite receiving glaucoma treatment and maintaining low IOP, some eyes continue to suffer glaucomatous damage, whereby glaucoma progression was defined by visual field (VF) loss or optic disc appearance (Schulzer et al., 1998; Heijl et al., 2002; Broman et al., 2008). In participants with a positive diagnosis of glaucoma, The Early Manifest Glaucoma Trial randomised participants to a treatment group and a non-treatment group (Heijl et al., 2002). After a median follow-up period of 6 years, glaucoma progression was less frequent in the treatment group (45%) than in the control group (62%) and occurred significantly later in treated participants. It is unknown why RGC death and vision loss can continue to occur in some cases despite the reduction of IOP.

I.2.1 Classification of glaucoma

Glaucoma can be classified as primary or secondary (Thylefors and Negrel, 1994; Weinreb and Khaw, 2004). In primary glaucoma, the disease is not caused by any other pathology, whereas secondary glaucoma can result from other pathology such as pigment dispersion or neovascular glaucoma whereby pigmentary cells or neovascularisation of the iris causes blockage of the trabecular meshwork and a subsequent rise in IOP. Typically, the raised IOP

in secondary glaucoma can be caused by, for example, trauma, cataract, uveitis, and such disorders that affect the structure of the anterior chamber angle and the drainage of the aqueous humour. Furthermore, glaucoma can be divided into categories according to whether the anterior chamber angle is open (i.e., open-angle glaucoma) or closed (i.e., angle-closure glaucoma). It is possible that both open-angle and angle-closure glaucoma can be primary diseases (Weinreb et al., 2014).

Primary open angle glaucoma (POAG) is the most common form of glaucoma and accounts for approximately 70% of glaucoma cases worldwide (Quigley and Broman, 2006; King, Azuara-Blanco and Tuulonen, 2013). The average age of glaucoma onset is 60, although the prevalence of glaucoma increases with age (Quigley, 2011; Schuster et al., 2020). POAG is a slow progressing disease, usually bilateral, although often asymmetrical in severity (Boland et al., 2008; Broman et al., 2008).

In primary angle closure glaucoma (PACG) the anterior chamber angle becomes blocked by the iris, thereby limiting outflow of aqueous humour via the trabecular meshwork (Congdon, Wang and Tielsch, 1992). In POAG and PACG, ONH and VF changes are similar, although, patients with PACG generally have a larger decline in visual function (Ang et al., 2004; Aung et al., 2004). Angle closure glaucoma accounts for roughly a quarter of glaucoma cases in the world, with higher prevalence in East Asian countries (Thylefors and Negrel, 1994; Friedman et al., 2004; Quigley and Broman, 2006; Day et al., 2012).

I.2.2 Intraocular pressure and aqueous humour drainage

Aqueous humour is a transparent, colourless fluid that fills the anterior segment of the eye. Aqueous humour provides nutrition to the avascular cornea and lens, and removal of metabolic waste products. Aqueous humour also generates an intraocular pressure (IOP), which is determined by the balance between aqueous production and drainage. The anterior chamber is encompassed on its front surface by the cornea, and posteriorly is formed by the iris and lens. The chamber depth is greatest axially and becomes progressively shallower peripherally. Aqueous humour is secreted by the ciliary epithelium into the posterior chamber, where it passes around the equator of the lens, flowing through the pupil and into the anterior chamber. It has been shown that the flow rate can vary with age, noting a 25%

decline from age 10 to 80 years (Brubaker, 1991). Temperature differences between the cornea and iris create convection currents which circulates the aqueous humour within the anterior chamber (Freddo, 2001).

Aqueous humour leaves the eye via two routes. The conventional pathway being through the trabecular meshwork into the canal of Schlemm, where it drains into episcleral veins. The uveoscleral pathway is through the ciliary muscle and into the supraciliary and suprachoroidal spaces. The vast majority (~90%) of aqueous outflow is accounted for by the trabecular route. In POAG, there has been reported to be an increased resistance to aqueous outflow via the trabecular meshwork, leading to an increase in IOP (Johnson, 2006); see Figure 1.4. With respect to glaucoma treatment, the mechanism of action for prostaglandin analogues is by increasing the uveoscleral outflow, not affecting aqueous inflow (Linden and Alm, 1999). These agents have proven to be effective ocular hypotensive drugs by increasing the proportion of aqueous leaving the eye via the uveoscleral route (Crowston and Weinreb, 2005; Garway-Heath et al., 2015).

The normal range of IOP is generally considered as 10-21 mmHg, with the mean IOP in 'normal' eyes estimated to be ~15-16mmHg, with a standard deviation of ~2.5mmHg (Morgan and Drance, 1975). In normal eyes, it has been reported that the distribution of IOP is skewed toward the high values, hence the upper limit of 'normal' is typically given as 21mmHg, a figure which is the mean IOP plus two standard deviations (Shiose, 1984). It is important to note that ocular hypertension describes cases where a raised IOP (usually above 21mmHg) exists, but in the absence of ONH damage or VF loss. Indeed, Tielsch et al. (1991) reported that only ~10% of patients with an IOP of 22mmHg or above had glaucoma. Additionally, approximately one in three patients with POAG did not present with raised IOP, and therefore it is reported that roughly a third of POAG is accounted for by normal tension glaucoma (Klein et al., 1992; Anderson, Feuer and Schiffman, 2008; King et al., 2013).

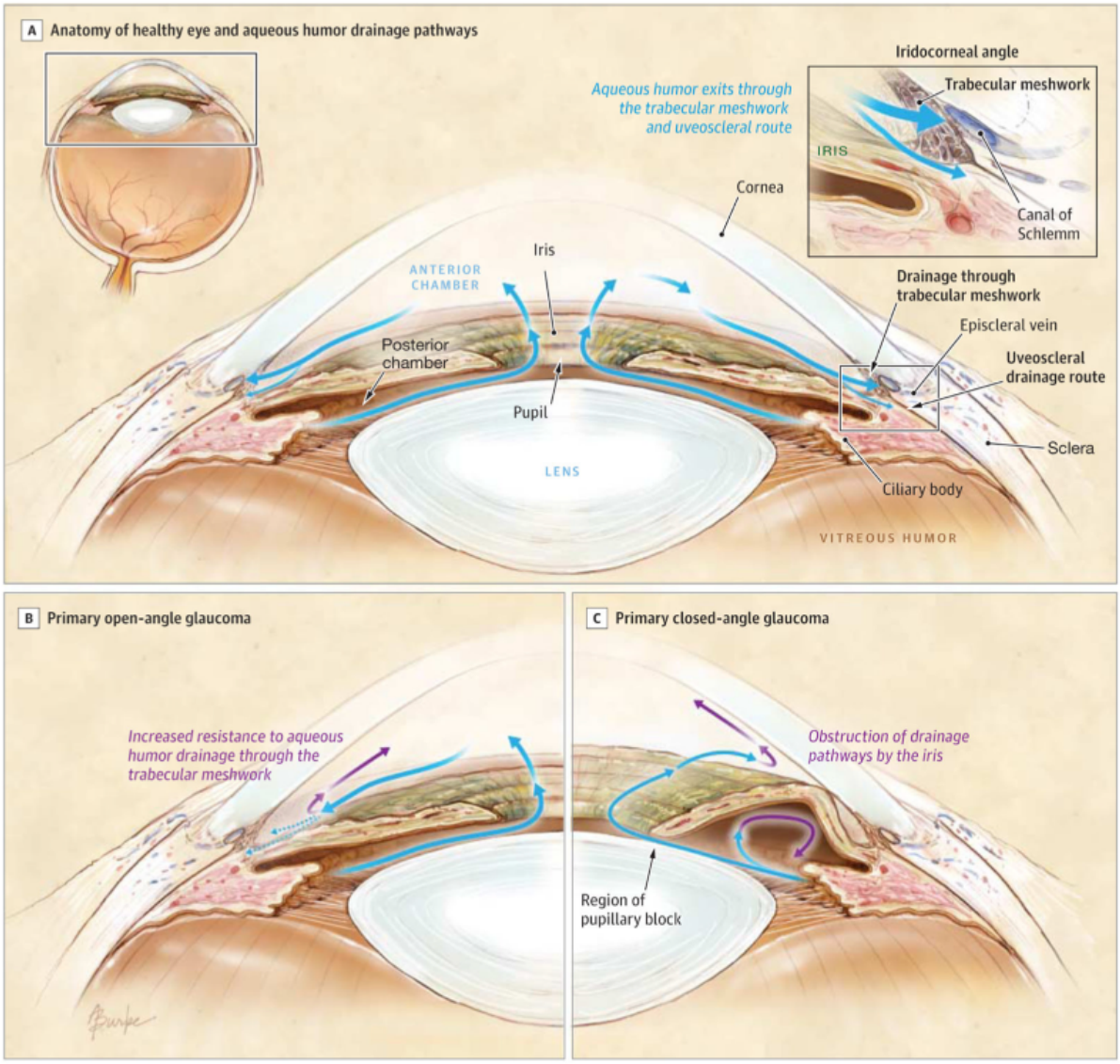

Figure 1.4: Drainage pathways of aqueous humour in healthy (a), primary open angle glaucoma (b), and primary closed-angle glaucoma (c). From Weinreb et al. (2014). Copyright permit shown in Appendix V.

Diurnal IOP variation refers to the fluctuations that occur throughout a daily cycle. There is a tendency for IOP to be higher in the morning and lower in the afternoon and evening (Syam, Mavrikakis and Liu, 2005). It is suggested that the characteristic afternoon/evening depression in IOP is more significant in males (Pointer, 1997). In a 'normal' eye, IOP could vary by up to 4mmHg throughout the day, although, in glaucoma, a larger change (≥ 5mmHg) may be observed (Fan et al., 2011; Liu et al., 2011).

I.2.3 Glaucomatous changes to the optic nerve head

In glaucoma, measurable VF defects do not develop at an early stage of disease, and VF defects do not often occur at homonymous locations within both VFs (Chauhan et al., 1989; Drance et al., 2001). Additionally, since POAG is a chronic, painless condition, patients with glaucoma are often not aware they have the disease until a relatively late stage (Khaw, Shah and Elkington, 2004; Weinreb and Khaw, 2004; Jonas et al., 2017). Therefore, the mainstay of glaucoma detection is the clinical examination of the ONH (Akagi et al., 2012; Patel, Sullivan-Mee and Harwerth, 2014b; Jung et al., 2015) and RNFL (Lee et al., 2010c; Akagi et al., 2013; Zhang et al., 2016). The characteristic appearance to the ONH seen in glaucoma disease involves progressive enlargement and deepening of the optic cup and thinning of the neuroretinal rim due to loss of RGC axons, which constitute the majority of the neuroretinal rim (Jonas, Fernandez and Sturmer, 1993; Reis et al., 2012c; Chauhan et al., 2013; Belghith et al., 2016b); see Figure 1.5.

A clinical assessment of an optic disc with respect to glaucoma disease involves evaluation of the neuroretinal rim regarding its thickness, symmetry, presence of notches, or indication of neuroretinal rim loss and enlargement of the optic cup (Foster et al., 2002; Gordon et al., 2002; Wang et al., 2010; Tatham et al., 2013; Fortune, 2019). Additionally, optic disc evaluation involves attention to vascular alterations including bayonetting of blood vessels or optic disc haemorrhages (Jonas et al., 1988c; Drance, 1989; Coleman, 1999; Kass et al., 2002; Keltner et al., 2006). Compression and backward bowing of the LC has been reported in human glaucoma (Quigley et al., 1983; Park, Jeon and Park, 2012a; Lee et al., 2017), and in monkey models of experimental glaucoma posterior migration of the LC has been reported (Yang et al., 2007b; Yang et al., 2011b). Therefore, due to this ONH compression and stretch imposed on the LC beams, capillaries contained within the prelamina and LC beams could rupture leading to an optic disc haemorrhage, which are associated with glaucoma disease progression (Drance, 1989; Gordon et al., 2002; Keltner et al., 2006; Chung et al., 2015).

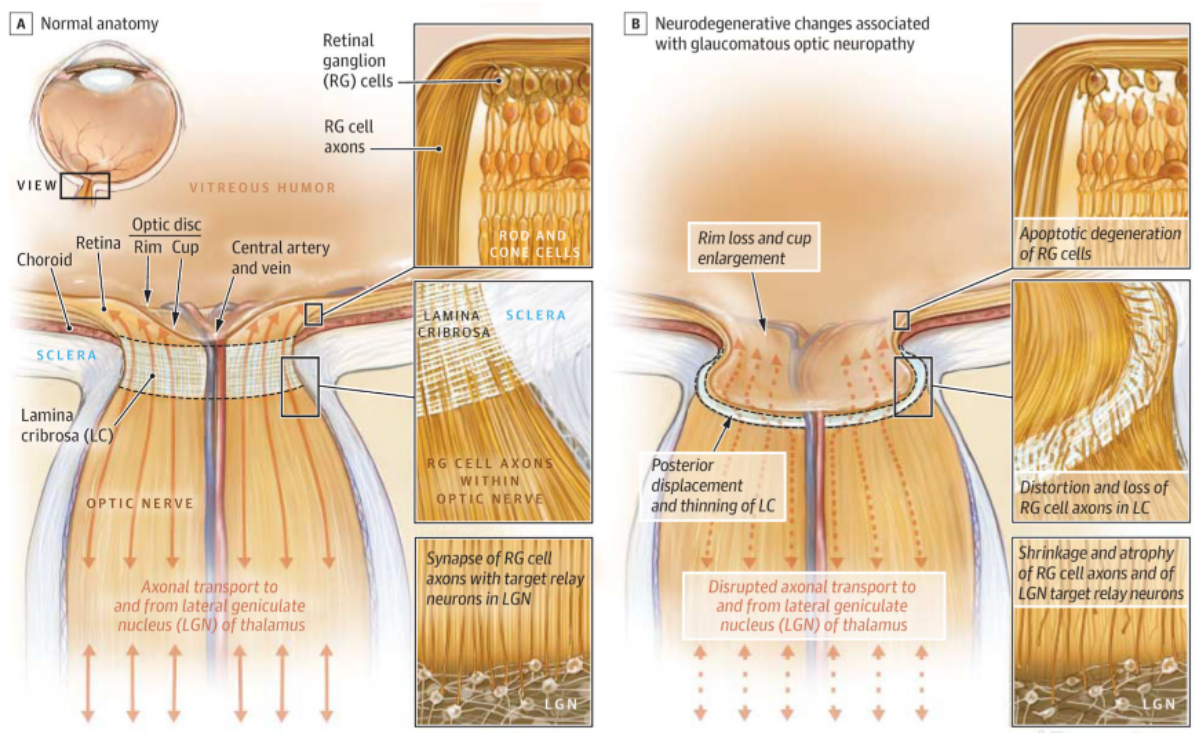

Figure 1.5: Schematic illustration of normal (left) and glaucomatous (right) ONH anatomy; including enlargement of the optic cup and loss of neuroretinal rim in glaucoma disease. Posterior displacement and deformation of the LC may induce RGC axonal damage and blockage of axoplasmic flow. From Weinreb et al. (2014). Copyright permit shown in Appendix V.

I.2.4 Glaucomatous visual field loss

In glaucoma, the death of RGCs and loss of RGC axons results in characteristic changes to the appearance of the ONH and NFL (Weinreb et al., 1998; Wu et al., 2015). Since a substantial number of RGC axons can be lost before VF defects are detected (Quigley et al., 1982; Kerrigan-Baumrind et al., 2000), evaluation of the ONH and RNFL are the most important aspects in glaucoma detection and can be identified through ophthalmoscopic inspection (Medeiros et al., 2009a; Weinreb et al., 2014; Kuang et al., 2015; Jonas et al., 2017). Visual field examination is an important consideration in glaucoma evaluation, which can confirm diagnosis, and is vital in the follow-up of glaucomatous ONH damage and vision loss (Drance et al., 2001; Broman et al., 2008; Parrish et al., 2009). However, it has been reported that as many as 30% to 50% of RGCs may be lost before VF defects are detected by standard VF testing (Quigley et al., 1981; Quigley et al., 1982; Harwerth and Quigley, 2006; Harwerth et al., 2010). Due to the slow progressive nature of glaucoma, using perimetry alone, it could take several years to identify glaucomatous disease as ~35% of RGC axons can be lost before

detection of a VF defect (Kerrigan-Baumrind et al., 2000). Pederson (1980) reported that glaucomatous expansion of the optic cup can typically precede VF loss by several years. Following evaluation of fundus photographs, Sommer et al. (1991a) stated that at the time VF loss was first detected, 60% of eyes already had NFL defects 6 years prior to VF loss. Indeed, Kuang et al. (2015) suggest that OCT evaluation of RNFL thickness could detect NFL damage in approximately a third of glaucomatous eyes up to 5 years before the appearance of a VF defect. However, it is important to note that in some instances the first indication of glaucoma is VF loss. Ohnell et al. (2016) reported that among glaucoma participants, in the fellow eyes with normal visual fields, progression was detected as frequently in the VF as in the optic disc. Indeed, in eyes with manifest glaucoma, VF progression was detected first more than four times as often as progression detected in the optic disc. Therefore, this indicates that the development and progression of glaucoma is largely variable (Heijl et al., 2013b; Ohnell et al., 2016), and clinical evaluation should not focus solely on structural or functional measures.

Loss of RGCs causes a progressive decline in VF function. Early glaucomatous VF defects usually begin in the mid-periphery as an isolated scotoma between 5° and 25° from fixation. Progression may occur in a centripetal manner within the arcuate NFL area (as described in section I.1) to touch the horizontal raphe nasal to fixation, then join to the blind spot until there remains only a central or peripheral island of vision; with the central 5° and temporal VF usually preserved until a late stage in the disease (Quigley et al., 1981; West et al., 2002; Musch et al., 2009; Weinreb et al., 2014); see Figure 1.6.

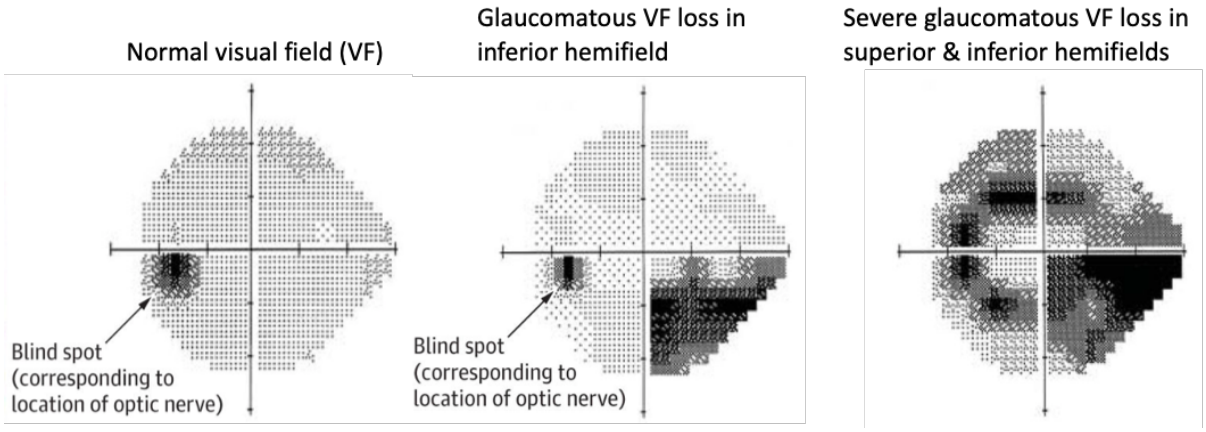

Figure 1.6: Appearance of normal left eye visual field plot (left); glaucomatous visual field loss in inferior hemifield (middle); severe glaucoma and associated visual field loss in superior and inferior hemifields (right). From Weinreb et al. (2014). Copyright permit shown in Appendix V.

A disadvantage of VF testing is the relatively high inter-visit variability of examinations, with an increase in variability shown with increasing VF damage (Heijl, Lindgren and Lindgren, 1989; Chauhan and Johnson, 1999). It is suggested that at least three VF examinations may be necessary to reliably detect deterioration in VF function (Heijl, Lindgren and Olsson, 1989; Keltner et al., 2006). Indeed, Keltner et al. (2000) reported that 86% of patients with a VF defect on initial testing, were not confirmed when VF testing was repeated; indicating the need for additional techniques for monitoring glaucoma disease progression.

I.2.5 Retinal ganglion cell and axonal damage

In glaucoma, regardless of the mechanism for neuropathy, the final pathway is RGC and axonal death, resulting in irreversible vision loss (McKinnon, 1997; Quigley, 1999). Neuronal cell death appears to be specific to RGCs, with the remainder of the inner retina and outer retina remaining largely unaffected (Osborne et al., 1999; Osborne et al., 2001). This RGC death has been shown to occur by apoptosis in human and experimental glaucoma (Kerrigan et al., 1997; Quigley, 1999). Optic nerve fibre size was examined in monkeys with experimentally induced glaucoma. It was found that all sizes of fibres were affected, but fibres with diameter larger than mean showed more rapid atrophy. The superior and inferior peripheral portions of the nerve contained a high proportion of large diameter nerve fibres and these areas were preferentially affected. Large diameter fibres were also lost in other areas of the nerve, which suggests an increased vulnerability to pressure related damage (Quigley et al., 1987). Another *ex vivo* study demonstrated preferential loss of larger nerve fibres in human eyes; whereby optic nerve fibres larger than the mean diameter were damaged more quickly than smaller fibres, although no fibre size was spared completely at any stage of atrophy. The superior and inferior poles of the nerve were the most damaged portions, and displayed an hourglass distribution, although large fibres were again lost throughout the nerve (Quigley, Dunkelberger and Green, 1988).

In glaucomatous eyes, a selective loss of RGCs with a larger soma diameter than the mean in non-foveal areas was observed, and RGC loss was associated with VF loss (Quigley et al., 1989). This corresponds with the observation of loss of large nerve fibres within the optic nerve (Quigley et al., 1988). However, the observation that RGCs with a large cell soma and

axon (parasol) cells are selectively damaged in early glaucoma (Quigley et al., 1989; Kerrigan-Baumrind et al., 2000) has been questioned, where it is suggested that the smaller (midget) cells also sustain early glaucomatous damage (Morgan, 1994). It is suggested that if RGCs shrink prior to RGC death, the result would be an apparent loss of RGCs with soma size larger than the mean RGC soma size (Morgan, 2002).

Apart from RGC death, there have been changes noted in RGC soma size in experimental glaucoma. An overall hypertrophy of all RGC types has been reported in rats after IOP elevation by episcleral vein cauterization (Ahmed, Chaudhary and Sharma, 2001). An increase in RGC soma size was also observed following optic nerve crush and axotomy (Moore and Thanos, 1996; Rousseau and Sabel, 2001). It is proposed that the increase in RGC soma size is likely to be a response to the space made available by the death of RGCs (Ahmed et al., 2001). Additionally, there have been changes observed in cell soma size following ocular hypertension in monkey eyes which suggests that both parasol and midget retinal ganglion cells undergo shrinkage prior to cell death (Weber, Kaufman and Hubbard, 1998; Morgan, Uchida and Caprioli, 2000). However, RGC shrinkage has not been documented in human RGC bodies (Quigley, 1999). Indeed, in post-mortem advanced glaucoma human eyes, the remaining RGCs had cell bodies which were normal in size, although had irregular silhouettes or swellings (Pavlidis et al., 2003).

During glaucoma disease, as RGC axons are lost there is thinning of the NFL in both the macula (Unterlauft et al., 2020) and peripapillary (Yang et al., 2020). The peripapillary NFL thinning can be diffuse or localised, with localised loss characterised by slit defects within the NFL which become larger with glaucoma progression (Pieroth et al., 1999). In glaucoma, thinning of the NFL around the optic disc (peripapillary) is associated with loss of the neuroretinal rim and corresponds to VF defects (Pieroth et al., 1999), and *in vivo* NFL thickness measures have been shown to discriminate between glaucomatous and healthy eyes (Weinreb et al., 1998; Anton et al., 2007).

Sommer et al. (1991a) reported that in glaucoma patients with VF loss, 60% of patients already had NFL defects 6 years before VF loss had occurred. Therefore, it is suggested that NFL thickness provides additive information to ONH parameters with respect to glaucoma

disease and therefore should be used alongside ONH evaluation (DeLeon-Ortega et al., 2006; Sakata et al., 2009), and for screening purposes for the early detection of glaucoma disease (Parikh et al., 2007; Blumberg et al., 2016).

I.3 Theories of glaucomatous disease

The exact mechanism for the initiation of RGC dysfunction in POAG remains unknown. The cause of the disease seems to be complex and multifactorial. A number of explanatory theories have been proposed and can be grouped into two broad categories; mechanical and vasogenic (Fechtner and Weinreb, 1994; Flammer and Mozaffarieh, 2007; Weinreb et al., 2014), which are discussed further below. However, since no single mechanism can explain entirely the variations in susceptibility to damage, and variable patterns of damage seen in glaucoma disease (Fechtner and Weinreb, 1994), there are likely interactions between theories that have been proposed and reviewed (Burgoyne et al., 2005; Burgoyne, 2011; Downs et al., 2011; Downs, 2015); outlined in Figure 1.7.

I.3.1 Mechanical theory

The mechanical theory supports damage to RGC axons within the ONH as a result of IOP-induced compression and deformation of the lamina cribrosa (LC), leading to axonal transport blockage (Quigley, 1987). It is proposed that within the tough corneoscleral envelope of the eye, the LC represents a weak point and is therefore vulnerable to the effects of raised IOP (Downs, Roberts and Burgoyne, 2008; Downs and Girkin, 2017). Within the superior and inferior poles of the LC there is typically less connective tissue and larger LC pores than the nasal-temporal regions (Radius, 1981; Dandona et al., 1990). Variations in proportions of supporting connective tissue content can lead to weakening and distortion at the upper and lower ONH poles hence increasing the risk of mechanical damage to RGC axons (Quigley et al., 1981; Quigley et al., 1983). It is suggested that IOP-related deformation of the LC and compression of the cribriform plates results in shearing, constriction, or extension of the RGC axons within the LC, resulting in direct mechanical damage to the axons and disruption of axonal transport (Minckler, 1981; Quigley et al., 1981; Radius, 1983).

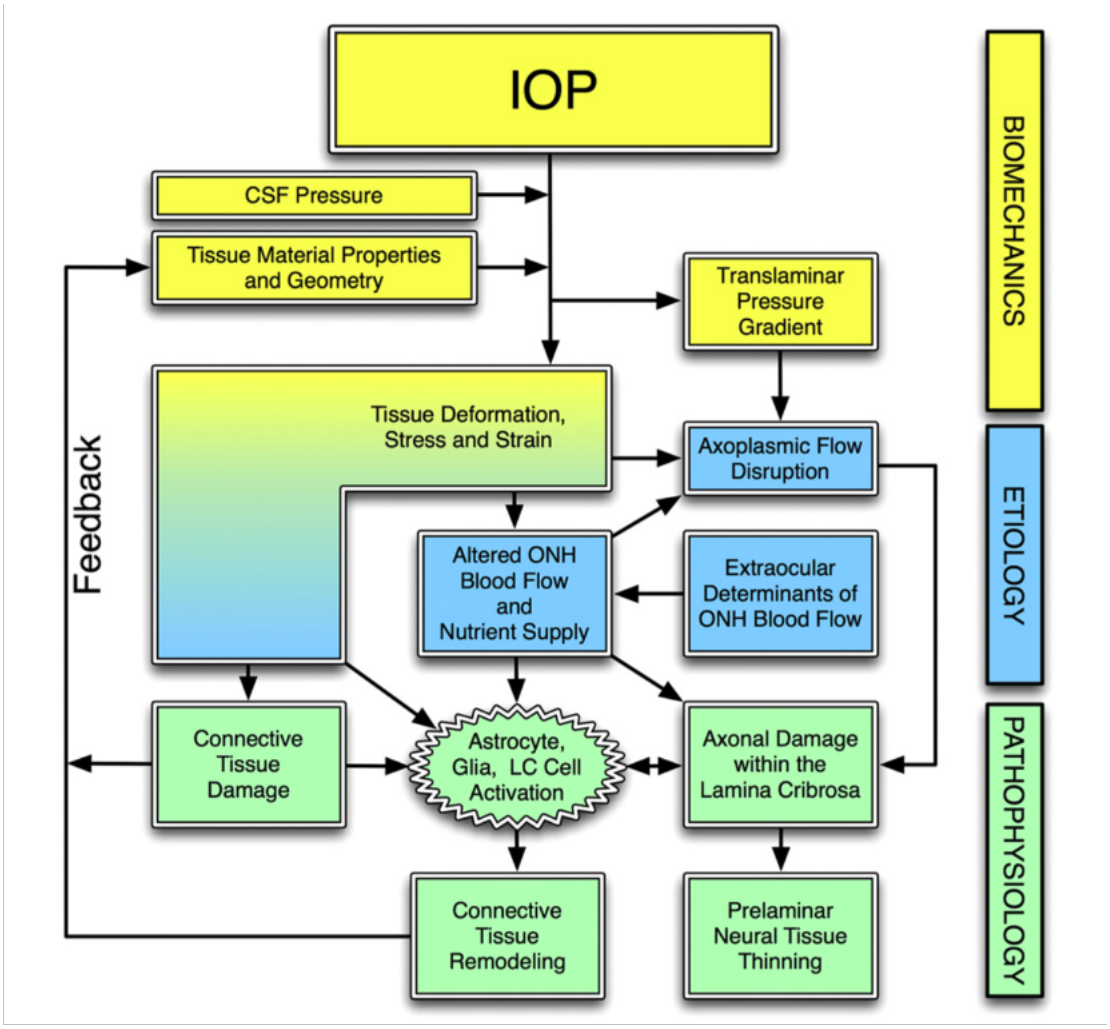

Figure 1.7: Schematic diagram illustrating the interactions between proposed mechanisms of glaucomatous disease which may result in RGC death in glaucoma. From Downs et al. (2011). Copyright permit shown in Appendix V.

In glaucoma, the excavated appearance of the ONH is also seen in a proportion of patients with IOP recorded within the normal range, i.e., normal tension glaucoma. In these cases, it is proposed that the LC connective tissue may display abnormalities that accounts for its susceptibility to deformation and subsequent axonal damage (Quigley et al., 1983). Quigley, Dorman-Pease and Brown (1991b) reported a lower degree of collagen density in the inferior and inferior-nasal regions of the LC. This aligns with that reported by Winkler et al. (2010) where low LC collagen density was reported in the inferior-temporal region of the ONH. It is suggested that these regions are more vulnerable to LC focal damage where the inferior LC is a common site for focal LC defects (Kiumehr et al., 2012). With the loss of anterior LC beams, focal LC defects correspond with RGC axon loss and VF defects, and can lead to deep excavations of the LC, i.e., acquired pits of the optic nerve (APONs) at the vertical poles of the

ONH (Quigley and Addicks, 1981; Faridi et al., 2014). Furthermore, in the *ex vivo* LC, Jones et al. (2015) reported an increased degree of LC connective tissue alignment in glaucoma eyes in the inferior-temporal ONH quadrant. Additionally, previous studies have reported alterations in LC connective tissue in glaucoma disease (Hernandez and Pena, 1997; Downs et al., 2011).

I.3.2 Vasogenic theory

The existence of normal tension glaucoma cannot be explained by an IOP-related theory alone. The vasogenic theory for glaucomatous optic neuropathy proposes that the blood supply to the ONH is disturbed, and can be either associated with, or independent of raised IOP (Flammer and Orgul, 1998). An impaired blood supply within the ONH can alter supplies of oxygen and nutrients, and removal of waste products (Prünte, 1998; Flammer et al., 2002). It is proposed that raised IOP may impair the quality of blood supply to the ONH, leading to hypoxia and reduced nutrition to optic nerve axons, ultimately leading to RGC death (Kaiser et al., 1997; Osborne et al., 2001). However, ONH blood supply may also be influenced by factors which are independent of IOP such as reduced arterial blood pressure, local vasospasm, increased blood viscosity or vascular dysregulation (Hayreh, 2001; Flammer and Mozaffarieh, 2007).

Gasser and Flammer (1991) reported that blood flow was significantly reduced in other parts of the body in glaucoma participants, particularly normal tension glaucoma, compared to controls. Therefore, haemodynamic alterations have been proposed as an important factor in the development of glaucomatous optic neuropathy (Flammer and Mozaffarieh, 2007). It is reported that RGCs have probably more mitochondria than any other neurone in the central nervous system (Osborne and del Olmo-Aguado, 2013). In ischaemia, it is proposed that the lack of blood supply effects RGC mitochondria causing oxidative stress and results in RGC loss (Osborne and del Olmo-Aguado, 2013). Dysfunction of RGC mitochondria causes increased production of reactive oxygen species (ROS) and can result in oxidative stress. It is not fully understood the mechanism by which oxidative stress can induce RGC death but may be related to direct neurotoxic effects from ROS, or indirect damage via oxidative stress resulting in the dysfunction of glial cells (Chrysostomou et al., 2013). Raised IOP and ischaemia can induce activation of ONH astrocytes which can release neurotoxins detrimental to RGCs and

alter connective tissues within the human ONH (Hernandez and Pena, 1997; Hernandez, Miao and Lukas, 2008). Therefore, mechanisms of glaucoma disease are considered to be interlinked and complicated (Burgoyne et al., 2005; Flammer and Mozaffarieh, 2007; Downs et al., 2008).

I.4 Lamina cribrosa in glaucoma

In the normal eye, the anterior surface of the LC is seen as a relatively shallow depression in the centre of the optic disc, whereas in glaucoma there is compression and backward bowing of the LC (Quigley et al., 1981; Quigley et al., 1983; Varma, Quigley and Pease, 1992a). The latter is more pronounced at the superior and inferior poles of the ONH (Quigley et al., 1983), consistent (as mentioned above) with the superior and inferior regions containing less connective tissue, compared to the nasal-temporal regions, and being more prone to deformation and structural alteration (Quigley and Addicks, 1981; Radius, 1981). With advancement of glaucoma disease, the posterior displacement of the LC in the superior and inferior regions changes from a ‘u’ shape to form a ‘w’ shape in the vertical meridian of the ONH (Quigley et al., 1983; Quigley, 2011); see Figure 1.8. The posterior migration of the LC contributes to the deepening of the optic cup, and thereby an increase in optic disc cupping seen in glaucoma disease (Radius, 1987). This structural deformation of the LC has been suggested to contribute to optic neuropathy by mechanical damage imposed on the RGC axons (i.e. compression, shearing, extension), resulting in a loss of prelamina tissue, and impeding axonal transport within the optic nerve fibres, resulting in apoptosis of RGCs (Quigley and Anderson, 1976; Quigley et al., 2000; Nuyen, Mansouri and Weinreb, 2012).

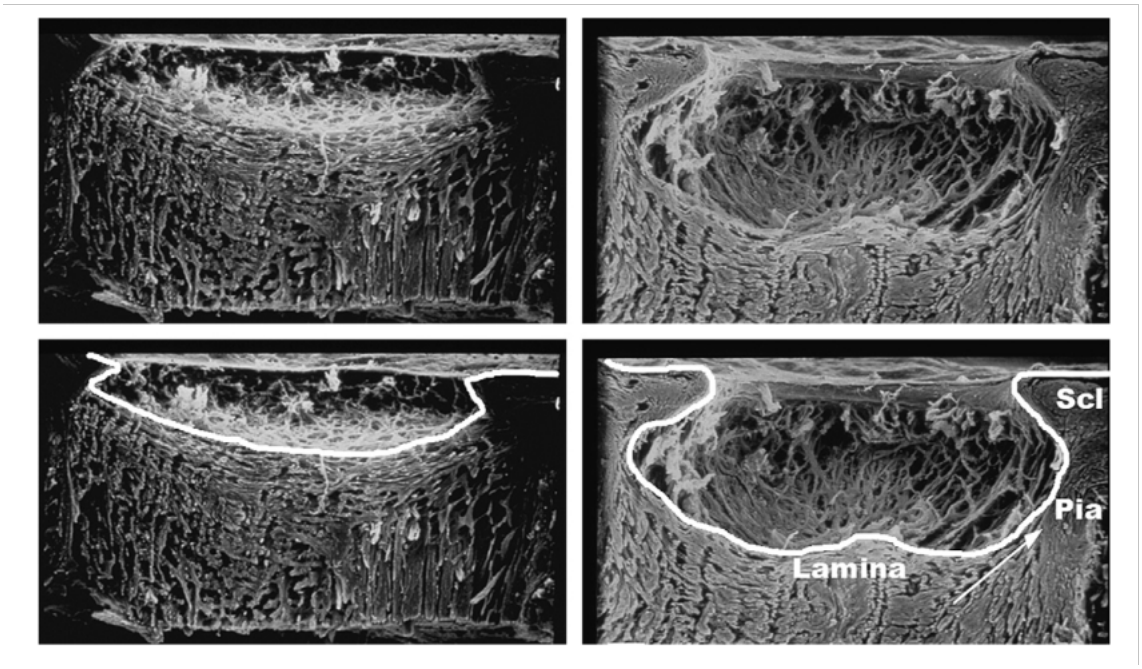

Figure 1.8: Scanning electron microscopy images from healthy (left) and advanced glaucoma (right) human ONHs. In glaucoma, the LC forms a 'w' shape demonstrating the posterior displacement and excavation beneath the scleral canal rim into the pia mater (arrow). Scl = sclera. From Downs et al. (2011). Copyright permit shown in Appendix V.

In vivo studies have reported the LC to be significantly thinner in early stage glaucoma patients than compared with control participants (Kwun, Han and Kee, 2015; Kim et al., 2020), which is consistent with that reported by *ex vivo* studies (Jonas, Hayreh and Tao, 2009; Ren et al., 2009; Jonas et al., 2012). Indeed, Park et al. (2012a) reported a central LC thickness of around 350µm in control participants, although thinner in POAG (~220µm) and normal tension glaucoma (~175µm). Other *in vivo* studies have reported thicker LCs in ocular hypertension compared to glaucoma participants (Kwun et al., 2015; Kim et al., 2020). This is consistent that reported by Inoue et al. (2009) where the average LC thickness in ocular hypertension was reported to be 245µm, 200µm in early glaucoma, and decreased to 130µm in advanced glaucoma. In *ex vivo* human eyes, Quigley et al. (1983) reported LC thickness in control eyes to be approximately 240µm, which decreased to 140µm in glaucoma participants. Such differences in measurements reported by *in vivo* and *ex vivo* studies could be related to tissue preparation techniques used in histology causing tissue shrinkage.

In glaucoma, elevated IOP has been shown to be associated with structural thinning (Yan et al., 1994; Jonas, Berenshtein and Holbach, 2003; Park et al., 2012a) and posterior

displacement of the LC (Wu et al., 2015; Lee et al., 2017), and alterations to LC pore morphological parameters (Akagi et al., 2012; Tian, Li and Song, 2017; Wang et al., 2018). This deformation of the LC pores can impede axoplasmic flow of the RGC axons passing through the pores, and therefore disrupt the transport of trophic factors important for RGC survival (Minckler et al., 1977; Quigley et al., 2000). Changes in LC pore shape and size has also been correlated with the severity and progression of glaucoma due to LC connective tissue stretch caused by raised IOP in glaucoma (Tezel, Trinkaus and Wax, 2004). In normal eyes, or glaucoma patients with minimal VF damage, the anterior LC surface pores are small and roughly round, whereas with increasing loss of visual function the pores become more elongated and oval in shape (Susanna, 1983; Miller and Quigley, 1988; Tezel et al., 2004). In healthy eyes, *in vivo* characterisation of the LC pores showed larger pores in the superior and inferior quadrants compared to temporal (Nadler et al., 2014). The nasal quadrant was excluded due to poor visualisation within the OCT image datasets. In another *in vivo* study, Wang et al. (2013) reported a significant decrease in pore diameter in glaucoma eyes, although LC beam thickness, and beam thickness to pore diameter ratio significantly increased. Such micro-architecture changes within the glaucomatous LC reflects LC beam remodelling and RGC axon loss, leading to a reduction in pore size and increased pore size variability (Wang et al., 2013). It is reported that LC pore morphologic features may continue to change in glaucoma, even when the appearance of the neuroretinal rim is clinically stable, and such LC alterations are probably associated with chronic connective tissue remodelling seen in the glaucomatous ONH (Hernandez, 2000; Tezel et al., 2004).

Within the ONH, non-neuronal cells also show evidence of disruption and altered function (Hernandez, Andrzejewska and Neufeld, 1990). The predominant glial cell within the ONH are astrocytes and these are essential for ganglion cell health. They are metabolically very active, vulnerable to physiological changes and are often the first cell to respond to injury (Hernandez, 2000; Hernandez et al., 2008). In glaucoma, astrocytes lining the LC pores are reduced in size and migrate into the nerve fibre bundles (Hernandez and Pena, 1997). Astrocytes can become transformed into a ‘reactive’ phenotype that release potential neurotoxins (Varela and Hernandez, 1997). During glaucomatous neurodegeneration it was suggested that astrocyte activation leads to an upregulation of extracellular matrix synthesis (Hernandez, 2000). In POAG, the LC extracellular matrix is altered, leading to a remodelled

and fibrotic tissue that is quantitatively different to that within the normal ONH (Hernandez et al., 1990; Hernandez and Pena, 1997; Burgoyne et al., 2005). Elevated IOP leads to deformation of the LC (Quigley et al., 1983; Jonas et al., 2003), including deposition of extracellular matrix molecules such as collagen and fibronectin (Hernandez et al., 1990), reviewed by (Hernandez, 2000; Wallace and O'Brien, 2016). As opposed to star-shaped astrocytes, LC cells are broad, flat, and polygonal (Hernandez, Igoe and Neufeld, 1988). These LC cells are localised to the LC between or within the cribriform plates, whereas astrocytes are found throughout the ONH and line the LC pores separating the unmyelinated RGC axons from the cribriform plates (Hernandez et al., 1988; Hernandez, 2000). Following mechanical stretch of LC cells *in vitro*, Kirwan et al. (2005) showed an increased production of extracellular matrix; suggesting LC cells play an important role in extracellular matrix remodelling. Additionally, the LC has been shown to undergo fibrosis and mechanical failure in POAG (Hernandez et al., 1990). In later glaucoma disease stages in human eyes the LC undergoes collapse of the LC plates, leading to a thin fibrotic connective tissue structure/scar (Jonas et al., 2003), where there is extracellular matrix remodelling (Hernandez et al., 1990; Burgoyne, 2011) and increased deposition of collagen and elastin (Hernandez and Pena, 1997; Pena et al., 1998). Therefore, LC cell activation and astrocyte dysfunction are likely to play an important role in RGC axonal damage and extracellular matrix changes seen within the ONH in glaucoma disease (Hernandez and Pena, 1997; Varela and Hernandez, 1997; Hernandez et al., 2008). Structural changes within the LC likely play an important role in neuronal death in glaucoma (Quigley et al., 1981; Quigley, 1999), hence visualisation of the LC *in vivo* holds great potential for glaucoma detection and/or staging of disease.

I.5 Clinical detection of glaucoma

In the UK, glaucoma detection currently depends largely on community-based optometrists, accounting for over 90% of POAG referrals to secondary hospital-based eye care (Bowling, Chen and Salmon, 2005). However, since there is no single perfect reference standard for glaucoma detection, early diagnosis of glaucoma can remain difficult (Weinreb et al., 2014). Currently, clinical diagnosis and follow-up of glaucoma disease is fundamentally based on the appearance of the ONH, IOP measurement, and VF examination (Coleman, 1999; Anderson, 2006; Weinreb et al., 2014). However, each of these three aspects have drawbacks. In

assessment of the ONH and NFL, clinical glaucoma indicators such as an increase in cup-disc ratio or reduction in NFL thickness indicates that RGC axon loss has already taken place (Gordon et al., 2002; Boland and Quigley, 2011; Yu et al., 2016). Further to this, there is reported to be disagreement amongst eye specialists in terms of ONH evaluation to suggest glaucomatous structural damage or disease progression (Azuara-Blanco et al., 2003; Parrish et al., 2005; Breusegem et al., 2011; Rossetto et al., 2017; Hong et al., 2018). Therefore, detection of subtle glaucomatous changes to the optic disc (i.e., suggesting disease onset or progression) is challenging and may go unnoticed by a given observer.

Tielsch et al. (1991) reported that only ~10% of patients with IOP greater than 21mmHg had glaucoma. Additionally, roughly a third of glaucoma patients do not present with raised IOP (Klein et al., 1992; King et al., 2013). Furthermore, a considerable amount of RGCs may be lost before glaucomatous VF defects are detected by perimetry (Quigley et al., 1982; Kerrigan-Baumrind et al., 2000; Harwerth and Quigley, 2006). Therefore, it is suggested that current screening mechanisms for glaucoma are limited (Tielsch et al., 1991). It is proposed that *in vivo* evaluation of the ONH and in particular the LC may provide further insights into structural change seen in glaucoma disease, and aid in glaucoma diagnosis and management (Inoue et al., 2009; Li et al., 2010; Nuyen et al., 2012; Wu et al., 2015). Optical coherence tomography provides us with a tool to image ONH structure *in vivo*.

I.6 Optical Coherence Tomography

Optical coherence tomography (OCT) is a non-invasive interferometric imaging technique that provides high-resolution cross-sectional images of the subsurface microstructure of biological tissue (Tearney et al., 1996; Schmitt, 1999). Since its introduction in 1991 (Huang et al., 1991), OCT has rapidly evolved and has been extensively adopted for the detection of glaucoma and retinal disease (Swanson et al., 1993; Hee et al., 1995; Schuman et al., 1995a). The past decade has seen OCT develop into one of the most important ancillary tests in optometric practice (Adhi and Duker, 2013). With an axial resolution of ~5-8µm, OCT provides an *in vivo* 'optical biopsy' of the retina and ONH (Schmitt, 1999; Fujimoto et al., 2000; Adhi and Duker, 2013).

Fundamentally, OCT imaging is analogous to ultrasound, although OCT measures back-scattering of infrared light, rather than sound (Fujimoto et al., 2000). Conversely to ultrasound, OCT has an advantage in that it does not require direct contact with the sample (Fujimoto et al., 2000; Li et al., 2000). However, due to the fact light is absorbed or scattered by most biological tissues, OCT imaging is restricted to structures that are optically accessible, and therefore is widely used for ocular imaging, with an imaging depth of typically ~1-2mm (Povazay et al., 2003; Unterhuber et al., 2005; Sarunic, Asrani and Izatt, 2008).

I.6.1 Principles of OCT

OCT imaging uses a broadband light source to illuminate an interferometer. The illuminating light source is split by a beam splitter into two beams and serves the reference arm and the sample arm. The sample beam is focused through the scanning optics of the system and via an objective lens towards the sample to be imaged. A reference mirror is used to reflect the reference beam back through the optical system. Light is reflected back from the sample from structural boundaries within the sample, and the light is scattered differently by tissues with different optical properties. Backscattered light from the sample interferes (recombines) with light from the reference arm. If the two path lengths are the same, the beams are 'in phase' and constructive interference occurs, whereby this interference is measured by an interferometer (Fujimoto et al., 2000; Izatt and Choma, 2008). The point where there is no delay between the two beams is known as the 'zero delay' and is where the maximum OCT signal is detected. If the reflected light within the two beams is not in phase, little or no signal is detected. This allows an image of reflected light from the sample to be created, which, at a single point is called an a-scan (Fercher et al., 1993; Schmitt, 1999; Sull et al., 2008). Lateral scanning of a sample by the OCT device generates individual a-scans, which are combined to form b-scans (i.e., a line of a-scans); see Figure 1.9. Multiple b-scans can be combined to form a 3D volumetric OCT image, also known as c-scans (Izatt and Choma, 2008; Schuman, 2008).

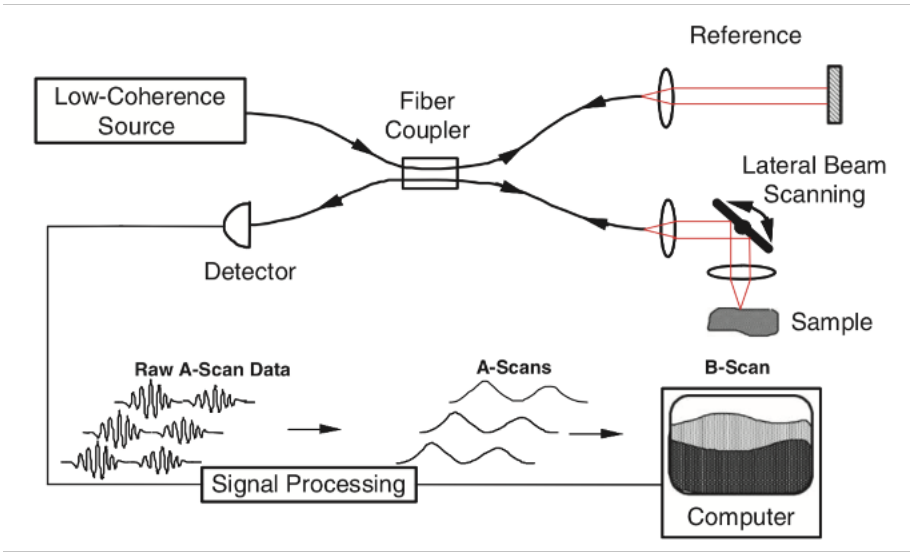

Figure 1.9: Schematic illustration of a generic OCT system. The low coherence light source is split into a reference and sample arm. Back reflected light from the sample is recombined with the reference arm and recorded by the detector. Signal processing forms a-scans, which are combined to form b-scans. From Izatt and Choma (2008). Copyright permit shown in Appendix V.

The spectral bandwidth of the light source dictates the axial resolution, and the centre wavelength of the light source determines the depth of tissue penetration into a sample. Lateral resolution is determined by the size of the focused transverse spot of the optical beam (Hitzenberger et al., 2003; Schuman, 2008). Commercial OCT systems used in ophthalmic imaging traditionally use a centre wavelength of ~840nm with a bandwidth of ~25nm, resulting in ~10µm axial resolution (Gabriele et al., 2010; Sull et al., 2010), although, there are now commercial OCT devices with long centre wavelength. Light sources with a broader spectral bandwidth have been used in OCT systems to improve axial resolution (Drexler et al., 1999; Drexler, 2004; Leitgeb et al., 2004).

I.6.2 Time Domain OCT

There are two type of OCT imaging; time domain OCT (TD-OCT), and Fourier domain OCT (FD-OCT), and both operate in different ways. Initially, OCT was developed as TD-OCT, which is the simplest form of OCT (Huang et al., 1991; Izatt et al., 1994; Schuman, 2008). In TD-OCT, image resolution is produced as a function of time, where a reflectivity profile (a-scan) is produced by adjusting the reference mirror to measure the reflectivity from various depths within a sample (Choma et al., 2003; Han and Jaffe, 2009). The need to oscillate the reference

mirror back and forth results in slow image acquisition (~400 a-scans per second), so that the resolution and clarity of the image is limited by the mechanical movement of the mirror (Drexler, 2004; Mumcuoglu et al., 2008). Images acquired using TD-OCT can be prone to motion artefacts related to eye movements due to the limited scan speed in TD-OCT (Gabriele et al., 2010). Therefore, early commercial TD-OCT devices such as the Stratus OCT (Carl Zeiss Meditec) are now considered obsolete and have been superseded by FD-OCT.

I.6.3 Fourier Domain OCT

In FD-OCT, there is no requirement for mechanical movement of the reference mirror. There are two types of FD-OCT: spectral domain OCT (SD-OCT) and swept source OCT (SS-OCT). Spectral domain OCT operates detection of the light echoes simultaneously by measuring the interference spectrum using an interferometer with a high-speed spectrometer, whereas TD-OCT uses a photodetector (Adhi and Duker, 2013). Backscattered light from the sample is recombined with reflected light from a stationary reference arm and collected by the spectrometer. Spectral discrimination is achieved using a dispersive spectrometer, and Fourier transform of the interference spectrum obtains the depth-reflectivity profile, i.e., the a-scan (Wojtkowski et al., 2002; Wojtkowski et al., 2004). In FD-OCT, as reflected light is measured along the entire depth of the sample (i.e., along the a-scan) simultaneously, rather than sequentially, this negates the requirement of a moving reference mirror. This results in a significantly faster a-scan acquisition rate (by ~50 times) and improved axial resolution compared to TD-OCT (Leitgeb, Hitzenberger and Fercher, 2003; Povazay et al., 2009). This high scan speed is appropriate in the reduction of image artefacts caused by small eye movements, and aids in examination of the ONH and retina in high spatial resolution (Wojtkowski et al., 2005).

The most recent development in OCT is swept source OCT (SS-OCT) which uses a photodiode detector and rapidly tunes a light source through a broad bandwidth to acquire the spectral data from the sample. As opposed to SD-OCT, in SS-OCT the spectral components are time encoded rather than spatially encoded (i.e., via use of a dispersive spectrometer in SD-OCT). In SS-OCT, the use of the photodiode detector allows for a higher scan speed and reduction in image acquisition time, and less attenuation of light. Swept source OCT is able to achieve the highest imaging speed of any commercially available OCT. For example, the DRI OCT Triton

(Topcon, Japan) uses a scan rate of 100,000 a-scans per second, whereas previous SD-OCT systems such as the Topcon 3D OCT-2000 operates at 50,000 a-scans per second. Therefore, long wavelength SS-OCT allows for improved visualisation of deeper ocular structures such as the lamina cribrosa (Nuyen et al., 2012; Omodaka et al., 2015) and the choroid (Agawa et al., 2011; Jirarattanasopa et al., 2012). A major advantage of the SS-OCT is the high imaging speed which helps to reduce patient eye movement artefacts. Additionally, the use of an invisible light source is less distracting for patients compared to the visible light used in SD-OCT, noting that photoreceptors are not sensitive to light >900nm (Srinivasan et al., 2006).

I.6.4 OCT light source wavelength

Several commercial SD-OCT devices utilise a light source with a central wavelength of ~830nm, although, OCT devices have been developed that use a longer central wavelength of ~1050nm. OCT systems with a longer wavelength provide enhanced visualisation of deeper ocular structures beneath the RPE (Agawa et al., 2011). In the healthy eye, if the RPE is intact there is limited visualisation of the choroid using OCT systems with central wavelength of ~800-860nm. Within the RPE there is a high concentration of melanin pigment, which readily absorbs and scatters light (Hammer et al., 1995). However, the light absorption properties of melanin are strongly wavelength dependent. In the 600-1200nm range, it has been reported that there is less scattering and absorption with longer wavelengths of light (Povazay et al., 2003; Unterhuber et al., 2005). Therefore, long wavelength OCT allows for improved visualisation of deeper ocular structures such as the LC and choroid. Additionally, it is reported that in long wavelength OCT, there is less image degradation due to less light scatter caused by intraocular media opacities such as cataracts and corneal haze (Povazay et al., 2007a; Drexler and Fujimoto, 2008). This has important clinical implications as this allows for OCT images to be acquired in patients with age-related ocular changes such as cataract, as age is a risk factor for glaucoma.

However, the vitreous within the eye is composed of ~90% water. At longer wavelengths, the water absorption of light increases, indicating that OCT light at longer wavelengths will be strongly attenuated by the vitreous (i.e., water absorption). According to the water absorption spectrum, there are two regions where absorption is relatively low; below ~950nm, and a narrow band between 1000-1100nm, also termed the water window (Drexler,

2004). Water comprises most of the ocular tissue (cornea, lens, vitreous) and the water absorption profile has a local dispersion and absorption minimum at ~1060nm (Hale and Querry, 1973; Drexler, 2004). The scattering coefficient of ocular tissue at 1060nm is reduced compared to that at 800nm, which provides the advantage of obtaining significantly better-quality OCT images in patients with ocular opacities (Povazay et al., 2007a; Povazay et al., 2009). Using 1060nm OCT, Esmaeelpour et al. (2010) reported better visualisation of deeper ocular structures in the presence of cataract, compared to those acquired using 800nm OCT. Additionally, Unterhuber et al. (2005) reported that OCT images acquired at 1040nm penetrated deeper into the choroid below the RPE by ~200µm compared to those acquired at 800nm.

I.6.5 OCT imaging developments

Advancements in optical coherence tomography (OCT), including enhanced depth imaging (EDI-OCT) and long wavelength OCT, has allowed for improved visualisation of deeper ONH structures, such as the LC *in vivo* (Spaide, Koizumi and Pozonni, 2008; Lee et al., 2011; Park et al., 2012b; Traber et al., 2017; Naz et al., 2020); see Figure 1.10.

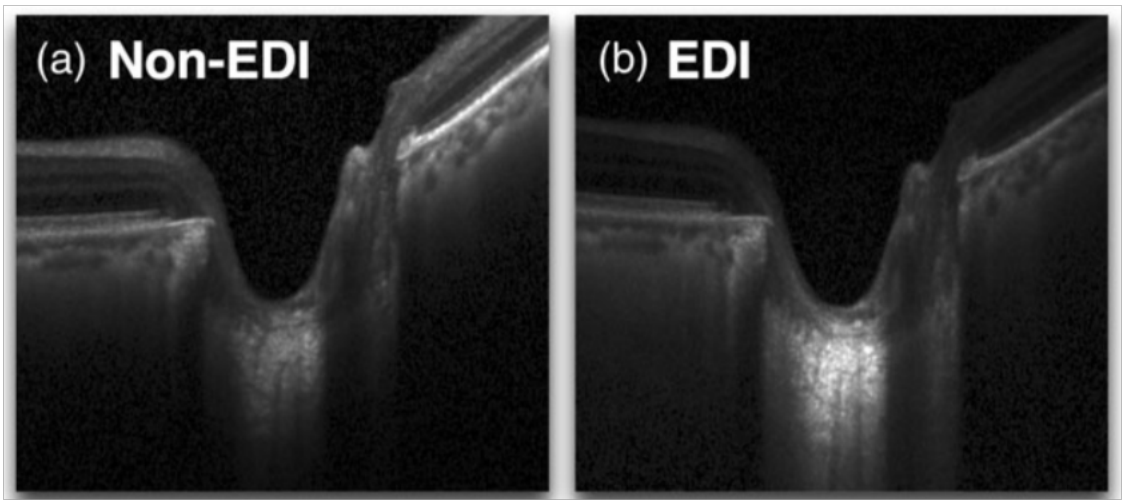

Figure 1.10: Optic nerve head OCT tomograms acquired without enhanced depth imaging (a), and with enhanced depth imaging (b). In (b), note improved visualisation of the LC positioned deep within the ONH. From Tan et al. (2018). Copyright permit shown in Appendix V.

The ‘zero delay line’ is the depth at which there is highest image sensitivity and the location where image acquisition is optimal. With increasing distance from the ‘zero delay line’, SD-OCT suffers from a depth-related signal roll off (i.e., a reduction in OCT signal). Therefore, due to this depth-dependent decrease in sensitivity and light scattering caused by melanin and

blood vessels, SD-OCT systems have a limited ability to visualise deep ocular structures in the posterior pole (Spaide et al., 2008). Clinically, often retinal layers are of interest and are therefore positioned closest to the zero delay, although, this results in limited visualisation of the LC and choroid as these are deeper structures located away from the 'zero delay line'. Enhanced depth imaging (EDI) OCT provides increased sensitivity of *in vivo* imaging of deeper layers by placing the instrument close enough to the eye to create an inverted representation of the fundus (Spaide et al., 2008). For EDI OCT, the OCT device is focused on the retina in the traditional way, then the device is moved closer to the eye, moving the reference plane more posterior within the eye, generating an inverted image with the inner retina facing down, and deeper ocular structures closer to the 'zero delay' (Spaide et al., 2008; Yeoh et al., 2010). Therefore, EDI OCT provides improved visualisation of deeper ocular structures such as the choroid and sclera (Yeoh et al., 2010), and ONH (Lee et al., 2011).

In OCT imaging, the lateral (or transverse) resolution of the system is limited by size of the beam of focussed light on the retina (Schmitt, 1999; Folio, Wollstein and Schuman, 2012). As the light passes through the ocular media optical aberrations occur. These aberrations within the eye limit OCT lateral resolution to ~15-20µm and can reduce overall image quality (Dong et al., 2017). Adaptive optics can be incorporated into OCT as a way to improve lateral resolution, whereby a deformable mirror can be used within the OCT system to compensate for wavefront distortions (Schuman, 2008; Dong et al., 2017). Adaptive optics OCT can be applied to allow *in vivo* 3D evaluation of the retina (Zawadzki et al., 2008) and ONH (Kim et al., 2013b), including LC beam thickness and pore parameters (Nadler et al., 2014) with improved lateral resolution.

I.6.6 OCT imaging of the ONH

Previous *ex vivo* work has implicated the LC within the ONH as a primary site of RGC axonal damage in glaucoma (Quigley et al., 1981; Quigley et al., 1983; Miller and Quigley, 1988). OCT imaging, and in particular EDI-OCT has been used to evaluate structural changes to the LC in glaucoma *in vivo* (Lee et al., 2011; Park et al., 2012b). Strouthidis et al. (2010) reported that ONH structures identified using SD-OCT accurately compared to histologic sections of a monkey eye throughout the extent of the ONH.

In healthy eyes, EDI-OCT has shown that the anterior shape of the LC has a horizontal central ridge ranging across the nasal-temporal LC, and the anterior LC insertion was more posteriorly located in the superior and inferior regions, compared to the nasal and temporal regions (Park et al., 2012c). In glaucoma, the anterior LC surface has shown significant alterations including increased concave curvature corresponding to an increased cupped shape (Tun et al., 2016; Tan et al., 2019), an increase in LC depth (Park et al., 2015; Tan et al., 2019), and detection of LC focal defects (Kiumehr et al., 2012). Furthermore, LC thickness has been shown to significantly differ between glaucoma and control participants (Park et al., 2012a; Omodaka et al., 2015). OCT imaging has been used to visualise LC pores (Inoue et al., 2009), and analyse LC beam thickness and pore parameters (Wang et al., 2013; Nadler et al., 2014), and evaluate the pathway taken by RGC axons as they traverse the LC (Wang et al., 2018).

I.6.7 Efficacy of OCT for glaucoma screening

Current clinical aspects of glaucoma diagnosis and evaluation are based upon structural assessment of the optic disc, and functional assessment of the VF based on standard automated perimetry (Medeiros et al., 2005a; Jonas et al., 2017). Early diagnosis and initiation of glaucoma treatment has been shown to reduce the rate of disease progression and improve the patient's quality of life (McKean-Cowdin et al., 2008; Garway-Heath et al., 2015). The diagnosis of glaucoma does not rely upon VF defects detected by perimetry, however, perimetry provides indispensable documentation for monitoring functional decline in glaucoma (Deeks, 2001; Fallon et al., 2017).

Biomicroscopy or stereophotography provide a subjective evaluation of the optic disc, whilst an objective assessment can be obtained from highly reproducible cross-sectional OCT images of the retina and ONH (Swanson et al., 1993; Schuman et al., 1996; Budenz et al., 2005; Sharma et al., 2008). For clinical glaucoma assessment, scanning and analysis of the peripapillary NFL is the OCT protocol most often used and has been widely adopted as an additional test for glaucoma detection (Leung et al., 2010a; Mwanza et al., 2010; Sung et al., 2011; Bussel, Wollstein and Schuman, 2014). In the UK, OCT has become increasingly utilised by community optometrists and hospital glaucoma clinics for the quantification of RNFL thickness measurements (Myint et al., 2011). Peripapillary NFL analyses offer clinical utility in glaucoma diagnosis as the pNFL comprises axons of the entire RGC population, although is

subject to inter-individual variability of ONH size and shape found in healthy and patients with glaucoma (Reus et al., 2010; Oddone et al., 2011). In a longitudinal study, thinner peripapillary NFL at baseline in the superior and inferior regions, along with the regional average, were associated with disease progression in glaucoma suspect eyes (Lalezary et al., 2006).

Since up to 50% of all RGCs are located within the macula region of the retina (Curcio and Allen, 1990), alterations in retinal thickness in the macula may be indicative of glaucoma disease (Zeimer et al., 1998). Analysis of macula thickness using TD-OCT has been shown to differentiate between glaucomatous and healthy individuals (Giovannini, Amato and Mariotti, 2002). However, the diagnostic accuracy of macula thickness was less than NFL thickness (Leung et al., 2005; Medeiros et al., 2005b; Sakamoto et al., 2010), likely a result of these macula thickness analyses including inner and outer retinal layers, the latter not being affected in glaucoma disease (Kendell et al., 1995). Spectral domain and swept source OCT have enabled selective analysis of segmented innermost retinal layers, including the NFL, ganglion cell layer, and inner plexiform layer, representing RGC axons, cell bodies, and dendrites respectively (Wang et al., 2009), with consequent better glaucoma diagnostic ability compared to total macula retinal thickness (Tan et al., 2009; Mori et al., 2010; Sakamoto et al., 2010).

In a clinical setting, commercial SD-OCT devices allow for automated NFL thickness measurements via inbuilt software allowing for monitoring of NFL thickness change, which has been shown to be able to distinguish between glaucomatous and healthy eyes, even in early stages of disease (Jeoung and Park, 2010; Mwanza et al., 2011a). Furthermore, the ganglion cell complex, which comprises the NFL, GCL, and IPL combined, along with the GCL and IPL combined have been shown to allow detection of glaucoma in early and preperimetric stages (Mwanza et al., 2011b; Arintawati et al., 2013; Zhang et al., 2014).

Recent reviews suggest that analysis of the RNFL via OCT remains the most diagnostically accurate parameter for glaucoma detection, although macula retinal thickness evaluation shows a comparable performance and is a useful alternative (Bussel et al., 2014; Michelessi et al., 2015; Oddone et al., 2016; Fallon et al., 2017; Kansal et al., 2018; Mwanza, Warren and Budenz, 2018). Analysis of the GCC for glaucoma detection may be more helpful in myopic

eyes where structural features, such as tilting or deformation of the optic disc, peripapillary atrophy, or variability in ONH size may decrease the diagnostic performance of peripapillary NFL thickness (Shoji et al., 2011; Oddone et al., 2016).

In clinical glaucoma assessment, fundus photos (Myers, Fudemberg and Lee, 2018) and OCT scanning techniques including RNFL thickness (Bussel et al., 2014) and MRW (Gardiner et al., 2015) have been shown to be useful modalities for glaucoma screening and diagnosis (Kansal et al., 2018; Fortune, 2019). Fundus photos can be used to assess parameters including the cup-disc ratio, peripapillary atrophy, blood vessel alterations, and examination of the NRR (Hagiwara et al., 2018). OCT scans provide micrometre resolution cross sectional images of the retina (Swanson et al., 1993) that can provide reproducible information about RNFL thickness, that can be used to differentiate between glaucomatous and healthy eyes (Chauhan et al., 2013; Grewal and Tanna, 2013). Indeed, RNFL thickness derived from OCT scans has been shown to highly correlate with VF function (Schuman et al., 1995b). Clinically, fundus photos and OCT scanning can be used concomitantly to aid in glaucoma diagnosis, along with other ocular pathologies such as macular degeneration or diabetic retinopathy (Agurto et al., 2011; Murtagh, Greene and O'Brien, 2020).

I.7 Artificial intelligence and deep learning in glaucoma diagnosis

Since there is no single perfect reference standard for the detection of glaucoma (Weinreb et al., 2016), diagnosis and prediction of disease progression is a complex, time consuming task which is subjective and depends on the clinician's experience and expertise, requiring multiple clinical examinations (Stroux et al., 2003; Schuman, 2012). Therefore, structural and functional evaluation of the eye may aid early diagnosis of glaucoma, and better predict its progression (Leske et al., 2003; Quigley, 2011; Weinreb et al., 2016).

Artificial intelligence (AI) has been applied for the diagnosis of retinal (Gulshan et al., 2016) and macula disease (Burlina et al., 2017; Fang et al., 2017b). Furthermore, deep learning (DL) AI tools have been applied to OCT image datasets for the automated segmentation of retinal layers (Fang et al., 2017a; Roy et al., 2017), and ONH structures (Devalla et al., 2018b), and

enhancement of ocular features within OCT image datasets (Devalla et al., 2018a; Halupka et al., 2018).

Algorithms used in AI can be broadly classified into two categories, according to the complexity of data under investigation. Included in the first category are machine learning classifiers (MLCs) and artificial neural networks (ANNs). MLCs are clustering algorithms which are based upon classical statistical modelling including logistic regression (LR), support vector machine (SVM), gaussian mixture model (GMM), and independent component analysis (ICA). Artificial neural networks are considered biologically inspired algorithms which pass input data through a series of interconnected artificial neurones, whilst modifying the weight of each neurone to achieve the desired classification (Devalla et al., 2020). Therefore, via a supervised or unsupervised learning process, these algorithms learn to utilise input data such as clinical parameters to automatically predict, for example, presence of disease or severity of glaucoma. Supervised learning algorithms including LR, SVM, and ANNs are trained using fully labelled datasets including disease diagnosis as the label (Burlina et al., 2017). Unsupervised learning algorithms such as GMM and ICA are trained with unlabelled datasets including only clinical parameters in attempt to identify patterns/trends within data and are well suited for low dimensionality numeric data such as cup-disc ratio, and IOP (Devalla et al., 2020).

The second category of AI algorithms are variants of ANNs, known as convolutional neural networks (CNNs) which are suited for high dimensionality data, such as OCT images, and uses multiple interconnected levels of data abstraction. Each convolutional layer (layers of filters) attempt to extract feature information e.g., edges, intensity, thickness, that best allow identification of disease, or specific structure, depending on the purpose of the algorithm. An iterative learning process is used to train the algorithm to minimise the error between the output of the algorithm i.e., the predicted diagnosis made by the network, and the clinical diagnosis. This involves continuously refining the weights/parameters of the extracted feature maps until the optimal weights of each feature are identified resulting in the least error between the algorithm output and the clinical diagnosis (Litjens et al., 2017; Devalla et al., 2020). Deep learning is an advancement of CNNs and has become the preferred AI approach with respect to diagnostic application, and image segmentation and enhancement

(Litjens et al., 2017). Deep learning techniques are often preferred over traditional methods due to their 'automated feature engineering', which automatically identifies the best set of features within the data that influence the algorithm's performance (Devalla et al., 2018a).

Deep learning AI approaches have been applied to colour fundus photographs for the extraction of glaucoma-related features including cup-disc ratio, notching of the NRR, and RNFL defects (Phene et al., 2019; Thompson, Jammal and Medeiros, 2019). Ting et al. (2017) used 125,189 glaucomatous fundus images to develop a DL system which was capable of discriminating glaucoma with high confidence; sensitivity: 96.4%, specificity: 87.2%, AUC: 0.942. Li et al. (2018) reported similar findings using 48,000 fundus photographs to develop a DL network to detect referable glaucomatous disease; sensitivity: 95.6%, specificity: 92.0%, AUC: 0.982.

Huang and Chen (2005) used OCT to train ANNs based on RNFL thicknesses and ONH parameters such as cup-disc ratio, cup area, and NRR area, resulting in successful discrimination between glaucomatous and healthy ONHs (AUC: 0.87). Similar results were found using MLCs based on OCT parameters measured in the macula (Burgansky-Eliash et al., 2005), peripapillary (Kim, Cho and Oh, 2017), and ONH (Barella et al., 2013; An et al., 2018) regions.

Even though AI studies report success in the ability to identify glaucomatous eyes based on quantitative OCT-derived data, the performance of the AI system depends on the accuracy with which such OCT parameters are measured. Within OCT image datasets, vascular shadowing can result in inaccurate ONH structural and RNFL measurements (Lucy et al., 2015; Ye, Yu and Leung, 2016; Halupka et al., 2018), thereby decreasing the discriminatory ability of such AI systems.

Using OCT images of the ONH, a DL network has allowed segmentation of the ONH neural and connective tissues to allow automatic measurement of ONH structures that may be critical to improve glaucoma management (Devalla et al., 2018a). The authors reported that the performance of the DL algorithm was significantly improved when adaptive compensation (Girard et al., 2015) was applied to training OCT images (Devalla et al., 2018a).

Using raw OCT volumes, Maetschke et al. (2019) developed a 3D DL system to classify healthy and glaucomatous eyes (AUC: 0.94) and reported that the DL algorithm focused on the NRR, optic disc area, and the LC to identify a glaucomatous ONH. Therefore, utilising 3D ONH structural information, the DL system is able to distinguish glaucoma disease significantly better than methods using RNFL thickness measures alone (Maetschke et al., 2019; Wang et al., 2019).

In glaucoma, since ONH structural changes often precede functional loss (Gordon et al., 2002; Harwerth et al., 2010), AI systems could aid in the segmentation (Devalla et al., 2018a) and enhancement (Girard et al., 2011; Devalla et al., 2018b) of ONH structures. This could offer improved clinical utility in better visualisation of OCT structural information which could further improve timely glaucoma diagnosis and initiation of appropriate treatment. Such AI systems may allow for improved personalised therapeutic interventions and monitoring of glaucoma treatment efficacy (Devalla et al., 2020; Ran et al., 2021).

I.8 Open data initiatives

Scientific progress is based upon data acquisition and analysis, providing evidence for the published body of scientific knowledge (Molloy, 2011). Historically, scientific data and reports have not been easily accessible. Such scientific reports were published in journals requiring paid subscriptions, and databases that were generated were considered the private and intellectual property of those who those who developed them (Huston, Edge and Bernier, 2019). However, the open provision of data in a useful format increases transparency and reproducibility, making the scientific process more efficient and a greater benefit to society (Molloy, 2011; Huston et al., 2019). Therefore, there is an urgent need to improve the infrastructure supporting the reuse and sharing of scientific/scholarly data (Wilkinson et al., 2016).

The rise of online journals in the 1990s has enabled the movement toward open science and open data; supporting scientific communication, transparency and collaboration in research (Gezelter, 2015). Open data not only has practical advantages relating to sharing and reuse

of data but would address issues of reproducibility of data results from publications (Ioannidis, 2005; Prinz, Schlange and Asadullah, 2011). This 'reproducibility crisis' has been associated with poor statistical analyses, loss of lab expertise through graduation of students, changing versions of data files, and inadequate methodology describing all necessary steps required to reproduce the work (Gezelter, 2015).

Since modern science relies on numerical experiments and increasingly computer simulations, attention must be paid to reproducibility in modelling and simulation (Donoho et al., 2009). As the complexity of numerical experiments increases and the datasets become larger, reproducibility of results is dependent upon the source code used for analysis, data, and meta-data (Donoho et al., 2009), triggering the suggestion for their accessibility upon publication and review (Gezelter, 2015), under an open source license (Stodden, 2009).

An advantage to open-source software and data is that reuse of data and software components lowers research grant funding costs and increases the scientist's efficiency (Gezelter, 2015), as well as increased scientific output as a result of potential collaborations (Wilkinson et al., 2016; Huston et al., 2019). Such open scientific resources provide a publicly accessible continuous repository of knowledge whereas previous 'closed knowledge' approaches do not (Gezelter, 2015).

Funders such as the UK Research Councils and Wellcome Trust, and the US National Institutes of Health support open data publications as essential for researchers to build upon, verify, and reproduce previously published results (Boulton et al., 2011; Walport and Brest, 2011). Since publications and citations are the primary method in science to attribute credit and recognise effort (Gezelter, 2015), sharing of data remains a challenge (Molloy, 2011). Researchers may fear exploitation of datasets that may yield numerous publications and/or the absence of career rewards/incentives to publish data, may make it less appealing to researchers to allocate time and effort required making data publicly available (Molloy, 2011).

Modern science and technologies will continue to create an explosive generation of data (Huston et al., 2019). The global movement towards open-source data indicates the desire by many to collaboratively address complex issues (Huston et al., 2019). Despite remaining

challenges, open data could result in better reproducibility, transparency, and increased scientific efficiency, ultimately leading to a greater benefit to society (Molloy, 2011).

I.9 Hypothesis and aims

Currently, there is no cure for glaucoma, and it is estimated that the disease affects around 60 million people worldwide (Quigley, 2011; Tham et al., 2014). Reduction of IOP is the only proven method of treatment for glaucoma (Boland et al., 2013). Several studies have demonstrated the benefit of lowering IOP in preventing disease development and maintaining visual function (Gordon et al., 2002; Heijl et al., 2002; Kass et al., 2002; Crowston and Weinreb, 2005; Kotecha et al., 2009; Garway-Heath et al., 2015; Karaskiewicz et al., 2017). The main goals for glaucoma treatment are to slow/halt disease progression and maintain patient quality of life (McKean-Cowdin et al., 2008; Patino et al., 2010; Boland et al., 2013). Since vision loss in glaucoma cannot be recovered, this highlights the importance of early glaucoma diagnosis and appropriate management.

Three-dimensional OCT imaging allows for *in vivo* evaluation of ONH structure in glaucoma disease, in an attempt to use ONH parameters as biomarkers to indicate early disease onset and/or hold potential to suggest disease progression. Therefore, such markers may aid in the clinical management of glaucoma to provide appropriate treatment prior to early (or further) VF loss.

The overall hypothesis of this thesis is that ONH microstructure changes as a function of glaucoma disease stage and impacts on visual function, and that the earliest ONH changes have potential to act as biomarkers to detect POAG in its earliest stages. Based on SD-OCT images, the overall aim of this thesis is to identify and evaluate ONH structural and axon-related parameter differences that occur between stages of POAG to determine potential ONH biomarkers critical to early diagnosis and detection of POAG disease.

To this purpose, specific aims are:

- To quantify *in vivo* ONH depth and thickness and axon parameters as a function of glaucoma disease stage, and with respect to VF sensitivity.

- To identify differences in volumetric ONH parameters that occur between different stages of glaucoma disease.
- To investigate regional and depth-related alterations in LC connective tissue coherence between glaucoma disease stages.
- To evaluate whether a group/combination of ONH parameters can be used to allow discrimination between healthy and glaucomatous eyes and predict early-stage disease.

II. Chapter 2: Methods

This chapter outlines participant recruitment and inclusion criteria, ocular assessments performed, OCT dataset acquisition and image processing techniques used within this thesis study. Additionally, the methodology used in each experimental chapter is described, including intra-session repeatability of ONH measurements and statistical analyses performed to identify ONH parameter changes as a function of glaucoma disease.

II.1 Participant recruitment

Participants with primary open angle glaucoma (POAG; diagnosed by a glaucoma specialist) were recruited from Professor James Morgan's Glaucoma clinic at the University Hospital of Wales, Cardiff, UK. Control participants were recruited from within Cardiff University School of Optometry and Vision Sciences which included staff, students, and family members. All recruitment and research were carried out in accordance with the tenets of the declaration of Helsinki, under ethical approval granted by NHS Wales Research Ethics Committee (Wales REC 2) and School of Optometry and Vision Sciences Research Audit Ethics Committee.

Before experimental proceedings began, participants were provided with a detailed written explanation of the study aims, and procedures to be undertaken. Prior to participation in the study and data acquisition, written informed consent was obtained. Participant recruitment during this project included 40 participants with POAG (mean age ± SD: 72.55 ± 8.41 years) and 19 control participants (mean age ± SD: 67.74 ± 6.59 years). Additionally, SD-OCT datasets, acquired from a previous study (11 control participants; mean age ± SD: 61.91 ± 4.55 years and 24 participants with POAG; mean age ± SD: 71.08 ± 9.78 years) were included in analyses performed in Chapters 3, 4 and 6.

To determine intra-session variation of ONH depth and thickness measurements, 20 participants aged 21 to 63 years (mean age ± SD: 36.0 ± 13.2 years) were recruited from staff and postgraduate students at the School of Optometry and Vision Sciences, Cardiff University.

II.2 Inclusion criteria

A brief medical history was taken from each participant which included general health and prescription medications (if appropriate) and ocular history. Exclusion criteria for the study included: pregnancy, epilepsy, non-glaucomatous ocular pathology, or systemic pathology with significant ocular complications, e.g., diabetes, systemic hypertension. Participant inclusion criteria for this study are summarised in Table 2.1.

Participant	Criteria	Status
All participants	Ocular health	• Clear optical media or mild cataract, providing view of posterior pole not restricted • No non-glaucomatous ocular pathology
	General health	• No systemic pathology with ocular complications (e.g., diabetes, systemic hypertension) • No pregnancy or epilepsy
	Refractive error	• Spherical error within $\pm$ 6.00 D • Cylindrical error less than 3.00 D
Control	IOP	• Average of triplicate readings $\leq$ 21 mmHg using a Goldmann tonometer
	Visual fields	• No visual field defect, as determined by standard automated perimetry
	Visual acuity	• 0.1 logMAR acuity or better
Glaucoma	Ocular health	• Positive diagnosis of POAG from a Consultant Ophthalmologist (Glaucoma Specialist) based on changes to ONH, IOP and/or functional loss of visual field, and open anterior chamber angle determined by gonioscopy

Table 2.1: Summary of study participant inclusion criteria.

Diagnosis of POAG was made by Prof JE Morgan and based upon the presence of typical glaucomatous optic disc features including diffuse or focal thinning/notching of the neuroretinal rim, increased vertical cup to disc ratio, inter-ocular difference in cup-disc ratio > 0.2, or RNFL defects, IOP > 21mmHg without topical treatment, and a VF defect consistent with glaucoma (Jonas et al., 1988c; Jonas et al., 1993; Foster et al., 2002; Cho et al., 2012). POAG participants that displayed characteristic optic disc changes without VF loss were classified as preperimetric glaucoma. POAG participants were divided into three groups according to visual field Mean Deviation (VF MD). The three groups being preperimetric glaucoma (no VF defect), early glaucoma (VF MD better than -6dB), and moderate-advanced glaucoma (VF MD worse than -6dB) (Budenz et al., 2002; Mills et al., 2006). VF examinations were performed at least three times by control participants, and once by glaucoma

participants, who all had previous experience in performing VF tests. Due to the strict inclusion criteria of this study, a disadvantage of this approach is that the results may be less generalisable to a wider population of glaucoma participants.

II.3 Preliminary ocular examinations

Prior to commencing OCT image acquisition, several procedures were carried out to evaluate ocular health, including confirmation that control participant eyes showed no signs of glaucoma. LogMAR visual acuity was recorded, and refractive error of each eye determined using Topcon KR 7500 Auto refractometer (Topcon Medical Systems, USA). Participant inclusion criteria was restricted to having a mean refractive error of less than $\pm$6.00 Dioptres (D), with less than 3.00 D of cylindrical error. This stipulation was to allow accurate focussing of the OCT device, and to ensure no bias on optic nerve head parameters due to axial myopia or hyperopia.

Visual field assessment was undertaken to obtain Mean Deviation (MD) values and was performed using SITA 24-2 Standard threshold visual field test (Humphrey Visual Field Analyser, Carl Zeiss Meditec Inc, Germany). Axial eye length (important in OCT image calibration) was determined using an IOL Master (Carl Zeiss Meditec Inc, Germany). Ocular biometry, including central corneal thickness and anterior chamber depth were measured with a Pentacam (Oculus Optikgeräte GmbH, Germany).

Participants underwent slit lamp examination to evaluate the health of the anterior eye and Volk lens retinal examination, in addition to ensuring the absence of significant corneal or lenticular opacities that would hinder the quality of OCT image data acquired. The anterior chamber angle was graded using the Van Herrick technique to confirm open angle glaucoma in POAG participants and to reduce the risk of angle closure during pupillary dilation. Pupillary dilation was achieved by the instillation of 1.0% Tropicamide (Bausch & Lomb, UK) in each eye.

Triplicate intraocular pressure (IOP) readings were recorded using Goldmann applanation tonometry (Haag Streight AG, Switzerland), with 0.5% Proxymetacaine Hydrochloride (Bausch

& Lomb, UK) instilled in each eye for anaesthesia. Additionally, digital fundus photography was performed using the DRS retinal camera (CenterVue Inc. USA).

II.4 Spectral Domain Optical Coherence Tomography

Before commencing acquisition of OCT images, the incident power output of the OCT system was measured using a power meter (Thorlabs Inc. USA) in order to confirm that power was less than 2.5mW at the cornea; the maximum permissible corneal exposure at this wavelength. This conforms with the American National Standard Institute (ANSI, 2000) and the International Commission on Non Ionizing Radiation Protection (ICNIRP, 2000) safety limits for a 10 seconds exposure at this wavelength.

Image datasets were acquired using a custom-built, laboratory-based Spectral Domain Optical Coherence Tomography (SD-OCT) system. The light source had a centre wavelength of 1040nm (bandwidth 70nm). The light source (1-ASE-HPE-S, NP Photonics, Tuscan, US) was fibre-optically linked to a 20/80 beam splitter which serves the sample arm and reference arm respectively, resulting in approximately 7-8µm axial resolution (assuming a retinal refractive index of 1.4), and maximum transverse resolution of ~17.5µm (Povazay et al., 2007a; Wood et al., 2011; Terry et al., 2016). The spectrometer within the system was grating-based, with a Goodrich SUI-LDH-1.7 camera. The beam diameter of the OCT system was 1.5 mm, and optical power at the cornea was 1.88 ± 0.03mW (see Figure 2.1). The SD-OCT system has an acquisition speed of 47,000 a-scans/second, resulting in approximately 6 seconds to acquire each scan composed of 512 x 512 x 1024 pixels.

A custom-built OCT system was used as this allowed for the OCT scan protocols for 3D dataset acquisition of 512 x 512 x 1024 pixels to be more easily adapted than provided by commercial instruments. For instance, data within chapter 5 were acquired using a 10° scan angle allowing a greater sampling rate and lateral resolution. Additionally, as outlined in sections II.6 and II.7, since data were acquired in raw spectral format this allowed for appropriate image processing techniques and that all images were calibrated to account for axial eye length.

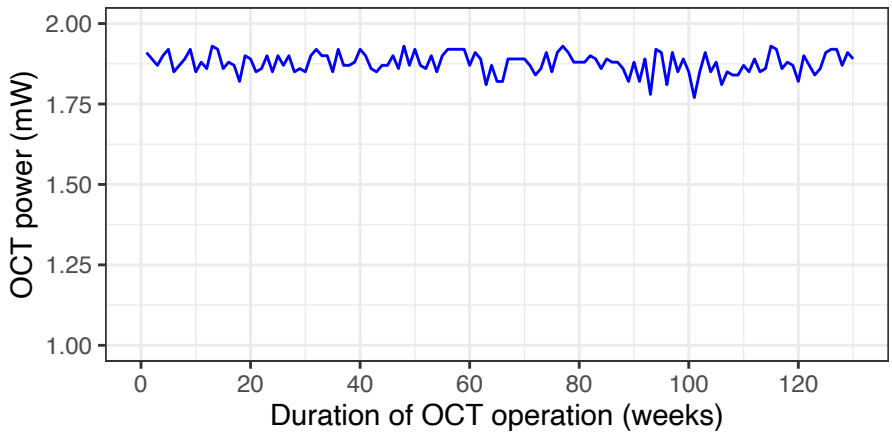

Figure 2.1: OCT system power recorded for each image acquisition session.

For SD-OCT image acquisition, participants were positioned accordingly, and asked to look at a fixation target set within the instrument for gaze control. Participants were instructed to fixate on a peripheral target for ONH imaging. For all participants, both 10° and 20° scans of the ONH were acquired. The ONH image was positioned close to the zero-delay line where image capture was optimal due to higher signal to noise ratio (Povazay et al., 2007a). Image acquisition of ONH scans were acquired with the image vertically inverted, allowing for enhanced depth image (EDI), as described by Spaide et al. (2008). This was achieved by adjusting the reference arm of the OCT system to invert the image, moving the lamina cribrosa (LC) closer to the zero-delay line, providing better definition of deeper structures within the ONH.

II.5 Processing of SD-OCT data

During OCT image acquisition, each image was saved in spectral data format (i.e., FD1 format). In order to view the collected data as a volumetric image, processing of the spectral data was performed and subsequently converted into a 16-bit TIFF image file. This was carried out using OCT1_FD1 data processing software (version 2.2, J Fergusson, VSBL, Cardiff University), a custom written MATLAB software v2014b (Math-Works, US).

II.6 Post processing of OCT TIFF images

Within Fiji ImageJ (Version 1.52a; National Institutes of Health, Bethesda, Maryland, USA, http://imagej.nih.gov.ij) the 3D OCT TIFF image dataset was registered to align the OCT tomograms and to account for small eye movements, using 'Stackreg' (Thevenaz, Ruttimann

and Unser, 1998), an ImageJ plugin (P Thevenaz, Biomedical Imaging Group, Swiss Federal Institute of Technology). Following image registration, OCT datasets were then cropped to remove areas of signal loss containing zero information, or excess vitreous within the image.

II.6.1 Method development: Determination of optimal filter for ONH measurements

Following processing of ONH derived OCT spectral data to TIFF image format, it was necessary to establish which 3D filter to apply to these OCT datasets. Image filtering was applied to reduce image noise in order to improve image detail and perform measurements of ONH depth and thickness parameters within the OCT image datasets.

Within ImageJ, it is possible to apply 3D digital filters to the OCT image dataset based on statistical calculation, set by pixel radii in the lateral and axial planes. For example, a median filter of set radii reduces noise in the image by replacing each pixel with the median of the neighbouring pixel values. A mean filter uses the mean value of neighbouring pixels. 'Neighbouring' pixels are determined by the specified pixel radii.

Determination of optimal filter was performed on 20° scans of the ONH (n=3). Following image registration, correct orientation of the 3D ONH OCT image dataset was established by comparison to the participant's fundus photograph. Next within ImageJ, a digital filter was applied to the 3D OCT image dataset. A comparison was made for both mean and median filters for a range of varying pixel radii and applied to each of the three ONH OCT image datasets, see Table 2.2.

For each participant a nasal-temporal image slice was extracted from the OCT dataset, and the slice number recorded so that the same OCT b-scan was analysed for each of the different filters (i.e., digital filters were applied to 3D OCT image datasets, and nasal-temporal b-scan used to evaluate the effect of each filter). The image was scaled to isotropic proportion, by dividing the lateral pixel calibration (10-12µm/pixel) by the axial pixel calibration (1.9µm/pixel). This factor (~5.5) was entered into the x-scale within ImageJ, so the OCT b-scan had the same scaling in both lateral and axial directions.

A vertical line plot profile of grayscale pixel values was analysed in each b-scan to determine filter potential to aid in differentiation between ONH layers. The plot-profile evaluation line was placed in the same position repeatedly, (using Image J region of interest manager) i.e., in the temporal ONH, equidistant between the ONH centre and BMO termination, see Figure 2.2.

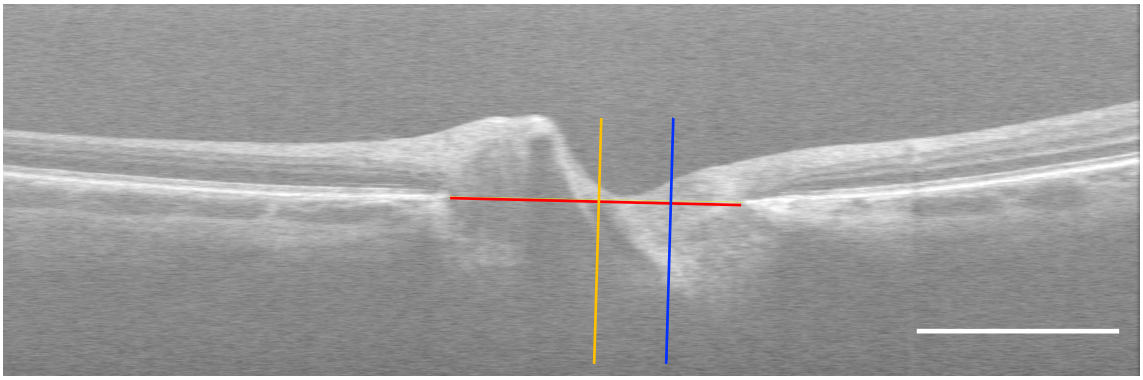

Figure 2.2: Scaled nasal-temporal OCT b-scan with Bruch's membrane opening marked in red. Orange line denotes ONH centre, perpendicular to and bisecting BMO. Blue line indicates location of plot profile for pixel grayscale values. Scale bar represents 1mm.

Following application of the filter to each image, the plot profile of the evaluation line was displayed as graphical representation of pixel grayscale values (as shown in Appendix I; Figures II.1 and II.2). Plot profiles were evaluated as to whether distinct fluctuations in grayscale value could be determined at tissue boundaries. Additionally, each OCT b-scan was graded with reference to the observer's ability to determine prelamina, anterior and posterior LC surfaces, see Figure 2.3.

Mean and median 3D digital filters	**Axis direction within 3D OCT image dataset**		
	X	**Y**	**Z**
Specified pixel radii for mean and median filters	2	2	0
	3	3	0
	2	2	1
	3	3	1
	1	1	2
	3	3	2
	2	2	3
	3	3	3

Table 2.2: Specified parameters of mean and median 3D digital filters in pixel radii.

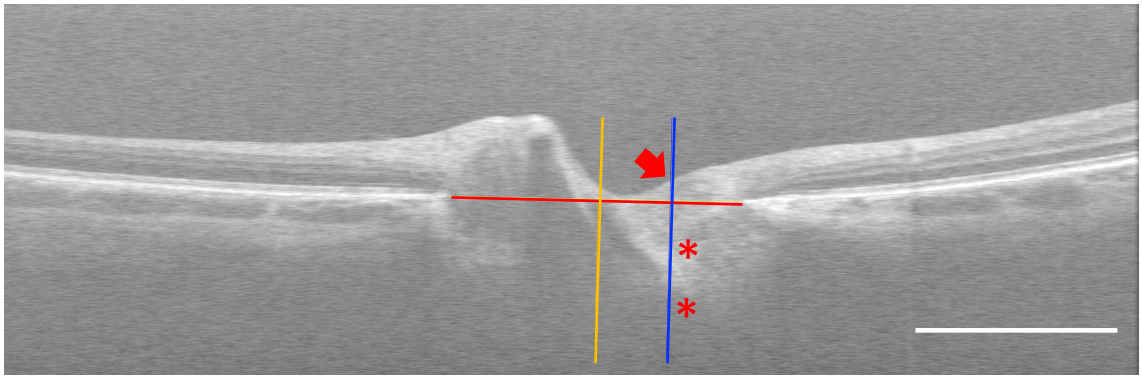

Figure 2.3: Evaluation of clarity of tissue boundaries from top of evaluation line, marked in blue. Surfaces being prelamina surface (red arrowhead), anterior and posterior LC surfaces (red asterisks). Scale bar represents 1mm.

Optimal filter was determined by scoring each image based on the line plot profile, in combination with observer visualisation, to detect ONH tissue boundaries. This yielded an optimal filter which was subsequently applied to ONH OCT image datasets for further analysis.

For each filter (mean or median) with specified pixel radii, there was clear delineation between the vitreous and prelamina surface in each nasal-temporal OCT b-scan. With increasing lateral and axial pixel radii, the result was a smoother image containing less noise and additionally, the intensity profile plot showed less variation in pixel grayscale and resulted in a smoother plot (as shown in Appendix I; Figures II.1 and II.2). However, despite providing a 'smoother' image with less noise, with increasing pixel radii, deeper ONH tissue borders (i.e., in the axial plane) became too blurred for accurate delineation, thereby hampering the ability to perform ONH depth and thickness measurements.

For each filter, following evaluation of the line plot profiles and the ability to visualise ONH tissue boundaries, it was decided that the optimal filter for ONH OCT image datasets was a median filter with pixel radii of 2-2-1 in the x-y-z planes respectively. This was deemed to provide adequate image noise reduction, whilst also allowing accurate delineation of deeper ONH structures. Therefore, subsequent ONH parameter analysis was performed on OCT image datasets following application of the median filter with radii 2-2-1 (x-y-z).

II.7 Calibration of OCT image datasets

The interferometric properties of OCT result in a decoupling of the transverse and axial resolution (Fujimoto et al., 2000). Therefore, image datasets obtained from the OCT device were not scaled correctly after image acquisition. Lateral scaling is related to the sampling rate in the lateral direction and is also dependent on the optics of the eye being imaged, whereas axial scaling is a property of the instrument. In order for an image to be produced, the OCT device produced a collimated beam that was focussed on the posterior pole of the eye. Therefore, the lateral scaling depends on the optics of the eye under investigation, whilst axial scaling is only affected by the refractive index of the eye.

If the eye is considered as a simple thin lens, where all refraction occurs at a single point in the eye's principal plane, then for accurate lateral scaling, the distance from the principal plane of the eye to the retina was estimated as:

$$P = AEL - 1.82\text{mm}$$ (Littmann, 1982; Bennett, Rudnicka and Edgar, 1994)

Where P is the distance from the principal plane of the eye to the retinal surface and AEL is the axial eye length in millimetres. The principal plane is not constant between participants as axial eye length varies, and currently there is no device to measure the distance from principal plane to retinal surface. In this study, 1.82mm was subtracted from the full axial eye length to calculate P. The quantity 1.82mm is based upon work by Bennett et al. (1994) who mentions that this method was as accurate as complete ray tracing of the eye.

The input scan angle of the OCT device (A), and the resulting scan angle (A_m), are also taken into consideration. The two angles are related by the refractive index (RI) of the scan medium when the stationary point of the scan is located at the principal plane of the lens (Bennett et al., 1994).

$$A_m = A / 1.336$$

Where A is the input OCT scan angle (i.e. 10° or 20° in this study), A_m is the resulting scan angle, and 1.336 is the refractive index of the eye, assuming a bulk refractive index of 1.336 (Bennett et al., 1994), see Figure 2.4.

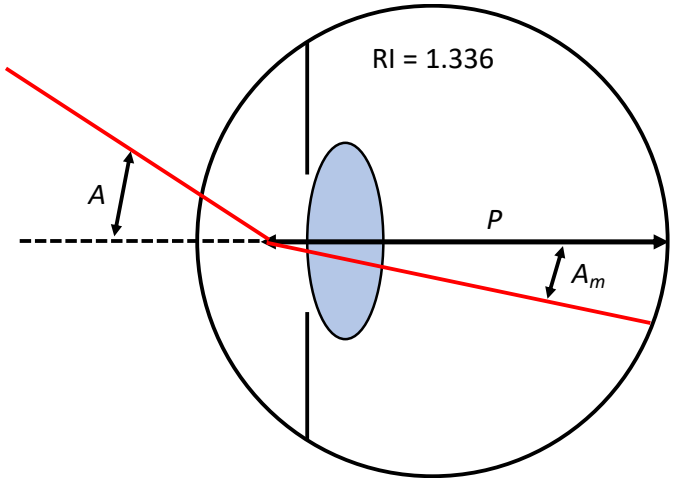

Figure 2.4: Schematic ray diagram illustrating the input scan angle *A,* and the resulting scan angle A_m. Where *P* is the distance from the principal plane to the retina and RI the refractive index of the eye.

Once A_m is known, the equation for the circumference of a circle, 2πr, can be used to find the scan size on the retina, i.e., the fraction of circumference covered by angle A_m.

$$\text{Scan size on retina} = 2\pi P\,(A_m / 360)$$

Where *P* is in millimetres and A_m is in degrees.

The lateral pixel calibration can then be calculated by dividing by the number of pixels in the scan (N_p), i.e., 512.

$$\text{Lateral pixel calibration} = (2\pi P\,(A_m / 360)) / N_p$$

Where *P* = distance from principal plane to the retina, A_m = resulting scan angle, and N_p = number of pixels in the scan. The lateral pixel calibration for a 20° OCT scan was 10-12µm per pixel, and for a 10° OCT scan was 5-6µm per pixel.

Lateral scaling of all OCT images was calculated based on previous work (Littmann, 1982; Bennett et al., 1994) to calculate the transverse size of any retinal feature using appropriate ocular biometry and instrument meta-data (Terry et al., 2016). This involved (a) an estimate of the distance from the eye's principal plane to the retina, calculated as AEL – 1.82mm, (b) the OCT scan angle in air, and (c) an estimate of the bulk refractive index of the eye (1.336).

Whilst differences in refractive index of ocular structures (corneal refractive index = 1.388, aqueous refractive index = 1.343) (Lehman et al., 2009) may affect the resultant scan angle at the retina, a generally accepted value of the bulk ocular refractive index is 1.336 (Bennett et al., 1994). Furthermore, this approach to calculate the transverse size of retinal features has been described to be sufficiently accurate within ±20° from the optical axis (Littmann, 1982; Bennett et al., 1994). In this thesis study, since the OCT scan angle did not exceed 20°, this method was deemed appropriate to allow a reasonably accurate lateral scaling of all OCT images, as outlined by Terry et al. (2016).

Since axial pixel calibration of the OCT instrument was not affected by the optics of the participant eye, this was a fixed quantity for all participants. Axial pixel calibration was calculated by imaging an object of known size using the OCT system (object being the air gap between two glass slides suspended 1mm apart measured to an accuracy of 1µm using a confocal microscope), then measuring the resulting image size in pixels. The image size in µm was then divided by the number of axial pixels in the image, resulting in the axial scaling of the OCT device in air. This has previously been found to be 2.664 µm per pixel. However, axial scaling is affected by the refractive index of the optical medium being investigated. To obtain correct axial pixel calibration, this was then divided by the refractive index of the retina, which was taken to be 1.4 (Wojtkowski et al., 2002). Therefore, the axial pixel calibration was 1.9µm per pixel for all OCT images.

II.8 Orientation of OCT image datasets

Correct orientation of the OCT datasets was ensured by comparing maximum intensity projections (MIP) of the OCT images with the participant fundus photograph. The OCT datasets were flipped and/or rotated as required, for example in enhanced depth image (EDI) acquisition, see Figure 2.5.

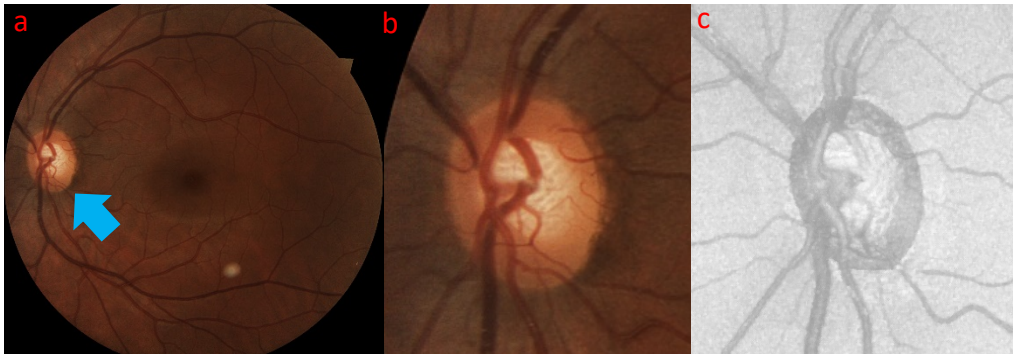

Figure 2.5: Orientation of the OCT datasets confirmed by comparing the participant fundus photograph (a) and (b) to a maximum intensity projection of the OCT image (c). OCT image was flipped vertically following EDI image acquisition. Blue arrow indicates location of optic disc in fundus photograph (a), as shown in (b) and (c).

II.9 Radial reslice of OCT image datasets

Following application of the 3D digital filter (median 2-2-1) to the registered ONH dataset, the image stacks were resliced into the *enface* plane. Within the 3D OCT dataset, the edge of the ONH border was demarcated using the oval selection tool in ImageJ; to determine the centroid location of the ONH, see Figure 2.6.

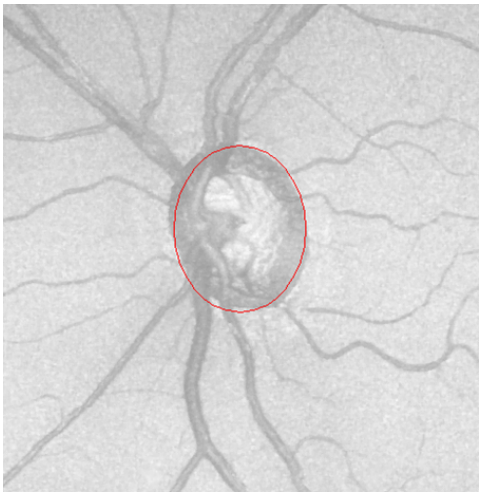

Figure 2.6: ONH centroid location; oval selection tool was used to demarcate optic disc edge to determine centroid prior to radial reslice.

After the centre of the ONH was located, each OCT data set was resliced radially at 45° intervals to produce four OCT tomograms at different orientations through the 3D ONH datasets. This was performed using the 'reslice_on_centroid_v2' macro in ImageJ (version 2,

J Fergusson, VSBL, Cardiff University). The orientations being vertically: superior (S) – inferior (I), horizontally: nasal (N) – temporal (T), and diagonally: IT-SN, and IN-ST (see Figure 2.7).

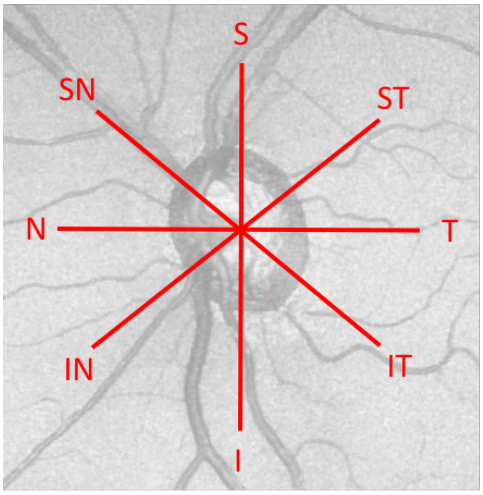

Figure 2.7: Indicated in red, four radial b-scans were created at 45° intervals, centred on ONH centroid location.

II.10 Brightness and contrast adjustment

OCT tomograms were imported into ImageJ (version 1.52a; NIH, USA, http://imagej.nih.gov.ij). Within ImageJ, the histogram of pixel intensities was used to adjust image brightness and contrast. Initially, pixel intensities were non-normally distributed. Pixel minimum limit was adjusted to the modal value of the histogram, and the maximum pixel limit was set to the upper tail of the curve. Image pixel values were then automatically redistributed across this range to aid in improving image contrast and visualisation of ONH structures. An example of an OCT tomogram before and after brightness and contrast adjustment is given in Figure 2.8.

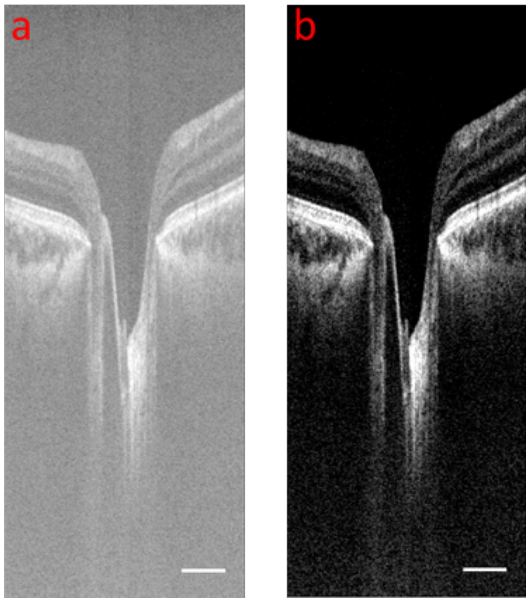

Figure 2.8: Nasal-temporal ONH b-scan before (a) and after (b) brightness and contrast adjustment. Note improved visibility of ONH structures. Scale bar represents 1mm.

II.11 Isotropic scaling of OCT b-scans

Following OCT image acquisition and initial processing, when viewed in ImageJ, the ONH or macula datasets appeared elongated in the axial plane and narrowed in the lateral plane. This is due to the fact that axial and lateral resolution in OCT are decoupled (Fujimoto et al., 2000). For image analysis and to enhance visibility of ONH structures, the OCT image was scaled to isotropic proportion. This was performed by dividing the lateral pixel calibration (10-12µm/pixel) by the axial calibration (1.9µm/pixel) and entering this factor (~5.5) into ImageJ to upscale laterally, see Figure 2.9.

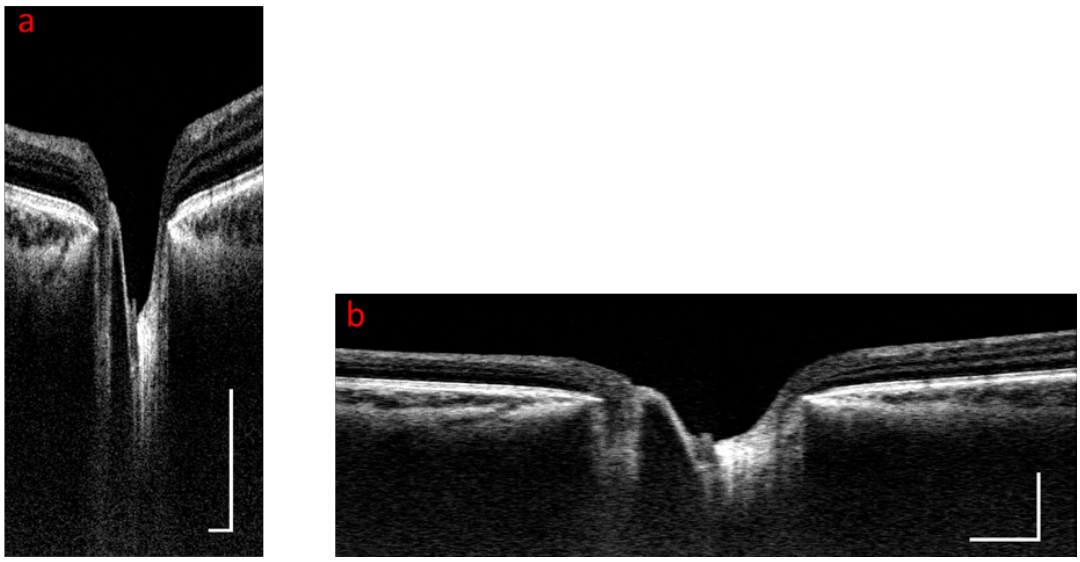

Figure 2.9: Example of nasal-temporal ONH b-scan prior to (a) and after applying isotropic scaling (b). Scale bar represents 500µm.

II.12 Stages of SD-OCT data and image processing

Figure 2.10 summarises stages involved from acquisition of OCT spectral data to final OCT images to perform measurements of ONH depth and thickness parameters.

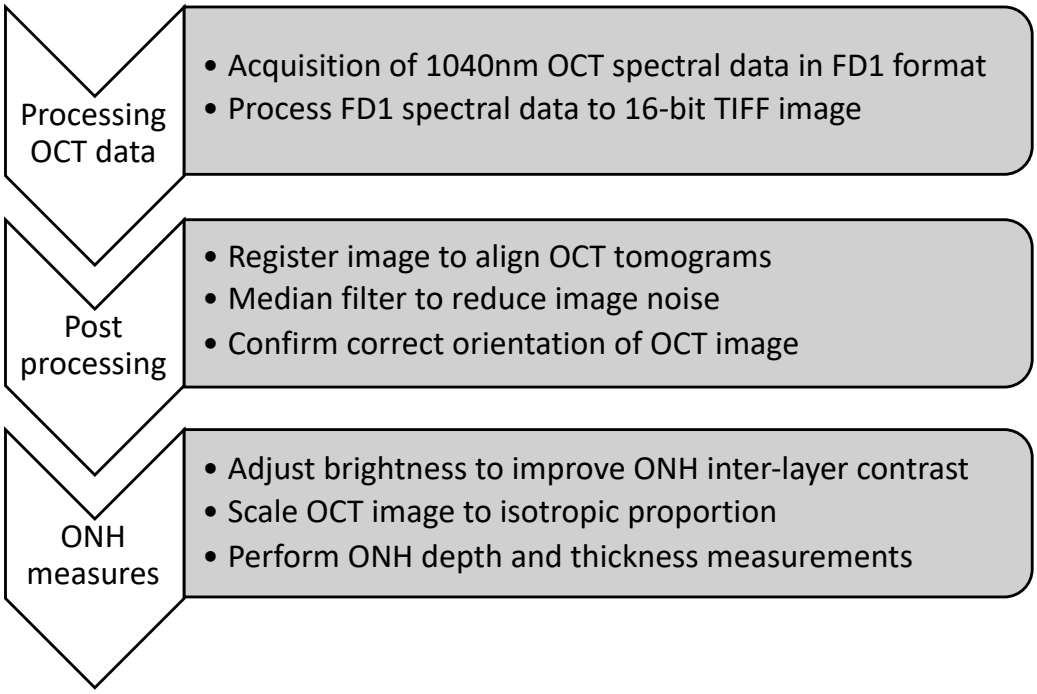

Figure 2.10: Summary of OCT data and image processing stages in order to perform ONH depth and thickness measurements.

II.13 Optic nerve head parameter measurements in OCT image slices (Chapter 3)

Subsequent to radial reslice of the ONH, four OCT tomograms were generated along the superior (S) – inferior (I), nasal (N) – temporal (T) and the diagonal (SN-IT and ST-IN) meridians of the ONH (see Figure 2.11). Regional ONH parameter measurements and BMO diameter were performed on these 2D OCT images.

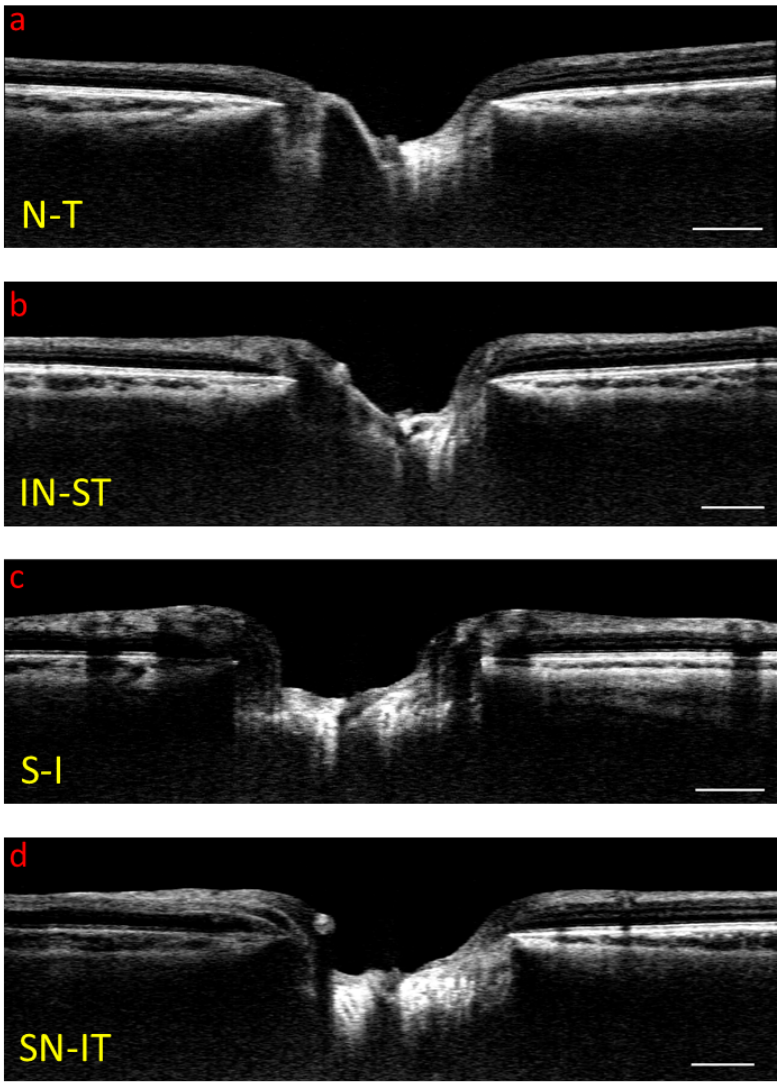

Figure 2.11: Example of four ONH radial OCT tomograms in the (a) nasal-temporal, (b) inferior nasal-superior temporal, (c) superior-inferior, and (d) superior nasal-inferior temporal meridians. Images are subsequent to brightness and contrast adjustment and have correct isotropic scaling. Scale bar represents 500µm.

BMO diameter measurement

Firstly, at the edge of the ONH, Bruch's membrane terminations were determined, and a line drawn across Bruch's membrane opening (BMO; see Figure 2.12). This line was measured, and also used as a reference plane from which further measurements were taken.

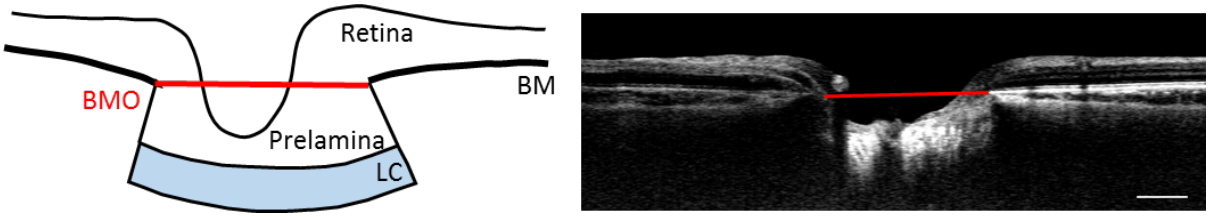

Figure 2.12: Schematic diagram and OCT image denoting Bruch's membrane opening (BMO) marked in red. BM = Bruch's membrane, LC = lamina cribrosa. Scale bar represents 500µm.

Prelamina, anterior and posterior LC surface depths

Using the pixel coordinates (x, y) of each side of the BMO, it was possible to calculate the midpoint and two quartiles of the BMO line. From these points, regional depth measurements were taken of the prelamina surface (Figure 2.13a), anterior LC surface (Figure 2.13b) and posterior LC surface (Figure 2.13c). In instances where the prelamina surface was above the BMO reference plane, these depth measures were recorded with a negative value. Whereas prelamina surfaces below BMO were recorded with a positive value, see Figure 2.14a.

Prelamina and LC thickness

Prelamina thickness was calculated as the difference between prelamina surface and anterior LC surface depths, see Figure 2.14b. Similarly, LC thickness was calculated as the difference between anterior and posterior LC surface depths, see Figure 2.14c.

Nerve fibre layer measurements

Peripapillary nerve fibre layer thickness (pNFL) was measured at a point 1.7 mm either side from the centre of BMO, to replicate nerve fibre thickness measures made by some commercial OCT devices. From each termination of Bruch's membrane, the vertical distance to prelamina surface directly above was also measured to provide retinal nerve fibre layer thickness at the optic disc border (bNFL), Figure 2.13d.

Minimum rim width (MRW) has been defined as the shortest distance from BMO termination to the inner limiting membrane (ILM) (Reis et al., 2012b; Chauhan et al., 2013). Within the radial OCT scans, MRW, and the angle between MRW and BMO plane, can then be used to calculate minimum rim area (MRA) to estimate the minimum area through which the RGC axons must pass (Gardiner et al., 2014), see Figure 2.13e.

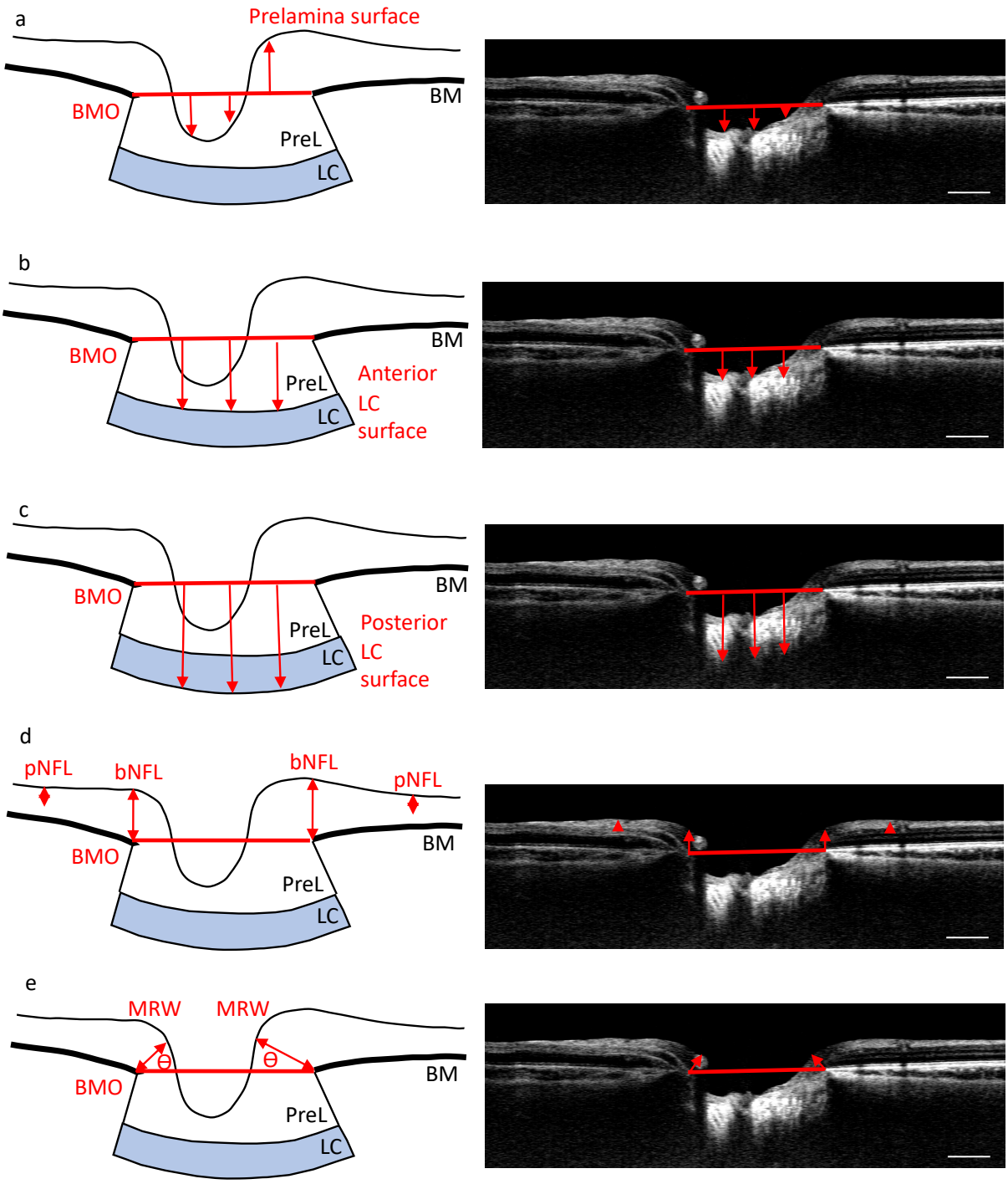

Figure 2.13: Schematic diagram and OCT image depicting depth measurements of prelamina surface (a), anterior LC surface (b), posterior LC surface (c), retinal nerve fibre layer thicknesses (d), and minimum rim width (e). Bruch's membrane opening (BMO) used as reference plane. Measurements taken at centre of BMO and two quartiles either side. Border nerve fibre layer (bNFL) and peripapillary nerve fibre layer (pNFL) thicknesses measured at edge of BMO and 1.7mm from centre of BMO. Minimum rim width measured from BMO termination to inner limiting membrane at angle θ from BMO plane. PreL = prelamina, LC = lamina cribrosa and BM = Bruch's membrane. Scale bar = 500µm.

Minimum rim area was calculated using the formula for area of a trapezium for each sector of the ONH. The base of the trapezium was calculated as 2πr/8, where r is the radius from ONH centre to BMO termination. The height of each trapezium equals the rim width at angle θ from BMO plane (RW_θ). The top length of the trapezium was calculated as: 2πr/8 x (r – RW_θ *cos(θ)). Therefore, the MRA for each sector was calculated as: (top + base) x RW_θ /2, as proposed by Gardiner et al. (2014).

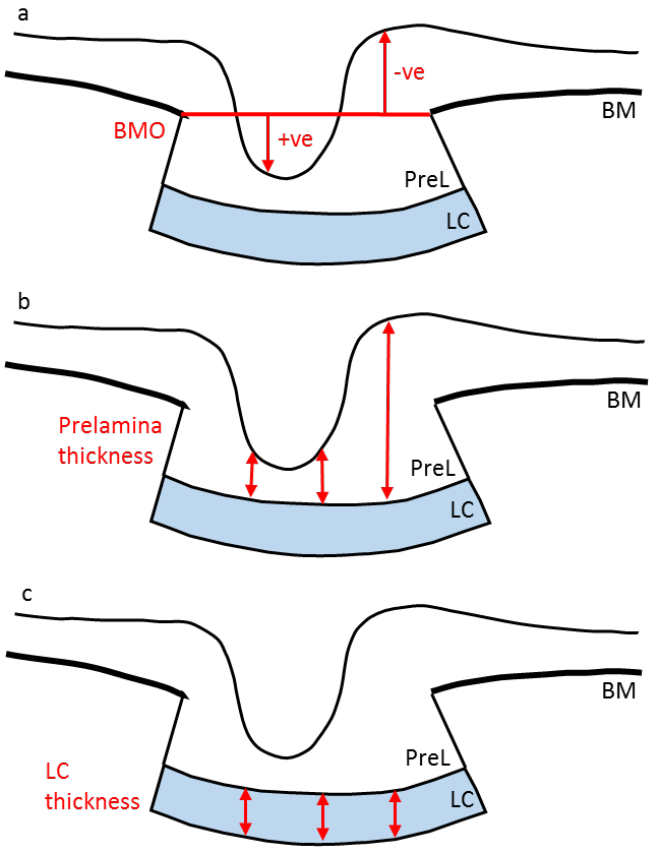

Figure 2.14: Schematic diagram annotating positive and negative recordings of prelamina surface using Bruch's membrane opening (BMO) as reference plane (a), followed by calculation of prelamina thickness (b) and lamina cribrosa thickness (c). BM = Bruch's membrane, PreL = prelamina and LC = lamina cribrosa.

II.13.1 Intra-session repeatability of ONH depth and thickness measurements

To determine intra-session repeatability of ONH measurements, 20 healthy control participants were recruited from within Cardiff University School of Optometry and Vision Sciences. Inclusion and exclusion criteria for the repeatability study was the same as for the control participants, as described in section II.2. ONH parameter measurements included: BMO diameter, prelamina depth and thickness, anterior and posterior LC depth, and LC

thickness. Repeatability was determined using data acquired from triplicate image datasets and analysed in the following ONH regions: superior (S), inferior (I), nasal (N), temporal (T), and central (C), obtained from N-T and S-I orientated OCT tomograms. As both orientations contain the central region of the ONH, central measures were recorded as the average obtained from both OCT tomograms.

Intra-session repeatability of regional ONH depth and thickness measurements was analysed in the Statistical Package for the Social Sciences (SPSS; version 25.0, Chicago, USA). Normality of data was determined using histograms and the Shapiro-Wilk test, $P > 0.05$ for normal distribution. Depending on normality of data, repeated measures ANOVA or the Friedman test were used to determine significant differences between regional ONH parameter measurements acquired from triplicate OCT image datasets. Statistical significance was assumed when $P<0.05$. Additionally, the intraclass correlation coefficient (ICC) was calculated to determine the agreement of a single observer's measurements using a two-way mixed-effects model (i.e., ICC 3,1), as outlined by (Shrout and Fleiss, 1979; Koo and Li, 2016). ICC scores ≥ 0.75, between 0.4 and 0.75, and ≤ 0.4 are considered excellent, moderate, and poor respectively (Fleiss, 1986).

The calculated ICCs for triplicate OCT image datasets from the C, S, I, N, T ONH parameters; prelamina depth and thickness, anterior and posterior LC depth, and vertical and horizontal BMO width showed excellent agreement between measurements, with the ICC being greater than 0.89 for each ONH parameter, in all regions. The calculated ICCs for LC thickness also showed moderate to excellent agreement, with the ICC being at least 0.7 in all ONH regions. Additionally, no significant differences were observed between triplicate image datasets of regional measures of any ONH parameter, as shown in Table 2.3.

Bland-Altman plots were used to assess agreement between measurements performed on triplicate images acquired at the same imaging session (Bland and Altman, 1996). The mean difference (bias) and 95% limits of agreement (LOA) were calculated for each pairwise comparison. The 95% LOA were defined as the mean difference $\pm$ 1.96 standard deviations (Bland and Altman, 1986). Bland -Altman plots were generated for central prelamina depth

and thickness (Figure 2.15), anterior and posterior LC depth (Figure 2.16), and LC thickness (Figure 2.17).

A limitation in the use of healthy controls to evaluate measurement variability is that the repeatability of such measures may be overestimated. Since ONH structure alters with advancement of glaucoma disease, the variability of ONH measures is likely to be higher in POAG participants. Furthermore, high myopia and ONH features such as a tilted disc may further influence ONH parameters (Oliveira et al., 2007; Jonas and Xu, 2014). This would add variability to the ONH parameters measured which was not evident in this study as refractive error of all participants was refined to within ±6.00 dioptres.

ONH Parameter	Region	ICC for Image Comparison			*P*-Value
		Image 1 vs 2	Image 1 vs 3	Image 2 vs 3	
Prelamina Depth	Centre	0.99	0.99	0.99	0.998*
	Superior	0.94	0.96	0.97	0.848φ
	Inferior	0.94	0.95	0.98	0.898φ
	Nasal	0.98	0.98	0.96	0.997*
	Temporal	0.99	0.99	0.99	0.980φ
Prelamina Thickness	Centre	0.99	0.99	0.98	0.986φ
	Superior	0.94	0.96	0.96	0.900φ
	Inferior	0.96	0.96	0.96	0.939φ
	Nasal	0.95	0.99	0.96	0.685φ
	Temporal	0.99	0.99	0.96	0.898φ
Anterior LC Depth	Centre	0.99	0.99	0.98	0.960φ
	Superior	0.98	0.99	0.99	0.969φ
	Inferior	0.94	0.99	0.94	0.848φ
	Nasal	0.89	0.99	0.91	0.996φ
	Temporal	0.95	0.99	0.98	0.855φ
Posterior LC Depth	Centre	0.98	0.99	0.99	0.891φ
	Superior	0.97	0.98	0.96	0.906 φ
	Inferior	0.96	0.97	0.98	0.845 φ
	Nasal	0.95	0.98	0.95	0.722φ
	Temporal	0.91	0.98	0.91	0.991φ
LC Thickness	Centre	0.90	0.92	0.90	0.792φ
	Superior	0.89	0.94	0.90	0.724 φ
	Inferior	0.72	0.94	0.75	0.991 *
	Nasal	0.73	0.85	0.74	0.756φ
	Temporal	0.81	0.95	0.80	0.971*
BMO Diameter	N-T	0.97	0.99	0.98	0.780*
	S-I	0.96	0.97	0.97	0.945φ

Table 2.3: ICC calculated for intra-session repeatability of ONH measurements acquired from triplicate OCT image datasets. *P*-value determined by repeated measures ANOVA (*) or Friedman test (φ).

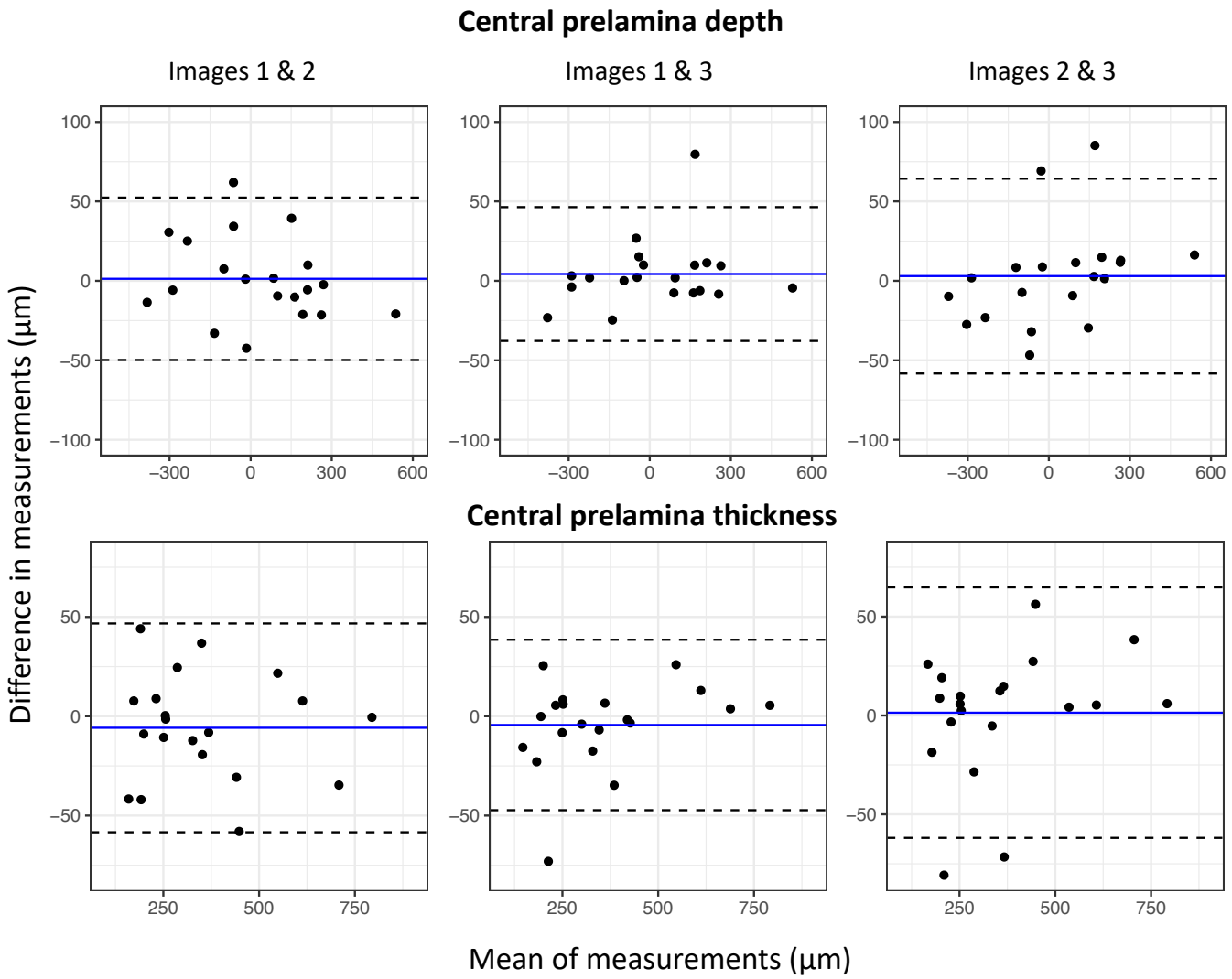

Figure 2.15: Bland-Altman plots for central prelamina depth and thickness for measurements performed on triplicate image datasets. Solid blue line indicates mean difference between measures, dashed black lines indicate mean ± 1.96 standard deviations.

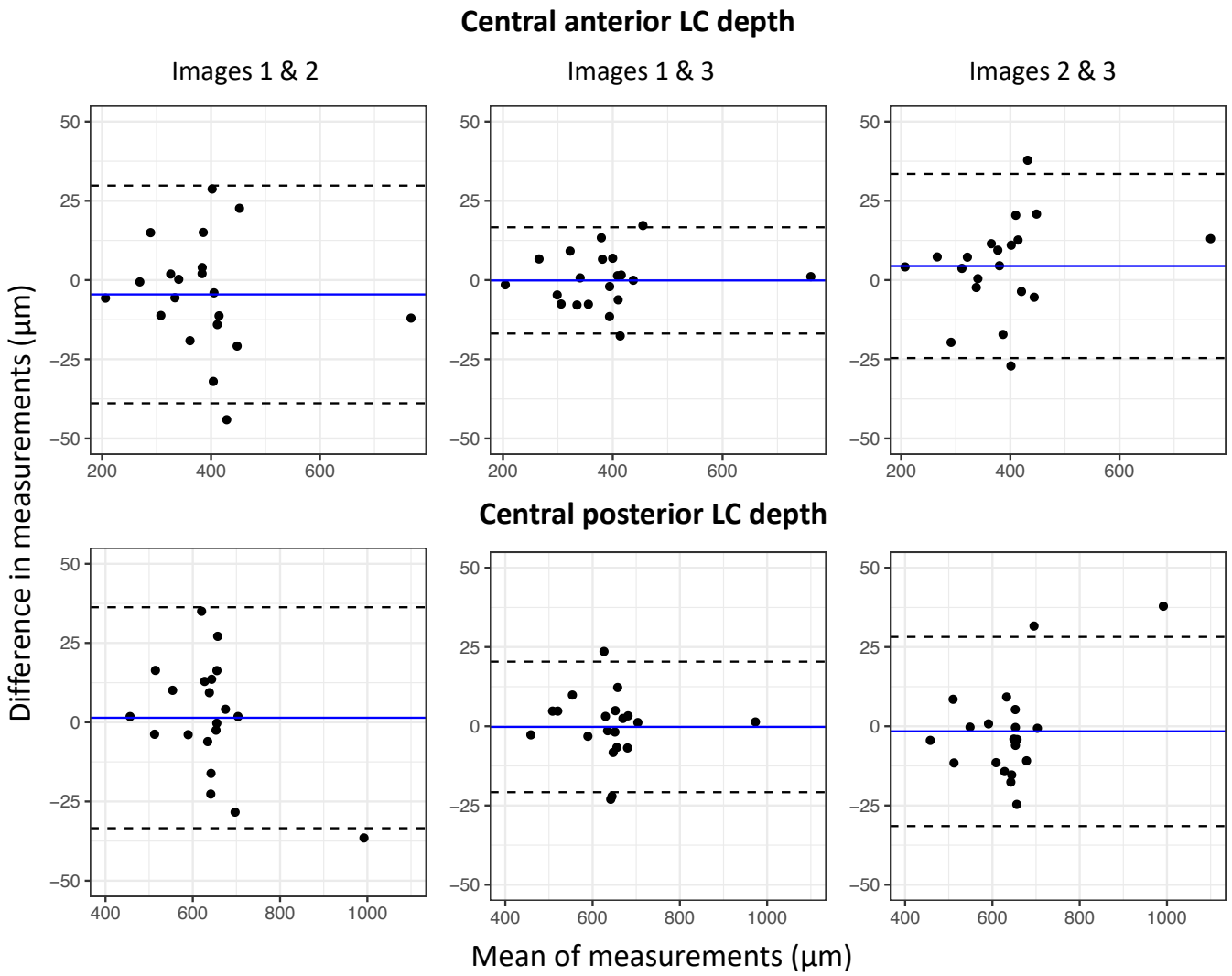

Figure 2.16: Bland-Altman plots for central anterior and posterior lamina cribrosa (LC) depth for measurements performed on triplicate image datasets. Solid blue line indicates mean difference between measures, dashed black lines indicate mean ± 1.96 standard deviations.

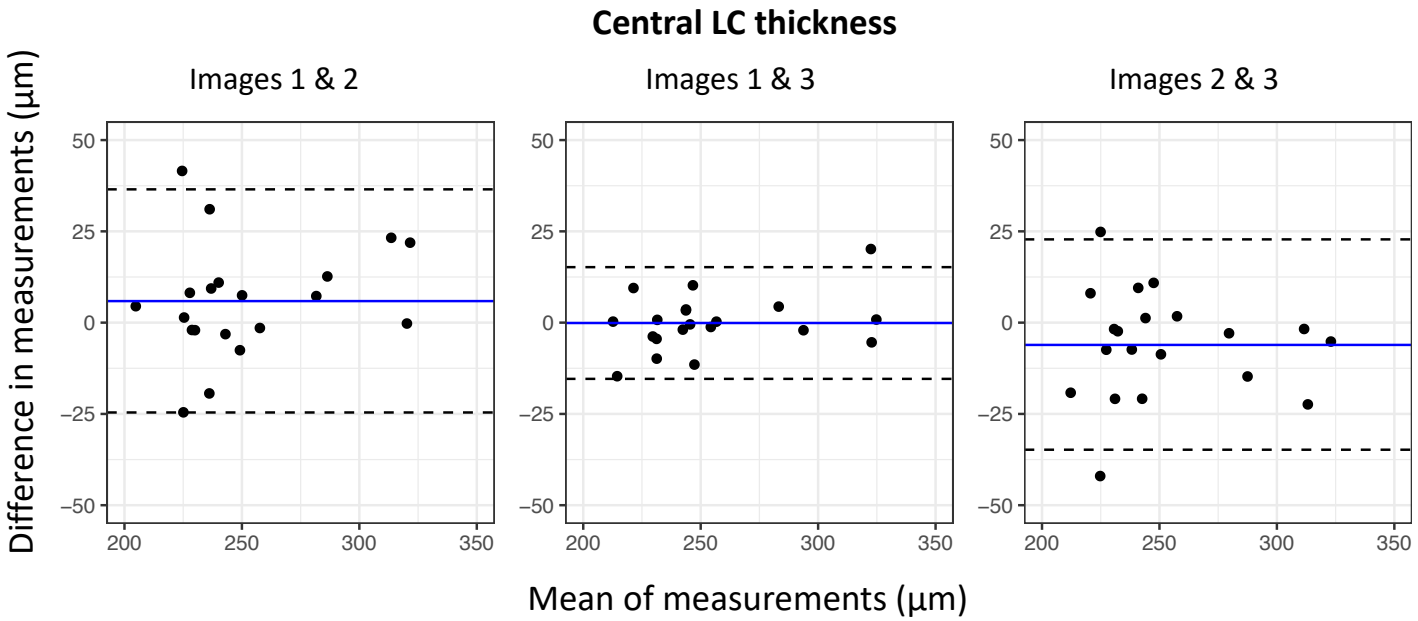

Figure 2.17: Bland-Altman plots for central lamina cribrosa (LC) thickness for measurements performed on triplicate image datasets. Solid blue line indicates mean difference between measures, dashed black lines indicate mean ± 1.96 standard deviations.

II.14 Volumetric measurements of 3D ONH parameters in Glaucoma (Chapter 4)

In healthy controls and participants with POAG, volumetric measurements of ONH parameters were quantified and included optic cup volume, prelamina volume, LC volume, and BMO surface area. The 3D analyses of volumetric ONH parameters were performed on 20° SD-OCT image datasets, subsequent to image registration, noise reduction using 3D median filter, and brightness and contrast adjustment within ImageJ. Additionally, within ImageJ, the OCT datasets were cropped to remove areas including excess vitreous or OCT signal loss.

Each 20° ONH OCT datasets was imported into Amira software (version 6.0, Thermo Fisher Scientific, UK). For each participant, correct lateral and axial pixel calibration was entered, as previously calculated. Within Amira, the ONH image dataset was viewed in the *enface* orientation and the centre of the ONH demarcated with the landmark editor, see Figure 2.18a. The pixel co-ordinates of the landmark denoting ONH centre were noted in the x-y-z axes. A radial reslice through the ONH was selected, with its origin set at the pixel co-ordinates of ONH centre. Within the ONH slice, landmarks were placed at BMO terminations, see Figure 2.18b.

The radial slice was rotated at 15° intervals around ONH centre. Additional landmarks were placed at BMO terminations around the ONH, see Figure 2.18c. Bruch's membrane terminations were demarcated around the entire ONH border, see Figure 2.18d. The ONH radial slice was then hidden, although with BMO landmarks remaining, see Figure 2.18e. Using the Point-wrap tool within Amira software, BMO landmarks were joined to create a surface (see Figures 2.18 f and g). The surface area of BMO plane when then quantified.

The BMO surface plane was used as a reference plane to acquire measurements of optic cup and prelamina volume. The ONH radial slice was unhidden, and the BMO surface plane superimposed over the OCT tomogram, see Figures 2.18h and 2.19a. Landmarks were placed along BMO surface and at the boundary of the optic cup, i.e., anterior prelamina surface, see Figure 2.19b. The radial slice was rotated around ONH centre at 15° intervals, and additional landmarks placed to demarcate the entire optic cup, see Figures 2.19c, 2.19d, and 2.19e. The

OCT tomogram was hidden, and the optic cup landmarks joined using the Point-wrap tool to generate a 3D surface. The volume of this surface was then quantified to provide optic cup volume posterior to BMO, see Figures 2.19f, 2.19g, and 2.19h.

The optic cup volumetric surface object, and its landmarks were then hidden. The ONH radial slice and BMO surface plane were reactivated. Landmarks were placed along anterior LC surface boundary and BMO surface, see Figures 2.20a and 2.20b. The entire prelamina was then demarcated throughout the ONH at 15° intervals, around ONH centre, see Figures 2.20c and 2.20d. The Point-wrap tool was used to generate a surface object including BMO reference plane and anterior LC surface, i.e., the optic cup and prelamina tissue posterior to BMO. The volume of this surface object was then quantified, see Figures 2.20e and 2.20f. Optic cup volume was then subtracted from this value to calculate prelamina volume posterior to BMO reference plane. The ONH radial slice was again rotated around ONH centre at 15° intervals, and landmarks placed at anterior and posterior LC surfaces. The Point-wrap tool was then used to create a volumetric surface object, and LC volume quantified.

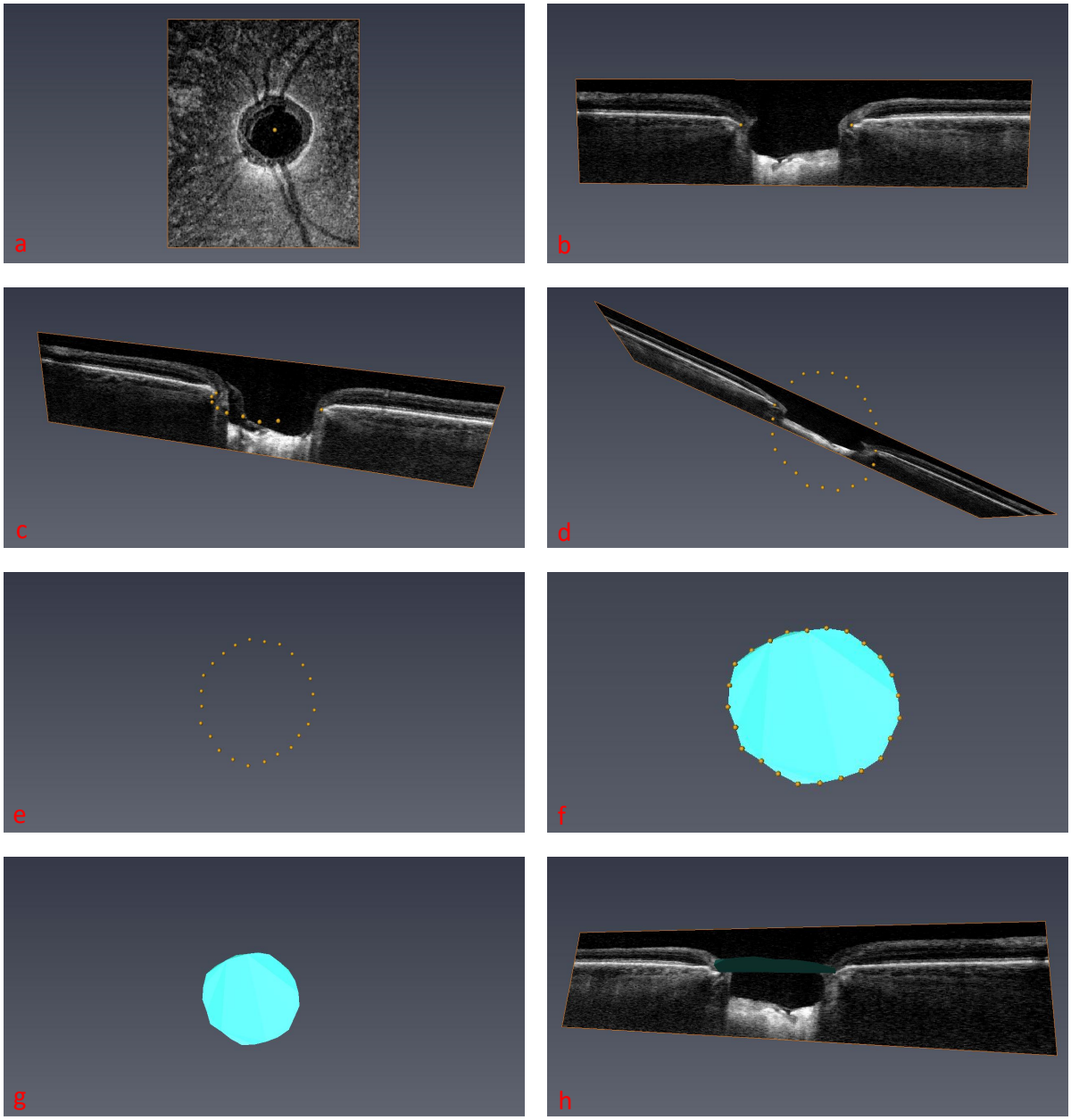

Figure 2.18: Quantification of BMO surface area in an optic nerve head dataset of a 67-year-old male with glaucoma. ONH viewed in *enface* orientation and ONH centre located (a). Bruch's membrane terminations demarcated in radial slice through ONH dataset (b). Radial slice rotated at 15° intervals and BMO demarcated around entire ONH (c and d), and then OCT tomogram hidden (e). Point-wrap tool used to construct BMO surface (f). Landmarks hidden and BMO surface area measured (g). BMO surface plane superimposed over ONH OCT tomogram (h).

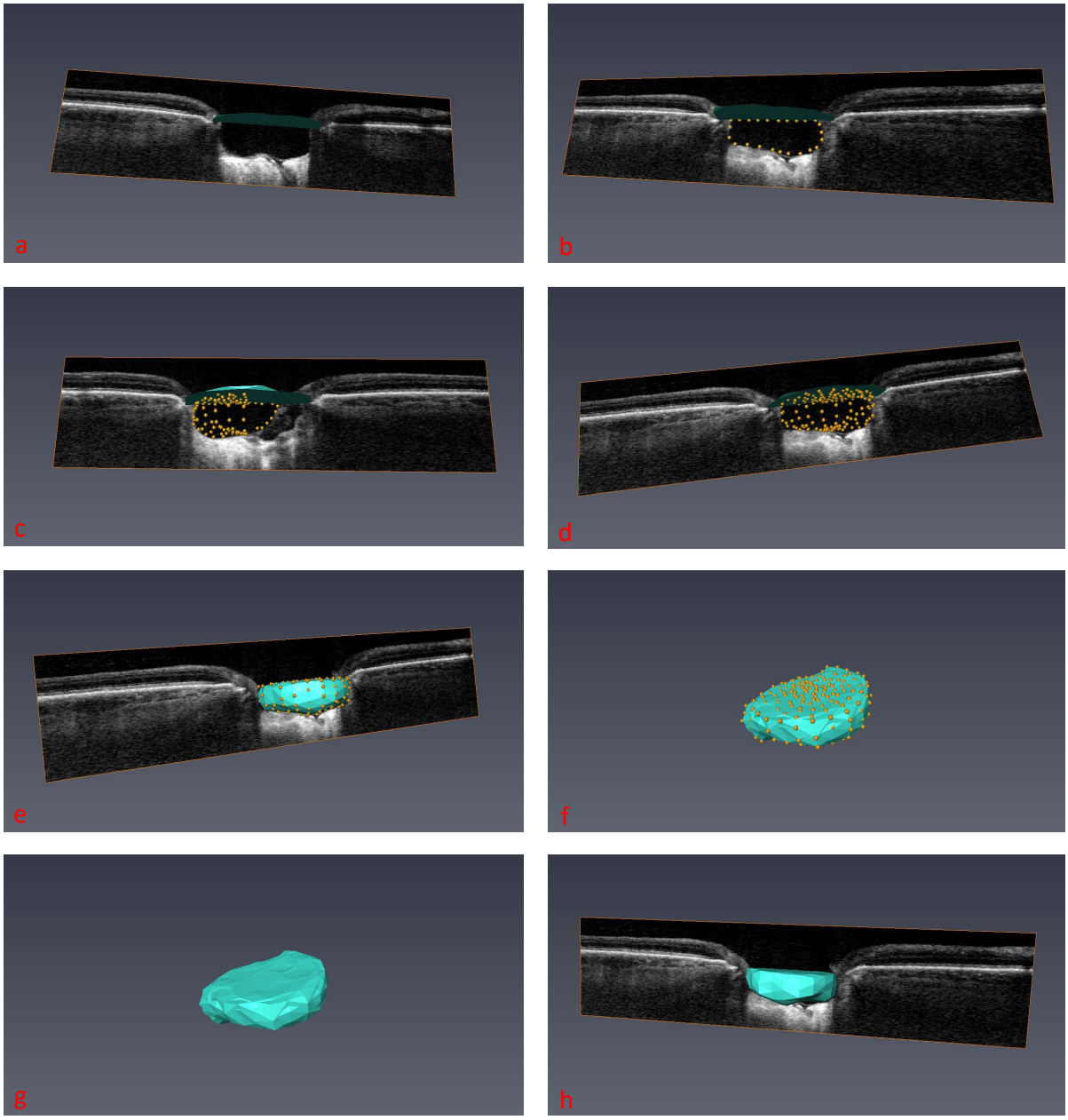

Figure 2.19: Quantification of optic cup volume in an optic nerve head dataset of a 67-year-old male with glaucoma. BMO surface plane superimposed over OCT tomogram (a). Landmarks are placed to demarcate BMO surface and anterior prelamina surface (b). ONH radial slice rotated at 15° intervals until optic cup demarcated throughout entire ONH dataset (c and d). Point-wrap tool used to construct optic cup volumetric surface (e) and OCT tomogram hidden (f). Landmarks were then hidden (g). Optic cup surface superimposed over OCT tomogram and volume quantified (h).

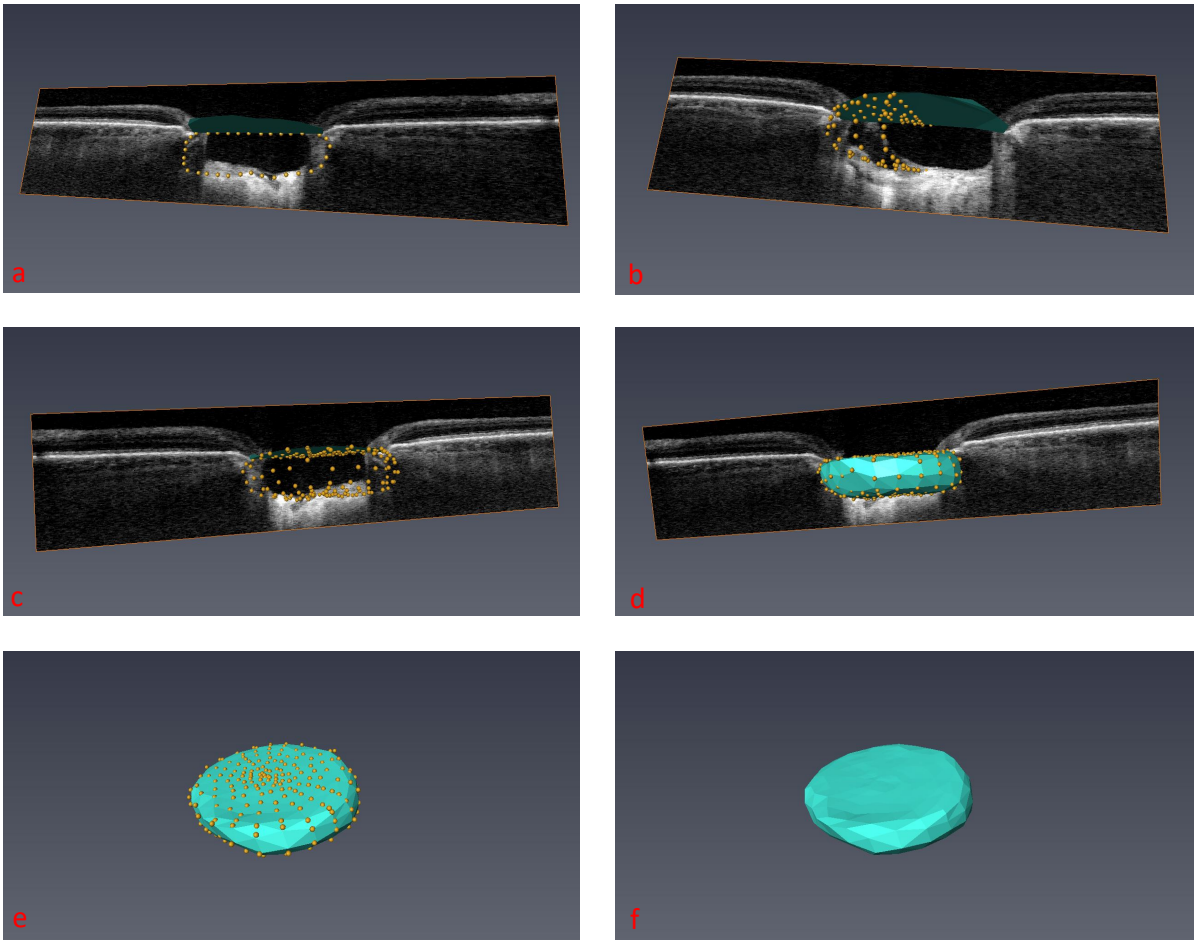

Figure 2.20: Quantification of prelamina volume in an optic nerve head dataset of a 67-year-old male with glaucoma. Landmarks were positioned to demarcate BMO surface and anterior LC surface (a). ONH radial slice rotated at 15° intervals until prelamina demarcated throughout entire ONH dataset (b and c). Point-wrap tool used to construct prelamina volumetric surface (d and e). Landmarks were then hidden and prelamina volume quantified (f).

II.15 Analysis of lamina cribrosa connective tissue microstructural-derived parameters in Glaucoma (Chapter 5)

The following methods were used to evaluate regional measures of LC connective tissue orientation and coherence throughout the depth of the LC in glaucoma and control participants. To allow for greater detail of the LC microstructure to be captured with increased resolution, 10° OCT scans were acquired centred on the ONH. Acquired spectral data was converted to TIFF image format as described in section II.5. Image noise was reduced with a Gaussian blur with sigma 1-1-3 in the x-y-z planes respectively. Each ONH OCT dataset was resliced to *enface* orientation to confirm correct orientation of the dataset against the

participant's fundus photo, as described in section II.8. Brightness and contrast of the image dataset was adjusted as described in section II.10.

Within ImageJ, using the *enface* ONH image dataset, the anterior surface of the LC was located so that central and peripheral LC were visible. Therefore, the anterior LC surface was determined from the central LC, rather than when peripheral LC was visible. Due to the curved nature of the LC, each ONH dataset was cropped 50µm prior to the axial location of the central anterior LC surface – containing both peripheral LC and some prelamina. From this location, the OCT datasets were cropped at 50µm intervals in the axial plane. Each 50µm section was then averaged to create an *enface* OCT slice. This resulted in 4-6 OCT slices per ONH dataset, referred to as S1-S6; representing increasing axial depth through the ONH dataset, shown in Figure 2.21.

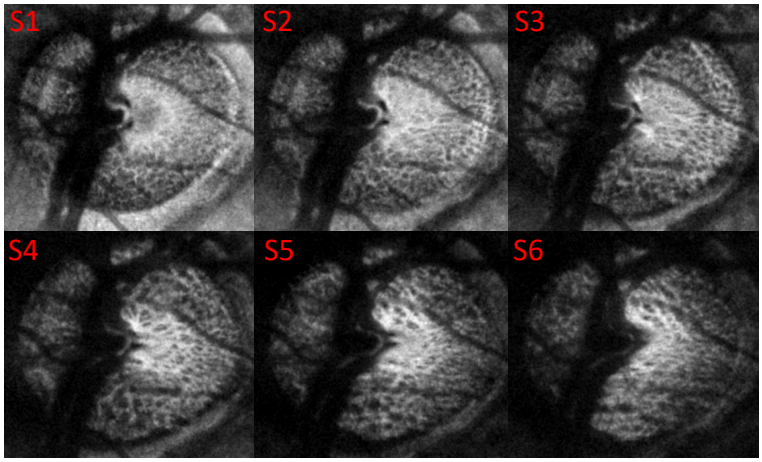

Figure 2.21: Average projections of ONH OCT image datasets of a 72-year-old male control participant created at 50µm intervals with slice 1 (S1) located 50µm prior to the first visibility of the anterior central LC surface – visible in S2.

Each OCT slice (S1-S6) was imported to ImageJ and regional analysis was performed using the 'ONHseg' macro (Version 1.0, N White, VSBL, Cardiff University). The plugin 'ONHseg' allows the ONH OCT slice to be divided into clock-hour segments, as shown in Figure 2.22.

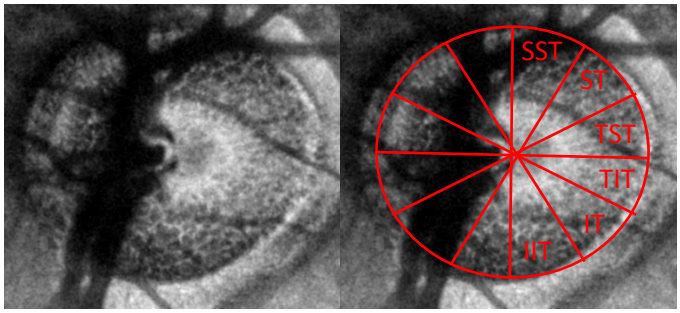

Figure 2.22: Averaged projections of ONH OCT image datasets of a 72-year-old male control participant divided into clock-hour segments for regional analysis of LC connective tissue. S = superior, I = inferior, T = temporal.

The ImageJ plugin 'OrientationJ' (Version 16.01.2018, Resakhaniha et al. 2012, Biomedical Imaging Group, Sweden) was used to determine the preferred orientation (direction of alignment) and coherence (degree of alignment) of ONH connective tissue within the regions specified by the 'ONHseg' macro. Orientation was defined as the dominant direction of features within a region of interest; specified as a value within ± 90°. A value of 0° represented features orientated in the horizontal x-axis, whereas +90° indicated the vertical y-axis in the superior meridian, and -90° indicated the inferior vertical meridian; outlined in Figure 2.23.

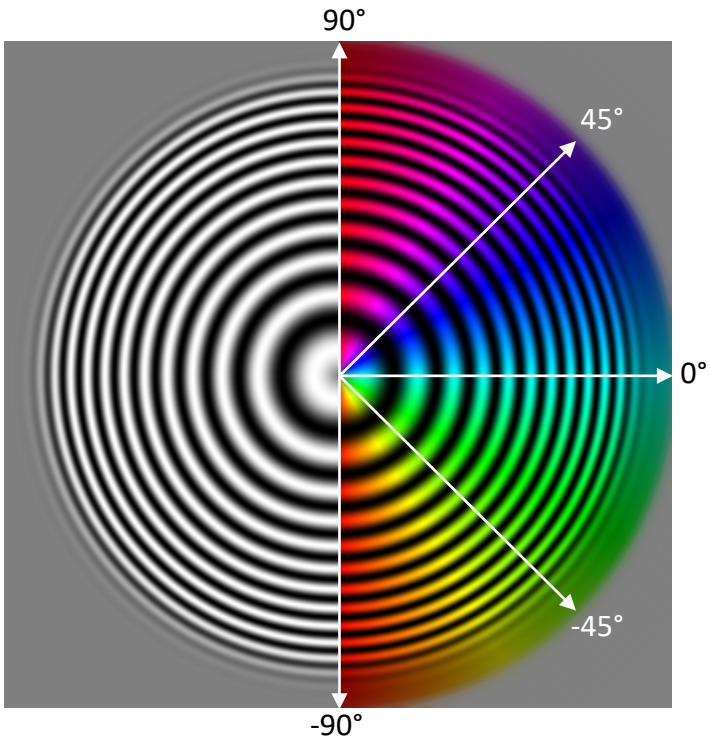

Figure 2.23: Colour map denoting orientation of LC connective tissue within OCT datasets.

Also using OrientationJ, coherence was recorded as a measure of degree of alignment of the features within the region of interest. A coherence result of 1 indicated the features were aligned in a uniform direction. A coherence of 0 indicated the features within the image were arranged randomly. For each OCT slice, colour-coded maps were generated using OrientationJ to represent connective tissue preferred orientation and coherence, allowing visualisation of ONH regions with a higher degree of tissue alignment and the dominant orientation of ONH features. Due to vascular shadowing within the OCT datasets no data was acquired from the nasal side of the ONH. Additionally, regions within the temporal side of the ONH which contained major blood vessels were also excluded from analysis. For example, as outlined in Figure 2.22; whereby region SST was excluded from analysis.

II.16 Statistical analysis

II.16.1 Statistical analyses to evaluate ONH structure with respect to Glaucoma disease

Statistical analyses were performed within RStudio, version 1.2.1335, RStudio Team (2015). RStudio: Integrated Development for R. RStudio, Inc, Boston, USA; www.rstudio.com. Normality of data was determined using histograms, density plots, and the Shapiro-Wilk test. For normally distributed data, associations were analysed using Pearson's correlation coefficient, $P < 0.05$ assumed statistical significance. For non-normally distributed data, associations were analysed using Spearman's rank correlation, $P < 0.05$ for significance. The package 'ggplot2' (Wickham, 2016; http://cran.r-project.org/package=ggplot2) was used to generate graphs.

II.16.2 Linear mixed-effects regression models

In analyses, where possible, data from both eyes of glaucoma and control participants were used in this study. To account for the correlation of data between eyes of the same participant, mixed-effects statistical models (i.e., general linear models) were constructed including a repeated-measures component (i.e., a random term specified by participant). Linear mixed-effects regression models were fitted using the package 'lme4' within R statistics (Bates et al., 2015; http://cran.r-project.org/package=lme4). Initially, each mixed-effects regression model included fixed effects such as participant age, and ocular parameters including stage of glaucoma (Dx), axial length (AxL), mean spherical refractive error (MS),

anterior chamber depth (ACD), central corneal thickness (CCT), and intraocular pressure (IOP). This approach allowed identification of which factors had a significant effect on a given ONH parameter. Linear mixed-effects regression models were optimised via stepwise deletion of the fixed effects, in order to determine the association between each fixed effect and each ONH parameter.

II.16.3 Model interpretation

The results of each optimised regression model indicated which of the fixed effects had a significant association with each ONH parameter. Within each model, for continuous variables, e.g., age, the effect sizes on each ONH parameter are presented as effect size ± standard error, t-value, *p*-value, i.e., how much a given ONH parameter will change per unit change in the independent variable. The t-value is the effect size divided by its standard error; and describes the effect size of a given association, while the *p*-value describes statistical significance. Independent variables were considered to have a significant effect on a given ONH parameter if $P < 0.05$.

For categorical independent variables (e.g., stage of glaucoma), inter-group differences were determined using Tukey post-hoc pairwise comparisons, and statistical significance assumed when $P < 0.05$ (following adjustment for multiple comparisons). Tukey post-hoc analysis was performed using the package 'emmeans' (Lenth et al., 2019; http://cran.r-project.org/package=emmeans).

II.16.4 Multivariate analysis (Chapter 6)

In Chapter 6, dimensional reduction was performed on a multivariate ONH dataset using principal component analysis (PCA) and linear discriminant analysis (LDA) with aim to elucidate which ONH parameters allow for the best characterisation of ONHs according to glaucoma disease stage. The multivariate ONH dataset contained regional measures of prelamina depth and thickness, LC thickness, bNFL, pNFL, MRW, MRA, and volumetric measurements of optic cup and prelamina volume, and BMO surface area. Principal component analysis was aimed at summarising the variation within several variables into fewer new variables: namely principal components (PCs). The resulting PCs were generated

as linear combinations of all the ONH variables and are uncorrelated (i.e., orthogonal) with each other. Within R, the function 'prcomp' was used to perform PCA.

Linear discriminant analysis identifies axes that allow for the maximum separation between known group classifications. The resulting linear discriminants (LDs) are linear combinations of all the ONH variables that provide the most effective discrimination between observations. Linear discriminant analysis was performed using the 'MASS' package (Venables and Ripley 2002, http://cran.r-project.org/package=MASS).

Cluster analysis was used to identify groups of observations according to glaucoma disease stage (i.e., controls, PG, EG, and MAG) that were similar/dissimilar to each other based upon the distance between pairs of observations within the multivariate dataset. Therefore, groups of observations that were similar to each other are clustered together. Within R, the 'hclust' function was used to perform hierarchical cluster analysis, and the 'kmeans' function was used to perform K-means clustering. More details are provided in chapter 6.

II.17 Summary

This chapter has described the methodology used for each experimental chapter along with statistical analyses performed, including the intra-session repeatability of regional ONH depth and thickness measurements. Experimental design and sample size included will be described in detail within each experimental chapter.

III. Chapter 3: Evaluation of ONH depth and thickness parameters in Glaucoma

III.1 Introduction

Since glaucomatous disease is characterised by optic nerve head (ONH) structural changes, including enlargement of the optic cup, and retinal nerve fibre layer (RNFL) thinning with consequent visual field impairment (Weinreb and Khaw, 2004; Balaratnasingam et al., 2007), their evaluation is essential for the detection and monitoring of glaucoma disease. Since there is a dissociation between structural and functional alterations in glaucoma, both assessment of the ONH and VF analysis are essential in glaucoma disease evaluation (Bowd et al., 2000; Weinreb and Khaw, 2004; Spaeth et al., 2006; Chauhan et al., 2013; Tatham et al., 2013; Weinreb et al., 2014; Jonas et al., 2017).

The ONH comprises the prelamina tissue with bundles of RGC axons, astrocytes and capillaries (Anderson and Hoyt, 1969; Hernandez et al., 1986; Ye and Hernandez, 1995; Hernandez and Pena, 1997) and the LC with its horizontally oriented connective tissue sheets (Anderson, 1969; Quigley and Addicks, 1981). The LC has been implicated as the primary site of injury to RGC axons, and an important factor in the pathogenesis of glaucoma (Quigley and Anderson, 1976; Quigley et al., 1981; Weinreb et al., 2014; Downs and Girkin, 2017). In glaucomatous optic neuropathy, posterior migration, compression (Yan et al., 1994), and deformation of the LC have been proposed as pathophysiological mechanisms accompanying RGC axonal transport disruption and damage (Minckler et al., 1977; Quigley et al., 1981; Quigley et al., 1983; Quigley, 1987; Balaratnasingam et al., 2007; Downs et al., 2011; Downs and Girkin, 2017).

Optical coherence tomography (OCT) allows for non-invasive, non-contact, *in vivo* imaging of the anterior eye (Izatt et al., 1994), as well as posterior ocular structures such as the optic disc (Fercher et al., 1993; Hee et al., 1995) and fovea (Swanson et al., 1993; Puliafito et al., 1995). In particular, *in vivo* imaging such as EDI-OCT has augmented evaluation of LC position (Park et al., 2012b), and thickness (Park et al., 2012a), and characterisation of the anterior LC

surface shape (Kiumehr et al., 2012; Park et al., 2012c) Focal LC defects (LC holes or disinsertions) have been reported (Takayama et al. (2013) in association with glaucomatous neuroretinal rim loss (You et al., 2013). Other *in vivo* studies have reported displacement of the prelamina following acute elevation of IOP in glaucomatous ONHs (Agoumi et al., 2011), and posterior LC displacement has been linked to increased visual field loss in glaucoma (Furlanetto et al., 2013).

Regional structural differences within the LC (Quigley and Addicks, 1981; Radius and Gonzales, 1981; Dandona et al., 1990), namely that the superior and inferior LC poles contain less connective tissue and larger LC pores than in the nasal-temporal LC, has been implicated in the development of the typical arcuate VF defect seen in glaucoma (Quigley et al., 1982; Quigley et al., 1983).

It is likely that ONH structure plays an important role in glaucoma pathophysiology. However, glaucomatous regional ONH alterations have not been investigated in detail, with the majority of studies focusing on the vertical (superior-inferior) ONH meridian (Lee et al., 2011; Furlanetto et al., 2013; Kim et al., 2013a; Park et al., 2015; Prata et al., 2017). Therefore, this current study is novel in that it is the first to quantify regional ONH structure as a function of glaucoma disease stage *in vivo*.

III.2 Aims of chapter

The hypothesis of this chapter is that regional ONH and axon-related parameters undergo structural changes in POAG that correspond to visual field loss in glaucoma.

The aim of this cross-sectional study was to assess regional microstructural optic nerve head parameters *in vivo* in control and glaucoma participants, at different stages of glaucomatous disease to determine changes in axon and ONH-related parameters that best describe early-stage disease.

III.3 Experimental design

Glaucoma (n=64) and control (n=30) participants were recruited according to defined inclusion and exclusion criteria described in section II.2. All participants underwent clinical ocular assessments as described in section II.3.

Enhanced depth imaging OCT was performed centred on the ONH (127 glaucomatous eyes and 60 control eyes) of all participants to acquire 20° scans, composed of 512 x 512 A-scans. Processing of acquired spectral data, OCT image registration, and 3D image filtering was performed, as described in sections II.5 and II.6. One glaucomatous eye was excluded from analyses due to OCT image artefacts preventing accurate measurement of ONH structures. Participant ONHs were subdivided into groups according to disease stage. Participant demographics are presented in Table 3.1.

Characteristic	**Control**	**PG**	**EG**	**MAG**
	N=60 eyes	N=32 eyes	N=69 eyes	N=26 eyes
	Mean ± Standard Deviation			
Age (years)	65.6 ± 6.4	68.2 ± 9.6	72.4 ± 8.5	74.2 ± 8.6
Gender	32 F & 28 M	18 F & 14 M	36 F & 33 M	12 F & 14 M
MS (D)	0.79 ± 1.89	-0.18 ± 2.81	0.29 ± 2.41	0.14 ± 2.13
VA (logMAR)	-0.04 ± 0.09	0.06 ± 0.10	0.11 ± 0.13	0.16 ± 0.17
IOP (mmHg)	15.2 ± 3.2	13.3 ± 2.1	13.3 ± 2.4	12.0 ± 2.5
AEL (mm)	23.7 ± 1.0	23.9 ± 1.7	23.9 ± 1.3	24.1 ± 1.3
CCT (μm)	560.4 ± 41.3	528.9 ± 30.8	530.1 ± 44.5	521.2 ± 34.2
ACD (mm)	2.83 ± 0.6	2.97 ± 0.7	3.21 ± 0.9	3.21 ± 0.9
VF MD (dB)	-0.45 ± 1.16	-0.34 ± 1.13	-3.02 ± 1.68	-10.65 ± 4.71

Table 3.1: Participant characteristics for glaucoma and control eyes, MS = mean sphere, VA = visual acuity, IOP = intraocular pressure, AEL = axial eye length, CCT = central corneal thickness, ACD = anterior chamber depth, VF MD = visual field Mean Deviation.

III.4 Analysis of regional ONH depth and thickness parameters

The volumetric 3D OCT image datasets were resliced radially every 45° around the centre of the ONH (using reslice_on_centroid_V2; J Fergusson, VSBL, Cardiff University, see section II. 9) to produce 4 radial OCT tomograms with ONH orientations: superior–inferior (S-I), nasal-temporal (N-T), and diagonally; SN-IT and ST-IN (see section 2.10). Following isotropic scaling (section II.10) and image contrast adjustment (section II.11.), the terminations of Bruch's

membrane opening (BMO) were determined and BMO diameter was drawn, measured and recorded in each OCT tomogram. As a measure of ONH ovality and to account for normal variation in ocular dimensions, the ratio of BMO diameter in the vertical and horizontal meridians was calculated (i.e., S-I BMO/N-T BMO); such that a larger ratio indicated a more vertically oval ONH.

Thereafter BMO diameter was used as a reference plane for subsequent regional ONH measurements at the midpoint of BMO diameter and at two quartiles either side of BMO centre. As described in section II.12, measurements of BMO diameter, NFL (border and peripapillary) thickness, minimum rim width (MRW) and area (MRA) were performed in the superior (S), inferior (I), nasal (N), temporal (T), SN, IT, ST and IN regions of the ONH. Prelamina depth and thickness, and LC depth and thickness measures were performed in the same regions, and additionally in the ONH centre (see section II.12).

III.5 Statistical analysis

Statistical analysis was performed within RStudio, version 1.2.1335, as described in section II.16. Normality of data was determined using histograms, density plots, and the Shapiro-Wilk test, with $P < 0.05$ as the level of significance. To account for data being used from both eyes of each participant, linear mixed-effects regression models were fitted using the package 'lme4' (Bates et al., 2015; http://cran.r-project.org/package=lme4). Inter-group differences were determined using Tukey's post-hoc analysis; package 'emmeans' (Lenth et al., 2019; http://cran.r-project.org/package=emmeans), and *P*-values adjusted for multiple comparisons; $P < 0.05$ as significance level. Correlations were examined using Pearson's correlation for normally distributed data, and Spearman's rank correlation for non-normally distributed data. Graphs were generated using the package 'ggplot2' (Wickham, 2016; http://cran.r-project.org/package =ggplot2).

III.6 Results

III.6.1 Multivariate analysis of ocular parameters effect on Bruch's membrane opening diameter

A number of factors were included in optimisation of a mixed effect regression model for analysis of BMO parameters to determine their contribution (see Table 3.3). Stage of glaucoma was found to be a significant factor in statistical models for the determination of inter-group differences in BMO diameter in all four ONH orientations and the BMO ratio ($P < 0.05$, Table 3.3). Axial length, with the exception of the vertical BMO diameter, significantly contributed to BMO variance in all orientations ($P \leq 0.001$), as well as the S-I/N-T ratio of BMO diameter ($P \leq 0.001$); i.e., a larger axial length was associated with larger BMO diameters and a smaller S-I/N-T ratio. The latter indicated that eyes with a longer axial length had a more circular ONH. This observation was not as expected as myopic eyes often display ONH structural features such as tilting and deformation of the optic disc and variation in ONH size and shape (Shoji et al., 2011; Jonas and Xu, 2014). However, this finding might be explained since the V:H BMO ratio accounts for normal biological variation in ONH size, therefore such findings that could be associated with increasing axial length may not be observed since variation in ONH size has been accounted for.

Anterior chamber depth had a significant negative association with ST-IN BMO diameter only ($P = 0.041$). Age, mean-spherical correction, central corneal thickness and intraocular pressure had no significant association with BMO diameters or the vertical-to-horizontal BMO ratio (see Table 3.3), and were therefore excluded from the optimised linear mixed-effects regression models used to determine inter-glaucoma stage differences described below.

III.6.2 Bruch's membrane opening as a function of glaucoma disease stage and visual field sensitivity

BMO diameter (vertical: S-I, horizontal: N-T, and diagonals: SN-IT and ST-IN) as a function of disease stage and visual field sensitivity is demonstrated in Figure 3.1 (data are shown in Table III.1 in Appendix II). The horizontal BMO diameter was significantly larger in MAG than that in EG ($P = 0.013$), but vertical and diagonal BMO diameters did not vary as a function of glaucoma disease stage. The V:H BMO ratio significantly increased in EG, compared to in PG

(*P* = 0.004). No other differences in V:H BMO ratio were determined between glaucoma stages (*P* > 0.05; see Table 3.2 and Figure 3.1). No significant correlations were observed between BMO diameters in any of the ONH orientations, or V:H BMO ratio and VF MD (see Figures 3.1 and 3.2).

BMO (µm)	**Tukey post-hoc Multiple Comparisons: Adjusted *P* values**					
	C-PG	**C-EG**	**C-MAG**	**PG-EG**	**PG-MAG**	**EG-MAG**
S – I	0.546	0.309	0.087	0.981	0.533	0.591
N – T	0.251	0.963	0.068	0.150	0.841	0.013
SN – IT	0.331	0.786	0.095	0.599	0.844	0.120
ST – IN	0.273	0.353	0.182	0.974	0.991	0.858
V:H ratio	0.466	0.189	1.000	0.004	0.553	0.289

Table 3.2: Regional BMO diameters as a function of glaucoma disease stage. S = superior, I =. Inferior, N = nasal, T = temporal, SN = superior-nasal, IT = inferior-temporal, ST = superior-temporal, IN = inferior-nasal, C = control, PG = preperimetric glaucoma, EG = early glaucoma, MAG = moderate-advanced glaucoma. Red text denotes significant differences at $p < 0.05$.

BMO (µm)	Dx (*p*-values)	Age (years)	Age^2 (years)^2	Age^3 (years)^3	AxL (mm)	MS (D)	ACD (mm)	CCT (µm)	IOP (mmHg)
S – I	C: <0.001	0.06 ± 2.19	-0.003 ± 0.17	-0.002 ± 0.01	27.06 ± 17.45	-3.17 ± 9.24	-25.73 ± 18.53	-0.66 ± 0.35	7.71 ± 5.96
t value	PG: 0.185	0.03	-0.02	-0.16	1.55	-0.34	-1.39	-1.86	1.29
p value	EG: 0.085	0.977	0.985	0.876	0.124	0.732	0.167	0.064	0.199
	MAG: 0.019								
N – T	C: 0.466	0.86 ± 2.38	-0.17 ± 0.19	0.002 ± 0.02	71.41 ± 13.35	-7.70 ± 10.09	-21.17	-0.40	4.64 ± 6.51
t value	PG: 0.065	0.36	-0.88	0.10	5.35	-0.76	-0.99	-0.98	0.71
p value	EG: 0.630	0.718	0.381	0.924	<0.001	0.447	0.319	0.328	0.478
	MAG: 0.014								
SN – IT	C: 0.673	-1.21 ± 2.45	-0.23 ± 0.19	0.009 ± 0.02	58.21 ± 13.78	0.91 ± 10.49	-17.01 ± 22.03	-0.33 ± 0.42	1.81 ± 6.70
t value	PG: 0.092	-0.50	-1.16	0.55	4.23	0.09	-0.77	-0.79	0.27
p value	EG: 0.351	0.621	0.251	0.582	<0.001	0.931	0.441	0.433	0.787
	MAG: 0.021								
ST – IN	C: 0.141	0.67 ± 2.28	0.14 ± 0.18	0.001 ± 0.02	48.50 ± 13.58	-2.95 ± 9.92	-42.46 ± 20.60	-0.50 ± 0.40	4.70 ± 6.33
t value	PG: 0.072	0.29	0.75	0.07	3.57	-0.30	-2.06	-1.23	0.74
p value	EG: 0.101	0.771	0.453	0.946	0.001	0.766	0.041	0.219	0.459
	MAG: 0.044								
V:H Ratio	C: <0.001	-0.001 ± 0.001	$6.2e^{-5}$ ± $8.5e^{-5}$	$-5.8e^{-6}$ ± $7.6e^{-6}$	-0.03 ± 0.006	0.009 ± 0.005	-0.004 ± 0.01	-0.0001 ±	0.002 ± 0.003
t value	PG: 0.145	-1.24	0.73	-0.82	-5.03	1.77	-0.33	0.0002	0.58
p value	EG: 0.046	0.217	0.466	0.413	<0.001	0.080	0.743	-0.60	0.563
	MAG: 0.997							0.551	

Table 3.3: Independent variables included in linear mixed-effects regression model for each BMO orientation. Presented as effect size ± standard error (i.e., how much BMO changes per one-unit change in the independent variable), also the t-value and *p*-value. Red text indicates the independent variable had a significant effect at $p < 0.05$. BMO = Bruch's membrane opening, Dx = stage of glaucoma, AxL = axial length, MS = mean sphere refractive error, ACD = anterior chamber depth, CCT = central corneal thickness, IOP = intraocular pressure, S = superior, I = inferior, N = nasal, T = temporal, SN = superior-nasal, IT = inferior-temporal, ST = superior-temporal, IN = inferior-nasal.

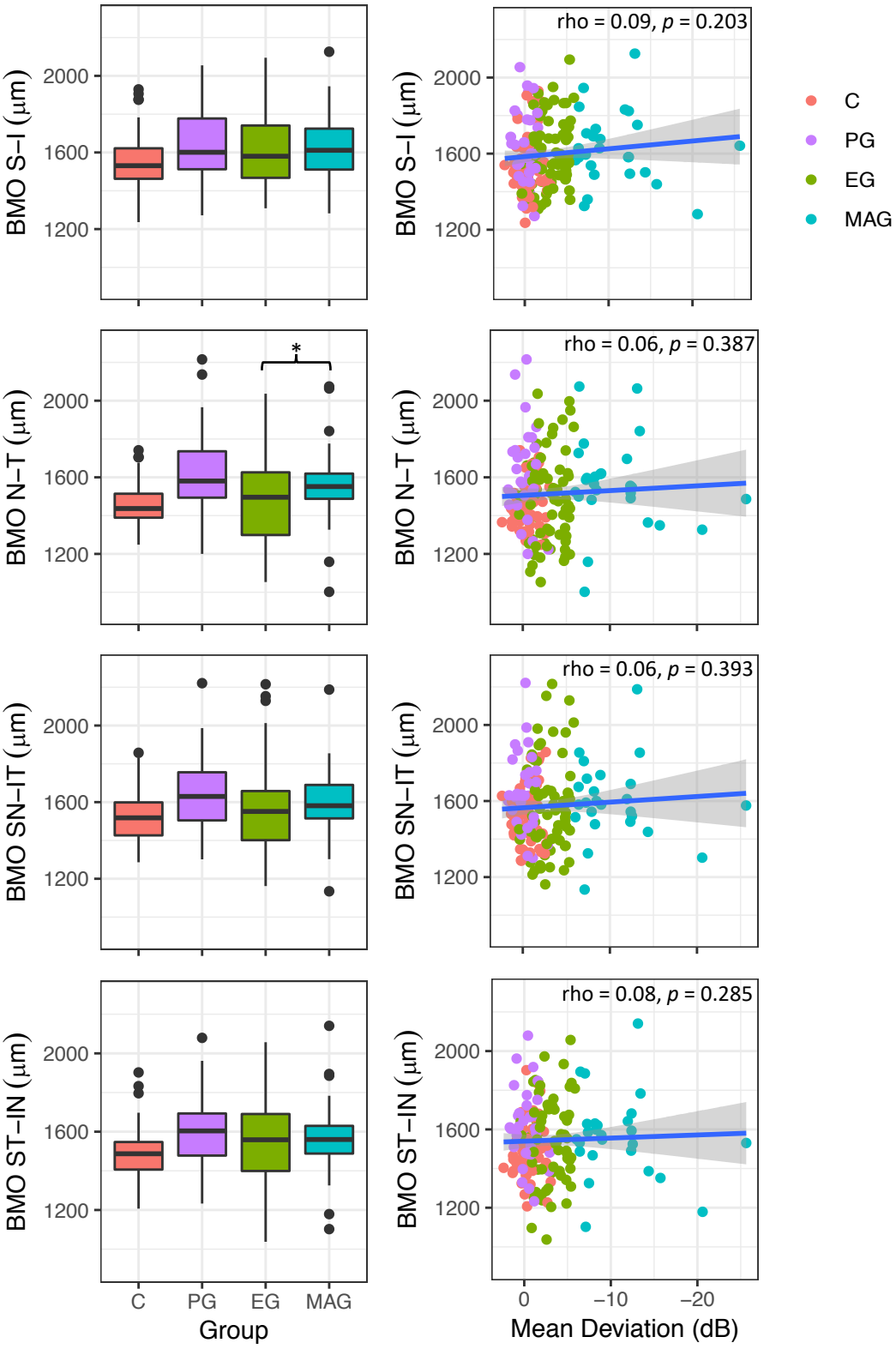

Figure 3.1: Regional measures of BMO diameter for each glaucoma disease stage and against VF Mean Deviation. Box plots denote group median value and 1st to 3rd quartiles. Whiskers represent data within 1.5x interquartile range. Black points denote outliers. * represents $P < 0.05$. Blue line represents regression line and grey shading represents 95% confidence intervals.

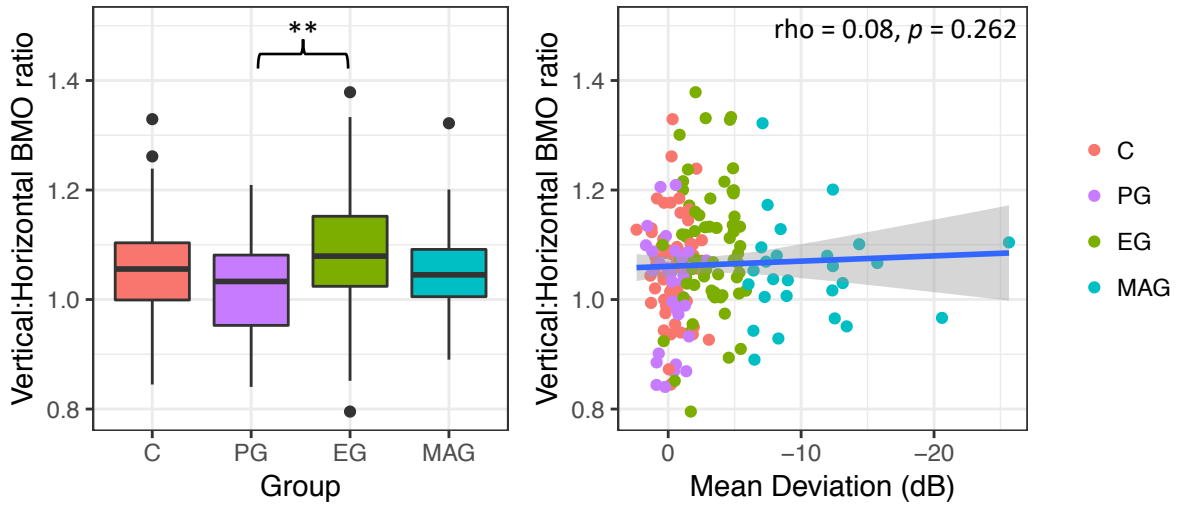

Figure 3.2: Vertical to horizontal BMO ratio for each glaucoma disease stage and against Mean Deviation. Box plots denote group median value and 1st to 3rd quartiles. Whiskers represent data within 1.5x interquartile range. Black points denote outliers. ** represents $P < 0.01$. Blue line on scatter plot is regression line and grey shading represents 95% confidence intervals.

III.6.3 Multivariate analysis of ocular parameters effect on prelamina depth and thickness

Multivariate analysis revealed that stage of glaucoma significantly contributed to prelamina depth and thickness in all ONH regions ($P < 0.001$, see Tables 3.4 and 3.5). Central corneal thickness (CCT) had a significant negative association with prelamina depth in all ONH regions ($P < 0.02$), except for the inferior-temporal and inferior-nasal regions i.e., eyes with thinner corneas were associated with greater prelamina depth (more posterior to BMO). Additionally, CCT significantly affected prelamina thickness in the superior (0.94 ± 0.34 µm/µm, $P = 0.006$) and superior-temporal regions (0.89 ± 0.28 µm/µm, $P = 0.002$); a greater prelamina thickness in these regions was associated with eyes with thicker corneas.

Axial eye length was significantly associated with prelamina depth in the nasal ONH region (42.09 ± 15.39 µm/mm, $P = 0.007$), meaning that eyes with larger axial length had a larger nasal prelamina depth. In the ST region, axial length had a significant negative effect on prelamina thickness (-25.55 ± 12.79 µm/mm, $P = 0.048$), i.e., eyes with larger axial length displayed thinner ST prelamina. Mean spherical refractive error was significantly associated with ST prelamina depth (14.14 ± 6.85 µm/D, $P = 0.041$), indicating that an eye with a more hyperopic correction had a greater ST prelamina depth. Mean sphere refractive error was negatively associated with ST prelamina thickness (-19.47 ± 6.87 µm/D, $P = 0.005$), as well as

the temporal (-11.66 ± 4.90 µm/D, *P* = 0.019) region, such that these prelamina regions were thinner in hyperopic eyes.

Age had a significant negative association with prelamina thickness in the inferior (-5.34 ± 1.66 µm/year, *P* = 0.002), SN (-5.47 ± 1.89 µm/year, *P* = 0.005), IT (-3.86 ± 1.35 µm/year, *P* = 0.005), and IN (-5.77 ± 2.03 µm/year, *P* = 0.006) regions, indicating prelamina thinning with increasing age (Table 3.6). However, age did not contribute to variance in prelamina depth in any ONH region (*P* > 0.05). Furthermore, anterior chamber depth and intraocular pressure had no significant association with prelamina depth or thickness in any region of the ONH (*P* > 0.05, Tables 3.4 and 3.5), so were excluded in optimised models.

To evaluate prelamina depth and thickness as a function of glaucoma disease stage, optimised regression models for each region included all significantly contributing factors outlined above and shown in Tables 3.4 and 3.5.

Prelamina depth (µm)	Dx (*p*-values)	Age (years)	Age^2 (years)^2	Age^3 (years)^3	AxL (mm)	MS (D)	ACD (mm)	CCT (µm)	IOP (mmHg)
Centre	C: 0.002	-1.85 ± 2.13	-0.16 ± 0.17	0.005 ± 0.01	1.99 ± 16.89	3.45 ± 8.95	2.01 ± 18.71	-0.84 ± 0.34	2.48 ± 5.79
t value	PG: 0.022	-0.87	-0.95	0.37	0.12	0.38	0.11	-2.50	0.43
p value	EG: 0.002	0.387	0.343	0.712	0.906	0.700	0.905	0.014	0.669
	MAG: <0.001								
Superior	C: 0.002	1.74 ± 2.64	-0.30 ± 0.21	-0.01 ± 0.02	27.79 ± 21.22	12.02 ± 11.22	-39.59 ± 23.97	-1.45 ± 0.44	8.67 ± 7.29
t value	PG: <0.001	0.66	-1.45	-0.74	1.31	1.31	-1.65	-3.33	1.19
p value	EG: <0.001	0.513	0.151	0.461	0.193	0.193	0.101	0.001	0.237
	MAG: <0.001								
Inferior	C: 0.059	2.86 ± 2.41	0.08 ± 0.19	-0.01 ± 0.02	20.42 ± 19.92	7.46 ± 10.63	-32.03 ± 23.63	-1.01 ± 0.42	-7.15 ± 6.78
t value	PG: 0.002	1.19	0.43	-0.77	1.03	0.70	-1.35	-2.41	-1.05
p value	EG: <0.001	0.238	0.668	0.445	0.308	0.484	0.178	0.017	0.295
	MAG: <0.001								
Nasal	C: 0.688	1.36 ± 2.72	-0.31 ± 0.21	0.01 ± 0.02	42.09 ± 15.39	-0.31 ± 11.87	-31.55 ± 26.12	-1.83 ± 0.46	-4.34 ± 7.67
t value	PG: 0.006	0.50	-1.45	0.65	2.74	-0.03	-1.21	-3.95	-0.56
p value	EG: 0.006	0.618	0.150	0.516	0.007	0.979	0.229	<0.001	0.572
	MAG: <0.001								
Temporal	C: 0.011	-0.04 ± 2.16	-0.05 ± 0.17	-0.01 ± 0.01	2.94 ± 17.63	13.06 ± 9.35	-11.41 ± 20.37	-0.92 ± 0.36	-2.99 ± 6.08
t value	PG: 0.021	-0.02	-0.28	-0.87	0.17	1.39	-0.56	-2.52	-0.49
p value	EG: 0.002	0.983	0.781	0.385	0.868	0.165	0.576	0.013	0.624
	MAG: <0.001								
SN	C: 0.003	3.64 ± 2.63	-0.21 ± 0.21	0.002 ± 0.02	25.79 ± 22.04	-6.49 ± 11.60	-45.74 ± 25.32	-1.57 ± 0.46	3.07 ± 7.43
t value	PG: 0.002	1.39	-1.04	0.11	1.17	-0.56	-1.81	-3.45	0.41
p value	EG: <0.001	0.169	0.303	0.916	0.244	0.576	0.073	<0.001	0.681
	MAG: <0.001								
IT	C: 0.107	0.96 ± 2.16	-0.07 ± 0.17	-0.009 ± 0.01	-4.84 ± 17.80	7.34 ± 9.35	-19.67 ± 20.06	-0.72 ± 0.38	-0.75 ± 6.04
t value	PG: <0.001	0.45	-0.38	-0.64	-0.27	0.79	-0.98	-1.88	-0.12
p value	EG: <0.001	0.657	0.705	0.522	0.786	0.434	0.328	0.062	0.901
	MAG: <0.001								
ST	C: 0.001	0.34 ± 2.24	-0.09 ± 0.18	-0.01 ± 0.01	26.31 ± 18.18	14.14 ± 6.85	-27.82 ± 20.86	-1.35 ± 0.37	4.42 ± 6.26
t value	PG: <0.001	0.15	-0.49	-0.75	1.45	2.07	-1.33	-3.62	0.71
p value	EG: <0.001	0.879	0.628	0.453	0.151	0.041	0.184	<0.001	0.482
	MAG: <0.001								
IN	C: <0.001	4.26 ± 2.99	-0.15 ± 0.24	-0.002 ± 0.02	24.15 ± 24.85	1.89 ± 13.17	-8.97 ± 29.03	-0.83 ± 0.55	0.72 ± 8.50
t value	PG: <0.001	1.42	-0.65	-0.01	0.97	0.14	-0.31	-1.51	0.08
p value	EG: <0.001	0.158	0.518	0.991	0.333	0.886	0.758	0.133	0.933
	MAG: <0.001								

Table 3.4: Independent variables included in regional analysis of prelamina depth. Presented as effect size ± standard error, also the t-value and *p*-value. Red text indicates the independent variable had a significant effect at $p < 0.05$ and therefore included in the mixed-effects regression models.

Prelamina thickness (µm)	Dx (*p*-values)	Age (years)	Age^2 (years)^2	Age^3 (years)^3	AxL (mm)	MS (D)	ACD (mm)	CCT (µm)	IOP (mmHg)
Centre	C: <0.001	-1.37 ± 1.37	-0.03 ± 0.15	0.003 ± 0.01	3.72 ± 11.23	4.25 ± 5.91	-9.15 ± 12.69	0.44 ± 0.24	-3.52 ± 3.83
t value	PG: <0.001	-0.99	-0.23	0.21	0.33	0.72	-0.72	1.82	-0.92
p value	EG: <0.001	0.321	0.816	0.834	0.741	0.473	0.472	0.071	0.360
	MAG: <0.001								
Superior	C: 0.469	-2.40 ± 1.98	-0.06 ± 0.21	0.02 ± 0.02	0.13 ± 16.46	2.29 ± 8.59	10.73 ± 19.47	0.94 ± 0.34	-3.52 ± 5.64
t value	PG: <0.001	-1.21	-0.29	1.09	0.01	0.27	0.55	2.78	-0.61
p value	EG: <0.001	0.227	0.770	0.279	0.994	0.790	0.582	0.006	0.546
	MAG: <0.001								
Inferior	C: <0.001	-5.34 ± 1.66	-0.19 ± 0.21	0.04 ± 0.02	-24.49 ± 15.28	0.09 ± 8.01	25.22 ± 18.26	0.61 ± 0.35	9.79 ± 5.14
t value	PG: 0.003	-3.21	-0.92	1.96	-1.60	0.01	1.38	1.69	1.90
p value	EG: <0.001	0.002	0.363	0.053	0.112	0.991	0.170	0.092	0.060
	MAG: <0.001								
Nasal	C: <0.001	-1.97 ± 3.06	0.23 ± 0.28	0.01 ± 0.02	31.30 ± 24.39	26.87 ± 14.28	-29.21 ± 30.33	-0.27 ± 0.55	11.38 ± 7.88
t value	PG: 0.007	-0.64	0.83	0.30	1.28	1.88	-0.96	-0.50	1.45
p value	EG: <0.001	0.522	0.410	0.768	0.203	0.063	0.338	0.621	0.153
	MAG: <0.001								
Temporal	C: <0.001	-1.89 ± 1.53	-0.14 ± 0.17	0.02 ± 0.01	-15.66 ± 12.66	-11.66 ± 4.90	8.88 ± 14.91	0.54 ± 0.28	2.21 ± 4.34
t value	PG: 0.007	-1.24	-0.86	1.56	-1.24	-2.38	0.596	1.92	0.51
p value	EG: <0.001	0.219	0.393	0.123	0.219	0.019	0.552	0.056	0.612
	MAG: <0.001								
SN	C: <0.001	-5.47 ± 1.89	0.13 ± 0.22	0.009 ± 0.02	-26.65 ± 17.83	7.93 ± 9.04	17.49 ± 21.55	0.75 ± 0.38	-1.86 ± 5.75
t value	PG: 0.004	-2.90	0.62	0.46	-1.49	0.88	0.81	1.97	-0.32
p value	EG: <0.001	0.005	0.541	0.645	0.138	0.383	0.419	0.052	0.748
	MAG: <0.001								
IT	C: <0.001	-3.86 ± 1.35	-0.07 ± 0.17	0.009 ± 0.01	-23.24 ± 12.60	-9.40 ± 6.68	21.41 ± 14.66	0.33 ± 0.28	0.11 ± 4.28
t value	PG: <0.001	-2.85	-0.38	0.59	-1.85	-1.14	1.46	1.20	0.03
p value	EG: <0.001	0.005	0.703	0.557	0.068	0.162	0.147	0.232	0.980
	MAG: <0.001								
ST	C: 0.770	-2.12 ± 1.61	-0.05 ± 0.19	0.02 ± 0.02	-25.55 ± 12.79	-19.47 ± 6.87	13.25 ± 15.53	0.89 ± 0.28	-3.16 ± 4.57
t value	PG: <0.001	-1.32	-0.30	1.48	-2.00	-2.84	0.85	3.19	-0.69
p value	EG: <0.001	0.191	0.769	0.143	0.048	0.005	0.395	0.002	0.491
	MAG: <0.001								
IN	C: 0.768	-5.77 ± 2.03	-0.11 ± 0.25	-0.001 ± 0.02	-22.44 ± 18.37	-1.55 ± 10.54	-12.61 ± 22.64	0.75 ± 0.42	8.42 ± 6.08
t value	PG: <0.001	-2.84	-0.44	-0.07	-1.22	-0.15	-0.56	1.79	1.39
p value	EG: <0.001	0.006	0.664	0.947	0.225	0.883	0.579	0.077	0.169
	MAG: <0.001								

Table 3.5: Independent variables included in regional analysis of prelamina thickness. Presented as effect size ± standard error, also the t-value and *p*-value. Red text indicates the independent variable had a significant effect at $p < 0.05$ and therefore included in the mixed-effects regression models.

III.6.4 Prelamina depth and thickness as a function of glaucoma disease stage and visual field sensitivity

Prelamina depth and thickness data are presented in Figures 3.3 and 3.4 respectively (mean and standard deviation are shown in Table III.2 of Appendix II). Inter-group differences in regional measures of prelamina depth and thickness were determined using linear mixed-effects regression models (Tables 3.4 and 3.5) with Tukey post-hoc analysis (see Table III.3 of Appendix II). The EG and MAG groups displayed significantly greater prelamina depth than controls in all regions of the ONH ($P < 0.03$). Prelamina depth was also significantly larger in PG ONHs than in controls in all regions ($P < 0.04$), apart from centre and temporal, but no differences were identified between PG and EG in any ONH region.

In MAG, prelamina depth was greater than PG in the superior (MAG: 333.21 $\pm$ 200.69 µm and PG: 215.71 $\pm$ 211.30 µm, $P < 0.001$) and inferior (MAG: 269.24 $\pm$ 168.91 µm and PG: 72.15 $\pm$ 229.94 µm, $P = 0.003$) regions, as well as in the superior ONH in EG (MAG: 333.21 $\pm$ 200.69 µm and EG: 238.87 $\pm$ 201.49 µm, $P = 0.011$), see Figure 3.3.

In all regions of the ONH, prelamina thickness was significantly lower in all three stages of glaucoma (PG, EG & MAG) than the control group ($P < 0.02$), apart from the PG nasal region ($P = 0.093$). Prelamina thickness was not significantly different between PG and EG in any region of the ONH.

Superior prelamina thickness was significantly lower in the MAG group than in the PG and EG groups (MAG: 127.83 $\pm$ 105.55 µm, PG: 200.56 $\pm$ 126.24 µm, EG: 175.90 $\pm$ 123.38 µm). Additionally, prelamina thickness in MAG was lower than in PG, in the inferior (MAG: 151.78 $\pm$ 87.69 µm and PG: 328.26 $\pm$ 193.12 µm, $P = 0.004$) and inferior-temporal regions (MAG: 158.36 $\pm$ 81.46 µm and PG: 280.77 $\pm$ 124.38 µm, $P < 0.001$), see Figure 3.4.

For the nine ONH regions analysed, prelamina depth increased and thickness decreased significantly with increasing VF loss in all regions of the ONH, see Figure 3.5.

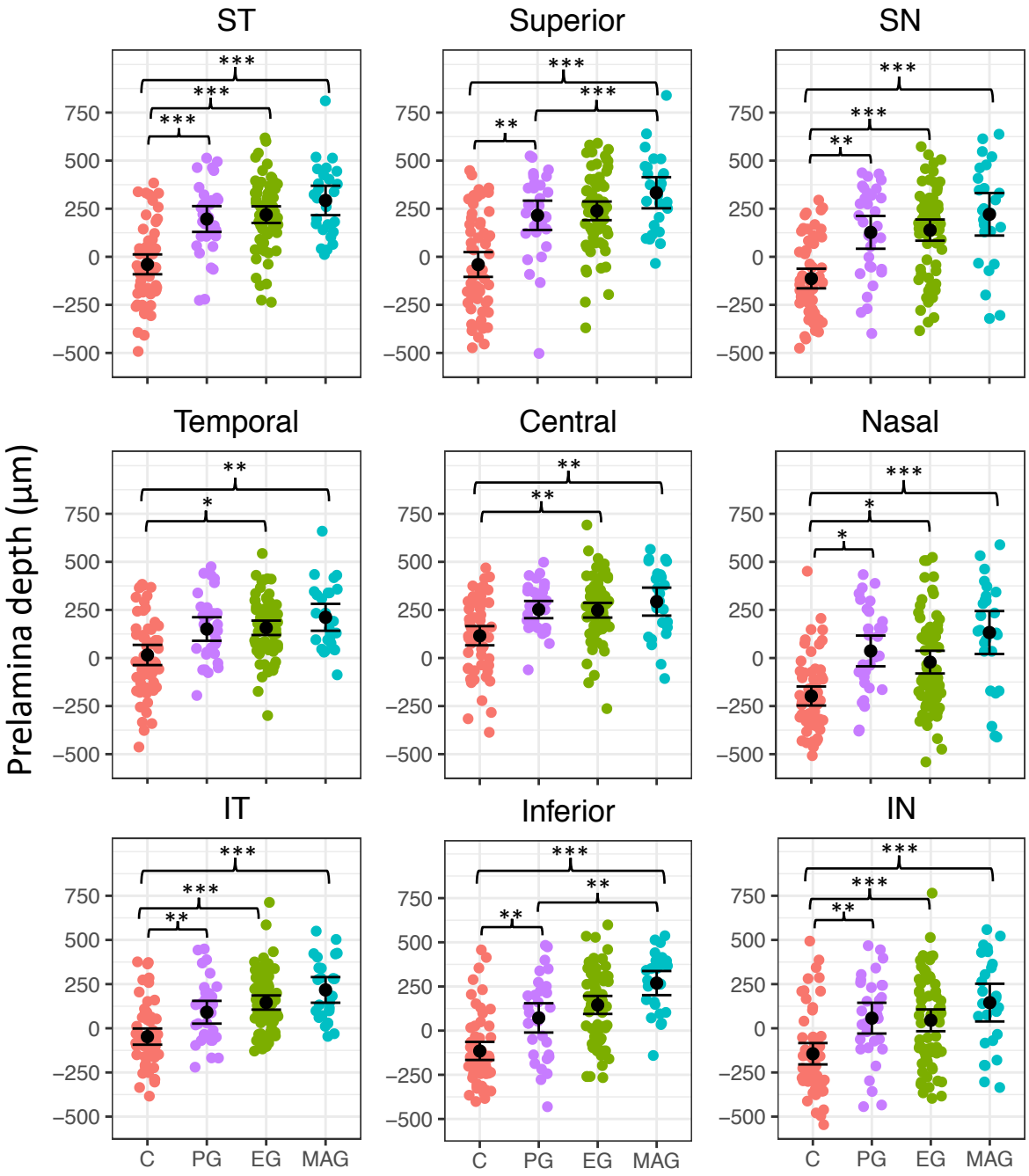

Figure 3.3: Inter-group comparisons of regional prelamina depth as a function of glaucoma disease stage. Black point represents group mean. Error bars represent 95% confidence intervals. * = $P < 0.05$, ** = $P < 0.01$, *** = $P < 0.001$.

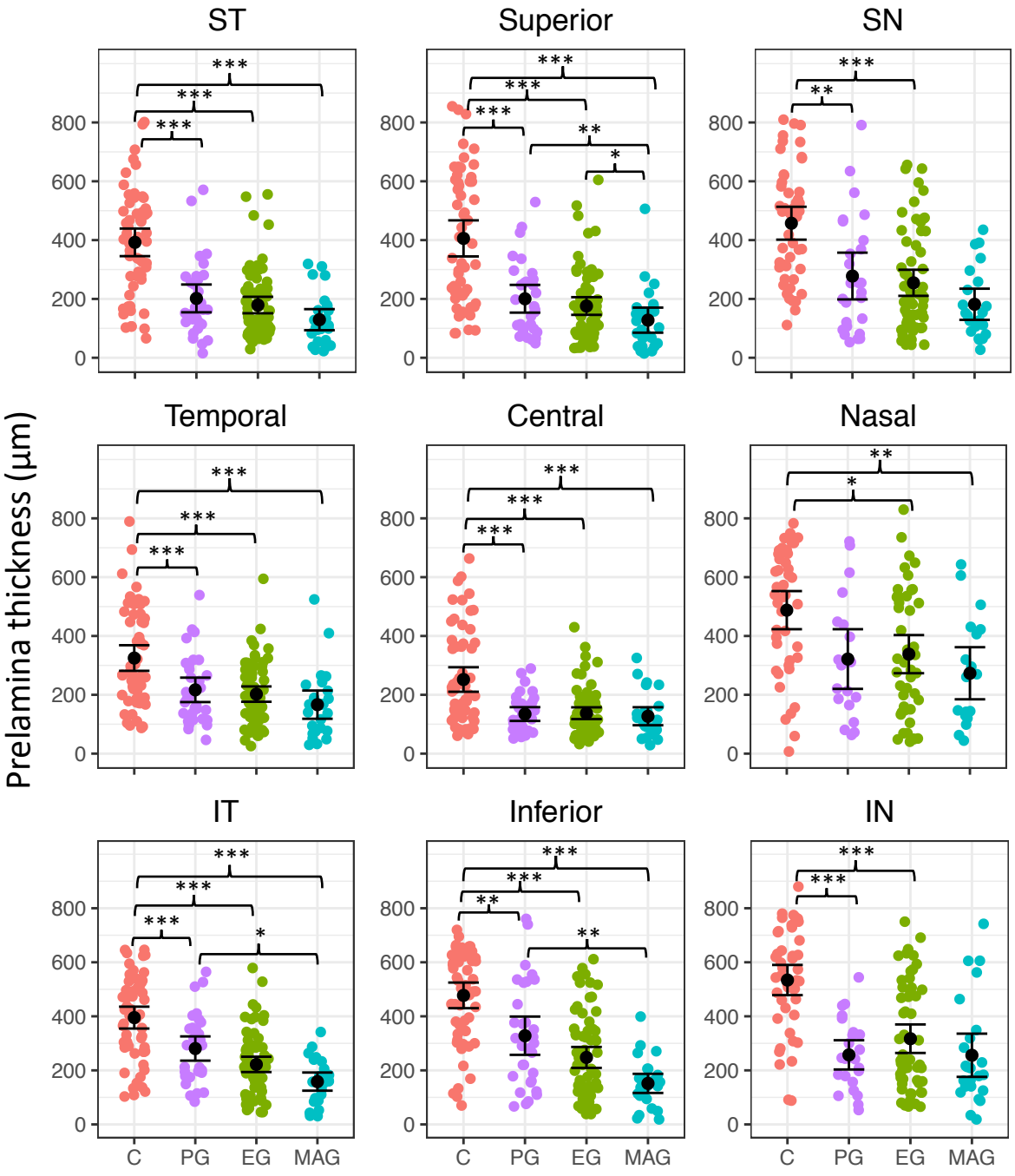

Figure 3.4: Inter-group comparisons of regional prelamina thickness as a function of glaucoma disease stage. Black point represents group mean. Error bars represent 95% confidence intervals. * = $P < 0.05$, ** = $P < 0.01$, *** = $P < 0.001$.

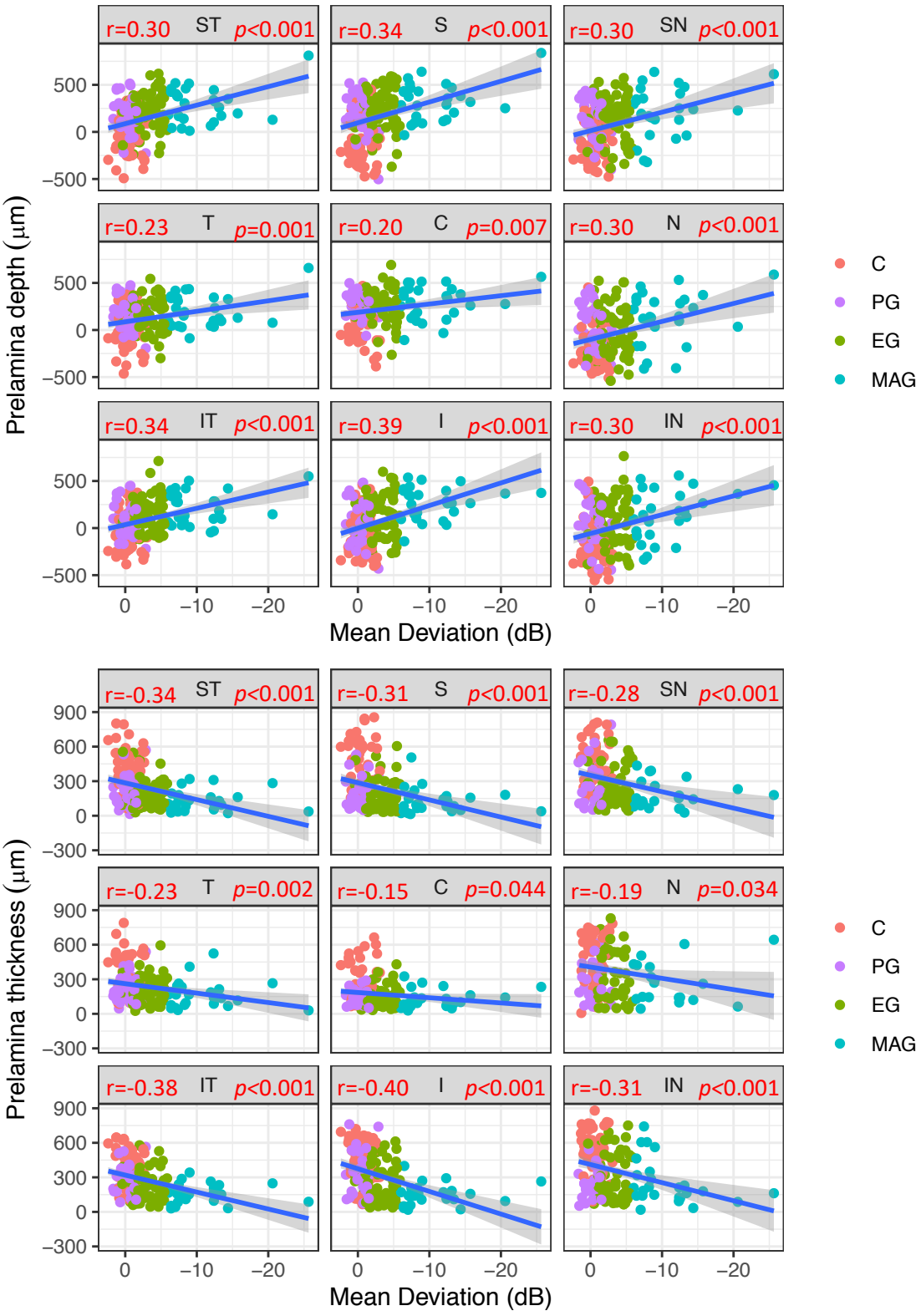

Figure 3.5: Regional prelamina depth and thickness as a function of visual field loss. Blue line represents regression line and grey shading represents 95% confidence intervals. Red text indicates significant Pearson's correlation at $P < 0.05$.

III.6.5 Multivariate analysis of ocular parameters effect on lamina cribrosa depth and thickness

Ocular parameters were included as independent variables in linear mixed-effects regression models to evaluate their association with LC depth and thickness. In all ONH regions, stage of glaucoma was a significant factor included in models for anterior LC depth ($P < 0.001$), posterior LC depth ($P < 0.001$), and LC thickness ($P \leq 0.002$), see Tables 3.6, 3.7, and 3.8 respectively. Age had a significant negative association with central anterior LC surface depth (-3.25 ± 1.34 µm/year, $P = 0.017$) and on central (-3.58 ± 1.40 µm/year, $P = 0.012$) and ST posterior LC depth (-2.87 ± 1.32 µm/year, $P = 0.033$. Age was not significantly associated with LC thickness in any region of the ONH.

In the inferior-temporal ONH, axial length had a significant negative association with anterior (-26.93 ± 7.49 µm/mm, $P < 0.001$) and posterior (-28.21 ± 8.41 µm/mm, $P = 0.001$) LC surface depth i.e., eyes with larger axial length displayed anterior and posterior LC surface depths less posterior to BMO in the IT region. Axial length had a positive association with LC thickness (between 8.92 and 14.21 µm/mm) in the central ($P = 0.006$), superior ($P = 0.022$), temporal ($P = 0.008$), SN ($P = 0.003$), IT ($P = 0.009$), and ST ($P = 0.006$) regions, in these regions, eyes with larger axial lengths had thicker LCs.

Mean spherical correction was not significantly associated with anterior or posterior LC depth in any ONH region but had a significant positive association with central ($P = 0.006$), superior ($P = 0.027$), temporal ($P = 0.017$), SN ($P = 0.006$), IT ($P < 0.001$), and ST ($P = 0.005$) LC thickness. In these regions eyes with increasing hyperopic correction had thicker LCs, while eyes with more myopic correction had thinner LCs.

Anterior chamber depth had a negative association with nasal anterior LC depth (-29.81 ± 13.19 µm/ µm, $P = 0.026$), and also on superior (-44.96 ± 14.45 µm/mm, $P = 0.002$) and inferior (-43.45 ± 14.08 µm/mm, $P = 0.003$) posterior LC depth, indicating the anterior and posterior LC surface was closer to BMO plane in eyes with larger anterior chamber depths. Anterior chamber depth was not significantly associated with LC thickness in any ONH region (Table 3.8).

Anterior LC depth (µm)	Dx (*p*-values)	Age (years)	Age^2 (years)^2	Age^3 (years)^3	AxL (mm)	MS (D)	ACD (mm)	CCT (µm)	IOP (mmHg)
Centre	C: <0.001	-3.25 ± 1.34	-0.07 ± 0.11	0.0007 ± 0.009	-7.81 ± 10.62	1.33 ± 5.49	-10.19 ± 10.83	-0.77 ± 0.21	-2.89 ± 3.62
t value	PG: 0.852	-2.42	-0.62	0.07	-0.74	0.24	-0.941	-3.63	-0.80
p value	EG: 0.277	0.017	0.536	0.941	0.463	0.809	0.348	<0.001	0.425
	MAG: 0.250								
Superior	C: <0.001	-1.94 ± 1.47	-0.13 ± 0.12	-0.0008 ± 0.009	-2.49 ± 12.33	2.55 ± 5.96	-26.06 ± 13.87	-0.83 ± 0.23	-3.03 ± 3.90
t value	PG: 0.224	-1.32	-1.13	-0.08	-0.20	0.43	-1.88	-3.59	-0.78
p value	EG: 0.290	0.189	0.262	0.935	0.840	0.670	0.062	<0.001	0.439
	MAG: 0.147								
Inferior	C: <0.001	-1.67 ± 1.38	-0.06 ± 0.11	-0.0002 ± 0.009	-15.75 ± 10.70	-3.16 ± 5.52	-5.70 ± 11.24	-0.34 ± 0.23	5.20 ± 3.70
t value	PG: 0.348	-1.19	-0.50	-0.03	-1.47	-0.57	-0.51	-1.49	1.40
p value	EG: 0.061	0.234	0.615	0.979	0.143	0.568	0.613	0.137	0.162
	MAG: 0.103								
Nasal	C: <0.001	-0.58 ± 1.50	-0.09 ± 0.11	0.006 ± 0.009	12.37 ± 11.81	4.62 ± 6.85	-29.81 ± 13.19	-0.52 ± 0.24	0.62 ± 3.89
t value	PG: 0.084	-0.39	-0.80	0.67	1.05	0.67	-2.26	-2.14	0.16
p value	EG: 0.231	0.699	0.428	0.504	0.298	0.502	0.026	0.035	0.874
	MAG: 0.076								
Temporal	C: <0.001	-2.47 ± 1.27	-0.03 ± 0.10	0.0001 ± 0.009	-10.69 ± 10.18	-0.79 ± 5.30	-4.23 ± 10.93	-0.60 ± 0.20	1.19 ± 3.46
t value	PG: 0.742	-1.95	-0.33	-0.02	-1.05	-0.15	-0.39	-2.96	0.34
p value	EG: 0.751	0.055	0.739	0.987	0.296	0.882	0.699	0.004	0.732
	MAG: 0.858								
SN	C: <0.001	-2.18 ± 1.41	-0.10 ± 0.11	-0.0002 ± 0.009	3.43 ± 11.67	1.96 ± 6.05	-20.52 ± 13.78	-0.64 ± 0.23	-2.18 ± 3.87
t value	PG: 0.518	-1.55	-0.92	-0.01	0.29	0.33	-1.49	-2.78	-0.56
p value	EG: 0.205	0.125	0.361	0.998	0.769	0.746	0.139	0.006	0.575
	MAG: 0.039								
IT	C: <0.001	-2.24 ± 1.22	-0.05 ± 0.11	-0.005 ± 0.009	-26.93 ± 7.49	-3.39 ± 5.37	9.41 ± 10.87	-0.37 ± 0.21	-1.42 ± 3.50
t value	PG: 0.736	-1.84	-0.46	-0.62	-3.60	-0.63	0.87	-1.76	-0.41
p value	EG: 0.222	0.069	0.644	0.538	<0.001	0.529	0.388	0.080	0.685
	MAG: 0.566								
ST	C: <0.001	-1.77 ± 1.35	-0.11 ± 0.11	-0.001 ± 0.009	-6.54 ± 10.88	0.80 ± 5.68	-11.62 ± 11.84	-0.70 ± 0.22	0.86 ± 3.71
t value	PG: 0.617	-1.31	-1.04	-0.11	-0.60	0.14	-0.98	-3.21	0.23
p value	EG: 0.327	0.194	0.302	0.911	0.549	0.888	0.328	0.002	0.816
	MAG: 0.190								
IN	C: <0.001	-1.05 ± 1.53	-0.09 ± 0.12	-0.005 ± 0.009	8.28 ± 11.97	0.65 ± 6.87	-22.99 ± 14.63	-0.51 ± 0.25	4.78 ± 4.08
t value	PG: 0.944	-0.69	-0.74	-0.51	0.69	0.09	-1.57	-2.04	1.17
p value	EG: 0.766	0.494	0.463	0.610	0.491	0.924	0.119	0.043	0.243
	MAG: 0.866								

Table 3.6: Independent variables included in regional analysis of anterior LC depth. Presented as effect size ± standard error, also the t-value and *p*-value. Red text indicates the independent variable had a significant effect at $p < 0.05$ and therefore included in the mixed-effects regression models.

Posterior LC depth (µm)	Dx (*p*-values)	Age (years)	Age^2 (years)^2	Age^3 (years)^3	AxL (mm)	MS (D)	ACD (mm)	CCT (µm)	IOP (mmHg)
Centre	C: <0.001	-3.58 ± 1.40	-0.11 ± 0.12	-0.001 ± 0.009	-0.361 ± 11.39	6.03 ± 5.95	-11.27 ± 12.02	-0.95 ± 0.24	1.63 ± 3.88
t value	PG: 0.361	-2.56	-0.96	-0.11	-0.03	1.02	-0.93	-3.99	0.42
p value	EG: 0.854	0.012	0.341	0.911	0.975	0.311	0.349	<0.001	0.674
	MAG: 0.722								
Superior	C: <0.001	-3.14 ± 1.68	-0.15 ± 0.13	-0.004 ± 0.01	5.02 ± 14.26	6.63 ± 7.01	-44.96 ± 14.45	-1.03 ± 0.27	-0.37 ± 4.60
t value	PG: 0.909	-1.86	-1.16	-0.37	0.35	0.95	-3.11	-3.82	-0.08
p value	EG: 0.722	0.066	0.252	0.713	0.725	0.346	0.002	<0.001	0.935
	MAG: 0.972								
Inferior	C: <0.001	-0.63 ± 1.61	-0.04 ± 0.12	-0.005 ± 0.01	10.82 ± 12.88	7.17 ± 6.87	-43.45 ± 14.08	-0.52 ± 0.27	6.28 ± 4.64
t value	PG: 0.960	-0.39	-0.36	-0.51	0.84	1.05	-3.09	-1.88	1.36
p value	EG: 0.440	0.696	0.720	0.613	0.403	0.298	0.003	0.062	0.178
	MAG: 0.921								
Nasal	C: <0.001	-2.08 ± 1.81	-0.15 ± 0.12	-0.002 ± 0.01	1.10 ± 13.96	7.24 ± 8.05	-0.96 ± 18.48	-0.77 ± 0.29	9.32 ± 4.28
t value	PG: 0.751	-1.16	-1.27	-0.19	0.08	0.89	-0.05	-2.69	2.17
p value	EG: 0.867	0.253	0.210	0.847	0.937	0.372	0.958	0.009	0.033
	MAG: 0.145								
Temporal	C: <0.001	-2.73 ± 1.48	-0.07 ± 0.12	-0.006± 0.01	-2.20 ± 11.75	4.40 ± 6.23	-8.02 ± 12.24	-0.74 ± 0.24	5.66 ± 3.95
t value	PG: 0.281	-1.84	-0.55	-0.06	-0.18	0.71	-0.66	-3.15	1.43
p value	EG: 0.402	0.069	0.581	0.956	0.852	0.481	0.513	0.002	0.155
	MAG: 0.114								
SN	C: <0.001	-3.27 ± 1.79	-0.15 ± 0.13	-0.008 ± 0.01	16.99 ± 15.29	9.39 ± 8.06	-17.19 ± 16.98	-0.97 ± 0.31	2.58 ± 4.96
t value	PG: 0.692	-1.83	-1.12	-0.75	1.11	1.17	-1.01	-3.11	0.52
p value	EG: 0.914	0.072	0.265	0.455	0.269	0.247	0.313	0.002	0.603
	MAG: 0.613								
IT	C: <0.001	-2.41 ± 1.36	-0.06 ± 0.11	-0.007 ± 0.009	-28.21 ± 8.41	5.29 ± 5.84	4.39 ± 11.29	-0.39 ± 0.23	4.19 ± 3.82
t value	PG: 0.231	-1.78	-0.54	-0.72	-3.36	0.91	0.39	-1.72	1.10
p value	EG: 0.947	0.079	0.590	0.474	0.001	0.366	0.698	0.087	0.275
	MAG: 0.244								
ST	C: <0.001	-2.87 ± 1.32	-0.12 ± 0.11	-0.001 ± 0.009	4.16 ± 10.97	7.99 ± 5.88	-11.81 ± 11.83	-0.96 ± 0.23	5.64 ± 3.78
t value	PG: 0.537	-2.17	-1.09	-0.14	0.38	1.36	-0.99	-4.12	1.49
p value	EG: 0.948	0.033	0.278	0.889	0.705	0.177	0.320	<0.001	0.138
	MAG: 0.756								
IN	C: <0.001	-0.60 ± 1.89	-0.09 ± 0.13	-0.008 ± 0.01	27.64 ± 14.72	9.53 ± 8.59	-34.11 ± 17.85	-0.89 ± 0.35	13.97 ± 4.97
t value	PG: 0.894	-0.32	-0.66	-0.73	1.88	1.11	-1.91	-2.58	2.81
p value	EG: 0.398	0.751	0.510	0.466	0.064	0.270	0.059	0.011	0.006
	MAG: 0.784								

Table 3.7: Independent variables included in regional analysis of posterior LC depth. Presented as effect size ± standard error, also the t-value and *p*-value. Red text indicates the independent variable had a significant effect at $p < 0.05$ and therefore included in the mixed-effects regression models.

LC thickness (µm)	Dx (*p*-values)	Age (years)	Age^2 (years)^2	Age^3 (years)^3	AxL (mm)	MS (D)	ACD (mm)	CCT (µm)	IOP (mmHg)
Centre	C: 0.563	0.13 ± 0.41	-0.04 ± 0.03	-0.0009 ± 0.003	8.92 ± 3.20	4.98 ± 1.77	-3.01 ± 4.07	-0.13 ± 0.08	4.99 ± 1.14
t value	PG: 0.207	0.33	-1.15	-0.37	2.79	2.82	-0.74	-1.63	4.37
p value	EG: 0.002	0.746	0.253	0.714	0.006	0.006	0.461	0.106	<0.001
	MAG: <0.001								
Superior	C: 0.477	-0.65 ± 0.55	-0.01 ± 0.04	-0.001 ± 0.003	10.87 ± 4.65	5.46 ± 2.44	-4.43 ± 5.75	-0.14 ± 0.11	5.02 ± 1.57
t value	PG: 0.037	-1.18	-0.24	-0.40	2.34	2.24	-0.77	-1.31	3.19
p value	EG: 0.001	0.240	0.811	0.690	0.022	0.027	0.443	0.192	0.002
	MAG: 0.002								
Inferior	C: <0.001	-0.44 ± 0.56	-0.0007 ± 0.04	-0.003 ± 0.004	8.44 ± 4.67	2.14 ± 1.70	-4.88 ± 5.58	-0.23 ± 0.10	2.82 ± 1.65
t value	PG: <0.001	-0.79	-0.02	-0.77	1.81	1.26	-0.87	-2.31	1.72
p value	EG: <0.001	0.429	0.987	0.447	0.074	0.210	0.384	0.023	0.090
	MAG: <0.001								
Nasal	C: <0.001	0.28 ± 0.76	-0.09 ± 0.05	-0.007 ± 0.004	1.45 ± 6.32	0.79 ± 3.71	5.17 ± 8.06	-0.18 ± 0.14	5.77 ± 1.90
t value	PG: 0.854	0.38	-1.67	-1.60	0.23	0.21	0.64	-1.33	3.03
p value	EG: 0.213	0.709	0.101	0.117	0.818	0.831	0.523	0.188	0.003
	MAG: 0.068								
Temporal	C: 0.814	-0.27 ± 0.54	-0.02 ± 0.04	-0.0009 ± 0.003	11.40 ± 4.23	5.73 ± 2.36	-2.82 ± 5.41	-0.21 ± 0.10	6.42 ± 1.51
t value	PG: 0.331	-0.49	-0.60	-0.26	2.69	2.43	-0.52	-2.17	4.25
p value	EG: 0.029	0.625	0.554	0.798	0.008	0.017	0.602	0.032	<0.001
	MAG: 0.002								
SN	C: 0.117	-0.55 ± 0.54	-0.07 ± 0.04	-0.002 ± 0.003	14.21 ± 4.69	7.03 ± 2.49	2.42 ± 5.52	-0.16 ± 0.10	4.50 ± 1.52
t value	PG: 0.005	-1.01	-1.79	-0.69	3.03	2.83	0.44	-1.57	2.95
p value	EG: 0.008	0.315	0.076	0.488	0.003	0.006	0.662	0.119	0.004
	MAG: <0.001								
IT	C: 0.306	-0.03 ± 0.45	-0.03 ± 0.03	-0.001 ± 0.003	9.57 ± 3.60	7.75 ± 1.96	-1.61 ± 4.39	-0.07 ± 0.09	5.50 ± 1.31
t value	PG: 0.139	-0.06	-0.97	-0.58	2.66	3.94	-0.37	-0.88	4.21
p value	EG: 0.093	0.954	0.336	0.565	0.009	<0.001	0.715	0.378	<0.001
	MAG: 0.002								
ST	C: 0.321	-0.50 ± 0.42	-0.03 ± 0.03	-0.0008 ± 0.003	9.59 ± 3.37	5.41 ± 1.88	-1.56 ± 4.24	-0.13 ± 0.08	5.03 ± 1.24
t value	PG: 0.043	-1.19	-1.06	-0.30	2.85	2.88	-0.37	-1.58	4.06
p value	EG: 0.003	0.239	0.291	0.767	0.006	0.005	0.714	0.118	<0.001
	MAG: <0.001								
IN	C: <0.001	-0.47 ± 0.58	-0.05 ± 0.04	0.0001 ± 0.003	5.04 ± 3.18	4.71 ± 2.60	-5.92 ± 5.86	-0.24 ± 0.10	3.56 ± 1.46
t value	PG: 0.009	-0.81	-1.05	0.04	1.58	1.82	-1.01	-2.33	2.45
p value	EG: 0.011	0.418	0.298	0.968	0.117	0.073	0.314	0.022	0.016
	MAG: <0.001								

Table 3.8: Independent variables included in regional analysis of LC thickness. Presented as effect size ± standard error, also the t-value and *p*-value. Red text indicates the independent variable had a significant effect at $p < 0.05$ and therefore included in the mixed-effects regression models.

Central corneal thickness (CCT) had a negative effect on anterior and posterior LC surface depth in all ONH regions, apart from inferior and IT; i.e. eyes with thicker corneas had anterior and posterior LC surface closer to BMO reference plane. Additionally, CCT had a negative effect on the inferior (-0.23 ± 0.10 µm/µm, P = 0.023), temporal (-0.21 ± 0.10 µm/µm, P = 0.032), and IN (-0.24 ± 0.10 µm/µm, P = 0.022) LC thickness; suggesting that eyes with thicker corneas had thinner LCs in these regions.

Intraocular pressure (IOP) had no significant effect on anterior LC depth in any region of the ONH, although IOP had a significant positive effect on posterior LC depth in the nasal (9.32 ± 4.28 µm/mmHg, P = 0.033) and IN (13.97 ± 4.97 µm/mmHg, P = 0.006) regions; indicating that a higher IOP was associated with a deeper posterior LC surface relative to BMO. IOP had a significant positive effect on LC thickness in all regions of the ONH, except for the inferior LC; suggesting that eyes with higher IOP had thicker LCs (see Tables 3.6, 3.7, and 3.8).

III.6.6 Lamina cribrosa depth and thickness as a function of glaucoma disease stage and visual field sensitivity

Mean and standard deviation for regional measures of anterior and posterior LC depth, and LC thickness for each stage of glaucoma disease are given in Appendix II, Table III.4, and Figures 3.6 to 3.8. Inter-group differences (Tukey post-hoc P-values) for regional measures of anterior and posterior LC surface depths and LC thickness are given in Table III.5 of Appendix II. Throughout all regions of the ONH, no significant differences were observed in anterior or posterior LC surface depths between glaucoma groups (PG, EG & MAG) or control groups (see Figures 3.6 and 3.7).

The LC was significantly thinner in PG than controls in the inferior (P = 0.005), SN (P = 0.026), and IN (P = 0.048) regions. The EG group displayed thinner LC than controls in the central (P = 0.035), superior (P = 0.010), inferior (P < 0.001), SN (P = 0.041), and ST (P = 0.015) ONH regions. The LC was significantly thinner in MAG than in controls in all ONH regions (P < 0.03), apart from nasal (P = 0.272). Lamina cribrosa thickness was not significantly different between PG and EG, or between EG and MAG in any region of the ONH, although central LC was thinner in MAG than in PG (P = 0.013), see Figure 3.8.

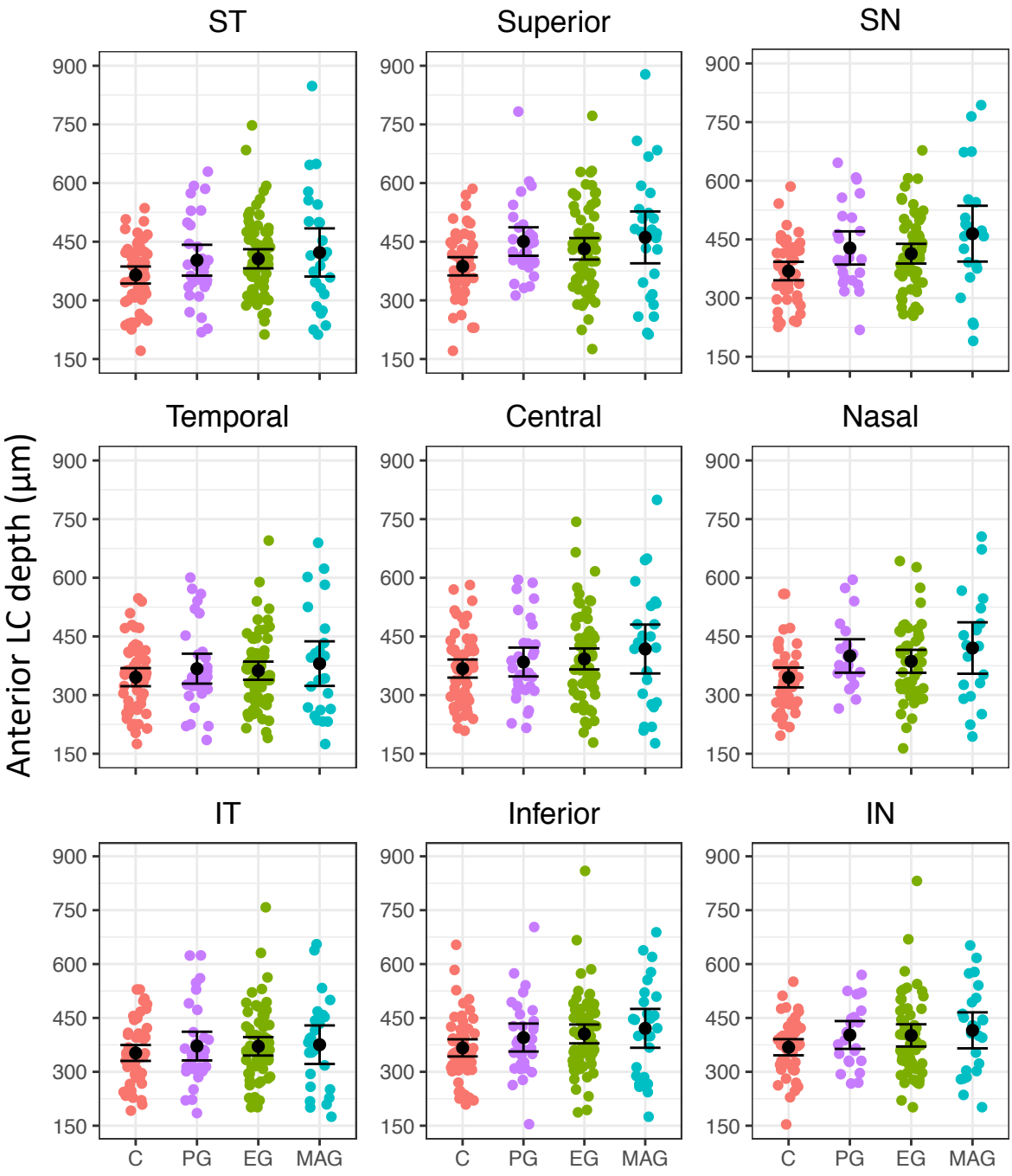

Figure 3.6: Inter-group comparisons of regional anterior LC surface depth as a function of glaucoma disease stage. Black point represents group mean. Error bars represent 95% confidence intervals.

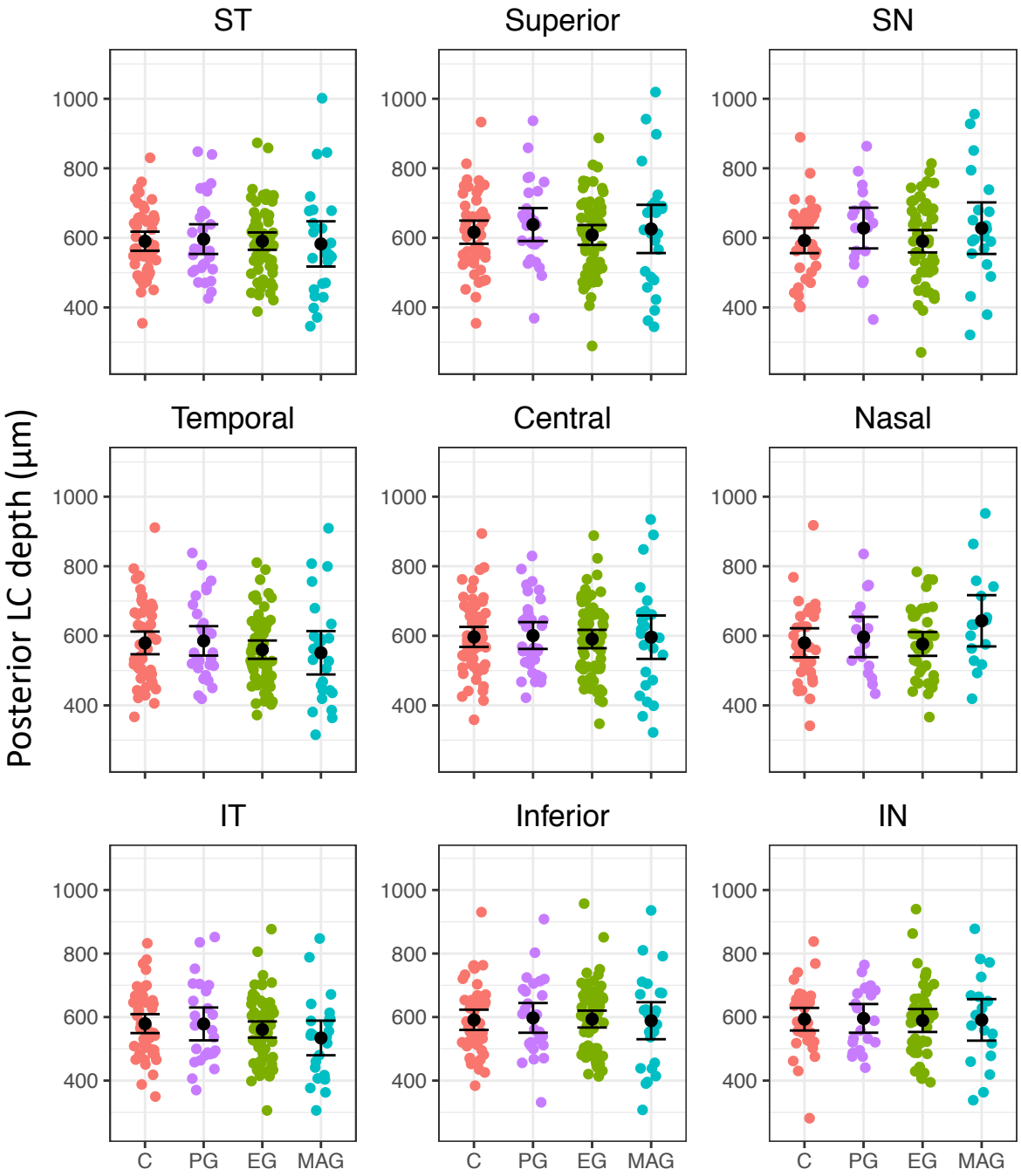

Figure 3.7: Inter-group comparisons of regional posterior LC surface depth as a function of glaucoma disease stage. Black point represents group mean. Error bars represent 95% confidence intervals.

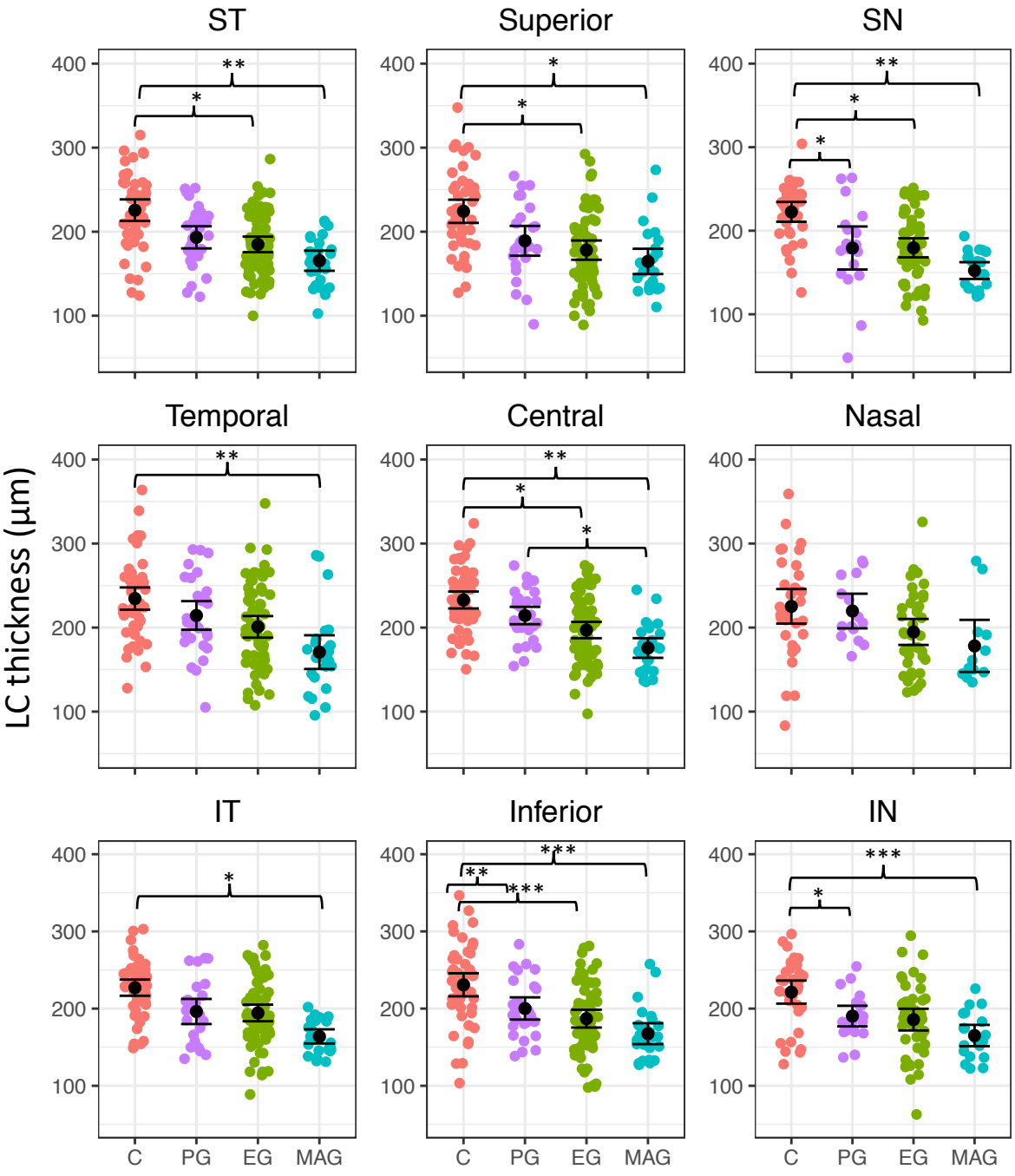

Figure 3.8: Inter-group comparisons of regional LC thickness as a function of glaucoma disease stage. Black point represents group mean. Error bars represent 95% confidence intervals. * = $P < 0.05$, ** = $P < 0.01$, *** = $P < 0.001$.

The association between regional LC depth and thickness, and visual field Mean Deviation is shown in Figures 3.9 and 3.10. Anterior LC depth showed a significant positive correlation with VF MD in all regions of the ONH, except for the temporal and IT, indicating an increased depth of the anterior LC surface (relative to BMO) with increasing VF loss (Figure 3.9). Posterior LC depth did not significantly alter with VF MD in any region of the ONH (Figure 3.9).

In all ONH regions, a significant negative correlation between VF MD and LC thickness was observed; indicating that with increasing VF loss, the LC thinned in all ONH regions, with the strongest correlation between IT LC thickness and VF MD ($r = -0.44$, $P < 0.001$), see Figure 3.10.

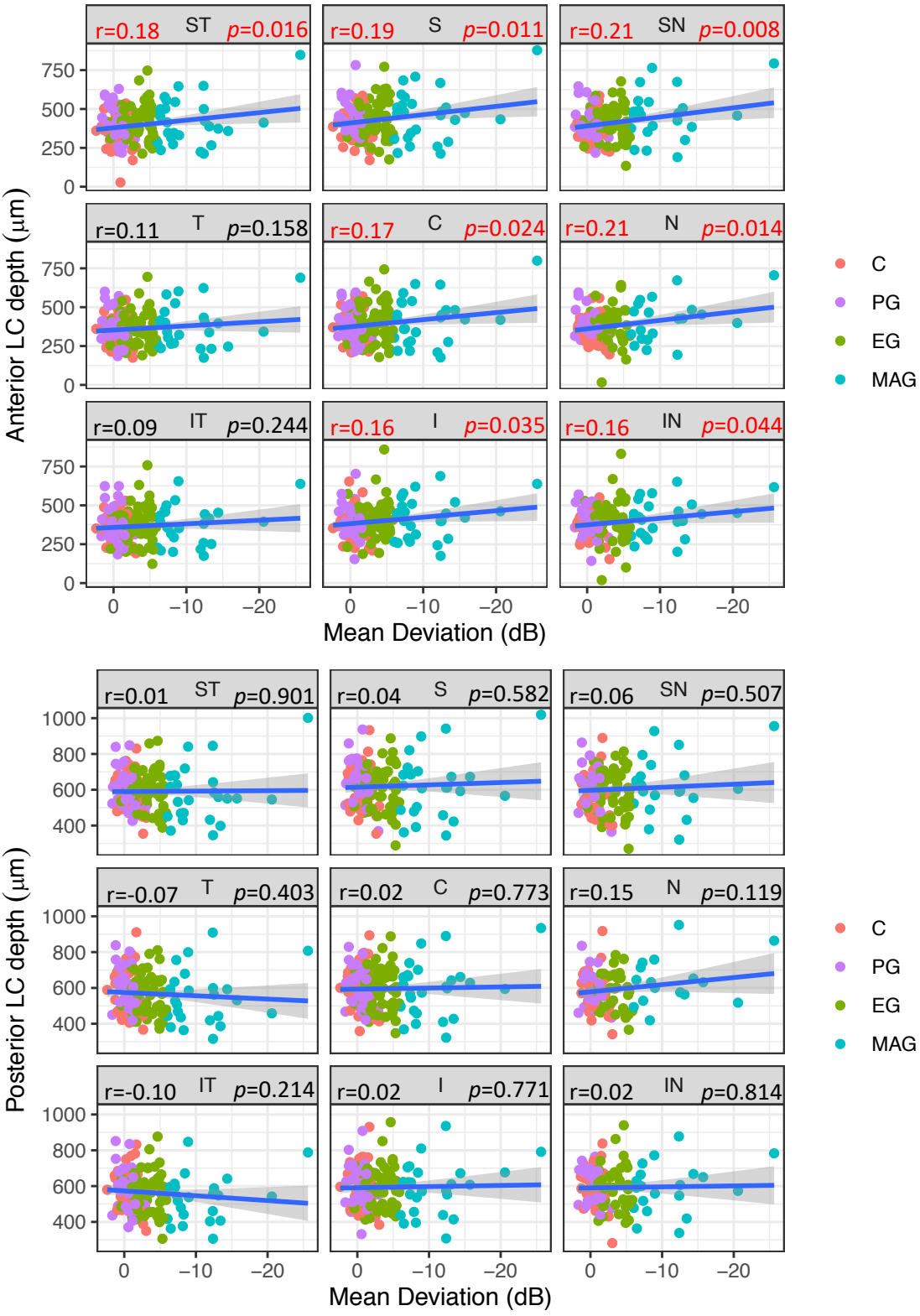

Figure 3.9: Regional anterior and posterior LC depth as a function of visual field loss. Blue line represents regression line and grey shading represents 95% confidence intervals. Red text indicates significant Pearson's correlation at $P < 0.05$.

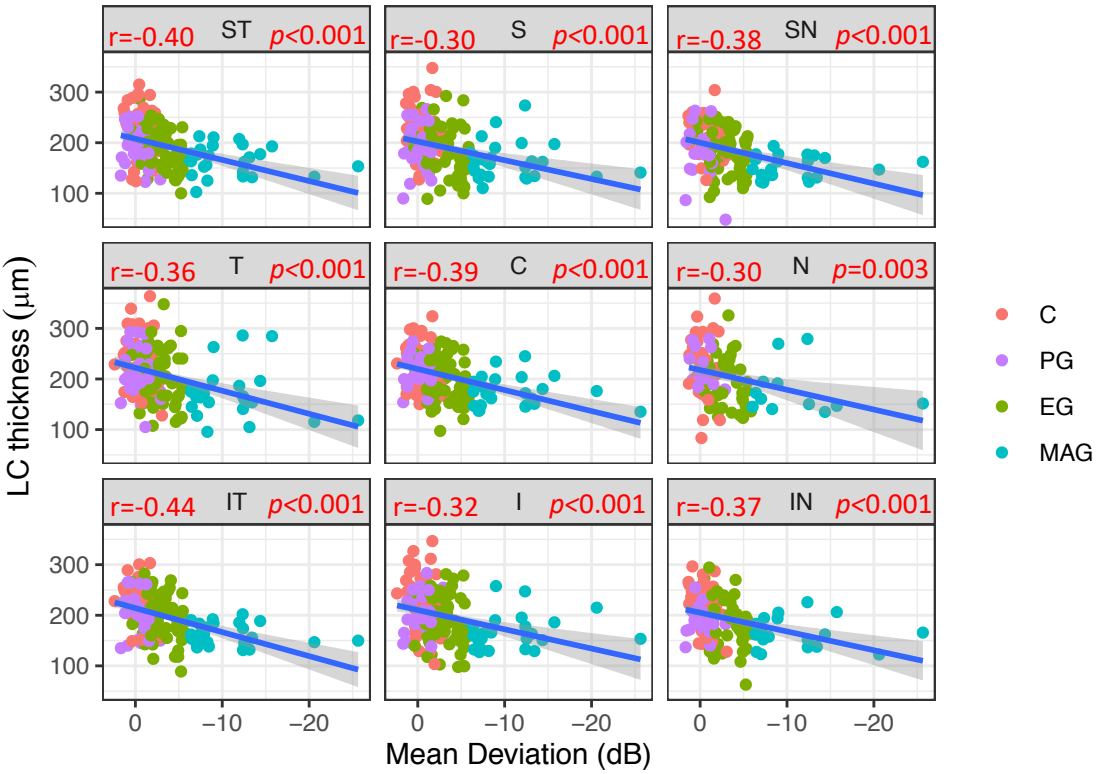

Figure 3.10: Regional LC thickness as a function of visual field loss. Blue line represents regression line and grey shading represents 95% confidence intervals. Red text indicates significant Pearson's correlation at $P < 0.05$.

III.6.7 Multivariate analysis of ocular parameters effect on border and peripapillary nerve fibre layer thickness

Stage of glaucoma was a significant factor in models for border and peripapillary NFL in all regions of the ONH ($P < 0.001$), see Tables 3.9 and 3.10. Age had a significant negative association with bNFL in the superior (-2.49 ± 0.73 µm/year, $P <. 0.001$), IT (-1.85 ± 0.56 µm/year, $P = 0.001$), and ST (-2.36 ± 0.57 µm/year, $P < 0.001$) ONH regions. Age also had a significant negative association with pNFL in the IT (-0.62 ± 0.26 µm/year, $P = 0.019$) and ST (-0.69 ± 0.26 µm/year, $P = 0.008$) regions; indicating there was significant thinning of the NFL in these regions with increasing age.

Axial length had a significant negative association with bNFL in all ONH regions, apart from nasal and IT, suggesting that in the majority of ONH regions, with increasing axial length there was a reduction in bNFL thickness. However, in the temporal region of the ONH, axial length had a significant positive association with pNFL (2.24 ± 0.90 µm/mm, $P = 0.014$); suggesting that with eyes with larger axial length had thicker pNFL in the temporal region.

Mean spherical correction was not significantly associated with bNFL or pNFL in any ONH region, apart from temporal, where there was a significant negative association (-6.46 ± 2.63 µm/D, *P* = 0.015); indicating that in the temporal region, eyes with more hyperopic correction had thinner bNFL. Additionally, anterior chamber depth was not significantly associated with bNFL or pNFL in any region of the ONH.

In the SN region, central corneal thickness had a significant positive association with bNFL (0.44 ± 0.14 µm/ µm, *P* = 0.003), and a significant positive association with pNFL in the superior ONH region (0.13 ± 0.05 µm/ µm, *P* = 0.012); meaning that eyes with thicker corneas displayed thicker bNFL and pNFL in these regions.

No significant association between IOP and bNFL was found in any ONH region. However, IOP had a significant positive association with pNFL in the superior (1.56 ± 0.77 µm/mmHg, *P* = 0.046), nasal (1.06 ± 0.46 µm/mmHg, *P* = 0.023), and IT (1.53 ± 0.76 µm/mmHg, *P* = 0.045) regions; suggesting that eyes with higher IOP displayed thicker pNFL in these regions.

Border NFL (µm)	Dx (*p*-values)	Age (years)	Age^2 (years)^2	Age^3 (years)^3	AxL (mm)	MS (D)	ACD (mm)	CCT (µm)	IOP (mmHg)
Superior	C: <0.001	-2.49 ± 0.73	0.04 ± 0.08	-0.006 ± 0.007	-17.92 ± 4.59	-5.70 ± 3.48	5.30 ± 7.75	0.15 ± 0.15	-0.38 ± 2.24
t value	PG: 0.059	-3.44	0.53	-0.86	-3.91	-1.64	0.69	1.04	-0.17
p value	EG: <0001	<0.001	0.599	0.394	<0.001	0.105	0.495	0.299	0.865
	MAG: <0.001								
Inferior	C: <0.001	-1.45 ± 0.78	0.16 ± 0.09	0.004 ± 0.008	-14.72 ± 4.64	-5.84 ± 3.42	4.92 ± 7.63	0.22 ± 0.14	-1.27 ± 2.20
t value	PG: 0.022	-1.88	1.81	0.57	-3.17	-1.70	0.65	1.52	-0.58
p value	EG: <0.001	0.064	0.075	0.567	0.002	0.091	0.520	0.130	0.563
	MAG: <0.001								
Nasal	C: <0.001	-1.22 ± 0.81	0.002 ± 0.09	-0.003 ± 0.008	-12.33 ± 6.69	-2.73 ± 3.57	5.46 ± 7.98	0.27 ± 0.15	-0.95 ± 2.30
t value	PG: 0.190	-1.51	0.02	-0.41	-1.84	-0.76	0.68	1.78	-0.42
p value	EG: <0.001	0.136	0.987	0.685	0.068	0.447	0.495	0.077	0.679
	MAG: <0.001								
Temporal	C: <0.001	-1.09 ± 0.56	-0.006 ± 0.06	0.004 ± 0.006	-11.13 ± 4.80	-6.46 ± 2.63	3.73 ± 6.03	0.01 ± 0.11	-1.73 ± 1.73
t value	PG: 0.014	-1.96	-0.09	0.67	-2.32	-2.46	0.62	0.08	-1.00
p value	EG: <0.001	0.053	0.926	0.505	0.022	0.015	0.538	0.937	0.319
	MAG: <0.001								
SN	C: <0.001	-1.45 ± 0.80	0.05 ± 0.09	-0.004 ± 0.008	-13.30 ± 4.71	-1.21 ± 3.61	4.52 ± 7.96	0.44 ± 0.14	-1.15 ± 2.29
t value	PG: 0.507	-1.81	0.61	-0.56	-2.82	-0.34	0.57	3.08	-0.51
p value	EG: 0.002	0.073	0.543	0.577	0.006	0.737	0.571	0.003	0.615
	MAG: <0.001								
IT	C: <0.001	-1.85 ± 0.56	0.06 ± 0.07	0.006 ± 0.006	-6.54 ± 5.31	-1.88 ± 2.80	1.19 ± 6.17	0.04 ± 0.12	-1.43 ± 1.78
t value	PG: 0.013	-3.31	0.79	0.94	-1.23	-0.67	0.19	0.31	-0.80
p value	EG: <0.001	0.001	0.430	0.348	0.221	0.502	0.848	0.761	0.425
	MAG: <0.001								
ST	C: <0.001	-2.36 ± 0.57	0.03 ± 0.07	-0.006 ± 0.006	-9.69 ± 3.62	-4.37 ± 2.78	5.29 ± 6.20	0.10 ± 0.12	-1.36 ± 1.80
t value	PG: 0.030	-4.12	0.47	-1.06	-2.68	-1.57	0.85	0.87	-0.75
p value	EG: <0.001	<0.001	0.637	0.295	0.009	0.118	0.395	0.385	0.453
	MAG: <0.001								
IN	C: <0.001	-0.94 ± 0.90	0.04 ± 0.09	-0.007 ± 0.008	-10.41 ± 5.18	-4.02 ± 3.98	8.31 ± 8.87	0.21 ± 0.17	0.07 ± 2.55
t value	PG: 0.119	-1.05	0.45	-0.87	-2.01	-1.01	0.94	1.25	0.03
p value	EG: <0.001	0.296	0.655	0.389	0.047	0.314	0.351	0.213	0.979
	MAG: <0.001								

Table 3.9: Independent variables included in regional analysis of border NFL thickness. Presented as effect size ± standard error (i.e. how much border NFL changes per one-unit change in the independent variable), also the t-value and *p*-value. Red text indicates the independent variable had a significant effect at $p < 0.05$ and therefore included in the mixed-effects regression models.

pNFL (µm)	Dx (*p*-values)	Age (years)	Age^2 (years)^2	Age^3 (years)^3	AxL (mm)	MS (D)	ACD (mm)	CCT (µm)	IOP (mmHg)
Superior	C: 0.142	0.46 ± 0.30	0.01 ± 0.03	-0.001 ± 0.002	0.43 ± 2.76	-2.16 ± 1.41	-1.38 ± 2.97	0.13 ± 0.05	1.56 ± 0.77
t value	PG: <0.001	1.57	0.35	-0.52	0.16	-1.53	-0.46	2.57	2.03
p value	EG: <0.001	0.120	0.721	0.602	0.877	0.129	0.644	0.012	0.046
	MAG: <0.001								
Inferior	C: <0.001	0.42 ± 0.29	0.001 ± 0.03	-0.002 ± 0.002	-1.51 ± 2.70	-2.11 ± 1.36	-4.42 ± 2.95	0.07 ± 0.06	0.49 ± 0.80
t value	PG: 0.006	1.42	0.04	-0.81	-0.56	-1.54	-1.50	1.32	0.61
p value	EG: <0.001	0.160	0.964	0.418	0.578	0.126	0.126	0.190	0.554
	MAG: <0.001								
Nasal	C: <0.001	-0.12 ± 0.18	0.01 ± 0.02	0.0007 ± 0.001	0.08 ± 1.67	0.07 ± 0.84	-0.08 ± 1.86	-0.01 ± 0.03	1.06 ± 0.46
t value	PG: 0.379	-0.66	0.67	0.49	0.05	0.08	-0.04	-0.38	2.32
p value	EG:0.034	0.511	0.506	0.628	0.961	0.934	0.965	0.707	0.023
	MAG: <0.001								
Temporal	C: 0.762	-0.23 ± 0.14	-0.002 ± 0.02	-0.001 ± 0.001	2.24 ± 0.90	0.73 ± 0.71	-0.50 ± 1.56	-0.06 ± 0.03	0.59 ± 0.41
t value	PG:0.579	-1.67	-0.14	-1.03	2.51	1.02	-0.32	-1.90	1.47
p value	EG: 0.002	0.099	0.886	0.303	0.014	0.309	0.748	0.061	0.147
	MAG: <0.001								
SN	C: <0.001	0.24 ± 0.36	-0.002 ± 0.03	-0.001 ± 0.001	0.08 ± 3.40	-0.88 ± 1.69	-1.48 ± 3.59	0.06 ± 0.06	-0.05 ± 0.977
t value	PG: 0.428	0.66	-0.06	-1.02	0.02	-0.52	-0.41	0.88	-0.05
p value	EG: 0.011	0.512	0.955	0.345	0.982	0.604	0.681	0.383	0.959
	MAG: <0.001								
IT	C: <0.001	-0.62 ± 0.26	0.005 ± 0.03	0.002 ± 0.003	0.34 ± 2.72	-0.49 ± 1.39	0.50 ± 2.86	0.03 ± 0.05	1.53 ± 0.76
t value	PG: 0.365	-2.39	0.19	0.89	0.13	-0.36	0.18	0.47	2.03
p value	EG: 0.009	0.019	0.851	0.378	0.900	0.722	0.861	0.638	0.045
	MAG: <0.001								
ST	C: <0.001	-0.69 ± 0.25	0.01 ± 0.03	-0.002 ± 0.003	4.19 ± 2.61	1.09 ± 1.34	-3.11 ± 2.88	-0.01 ± 0.06	0.78 ± 0.78
t value	PG: 0.479	-2.73	0.41	-0.73	1.60	0.82	-1.08	-0.10	1.00
p value	EG: <0.001	0.008	0.685	0.470	0.113	0.417	0.281	0.920	0.319
	MAG: <0.001								
IN	C: <0.001	-0.16 ± 0.27	0.02 ± 0.03	-0.004 ± 0.002	2.64 ± 2.53	0.06 ± 1.25	-3.01 ± 2.66	-0.06 ± 0.05	-0.20 ± 0.73
t value	PG: 0.014	-0.60	0.54	-1.76	1.05	0.05	-1.13	-1.38	-0.28
p value	EG: <0.001	0.551	0.595	0.084	0.299	0.959	0.262	0.172	0.780
	MAG: <0.001								

Table 3.10: Independent variables included in regional analysis of peripapillary NFL thickness. Presented as effect size ± standard error (i.e. how much peripapillary NFL changes per one-unit change in the independent variable), also the t-value and *p*-value. Red text indicates the independent variable had a significant effect at $p < 0.05$ and therefore included in the mixed-effects regression models.

III.6.8 Border and peripapillary nerve fibre layer as a function of glaucoma disease stage and visual field sensitivity

In eight regions around the ONH, border NFL was measured directly above BMO terminations, and peripapillary NFL was measured at a point 1.7mm from ONH centre. Mean and standard deviation for regional measures of border and peripapillary NFL thickness for each stage of glaucoma disease are presented in Appendix II, Table III.6, and Figures 3.11 and 3.12 respectively. Tukey post-hoc pairwise comparisons identified inter-group differences for regional measures of border and peripapillary NFL thickness (see Table III.7 of Appendix II).

Border NFL was significantly thinner in EG and MAG than controls in all ONH regions ($P < 0.001$). Compared to controls, pNFL was significantly thinner in MAG in all regions ($P \leq 0.009$). Peripapillary NFL did not significantly differ between controls and EG in the nasal, SN, or IT regions ($P \geq 0.136$). Border NFL was significantly less in EG than in PG in the superior, inferior, SN, and ST regions ($P \leq 0.035$). Peripapillary NFL was also significantly less in EG than PG, only in the ST region of the ONH ($P = 0.038$).

In MAG, bNFL was significantly thinner than PG and EG in all ONH regions, apart from temporal, where EG and MAG did not significantly differ ($P = 0.464$). The MAG group displayed significantly thinner pNFL than PG in all regions, apart from superior ($P = 0.419$) and nasal ($P = 0.059$). Compared to EG, pNFL was significantly thinner in MAG in four of the regions; inferior ($P = 0.008$), temporal ($P = 0.016$), IT ($P = 0.003$), and ST ($P = 0.007$). See Figures 3.11 and 3.12. The control group displayed significantly thicker bNFL than PG in the inferior ($P = 0.014$), temporal ($P = 0.017$), and IT ($P = 0.021$) ONH regions. Peripapillary NFL was significantly thinner in PG than in controls, however, only in the superior ($P = 0.009$) region of the ONH.

When assessing the association between border or peripapillary NFL and visual field Mean Deviation, all regions of border or peripapillary NFL thinned significantly with progression of VF loss (Figure 3.13). The strongest correlations identified were between VF MD and superior border NFL ($r = -0.54$, $P < 0.001$) and the superior-temporal peripapillary NFL ($r = -0.50$, $P < 0.001$).

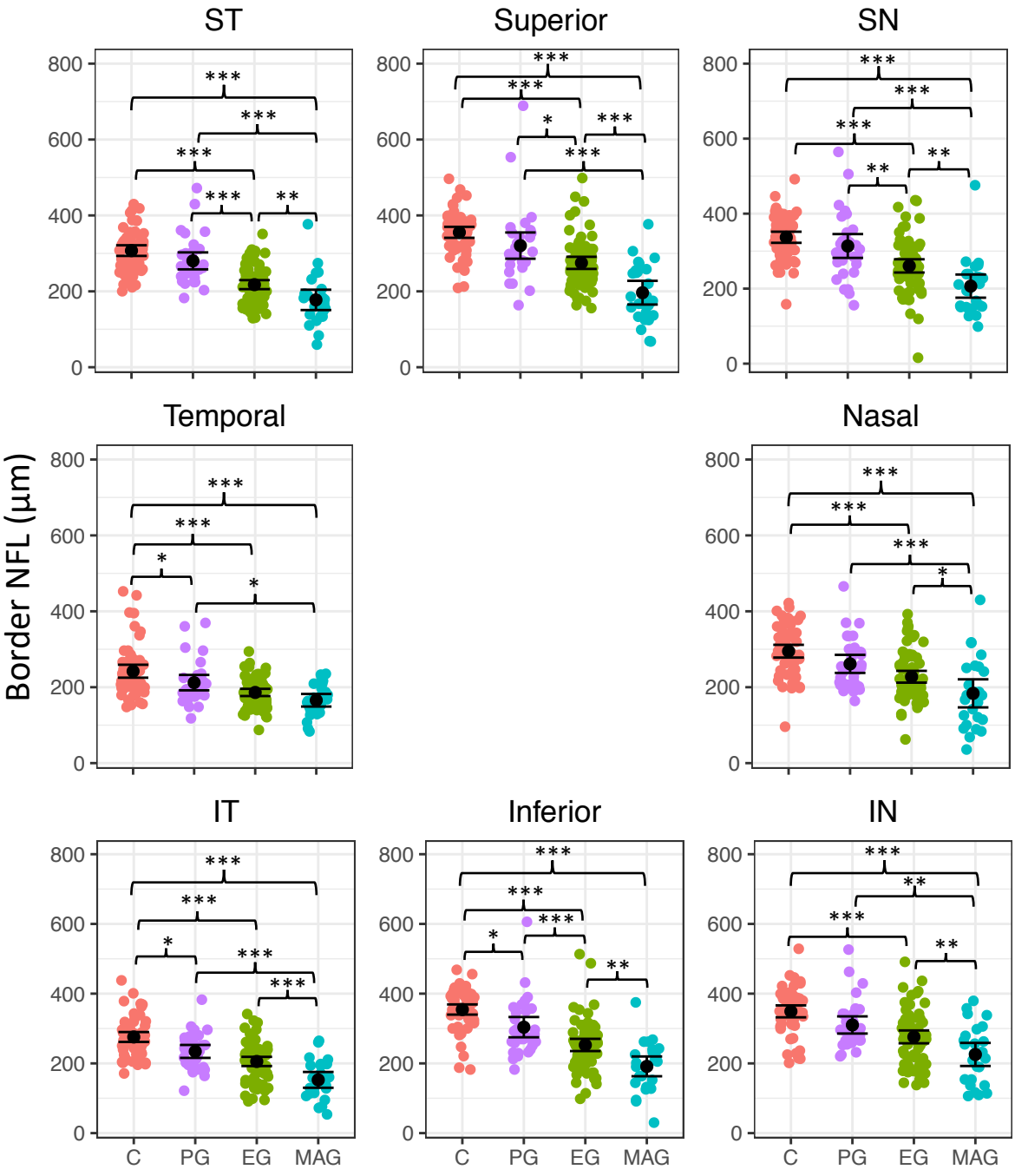

Figure 3.11: Inter-group comparisons of regional border NFL thickness as a function of glaucoma disease stage. Black point represents group mean. Error bars represent 95% confidence intervals. * = $P < 0.05$, ** = $P < 0.01$, *** = $P < 0.001$.

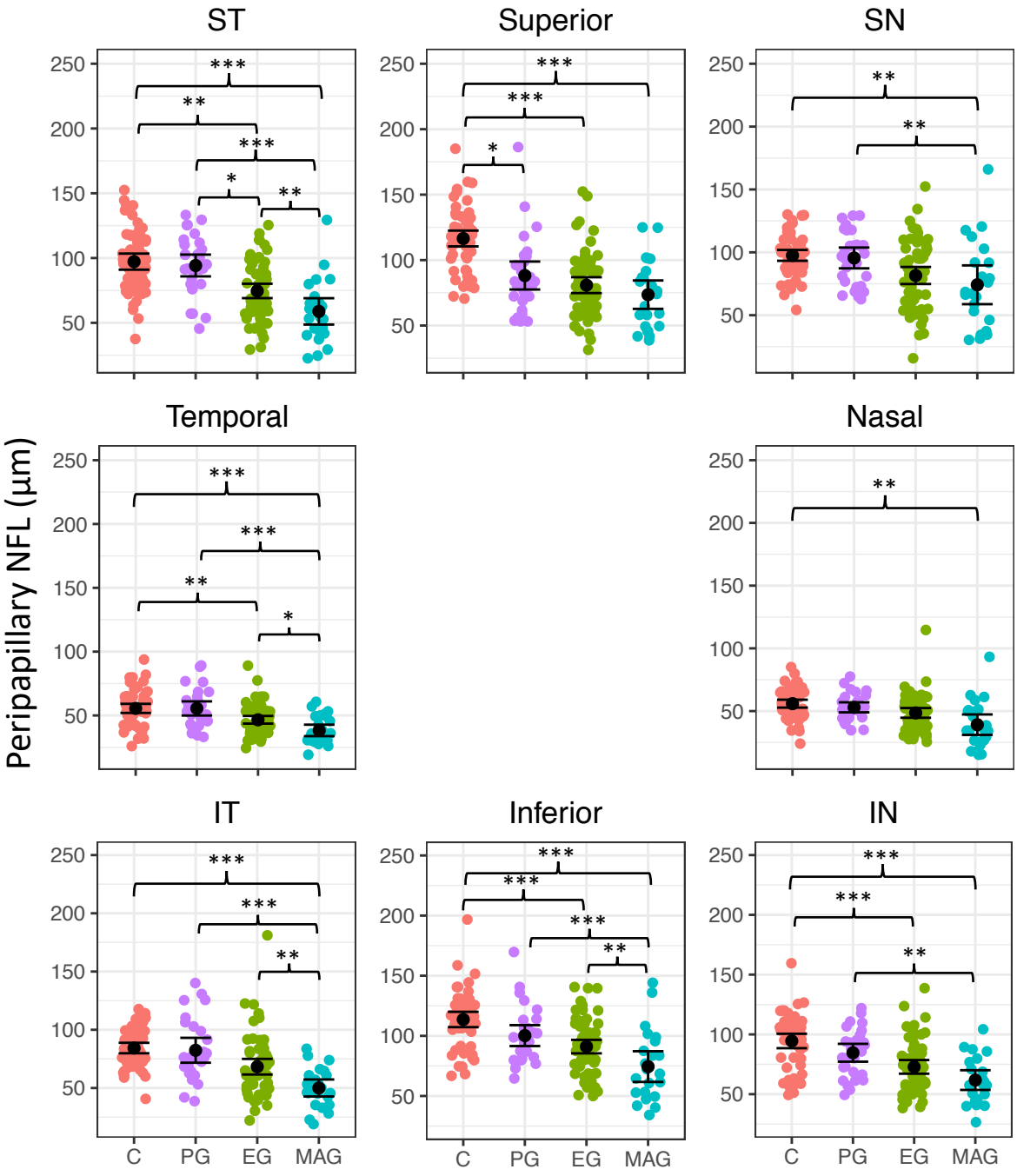

Figure 3.12: Inter-group comparisons of regional peripapillary NFL thickness as a function of glaucoma disease stage. Black point represents group mean. Error bars represent 95% confidence intervals. * = $P < 0.05$, ** = $P < 0.01$, *** = $P < 0.001$.

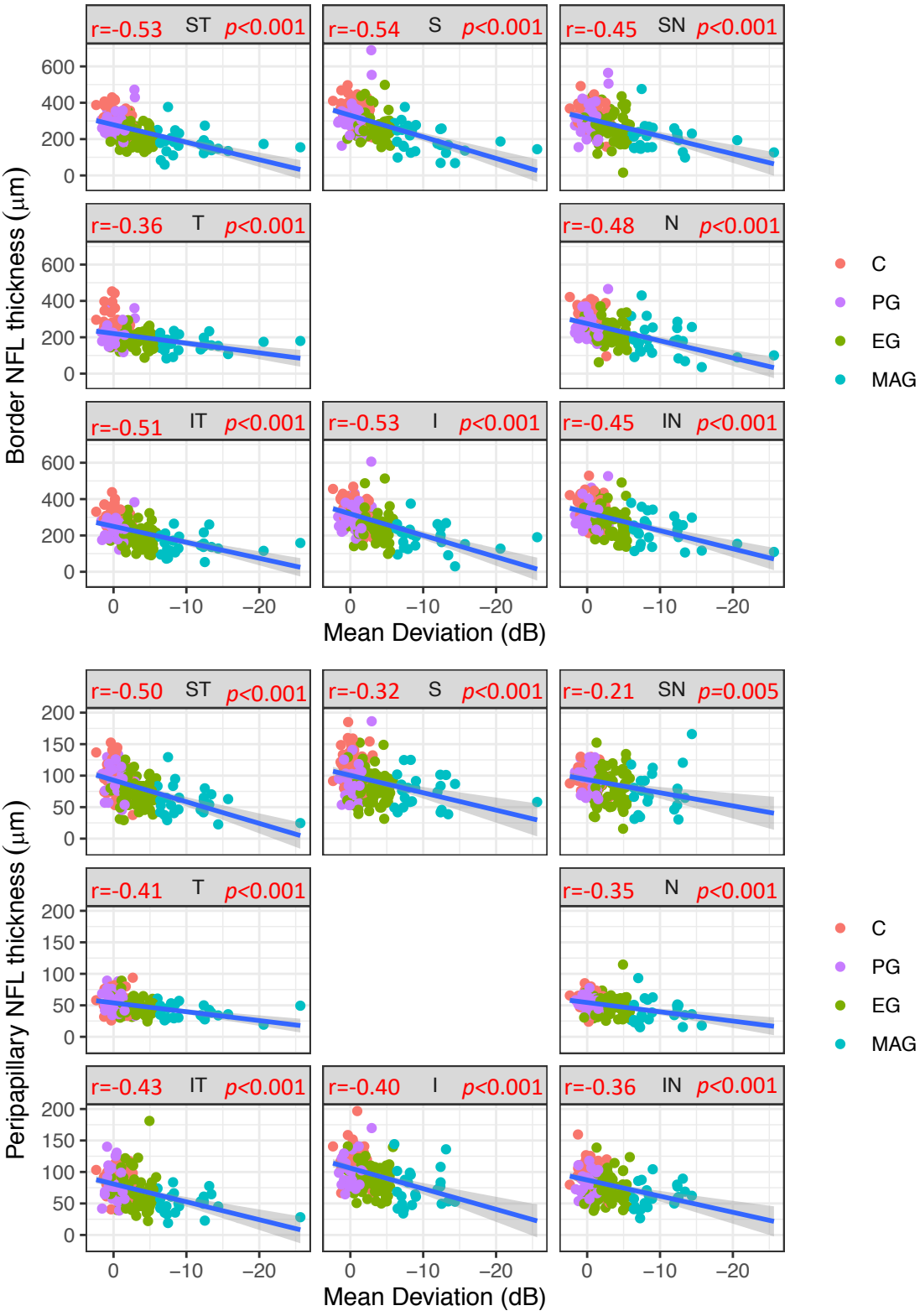

Figure 3.13: Regional border and peripapillary NFL thickness as a function of visual field loss. Blue line represents regression line and grey shading represents 95% confidence intervals. Red text indicates significant Pearson's correlation at $P < 0.05$.

III.6.9 Multivariate analysis of ocular parameters effect on minimum rim width and area

Stage of glaucoma was a significant factor in models for MRW and MRA ($P < 0.001$) in all ONH regions. See Tables 3.11 and 3.12 for all factors that were associated with MRW and MRA parameters. Age had a significant negative association with MRW in all ONH regions ($P \leq 0.005$), apart from IN ($P = 0.074$). Additionally, age had a significant negative association with MRA in all ONH regions ($P < 0.001$), apart from temporal ($P = 0.057$) and IN ($P = 0.128$), indicating a reduction in minimum rim width and area with increasing age.

Axial length had a significant negative association with MRW in the superior (-12.48 ± 5.12 µm/mm, $P = 0.017$), inferior (-14.54 ± 4.94 µm/mm, $P = 0.004$) and SN (-9.74 ± 4.84 µm/mm, $P = 0.047$) regions; meaning that eyes with larger axial length had thinner MRW in these regions. Axial length was not significantly associated with MRA in any region of the ONH. Mean spherical correction and anterior chamber depth were not significantly associated with MRW or MRA in any region of the ONH.

Central corneal thickness had a significant positive association with superior-nasal MRW (0.38 ± 0.15 µm/µm, $P = 0.014$); meaning that eyes with thicker corneas had thicker MRW in the SN region. Central corneal thickness was not significantly associated with MRA in any region of the ONH. Intraocular pressure was not significantly associated with MRW in any region of the ONH but had a significant negative association with superior-nasal MRA (-0.003 ± 0.001 mm^2/mmHg, $P = 0.041$). The latter suggested that eyes with a higher IOP had smaller superior-nasal MRA.

MRW (µm)	Dx (*p*-values)	Age (years)	Age^2 (years)^2	Age^3 (years)^3	AxL (mm)	MS (D)	ACD (mm)	CCT (µm)	IOP (mmHg)
Superior	C: <0.001	-3.79 ± 0.81	-0.02 ± 0.10	0.001 ± 0.009	-12.48 ± 5.12	-2.32 ± 4.05	-2.30 ± 8.94	0.23 ± 0.17	-1.41 ± 2.55
t value	PG: 0.021	-4.69	-0.29	0.14	-2.44	-0.57	-0.26	1.38	-0.55
p value	EG: <0.001	<0.001	0.774	0.892	0.017	0.567	0.797	0.171	0.580
	MAG: <0.001								
Inferior	C: <0.001	-3.49 ± 0.78	0.12 ± 0.09	0.004 ± 0.008	-14.54 ± 4.94	-5.02 ± 3.84	5.71 ± 8.48	0.26 ± 0.16	0.79 ± 2.41
t value	PG: 0.005	-4.48	1.31	0.45	-2.94	-1.31	0.67	1.67	0.33
p value	EG: <0.001	<0.001	0.194	0.653	0.004	0.194	0.502	0.098	0.743
	MAG: <0.001								
Nasal	C: 0.934	-2.79 ± 0.87	-0.10 ± 0.11	-0.005 ± 0.009	-13.03 ± 7.89	-4.89 ± 4.21	13.82 ± 9.11	0.34 ± 0.17	-2.50 ± 2.69
t value	PG: 0.428	-3.19	-0.90	-0.54	-1.65	-1.16	1.52	1.95	-0.93
p value	EG: 0.001	0.002	0.371	0.588	0.101	0.248	0.131	0.054	0.354
	MAG: <0.001								
Temporal	C: <0.001	-1.65 ± 0.58	-0.07 ± 0.07	0.005 ± 0.006	-1.53 ± 5.26	-1.22 ± 2.81	0.89 ± 6.06	0.10 ± 0.11	-0.38 ± 1.80
t value	PG: 0.057	-2.87	-0.92	0.77	-0.29	-0.44	0.15	0.86	-0.21
p value	EG: 0.004	0.005	0.362	0.445	0.772	0.665	0.883	0.389	0.831
	MAG: <0.001								
SN	C: 0.043	-2.90 ± 0.80	-0.05 ± 0.09	0.004 ± 0.008	-9.74 ± 4.84	-2.90 ± 3.76	5.26 ± 8.26	0.38 ± 0.15	-3.53 ± 2.37
t value	PG: 0.007	-3.64	-0.57	0.49	-2.01	-0.77	0.64	2.49	-1.49
p value	EG: <0.001	<0.001	0.571	0.627	0.047	0.442	0.525	0.014	0.140
	MAG: <0.001								
IT	C: <0.001	-2.21 ± 0.60	-0.05 ± 0.07	0.005 ± 0.007	-4.50 ± 5.61	-2.24 ± 3.01	2.34 ± 6.63	0.13 ± 0.12	-1.29 ± 1.90
t value	PG: 0.092	-3.67	-0.60	0.81	-0.80	-0.74	0.35	1.03	-0.68
p value	EG: <0.001	<0.001	0.548	0.423	0.425	0.460	0.724	0.307	0.498
	MAG: <0.001								
ST	C: <0.001	-2.93 ± 0.62	0.04 ± 0.08	0.002 ± 0.007	-6.87 ± 5.86	-2.51 ± 3.16	-1.16 ± 6.97	0.13 ± 0.13	-0.25 ± 1.98
t value	PG: 0.010	-4.72	0.47	0.25	-1.17	-0.80	-0.17	1.02	-0.13
p value	EG: <0.001	<0.001	0.639	0.802	0.243	0.428	0.868	0.309	0.899
	MAG: <0.001								
IN	C: 0.405	-1.68 ± 0.93	-0.008 ± 0.11	-0.007 ± 0.009	-9.59 ± 5.89	-4.74 ± 4.46	12.62 ± 9.77	0.35 ± 0.18	-0.04 ± 2.83
t value	PG: 0.145	-1.81	-0.08	-0.74	-1.63	-1.06	1.29	1.90	-0.02
p value	EG: <0.001	0.074	0.939	0.462	0.106	0.290	0.199	0.060	0.988
	MAG: <0.001								

Table 3.11: Independent variables included in regional analysis of minimum rim width. Presented as effect size ± standard error (i.e. how much minimum rim width changes per one-unit change in the independent variable), also the t-value and *p*-value. Red text indicates the independent variable had a significant effect at $p < 0.05$ and therefore included in the mixed-effects regression models.

MRA (mm^2)	Dx (*p*-values)	Age (years)	Age^2 $(years)^2$	Age^3 $(years)^3$	AxL (mm)	MS (D)	ACD (mm)	CCT (µm)	IOP (mmHg)
Superior	C: <0.001	-0.002 ± 0.0005	$-1.92e^{-5} \pm 6.01e^{-5}$	$1.38e^{-6} \pm 5.26e^{-6}$	-0.003 ± 0.005	-0.0004 ± 0.003	-0.005 ± 0.006	-0.00003 ± 0.0001	-0.0003 ± 0.002
t value	PG: 0.297	-4.64	-0.32	0.26	-0.65	-0.16	-0.82	-0.27	-0.20
p value	EG: 0.029	<0.001	0.750	0.794	0.517	0.876	0.415	0.790	0.851
	MAG: <0.001								
Inferior	C: <0.001	-0.002 ± 0.0005	$5.50e^{-5} \pm 6.06e^{-5}$	$2.57e^{-7} \pm 5.31e^{-6}$	-0.004 ± 0.005	-0.0009 ± 0.002	0.0002 ± 0.005	0.00006 ± 0.0001	-0.00004 ± 0.002
t value	PG: 0.251	-3.90	0.91	0.05	-0.92	-0.35	0.04	0.58	-0.02
p value	EG: <0.001	<0.001	0.366	0.962	0.362	0.731	0.971	0.567	0.981
	MAG: <0.001								
Nasal	C: <0.001	-0.002 ± 0.0005	$-9.20e^{-5} \pm 6.43e^{-5}$	$6.38e^{-7} \pm 5.63e^{-6}$	-0.004 ± 0.005	-0.003 ± 0.003	0.004 ± 0.006	0.0001 ± 0.0001	-0.002 ± 0.002
t value	PG: 0.874	-3.49	-1.43	0.11	0.84	-1.23	0.78	1.02	-1.03
p value	EG: 0.025	<0.001	0.156	0.910	0.404	0.222	0.436	0.308	0.306
	MAG: 0.008								
Temporal	C: <0.001	-0.0008 ± 0.0004	$-8.32e^{-5} \pm 4.71e^{-5}$	$3.48e^{-6} \pm 4.11e^{-6}$	0.006 ± 0.003	-0.002 ± 0.002	-0.002 ± 0.004	0.00004 ± 0.001	-0.0005 ± 0.001
t value	PG: 0.894	-1.93	-1.77	0.85	1.84	-0.87	-0.48	-0.39	-0.39
p value	EG: 0.102	0.057	0.081	0.400	0.069	0.389	0.635	0.698	0.698
	MAG: 0.162								
SN	C: <0.001	-0.002 ± 0.0005	$-5.76e^{-5} \pm 5.70e^{-5}$	$6.01e^{-6} \pm 4.94e^{-6}$	-0.001 ± 0.004	-0.003 ± 0.002	0.001 ± 0.005	0.0001 ± 0.0001	-0.003 ± 0.001
t value	PG: 0.086	-4.94	-1.01	1.22	-0.27	-1.22	0.22	1.04	-2.07
p value	EG: <0.001	<0.001	0.315	0.228	0.787	0.226	0.828	0.303	0.041
	MAG: <0.001								
IT	C: <0.001	-0.002 ± 0.0004	$-5.94e^{-5} \pm 5.47e^{-5}$	$5.35e^{-6} \pm 4.75e^{-6}$	0.005 ± 0.004	-0.002 ± 0.002	-0.001 ± 0.005	$-0.000006 \pm 8.8e^{-5}$	-0.001 ± 0.001
t value	PG: 0.818	-3.74	-1.09	1.12	1.18	-0.83	-0.32	-0.07	-0.91
p value	EG: 0.037	<0.001	0.281	0.264	0.242	0.409	0.753	0.947	0.367
	MAG: <0.001								
ST	C: <0.001	-0.002 ± 0.0003	$1.69e^{-5} \pm 4.43e^{-5}$	$-9.20e^{-7} \pm 3.88e^{-6}$	0.002 ± 0.003	-0.001 ± 0.002	-0.004 ± 0.004	0.00002 ± 0.00008	0.0003 ± 0.001
t value	PG: 0.672	-4.46	0.38	-0.24	0.68	-0.65	-0.88	0.28	0.25
p value	EG: <0.001	<0.001	0.703	0.813	0.501	0.520	0.380	0.784	0.805
	MAG: <0.001								
IN	C: 0.623	-0.0009 ± 0.0006	$7.49e^{-6} \pm 5.95e^{-5}$	$-2.81e^{-6} \pm 5.20e^{-6}$	-0.004 ± 0.005	-0.003 ± 0.003	0.003 ± 0.006	0.0001 ± 0.0001	0.0003 ± 0.002
t value	PG: 0.869	-1.54	0.13	-0.54	-0.84	-1.10	0.61	1.41	0.18
p value	EG: 0.008	0.128	0.900	0.591	0.404	0.274	0.545	0.162	0.857
	MAG: <0.001								

Table 3.12: Independent variables included in regional analysis of minimum rim area. Presented as effect size ± standard error (i.e. how much minimum rim area changes per one-unit change in the independent variable), also the t-value and *p*-value. Red text indicates the independent variable had a significant effect at $p < 0.05$ and therefore included in the mixed-effects regression models.

III.6.10 Minimum rim width and area as a function of glaucoma disease stage and visual field sensitivity

Mean and standard deviation for regional measures of minimum rim width (MRW) and area (MRA) for each stage of glaucoma disease are presented in Appendix II, Table III.8. Inter-group differences for regional measures of MRW and MRA are presented in Table III.9 of Appendix II, and Figures 3.14 and 3.15. MRW was significantly less in PG than in controls in the superior (P = 0.028), inferior (P = 0.015), SN (P = 0.011), ST (P = 0.014), and IN regions (P = 0.024). No significant difference in minimum rim area (MRA) was found between controls and PG in any ONH region.

All regional MRWs were significantly less in EG and MAG when compared to controls ($P \leq 0.007$). MRA was significantly less in EG than controls in the inferior (P <0.001), SN (P = 0.002), ST (P = 0.001), and IN (P < 0.001) regions. In all regions of the ONH MRA was significantly less in MAG than controls, apart from the temporal region (P = 0.181).

Significant differences were found between PG and EG MRW in the inferior (P = 0.013) and ST (P = 0.034) regions, whereas MRA differences were observed between PG and EG in the inferior (P = 0.017), nasal (P = 0.041), IT (P = 0.030), and ST (P = 0.019) regions. MRW and MRA were significantly lower in MAG than PG in all regions of the ONH, apart from temporal. In MAG, MRW was also significantly lower than EG in all regions of the ONH, apart from the nasal (P = 0.392) and temporal (P = 0.447) regions. MRA was significantly lower in MAG than in EG in the superior (P = 0.009) and inferior (P = 0.043) regions.

In all regions of the ONH there was a significant negative correlation between VF MD and minimum rim width and area (see Figure 3.16). This suggested that with progression of VF loss, there is thinning of the minimum rim width, and a decrease in minimum rim area. The strongest correlation found between VF MD and minimum rim width was is the inferior, IT, and ST regions (r = -0.52, P < 0.001), and with the ST minimum rim area (r = -0.45, P < 0.001).

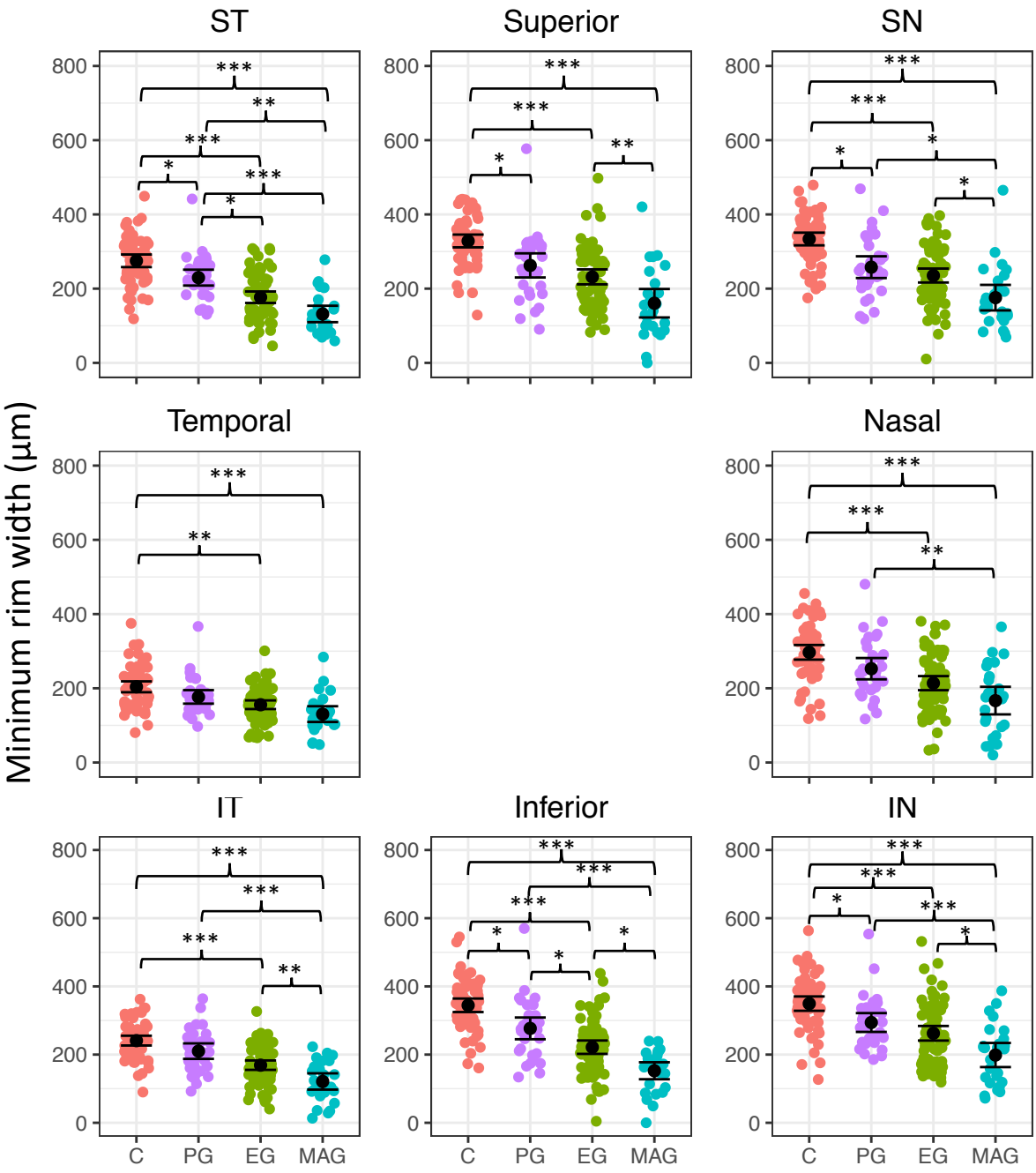

Figure 3.14: Inter-group comparisons of regional minimum rim width as a function of glaucoma disease stage. Black point represents group mean. Error bars represent 95% confidence intervals. * = $P < 0.05$, ** = $P < 0.01$, *** = $P < 0.001$.

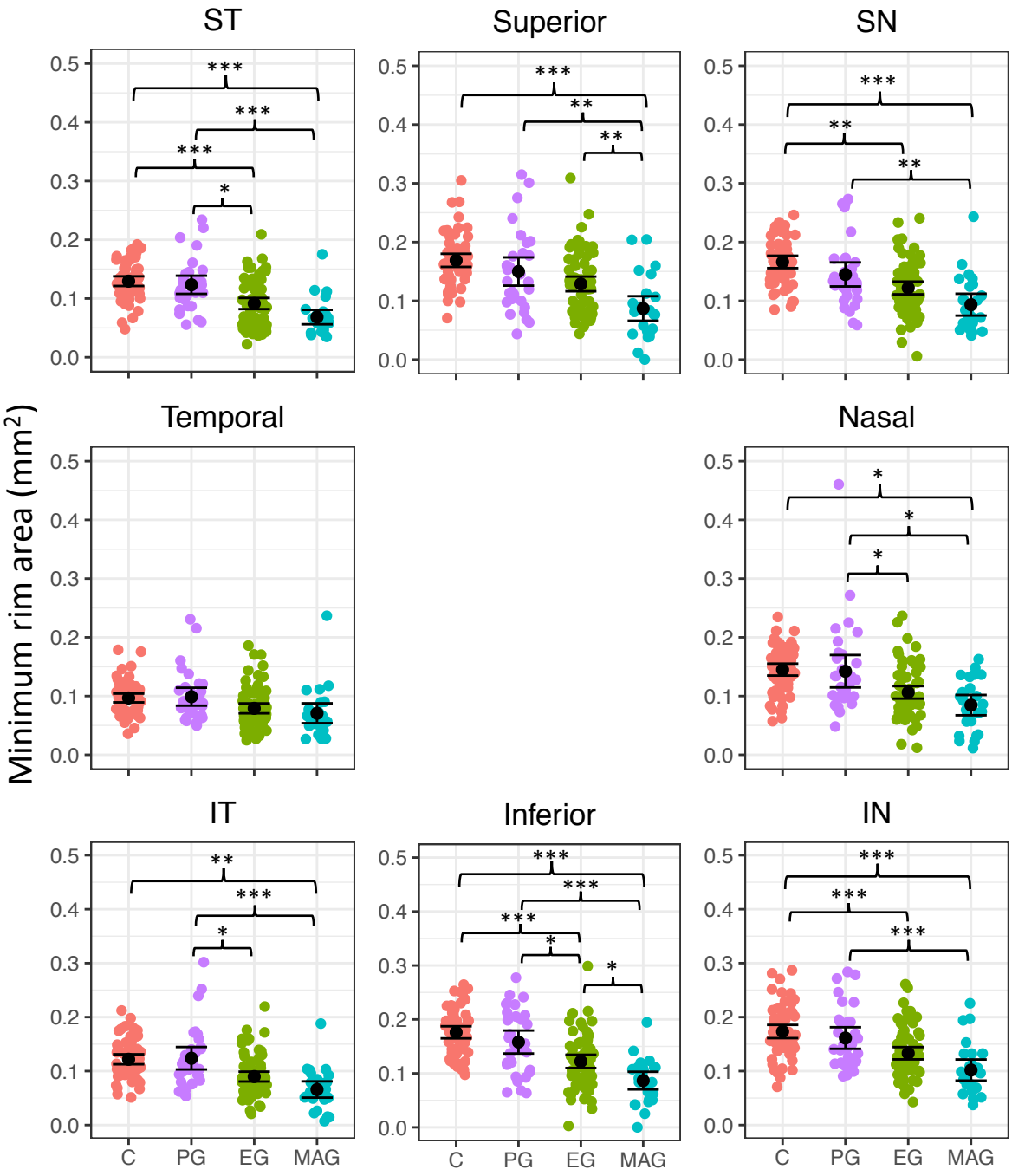

Figure 3.15: Inter-group comparisons of regional minimum rim area as a function of glaucoma disease stage. Black point represents group mean. Error bars represent 95% confidence intervals. * = $P < 0.05$, ** = $P < 0.01$, *** = $P < 0.001$.

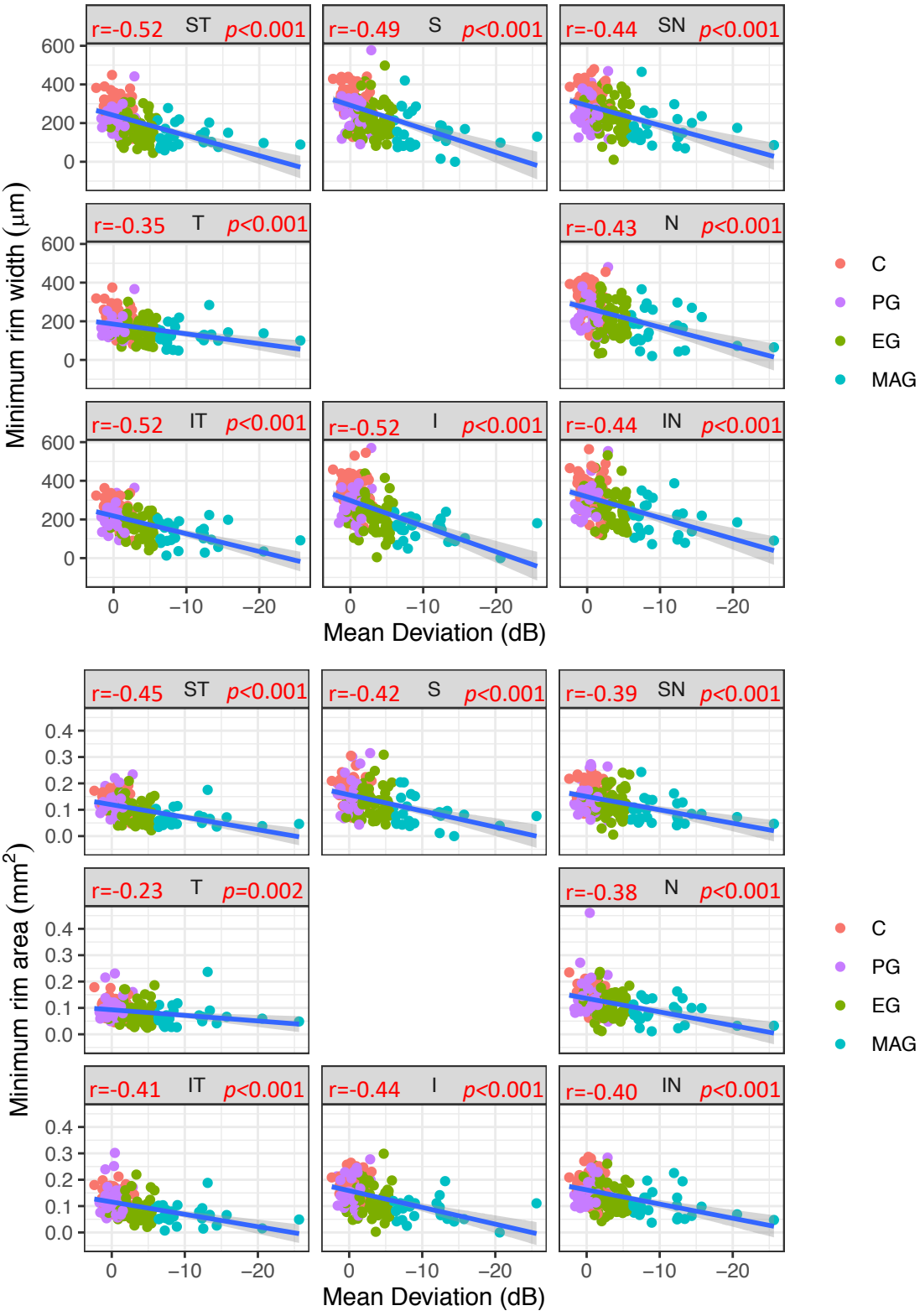

Figure 3.16: Regional minimum rim width and area as a function of visual field loss. Blue line represents regression line and grey shading represents 95% confidence intervals. Red text indicates significant Pearson's correlation at $P < 0.05$.

III.7 Discussion

A characteristic sign of glaucomatous optic neuropathy is morphological changes to the optic disc due to mechanical compression and damage to ONH neural and connective tissues (Quigley, 1993; Gandhi and Dubey, 2013; Wu et al., 2015). This leads to thinning of the neuroretinal rim, enlargement of the optic cup and characteristic excavation of the ONH (Quigley and Green, 1979; Jonas et al., 1988c; Weinreb and Khaw, 2004).

This chapter evaluated changes in ONH depth and thickness parameters as a function of glaucoma disease stage, and with respect to visual function in order to elucidate ocular parameters that characterise ONH changes in glaucoma and hold potential as biomarkers of disease. This study is original as it evaluates *in vivo* regional ONH depth and thickness parameters according to glaucoma disease stage. To address this aim, this study used OCT image slices extracted from 3D OCT image datasets to quantify regional measurements of BMO diameter, prelamina depth and thickness, LC depth and thickness, MRW and MRA, and NFL thickness at the ONH border and peripapillary. Significant findings of this study, according to glaucoma disease stage, are summarised in Tables 3.13 and 3.14, and Figures 3.17 and 3.18.

Alteration to RGC axon-related parameter according to glaucoma stage		
Control to PG	**PG to EG**	**EG to MAG**
• ↓ prelamina thickness in all regions, apart from nasal • ↓ bNFL in inferior, temporal, and IT regions • ↓ superior pNFL • ↓ MRW in all regions, apart from nasal, temporal, and IT • No significant difference in MRA	• ↓ bNFL in the superior, inferior, SN and ST regions • ↓ pNFL in the ST region • ↓ MRW in the inferior and ST regions • ↓ MRA in the inferior, nasal, IT, and ST regions • No significant difference in prelamina thickness	• ↓ prelamina thickness in superior ONH region • ↓ bNFL in all regions, apart from temporal • ↓ pNFL in inferior, temporal, IT, and ST regions • ↓ MRW in all regions, apart from nasal and temporal • ↓ MRA in superior and inferior regions
Alteration to RGC axon-related parameter versus VF MD		
↓ in prelamina thickness in all ONH regions with VF loss ↓ bNFL, pNFL, MRW, and MRA in all regions with loss of VF function		

Table 3.13: Summary of regional axon-related parameter alterations as a function of glaucoma disease stage and VF MD. Red text indicates significant alteration in axon-related parameters.

Alteration in ONH structural parameters according to glaucoma stage		
Control to PG	**PG to EG**	**EG to MAG**
• ↑ prelamina depth in all regions; except temporal and centre • ↓ LC thickness in inferior, SN, and IN regions • No significant difference in BMO diameter • No significant difference in anterior or posterior LC depth	• ↑ BMO V:H ratio • No significant difference in prelamina depth • No significant difference in anterior or posterior LC depth, or LC thickness	• ↑ N-T BMO diameter • ↑ prelamina depth in superior ONH region • No significant difference in anterior or posterior LC depth, or LC thickness
Alteration in ONH structural parameters versus VF MD		
↑ prelamina depth in all ONH regions with VF loss ↑ anterior LC depth with VF loss in all ONH regions, apart from temporal and IT ↓ LC thickness in all regions with loss of VF sensitivity No significant association between BMO diameter and VF MD No significant alteration in posterior LC depth with VF loss		

Table 3.14: Summary of regional ONH structural parameter alterations as a function of glaucoma stage and VF MD. Red text indicates significant alteration in ONH structure.

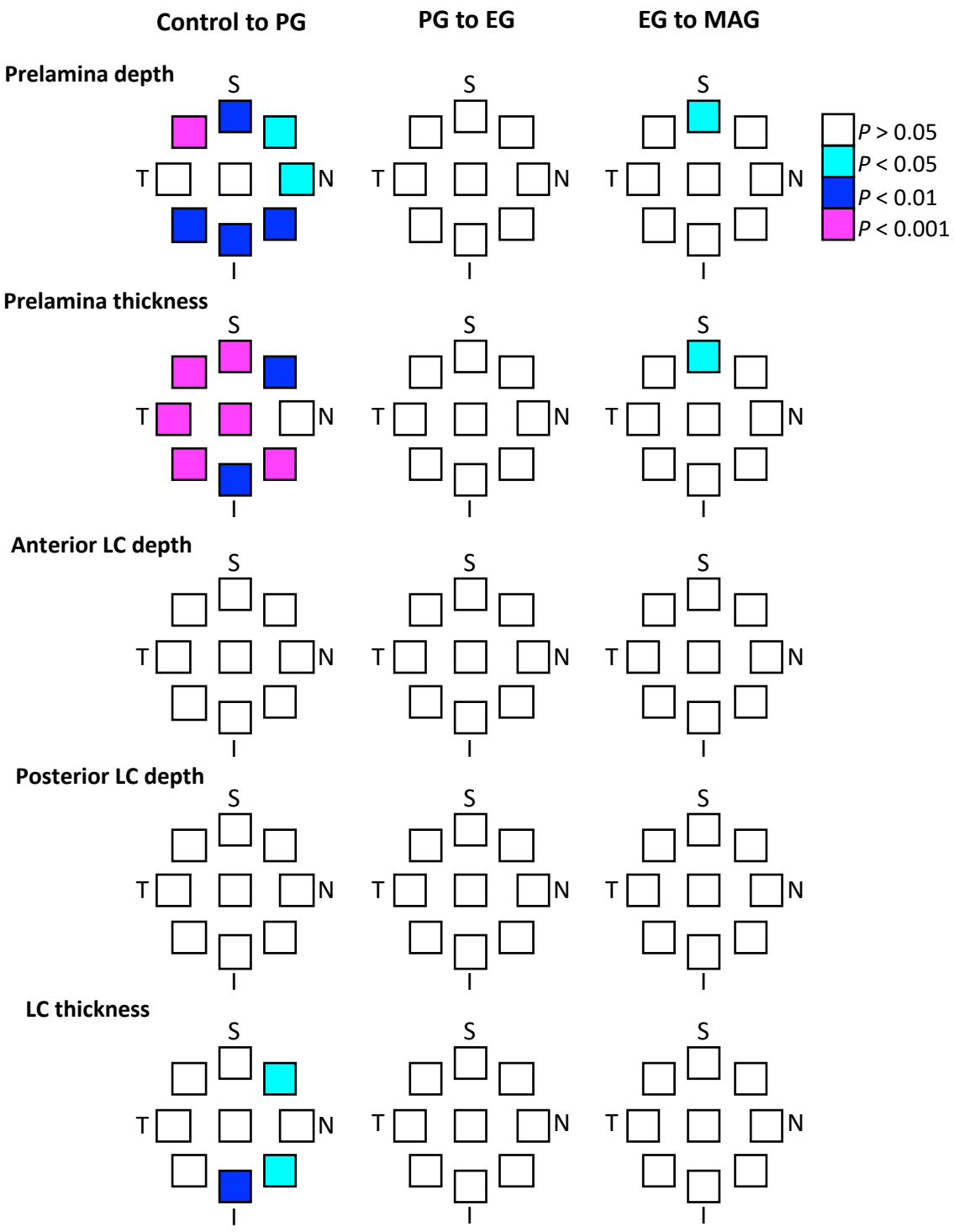

Figure 3.17: Summary of alteration in prelamina depth and thickness, and LC depth and thickness according to glaucoma disease stage.

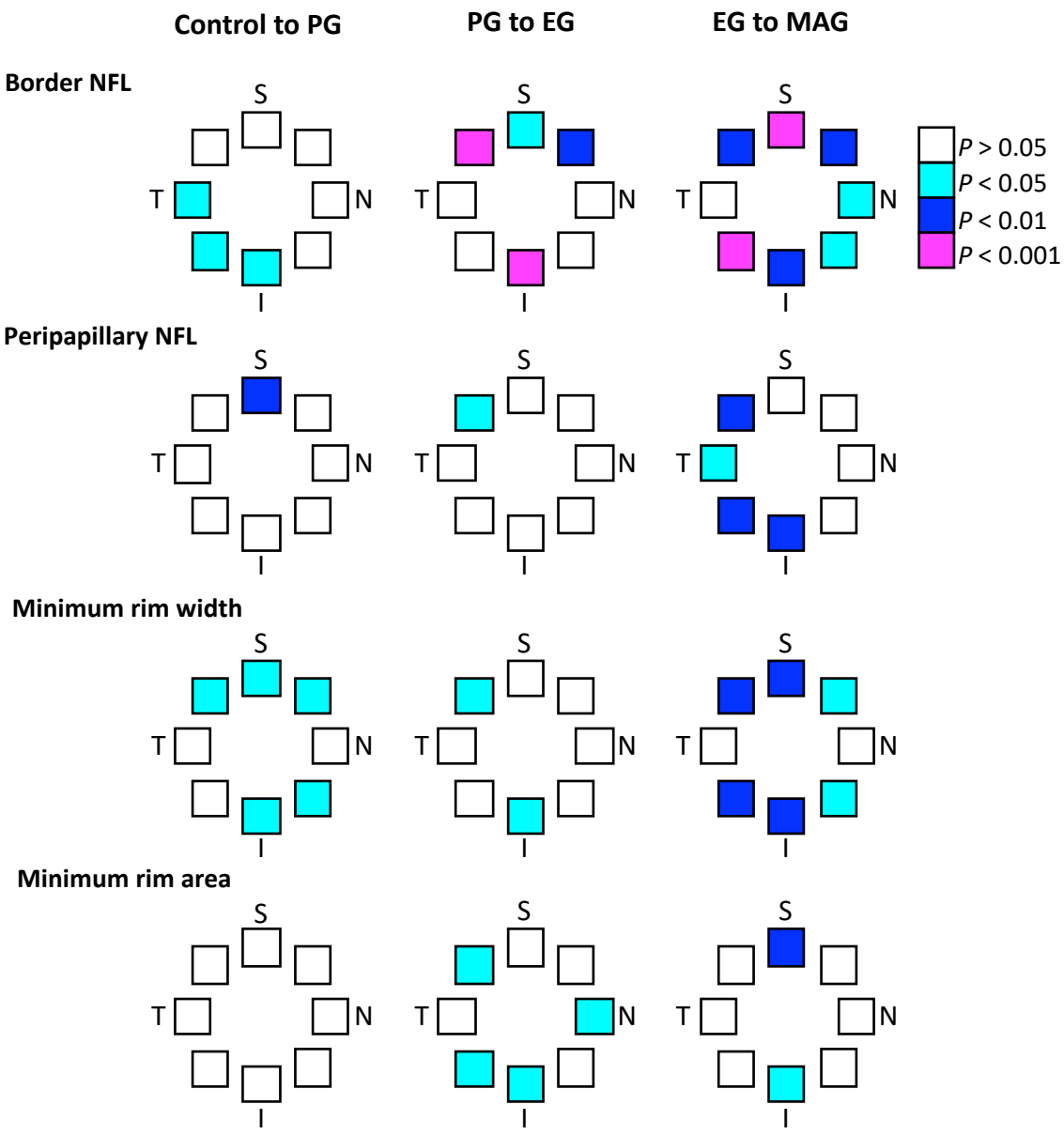

Figure 3.18: Summary of alteration in bNFL, pNFL, MRW, and MRA according to glaucoma disease stage.

III.7.1 Bruch's membrane opening in glaucoma disease

In this current study BMO diameter across four orientations of the ONH was used as a surrogate measure for optic disc size as a function of glaucoma disease stage, however BMO diameter did not differ between controls and glaucoma stages (namely PG, EG, or MAG). Additionally, except for an increased nasal-temporal BMO diameter in MAG, compared to EG, BMO diameter did not differ between PG, EG, and MAG. The vertical-to-horizontal (V:H) BMO ratio was larger, i.e., more vertically oval in EG than PG, but no difference was observed between EG and MAG, or controls and glaucoma stages. This study found that BMO diameter

did not significantly correlate with progression of visual field loss in any of the four ONH orientations; superior-inferior, nasal-temporal, SN-IT, and SN-IT, which is in agreement with Jonas, Fernandez and Naumann (1991).

Controversy exists as to the role of optic disc size in glaucoma. Optic discs that are larger in diameter have been reported to be at higher risk of glaucomatous ONH damage at normal levels of IOP (Chi et al., 1989; Burk et al., 1992). Additionally, Tuulonen and Airaksinen (1992) report that optic disc area in low-tension glaucoma was statistically significantly larger than in primary open angle and exfoliative glaucoma. Optic disc area did not significantly differ between POAG and exfoliative glaucoma, although smaller optic discs were more frequent in exfoliative glaucoma, whereas larger discs were more frequent in low-tension glaucoma. The authors mentioned that eyes with larger optic disc size could be more vulnerable to glaucomatous damage even at low levels of IOP due to extracellular matrix properties within the ONH (Hernandez et al., 1990; Tuulonen and Airaksinen, 1992; Hernandez and Pena, 1997; Varela and Hernandez, 1997). Other studies have not found optic disc size to be significantly different between POAG and control eyes, nor does optic disc size significantly correlate with loss of optic nerve fibres in glaucoma (Jonas et al., 1988c; Jonas et al., 1991).

The significant positive association between axial eye length and BMO diameter in all orientations of the ONH, apart from superior-inferior, is in agreement with Zhang et al. (2019) who reported that a larger horizontal BMO diameter was associated with increasing axial length (up to 26.0mm), with no effect on vertical BMO diameter. Also Zhang et al. (2019) reported that BMO diameter had a positive linear association with axial eye length (beyond 26.0mm) in both meridians. As described in section II.7, in this study, participant axial eye length was included in the calculation for OCT image pixel calibration, which potentially explains why axial length was not found to have a significant association with BMO diameter in all ONH orientations. Zhang et al. (2019) do not describe the incorporation of axial eye length in OCT image pixel calibration, and therefore may explain the significant positive association between axial length and BMO diameter reported with increasing axial length. This current study did not find that BMO diameter was significantly associated with axial length in all orientations of the ONH, although this study agrees with the importance of

including axial length in statistical models to investigate alterations to BMO diameter as a process of glaucomatous disease.

III.7.2 Prelamina depth and thickness in glaucoma disease

Within the ONH, the prelamina tissue is primarily composed of RGC axons, capillaries and glial cells (Lucy et al., 2015; Wang et al., 2017). This study found that prelamina depth was significantly greater, and prelamina tissue significantly thinner than control eyes in all stages of glaucoma. Additionally, in all regions of the ONH, an increase in prelamina depth and a decrease in prelamina thickness was significantly associated with loss of VF sensitivity. These results suggest that during the progression of glaucoma disease, thinning of prelamina tissue is consistent with increased loss of RGC axons, and the prelamina surface is positioned more posteriorly within the ONH. These features relate to the increased ONH cupping with the advancement of glaucomatous optic neuropathy (Vrabec, 1976; Quigley and Green, 1979; Jonas et al., 1988c; Yang et al., 2007a; Downs et al., 2011).

In all regions of the ONH, this study found that prelamina depth (relative to BMO) was significantly greater in each of the glaucoma groups compared to controls, apart from the centre and temporal ONH regions where prelamina depth did not significantly differ between controls and PG. With advancement of glaucoma disease stage, prelamina depth was also significantly greater in MAG than PG in the superior and inferior regions, and greater in MAG than EG in the superior region.

Glaucomatous damage results in a distinctive change in ONH structure, clinically termed ‘cupping’. ONH cupping can be divided into two parts; the prelamina component, and the LC component (Quigley and Green, 1979; Yang et al., 2007a; Tun et al., 2016; Tan et al., 2019). The prelamina component is characterised by progressive loss of the prelamina neural tissues, which increases cup depth and width, thereby also increasing the cup to disc ratio. The LC component involves the connective tissue, causing progressive posterior movement of the LC and excavation beneath the anterior scleral canal (Downs et al., 2011). Glaucomatous cupping is mostly a combination of both prelamina and LC components, reflecting both damage to, deformation and remodelling of the LC connective tissues, and progressive loss of RGC axons (Quigley, 1999; Downs et al., 2011). Therefore, these observations in glaucoma disease align

with that reported in this current study whereby an increase in prelamina depth and decrease in prelamina thickness corresponds to the characteristic ONH appearance seen in glaucoma disease.

In this study, quantitative analysis of prelamina depth in the central region of the ONH found a comparable trend to that reported by Kim et al. (2016). Central prelamina depth for control participants in this study was 115.78 ± 193.13µm, for PG: 251.74 ± 124.08 µm, for EG: 248.45 ± 158.95 µm, and for MAG: 293.19 ± 180.06µm. In POAG participants with unilateral VF loss, Kim et al. (2016) investigated central prelamina depth. They report that POAG participants with VF loss displayed significantly greater central prelamina depth (460.88 ± 139.05µm) than POAG eyes with no VF defect (384.35 ± 131.67µm), and also compared to control participants (296.00 ± 154.98µm). Further to this, the fellow eyes of POAG participants with unilateral VF loss displayed significantly greater central prelamina depth than healthy controls (Kim et al., 2016). Differences in values reported for central prelamina depth by this study and those reported by Kim et al. (2016) could be related to differences in axial eye length and refractive error. The participants included in this thesis had a mean spherical refraction of +0.36 ± 2.31 DS, and an average axial length of 23.86 ± 1.27mm, whereas in the study conducted by Kim et al. (2016), the POAG group with unilateral VF loss had a mean spherical refraction of -1.75 ± 3.00 DS, and axial length of 24.24 ± 0.21 mm. With larger axial length and more myopic refractive error, hence larger optic discs (Saw et al., 2005; Jonas and Xu, 2014), this could partly account for the larger values of central prelamina depth reported by Kim et al. (2016). For example, in the nasal ONH, this study found that axial length had a significant positive effect on prelamina depth, meaning that eyes with longer axial length displayed larger prelamina depth.

In this current study, compared to control participants, prelamina tissue was significantly thinner in PG, EG, and MAG in all regions of the ONH, apart from nasal ONH, where prelamina thickness was not significantly different between PG and controls. Each group of glaucoma participants displayed significantly thinner prelamina tissue than controls, although not always different between each stage of glaucoma. For example, only in the superior ONH was prelamina significantly thinner in MAG than PG and EG. Prelamina thickness was also significantly lower in MAG than PG in the inferior and inferior-temporal regions. Note that

inferior prelamina thickness was over twice as thick in PG (328.26 ± 193.12μm) than in MAG (151.78 ± 87.69μm). Additionally, in the superior, inferior, and central regions of the ONH, prelamina thickness was reduced by approximately 50% from controls to PG. This suggests that regional measures of prelamina thickness could act as key biomarkers for the early detection of glaucoma onset and could act to indicate disease progression.

Conversely to this study, Lee et al. (2011) found no significant difference in central prelamina thickness between controls, glaucoma suspects, and glaucoma participants. This study found central prelamina thickness for control participants to be: 251.98 ± 161.20μm, for PG: 134.52 ± 64.95μm, for EG: 137.37 ± 82.71μm, and for MAG: 127.08 ± 75.78μm. Lee et al. (2011) reported lower values for central prelamina thickness in controls; 111.43 ± 34.98μm, and in glaucoma: 95.70 ± 28.46μm. Also, interestingly, they reported thinner prelamina tissue in glaucoma suspects (93.83 ± 18.74μm) than in glaucoma patients. These differences in findings could be the result of differences in methodology. This study used the mid-point of BMO to define the centre of the ONH, whereas Lee et al. (2011) recorded measures as centrally as possible within the ONH where there was least vascular shadowing. Also the sample size included by Lee et al. (2011) was smaller than this study, where they evaluated 10 controls, 7 glaucoma suspects, and 18 glaucoma participants. Lee et al. (2011) did not provide patient ages for the three groups of their participants, only mean age for the total of their 35 participants, and likewise for VF MD. Therefore, it is hard to determine the stage of disease of the glaucoma participants. If the majority of glaucoma participants were preperimetric or early glaucoma, in addition to a small sample size, these factors could potentially explain the difference in findings between their study and ours.

According to glaucoma disease stage, this study has determined significant regional alterations to prelamina depth and thickness. Indeed, following acute IOP elevation in human eyes, Agoumi et al. (2011) reports compression of the prelamina tissue. An increase in prelamina thickness has been reported following IOP reduction surgery where it is reported that the prelamina tissue acts as a 'buffer' in response to IOP changes; where it compresses under increased IOP and becomes thicker when IOP is lowered (Reis et al., 2012a; Barrancos et al., 2014; Krzyzanowska-Berkowska et al., 2018). Therefore, this suggests that the prelamina is a dynamic structure that significantly alters in disease and in response to IOP

alterations, suggesting prelamina depth and thickness as useful indicators for not only glaucoma detection, but also as therapy outcome measures.

This study found that stage of glaucoma was significantly associated with prelamina depth and thickness in all regions of the ONH. Age was not found to be significantly associated with prelamina depth, although it had a significant negative association with prelamina thickness in the inferior, IT, IN, and SN regions, suggesting significant thinning of prelamina tissue with increasing age. This corresponded to previous work that mentioned that loss of RGCs is part of the normal aging process, and causes reduced visual sensitivity across the visual field (Johnson, Adams and Lewis, 1989). Harwerth et al. (2008) report an age dependent reduction of 0.5% per year in the density of RGC axons.

This current study also found that central corneal thickness had a significant negative association with prelamina depth in all regions of the ONH, apart from inferior-temporal and inferior-nasal; meaning that eyes with thicker corneas displayed prelamina surface closer to BMO. This study reports on the potential of regional measures of prelamina depth and thickness being important biomarkers in the detection and assessment of glaucomatous disease. However, multivariate analyses performed in this study highlights the importance of ocular parameters such as axial length, refractive error, and central corneal thickness, along with participant age being taken into consideration when using OCT-derived measurements of prelamina depth and thickness in the evaluation of the glaucomatous ONH.

III.7.3 Lamina cribrosa depth and thickness in glaucoma disease

Anterior and posterior LC surface depth did not alter as a function of glaucoma disease stage in any region of the ONH. This is inconsistent with Quigley et al. (1983) who reported that posterior bowing of the LC was a later change involving the superior and inferior poles more than the mid nerve head region, compatible with regional differences in the structure of the LC (Quigley and Addicks, 1981; Radius and Gonzales, 1981).

Enlargement of the scleral canal and posterior displacement of the LC has also been described in non-human primate models of experimental glaucoma (Bellezza et al., 2003; Yang et al., 2011a; Yang et al., 2011b). This study reported contradictory findings to previous studies

whereby this present study did not find significant alterations in anterior or posterior LC surface depth according to glaucoma disease stage in any ONH region. This may be related to a difference in participant numbers included in this study for each of the glaucoma groups, in PG; n = 32, in EG; n = 69, and MAG; n = 26; a larger sample size in the PG and MAG groups and a longitudinal study is required to confirm any alterations in LC depth as a function of glaucoma disease stage.

Converse to this study, Park et al. (2015) found that mean LC depth was significantly greater in PG compared to controls, and mild-to-moderate glaucoma participants displayed significantly greater LC depth than PG. They did not report a significant difference in LC depth between mild-to-moderate and severe glaucoma. Differences in these findings to this study could be related to the grouping of glaucoma participants. Their groups included preperimetric, mild-to-moderate (VF MD better than -12 dB), and severe glaucoma (VF MD worse than -12dB), whereas our glaucoma groups included preperimetric, early (VF MD better than -6 dB), and moderate-advanced glaucoma (VF MD worse than -6 dB). Their sample size was also larger, including normal (n = 86), preperimetric (n = 47), mild-to-moderate (n = 55), and severe (n = 60). Therefore, their analysis included more cases of preperimetric and severe glaucoma cases than our study. Also, the methodology for obtaining LC depth measures was different between studies. In our study, LC depth was measured in 9 different locations/regions within the ONH. Park et al. (2015) measured LC depth at 11 points on the vertical meridian of the ONH and calculated the mean LC depth. Therefore, the LC depth in each group was approximated and may not accurately represent the true depth of the entire anterior LC surface in each group. Additionally, Park et al. (2015) appear not to have taken axial eye length into consideration when performing OCT image analysis, thereby erroneously recording with the magnitude of error confounded by axial length (Terry et al., 2016). Discrepancies in findings between Park et al. (2015) and our study could be explained by omitting axial length from analyses as Seo, Kim and Weinreb (2014) report larger LC depths in eyes with shorter axial length.

Furthermore, the mean age of glaucoma participants included by Park et al. (2015) is approximately 60 years of age. In this study, the mean age of glaucoma participants is over 70 years of age. Differences in participant ages between studies could explain why Park et al.

(2015) found significant differences in LC depth with advancing glaucomatous disease, as older participants with less compliant LC (Albon et al., 2000b; Midgett et al., 2017), may demonstrate less alteration in LC depth as a function of glaucoma disease stage. Further to this, in participants of European descent (which describes participants included in this study), Rhodes et al. (2014) reported that with increasing age there was significant anterior movement of the LC; potentially explaining why participants of greater age included in this study did not display significant alteration in LC depth.

Another possible explanation for the reason that this study did not observe significant differences in LC depth between control and glaucoma participants, or between PG, EG, and MAG is that all the glaucoma participants recruited in this study were continuing with ongoing topical glaucoma treatment. Following reduction of IOP in POAG patients, it is well documented that there is reversal of LC posterior displacement (Lee, Kim and Weinreb, 2012; Reis et al., 2012a; Lee et al., 2013a; Yoshikawa et al., 2014; Krzyzanowska-Berkowska et al., 2018). Due to the cross-sectional design of this study, therefore it would not be possible to detect alterations in LC depth as a function of glaucoma disease stage if reversal of LC depth following IOP reduction treatment had already occurred prior to OCT image acquisition and data analysis.

This study found that anterior LC depth significantly correlated with VF MD in all ONH regions, apart from the temporal and inferior-temporal ONH regions, i.e., anterior LC depth significantly increased with increasing VF loss, although posterior LC depth did not significantly correlate with VF MD in any ONH region. However, Park et al. (2015) did not find a significant correlation between LC depth and VF MD, nor between LC depth and NFL thickness, perhaps due to the lack of inclusion of control participants in performing these analyses.

In this study, LC thickness was significantly less in all stages of glaucoma than control eyes and thinning of the LC was significantly associated with loss of VF sensitivity in all regions of the ONH, with the strongest association being found in the inferior-temporal region. LC thickness was significantly lower in PG than controls in the inferior, inferior-nasal and superior-nasal ONH regions. LC thickness was also significantly different between controls and EG in the

central, superior, inferior, superior-nasal, and superior-temporal regions, but not between PG and EG, or between EG and MAG. In MAG, the LC was significantly thinner than controls in all ONH regions, apart from nasal, and central MAG LC thickness was significantly lower than in PG.

In this study, central LC thickness for control participants was found to be 232.81 ± 37.24μm, which was significantly different to EG: 197.07 ± 40.10μm and MAG: 175.69 ± 28.98μm. Other *in vivo* studies using EDI SD-OCT have found similar results; Lee et al. (2011) found central LC thickness to be 254.80 ± 69.31 μm in the control group, 242.67 ± 68.02 μm for glaucoma suspects, and 215.67 ± 58.26 μm for glaucoma participants. Inoue et al. (2009) found central LC thickness in ocular hypertensive eyes with no vision loss to be 244.44 ± 47.2μm and 198.0 ± 43.7μm, 182.0 ± 22.9μm, 130.1 ± 32.7μm for early, moderate, and advanced glaucoma respectively, which were significantly different between groups. This study performed measurements of central LC thickness in a slightly different location within the ONH than Inoue et al. (2009) as central LC depth and thickness was measured at the mid-point on a BMO reference plane, whereas Inoue et al. (2009) performed measurements near to ONH centre where both the anterior and posterior boundary of the LC could be identified on an OCT B-scan without vascular shadowing. Consistent with this study, Park et al. (2012a) measured LC thickness in the central ONH, and mid-superior and mid-inferior regions for healthy controls, POAG, and also a normal tension glaucoma (NTG) group, reporting a thinner LC thickness in all three ONH regions in POAG and NTG group, compared to the control group.

Age was found to have a significant negative association with anterior LC depth in the central region, and in the central and ST region for posterior LC depth. This aligns with that reported by Rhodes et al. (2014) who found an anterior migration of the LC with increasing age. This study found that age had no significant association with LC thickness in any region of the ONH. However, previous work, in *ex vivo* tissue, has described an increase in human LC thickness with increasing age (Kotecha, Izadi and Jeffery, 2006).

This study found that central corneal thickness had a significant negative association with anterior and posterior LC depth in all ONH regions, apart from the inferior and inferior-temporal regions; indicating that in eyes with thicker corneas the LC is positioned closer to

BMO. In the majority of ONH regions, central corneal thickness was not significantly associated with LC thickness. This aligns with previous work suggesting no significant association between central corneal thickness and LC thickness in healthy eyes (Jonas and Holbach, 2005; Ren et al., 2010; Lee et al., 2013b). The observations from this study of central corneal thickness having a negative association with prelamina and LC depth imply that eyes with thinner corneas display greater prelamina and LC depth relative to BMO, which would result in a more cupped or excavated appearance to the ONH. This coincides with the findings that thinner central corneal thickness is a risk factor for glaucoma, although the reason for this is yet to be determined (Gordon et al., 2002; Herndon, Weizer and Stinnett, 2004; Jonas et al., 2005). Perhaps a thinner cornea provides less structural support in the wall of the eye, allowing the prelamina tissue and LC to be more easily displaced posteriorly with IOP.

Interestingly, IOP had a significant positive association with LC thickness in all regions of the ONH, apart from inferior, suggesting that eyes with higher IOP displayed thicker LCs. As mentioned earlier, all participants diagnosed with POAG in this study were receiving ongoing IOP lowering topical medication and displayed lower IOP than the control participants. Therefore, it holds true that participants with higher IOP (controls) also displayed greater LC thickness.

III.7.4 Nerve fibre layer thickness and area in glaucoma

Glaucoma impedes visual function by the loss of RGC axons and the death of RGCs, ultimately leading to blindness (Quigley, 1999). Therefore, it is vital that glaucoma is diagnosed as early as possible to commence treatment to slow or prevent further permanent vision loss. This current study found that bNFL, pNFL, MRW, and MRA significantly altered as a function of glaucoma stage, and significantly decreased in all ONH regions with loss of VF sensitivity. Measures of bNFL, pNFL, and MRW were able to distinguish PG from control eyes, hence prior to VF loss. This corresponds with previous work where it has been suggested that significant structural damage to the ONH and RNFL may precede vision loss (Gordon et al., 2002; Harwerth and Quigley, 2006; Harwerth et al., 2010).

In the present study, in all ONH locations, bNFL and MRW was significantly less in EG and MAG than in the control group. Border NFL was significantly thinner in PG than controls in the

inferior, temporal, and inferior-temporal ONH regions, whereas MRW differed between controls and PG in the superior, inferior, SN, ST, and IT regions of the ONH. Additionally, superior pNFL was significantly less in PG than in control eyes. However, MRA did not significantly differ between controls and PG in any ONH region. Border NFL and MRA was significantly different between PG and EG in several regions of the ONH. Minimum rim width differed between PG and EG in the inferior and ST regions and pNFL also differed in the ST region. The common region that was significantly different between PG and EG for bNFL, pNFL, MRW, and MRA was the superior-temporal region of the ONH. Border NFL was significantly less in MAG than EG in all ONH regions, apart from temporal, and pNFL significantly differed between EG and MAG in the inferior, temporal, IT, and ST regions. In MAG, MRW was significantly lower than EG in all regions, apart from nasal and temporal, and MRA significantly differed between EG and MAG in the superior and inferior ONH regions. Therefore, these findings suggest that parameters such as bNFL, pNFL, MRW, and MRA are useful in the early detection of glaucoma onset and could inform of potential disease progression.

In all regions of the ONH, this study determined a significant reduction in bNFL, pNFL, MRW, and MRA with loss of VF function. There has been shown to be a strong linear relationship between the number of RGC axons remaining and RNFL thickness measured *in vivo* by SD-OCT (Cull et al., 2012). Wollstein et al. (2012) used SD-OCT to evaluate RNFL thickness in 72 healthy controls and 40 glaucoma participants to determine the RNFL thickness at which VF defects become detectable and associated with structural loss. They concluded that substantial RNFL thickness loss (approximately 17%) appears to be necessary for visual function loss to be detectable using current VF testing. These findings align with the current clinical assessment of glaucoma in that measurement of RNFL thickness by OCT has become a standard clinical observation (Medeiros et al., 2009b; Na et al., 2013; Fortune, 2019).

Peripapillary (pNFL) thickness has been shown to have good diagnostic ability in distinguishing normal eyes from those with glaucoma (Leung et al., 2010b; Li et al., 2010), and using measurements of RNFL derived from SD-OCT images are a useful clinical tool in the screening and detection of glaucoma progression (Mwanza et al., 2013; Bussel et al., 2014). *In vivo* measures of pNFL has been reported to be an accurate parameter for glaucoma detection

using both TD-OCT (Leung et al., 2008) and SD-OCT (Jeoung and Park, 2010; Leung et al., 2010b; Bussel et al., 2014). Lee et al. (2010b) determined that compared to TD-OCT, SD-OCT allows for an improved structure-function correlation between RNFL thicknesses and VF MD. Indeed, Lisboa et al. (2013) report that RNFL measurements derived from SD-OCT performed better than macula and ONH measurements in the detection of preperimetric glaucomatous damage. Additionally, Fang et al. (2010) determined the diagnostic capabilities of glaucoma detection using SD-OCT and suggested that pNFL measurements and the vertical cup-disc ratio were better indicators of glaucoma detection than measurements of the ganglion cell complex.

Minimum rim width is an ONH parameter similar to bNFL, although instead of being the distance directly above BMO terminations to inner limiting membrane (ILM), MRW has been defined as the shortest distance between BMO and the ILM in SD-OCT scans (Povazay et al., 2007b; Reis et al., 2012b; Chauhan et al., 2013). Therefore, the angle between BMO plane and the position that MRW is measured can vary. Even though potentially performed at different angles from BMO plane, both bNFL and MRW measure the same structure; the neuroretinal rim tissue, containing RGC axons and supporting connective tissue. In this study, MRW significantly differed between controls and PG in all ONH regions, apart from nasal, temporal, and IT. In PG, pNFL was significantly thinner than controls, although, in the superior ONH region only; suggesting MRW may be a better parameter for the early detection of glaucoma disease. Correspondingly, measures of MRW have been shown to have better glaucoma diagnostic abilities than measurements of pNFL thickness (Chauhan et al., 2013). Using the 3D SD-OCT image dataset, radial scans can be used to derive the ONH parameter minimum rim area (MRA) through which RGC axons must pass (Gardiner et al., 2014). The ONH parameter MRA adjusts for the fact that optic disc size will influence MRW, and not just the number of axons. The measures MRW and MRA have been shown to correlate better with visual function than the previously used ‘horizontal’ rim measurements (Chauhan et al., 2013; Gardiner et al., 2014).

In this study, age had a significant negative association with MRW and MRA in all ONH regions, apart from the inferior-nasal region. Additionally, age was not significantly associated with MRA in the temporal region. Age also had a significant negative association with bNFL and

pNFL in the inferior-temporal and superior-temporal ONH regions, including the superior regions for bNFL, suggesting a decrease in bNFL, pNFL, MRW, and MRA with increasing age. In a cross-sectional analysis of one hundred normal individuals, Leung et al. (2012) also found significant thinning of pNFL with increasing age. In the inferior region they found that pNFL thinned at a rate of -0.45µm/year, in the temporal region -0.31µm/year, and on average pNFL thinned by -0.33µm/year. Axial length also had a significant negative association with bNFL and MRW, indicating that eyes with greater axial length displayed thinner bNFL and MRW. This could be related to findings that larger eyes also have larger ONHs (Saw et al., 2005; Oliveira et al., 2007; Jonas and Xu, 2014), therefore, in the larger ONH, the RGC axons could be more dispersed resulting in a thinner bNFL and MRW.

It has been previously suggested that MRW and MRA may be more sensitive for the early detection of glaucomatous damage, although RNFL thickness measured by SD-OCT may be preferable for monitoring change in glaucoma disease (Gardiner et al., 2015). However, as discussed, evidence from this study suggests that age and axial length have a significant influence over these NFL parameters and should be taken into consideration if they are to be used as clinical biomarkers for the identification of glaucoma onset or to indicate disease progression.

III.7.5 Study limitations

One of the limitations to this study, as with other *in vivo* OCT ONH imaging studies was the ability to visualise the entire LC throughout the regions of the ONH, thereby on some occasions inhibiting measurements of prelamina thickness, and LC depth and thickness. This was related to overlaying blood vessels or prelamina tissue causing shadows in the OCT image, and signal attenuation of the light source as the beam passes through tissue. In control eyes, where prelamina tissue was thicker than glaucoma participants, the anterior and particularly the posterior surface of the LC was less visible than glaucomatous eyes. However, in regions whereby the LC could not be accurately delineated no measurement was recorded, and not used to calculate prelamina or LC thickness.

This study performed regional analysis of ONH parameters using radial OCT scans set at 45° intervals, allowing measurements to be performed in nine regions within the ONH. Future

work may consider using radial scans at a closer interval, allowing analysis in more regions of the ONH to determine whether more ONH structural information could be gained in the study of the glaucomatous ONH.

Participant numbers in the four groups included in this study were not equal. In the control group: n=60, PG: n=32, EG: n=69, MAG: n=26. The addition of participants to the PG and MAG groups could add statistical power and allow for a more comprehensive analysis. Additionally, the age of the glaucoma participants included in this study was greater than the control participants. Increasing age is a well-established risk factor for glaucoma, therefore, this difference in age could be considered a weakness in this study.

Typically, researchers do not know with certainty which explanatory variables are appropriate to be included in multiple regression models. In data analysis, stepwise regression is a popular tool that uses statistical significance to select which explanatory variables are to be used in a multiple regression model (Smith, 2018). The stepwise regression method involves evaluation of the explanatory variables, one by one, typically using the *t*-statistic and *p*-values for the coefficients of each variable being considered (Thompson, 1995; Smith, 2018).

Starting with no explanatory variables, a forward selection method adds variables, one by one, according to which variable is the most statistically significant, until there are no statistically significant variables remaining. However, where there is not an obvious rationale for the order in which variables are sequentially added, a stepwise deletion method is usually preferred for statistical model optimisation (Walter and Tiemeier, 2009). As performed in this thesis study, a backward elimination stepwise method starts with all possible explanatory variables, then discards, one by one, the least statistically significant variables, until each variable included in the model is statistically significant (Whittingham et al., 2006).

Since statistical models are derived from the imperfect process of sampling, it must be deduced which 'significant' findings should be believed, and which should not (Babyak, 2004). In stepwise regression methods, when using a sequence of steps to determine the inclusion of explanatory variables, the standard errors of the coefficient estimates are underestimated, making the confidence intervals too narrow, the *t*-statistic too high, and the *p*-value too low

(Babyak, 2004). This leads to overfitting, creating a false confidence in the final model (Hurvich and Tsai, 1990; Smith, 2018). Overfitted regression-type models capitalise on the idiosyncratic characteristics of the data sample obtained which yields overly optimistic model results. Therefore, findings that appear in an overfitted model may not really exist at a population level and hence will not replicate, thereby reducing the generalisability of the statistical model for data outside of the sample obtained (Babyak, 2004). Therefore, due to the stepwise approach taken in this thesis study for the optimisation of regression models, resulting associations reported may not exist in a wider population of participants.

III.7.6 Conclusion

The findings from this study suggest that regional measures of prelamina depth and thickness, LC thickness, MRW, and border and peripapillary NFL thicknesses are able to discriminate between controls and PG, being the earliest stage of glaucoma, before vision loss is detected. Indeed, prelamina thickness significantly differed between PG and controls in 8 out of 9 ONH regions analysed, suggesting prelamina thickness as an important glaucoma indicator. Identifying ONH parameters that can discriminate between controls and PG could potentially act as biomarkers to aid in the diagnosis of glaucoma and therefore commence treatment prior to irreversible vision loss. Additionally, these parameters were able to detect differences between glaucoma participants based on disease stage, which could be useful to indicate glaucoma progression. This study did not find significant differences in anterior or posterior LC depth between glaucoma and control participants, nor with the progression of glaucomatous disease stage.

To conclude, significant differences in ONH structure between glaucoma and controls throughout nine regions of the ONH, i.e., not only the central ONH, or the vertical meridian of the ONH were demonstrated. As this was a cross-sectional study, a further *in vivo* longitudinal study may elucidate the relationship between regional ONH structural changes and the progression of glaucomatous optic neuropathy.

IV. Chapter 4: Volumetric measures of ONH parameters in Glaucoma

IV.1 Introduction

Clinically, a glaucoma consultation involves a subjective assessment made by the clinician of the 'cup to disc' ratio along the vertical meridian of the ONH, which is a ratio of the size of the optic cup compared to the size of the optic disc (Weisman et al., 1973; Garway-Heath et al., 1998). As mentioned, this observation is subjective to the glaucoma specialist and is prone to large inter-observer differences in recording the cup to disc ratio, and evaluation of the ONH (Schwartz, 1976; Parrish et al., 2005; Breusegem et al., 2011; Rossetto et al., 2017). Lichter (1976) mentions that an individual clinician can display substantial inconsistencies in the assessment of the ONH and cup-disc ratio, and that a single cup to disc ratio is not informative to describe whether an ONH displays normal or glaucomatous features. Therefore, these inconsistencies suggest that the cup to disc ratio is an inexact method of recording ONH status.

An increase in cup-disc ratio indicates enlargement of the optic cup and loss of prelamina neural tissue. However, due to the high inter-observer variability in the assessment of cup-disc ratio, significant ONH structural changes may go unnoticed. Indeed, Abrams et al. (1994) reported only moderate agreement between optometrists and ophthalmologists when assessing the cup-disc ratio, and suggest the need to develop standardised techniques when assessing the glaucomatous ONH (Arthur et al., 2006; Jampel et al., 2009; Hong et al., 2018).

Compression of ONH structures, loss of prelaminar neural tissue, and backward bowing of the LC are established ONH features of glaucomatous optic neuropathy; leading to excavation of the ONH (Quigley and Green, 1979; Quigley et al., 1983; Jung et al., 2015; Tan et al., 2019). Chapter 3 quantified *in vivo* regional measures of ONH depth and thickness parameters in different stages of glaucoma disease. Chapter 3 reported a significant increase in prelamina depth and reduction in prelamina thickness in preperimetric glaucoma (PG) compared to control eyes. However, prelamina depth and thickness did not significantly differ between PG and early glaucoma (EG) in any region of the ONH. With loss of VF sensitivity, prelamina depth significantly increased, and prelamina thickness significantly decreased in all ONH regions.

Therefore, early detection of RGC axon loss may be better visualised via *in vivo* measurements of optic cup and prelamina volume. Additionally, significant regional thinning of the LC was identified between controls and PG, although not between PG and EG, nor between EG and MAG. In chapter 3, LC thickness significantly decreased with VF loss in all regions of the ONH. Therefore, measures of LC volume may allow better detection of early glaucomatous changes (i.e., between controls and PG, and between PG and EG), and also act to suggest disease progression.

Due to its high imaging scan rate, and high axial resolution, SD-OCT enables visualisation and analysis of 3D structures within the ONH (Wojtkowski et al., 2005; Mumcuoglu et al., 2008). As discussed in chapter 3 (section III.6.6), in glaucoma disease, the thickness of the LC is reported to decrease (Inoue et al., 2009; Park et al., 2012a). However, in monkey models of experimental glaucoma the LC is reported to thicken during early stages of disease (Yang et al., 2007b; Yang et al., 2011b). Therefore, this cross-sectional study will consider volumetric measurements of ONH parameters to determine whether ONH structural alterations occur in human glaucoma and can be distinguished between different stages of disease. This study is novel as it is the first to investigate 3D volumetric ONH parameter changes as a function of glaucoma stage in OCT image datasets.

IV.2 Aims of study

Therefore, this study aimed to determine if a single 3D ONH parameter (equivalent to those found to significantly alter in glaucoma in Chapter 3) could be used in the early identification of ONH structural change in glaucoma.

To achieve this overall aim, quantitative 3D volumetric measures within the ONH, namely cup, prelamina and LC volumes, were performed and data were analysed as a function of disease stage in glaucoma or with respect to VF function.

IV.3 Experimental design

In this cross-sectional study, glaucoma (n=55) and control (n=30) participants were recruited as described previously in section II.1. Glaucoma participants were grouped into disease

stages: preperimetric glaucoma (PG; n=14), early glaucoma (EG; n=29), and moderate-advanced glaucoma (MAG; n=12) according to VF MD. As described in section II.3, prior to OCT image acquisition, preliminary clinical assessments of both eyes in all participants were performed. Participant characteristics are presented in Table 4.1.

Characteristic	**Control**	**PG**	**EG**	**MAG**
	N=60 eyes	N=28 eyes	N=58 eyes	N=23 eyes
	Mean ± Standard Deviation			
Age (years)	65.48 ± 6.46	68.93 ± 9.32	73.10 ± 8.17	75.73 ± 6.99
Gender	33 F, 28 M	16 F, 12 M	29 F, 29 M	11 F, 12 M
MS (D)	0.77 ± 1.88	-0.21 ± 3.13	0.15 ± 2.06	0.08 ± 2.26
VA (logMAR)	-0.04 ± 0.09	0.07 ± 0.10	0.11 ± 0.13	0.17 ± 0.16
IOP (mmHg)	15.10 ± 3.25	13.64 ± 2.00	13.41 ± 2.33	11.89 ± 2.49
AEL (mm)	23.72 ± 0.97	23.99 ± 1.55	23.95 ± 1.07	24.07 ± 1.33
CCT (μm)	559.80 ± 41.14	528.00 ± 30.34	525.15 ± 39.34	517.04 ± 32.75
ACD (mm)	2.81 ± 0.57	2.95 ± 0.74	3.24 ± 0.88	3.29 ± 0.92
VF MD (dB)	-0.54 ± 1.34	-0.35 ± 1.01	-3.16 ± 1.66	-11.03 ± 4.88

Table 4.1: Participant characteristics for glaucoma participants and age-similar controls. MS = mean sphere, VA = visual acuity, IOP = intraocular pressure, AEL = axial eye length, CCT = central corneal thickness, ACD = anterior chamber depth, VF MD = visual field Mean Deviation.

IV.4 Spectral Domain OCT imaging

OCT image datasets were acquired using enhanced depth imaging with 20° scans centred on the ONH of all participants. OCT image processing, registration, noise reduction, and image scaling were performed as described in sections II.5-II.7.

IV.5 Volumetric analysis of ONH structures

The 3D volumetric SD-OCT image datasets (TIFF image format) were imported into Amira image analysis software (version 6.0, Thermo Fisher Scientific, UK). Bruch's membrane opening surface area, optic cup volume, prelamina volume and LC volume were quantified as described in section II.14. In brief, BMO was demarcated using landmarks around the circumference of the ONH, pivoting on the ONH centre to create a reference plane. BMO surface area, and additionally, optic cup, prelamina and LC volumes, relative to the BMO reference plane, were quantified. An example of the process to construct a 3D ONH structure is given in section II.14.

IV.6 Statistical analysis

Statistical analysis was performed within RStudio, version 1.2.1335, as described in section II.16. To account for data being used from both eyes of each participant, linear mixed-effects regression models were fitted using the package 'lme4' (Bates et al., 2019; http://cran.r-project.org/package=lme4), and to determine which ocular parameters had a significant effect on volumetric ONH measures. Tukey's post-hoc analysis was performed to determine inter-group differences for each ONH parameter using the package 'emmeans' (Lenth et al., 2019; http://cran.r-project.org/package=emmeans). Pearson's correlation coefficient was used to determine the association between each ONH parameter and VF MD. The package 'ggplot2' (Wickham, 2016; http://cran.r-project.org/package=ggplot2) was used to generate graphs.

IV.7 Results

IV.7.1 Generation of mixed-effects regression models for analysis of 3D ONH parameters

Initially, parameters such as participant age, axial length, refractive error, anterior chamber depth, central corneal thickness, and intraocular pressure were included as independent variables in each mixed-effects regression model for each ONH volume parameter. Stage of glaucoma was found to be the only independent variable in mixed-effects regression models that was significantly associated with BMO surface area (P<0.001), prelamina volume (P<0.001) and LC volume (P<0.001), as shown in Table 4.2. Since age, axial length (AxL), mean spherical correction (MS), anterior chamber depth (ACD), central corneal thickness (CCT), and intraocular pressure (IOP) were not significantly associated with these parameters, these were excluded from the respective regression models. Additionally, mixed-effects models identified that stage of glaucoma disease significantly contributed to variance in optic cup volume (P<0.001). Mean sphere (-0.010 $\pm$ 0.005 mm^3/D, t=-2.04, p=0.044), anterior chamber depth (-0.038 $\pm$ 0.014 mm^3/mm, t=-2.72, p=0.007), central corneal thickness (-0.0009 $\pm$ 0.0003 $mm^3/\mu m$, t=-3.14, p=0.002) also indicated significant negative associations with optic cup volume (see Table 4.5). This suggested that eyes with a more hyperopic prescription, thicker corneas, or deeper anterior chambers had a smaller optic cup volume. Therefore, MS, ACD, and CCT parameters were included in the regression models for further analysis of optic cup volume.

ONH Parameter	Dx (*p*-value)	Age (years)	AxL (mm)	MS (D)	ACD (mm)	CCT (µm)	IOP (mmHg)
BMO surface area (mm^2)	C: <0.001 PG: 0.022 EG: 0.079 MAG: 0.004	-0.001 ± 0.007 -0.16 0.875	0.081 ± 0.051 1.58 0.116	-0.043 ± 0.026 -1.67 0.100	-0.073 ± 0.051 -1.43 0.154	-0.002 ± 0.001 -1.77 0.079	0.011 ± 0.016 0.68 0.499
Optic cup volume (mm^3)	C: <0.001 PG: 0.006 EG: 0.005 MAG: <0.001	0.001 ± 0.002 0.32 0.753	-0.025 ± 0.015 -1.70 0.091	-0.010 ± 0.005 -2.04 0.044	-0.038 ± 0.014 -2.72 0.007	-0.0009 ± 0.0003 -3.14 0.002	-0.007 ± 0.005 -1.49 0.139
Prelamina volume (mm^3)	C: <0.001 PG: 0.231 EG: 0.021 MAG: <0.001	-0.003 ± 0.002 -1.58 0.118	0.015 ± 0.015 0.99 0.324	0.009 ±0.008 1.23 0.220	-0.010 ± 0.016 -0.63 0.531	-0.0004 ± 0.0003 -1.37 0.175	0.004 ± 0.004 0.97 0.333
Lamina cribrosa volume (mm^3)	C: <0.001 PG: 0.032 EG: 0.003 MAG: <0.001	0.00004 ± 0.002 0.02 0.982	0.025 ± 0.016 1.61 0.111	0.003 ± 0.008 0.39 0.695	-0.013 ± 0.015 -0.89 0.374	-0.0001 ± 0.0003 -0.34 0.735	0.003 ± 0.005 0.69 0.490

Table 4.2: Independent variables included in linear mixed-effects regression model for each optic nerve head (ONH) parameter. Presented as effect size ± standard error (i.e., how much ONH parameter changes per one-unit change in the independent variable), also the t-value and *p*-value. Red text indicates the independent variable had a significant effect at $p < 0.05$. BMO = Bruch's membrane opening, Dx = stage of glaucoma, AxL = axial length, MS = mean sphere refractive error, ACD = anterior chamber depth, CCT = central corneal thickness, IOP = intraocular pressure.

IV.7.2 ONH parameters as a function of glaucoma disease and visual field sensitivity.

BMO surface area, optic cup volume, prelamina volume, and LC volume data for each experimental group are shown in Table 4.3. Inter-group differences for each ONH parameter, and *P* values adjusted for multiple comparisons are shown in Table 4.4.

ONH Parameter	Control	PG	EG	MAG
	N=61	N=28	N=58	N=23
	Mean ± Standard Deviation			
BMO surface area (mm^2)	1.81 ± 0.28	2.13 ± 0.63	1.98 ± 0.47	2.08 ± 0.50
Optic cup volume (mm^3)	0.05 ± 0.06	0.15 ± 0.13	0.16 ± 0.15	0.28 ± 0.23
Prelamina volume (mm^3)	0.58 ± 0.13	0.56 ± 0.11	0.51 ± 0.12	0.42 ± 0.11
Lamina cribrosa volume (mm^3)	0.48 ± 0.10	0.42 ± 0.11	0.41 ± 0.09	0.36 ± 0.12

Table 4.3: Volumetric quantification of 3D ONH parameters.

ONH Parameter	Multiple Comparisons: Adjusted *P* values					
	C-PG	C-EG	C-MAG	PG-EG	PG-MAG	EG-MAG
BMO surface area	0.097	0.291	0.020	0.670	0.783	0.113
Optic cup volume	0.033	0.026	<0.001	1.000	<0.001	<0.001
Prelamina volume	0.629	0.094	<0.001	0.787	0.004	0.014
LC volume	0.143	0.015	0.002	0.937	0.348	0.531

Table 4.4: Tukey post-hoc pairwise comparisons of ONH parameter as a function of glaucoma disease stage. Red text indicates significant differences at $p < 0.05$.

IV.7.2.1 Bruch's membrane opening surface area as a function of glaucoma disease stage and visual field sensitivity

The surface area of BMO was significantly greater in the MAG group, compared to the control group (*P* = 0.020, Tables 4.3 and 4.4, Figure. 4.1), but no significant difference was observed between control eyes and PG (*P* = 0.097) or EG (*P* = 0.291), nor between glaucoma participant groups (PG versus EG: *P* = 0.670; PG versus MAG: *P* = 0.783; EG versus MAG: *P* = 0.113, see Figure 4.1). Additionally, BMO surface area did not significantly correlate with VF MD (Pearson's r = 0.08, *P* = 0.287); see Figure 4.1.

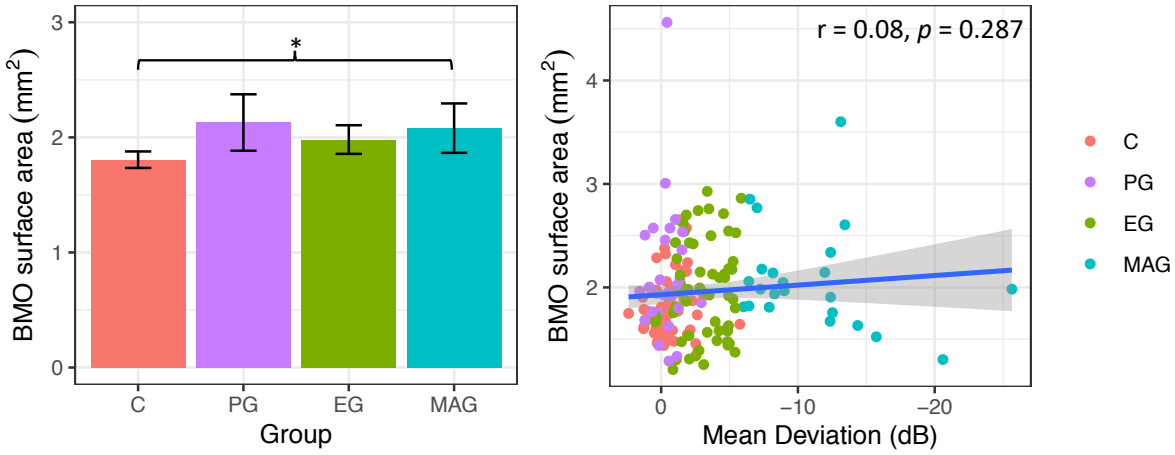

Figure 4.1: BMO surface area as a function of glaucoma disease stage and VF MD. * represents $P < 0.05$. Error bars represent 95% confidence intervals. Blue line represents regression line and grey shading represents 95% confidence intervals.

IV.7.2.2 Optic cup volume as a function of glaucoma stage and visual field sensitivity

Presented in Table 4.4, optic cup volume was significantly greater at all three stages of glaucoma, compared to control eyes (PG: $P = 0.03$; EG: $P = 0{,}026$; MAG: $P < 0.001$). Additionally, the MAG group had significantly larger optic cup volumes than PG and EG ($P < 0.001$), although optic cup volume was not significantly different between PG and EG ($P = 1.000$), see Figure 4.2. Optic cup volume was significantly associated with VF MD; with enlargement of optic cup volume as a function of VF loss (Pearson's r = 0.44, $P < 0.001$); see Figure 4.2.

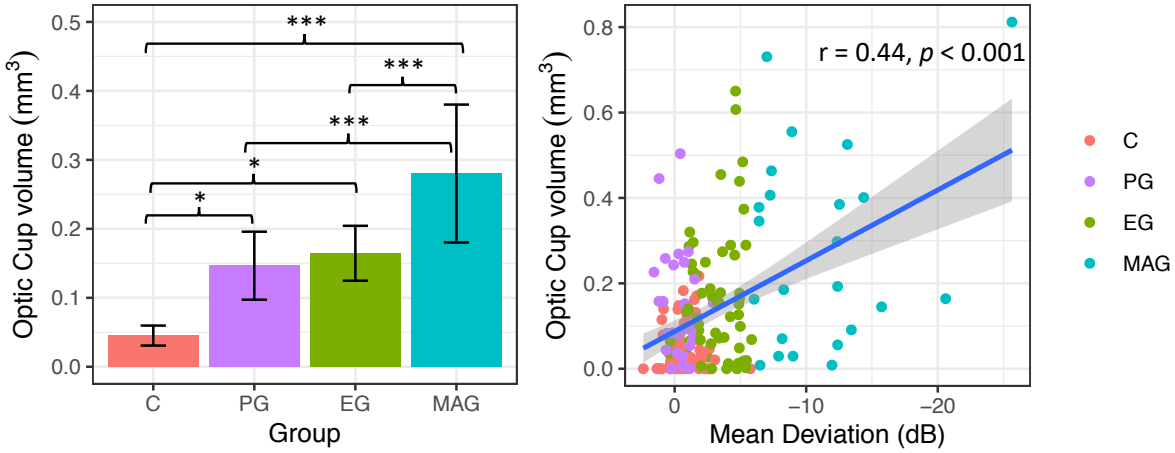

Figure 4.2: Optic cup volume as a function of glaucoma disease stage and VF MD. * represents $P < 0.05$. *** represents $P < 0.001$. Error bars represent 95% confidence intervals. Blue line represents regression line and grey shading represents 95% confidence intervals.

IV.7.2.3 Prelamina volume as a function of glaucoma stage and visual field sensitivity

Prelamina volume was significantly less in the MAG group compared to controls ($P < 0.001$), PG ($P = 0.004$), and EG ($P = 0.014$), see Table 4.4 and Figure 4.3. Prelamina volume was not significantly different between PG and EG ($P = 0.787$), or between control ONHs and PG ($P = 0.629$) and EG ($P = 0.094$), see Figure 4.3. Prelamina volume was significantly associated with VF MD; with increasing VF loss there was a reduction in prelamina volume (Pearson's r = -0.35, $P < 0.001$, Figure 4.3). Measurement of prelamina volume was not possible in 8/170 (5%) OCT image datasets due to shadowing caused by overlying tissue or blood vessels within the OCT image preventing clear delineation of the anterior LC surface.

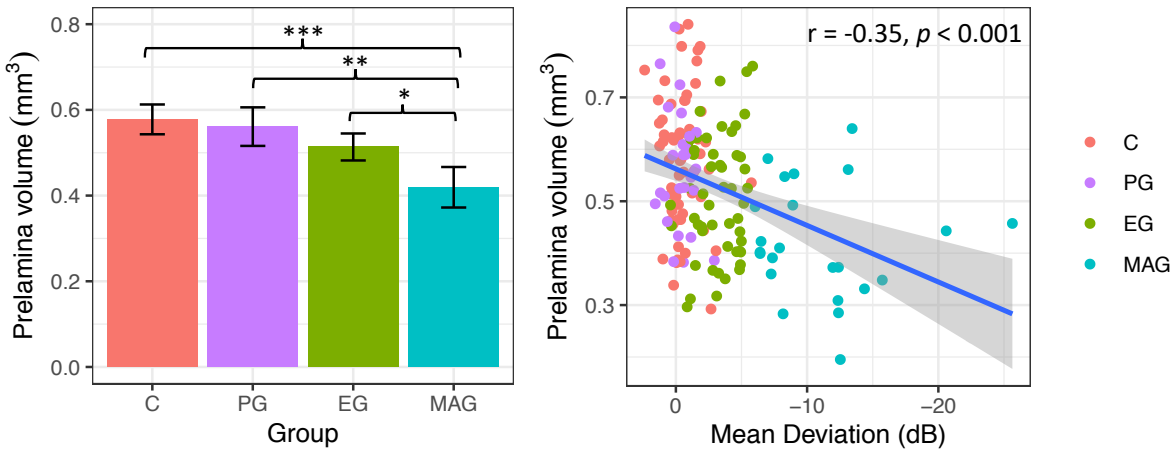

Figure 4.3: Prelamina volume as a function of glaucoma disease stage and VF MD. * represents $P < 0.05$. ** represents $P < 0.01$. *** represents $P < 0.001$. Error bars represent 95% confidence intervals. Blue line represents regression line and grey shading represents 95% confidence intervals.

IV.7.2.4 Lamina cribrosa volume as a function of glaucoma stage and visual field sensitivity

Compared to control eyes, LC volume was significantly less in the EG ($P = 0.015$) and MAG groups ($P = 0.002$), see Table 4.4. No significant difference in LC volume was observed between the PG group and control eyes ($P = 0.143$), EG ($P = 0.937$), or MAG ($P = 0.348$). Also, LC volume was not significantly different between EG and MAG ($P = 0.531$), see Figure 4.4. Lamina cribrosa volume was significantly associated with VF MD. With loss of VF function there was a significant decrease in LC volume (Pearson's r = -0.40, $P < 0.001$); see Figure 4.4. Due to unclear delineation of anterior and/or posterior LC surfaces, measurement of LC volume was not possible in 54/170 (32%) OCT image datasets.

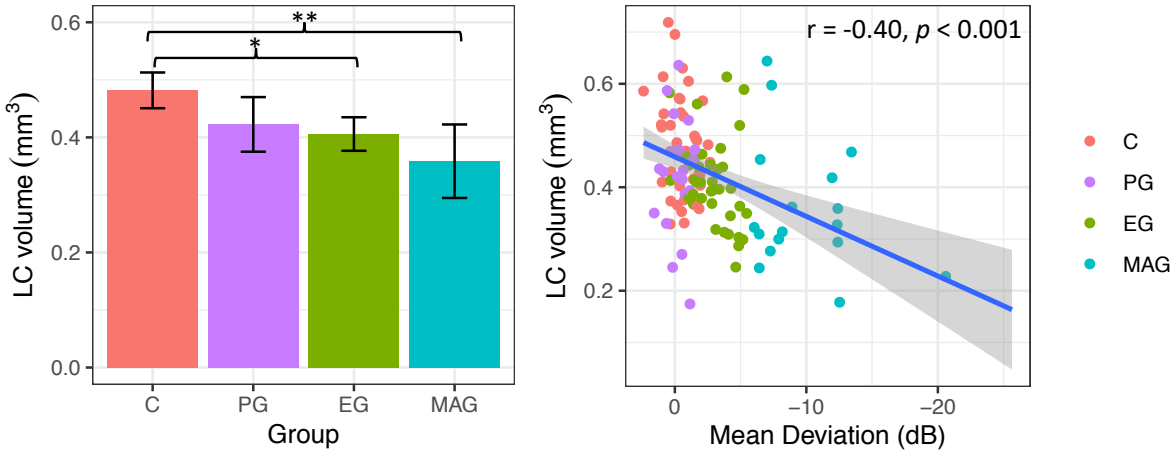

Figure 4.4: LC volume as a function of glaucoma disease stage and VF MD. * represents $P < 0.05$. ** represents $P < 0.01$. Error bars represent 95% confidence intervals. Blue line represents regression line and grey shading represents 95% confidence intervals.

IV.8 Discussion

The ONH is a complex, 3D structure. Therefore, this study aimed to identify 3D volumetric ONH parameters that hold potential to identify ONHs at risk of glaucoma onset, as early as possible. Additionally, there is clinical importance in being able to stage the ONH structure in glaucoma patients i.e., determine the stage of disease. This study is novel in its approach as it is the first to assess volumetric ONH parameters *in vivo* as a function of glaucoma disease stage, and in relation to visual function. Significant alterations in volumetric ONH parameters identified in this study between glaucoma stages and with VF loss are summarised in Table 4.5.

Alteration in volumetric ONH parameters according to glaucoma stage		
Control to PG	**PG to EG**	**EG to MAG**
↑ in optic cup volume	No alteration in BMO surface area, optic cup, prelamina, or LC volume	↑ in optic cup volume ↓ in prelamina volume
Alteration in volumetric ONH parameters versus VF MD		
↑ in optic cup volume with VF loss ↓ in prelamina volume with VF loss ↓ in LC volume with VF loss No significant alteration in BMO surface area with VF loss		

Table 4.5: Summary of volumetric ONH parameter alterations according to glaucoma disease stage and VF MD. Red text indicates significant alteration to ONH parameter.

In this study, BMO surface area did not differ significantly between control eyes and the PG or EG groups, although BMO surface area was significantly larger in the MAG group compared to control eyes. These findings in this *in vivo* human study suggest that expansion of the neural canal occurs at a later stage in glaucoma disease, than reported in *ex vivo* glaucoma studies using monkey eyes (Bellezza, Hart and Burgoyne, 2000; Bellezza et al., 2003). The term 'neural canal' has been proposed for the exit pathway of RGC axons through the eye wall, which includes a pre-scleral region, and the scleral canal (Burgoyne et al., 2004). The most anterior portion of the canal is the BMO (clinically termed the optic disc margin) and extends to the posterior scleral canal opening. Following laser-induced glaucoma in monkey eyes, it has been reported that in early glaucoma there is posterior deformation of the central LC, along with expansion of the anterior and posterior neural canal openings, when compared to the contralateral control eyes (Burgoyne et al., 2004; Downs et al., 2007).

In this current study, BMO surface area did not significantly correlate with VF MD which aligns with previous studies where no significant correlation was found between optic disc size and glaucomatous optic nerve fibre loss (Jonas et al., 1988c; Jonas et al., 1991). It has been previously suggested that the size of the ONH may be an important factor in glaucoma disease. Burk et al. (1992) reported that eyes with larger optic disc area have higher susceptibility to glaucomatous VF damage at IOP readings within statistically normal range, and with increased IOP are more vulnerable to ONH damage. It has been suggested that the larger optic disc area seen in a black population could be a factor accounting for higher glaucoma susceptibility in a black population than whites (Chi et al., 1989; Quigley et al., 1990). Furthermore, after adjusting for age and sex, the LC and peripapillary sclera have been reported to be thinner in participants of African descent than participants of European descent (Girkin et al., 2017). Potentially the thinner sclera and LCs are more prone to compression and structural alterations and are therefore more susceptible to glaucomatous damage.

This study used BMO as a reference plane from which to perform 3D measures of optic cup, prelamina, and LC volume. The use of BMO as a reference plane is supported by Belghith et al. (2016a) who evaluated BMO location longitudinally in healthy eyes and glaucoma eyes using SD-OCT. They used features including sclera, outer plexiform layer, and external limiting

membrane to align follow-up OCT scans and compare BMO location. They reported that after a mean follow up period of 3.7 years, BMO location was stable in normal and glaucomatous eyes; indicating that BMO can be used as a reference point in the monitoring of glaucoma progression.

This study demonstrated that optic cup volume significantly increased at all stages of glaucoma compared to control eyes. Importantly, optic cup volume displayed significant differences between control eyes and PG (prior to VF defect) and was the only 3D parameter to differentiate PG from control eyes. Optic cup volume was also able to discern differences between PG and EG from MAG, although optic cup volume did not significantly differ between PG and EG. With progression of glaucoma disease and loss of visual function, optic cup volume significantly correlated with VF MD. Therefore, using novel, volumetric quantification of ONH parameters, this study is in agreement with the optic cup being an important biomarker in the identification of early glaucoma disease onset and as an indicator to suggest disease progression. A widely acknowledged clinical feature of glaucomatous optic neuropathy is 'cupping' of the human ONH (Quigley and Green, 1979; Quigley et al., 1983; Jonas et al., 1988b). In monkey eyes, it has been suggested that cupping of the ONH can be considered as having two factors; prelamina, and alterations to the LC (Yang et al., 2007b; Burgoyne and Downs, 2008). Shown in monkey models of experimental glaucoma, ONH cupping regarding the LC is connective tissue based, with posterior migration of the LC, and excavation beneath the anterior scleral canal (Bellezza et al., 2003; Downs et al., 2011). Prelamina cupping of the ONH involves compression of prelamina tissue and progressive loss of RGC axons, relating to a clinical appearance of an increase in the depth and width of the optic cup, hence an increase in the cup to disc ratio (Quigley et al., 1982; Yang et al., 2007a; Gandhi and Dubey, 2013).

This study quantified prelamina volume *in vivo*. The MAG group displayed significantly less prelamina volume than control eyes, and the PG and EG groups. Prelamina volume did not significantly differ between PG and EG, and prelamina volume in the PG and EG groups was not significantly different to the control group. Additionally, a significant reduction in prelamina volume was determined with VF loss. This suggests that volumetric measurements of prelamina tissue may have clinical relevance in monitoring disease stage/progression in glaucoma. These findings are consistent with the advancement of glaucomatous disease and

cupping to the ONH, there is progressive loss of prelamina neural tissue (Garway-Heath and Hitchings, 1998; Gardiner, Johnson and Demirel, 2011; Jung et al., 2015).

In *ex vivo* monkey eyes with induced early glaucoma (n=3), Yang et al. (2007a) report regional (inferior, inferior-nasal, superior) increases in prelamina tissue volume when compared to normal contralateral eyes in two out of three eyes. However, they also report that prelamina volume decreased in the inferior-temporal and superior-nasal regions in two of the three eyes. This differs to that found by this study where prelamina volume was not significantly different in preperimetric and early stages of glaucoma compared to control eyes, although this study did not quantify prelamina volume regionally. The difference in these findings could be related to the expansion of the scleral canal found in monkey eyes with experimental glaucoma (Bellezza et al., 2003), which has not been shown in human eyes. Such differences in findings could be as scleral expansion was reported in young adult monkeys with early experimental glaucoma, in a smaller sample (n=17). Additionally, as the scleral canal expands in monkey eyes, if this expansion is included in the measurement of prelamina tissue volume, this may result in an increased quantity of prelamina tissue recorded in early experimental glaucoma.

This current study is the first of its kind to analyse LC volume *in vivo* in human glaucoma. LC volume did not significantly differ between controls and PG, or between PG and EG, nor between EG and MAG. However, LC volume was significantly less in the EG and MAG groups, compared to the control group. Furthermore, this study found that LC volume was significantly associated with VF function; with LC volume decreasing as a function of VF MD. This is consistent with previous histologic studies reporting a thinner LC in glaucoma patients than in normal eyes (Quigley et al., 1983; Jonas et al., 2003) and corresponds with LC thinning identified in other *in vivo* studies of human glaucoma (Park et al., 2012a; Kwun et al., 2015). Compression and backward bowing of the LC in glaucoma has long been reported and considered an important factor in the pathophysiology of glaucoma (Quigley et al., 1981; Quigley et al., 1983). More recently, Omodaka et al. (2015) used SS-OCT to evaluate average LC thickness in normal eyes, preperimetric, and normal tension glaucoma. They reported significant differences in LC thickness between the groups; with average LC thickness being greatest in the control group, and thinnest in normal tension glaucoma.

This study reports a significant reduction in LC volume in early glaucoma (i.e., between controls and EG). However, this differs to that reported by Yang et al. (2007b) in experimental glaucoma in monkey eyes, as thickening of the LC (i.e. an increase in LC volume) in early glaucoma was not observed in this study. Studies of monkey models of early experimental glaucoma (Yang et al., 2007b; Yang et al., 2011b) suggested that in early stages of glaucoma there was LC thickening as a result of LC remodelling. They report that it was not until a later disease stage that there was LC thinning. Also in monkey experimental glaucoma, Roberts et al. (2009) reported that the volume of the connective tissue within the LC is 40% to 80% larger in the glaucomatous eyes, compared to their contralateral control eyes.

IV.8.1 Study limitations

Each of the SD-OCT image datasets used in this study were acquired with enhanced depth imaging OCT to provide better visualisation of the deeper ONH structures (Spaide et al., 2008). Despite the use of EDI-OCT, in some image datasets there was not clear visualisation of the LC due to obscurities within the image caused by overlaying blood vessels or prelamina tissue.

Within Amira software, landmarks were manually placed to delineate a volumetric structure. If landmarks were not able to be placed within the image, for example due to shadowing in one meridian of the ONH, the 'Point-wrap triangulation' tool was still able to construct a 3D representation of the ONH structure, to allow for volumetric measurement. In some instances, a larger area of the LC was obscured within the OCT image, hence accurate delineation of the anterior LC surface was not possible. This not only inhibited measurement of LC volume, but also the prelamina volume. Additionally, even if the anterior surface of the LC was visible, to calculate LC volume, the posterior surface of the LC also had to be visible. It was not always possible to determine this boundary with confidence, due to OCT signal attenuation or shadowing within the OCT image. Therefore, in this study, out of the 170 image datasets included measurement of prelamina volume was not possible in 8 (5%) datasets, and LC volume was not possible in 54 (32%) OCT image datasets.

Furthermore, the glaucoma participants included in this study were divided into groups based on stage of glaucoma disease. This resulted in the participant numbers in each group not

being equal. For example, the EG group (n=58) contained more than double than included in the PG (n=28) group and the MAG group (n=23). An increased number of participants included in the PG and MAG groups would provide greater accuracy to the analyses and provide better insights into 3D ONH parameter change with the progression of glaucomatous disease.

IV.8.2 Conclusion

This study presented novel *in vivo* quantification of volumetric ONH parameters with respect to glaucoma disease stage and VF function. Optic cup volume was significantly smaller in control eyes than PG, therefore allowing identification of glaucomatous ONH structural changes prior to vision loss. Additionally, optic cup, prelamina, and LC volume were all significantly associated with VF MD. This study suggests that volumetric ONH parameters may provide an objective technique for ONH assessment and hold potential for the early detection and monitoring of glaucomatous disease.

V. Chapter 5: Analysis of lamina cribrosa microstructural parameters in Glaucoma

V.1 Introduction

Raised IOP is considered a major risk factor for glaucomatous disease and can result in cupping of the optic disc and stretching and rearrangement of the LC cribriform plates (Quigley et al., 1981; Quigley et al., 1983). In glaucoma, the compression and collapse of the LC connective tissue beams is accompanied by RGC axonal damage and blockage of axonal transport, and vision loss (Quigley and Anderson, 1976; Gaasterland et al., 1978; Quigley and Green, 1979; Radius, 1987). It is proposed that to withstand intraocular pressure (IOP) related forces, the LC connective tissue beams are anchored to a circumferential ring of collagen and elastic fibres within the peripapillary sclera (Quigley et al., 1991b; Hernandez, 1992; Albon et al., 1995; Albon et al., 2000b; Jones et al., 2015). However, onset and progression of glaucomatous ONH damage has been shown to occur even at IOP levels considered to be within the normal range (Van Veldhuisen et al., 2000; Kass et al., 2002; Leske et al., 2003). The findings that glaucomatous ONH damage can occur at all levels of IOP suggests that certain optic nerve heads are more susceptible to glaucomatous damage than others.

Current *in vivo* LC studies have reported on parameters such as LC depth and thickness (Lee et al., 2011; Park et al., 2012a), anterior LC surface morphology (Thakku et al., 2015; Tun et al., 2016), LC focal defects (Kiumehr et al., 2012), and analysis of the LC pores (Ivers et al., 2011; Akagi et al., 2012; Wang et al., 2018). In *ex vivo* studies evaluating the connective tissue of the glaucomatous ONH, an increase in collagen type VI density within the LC (Hernandez and Pena, 1997) has been reported, and in advanced glaucoma, bundles of collagen type I fibrils appear compacted in the cribriform plates closest to the myelinated nerve (Hernandez et al., 1990). Additionally, there has been shown to be a decrease in the total number of collagen fibrils within the LC and surrounding elastic fibres (Quigley et al., 1991b; Hernandez, 1992). Therefore, in glaucoma, there may be redistribution of different types of collagen in the LC, depending on the regions of the cribriform plates that are exposed to IOP-related stress (Hernandez and Pena, 1997). Furthermore, in glaucoma, changes to LC elastic fibres

include degeneration and curling of elastic fibres (Quigley, Brown and Dormanpease, 1991a; Hernandez, 1992), although Quigley et al. (1991b) reported that elastic fibre density remained unchanged in the glaucomatous ONHs studied.

Connective tissue and structural changes have been observed in glaucomatous eyes indicative of ONH remodelling, as described by (Hernandez et al., 2008; Roberts et al., 2009; Burgoyne, 2011; Downs et al., 2011). Such changes in LC connective tissue are likely to impact on the ability of the structure to respond to alterations in IOP, which is suggested to lead to a decrease in compliance, with a higher tendency to collapse under raised IOP (Hernandez and Pena, 1997). Additionally, the disruption to LC beam structure, including stretching and reorganisation of their connective tissue properties, may play a role in the susceptibility of an ONH to glaucomatous damage. In *ex vivo* human eyes, Jones et al. (2015) reported that LC connective tissue fibres in the inferior-temporal region displayed a higher degree of alignment in glaucomatous ONHs, compared to control eyes. However, such analysis of LC connective tissue fibre alignment has yet to be determined *in vivo*.

The hypothesis of this chapter is that such LC connective tissue changes, as those reported in *ex vivo* ONHs, can be detected in OCT image datasets of the human ONH *in vivo.* Such determinants would further our understanding of whether *in vivo* detection of LC regional microstructure can identify ONHs with a higher degree of susceptibly to develop glaucoma, or whether these regions are a consequence of the glaucoma disease process. Additionally, regional investigation of LC connective tissue alignment as a function of depth within the ONH in control and glaucoma participants may aid in the detection of abnormalities in LC beam orientation and coherence in early disease. Such parameters could allow for earlier detection of glaucomatous disease and/or monitoring of disease stage progression; thereby aiding in diagnosis and more timely therapeutic intervention.

V.2 Aims of study

This study was aimed at the *in vivo* evaluation of structural differences regionally within the LC, based on connective tissue orientation and coherence, throughout the depth of the LC, in control and glaucomatous eyes.

V.3 Experimental design

This cross-sectional study included 38 glaucoma participants and 19 healthy controls. Participants were recruited as outlined in section II.1, and in accordance with inclusion and exclusion criteria outlined in section II.2. Each participant underwent preliminary ocular assessments, as described in section II.3, including visual acuity, Goldmann applanation tonometry, axial eye length, anterior chamber depth, central corneal thickness, and refractive error. Visual field testing was performed using Humphrey Visual Field Analyser (SITA Standard 24-2 test). Participant eyes were divided into groups based on being a healthy control eye or by glaucoma disease stage. Participant characteristics are presented in Table 5.1.

Characteristic	**Control**	**Preperimetric Glaucoma**	**Early Glaucoma**	**Moderate-Advanced Glaucoma**
	N = 38 eyes	N = 23 eyes	N = 39 eyes	N = 14 eyes
	Mean ± Standard Deviation			
Age (years)	67.7 ± 6.5	67.8 ± 9.2	74.2 ± 7.8	74.8 ± 6.6
Gender	22 F &16 M	14 F & 9 M	20 F & 19 M	8 F & 6 M
MS (D)	0.96 ± 1.58	0.22 ± 2.73	0.20 ± 1.91	-0.48 ± 2.35
VA (logMAR)	0.01 ± 0.07	0.06 ± 0.09	0.13 ± 0.10	0.16 ± 0.10
IOP (mmHg)	16.6 ± 2.5	14.0 ± 2.0	13.8 ± 2.5	12.9 ± 2.5
AEL (mm)	23.6 ± 0.7	23.9 ± 1.5	24.0 ± 0.9	24.2 ± 1.1
CCT (μm)	549.5 ± 33.9	528.6 ± 30.3	515.5 ± 32.9	516.2 ± 32.9
ACD (mm)	2.80 ± 0.5	2.81 ± 0.6	3.32 ± 0.9	3.44 ± 1.0
VF MD (dB)	-0.44 ± 1.18	-0.18 ± 0.94	-2.88 ± 1.56	-9.69 ± 2.68

Table 5.1: Participant characteristics for glaucoma and control participants. MS = mean sphere, VA = visual acuity, IOP = intraocular pressure, AEL = axial eye length, CCT = central corneal thickness, ACD = anterior chamber depth, VF MD = visual field Mean Deviation.

Enhanced depth imaging OCT (EDI-OCT) was performed on the ONH of all participants (76 glaucomatous eyes and 38 control eyes) with a scan angle of 10°, with each scan composed of 512 x 512 A-scans. Acquired spectral data was processed as described in section II.5 and OCT image registration was performed as described in section II.6. Image noise was reduced using a Gaussian blur filter with sigma 1-1-3 in the x-y-z planes respectively. Image brightness and contrast was adjusted as described in section II.10.

V.4 Analysis of lamina cribrosa connective tissue alignment

As described in section II.15, each SD-OCT ONH dataset was resliced to the *enface* orientation and the central anterior LC surface located. Orientation of the datasets, to ensure superior ONH region was uppermost, was confirmed using fundus photography as described in section II.8. Each ONH dataset was cropped axially to create five to six (dependent on LC thickness) 50µm thick optical sections beginning 50µm anterior to the first appearance of the central LC surface. Then each 3D section was flattened in an averaged projection to generate an *enface* OCT image slice.

Within ImageJ, the macro 'ONHseg' (Version 1.0, N White, VSBL, Cardiff University) was applied to subdivide each ONH slice into clock-hour regions, as shown in Figure 5.1. Then the preferred orientation and coherence of each LC connective tissue region was determined using ImageJ plugin 'OrientationJ' (Version 16.01.2018, Resakhaniha et al. 2012, Biomedical Imaging Group, Sweden). Data was not acquired on the nasal side of the ONH due to vascular shadows within the OCT image, or within temporal regions of the ONH where major blood vessels encroached into the clock-hour regions; as shown in Figure 5.1 in region SST of the temporal ONH.

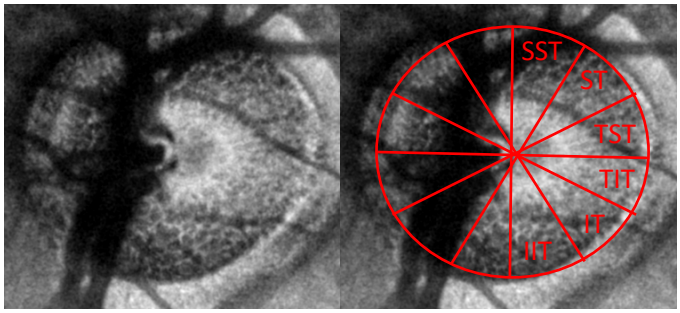

Figure 5.1: Left eye ONH OCT image datasets divided into clock-hour segments for regional analysis of LC connective tissue. Data was not acquired from the nasal ONH due to vascular shadowing. S = superior, I = inferior, T = temporal. (Figure repeated from section II.15).

Preferred orientation values were within ± 90°; a value of 0° indicated features aligned to the horizontal x-axis, +90° represented the vertical y-axis in the superior meridian, and -90° indicated the inferior vertical meridian, see Figure 5.2.

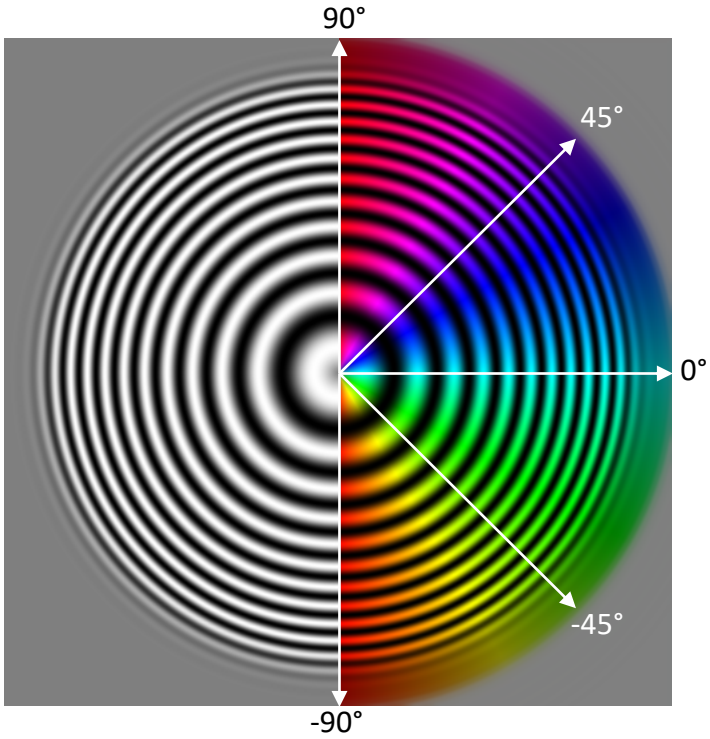

Figure 5.2: Colour map denoting orientation of LC connective tissue within OCT datasets, (figure repeated from section II.15). Image adapted from OrientationJ, Biomedical Imaging Group website; http://bigwww.epfl.ch/demo/orientation; accessed 01/05/2020.

Additionally, coherence was used as an indication of degree of alignment of ONH features within a region of interest. Coherence recorded as 1 indicated that features within the region were aligned in the same direction, whereas a coherence of 0 indicated the ONH features were arranged randomly. OrientationJ was also used to generate colour-coded maps to represent preferred orientation and coherence for each OCT slice. This allowed visualisation of areas within the ONH showing a higher degree of LC connective tissue alignment in a particular orientation.

V.5 Statistical analysis

Statistical analysis was performed as described in section II.16. Normality of data was determined using histograms and Shapiro-Wilk test. Linear mixed-effects regression models were constructed using the package 'lme4' to account for data being used from both eyes of participants, and to determine which factors had a significant effect on LC coherence. Parameters that did not have a significant effect on LC coherence were excluded from final regression models. Inter-group differences for regional depth-related LC coherence were

determined using Tukey's post-hoc analysis, including identification of regional differences in LC coherence for each stage of glaucoma. The association between LC coherence and VF MD was determined using Pearson's correlation coefficient. Graphs were generated using the package 'ggplot2'.

V.6 Results

V.6.1 Lamina cribrosa connective tissue orientation and coherence in glaucoma

Examples of average projections of serial 50µm ONH slices of each experimental group are shown in Figure 5.3. Regional LC beam orientation and coherence was then recorded for each projection within the ONH. LC coherence presented as mean values for each stage of glaucoma in Table V.1 in Appendix III.

V.6.2 Multivariate analysis of ocular parameters on LC connective tissue coherence

Stage of glaucoma was included as a contributing factor in all mixed-effects regression models for the determination of inter-group differences in regional depth-related LC coherence, as outlined in Tables V.2 to V.7 in Appendix III. Stage of glaucoma was a significant contributing factor to LC coherence in all regions except for: TST in OCT slice 1, ST and IIT in slice 2, TIT and IIT in Slice 3 and the IT quadrant in slice 4.

Age had a significant positive association, indicating an age-related increase in LC coherence in the SST regions of posterior LC slices 4 and 5 ($P < 0.02$). In slices 2 and 5, axial length had a significant positive association with LC coherence in the ST region; a higher level of LC coherence was associated with increasing axial length ($P < 0.03$). However, in slice 4, in the SST region, a negative association with LC coherence and axial length was found ($P = 0.006$). A significant positive association between mean spherical refractive error and LC coherence was found only in the superior-temporal region in slice 5, ($P = 0.005$).

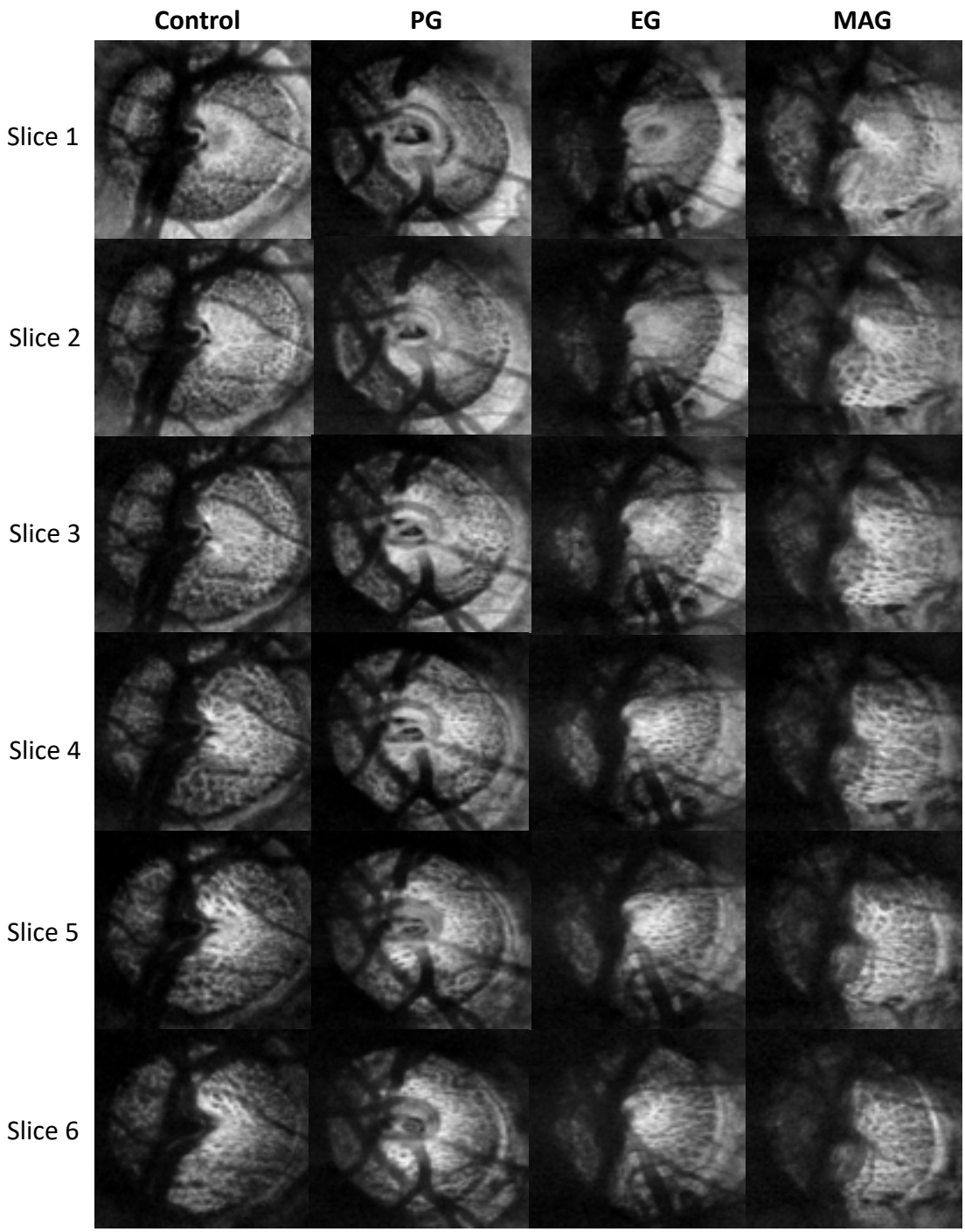

Figure 5.3: Example of left eye average projections of 50µm OCT slices (1 to 6) with increasing axial depth through the LC for each stage of glaucoma disease. PG = preperimetric glaucoma, EG = early glaucoma, MAG = moderate-advanced glaucoma.

Anterior chamber depth had a significant positive association with temporal LC coherence; in slice 1; TST region ($P = 0.026$), slice 2 IIT region ($P < 0.001$), and slice 3 TIT region ($P < 0.008$) and in the inferior-temporal quadrant of the ONH slice 4 ($P < 0.007$), indicating a higher LC coherence in eyes with a larger anterior chamber depth. Central corneal thickness and

intraocular pressure were not significantly associated with LC coherence in any of the ONH regions analysed; and were therefore excluded from the linear mixed-effects regression models.

V.6.3 Lamina cribrosa coherence as a function of axial depth and glaucoma disease stage

Lamina cribrosa beam orientation and coherence were recorded for each projection, with consequent colour coded maps used to visualise orientation and coherence, as shown in image slices 2 to 5 in Figures 5.4 to 5.7. In coherence colour maps, warmer colours indicated regions with features displaying a higher degree of alignment (i.e., higher coherence), whereas cooler colours indicated features with a lower degree of alignment. Within these maps, it was possible to visualise regional differences in LC coherence between glaucoma disease stages at varying depths within the LC. In moderate-advanced glaucoma, within the anterior LC, there appeared to be an increased degree of LC alignment in the inferior-temporal quadrant, as shown in Figures 5.4 and 5.5. However, in the mid to posterior LC there seemed to be increased LC coherence in the superior-temporal quadrant in glaucoma disease, shown in Figures 5.6 and 5.7.

Inter-group differences in regional LC connective tissue coherence through LC OCT slices 1 to 6 are presented in Table 5.2. For each stage of glaucoma disease, regional measures of LC coherence with increased axial depth through the LC are presented as mean values in Appendix III, Table V.1. Determination of inter-group differences in LC coherence as a function of glaucoma stage (see Table 5.2) showed that LC coherence, in the inferior-temporal region of OCT slice 2, was significantly greater in EG and MAG, compared to PG; see Figure 5.8. In slice 3 also, LC coherence in the inferior-temporal region was significantly greater in MAG than in PG, see Figure 5.9. In slices 2 and 3, LC coherence did not vary in other ONH regions as a function of glaucoma disease stage. With increased axial depth i.e., within slices 4 and 5, LC coherence was significantly greater in the SST region of PG ONHs, compared to that of control and moderate-advanced glaucoma LC; see Figures 5.9 and 5.10. Other ONH regions within slices 4 and 5 did not show any significant alteration in LC coherence as a function of glaucoma disease stage. OCT slice 1 (cropped 50µm anterior to the central LC surface), and OCT slice 6 (included the posterior LC surface) of the ONH showed no significant differences

in LC coherence in any of the ONH regions analysed between control or glaucomatous eyes, nor between glaucoma participants based on disease stage.

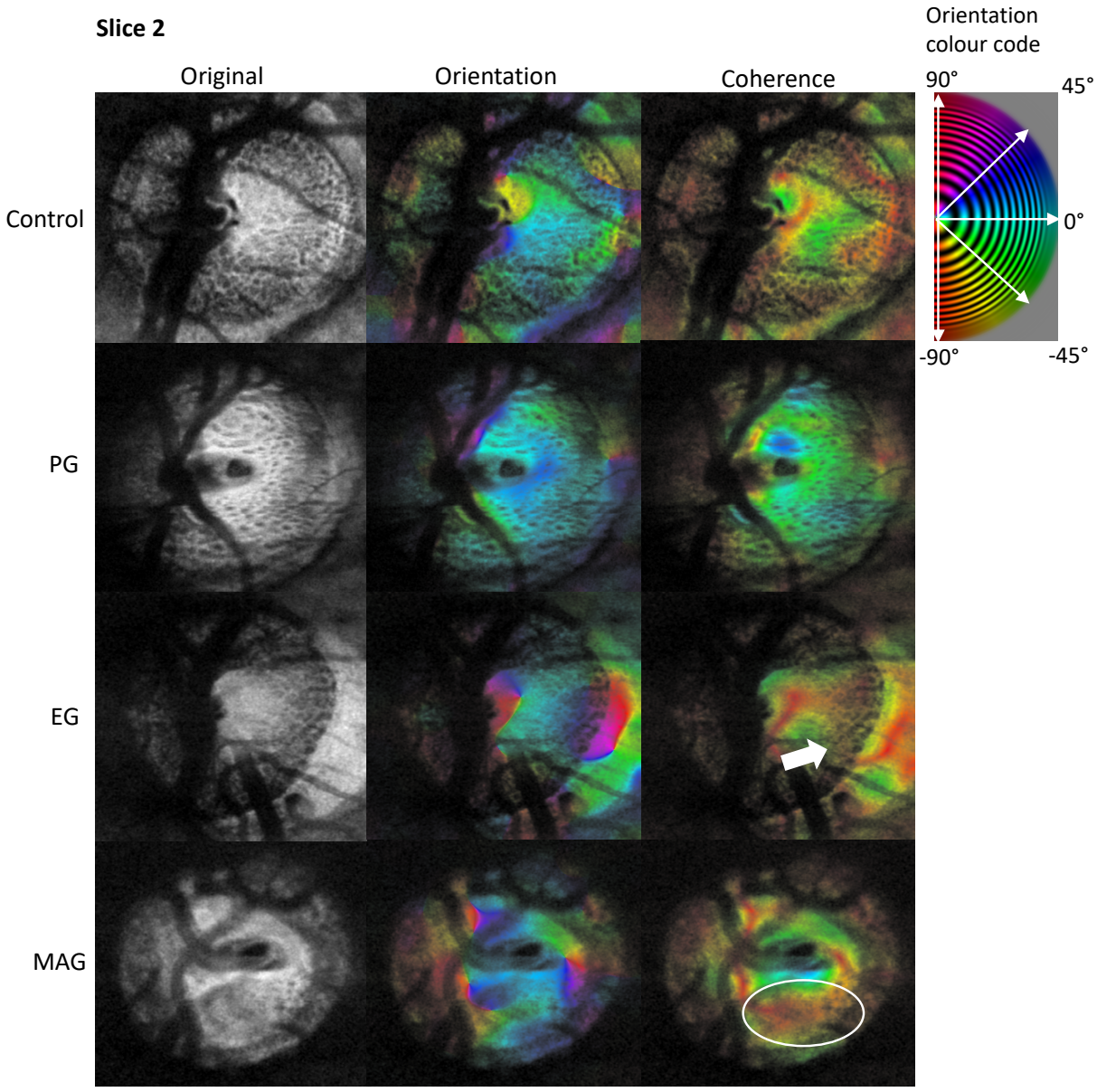

Figure 5.4: Example of left eye OCT image for slice 2, including colour coded maps for LC beam orientation and coherence for each stage of glaucoma disease. White oval indicates higher LC coherence in the inferior-temporal ONH region in MAG and white arrow indicates higher IT LC coherence in EG.

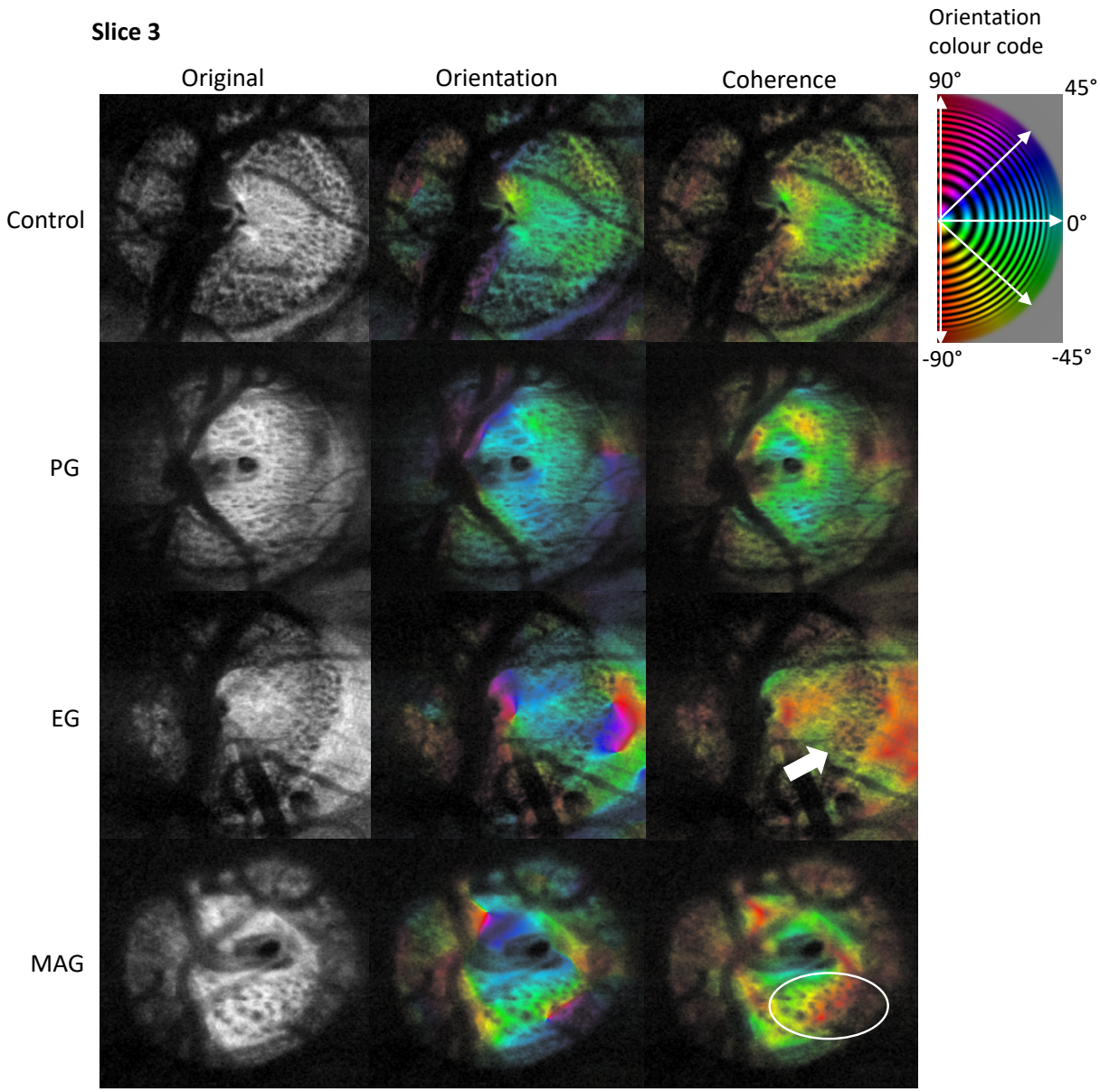

Figure 5.5: Example of left eye OCT image for slice 3, including colour coded maps for LC beam orientation and coherence for each stage of glaucoma disease. White oval indicates higher LC coherence in the inferior-temporal ONH region in MAG and white arrow indicates higher IT LC coherence in EG. LC beam orientation appeared to alter in MAG in the inferior-temporal quadrant compared to controls, PG, and EG.

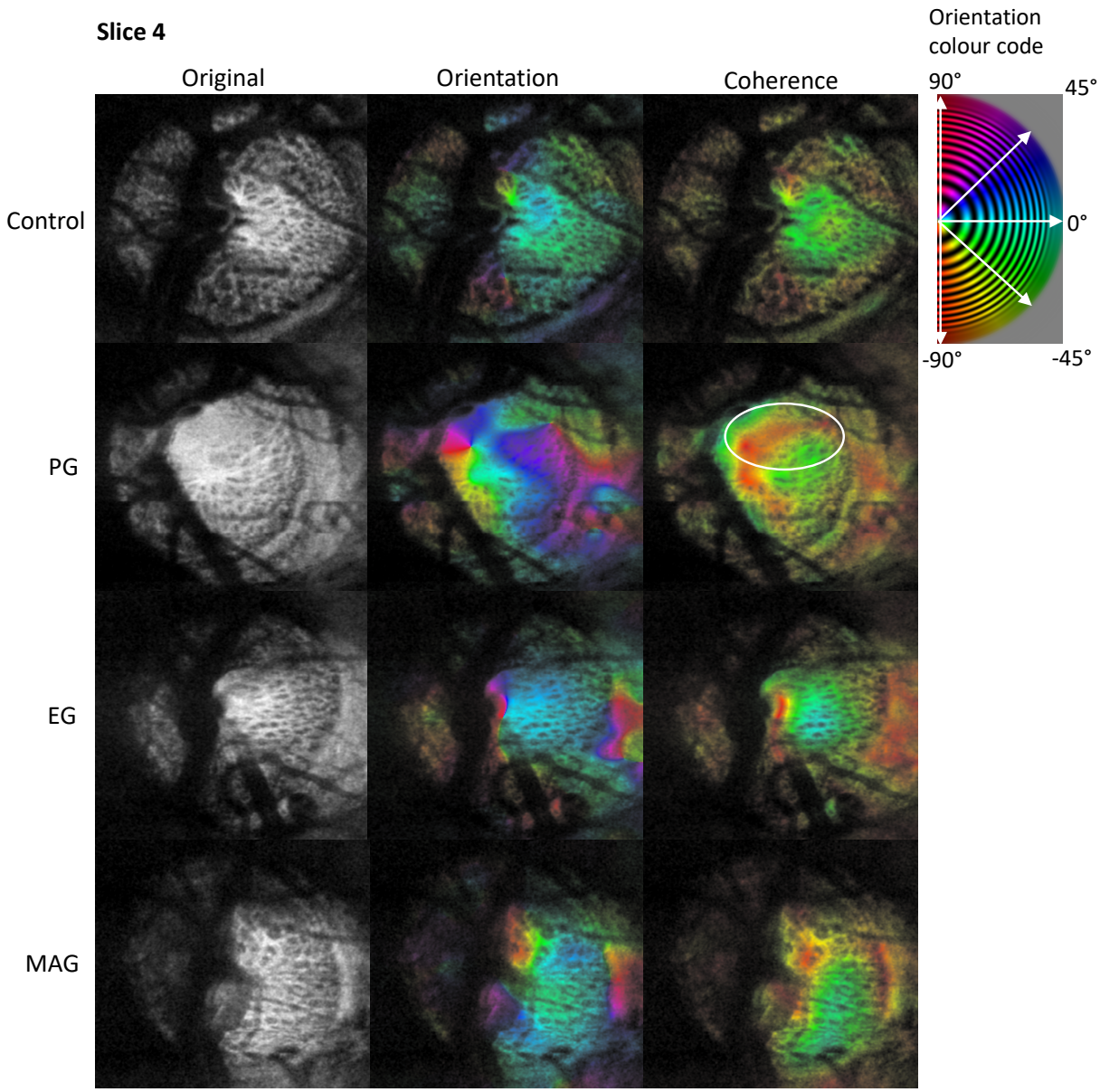

Figure 5.6: Example of left eye OCT image for slice 4, including colour coded maps for LC beam orientation and coherence for each stage of glaucoma disease. White oval indicates higher LC coherence in the superior-temporal ONH region in PG.

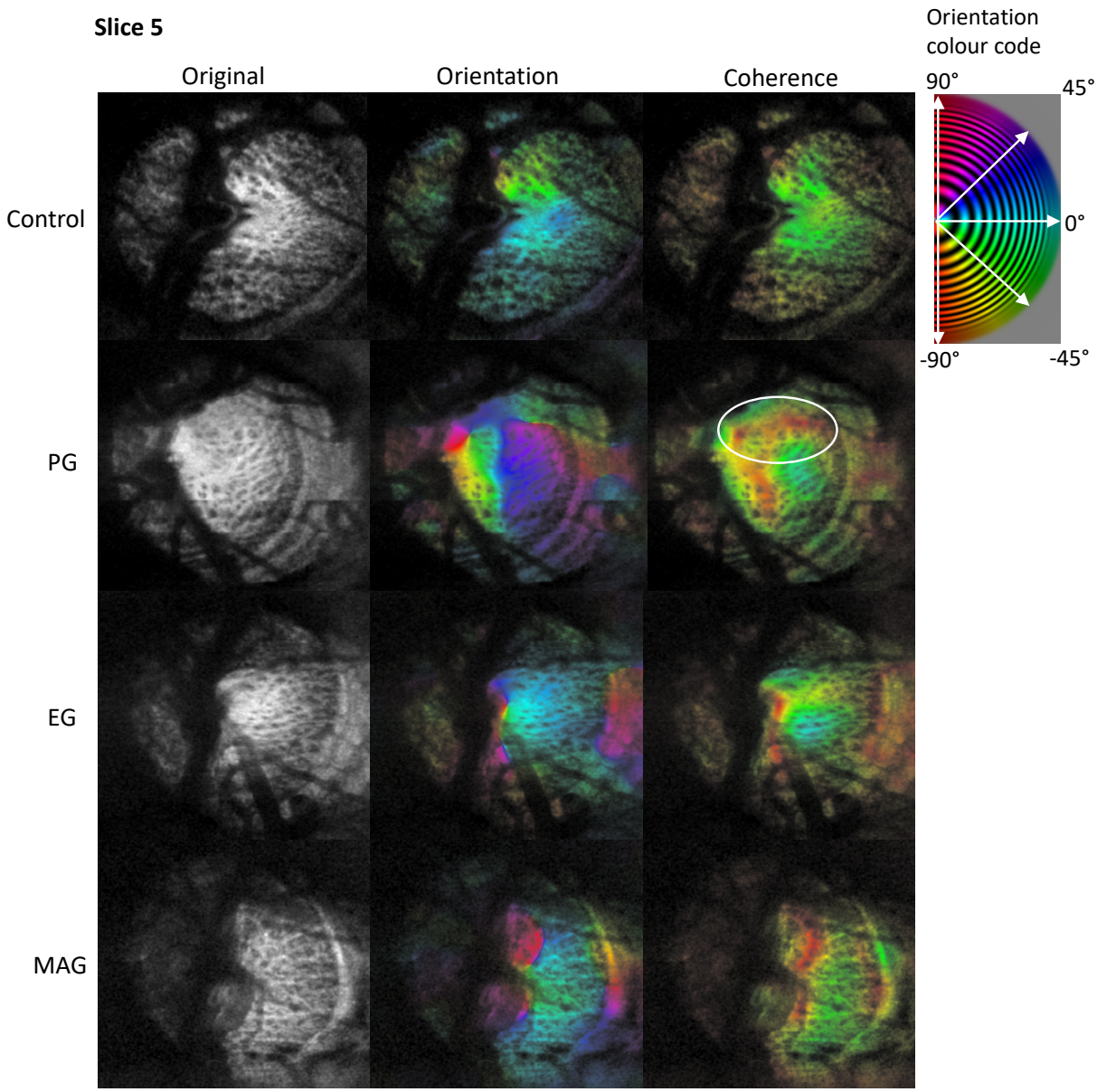

Figure 5.7: Example of left eye OCT image for slice 5, including colour coded maps for LC beam orientation and coherence for each stage of glaucoma disease. White oval indicates higher LC coherence in the superior-temporal ONH region in PG.

ONH OCT Slice	Region	Inter-group comparisons: Adjusted *P*-values					
		C-PG	C-EG	C-MAG	PG-EG	PG-MAG	EG-MAG
1	SST	0.996	0.999	0.692	0.991	0.692	0.722
	ST	0.905	0.707	0.368	0.992	0.773	0.836
	TST	0.981	0.971	0.412	0.833	0.251	0.539
	TIT	0.965	0.723	0.234	0.462	0.125	0.664
	IT	0.904	0.732	0.302	0.288	0.099	0.724
	IIT	1.000	0.999	0.871	0.999	0.910	0.817
2	SST	0.999	0.922	0.159	0.977	0.355	0.319
	ST	0.923	0.991	0.761	0.709	0.356	0.815
	TST	0.809	0.999	0.973	0.705	0.649	0.985
	TIT	0.760	0.863	0.994	0.169	0.595	0.959
	IT	0.378	0.836	0.565	0.040	0.035	0.892
	IIT	0.999	0.934	0.939	0.907	0.926	0.899
3	SST	0.945	0.976	0.989	0.750	0.845	0.999
	ST	0.999	0.868	0.544	0.888	0.571	0.852
	TST	0.924	0.997	0.594	0.844	0.902	0.478
	TIT	0.359	0.627	0.994	0.933	0.613	0.829
	IT	0.359	0.966	0.362	0.113	0.017	0.509
	IIT	0.999	0.986	0.624	0.996	0.610	0.356
4	SST	0.002	0.292	0.962	0.165	0.014	0.428
	ST	0.934	0.640	0.932	0.962	1.000	0.962
	TST	0.817	0.983	0.970	0.944	0.990	0.998
	TIT	0.727	0.819	0.999	0.994	0.737	0.795
	IT	0.674	0.842	0.987	0.981	0.610	0.706
	IIT	1.000	0.557	0.999	0.646	0.999	0.665
5	SST	0.020	0.959	1.000	0.112	0.049	0.937
	ST	0.924	0.738	0.754	0.997	0.988	0.997
	TST	0.996	0.989	0.987	1.000	0.999	0.999
	TIT	0.999	0.999	0.969	0.999	0.966	0.974
	IT	0.721	0.995	1.000	0.826	0.839	0.997
	IIT	0.926	0.918	0.876	0.541	0.598	0.992
6	SST	-	-	-	-	-	-
	ST	0.566	0.776	0.749	0.913	0.999	0.986
	TST	0.785	0.766	0.997	0.998	0.809	0.839
	TIT	0.931	0.995	0.987	0.875	0.997	0.961
	IT	0.989	0.999	0.722	0.983	0.669	0.787
	IIT	0.938	0.904	0.391	1.000	0.273	0.207

Table 5.2: Tukey post-hoc comparisons of regional LC coherence throughout the thickness of the LC (OCT slices 1 to 6) as a function of glaucoma disease stage. C = control, PG = preperimetric glaucoma, EG = early glaucoma, MAG = moderate-advanced glaucoma, S = superior, I = inferior, T = temporal. Dash (-) indicates insufficient data for that region due to vascular shadowing within the OCT dataset.

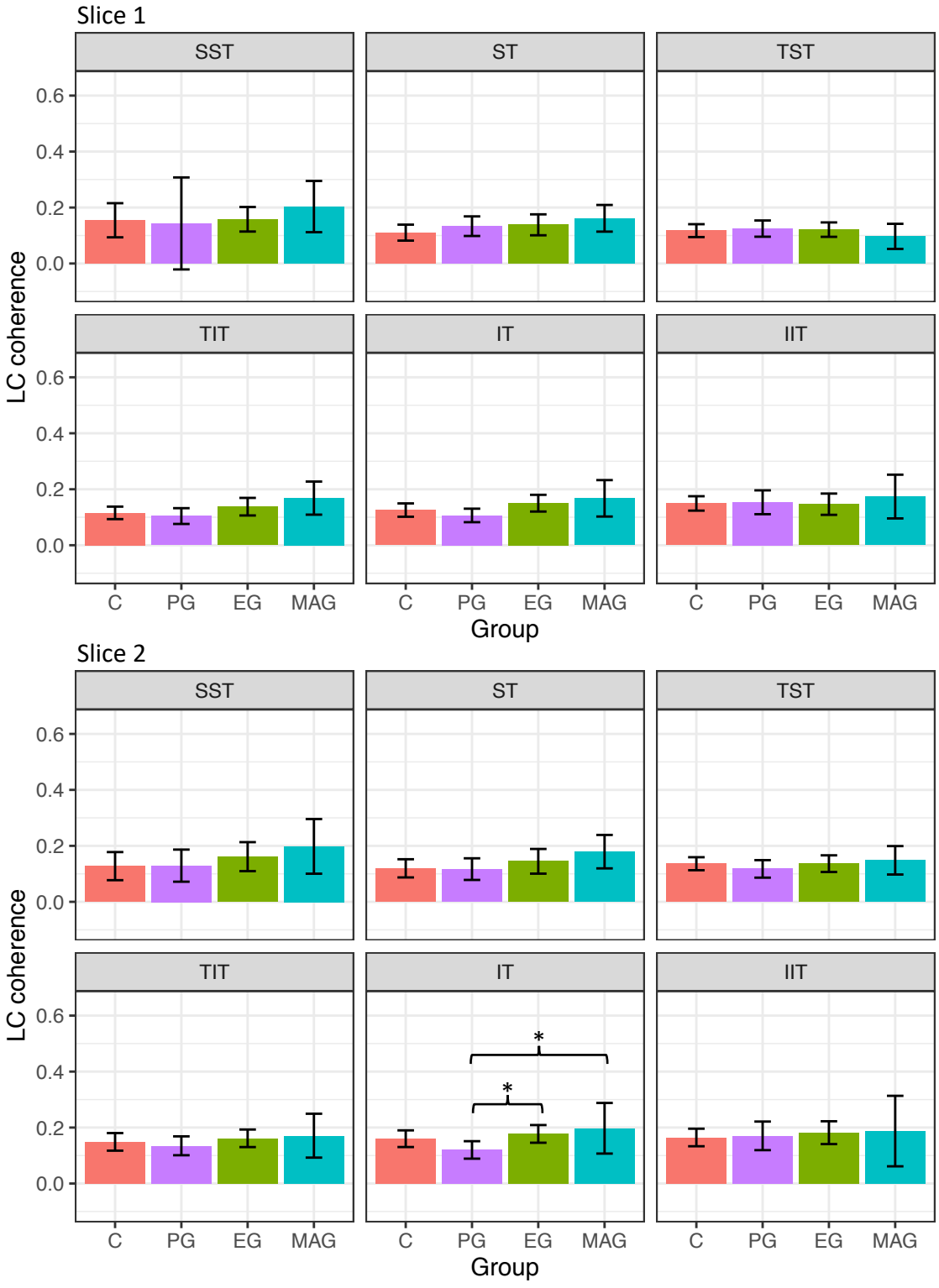

Figure 5.8: Regional LC coherence as a function of glaucoma disease stage for OCT slices 1 and 2. S = superior, I = inferior, T = temporal. * represents $P < 0.05$. Error bars represent 95% confidence intervals.

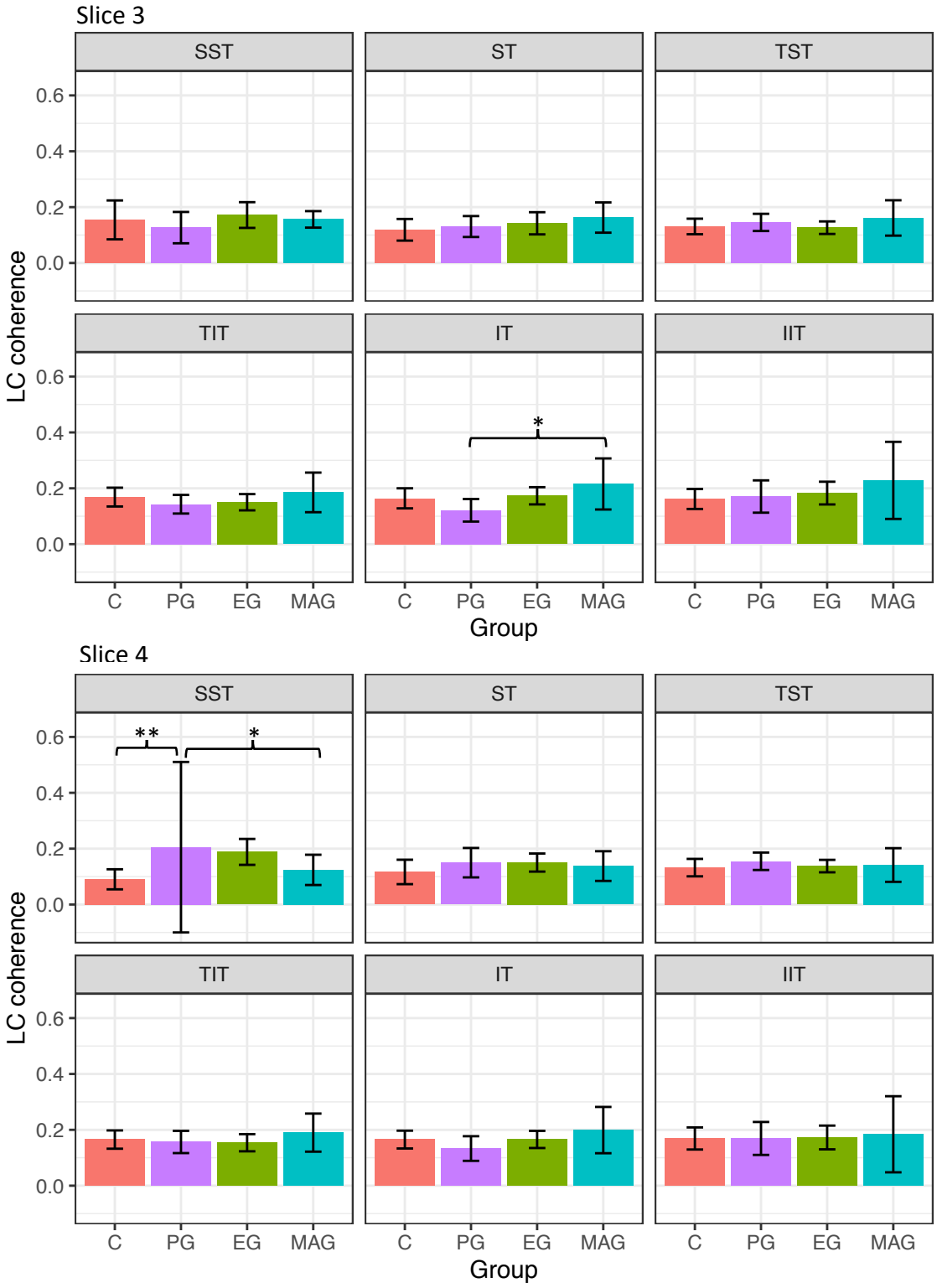

Figure 5.9: Regional LC coherence as a function of glaucoma disease stage for OCT slices 3 and 4. S = superior, I = inferior, T = temporal. * represents $P < 0.05$. ** represents $P < 0.01$ Error bars represent 95% confidence intervals.

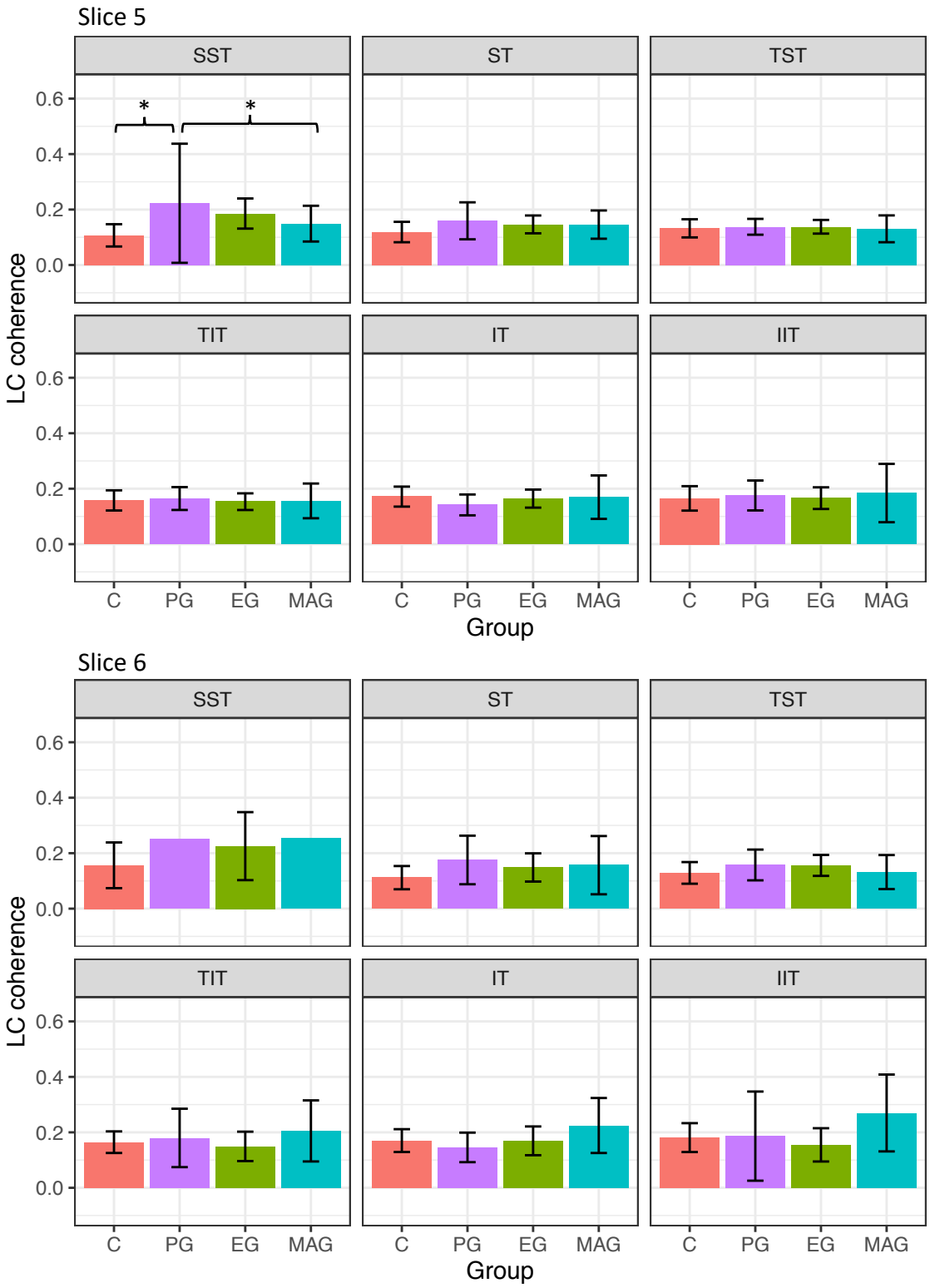

Figure 5.10: Regional LC coherence as a function of glaucoma disease stage for OCT slices 5 and 6. S = superior, I = inferior, T = temporal. * represents $P < 0.05$. Error bars represent 95% confidence intervals. In OCT slice 6, insufficient data to calculate confidence intervals for PG and MAG in region SST.

V.6.4 Regional LC coherence as a function of visual field sensitivity

A significant increase in LC coherence with worsening VF MD ($P < 0.03$) was identified in the IT quadrant within OCT slices 1 to 4 (i.e., anterior to mid LC); see Figures 5.11 and 5.12 and Table V.8 in Appendix III. No significant association between LC coherence and VF MD was found in any ONH region in OCT slices 5 and 6 (i.e., posterior LC); see Figure V.1 in Appendix III.

V.6.5 Regional differences in LC coherence for each stage of glaucoma

In control participants, LC coherence was significantly greater in the TIT region than ST in slice 4 ($P = 0.034$), and greater in IT than ST in slice 5 ($P = 0.046$); see Figure 5.13 and Table V.9 in Appendix III. In PG, no significant regional differences in LC coherence were identified throughout the thickness of the LC. In EG, LC coherence was significantly greater in IIT than TST in slices 2 ($P = 0.012$) and 3 ($P = 0.001$), and greater in IIT than ST in slice 3 ($P = 0.014$); see Figure 5.13. In MAG, LC coherence in slice 1 was significantly lower in TST than ST ($P = 0.023$), SST ($P = 0.001$), TIT ($P = 0.006$), IT ($P = 0.008$), and IIT ($P = 0.001$). In slice 6, LC coherence in MAG was significantly greater in IT ($P = 0.028$) and IIT ($P = 0.002$) than ST. Additionally, compared to TST, LC coherence was significantly greater in TIT ($P = 0.036$), IT ($P = 0.007$), and IIT ($P < 0.001$).

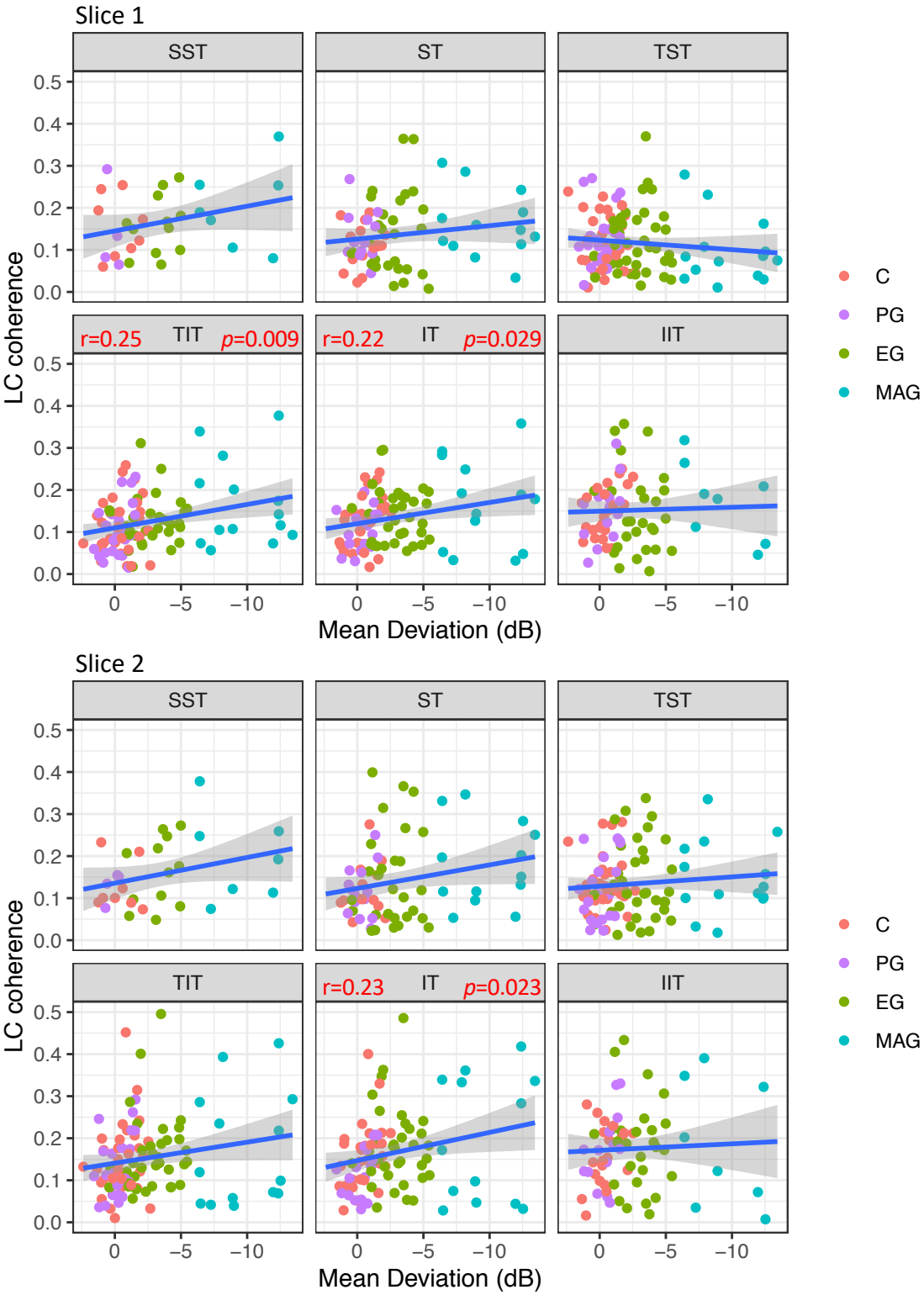

Figure 5.11: Regional LC coherence as a function of VF MD for OCT slices 1 and 2. S = superior, I = inferior, T = temporal. Blue line indicates regression line and grey shading represents 95% confidence intervals. Region SST contains relatively fewer observations due to vascular shadowing in this region within OCT image datasets.

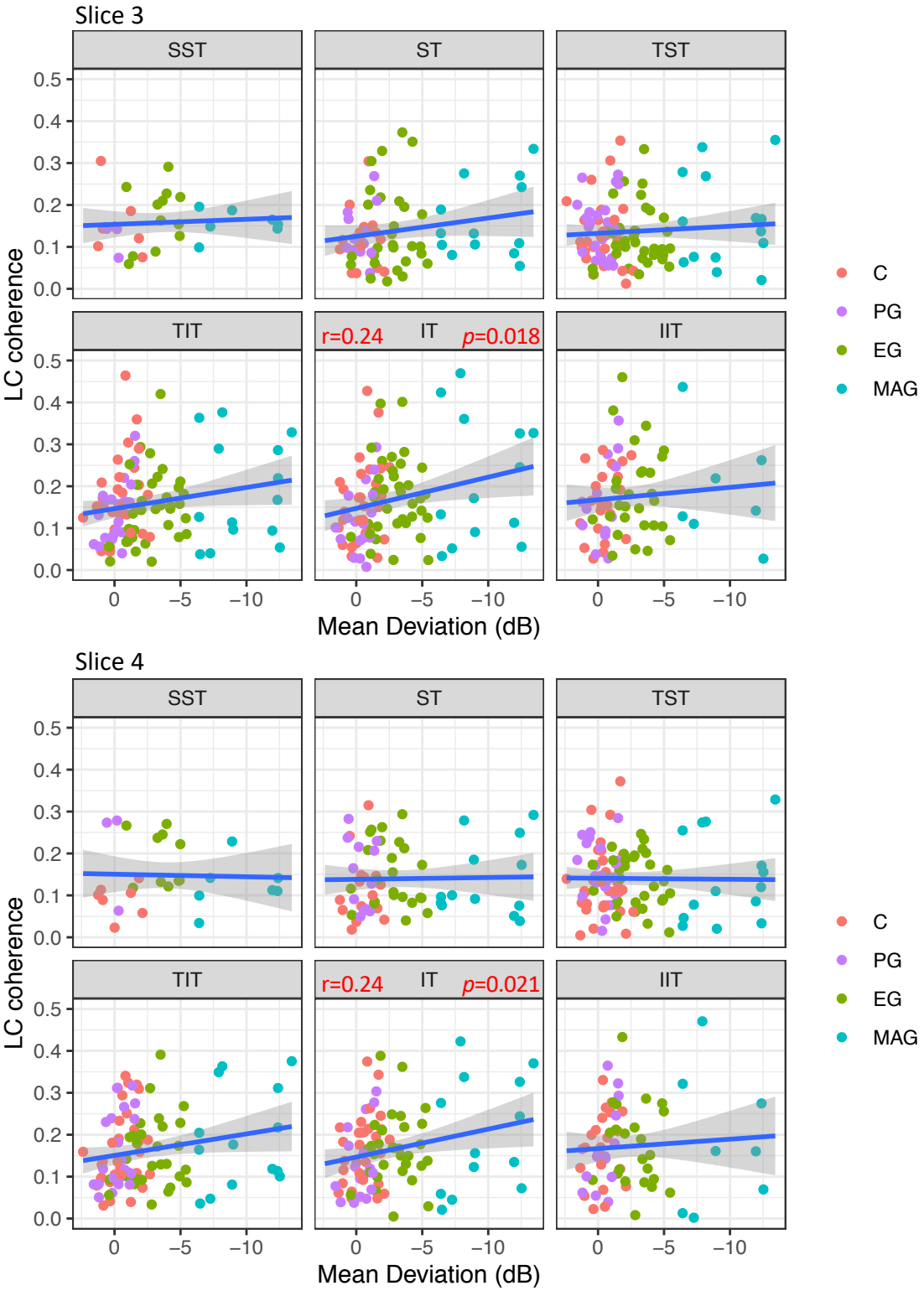

Figure 5.12: Regional LC coherence as a function of VF MD for OCT slices 3 and 4. S = superior, I = inferior, T = temporal. Blue line indicates regression line and grey shading represents 95% confidence intervals. Region SST contains relatively fewer observations due to vascular shadowing in this region within OCT image datasets.

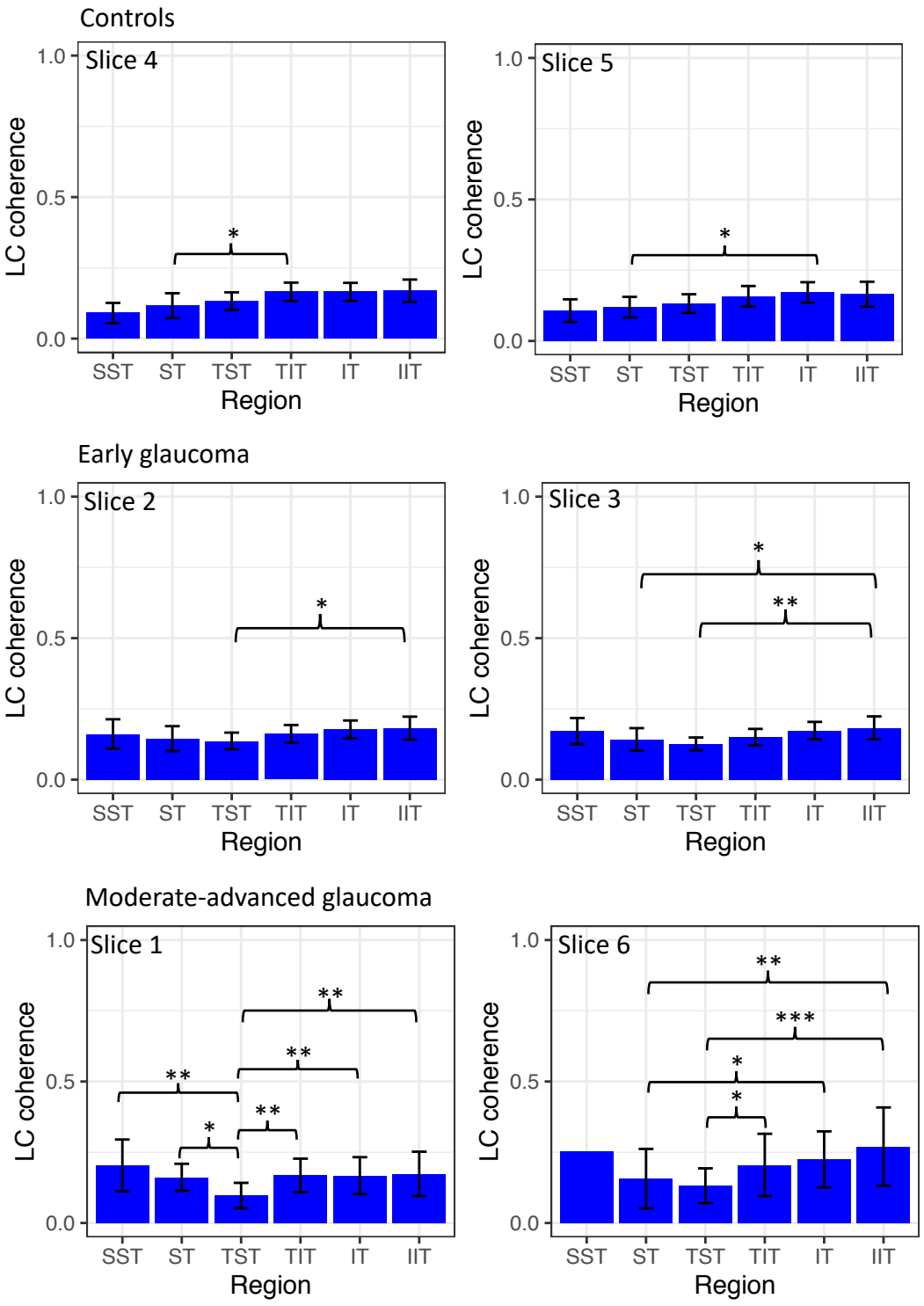

Figure 5.13: Regional difference in LC coherence for controls, early glaucoma, and moderate-advanced glaucoma with increased axial depth (i.e., OCT slices 1 to 6). S = superior, I = inferior, T = temporal. Error bars represent 95% confidence intervals. * represents $P < 0.05$.

V.7 Discussion

This study aimed to investigate *in vivo* regional alterations in LC connective tissue coherence as a function of glaucoma disease stage. Here, the organisation of connective tissue fibres was attributed to LC connective tissue light scatter within the OCT image datasets. As previously described, the LC is composed of cribriform plates that form a mesh-like structure containing pores to allow passage of RGC axons. In the *enface* orientation, this network of interweaving connective tissue beams results in a criss-cross appearance to the LC which provide relatively low levels of LC coherence (i.e., low degree of alignment). Since OCT imaging is based upon the backscatter of light from a sample; with greater backscatter from LC connective tissue than LC pores or blood vessels, this *in vivo* study probed LC coherence as a measure indicative of potential structural alterations in LC connective tissue in glaucoma disease at different stages.

Significant regional differences in LC coherence were identified between control eyes, preperimetric glaucoma, and moderate-advanced glaucoma. Furthermore, these regional differences (SST and IT) in LC coherence were specific to certain axial depths within the LC; summarised in Table 5.3. In Figures 5.4 to 5.7, the orientation colour maps denote which direction the dominant LC coherence was found. However, no statistical analysis regarding LC orientation was performed here.

Alteration in LC coherence according to glaucoma stage		
Control to PG	**PG to EG**	**EG to MAG**
↑ SST coherence within mid-posterior LC (slices 4 and 5)	↑ IT coherence within anterior LC (slices 2 and 3).	No alteration in regional LC coherence at any depth.
Alteration in LC coherence versus VF MD		
↑ LC coherence with VF loss in IT quadrant of anterior-to-mid LC. No significant association between regional LC coherence and VF MD in posterior LC.		

Table 5.3: Summary of regional LC coherence alterations as a function of glaucoma stage and VF MD. Red text indicates significant alteration in LC coherence.

Consistent with these findings, an *ex vivo* study of human eyes, Jones et al. (2015) discovered significantly higher LC connective tissue coherence in the inferior-temporal quadrant of the LC in glaucomatous eyes compared to control eyes, throughout the entire thickness of the LC,

divided into 100µm thick tissue sections. Until now, such findings of alterations in LC coherence as a function of glaucoma disease has not been indicated in the *in vivo* LC.

In this current study, LC coherence was significantly higher in PG than controls in the mid-posterior LC in the superior pole of the ONH. Furthermore, in the anterior LC, EG displayed significantly higher LC coherence than PG in the IT region of the ONH. Regional differences in LC coherence according to glaucoma stage found in this study could be related to regional structural differences within the LC. In glaucoma, regional variation of LC structure has been hypothesised to correlate with early patterns of visual field defects characteristic of glaucomatous optic neuropathy and structural damage to the LC. According to previous *ex vivo* studies, the superior and inferior poles of the LC contain larger pores and less connective tissue than the nasal and temporal regions (Quigley and Addicks, 1981; Radius and Gonzales, 1981). With the nasal-temporal ONH regions displaying greater connective tissue and glial cell structural elements, consistent with compression and backward bowing of the LC with glaucoma disease being more pronounced in the superior and inferior poles (Quigley et al., 1983). Therefore, such regional differences in LC structure described above may contribute to the significant changes in LC coherence in glaucoma reported in this study. Significant alterations in LC coherence in the superior and IT ONH regions, along with a significant association between IT LC coherence and VF MD in the anterior to mid LC suggest these regions are prone to LC structural alterations in the early stages of glaucoma disease.

This *in vivo* study is the first to report significant alterations to LC connective tissue coherence in glaucoma participants. This indicates that in glaucomatous disease, there is significant LC connective tissue microstructural changes, which is consistent with LC remodelling reported in early experimental glaucoma in monkey eyes. For instance, following IOP elevation in monkey eyes, Roberts et al. (2009) reported an increase in LC connective tissue volume (i.e. the LC incorporating more connective tissue) and an increased number of LC beams throughout the thickness of the LC compared to control eyes.

This study identified that increasing LC coherence was significantly associated with VF loss in the IT quadrant of the anterior to mid LC. This suggests that LC structure in the IT region of the ONH may be different to other ONH regions and therefore less resistant to glaucomatous

LC changes, in that no other ONH region displayed a significant association between LC coherence and VF MD. In a previous *ex vivo* study, Winkler et al. (2010) quantified the density and distribution of collagen across the LC, suggesting a non-uniform structural stiffness across the LC, which may correspond to increased susceptibility to RGC axon damage in glaucoma disease. Winkler et al. (2010) reported that the inferior-temporal region of the ONH contained a lower collagen density than other regions, which could relate to previous clinical observations reporting the IT region was more susceptible to ONH damage during the early stages of glaucoma (Caprioli, Sears and Miller, 1987; Jonas et al., 1993). Further to this postulation of LC structural vulnerability within the IT region, it has been reported by *in vivo* OCT evaluation that in glaucoma, LC focal defects predominantly occurred in the inferior and inferior-temporal regions of the LC (Kiumehr et al., 2012). Focal defects were defined as an anterior LC surface irregularity which violated the normal smooth curvilinear LC surface, with a diameter > 100µm, and depth > 30µm. The authors reported that in glaucoma, LC deformation included focal loss of LC beams, which may cause an acquired pit of the optic nerve (APON). Such focal LC defects occurred in conjunction with neuroretinal rim and VF loss. For instance, focal LC defects in the inferior half of the ONH displayed greater VF sensitivity loss in the superior visual hemifield and vice versa (Kiumehr et al., 2012). Furthermore, APONs have been reported to occur more often in the inferior ONH (70%), rather than the superior ONH region (30%), and are nearly always associated with dense visual field defects close to fixation (Nduaguba, Ugurlu and Caprioli, 1998; Ugurlu et al., 1998; Oh and Park, 2004; Faridi et al., 2014). These LC defects represent localised loss of LC tissue, which correlate spatially with ophthalmoscopic structural changes seen in glaucoma, such as loss of neuroretinal rim and APONs (Kiumehr et al., 2012; You et al., 2013; Faridi et al., 2014).

In the anterior LC, this study determined significantly higher LC coherence in EG and MAG than PG in the IT region of the ONH. Therefore, this suggests that the inferior-temporal sector of the anterior LC may be structurally vulnerable and more prone to LC alteration and deformation, hence damage to RGC axons with advancement of glaucoma disease. LC structural alterations and damage to RGC axons that occur within the inferior ONH will result in loss of inferior neuroretinal rim, and reduction of visual function in the superior VF (Quigley et al., 1981; Radius and Gonzales, 1981; Kiumehr et al., 2012). Clinically, from a topographic evaluation of the ONH, the localisation of VF loss can be related to the damaged area of the

neuroretinal rim within the optic disc (Quigley et al., 1981; Jonas et al., 1988c). This study has shown ONH sectoral alterations to LC coherence as a function of glaucoma stage which could impact on RGC axon viability within these regions, therefore resulting in RGC axonal damage and regional loss of the neuroretinal rim. In glaucoma, loss of the neuroretinal rim has been shown to be more pronounced in the inferior-temporal region of the optic disc (Caprioli et al., 1987). Using stereoscopic optic disc photographs, Jonas et al. (1993) report that glaucomatous neuro-retinal rim loss occurred in a sequence of sectors. In eyes with modest glaucomatous damage, the inferior-temporal region usually showed more pronounced rim loss. Generally, loss of the neuroretinal rim began in the inferior-temporal region and then progressed to the superior-temporal, temporal-horizontal, inferior-nasal, and finally superior-nasal.

To date, limited research has investigated regional assessment of LC beam coherence and preferred orientation in humans. This current study reported significant changes in LC structure in early glaucoma disease stages. For instance, in the superior pole of the mid-posterior LC, LC coherence significantly differed between controls and PG, and in the IT quadrant of the anterior LC, coherence significantly differed between PG and EG. These findings suggest that throughout the thickness of the LC, there is regional alteration to LC coherence as a function of glaucoma stage, suggesting significant changes to LC connective tissue. This increased LC tissue alignment could lead to areas within the LC that are more susceptible to glaucomatous damage. Within these regions, an alteration in LC coherence may hinder the LC's ability to cope with IOP-related stress; making these LC regions more likely to induce damage to RGC axons. Regional differences in LC coherence in glaucoma have also been reported in *ex vivo* human eyes (Jones et al., 2015). However, the authors acknowledge that it remains unclear whether regions of increased LC coherence suggest ONH susceptibility to glaucoma or are indicators of disease progression, or are related to a LC compensation mechanism as a result of disordered structure in other regions of the ONH. Jones et al. (2015) suggest that this increase in LC coherence likely assists in the LC's ability to resist tensional forces exerted in the direction of fibre alignment. This may also be a factor in the increased susceptibility of RGC axons regionally within the glaucomatous LC (Quigley and Addicks, 1981; Radius and Gonzales, 1981).

As determined in this study, an alteration in LC connective tissue coherence corresponds to the LC remodelling reported in monkey models of experimental glaucoma. With advancement of glaucomatous disease and respective cupping of the ONH due to elevated IOP, Yang et al. (2011b) report that posterior migration of the LC is a component in early cupping of the ONH in monkey eyes with early experimental glaucoma. This posterior migration of the LC could impose stress on the LC beams and potentially induce cell activation, leading to remodelling of the LC connective tissue (Yang et al., 2011a). Indeed, in monkey eyes with early experimental glaucoma there was a substantial increase in LC connective tissue volume compared to contralateral normal eyes; suggesting significant alterations in connective tissue components within the LC in the early stages of glaucoma disease (Roberts et al., 2009; Roberts et al., 2010a; Roberts et al., 2010b).

Such alterations to LC connective tissue in glaucoma could impact on LC beam and pore structure, which could be investigated with techniques outlined in this study. It has been reported that in control eyes the LC pores were approximately round, whereas in glaucoma participants, the LC pores were more elongated and less circular with increasing visual field loss (Bhandari et al., 1997; Fontana et al., 1998; Ivers et al., 2011; Lee et al., 2011). With advancements in OCT imaging including swept-source OCT, Wang et al. (2013) analysed LC microarchitecture *in vivo*, including LC beam thickness, LC pore counts, pore diameter, and aspect ratio in healthy and glaucomatous participants. They reported a significant increase in LC beam diameter, and a significant reduction in LC pore diameter with increasing VF loss (worse MD). The authors suggest that the advancement of glaucomatous disease leads to LC connective tissue remodelling (i.e., new connective tissue), resulting in an increase in LC beam thickness, and a corresponding reduction in LC pore diameter. Therefore, OCT imaging systems could allow for the novel investigation of LC beam and pore orientation and coherence *in vivo* in glaucomatous disease with aim to elucidate disease biomarkers within the LC microarchitecture.

V.7.1 Limitations of study

One of the limitations in this study was that the presence of blood vessels within the ONH cause extensive shadowing within the OCT image datasets. For example, in this study the nasal side of the ONH OCT images were immediately disregarded from investigation.

Additionally, the remaining temporal portion of the ONH images were examined, and sectors which contained major blood vessels or vascular shadowing within the OCT image were excluded from analysis. For example, the regions SST and IIT (i.e., the regions closest to the nasal portion of the ONH) often had to be excluded from analysis due to encroachment of vessels into these regions. In the SST region, 70% of images contained vascular shadowing and 40% in the IIT region; thereby lowering the amount of data included for these regions and potentially weakening statistical analysis.

The approach taken by this study to investigate LC connective tissue microstructure *in vivo* could be improved if accurate removal of vascular shadows from OCT image datasets was possible, and therefore obtain more sample data for stronger statistical analysis. Adaptive compensation algorithms have made progress in shadow removal within OCT images, including significant enhancements in inter-layer contrast (a measure of boundary visibility), in particular the posterior LC boundary by eliminating noise overamplification with increasing depth within the OCT image. Such adaptive compensation in OCT image datasets could aid *in vivo* ONH investigations for the diagnosis and monitoring of glaucoma (Girard et al., 2011; Mari et al., 2013). However, such algorithms in previously published work have not been deemed effective in image enhancement in our OCT image datasets, acquired using the custom-built research-based OCT device in this study.

This current study analysed data acquired from 10° SD-OCT scans centred on the ONH. The 10° scan angle resulted in a scan width of approximately 3mm at the retina. With such a narrow scan width these OCT image datasets were prone to motion artefacts and 4 OCT datasets were discarded due to excessive eye movements. The research-based OCT device used in this study does not currently employ an eye-tracking system. If this technology was incorporated during OCT image acquisition this would allow for less motion artefacts within the OCT images, and fewer exclusion of OCT datasets, resulting in an increase in data acquisition and therefore more powerful statistical analysis.

Another limitation of this study is that analysis was performed on data acquired from 2D OCT image projections of the complex 3D LC structure. This study used average projections of the LC at 50µm intervals which may not accurately represent such a complex structure.

Additionally, the 2D *enface* OCT projections used in this study do not take into consideration the natural curvature of the LC, which therefore could potentially influence the results obtained.

To further this investigation, an increase in sample size is important to confirm that the regional differences in LC connective tissue coherence reported in this study are due to glaucomatous disease, and not as a result of natural inter-participant biological variation. Due to the cross-sectional design of this study, longitudinal studies using techniques described here to evaluate LC coherence *in vivo* could allow for a better understanding of LC connective tissue changes in human eyes with the progression of glaucoma disease. The use of adaptive compensation in future studies could allow for removal of vascular shadowing, and analysis of data from the nasal side of the ONH. Furthermore, the use of eye tracking, adaptive optics, and swept-source OCT could benefit *in vivo* investigations of LC connective tissue with enhancements in data acquired throughout the depth of the LC, at greater image resolution, with OCT images less prone to motion artefacts.

V.7.2 Conclusion

This study has presented novel *in vivo* analysis on the degree of LC connective tissue alignment. The results from this study suggest that in glaucoma disease there are regional differences in degree of LC connective tissue alignment, which can occur at different levels within the LC. Such differences in LC structure may highlight the predisposition and susceptibility of some ONHs to regional damage to the LC, and therefore loss of RGC axons.

The findings from this study emphasise the importance and relevance of utilising *in vivo* high-resolution OCT imaging of the LC microstructure to gain a better understanding of the LC connective tissue structural alterations as a function of glaucoma disease stage. Such investigations may allow for the prediction of LC regions suspect to damage, and RGC axon loss in glaucoma disease.

VI. Chapter 6: Statistical modelling to determine ONH factors that characterise disease stage in Glaucoma

VI.1 Introduction

Glaucoma remains a leading cause of worldwide blindness (Coleman, 1999; Quigley and Broman, 2006; Tham et al., 2014; Flaxman et al., 2017). Historically, clinical detection of glaucoma is based upon progressive changes in the appearance of the optic disc, and reproducible deterioration in standard automated visual field testing (Weinreb et al., 2014). Structural alterations to the optic nerve head (ONH) (Varma et al., 1992a; Park et al., 2015; Kim et al., 2016) or NFL (Medeiros et al., 2008; Jeoung and Park, 2010) can occur prior to visual field abnormalities, and it has been reported that as many as 30% to 50% of RGCs may be lost before detection of VF defects using standard testing (Quigley et al., 1981; Harwerth and Quigley, 2006; Harwerth et al., 2010; Medeiros et al., 2013). This highlights the importance of longitudinal assessment and documentation of ONH structural damage in the diagnosis of glaucoma (Medeiros et al., 2009a; Medeiros et al., 2009b). However, there has been reported to be disagreement between glaucoma specialists in grading glaucomatous ONH appearance; therefore, making subjective identification of optic disc damage in glaucoma difficult (Varma, Steinmann and Scott, 1992b; Jampel et al., 2009; Breusegem et al., 2011; Rossetto et al., 2017; Hong et al., 2018).

Optical coherence tomography (OCT) imaging has allowed objective and quantitative information about ONH structure and nerve fibre layer (NFL) loss in glaucoma, thereby aiding in the early identification of disease, and the observation of RGC axon loss over time (Medeiros et al., 2009b; Leung et al., 2010b; Chauhan et al., 2013; Lee et al., 2017). In a clinical setting, OCT instruments are used for glaucoma diagnosis and management, and report parameters including NFL thickness, neuroretinal rim thickness and area, and have been shown to aid in glaucoma diagnostic ability (Hwang and Kim, 2012; Mwanza et al., 2013; Larros et al., 2015). However, we suggest that other ONH structural parameters could be important factors to further enhance early glaucoma detection.

Primary open angle glaucoma is a chronic condition that must be monitored for life. Early diagnosis of glaucoma, including the ability to detect disease progression, are key elements in the preservation of visual function. According to Kokotas et al. (2012), biomarkers are characteristics that are specifically measured and evaluated as indicators of normal biological or disease processes, or for monitoring responses to a therapeutic intervention. Therefore, these biomarkers may act as invaluable tools for the identification of individuals at risk of disease onset or progression, including glaucomatous optic neuropathy, and have potential to measure therapy outcomes (Golubnitschaja and Flammer, 2007; Kokotas et al., 2012).

Previous chapters have demonstrated significant alterations in various ONH parameters as a function of glaucoma disease stage. As described in Chapter 3, such ONH parameters include regional measures of prelamina depth and thickness, LC thickness, and NFL thickness and area. In Chapter 4, significant differences in volumetric ONH parameters were also found in glaucomatous disease including, optic cup volume, prelamina volume, LC volume, and BMO surface area. Chapter 5 reported a significant alteration in regional LC coherence in glaucoma disease.

The hypothesis of this chapter is that a subset of ONH parameters can act as a biomarker for the classification of ONHs, according to disease stage in glaucoma. This would allow for *in vivo* characterisation of ONH structural appearance in control and glaucoma participants to determine which ONH parameters hold potential to identify onset or stage of glaucomatous disease. As discussed, in glaucoma, early diagnosis of disease and/or the ability to identify disease stage is crucial in a clinical setting for clinical decision making in therapeutic and/or surgical intervention.

VI.2 Aims

This chapter aimed to develop an ONH classification based on glaucoma disease stage, using previously obtained quantitative measures of ONH and RGC axon-related parameters.

VI.3 Experimental design

Participant demographics and ocular characteristics are presented in Table 6.1. All participants were recruited according to study inclusion and exclusion criteria previously defined in section II.2. Data (81 variables) were collated from previous chapters. These data included regional ONH parameters analysed in Chapter 3; namely, centre, superior (S), inferior (I), nasal (N), temporal (T), ST, SN, IT and IN measurements of prelamina and LC depth and thickness, NFL measures at the ONH border (bNFL) and peripapillary (pNFL), minimum rim width (MRW) and area (MRA). Additionally, volumetric ONH parameters, from Chapter 4, included optic cup volume, prelamina volume, LC volume and BMO surface area. Table 6.2 presents the total number of ONH parameters quantified in Chapters 3 and 4.

Characteristic	**Control**	**Preperimetric Glaucoma**	**Early Glaucoma**	**Moderate-Advanced Glaucoma**
	N = 60 eyes	N = 28 eyes	N = 58 eyes	N = 23 eyes
	Mean ± Standard Deviation			
Age (years)	65.6 ± 6.4	68.9 ± 9.3	73.1 ± 8.2	75.7 ± 7.0
Gender	33 F & 27 M	16 F & 12 M	29 F & 29 M	11 F & 12 M
MS (D)	0.79 ± 1.89	-0.07 ± 2.75	0.15 ± 2.06	0.08 ± 2.26
VA (logMAR)	-0.04 ± 0.09	0.07 ± 0.10	0.11 ± 0.13	0.17 ± 0.16
IOP (mmHg)	15.17 ± 3.23	13.64 ± 2.00	13.41 ± 2.33	11.89 ± 2.49
AEL (mm)	23.73 ± .97	23.99 ± 1.55	23.95 ± 1.07	24.08 ± 1.34
CCT (μm)	560.35 ± 41.26	528.00 ± 30.34	525.16 ± 39.34	517.04 ± 32.75
ACD (mm)	2.83 ± 0.56	2.95 ± 0.74	3.24 ± 0.88	3.29 ± 0.92
VF MD (dB)	-0.46 ± 1.16	-0.35 ± 1.01	-3.16 ± 1.66	-11.03 ± 4.88

Table 6.1: Participant characteristics for glaucoma participants and controls. MS = mean sphere, VA = visual acuity, IOP = intraocular pressure, AEL = axial eye length, CCT = central corneal thickness, ACD = anterior chamber depth, VF MD = visual field Mean Deviation.

VI.4 Variable selection and data imputation

The first step was to undertake dimensional reduction of the data using principal component analysis (PCA). Since no significant differences in regional anterior or posterior LC depth data (n=18 ONH variables in chapter 3) were observed as a function of glaucoma disease stage, these data were excluded from PCA, as indicated in Figure 6.2. To execute PCA, datasets must not contain missing values within each variable. Therefore, since LC coherence was quantified in 114 of the 169 OCT datasets only, these data were excluded from PCA. Additionally, OCT

image analysis data sets contained missing values as a results of image artefacts or vascular shadowing, which prevented accurate measurement of a given ONH parameter.

ONH parameter	Number of regions quantified	Cumulative number of variables
Prelamina depth	9	9
Prelamina thickness	9	18
Anterior LC depth	9	27
Posterior LC depth	9	36
LC thickness	9	45
bNFL	8	53
pNFL	8	61
MRW	8	69
MRA	8	77
Volumetric ONH parameters		
Optic cup volume	N/A	78
Prelamina volume	N/A	79
LC volume	N/A	80
BMO surface area	N/A	81

Table 6.2: Summary of total number of variables measured as a function of glaucoma disease stage in chapters 3 and 4.

The proportion of missing observations within each ONH variable was visualised using 'naniar' software; (Tierney et al., (2020), http://cran.r-project.org/package=naniar). Each regional ONH parameter datasets were evaluated with respect to missing values. Figure 6.1 demonstrates the numbers and percentages of missing data for each ONH parameter quantified; 28 ONH variables had complete data sets and so could be included in the analyses performed in this chapter.

In datasets that contain relatively small amounts of missing observations, data imputation can be performed to determine values for missing values; thereby minimising bias and enabling use of 'expensive to collect' data, which would otherwise be discarded (Scheffer, 2002). One data imputation method is to replace each missing value with the mean of the variable. However, this reduces the resulting dataset variance which is important for PCA. Another method for data imputation is regression imputation; whereby missing values are imputed based on the relationship between the variable containing missing values, and another variable. This has the advantage of maintaining the relationship between the variable

to be imputed and another variable within the dataset. Regression imputation methods are acceptable for data imputation when less than 10% of the data are missing (Scheffer, 2002).

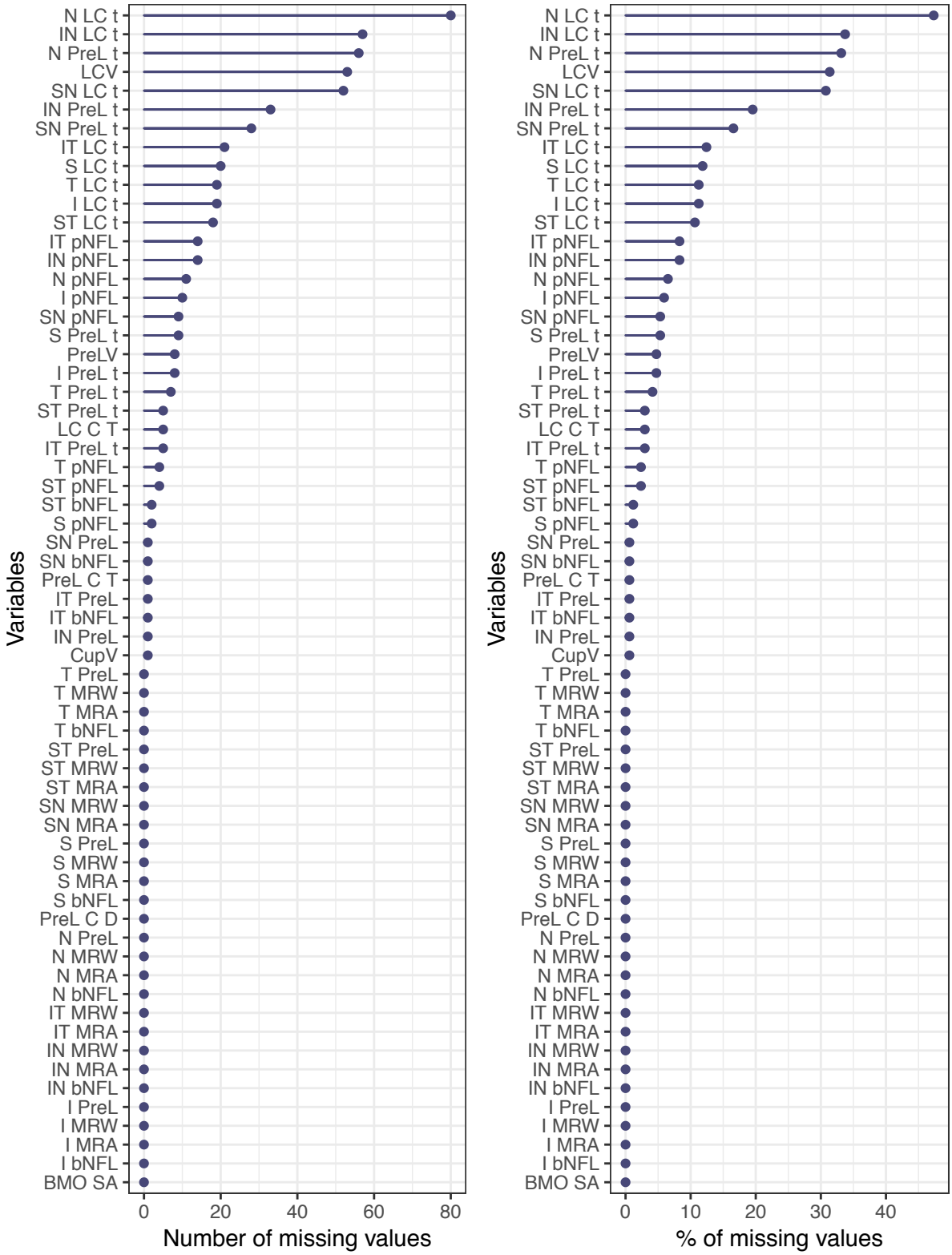

Figure 6.1: Indication of 63 ONH variables with number of missing values (left), and percentage of missing values (right) within each variable. Due to excessive numbers of missing observations, the first seven variables were excluded from PCA.

Since variables nasal, SN, and IN prelamina and LC thickness, as well as LC volume had > 10% missing values (see Figure 6.1), these 7 variables were excluded from PCA. However, other variable datasets, namely IT, S, T, I, and ST LC thicknesses, that contained > 10% (but <15%) missing observations were included in the PCA. The rationale for including these was that significant LC structural alterations in these regions in glaucoma, were indicated by LC coherence in Chapter 5, consistent with our previous *ex vivo* data (Jones et al., 2015). Additionally, data imputation was performed on a further 28 ONH variables which had <10% missing values. Imputed ONH variables were derived from the regression equations (using the 'linear model' function within R statistics) identified when each variable was significantly correlated with VF MD (see Chapters 3 and 4, and Table VI.1 in Appendix IV).

The sequence of ONH variable selection and data imputation in this chapter has been summarised in Figure 6.2. To conclude, 56 ONH variables, following data imputation were included in PCA, as shown in Table 6.3.

Regional ONH parameters	**Region**								
	C	**S**	**I**	**N**	**T**	**SN**	**IT**	**ST**	**IN**
Prelamina depth	✓	✓	✓	✓	✓	✓	✓	✓	✓
Prelamina thickness	✓	✓	✓	✗	✓	✗	✓	✓	✗
LC thickness	✓	✓	✓	✗	✓	✗	✓	✓	✗
Border NFL	N/A	✓	✓	✓	✓	✓	✓	✓	✓
Peripapillary NFL	N/A	✓	✓	✓	✓	✓	✓	✓	✓
Minimum rim width	N/A	✓	✓	✓	✓	✓	✓	✓	✓
Minimum rim area	N/A	✓	✓	✓	✓	✓	✓	✓	✓
Volumetric ONH parameters									
Optic cup volume	✓								
Prelamina volume	✓								
LC volume	✗								
BMO surface area	✓								

Table 6.3: Summary of 56 ONH variables included in PCA. Tick indicates variable inclusion. Cross indicates variable exclusion. C = centre S = superior, I = inferior, N = nasal, T = temporal.

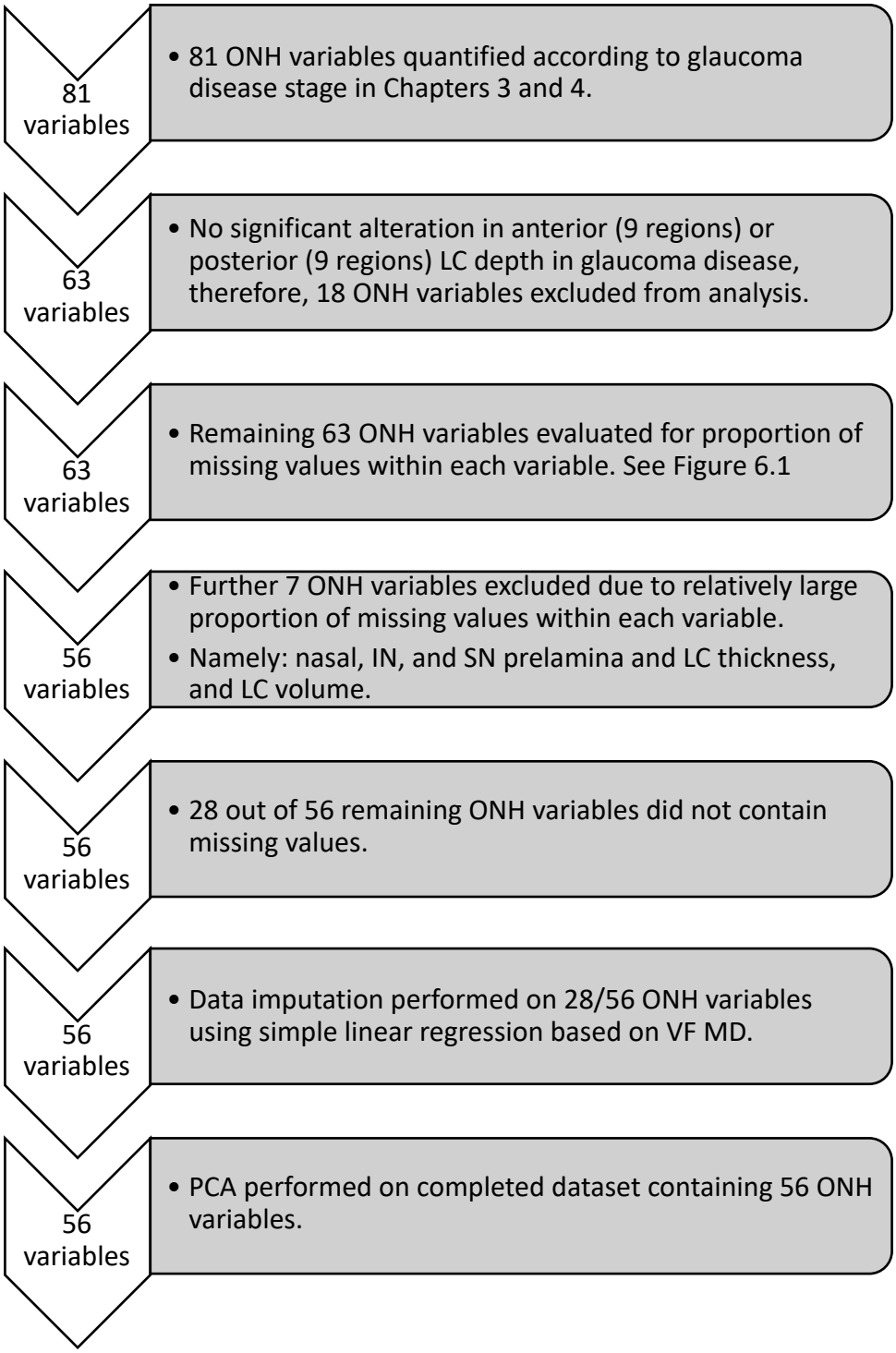

Figure 6.2: Summary of stages involved in ONH variable selection and data imputation prior to performing PCA.

VI.5 Principal component selection

Within this chapter 6, PCA was preferred over multivariate linear regression in an attempt to determine patterns/trends in ONH parameters according to glaucoma disease stage, via

dimensional reduction of quantified OCT-based parameters, whilst preserving as much variability (i.e., statistical information) as possible.

Controversy exists as to the required sample size required to perform regression analysis. A general rule of thumb is no fewer than 50 participants for a correlation or simple regression, with the number of observations required increasing with larger numbers of independent variables, i.e. in multivariate regression (Strasak et al., 2007). For instance, Green (1991) suggests a requirement of 8 observations per independent variable. This is similar to that described by Cohen (1992) where 10 observations per independent variable is suggested as an absolute minimum. However, previous studies have suggested that approximately 30 participants per independent variable would be required to detect a small effect size with 80% power (Guadagnoli and Velicer, 1988; VanVoorhis and Morgan, 2007). Therefore, if a multivariate linear regression were to be constructed including all 56 OCT-based ONH parameters, the sample size required would be ~500 as a minimum, as opposed to the 169 included in PCA.

Large datasets are increasingly frequent across many disciplines, and often, such datasets contain fewer observations than variables. However, in such contexts, nothing prevents the use of PCA and determination of PCs that account for data variability (Cadima and Jolliffe, 2009; Jolliffe and Cadima, 2016). For example, Lee et al. (2010a) performed PCA on genomic data containing 21,225 variables with a sample size of 59. PCA is a widely utilised data analysis tool that is useful for a variety of data types in numerous disciplines, including those with limited sample size in high dimensional datasets (Johnstone and Lu, 2009; Birnbaum et al., 2013; Jolliffe and Cadima, 2016).

Principal components are generated as linear combinations of the original variables within the dataset. Each of the original variables is given a 'loading coefficient' (i.e., the relative contribution of the original variable for each resulting PC) which is used to generate PC scores for each resulting PC. The analysis determines the PC axes that represent the largest amount of variance within the original data. The first axis (i.e., PC 1) explains the most variance in the data. Principal component 2 is orthogonal to PC 1 (i.e. uncorrelated with PC 1) and explains the second most variance within the data, and so forth (Cadima and Jolliffe, 1996). In PCA,

generally the first two PCs are the most important as these explain the most variance within the dataset. Following PCA, there are as many PCs as the number of original variables (Jolliffe and Cadima, 2016; Kumar, 2017).

Dimensional reduction is achieved as a large proportion of variance within the original dataset is explained by a considerably smaller number of PCs (Jolliffe, 1972; Jolliffe, 1973). The variance along each PC axis is termed its eigenvalue. The contribution of each PC can be made by comparing eigenvalues, and visualised using a 'scree-plot' (Cattell, 1966). The first PC, which captures the most variance in the data has the largest eigenvalue. The second PC has second largest eigenvalue, and so on. For dimensional reduction, there is no robust method in determining the number of PCs that should be discarded, and the number that should remain. Cattell (1966) proposed that one method was to visualise the 'scree-plot' to detect a sudden kink in the plot; and where the plot begins to level the remaining PCs should be discarded. However, another method for determination of the number of PCs to include, is that PCs with an eigenvalue less than 1.0 should be discarded (Kaiser, 1960). Additionally, the number of PCs retained should account for 80% of the variance in the data (Jolliffe, 1972; Jolliffe, 1973; Kumar, 2017).

VI.5.1 Performing principal component analysis

Principal component analysis was carried out on the 56 ONH variables as previously described. The purpose of PCA is the reduction of multidimensional data, in this case comprised of 56 ONH variables; by the generation of linear combinations of all of the variables. The resulting principal components (PCs) aimed to explain as much variance in the original data as possible (Daling and Tamura, 1970; Jolliffe and Cadima, 2016). Principal component analysis was performed using the 'prcomp' function within R (RStudio, version 1.2.1335, RStudio Team (2015). RStudio; Integrated Development for R. RStudio, Inc, Boston, USA, www.rstudio.com.) Graphs were generated using the package 'ggplot2'; http://cran.r-project.org/package=ggplot2, Wickham H (2016).

VI.5.2 Evaluation of resulting principal components

To evaluate the effect of PCs on VF MD, multiple linear regression models were constructed using the 'linear model' function within R. Ordinal regression ('ordinal' package; Christensen RHB (2019); http://cran.r-project.org/package =ordinal) was performed to evaluate the effect of PCs on an ordinal categorical variable; denoting control, preperimetric glaucoma (PG), early glaucoma (EG), and moderate-advanced glaucoma (MAG).

The interpretation of PCA usually involves examining the loading coefficients of a PC, and hence deciding which variables are important contributors for that PC. It is common practice to ignore variables with small loading coefficients for a given PC and approximate that PC by the linear combination of only the remaining variables (Al-Kandari and Jolliffe, 2005). However, Cadima and Jolliffe (1995) suggest this technique is misleading as determination of 'small' loadings is subjective and depends on the relative size of loadings for the PC. Therefore, an alternative is to evaluate the relationship between the variables and a given PC; with a good approximation of given PC involving a good correlation between the PC and its variables (Cadima and Jolliffe, 1995). Al-Kandari and Jolliffe (2005) define a 'good correlation' as correlations above 0.70. In this study, in order to investigate which of the ONH variables contributed most to the resulting PCs, the association between the ONH variables and resulting PCs was determined using Pearson's correlation coefficient (Al-Kandari and Jolliffe, 2005; Kumar, 2017). A correlation coefficient < 0.4 was considered a weak association, 0.4 to < 0.7 a moderate association, and ≥ 0.7 a strong association (Akoglu, 2018). Therefore, variables that were strongly correlated (Pearson's $r \geq 0.7$) with the resulting PCs were considered important factors for a given PC.

VI.5.3 Cluster analysis

In an attempt to achieve a more effective separation of observations as a function of glaucoma disease stage, cluster analysis was performed on resulting PCs 1 and 2 generated to describe the 56 ONH variables. The aim of cluster analysis is to identify groups (i.e., clusters) of similar observations based on measurements that are similar/dissimilar to each other within a multivariate dataset. Cluster analysis is based upon pairwise distances between observations within the multidimensional dataset. Based upon this distance between observations, similar observations are clustered together. Hierarchical clustering was

performed using the 'hclust' function, and K-means cluster analysis was performed using the 'kmeans' function, both within R statistics.

VI.5.4 Linear discriminant analysis of ONH variables between glaucoma disease stages

Linear discriminant analysis (LDA) is another statistical tool that can be used for dimensional reduction of multivariate data. The aim of LDA is to generate axes (i.e. linear combinations of original variables) that allow the maximum separation (discrimination) amongst known group classifications (Jolliffe, Morgan and Young, 1996). Pearson's correlation coefficient was used to determine the association between the original ONH variables and the resulting linear discriminants (LDs); with a stronger correlation suggesting which ONH parameters contribute most to the LDs. Linear discriminant analysis was performed using the 'MASS' package; Venables and Ripley (2002), http://cran.r-project.org/package=MASS.

In order to compare the ability of the discriminatory function of the resulting LDs 1 and 2 on a binary classifier (control or glaucoma), receiver operator characteristic (ROC) curves were generated and area under the curve (AUC) calculated. The ROC curves were generated using 'pROC' package; Robin X et al., (2011), http://cran.r-project.org/package=pROC.

VI.6 Results

VI.6.1 Derived principal components

Fifty-six principal components (PCs), each a linear combination of the original ONH variables, were generated. Since the first two PCs are considered to describe the most variance in the ONH dataset, the relationship between PC1 and PC2 for each stage of glaucoma disease was explored. Figure 6.3 indicates that although there was some separation of PC scores along axes 1 and 2 there was considerable overlap between participant groups, particularly between controls, PG, and EG.

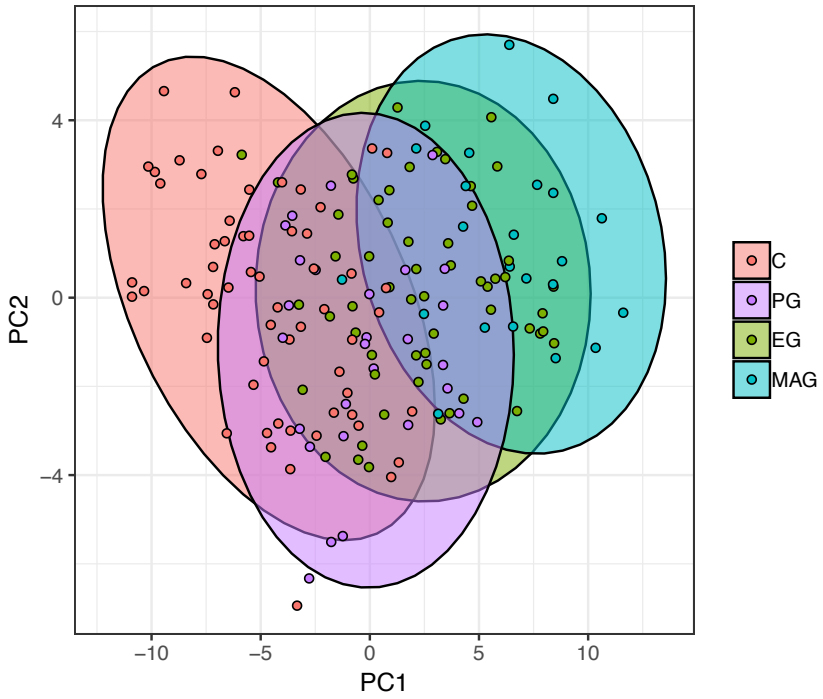

Figure 6.3: Scatter plot of the relationship between PC1 and PC2 for each stage of glaucoma disease. Oval polygons represent 95% confidence intervals for C = controls, PG = preperimetric glaucoma, EG = early glaucoma, MAG = moderate-advanced glaucoma.

The eigenvalues (i.e., the variance along each PC axis) for each of the 56 resulting PCs are summarised in Table 6.4, which indicated that 10 PCs described the 56 ONH parameters (i.e., had an eigenvalue greater than 1.0).

PC	EV	PC	EV	PC	EV	PC	EV
PC 1	24.95	PC 16	0.58	PC 31	0.18	PC 46	0.03
PC 2	5.49	PC 17	0.56	PC 32	0.16	PC 47	0.03
PC 3	3.68	PC 18	0.54	PC 33	0.16	PC 48	0.02
PC 4	2.28	PC 19	0.45	PC 34	0.14	PC 49	0.02
PC 5	2.10	PC 20	0.41	PC 35	0.12	PC 50	0.02
PC 6	1.80	PC 21	0.37	PC 36	0.11	PC 51	0.01
PC 7	1.29	PC 22	0.35	PC 37	0.11	PC 52	0.01
PC 8	1.14	PC 23	0.32	PC 38	0.10	PC 53	0.01
PC 9	1.09	PC24	0.31	PC 39	0.09	PC 54	0.01
PC 10	1.07	PC 25	0.30	PC 40	0.08	PC 55	0.01
PC 11	0.88	PC 26	0.27	PC 41	0.07	PC 56	0.01
PC 12	0.84	PC 27	0.25	PC 42	0.07		
PC 13	0.78	PC 28	0.22	PC 43	0.06		
PC 14	0.68	PC 29	0.22	PC 44	0.04		
PC 15	0.63	PC 30	0.20	PC 45	0.04		

Table 6.4: Eigenvalues for 56 PCs following PCA on 56 ONH variables. PC = principal component, EV = Eigenvalue.

A scree plot of eigenvalues for these first 10 PCs showed that eigenvalues began to level off after PC 4, Figure 6.4 (a), indicating that these 4 PCs were sufficient to describe the variance within the ONH datasets. However, 80% of variance was contributed to by the first 10 PCs, Figure 6.4 (b); indicating the retention of 10 PCs.

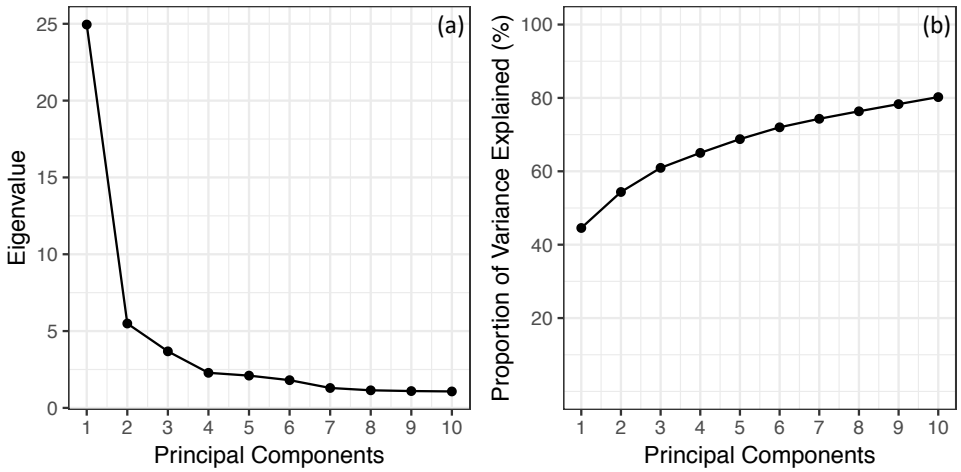

Figure 6.4: Scree-plot indicating eigenvalues for the first ten principal components (a), and cumulative proportion of variance explained by the first ten principal components (b).

The association between these first 10 PCs and VF MD is summarised in Table 6.5; showing that beyond PC 4, consistent with Figure 6.4 (a), the remaining PCs had no significant association with VF MD. Although PC 3 had no association with VF MD, it was retained as its eigenvalue was larger than that of PC 4 (see Figure 6.4 and Table 6.4).

Coefficients	Estimate	Standard Error	T-value	*P*-value
Intercept	-2.80	0.23	-12.16	$< 2e^{-16}$
PC 1	-0.50	0.04	-10.97	$< 2e^{-16}$
PC 2	-0.46	0.09	-4.68	$5.93e^{-06}$
PC 3	0.11	0.12	0.92	0.357
PC 4	-0.40	0.15	-2.62	0.009
PC 5	0.17	0.15	1.07	0.284
PC 6	-0.06	0.17	-0.39	0.692
PC 7	-0.39	0.20	-1.94	0.054
PC 8	-0.36	0.21	-1.68	0.094
PC 9	0.08	0.22	0.39	0.695
PC 10	0.21	0.22	0.96	0.334

Table 6.5: Output of multiple linear regression with VF MD modelled as a function of the first 10 principal components. Red text indicates the independent variable had a significant effect at $p < 0.05$. PC = principal component.

The output from ordinal regression modelling of the relationship between glaucoma disease stage (control, PG, EG, and MAG) and the first 10 PCs showed that beyond PC 5, PCs had no significant association with stage of glaucoma disease (Table 6.6). Additionally, PCs 2, 3, and 4 had no significant association with stage of glaucoma, but since their eigenvalues were larger than for PC 5, PCs 2, 3, and 4 were retained.

Coefficients	Estimate	Standard Error	Z-value	*P*-value
PC 1	0.25	0.03	7.03	$1.98e^{-12}$
PC 2	-0.07	0.06	-1.07	0.283
PC 3	-0.13	0.07	-1.82	0.068
PC 4	0.05	0.10	0.52	0.600
PC 5	-0.38	0.10	-3.58	< 0.001
PC 6	0.08	0.12	0.73	0.464
PC 7	-0.15	0.14	-1.12	0.262
PC 8	0.09	0.14	0.67	0.498
PC 9	0.17	0.13	1.22	0.219
PC 10	0.03	0.13	0.23	0.816

Table 6.6: Output of ordinal regression with stage of glaucoma (control, PG, EG, MAG) modelled as a function of the first 10 principal components. Red text indicates the independent variable had a significant effect at $p < 0.05$. PC = principal component.

PCs 1 and 2 showed the largest separation of ONH observations as a function of glaucoma disease stage, Figure 6.5 (a). However, Figure 6.5 (a) indicates considerable overlap remained between participant groups, for example controls, PG, and EG along PC axes 1 and 2. Less separation was observed using PCs 3, 4, and 5, Figure 6.5 (b-j), due to the relatively lower contribution of these PCs to variance for each stage of glaucoma, compared to PCs 1 and 2.

VI.6.2 Correlation between ONH parameters and resulting principal components

Since PCs greater than PC 5 had no significant effect on an ordinal categorical variable (i.e., control, PG, EG, MAG; Table 6.6), the remaining PCs were discarded. The association between regional measures of prelamina depth and thickness (Table VI.2), LC thickness and volumetric ONH parameters (Table VI.3), bNFL and pNFL (Table VI.4), and MRW and MRA (Table VI.5) and the first 5 PCs is shown in Appendix IV. As presented in Table 6.7, prelamina depth was strongly associated with PC 1 in the superior (r=0.78), inferior (r=0.81), temporal (r=0.70), SN (r=0.72), IT(r=0.80), and ST (r=0.80) regions. A strong association between prelamina

thickness and PC 1 was identified in the inferior (r=-0.76), IT (r=-0.81), and ST (r=-0.74) regions of the ONH.

LC thickness was moderately associated with PCs 1, 2, and 3 in all regions of the ONH (r = 0.4 to < 0.7, see Table VI.3 in Appendix IV). A strong correlation (r≥0.70) was found between optic cup volume and PC 1 (r=0.71), but not prelamina volume (r=-0.25) or BMO surface area (r=0.18). Prelamina volume (r=-0.53), and BMO surface area (r=-0.50) were moderately associated with PC 2, whereas optic cup volume displayed a weak correlation with PC 2 (r=-0.37).

A strong association was found between bNFL and PC 1 in all ONH regions (r>0.7) apart from temporal (r=-0.56, see Table 6.7). A moderate association between pNFL and PC 1 was found in all regions (r>0.4), apart from the SN region where pNFL and PC 1 were weakly correlated (r=-0.33). A strong association between MRW and PC 1 was found in all ONH regions (r>0.7, Table VI.5 in Appendix IV), and between MRA and PC 1 in the SN region (r=-0.71.). Moderate associations were found between other MRA regions and PC 1 (r=0.4 to <0.7).

Since all ONH parameters included in PCA were weakly correlated with resulting PCs 4 and 5 (Tables VI.2 to VI.5 in Appendix IV), loading coefficients, to determine the relative contributions of each ONH parameter on PCs 1, 2, and 3 only, were evaluated (see Tables 6.8, 6.9 and 6.10).

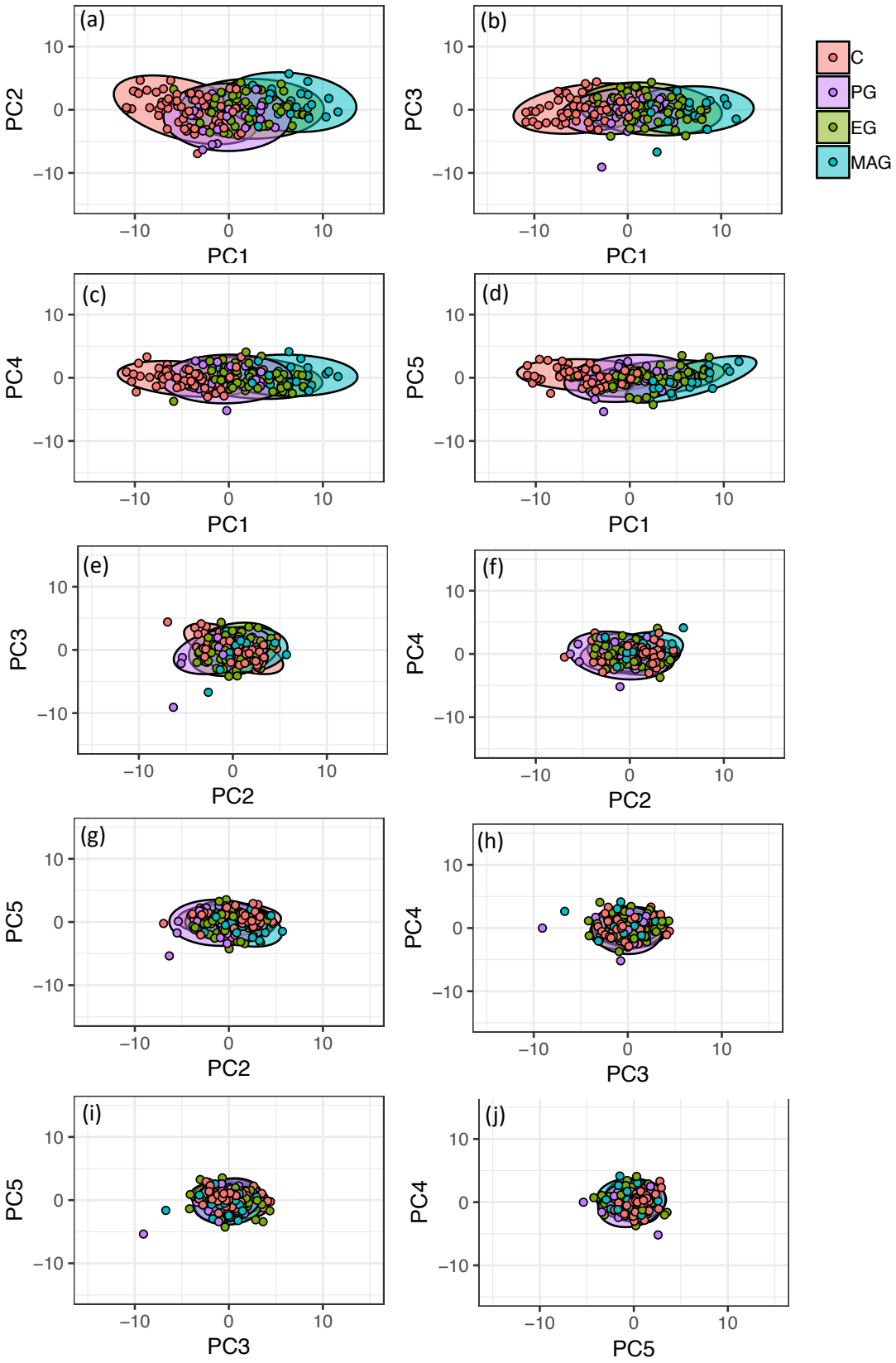

Figure 6.5: Scatter plots indicating separation of ONH observations as a function of glaucoma disease stage; plotted as PC2 against PC1 (a), PC3 against PC1 (b), PC4 against PC1 (c), PC5 against PC1 (d), PC3 against PC2 (e), PC4 against PC2 (f), PC5 against PC2 (g), PC4 against PC3 (h), PC5 against PC3 (i), PC4 against PC5 (j).

Regional ONH parameter	Pearson's correlation coefficient (r) between ONH parameter and PC 1								
	Centre	**Superior**	**Inferior**	**Nasal**	**Temporal**	**SN**	**IT**	**ST**	**IN**
Prelamina depth	0.66	0.78	0.81	0.65	0.70	0.72	0.80	0.80	0.67
Prelamina thickness	-0.61	-0.69	-0.76	Excluded	-0.66	Excluded	-0.81	-0.74	Excluded
LC thickness	-0.52	-0.49	-0.46	Excluded	-0.43	Excluded	-0.50	-0.56	Excluded
bNFL	N/A	-0.77	-0.80	-0.74	-0.56	-0.74	-0.74	-0.75	-0.72
pNFL	N/A	-0.52	-0.58	-0.42	-0.51	-0.33	-0.47	-0.66	-0.54
MRW	N/A	-0.80	-0.83	-0.79	-0.74	-0.83	-0.82	-0.85	-0.80
MRA	N/A	-0.61	-0.69	-0.65	-0.50	-0.71	-0.62	-0.69	-0.68
Volumetric ONH parameter									
Optic cup volume									0.71
Prelamina volume									-0.25
BMO surface area									0.18

Table 6.7: Pearson's correlation between 56 ONH parameters and PC 1. All correlations significant at $p < 0.05$. Red text indicates a strong association at $r \geq 0.70$.

Region	Loading coefficients of ONH parameter on PC 1									
	Prelamina depth	**Prelamina thickness**	**LC thickness**	**bNFL**	**pNFL**	**MRW**	**MRA**	**Optic Cup volume**	**Prelamina volume**	**BMO SA**
Centre	0.13	-0.12	-0.10	N/A	N/A	N/A	N/A	0.14	-0.05	0.04
Superior	0.16	-0.14	-0.10	-0.15	-0.10	-0.16	-0.12			
Inferior	0.16	-0.15	-0.09	-0.16	-0.12	-0.17	-0.14			
Nasal	0.13	Excluded	Excluded	-0.15	-0.08	-0.16	-0.13			
Temporal	0.14	-0.13	-0.09	-0.12	-0.10	-0.15	-0.10			
SN	0.14	Excluded	Excluded	-0.15	-0.07	-0.17	-0.14			
IT	0.16	-0.16	-0.10	-0.15	-0.09	-0.17	-0.12			
ST	0.16	-0.15	-0.11	-0.15	-0.13	-0.17	-0.14			
IN	0.14	Excluded	Excluded	-0.14	-0.11	-0.16	-0.14			

Table 6.8: Loading coefficients of regional ONH parameters on PC 1. Red text indicates regions with largest loading coefficients on PC 1 and strongest association with PC 1 for each ONH parameter. Measurements of prelamina and LC thickness acquired in the nasal, SN, and IN regions were excluded from PCA.

Region	Loading coefficients of ONH parameter on PC 2									
	Prelamina depth	**Prelamina thickness**	**LC thickness**	**bNFL**	**pNFL**	**MRW**	**MRA**	**Optic Cup volume**	**Prelamina volume**	**BMO SA**
Centre	-0.25	0.18	-0.20	N/A	N/A	N/A	N/A	-0.16	-0.23	-0.21
Superior	-0.19	0.12	-0.18	-0.04	-0.06	0.01	-0.08			
Inferior	-0.11	0.03	-0.21	-0.03	-0.10	-0.03	-0.09			
Nasal	-0.18	Excluded	Excluded	-0.01	-0.10	0.06	-0.03			
Temporal	-0.20	0.14	-0.21	-0.03	-0.13	0.04	-0.08			
SN	-0.20	Excluded	Excluded	-0.02	-0.16	0.07	-0.01			
IT	-0.14	0.07	-0.18	-0.09	-0.17	-0.09	-0.15			
ST	-0.19	0.11	-0.19	-0.08	-0.14	-0.06	-0.16			
IN	-0.14	Excluded	Excluded	-0.01	-0.12	0.05	-0.06			

Table 6.9: Loading coefficients of regional ONH parameters on PC 2. Red text indicates regions with largest loading coefficients on PC 2 and strongest association with PC 2 for each ONH parameter. Measurements of prelamina and LC thickness acquired in the nasal, SN, and IN regions were excluded from PCA.

Region	Loading coefficients of ONH parameter on PC 3									
	Prelamina depth	**Prelamina thickness**	**LC thickness**	**bNFL**	**pNFL**	**MRW**	**MRA**	**Optic Cup volume**	**Prelamina volume**	**BMO SA**
Centre	-0.02	0.04	0.26	N/A	N/A	N/A	N/A	-0.15	-0.06	-0.30
Superior	-0.01	0.02	0.28	0.03	0.03	-0.05	-0.16			
Inferior	-0.03	0.04	0.29	-0.02	-0.01	-0.05	-0.17			
Nasal	-0.12	Excluded	Excluded	0.01	0.03	-0.01	-0.19			
Temporal	0.01	0.02	0.29	-0.07	0.09	-0.12	-0.27			
SN	-0.04	Excluded	Excluded	0.07	0.01	0.02	-0.15			
IT	0.01	-0.01	0.29	-0.12	-0.07	-0.15	-0.27			
ST	-0.01	0.02	0.25	-0.02	-0.01	-0.07	-0.17			
IN	-0.09	Excluded	Excluded	0.05	0.02	0.03	-0.10			

Table 6.10: Loading coefficients of regional ONH parameters on PC 3. Red text indicates regions with largest loading coefficients on PC 3 and strongest association with PC 3 for each ONH parameter. Measurements of prelamina and LC thickness acquired in the nasal, SN, and IN regions were excluded from PCA.

Consistent with data above, the largest loading coefficient of prelamina depth on PC 1 was in the superior, inferior, IT, and ST regions, and for prelamina thickness the largest loadings were in the inferior, IT, and ST regions (see Table 6.8). This suggested that measures of prelamina depth and thickness in these regions contributed the most to PC 1. LC thickness and pNFL contained relatively low loading coefficients for PC 1 in all regions, suggesting a lower contribution from these variables to PC 1. Border NFL and MRW displayed high loadings on PC 1 in all regions (apart from temporal for bNFL), and the highest loadings from MRA were found in the inferior, SN, ST, and IN regions. Optic cup volume displayed a relatively large loading coefficient on PC 1, whereas prelamina volume and BMO surface area displayed low loadings on PC 1.

The strongest associations between prelamina depth and thickness and PC 2 were found in the central region of the ONH, and also had the largest loading coefficient on PC 2 (see Tables 6.9 and VI.2), although these variables were moderately associated with PC 2. The inferior and temporal ONH regions showed the largest loading of LC thickness on PC 2 and were also moderately associated. The largest loading of bNFL, pNFL, and MRW on PC 2 was in the IT region, and the ST region for MRA, although displayed a relatively weak association with PC 2. Prelamina volume and BMO surface area had larger loading coefficients on PC 2 than optic cup volume, and were moderately associate with PC 2, see Tables VI.3, VI.4, and VI.5.

The largest loading coefficient of prelamina depth on PC 3 was in the nasal ONH region, and prelamina thickness displayed small loadings on PC 3 in all ONH regions, see Table 6.10. The inferior, temporal, and IT regions displayed the largest loadings of LC thickness on PC 3, and were moderately associated with PC 3, see Table VI.3. The largest loadings of bNFL and MRW on PC 3 were in the IT region, and temporal for pNFL, although were weakly associated with PC 3. The temporal and IT regions displayed largest loadings for MRA and were moderately associated with PC 3. The loadings on PC 3 were higher for optic cup volume and BMO surface area than prelamina volume, and BMO surface area was moderately associated with PC 3, see Table 6.10.

VI.6.3 Cluster analysis of ONH principal components 1 and 2

PCs 1 and 2 were considered the most important as these possess the largest eigenvalues and explain the most amount of variance within the 56 ONH parameter variables (see Table 6.4 and Figure 6.4). Furthermore, PCs 1 and 2 showed the largest separation of observations as a function of glaucoma disease stage (Figures 6.3 and 6.5). However, along PC axes 1 and 2 there remained considerable overlap between observations for each stage of glaucoma, particularly between controls, PG, and EG. Therefore, with the aim to achieve a better separation of observations according to glaucoma stage, cluster analysis was performed on PCs 1 and 2. Using hierarchical clustering it was possible to group observations with similar PC scores (i.e., along PC axes 1 and 2) into four clusters, see dendrogram in Figure 6.6. As shown in Figure 6.6, the hierarchical cluster analysis assigns each observation into predicted classifications (i.e., four groups). However, on comparison of cluster assignment to the known participant stage of glaucoma, not all observations were correctly assigned according to glaucoma disease stage, see Table 6.11.

Table 6.11 indicates that out of 60 control eyes, 25 were correctly assigned as controls. Twelve out of 28 PG eyes were correctly assigned, and 24/58 were correctly assigned as EG. Additionally, 20/23 were correctly assigned as MAG. Therefore, although four groups of similar observations were identified using hierarchical cluster analysis, the cluster assignment according to glaucoma stage was not completely accurate.

Known glaucoma stage	**Cluster assignment**			
	C	**PG**	**EG**	**MAG**
C (n=60)	25	22	11	2
PG (n=28)	0	12	15	1
EG (n=58)	1	9	24	24
MAG (n=23)	0	1	2	20

Table 6.11: Comparison of cluster analysis assignment and known participant stage of glaucoma disease. Red text indicates correct group assignment following cluster analysis.

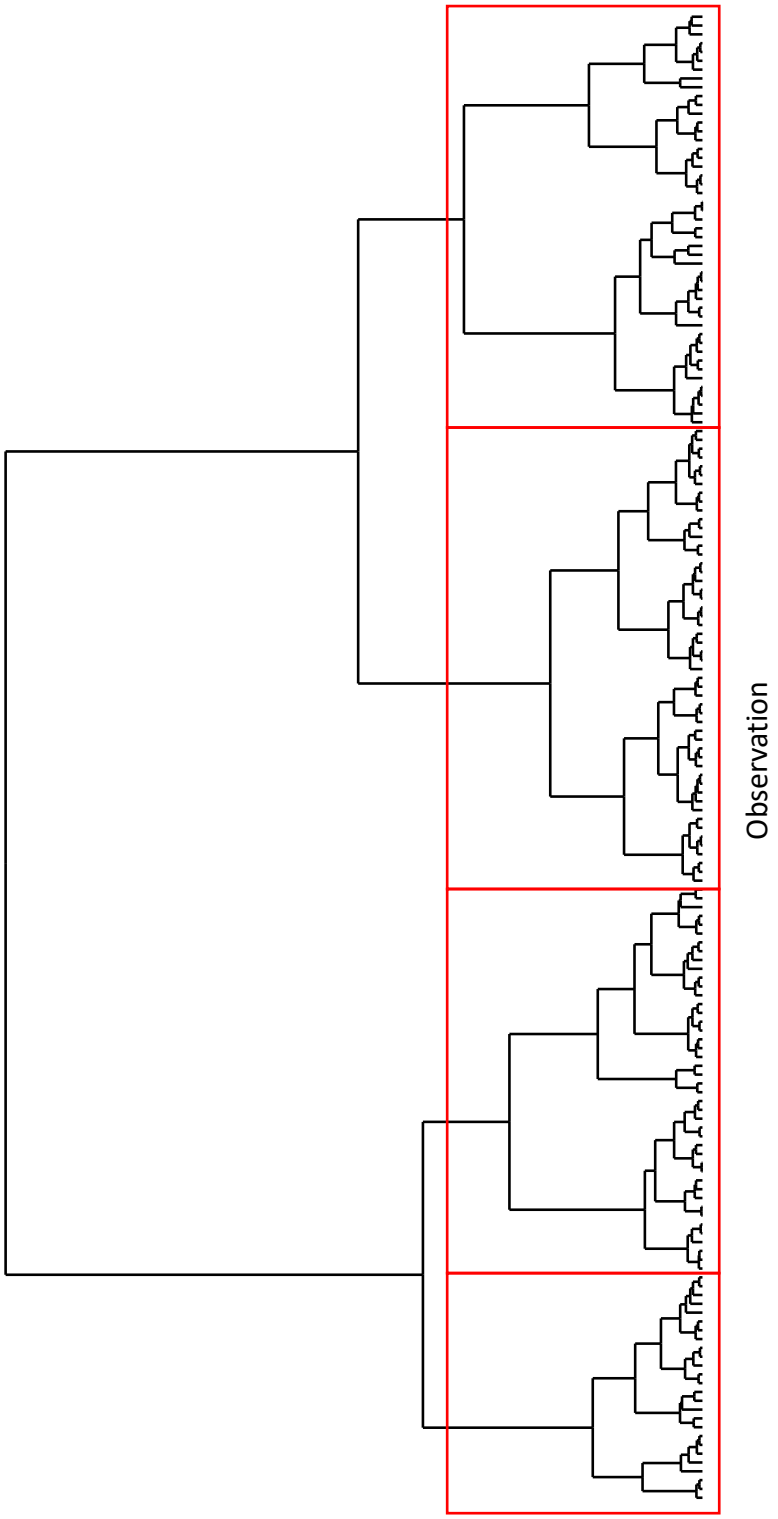

Figure 6.6: Dendrogram representing hierarchical cluster analysis on PCs 1 and 2. Red boxes indicate four clusters of similar observations.

Cluster analysis on ONH PCs 1 and 2 was also performed using k-means clustering, where the number of clusters to obtain is specified *a priori*. In this instance, the number of clusters was specified as four; controls, PG, EG, and MAG. Figure 6.7 (a) indicates that following k-means cluster analysis on PCs 1 and 2 there was close groupings of participant subsets and clear delineation between groups as a function of glaucoma disease stage. However, when this was compared to the known participant groups according to glaucoma stage in Figure 6.7 (b), again some data points had been allocated incorrectly to certain groups of glaucoma stage. As indicated by Figure 6.7 (b), this is due to the fact that even when group identity is known, there was considerable overlap in observations for PCs 1 and 2, as a function of glaucoma disease stage, particularly between controls, PG, and EG; suggesting these groups are difficult to differentiate between.

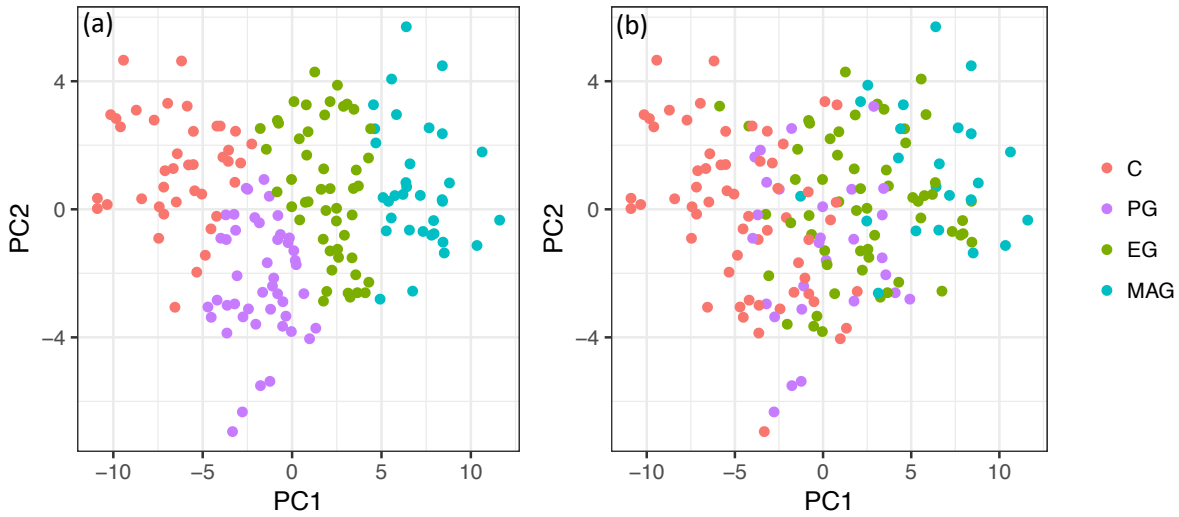

Figure 6.7: Comparison of stage of glaucoma disease following k-means clustering (a) and known participant stage of glaucoma (b).

VI.6.4 Principal component analysis on each ONH parameter

To determine whether a particular ONH parameter (e.g., prelamina depth) achieved better separation of observations according to glaucoma stage than another ONH parameter (e.g., prelamina thickness), PCA was performed on each regional ONH parameter separately. For instance, PCA was performed on prelamina depth, prelamina thickness, LC thickness, bNFL, pNFL, MRW, and MRA. Furthermore, PCA was performed on volumetric ONH data including optic cup and prelamina volume, and BMO surface area.

PCA performed separately on prelamina depth and thickness, and LC thickness resulted in considerable overlap of observations according to glaucoma stage. Therefore, PCA performed on these ONH parameters did not achieve distinct separation of participants as a function of glaucoma disease stage; data shown in Appendix IV, Figures VI.1, VI.2, and VI.3 for prelamina depth, prelamina thickness, and LC thickness respectively.

Table 6.12 summarises the loading coefficients on PC 1 and 2 for prelamina depth and thickness, and LC thickness. All regional measures of prelamina depth and thickness, and LC thickness displayed a strong correlation with PC 1 (Pearson's $r \geq 0.7$) and a relatively weak correlation with PC 2. The loading coefficients for prelamina depth and thickness, and LC thickness were similar for each region of the ONH. The largest loading and strongest association with PC 1 for prelamina depth was in the ST region. Prelamina thickness had the largest coefficients and strongest correlations in the IT and ST regions. The largest loading and strongest correlation for LC thickness and PC 1 was in the central region of the ONH.

Following PCA performed on bNFL and pNFL separately, a considerable overlap of observations along PC axes 1 and 2 for each stage of glaucoma was demonstrated (see Appendix IV, Figures VI.4 and VI.5). Table 6.13 indicates the loading coefficients for bNFL and pNFL on PCs 1 and 2, and Pearson's correlation for regional measures of bNFL and pNFL and PCs 1 and 2. All regional measures of bNFL were strongly correlated with PC 1 ($r>0.75$), apart from temporal where a moderate association was found ($r=0.67$). Peripapillary NFL was strongly associated with PC 1 in the inferior and ST regions, and these regions displayed the largest loading coefficients. The loading coefficients on PC 1 for bNFL were highest in the superior and inferior ONH regions and showed the strongest association with PC 1.

Following PCA performed on regional measures of MRW, MRA, and volumetric ONH parameters there was overlap between glaucoma disease stages; shown in Appendix IV, Figures VI.6, VI.7, and VI.8 respectively. The largest separation of observations is illustrated in Figure VI.6 along PC 1 axis describing MRW. Figures VI.7 and VI.8 illustrating PCA performed on MRA and volumetric ONH parameters show relatively little separation of glaucoma stages.

ONH Parameter	Region	Loadings		Pearson's Correlation			
		PC 1	PC 2	PC 1 (r)	*P*-value	PC 2 (r)	*P*-value
Prelamina depth	Centre	-0.34	0.01	-0.90	<0.001	0.01	0.952
	Superior	-0.34	-0.04	-0.90	<0.001	-0.04	0.645
	Inferior	-0.33	0.13	-0.87	<0.001	0.10	0.193
	Nasal	-0.31	-0.28	-0.82	<0.001	0.36	<0.001
	Temporal	-0.32	0.09	-0.86	<0.001	-0.39	<0.001
	SN	-0.34	-0.42	-0.89	<0.001	0.17	0.027
	IT	-0.34	0.30	-0.90	<0.001	-0.29	<0.001
	ST	-0.35	-0.33	-0.91	<0.001	-0.27	<0.001
	IN	-0.31	0.51	-0.82	<0.001	0.41	<0.001
Prelamina thickness	Centre	-0.39	-0.41	-0.80	<0.001	-0.30	<0.001
	Superior	-0.39	-0.58	-0.82	<0.001	-0.42	<0.001
	Inferior	-0.38	-0.24	-0.79	<0.001	-0.18	0.021
	Temporal	-0.42	0.48	-0.87	<0.001	0.36	<0.001
	IT	-0.43	0.39	-0.89	<0.001	0.25	0.001
	ST	-0.43	0.30	-0.89	<0.001	0.22	0.004
Lamina cribrosa thickness	Centre	-0.42	0.09	-0.91	<0.001	0.05	0.480
	Superior	-0.41	-0.52	-0.89	<0.001	-0.33	<0.001
	Inferior	-0.41	-0.35	-0.89	<0.001	-0.22	0.004
	Temporal	-0.41	-0.24	-0.90	<0.001	-0.15	0.046
	IT	-0.40	0.58	-0.88	<0.001	0.36	<0.001
	ST	-0.41	0.46	-0.89	<0.001	0.29	<0.001

Table 6.12: Loading coefficients for PC 1 and 2 for regional measures of prelamina depth and thickness, and LC thickness. Additionally, Pearson's correlation coefficient for PC 1 and 2, and prelamina depth and thickness, and LC thickness. Red text indicates a strong relationship with Pearson's r ≥ 0.70.

Presented in Table 6.14 are the loading coefficients for PCs 1 and 2 for MRW, MRA, and 3D volumetric ONH parameters. Additionally, Pearson's correlation coefficient for each ONH parameter and PCs 1 and 2.

ONH Parameter	Region	Loadings		Pearson's correlation			
		PC 1	PC 2	PC 1 (r)	*P*-value	PC 2 (r)	*P*-value
bNFL	Superior	-0.38	0.13	-0.86	<0.001	0.14	0.071
	Inferior	-0.38	0.04	-0.87	<0.001	0.05	0.538
	Nasal	-0.34	0.37	-0.77	<0.001	0.40	<0.001
	Temporal	-0.30	-0.59	-0.67	<0.001	-0.63	<0.001
	SN	-0.36	0.36	-0.81	<0.001	0.39	<0.001
	IT	-0.34	-0.42	-0.78	<0.001	-0.45	<0.001
	ST	-0.37	-0.31	-0.84	<0.001	-0.33	<0.001
	IN	-0.34	0.32	-0.76	<0.001	0.35	<0.001
pNFL	Superior	-0.34	0.46	-0.64	<0.001	0.48	<0.001
	Inferior	-0.40	0.20	-0.76	<0.001	0.21	0.006
	Nasal	-0.29	0.07	-0.55	<0.001	0.08	0.329
	Temporal	-0.36	-0.43	-0.67	<0.001	-0.45	<0.001
	SN	-0.32	0.47	-0.61	<0.001	0.49	<0.001
	IT	-0.34	-0.50	-0.64	<0.001	-0.52	<0.001
	ST	-0.40	-0.28	-0.76	<0.001	-0.29	<0.001
	IN	-0.36	0.08	-0.69	<0.001	0.08	0.306

Table 6.13: Loading coefficients for PC 1 and 2 for regional measures of bNFL and pNFL. Additionally, Pearson's correlation coefficient for PC 1 and 2, and bNFL and pNFL. Red text indicates a strong relationship with Pearson's r ≥ 0.70.

Table 6.14 indicates that the loading coefficients on PCs 1 and 2 for MRW and MRA were similar between ONH regions. Measures of MRW and MRA were strongly associated with PC 1 in all regions of the ONH. The highest loading coefficient, and strongest association between MRW and PC 1 was in the ST region, and the IT region for MRA. Regarding PCA on volumetric ONH parameters, BMO surface area displayed the largest loading and strongest association with PC 1, and prelamina volume displayed the largest loading and strongest association with PC 2.

Following PCA being performed on each group of ONH parameters, this did not result in sufficient separation of observations as a function of glaucoma disease stage; shown in Appendix IV, Figures VI.1 to VI.8. The 'scree-plots' in Figures VI.1 to VI.8 indicate that PC 1 is the most important as this explains the most variance in the data and therefore has the largest eigenvalue. For each group of ONH parameters, the loading coefficients were relatively similar between ONH regions for PC 1. Therefore, following PCA for each regional ONH parameter, there does not appear to be a particular ONH region that makes a marked contribution to the separation of observations along PC 1 axis according to glaucoma stage.

ONH Parameter	Region	Loadings		Pearson's correlation			
		PC 1	PC 2	PC 1 (r)	*P*-value	PC 2 (r)	*P*-value
MRW	Superior	-0.36	-0.01	-0.84	<0.001	-0.01	0.883
	Inferior	-0.36	-0.06	-0.86	<0.001	-0.05	0.485
	Nasal	-0.35	0.44	-0.82	<0.001	0.39	<0.001
	Temporal	-0.32	-0.52	-0.76	<0.001	-0.45	<0.001
	SN	-0.36	0.40	-0.85	<0.001	0.35	<0.001
	IT	-0.36	-0.34	-0.86	<0.001	-0.30	<0.001
	ST	-0.37	-0.32	-0.88	<0.001	-0.28	<0.001
	IN	-0.34	0.40	-0.81	<0.001	0.35	<0.001
MRA	Superior	-0.32	-0.58	-0.73	<0.001	-0.55	<0.001
	Inferior	-0.36	-0.47	-0.80	<0.001	-0.44	<0.001
	Nasal	-0.36	0.28	-0.81	<0.001	0.26	<0.001
	Temporal	-0.33	0.50	-0.74	<0.001	0.47	<0.001
	SN	-0.36	-0.18	-0.81	<0.001	-0.17	0.030
	IT	-0.38	0.03	-0.86	<0.001	0.02	0.757
	ST	-0.36	0.21	-0.81	<0.001	0.19	0.011
	IN	-0.35	0.20	-0.78	<0.001	0.19	0.014
Volumetric ONH Parameters							
Optic cup volume		0.55	-0.63	0.68	<0.001	-0.63	<0.001
Prelamina volume		0.45	0.78	0.56	<0.001	0.77	<0.001
BMO surface area		0.70	-0.01	0.87	<0.001	-0.01	0.953

Table 6.14: Loading coefficients for PC 1 and 2 for regional measures of MRW and MRA, and volumetric ONH parameters. Additionally, Pearson's correlation coefficient for PC 1 and 2, and MRW, MRA, and volumetric ONH parameters. Red text indicates a strong relationship with Pearson's r ≥ 0.70.

VI.6.5 Linear discriminant analysis

Linear discriminant analysis (LDA) was performed on the 56 ONH variables that were included in PCA. The loading coefficients and Pearson's correlation of linear discriminants for regional measures of prelamina depth and thickness, and LC thickness are presented in Table 6.15. A moderate correlation between LD 1 and prelamina depth was found in the superior, inferior, and ST regions of the ONH (r > 0.6), and the superior and inferior regions displayed the largest loading coefficients on LD 1. Prelamina thickness showed a moderate association with LD 1 in the superior, inferior, IT, and ST regions (r > 0.6), although the largest loadings on LD 1 were in the inferior and temporal regions. A moderate association between LC thickness and LD 1 was found in all regions of the ONH (r=0.4-<0.7) and loading coefficients on LD 1 for LC thickness were largest in the inferior and temporal ONH regions.

Table 6.16 presents the loading coefficients and Pearson's correlation coefficient of LDs for regional measures of border and peripapillary NFL thickness. There was a strong association ($r > 0.7$) between bNFL and LD 1 in superior, inferior, IT, and ST regions. A weak to moderate association between pNFL and LD 1 was found in all ONH regions. The strongest association and largest loading coefficients for bNFL and pNFL on LD 1 were found in the ST region of the ONH.

Presented in Table 6.17 are the loading coefficients and Pearson's correlation for LDs describing regional measures of MRW and MRA, and volumetric ONH parameters, including optic cup volume, prelamina volume, and BMO surface area. A strong association ($r>0.7$) was found between MRW and LD 1 in the superior, inferior, SN, IT, and ST ONH regions, although the largest loading coefficient was in the nasal region. MRA displayed a moderate ($r\geq0.6$) association with LD 1 in the inferior and ST regions, and the ST region also contained the largest loading coefficient on LD 1. A moderate association ($r > 0.4$) was found between optic cup volume and prelamina volume with LD 1, and out of the volumetric ONH parameters, prelamina volume contained the largest loading coefficient on LD 1.

Figure 6.8 presents separation of observations according to glaucoma disease stage along the axes of the resulting LDs describing the 56 ONH variables. Indicated by Figure 6.8 (a), the largest discrimination of participant groups was along axes LD 1 and LD 2. Figure 6.8 (a) shows that the control group is fully separated from the MAG group. However, there is overlap between controls, PG, and EG. Additionally, there is considerable overlap between PG and EG, and EG and MAG. Figures 6.8 (b) and (c) indicate significant overlap of observations according to glaucoma stage along the axis of LD 3.

ONH Parameter	Region	Loading coefficients			Pearson's correlation					
		LD 1	LD 2	LD 3	LD 1 (r)	*P*-value	LD 2 (r)	*P*-value	LD 3 (r)	*P*-value
Prelamina depth	Centre	-0.74	1.70	-0.63	0.41	<0.001	-0.18	0.022	-0.06	0.456
	Superior	-0.91	-0.98	-0.98	0.62	<0.001	-0.23	0.002	-0.08	0.285
	Inferior	0.99	0.31	0.18	0.65	<0.001	-0.07	0.330	0.02	0.831
	Nasal	0.20	-0.36	-0.72	0.53	<0.001	-0.13	0.074	-0.29	<0.001
	Temporal	0.26	-0.34	-0.01	0.44	<0.001	-0.15	0.057	-0.03	0.691
	SN	0.45	-0.53	0.31	0.59	<0.001	-0.18	0.017	-0.10	0.180
	IT	0.26	-1.65	1.28	0.58	<0.001	-0.09	0.255	0.07	0.379
	ST	0.39	-0.91	0.85	0.64	<0.001	-0.24	0.001	-0.01	0.985
	IN	-0.35	-0.06	-0.16	0.49	<0.001	-0.12	0.110	-0.16	0.041
Prelamina thickness	Centre	-0.31	-0.06	0.16	-0.46	<0.001	0.27	<0.001	0.04	0.621
	Superior	-0.59	-0.59	-0.80	-0.63	<0.001	0.20	0.010	0.05	0.530
	Inferior	0.66	0.18	-0.12	-0.68	<0.001	0.02	0.753	-0.04	0.578
	Temporal	0.67	-0.43	0.55	-0.48	<0.001	0.15	0.054	0.02	0.772
	IT	-0.01	-1.25	0.05	-0.67	<0.001	0.05	0.532	-0.04	0.645
	ST	-0.32	-0.15	0.05	-0.69	<0.001	0.25	<0.001	-0.01	0.983
Lamina cribrosa thickness	Centre	0.03	-0.25	-0.15	-0.49	<0.001	-0.16	0.039	-0.01	0.876
	Superior	-0.04	0.24	-0.37	-0.48	<0.001	0.08	0.332	0.01	0.940
	Inferior	-0.22	0.51	-0.20	-0.50	<0.001	-0.06	0.441	-0.02	0.761
	Temporal	0.18	-0.18	0.13	-0.43	<0.001	-0.16	0.037	0.07	0.393
	IT	-0.09	-0.49	0.11	-0.54	<0.001	-0.13	0.099	0.08	0.292
	ST	-0.05	0.79	0.56	-0.56	<0.001	-0.01	0.935	0.05	0.547

Table 6.15: Loading and Pearson's correlation coefficients for LDs describing regional measures of prelamina depth and thickness, and LC thickness.

ONH Parameter	Region	Loading coefficients			Pearson's correlation					
		LD 1	LD 2	LD 3	LD 1 (r)	*P*-value	LD 2 (r)	*P*-value	LD 3 (r)	*P*-value
bNFL	Superior	0.04	-0.56	0.44	-0.75	<0.001	-0.19	0.015	0.09	0.255
	Inferior	0.11	-0.04	-0.50	-0.77	<0.001	-0.08	0.281	-0.01	0.978
	Nasal	-0.22	0.41	0.15	-0.64	<0.001	-0.09	0.249	-0.04	0.598
	Temporal	0.06	0.25	0.42	-0.57	<0.001	0.09	0.245	-0.01	0.883
	SN	0.09	-0.59	-0.33	-0.69	<0.001	-0.19	0.013	-0.05	0.520
	IT	0.02	0.35	0.64	-0.71	<0.001	-0.02	0.822	0.08	0.293
	ST	-0.62	-0.63	-1.18	-0.80	<0.001	-0.13	0.102	-0.12	0.114
	IN	0.12	-0.01	-0.58	-0.58	<0.001	-0.08	0.304	-0.03	0.696
pNFL	Superior	-0.50	0.35	-0.05	-0.59	<0.001	0.13	0.080	0.01	0.972
	Inferior	-0.02	-0.13	0.51	-0.56	<0.001	-0.12	0.109	0.07	0.370
	Nasal	0.17	-0.15	0.15	-0.39	<0.001	-0.18	0.019	0.07	0.353
	Temporal	0.16	-0.37	0.09	-0.49	<0.001	-0.21	0.007	0.01	0.886
	SN	0.26	-0.01	-0.31	-0.32	<0.001	-0.18	0.016	-0.18	0.022
	IT	-0.11	-0.35	0.07	-0.50	<0.001	-0.25	0.001	0.04	0.616
	ST	-0.41	-0.17	-0.01	-0.64	<0.001	-0.26	0.001	-0.06	0.459
	IN	-0.43	-0.08	-0.05	-0.57	<0.001	-0.11	0.157	0.03	0.747

Table 6.16: Loading and Pearson's correlation coefficients for LDs describing regional measures of bNFL and pNFL. Red text indicates a strong correlation at $r \geq 0.70$.

ONH Parameter	Region	Loading coefficients			Pearson's correlation					
		LD 1	LD 2	LD 3	LD 1 (r)	*P*-value	LD 2 (r)	*P*-value	LD 3 (r)	*P*-value
MRW	Superior	0.23	-0.04	-0.21	-0.74	<0.001	-0.05	0.556	0.14	0.070
	Inferior	-0.28	0.28	0.78	-0.78	<0.001	-0.03	0.675	-0.01	0.914
	Nasal	0.70	-0.54	-0.87	-0.63	<0.001	-0.03	0.672	-0.03	0.681
	Temporal	-0.46	-0.23	0.74	-0.57	<0.001	0.03	0.719	-0.01	0.850
	SN	-0.18	0.28	0.17	-0.73	<0.001	0.03	0.724	0.12	0.106
	IT	0.01	0.98	-0.32	-0.70	<0.001	-0.10	0.205	-0.05	0.528
	ST	-0.45	1.25	-1.40	-0.78	<0.001	-0.05	0.503	-0.07	0.353
	IN	0.17	0.78	2.33	-0.64	<0.001	-0.04	0.641	0.05	0.508
MRA	Superior	-0.14	-0.13	0.52	-0.58	<0.001	-0.15	0.052	0.13	0.088
	Inferior	-0.03	-0.28	-0.88	-0.63	<0.001	-0.13	0.083	-0.05	0.556
	Nasal	-0.79	0.02	0.14	-0.48	<0.001	-0.15	0.052	-0.15	0.052
	Temporal	0.69	-0.45	-0.73	-0.31	<0.001	-0.08	0.312	-0.14	0.070
	SN	0.04	0.19	0.74	-0.59	<0.001	-0.09	0.262	0.07	0.373
	IT	-0.13	-1.04	0.18	-0.49	<0.001	-0.22	0.005	-0.13	0.085
	ST	0.83	-0.28	2.23	-0.60	<0.001	-0.16	0.039	-0.11	0.165
	IN	-0.34	-0.97	-1.94	-0.52	<0.001	-0.12	0.113	-0.07	0.389
Volumetric ONH Parameters										
Optic cup volume		-0.10	1.29	-0.12	0.56	<0.001	0.04	0.637	-0.17	0.024
Prelamina volume		-0.61	0.09	-0.10	-0.43	<0.001	-0.23	0.003	0.07	0.371
BMO surface area		0.35	0.77	-0.32	0.23	0.002	-0.19	0.012	-0.19	0.013

Table 6.17: Loading and Pearson's correlation coefficients for LDs describing regional measures of MRW and MRA, and volumetric ONH parameters. Red text indicates a strong correlation at r ≥ 0.70.

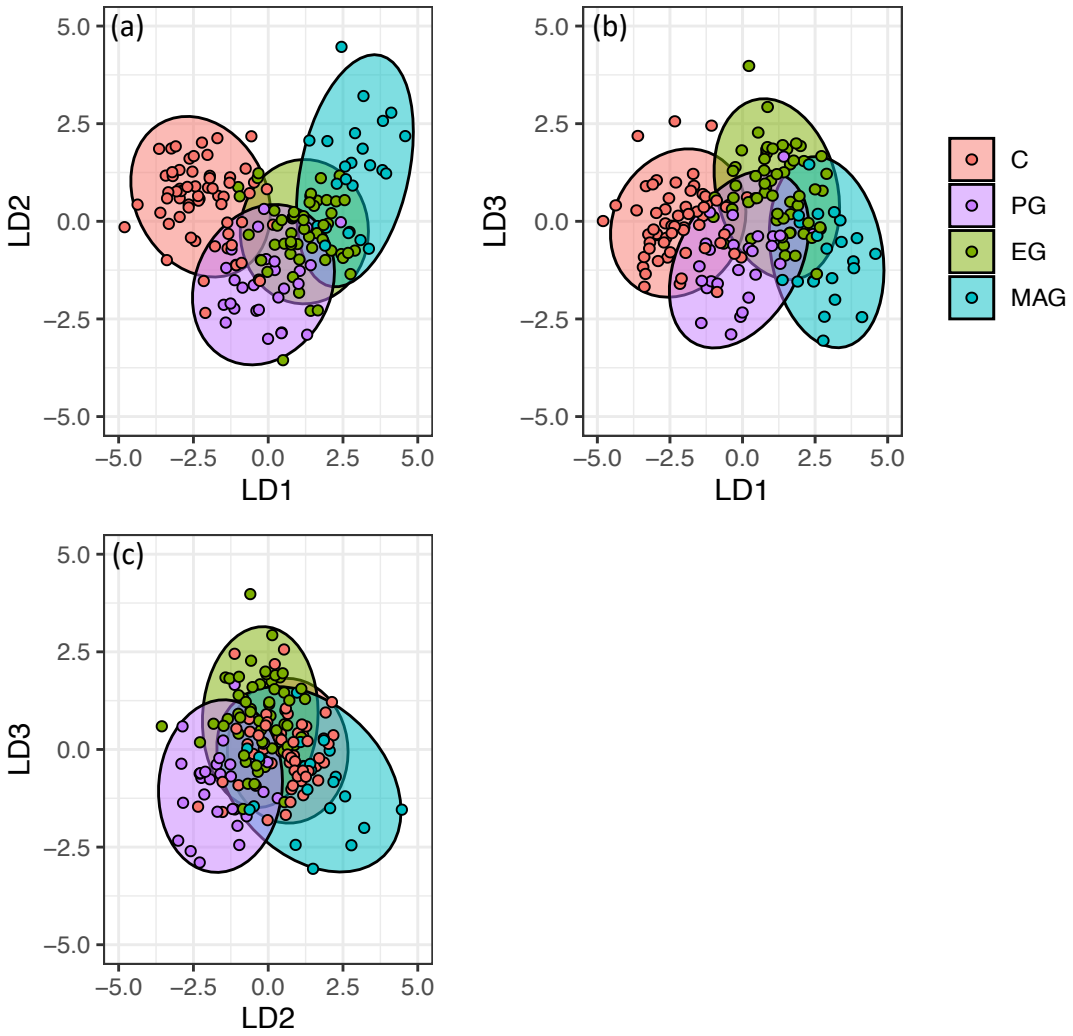

Figure 6.8: Scatter plot indicating separation of observations along LDs as a function of glaucoma stage; with LD 2 against LD 1 (a), LD 3 against LD 1 (b), LD 3 against LD 2 (c). Oval polygons represent 95% confidence intervals.

Figures 6.5 and 6.8 indicate that the largest separation of observations as a function of glaucoma stage was achieved with PCs 1 and 2, and LDs 1 and 2. Therefore, logistic regression was used to determine the ability of PCs 1 and 2, and LDs 1 and 2 to model a binary outcome variable (i.e., indicating control or glaucoma); summarised in Table 6.18. PCs 1 and 2 were found to have no significant effect on modelling a binary outcome variable (indicated by low Z-value and high *P*-value) and were therefore excluded from the logistic regression model. Table 6.19 summarises the logistic regression model describing control or glaucoma as a function of LDs 1 and 2. Both LD 1 and LD 2 had a significant effect on modelling a binary classifier indicating control or glaucoma. Receiver operator characteristic (ROC) curves were generated for LD 1 and LD 2 (Figure 6.9), and the area under the curve (AUC) indicated that

LD 1 (AUC = 0.975) performed better than LD 2 (AUC = 0.705) and LD 3 (AUC = 0.505) as a discriminatory function between control and glaucoma participants.

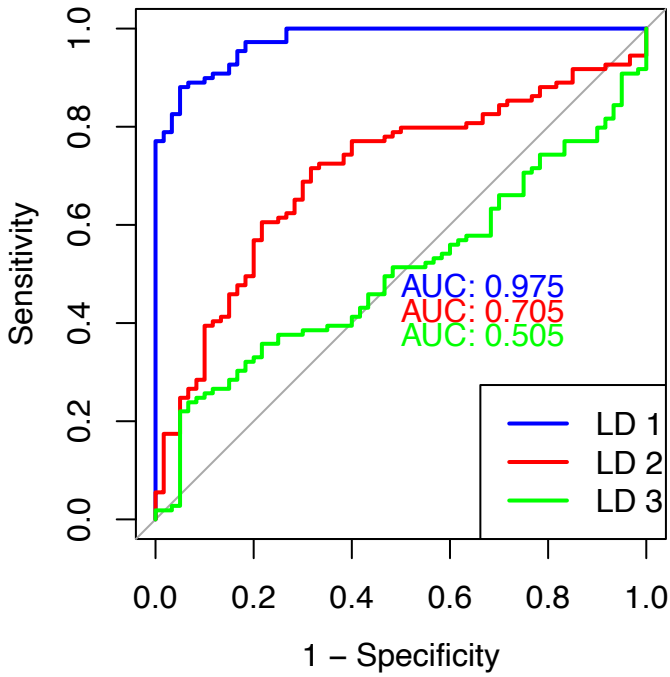

Figure 6.9: Receiver operator characteristic (ROC) curve of LDs 1-3 when applied to binary classifier indicating control or glaucoma.

Tables 6.15, 6.16, and 6.17 suggest that the regional and volumetric ONH parameters were stronger correlated with LD 1 than LD 2. Indeed, all the 56 ONH variables included in LDA were weakly correlated with LD 2. Therefore, the ONH parameters that were strongly associated with LD 1 were considered to provide the best differentiation of participants as a function of glaucoma disease stage.

Coefficients	Estimate	Standard Error	Z-value	*P*-value
Intercept	2.01	0.57	3.51	0.0004
PC 1	0.07	0.19	0.34	0.733
PC 2	0.05	0.19	0.27	0.785
LD 1	2.54	0.65	3.94	$8.29e^{-5}$
LD 2	-1.21	0.37	-3.26	0.001

Table 6.18: Output of logistic regression with binary outcome variable (control or glaucoma) modelled as a function of PC 1, PC 2, LD 1, and LD 2. Red text indicates the independent variable had a significant effect at $p < 0.05$.

Coefficients	Estimate	Standard Error	Z-value	*P*-value
Intercept	2.02	0.57	3.54	0.0004
LD 1	2.66	0.56	4.72	$2.37e^{-6}$
LD 2	-1.17	0.34	-3.42	0.0006

Table 6.19: Output of logistic regression with binary outcome variable (control or glaucoma) modelled as a function of LD 1 and LD 2. Red text indicates the independent variable had a significant effect at $p < 0.05$.

VI.6.6 Subset of ONH variables and subsequent PCA and LDA

Following PCA and LDA of 56 ONH variables, the relationship between each ONH variable and resulting PCs and LDs was examined using Pearson's correlation coefficient; outlined in Tables VI.2 to VI.5 in Appendix IV, and Tables 6.15 to 6.17. ONH variables were selected which showed a strong association with the resulting PCs and LDs, defined as Pearson's r ≥ 0.7 (Cadima and Jolliffe, 1995; Al-Kandari and Jolliffe, 2005). Table 6.20 summarises selection of 26 ONH variables showing a strong association with resulting PCs and LDs.

Regional ONH parameters	**Region**								
	C	**S**	**I**	**N**	**T**	**SN**	**IT**	**ST**	**IN**
Prelamina depth		✓	✓		✓	✓	✓	✓	
Prelamina thickness			✓				✓	✓	
LC thickness									
Border NFL	N/A	✓	✓	✓		✓	✓	✓	✓
Peripapillary NFL	N/A								
Minimum rim width	N/A	✓	✓	✓	✓	✓	✓	✓	✓
Minimum rim area	N/A					✓			
Volumetric ONH parameters									
Optic cup volume	✓								
Prelamina volume									
LC volume									
BMO surface area									

Table 6.20: Selection of 26 ONH variables which were strongly associated with resulting PCs and LDs, defined as Pearson's r ≥ 0.70.

The selected 26 ONH variables were then used to perform PCA and LDA. Figure 6.10 presents the relationship between PCs 1 and 2 according to glaucoma disease stage describing the subset of 26 ONH variables. As shown in Figure 6.10 there is reasonable separation of control and MAG stages, with largest separation of participant groups along axis PC 1. However,

considerable overlap between early glaucoma stages remains, particularly between controls, PG, and EG.

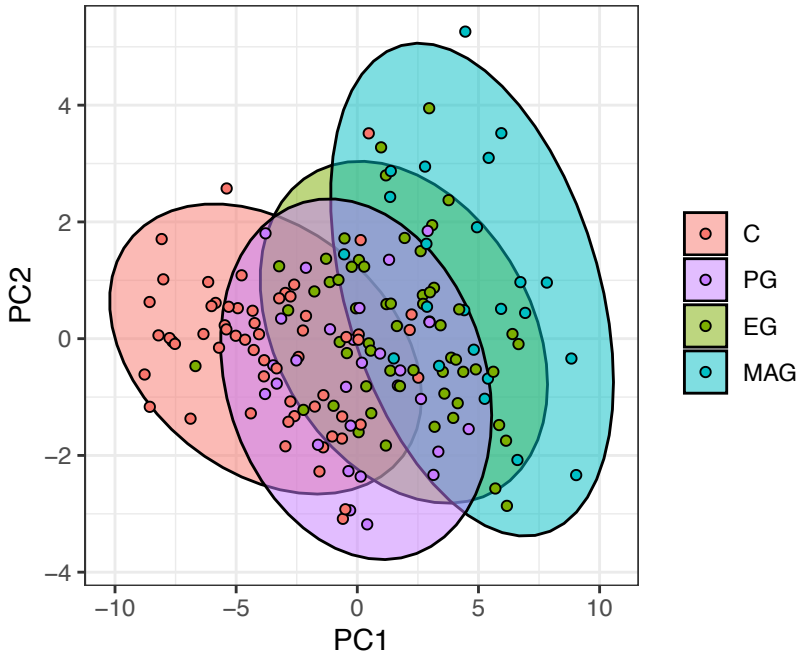

Figure 6.10: Relationship between PC1 and PC2 according to glaucoma disease stage describing subset of 26 ONH variables. Oval polygons represent 95% confidence intervals.

Following PCA on the subset of 26 ONH variables, Table 6.21 presents the loading coefficients for PCs 1 and 2, and their association with the 26 ONH variables. All of the 26 ONH variables were strongly correlated with PC 1 and showed a weak to moderate association with PC 2. The loading coefficients for PC 1 were relatively similar for each variable, suggesting a relatively equal contribution to PC 1 from each of the ONH variables.

Figure 6.11 presents the relationship between LDs 1 to 3 describing the subset of 26 ONH variables for each stage of glaucoma. The largest separation of observations according to glaucoma stage was along axes LD 1 and LD 2, with relatively little separation of groups along LD 3. Along axis LD 1 the control and MAG groups were fully separated, although overlap was observed between controls, PG, and EG.

Table 6.22 presents the loading coefficients for LDs 1 to 3, and the correlation with selected measures of prelamina depth and thickness. A strong correlation was found between inferior

prelamina depth and LD 1. The highest loading coefficient of prelamina depth on LD 1 was in the temporal region, although this showed a moderate correlation with LD 1. Inferior, IT, and ST prelamina thickness were strongly correlated with LD 1, with the highest loading coefficient found in the ST region.

Presented in Table 6.23, bNFL and MRW strongly correlated with LD 1 in all ONH regions apart from nasal, temporal, and IN, where a moderate association was found. The strongest correlation between bNFL and LD 1 was found in the ST region, which also showed the highest loading coefficient on LD 1. The highest loading of MRW on LD 1 was in the IT region and the strongest association between MRW and LD 1 was found in the inferior and ST regions.

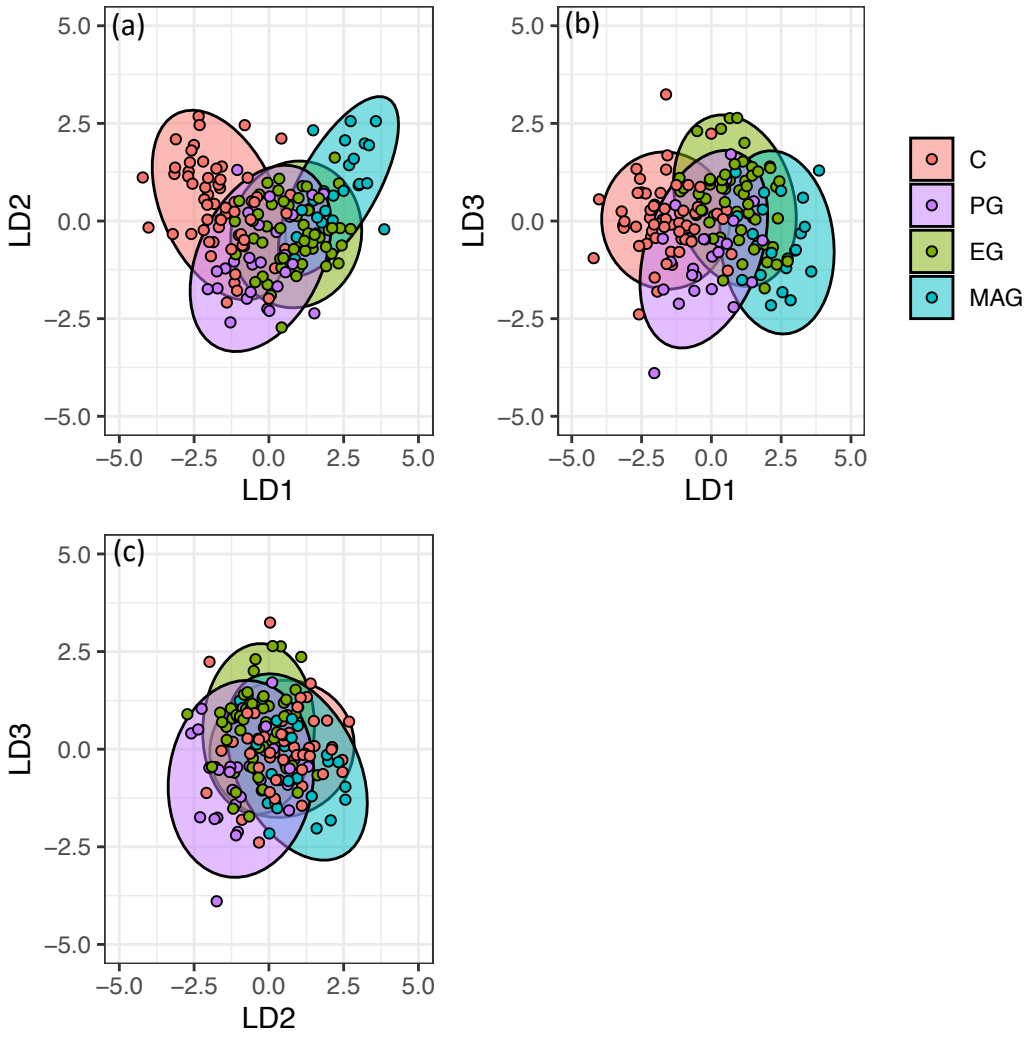

Figure 6.11: Separation of glaucoma disease stages along LDs 1 to 3 describing subset of 26 ONH variables; with LD 2 against LD 1 (a), LD 3 against LD 1 (b), LD 3 against LD 2 (c). Oval polygons represent 95% confidence intervals.

ONH Parameter	Region	Loading coefficients		Pearson's correlation			
		PC 1	PC 2	PC 1 (r)	*P*-value	PC 2 (r)	*P*-value
Prelamina depth	Superior	0.20	-0.24	0.82	<0.001	-0.34	<0.001
	Inferior	0.21	-0.16	0.83	<0.001	-0.23	0.003
	Temporal	0.19	-0.37	0.74	<0.001	-0.53	<0.001
	SN	0.19	-0.25	0.77	<0.001	-0.36	<0.001
	IT	0.21	-0.28	0.83	<0.001	-0.40	<0.001
	ST	0.21	-0.29	0.84	<0.001	-0.42	<0.001
Prelamina thickness	Inferior	-0.19	0.01	-0.77	<0.001	0.01	0.934
	IT	-0.21	0.11	-0.82	<0.001	0.16	0.036
	ST	-0.19	-0.25	-0.77	<0.001	0.22	0.004
bNFL	Superior	-0.19	-0.25	-0.77	<0.001	-0.36	<0.001
	Inferior	-0.20	-0.23	-0.81	<0.001	-0.33	<0.001
	Nasal	-0.19	-0.13	-0.75	<0.001	-0.18	0.019
	SN	-0.19	-0.20	-0.74	<0.001	-0.29	<0.001
	IT	-0.18	-0.22	-0.71	<0.001	-0.32	<0.001
	ST	-0.18	-0.24	-0.73	<0.001	-0.35	<0.001
	IN	-0.18	-0.12	-0.72	<0.001	-0.17	0.027
MRW	Superior	-0.20	-0.17	-0.81	<0.001	-0.24	0.001
	Inferior	-0.21	-0.20	-0.83	<0.001	-0.29	<0.001
	Nasal	-0.20	0.01	-0.81	<0.001	0.01	0.864
	Temporal	-0.18	0.01	-0.73	<0.001	0.02	0.801
	SN	-0.21	-0.02	-0.85	<0.001	-0.03	0.739
	IT	-0.20	-0.21	-0.80	<0.001	-0.30	<0.001
	ST	-0.21	-0.17	-0.83	<0.001	-0.25	0.001
	IN	-0.20	-0.01	-0.80	<0.001	-0.02	0.818
MRA	SN	-0.17	-0.05	-0.71	<0.001	-0.07	0.358
Volumetric ONH parameter							
Optic cup volume		0.18	-0.29	0.74	<0.001	-0.42	<0.001

Table 6.21: Loading and Pearson's correlation coefficient of PC1 and PC2 describing subset of 26 ONH variables. Red text indicates a strong association at r ≥ 0.70.

ONH Parameter	Region	Loading coefficients			Pearson's correlation					
		LD 1	LD 2	LD 3	LD 1 (r)	*P*-value	LD 2 (r)	*P*-value	LD 3 (r)	*P*-value
Prelamina depth	Superior	-0.15	-0.42	-0.03	0.67	<0.001	-0.36	<0.001	-0.18	0.020
	Inferior	0.14	-0.02	-0.22	0.70	<0.001	-0.17	0.024	-0.01	0.875
	Temporal	-0.63	0.64	-0.59	0.46	<0.001	-0.23	0.002	-0.09	0.269
	SN	0.18	-0.55	0.15	0.62	<0.001	-0.29	<0.001	-0.20	0.011
	IT	0.28	-1.05	1.28	0.61	<0.001	-0.19	0.014	0.06	0.463
	ST	-0.18	-0.98	0.75	0.68	<0.001	-0.39	<0.001	-0.07	0.350
Prelamina thickness	Inferior	-0.06	-0.07	-0.63	-0.73	<0.001	0.12	0.136	-0.03	0.662
	IT	0.04	-0.84	0.30	-0.71	<0.001	0.14	0.063	-0.02	0.806
	ST	-0.60	0.49	0.26	-0.72	<0.001	0.41	<0.001	0.07	0.353

Table 6.22: Loading and Pearson's correlation coefficient of LDs 1-3 describing subset of regional measures of prelamina depth and thickness. Red text indicates a strong association at r ≥ 0.70.

ONH Parameter	Region	Loading coefficients			Pearson's correlation					
		LD 1	LD 2	LD 3	LD 1 (r)	*P*-value	LD 2 (r)	*P*-value	LD 3 (r)	*P*-value
bNFL	Superior	-0.27	-0.35	0.72	-0.82	<0.001	-0.17	0.027	0.10	0.197
	Inferior	-0.16	-0.03	-0.66	-0.84	<0.001	-0.02	0.796	0.01	0.990
	Nasal	-0.22	0.23	0.31	-0.69	<0.001	-0.04	0.636	-0.06	0.466
	SN	-0.07	-0.41	-0.75	-0.75	<0.001	-0.16	0.038	-0.09	0.250
	IT	-0.26	0.31	0.94	-0.77	<0.001	0.05	0.552	0.13	0.102
	ST	-0.63	-0.37	-1.06	-0.87	<0.001	-0.05	0.485	-0.17	0.028
	IN	0.05	0.26	-0.36	-0.62	<0.001	-0.03	0.669	-0.04	0.589
MRW	Superior	0.01	-0.37	-1.06	-0.80	<0.001	0.01	0.961	0.20	0.009
	Inferior	-0.05	0.19	0.33	-0.84	<0.001	0.05	0.536	0.01	0.963
	Nasal	0.06	-0.50	-0.65	-0.68	<0.001	0.03	0.661	-0.03	0.676
	Temporal	-0.04	0.08	0.21	-0.61	<0.001	0.10	0.185	0.01	0.979
	SN	0.06	1.25	1.35	-0.78	<0.001	0.10	0.197	0.19	0.011
	IT	0.16	-0.03	-0.44	-0.76	<0.001	-0.04	0.604	-0.07	0.383
	ST	0.09	0.19	0.23	-0.84	<0.001	0.03	0.683	-0.09	0.264
	IN	-0.09	-0.29	0.58	-0.67	<0.001	0.02	0.818	0.08	0.305
MRA	SN	-0.22	-1.04	-0.42	-0.63	<0.001	-0.06	0.470	0.09	0.240
Volumetric ONH parameter										
Optic cup volume		0.25	1.35	-0.95	0.60	<0.001	0.01	0.893	-0.24	0.001

Table 6.23: Loading and Pearson's correlation coefficient of LDs 1-3 describing subset of regional measures of bNFL, MRW, MRA, and optic cup volume. Red text indicates a strong association at r ≥ 0.70.

The association between the 26 'optimal' ONH parameters and age was evaluated using Pearson's correlation coefficient, presented in Table 6.24.

ONH parameter	Region	Pearson's correlation with age	*P*-value
Prelamina depth	Superior	0.31	<0.001
	Inferior	0.32	<0.001
	Temporal	0.22	0.002
	SN	0.29	<0.001
	IT	0.27	<0.001
	ST	0.30	<0.001
Prelamina thickness	Inferior	-0.42	<0.001
	IT	-0.40	<0.001
	ST	-0.38	<0.001
Border NFL	Superior	-0.39	<0.001
	Inferior	-0.36	<0.001
	Nasal	-0.32	<0.001
	SN	-0.35	<0.001
	IT	-0.43	<0.001
	ST	-0.46	<0.001
	IN	-0.27	<0.001
Minimum rim width	Superior	-0.48	<0.001
	Inferior	-0.47	<0.001
	Nasal	-0.41	<0.001
	Temporal	-0.37	<0.001
	SN	-0.47	<0.001
	IT	-0.45	<0.001
	ST	-0.51	<0.001
	IN	-0.31	<0.001
Minimum rim area	SN	-0.49	<0.001
Volumetric ONH parameter			
Optic cup volume		0.23	0.003

Table 6.24: Association between regional and volumetric ONH parameters and age determined using Pearson's correlation coefficient. Red text indicates significant correlation at $p<0.05$.

Table 6.24 indicates that all 26 regional and volumetric ONH parameters that were deemed optimal in the classification of ONHs with respect to glaucoma disease stage were significantly associated with age. This coincides with increasing age as a prominent risk factor for POAG (Quigley, 2011; Schuster et al., 2020), and age-related changes to RNFL and ONH structure (Kergoat et al., 2001; Burgoyne and Downs, 2008; Downs, 2015). However, within chapters 3 and 4, in evaluation of ONH parameter differences according to glaucoma disease stage, age was controlled for via the use of linear mixed-effects regression models. This aligns with previous studies where it is suggested that age-related changes to the ONH are significant

and measurable, which should be taken into account when assessing potential glaucoma onset, and estimation of disease progression in patients with established glaucoma (Garway-Heath, Wollstein and Hitchings, 1997; Patel et al., 2014a).

Logistic regression was used to model participant gender as a function of the 26 'optimal' ONH parameters (see Table 6.25). Table 6.25 indicates that the only ONH parameter to significantly contribute to participant gender was ST bNFL. Correspondingly, ST bNFL significantly differed between male (mean ± SD: 236.81 ± 69.71µm) and female (mean ± SD: 262.53 ± 73.48µm) participants (t-test: p=0.022). However, the remaining 'optimal' ONH parameters were not considered to significantly describe information regarding participant gender.

ONH parameter	Region	Estimate	Standard Error	Z-value	*P*-value
Intercept		1.93	1.75	1.09	0.272
Prelamina depth	Superior	-0.001	0.002	-0.44	0.663
	Inferior	0.002	0.005	0.52	0.606
	Temporal	0.002	0.003	0.69	0.488
	SN	0.002	0.002	1.33	0.184
	IT	-0.001	0.005	-0.27	0.789
	ST	-0.007	0.005	-1.38	0.167
Prelamina thickness	Inferior	0.006	0.005	1.32	0.189
	IT	-0.008	0.005	-1.57	0.117
	ST	-0.002	0.005	-0.50	0.620
Border NFL	Superior	0.007	0.006	1.20	0.230
	Inferior	0.012	0.006	1.83	0.067
	Nasal	-0.009	0.007	1.20	0.158
	SN	-0.002	0.006	-1.41	0.158
	IT	-0.001	0.006	-0.12	0.902
	ST	-0.005	0.002	-2.25	0.024
	IN	-0.001	0.005	-0.18	0.859
MRW	Superior	-0.002	0.005	-0.43	0.669
	Inferior	-0.008	0.006	-1.51	0.132
	Nasal	0.003	0.006	0.42	0.676
	Temporal	0.05	0.003	1.70	0.090
	SN	-0.001	0.007	-0.07	0.945
	IT	0.003	0.007	0.45	0.650
	ST	0.001	0.007	0.02	0.984
	IN	-0.003	0.005	-0.65	0.516
MRA	SN	-1.18	8.92	-0.13	0.895
Volumetric ONH parameter					
Optic cup volume		0.408	2.72	0.15	0.881

Table 6.25: Output of logistic regression with participant gender modelled as a function of 26 optimal ONH parameters. Red text indicates a significant association at p<0.05.

VI.6.7 Cross-validation of LDs 1, 2, and 3

Cross-validation is a method to guard against over-fitting. An over-fit model captures information within the sample obtained, however may not be generalisable to data outside of the sample. Therefore, an over-fit model would perform poorly with out-of-sample data, thereby reducing its applicability to 'real world' data (Babyak, 2004; Smith, 2018).

Here, a 10-fold cross-validation (i.e., k-fold cross-validation) involves randomly dividing the training data into ten equal parts. Each of these ten parts serves in turn as a test set while the model is trained on the remaining data. The results of the ten tests are averaged and the model achieving the highest accuracy is selected. This model is then run on the full training set to produce a prediction model and evaluate its predictive performance (Schaffer, 1993). Cross-validation was performed to evaluate the ability of LDs 1, 2, and 3 to model a binary classifier indicating control or glaucoma. The model produced by cross-validation is thus the one of the three LDs that cross-validation suggests will be most predictive.

Table 6.26 summarises the performance of LDs 1, 2, and 3 to predict classification as control or glaucoma.

	LD1		**LD2**		**LD3**	
	Reference		**Reference**		**Reference**	
Prediction	Control	Glaucoma	Control	Glaucoma	Control	Glaucoma
Control	51	10	12	13	0	0
Glaucoma	9	99	48	96	60	109

Table 6.26: Confusion matrix to compare group prediction (i.e., control or glaucoma) made by LDs 1, 2, and 3, compared to known classification. Red text indicates correct group prediction made by each LD.

Tables 6.26 and 6.27 indicate that LD1 correctly predicted 51/60 controls and 99/109 glaucoma participants resulting in accuracy of 88.76%. LD2 correctly identified 12/60 controls and 96/109 glaucoma participants, whereas LD3 did not correctly identify any control participants, although correctly identified all 109 glaucoma participants, resulting in accuracy of 63.91% and 64.5% for LDs 2 and 3 respectively. Therefore, LD1 was deemed the most appropriate discriminatory function of ONHs with respect to glaucomatous disease.

Performance	LD1	LD2	LD3
Accuracy	0.8876	0.6391	0.6450
Sensitivity	0.8500	0.2000	0.0000
Specificity	0.9083	0.8807	1.0000

Table 6.27: Performance of LDs 1, 2, and 3 to correctly predict control or glaucoma, compared to known group classification.

VI.7 Discussion

This study aimed to determine which ONH and/or NFL parameters, and within which region, were important factors in differentiating ONHs as a function of glaucoma stage. This study is novel as it is the first to include 56 parameters describing NFL thickness, neuroretinal rim, and ONH structure to determine a classifier system of glaucoma disease stage. Additionally, this study aimed to reveal which ONH parameters provide the best indication of glaucomatous disease.

The largest differentiation of ONHs according to glaucoma stage was along the axes of PC 1 and LD 1. However, since each PC and LD are generated as linear combinations of *all* of the 56 ONH variables, interpretation of the resulting PCs and LDs was not simple (Jolliffe, 1972; Al-Kandari and Jolliffe, 2005; Jolliffe and Cadima, 2016). In this study, ONH variables that showed a strong association with the resulting PCs and LDs were considered to contribute most to a given PC or LD (Cadima and Jolliffe, 1995; Al-Kandari and Jolliffe, 2005).

Table 6.28 summarises the ONH variables deemed to contribute most to the resulting PCs and LDs; indicating that a combination of regional measures of prelamina depth and thickness, bNFL, MRW, MRA and optic cup volume are important biomarkers for the characterisation of POAG. For instance, in the superior, inferior, temporal, SN, IT, and ST regions of the ONH, a strong association was found between prelamina depth and PC 1, and inferior prelamina depth was strongly associated with LD 1. Similarly, prelamina thickness was strongly associated with PC 1 and LD 1 in the inferior, IT, and ST regions. Border NFL and MRW were found to be important parameters to characterise ONHs with respect to glaucoma stage in all ONH regions, apart from temporal bNFL. Optic cup volume and superior-nasal MRA were also found to contribute to the characterisation of ONHs in glaucoma disease. These findings indicate that these are important factors, and potentially biomarkers for the differentiation

of participants with glaucoma disease; with PC 1 and LD 1 showing large separation between controls and MAG. However, in this study, overlap remained between early glaucoma stages, such as controls, PG, and EG. This suggests that during the early stages of glaucoma disease it remains difficult to characterise and fully differentiate ONHs according to disease stage.

Regional ONH parameter	**Region**								
	C	**S**	**I**	**N**	**T**	**SN**	**IT**	**ST**	**IN**
Prelamina depth		✓	✓		✓	✓	✓	✓	
Prelamina thickness			✓				✓	✓	
bNFL	N/A	✓	✓	✓		✓	✓	✓	✓
MRW	N/A	✓	✓	✓	✓	✓	✓	✓	✓
MRA	N/A					✓			
Volumetric ONH parameter									
Optic cup volume	✓								

Table 6.28: Summary of important ONH parameters for the differentiation of ONHs according to glaucoma disease stage.

Central prelamina depth and thickness showed a significant, albeit moderate association with PC and LD 1, and was therefore considered a less important parameter than measures of prelamina depth and thickness made in the superior and inferior ONH quadrants. This aligns with that reported in chapter 3 where central prelamina depth did not significantly differ between controls and PG, or between PG and EG, nor between EG and MAG. However, in chapter 3, central prelamina depth was significantly greater in EG compared to controls. Furthermore, central prelamina depth has been shown to be significantly more posterior within the ONH, and thinner in glaucomatous eyes compared to controls (Kim et al., 2016; Prata et al., 2017; Lopes et al., 2019). However, these *in vivo* studies did not evaluate regional measures of prelamina depth and thickness, whereas this present study suggests that regional prelamina depth and thickness parameters could act as important glaucoma biomarkers.

Optic cup volume was strongly associated with PC 1 and therefore considered an important parameter in the differentiation of ONHs with respect to glaucoma disease. A moderate association was found between prelamina volume and LD 1, although weakly associated with PC 1. BMO surface area was weakly correlated with PC and LD 1. Therefore, optic cup volume was considered a more important parameter than prelamina volume and BMO surface area

in distinguishing participants with glaucoma disease. These findings were consistent with the characteristic glaucomatous ONH changes that includes enlargement of the optic cup (Jonas et al., 1988c; Garway-Heath et al., 1998; Quigley, 2011), and therefore an increase in optic cup volume. However, with progression of glaucomatous disease there is loss of RGC axons (Hayreh, 1972; Pederson, 1980), which would result in a reduction in prelamina volume. Furthermore, as shown in monkey models of experimental glaucoma, the loss of optic nerve fibres combined with posterior movement of the LC results in an increase in optic disc cupping and widening of BMO (Burgoyne et al., 2010; Yang et al., 2011a), i.e., resulting in an increase to BMO surface area. This contradicts that reported in this study whereby BMO surface area was weakly correlated with PC and LD 1. Although prelamina volume could be a useful ONH parameter to indicate loss of RGC axons, and indeed was moderately associated with LD 1, data in this study suggests optic cup volume is a more important parameter to indicate glaucoma disease. Previous studies have reported that 'cup shape' was the best ONH parameter to differentiate between glaucomatous and normal eyes (Uchida, Brigatti and Caprioli, 1996; Iester et al., 1997a). Although this current study identified optic cup volume as an important ONH parameter for the detection of glaucoma disease, 'cup shape' was not quantified. Furthermore, Iester et al. (2002) reported that a combination of four sectoral ONH parameters, including variables such as rim area and volume, and NFL thickness outperformed 'cup shape' to detect glaucomatous VF defects.

In this study, regional measures of prelamina depth and thickness, NFL, neuroretinal rim, and optic cup volume were identified as important ONH parameters in glaucomatous disease. Indeed, in the early stages of glaucoma disease, Jonas et al. (1993) reported that loss of the neuroretinal rim began in the IT and ST ONH sectors. Furthermore, other studies have reported on the need to determine which parameters best distinguish between control and glaucoma participants with VF defects according to sectoral ONH measurements (Iester, Swindale and Mikelberg, 1997b; Bathija et al., 1998; Iester, Courtright and Mikelberg, 1999), or RNFL measures (Weinreb et al., 1998). It was concluded, in agreement with this thesis study, that the latter was improved when a combination of a number of ONH variables were evaluated (Iester et al., 1997a; Iester et al., 2000; Iester et al., 2008).

In all regions of the ONH, a moderate association between LC thickness and PC 1 and LD 1 suggested a lower contribution by LC thickness for the differentiation of ONHs with respect to glaucoma disease. Therefore, measures of LC thickness were considered less important than parameters such as prelamina depth and thickness, bNFL, MRW, or optic cup volume. This differs from *ex vivo* work where it is noted that compression of the LC plates (i.e. LC thinning) is an early abnormality detected in the glaucomatous ONH (Quigley et al., 1983). Additionally, *in vivo* studies have reported significant differences in LC thickness in glaucomatous and control eyes; with central, mid-superior, and mid-inferior LC thinner in POAG and normal tension glaucoma (NTG) than control eyes (Park et al. (2012a). Additionally, Omodaka et al. (2015) determined that average LC thickness significantly differed between controls eyes, NTG, and PG. However, Omodaka et al. (2015) included fewer eyes than this current study where they included 18 eyes in each participant group. Therefore, in a smaller sample than this study, differences in LC thickness may correspond to ONH structural alterations in early glaucoma, although this study suggests that parameters such as prelamina depth and thickness, bNFL, MRW, and optic cup volume are more appropriate than LC thickness for ONH characterisation according to glaucoma disease stage. Inoue et al. (2009) reported that central LC thickness decreased as a function of glaucoma disease stage, and was significantly correlated with VF MD. Therefore, although LC thickness may provide an indication of ONH structural alteration in glaucoma, this current study determined that parameters related to loss of RGC axons, including optic cup volume contributed more than LC thickness for the differentiation of ONHs with glaucoma. This aligns with that reported by Lopes et al. (2019) who determined that prelamina neural tissue thickness and area provided a better correlation with VF status than LC thickness, area, and anterior LC depth.

Measurements of pNFL were moderately associated with PC and LD 1 in all regions of the ONH, whereas bNFL and MRW were strongly associated with PC 1 in all regions (except temporal bNFL), and also showed a strong correlation with LD 1 in the superior, inferior, IT, and ST regions. A strong association between MRA and PC 1 was found in the SN region. To date this is the first study to report on bNFL in glaucomatous disease. Regional measures of bNFL, MRW, and MRA were closer related to PC and LD 1 than pNFL and were therefore considered to provide better differentiation of ONHs with respect to glaucomatous disease than pNFL.

Clinically, *in vivo* evaluation of RNFL thickness has augmented clinical assessment of glaucoma disease (Medeiros et al., 2009b); with measurements of pNFL shown to have high sensitivity for the detection of VF abnormalities (Wollstein et al., 2004). Medeiros et al. (2005b) identified the inferior pNFL as the best discriminator between control and glaucoma participants, and in agreement with Leung et al. (2005), that the pNFL performed better than total macula retinal thickness. In agreement with this current study, Medeiros et al. (2005b) reported that a combination of ONH and NFL parameters resulted in the best discriminatory function for glaucoma detection. Additionally, in longitudinal studies, pNFL has been reported to detect glaucoma disease progression (Leung et al., 2010a; Li et al., 2010). However, consistent with this study, Chauhan et al. (2013) determined that MRW measurements have better glaucoma diagnostic capabilities than those of pNFL and horizontal rim width. Additionally, in a longitudinal study, Gardiner et al. (2015) showed that NFL thickness measurements showed a better rate of change over time than MRW or MRA, thus preferable for monitoring change in disease; but that that MRW or MRA may be more sensitive for the early detection of glaucomatous ONH damage. This current study also suggests that MRW and MRA are important parameters for glaucoma detection, however, as this was a cross-sectional study no evaluation was made as to which parameters are optimal to monitor disease progression over time.

In this study, when PCA was performed on individual ONH parameters (e.g., prelamina depth), this did not achieve adequate separation of participants according to glaucoma disease stage. Better separation of participant groups (i.e., glaucoma stages) was obtained when PCA or LDA was performed using all 56 ONH variables included in analyses. Therefore, this suggests that using a combination of ONH and NFL OCT-derived parameters allows for the best discrimination of ONHs with respect to glaucoma stage. Furthermore, when cluster analysis was performed on the resulting PCs 1 and 2, distinct groupings and separation of observations for each stage of glaucoma were determined. However, when group allocations (following cluster analysis) were compared with known glaucoma stages this revealed incorrect classifications according to disease stage. This suggests that following PCA and cluster analysis it remains difficult to distinguish between early stages of glaucoma, particularly PG and EG from controls. This overlap between participant groups may be related to the pronounced

inter-individual variability of ONH parameters in the normal population (Jonas et al., 1988a; Jonas et al., 1988b; Varma et al., 1994; Tan, Garway-Heath and Hitchings, 2003). Therefore, due to variability in the quantitative ONH parameters measured, this may be the reason there was overlap between participant groups as a function of glaucoma stage.

In a clinical setting, the standard for detecting glaucoma progression has been automated perimetry (Kotowski et al., 2014). However, in many cases, structural damage to the ONH and/or RNFL can precede VF loss or occurs without simultaneous defects to the VF (Sommer et al., 1991a; Quigley et al., 1992; Centofanti et al., 2005). Therefore, there is a need for diagnostic tools that enhance objective, reliable evaluation of glaucomatous structural changes. The role of OCT in glaucoma diagnosis and follow-up has increased in recent years due to the ease of data acquisition offering objective, automated, accurate and reliable quantitative structural measurements *in vivo* (Fallon et al., 2017). However, there is a lack of a commonly accepted 'gold standard' to indicate glaucomatous progression. Therefore, it remains difficult to determine whether progression identified by an imaging device e.g., OCT, without decline of the VF, reflects structural alterations that precede loss of visual function as measured by standard automated perimetry, or indeed is a false positive (Kotowski et al., 2014).

Compared to TD-OCT, SD-OCT allowed for improved intra-visit and inter-visit reproducibility of measurements, highlighting the instrument's advantages for detecting early glaucoma progression (Leung et al., 2012). For instance, 128 glaucomatous eyes were monitored for a minimum of two years, whereby 19 eyes were identified as progressive disease using SD-OCT, compared to 4 eyes identified using TD-OCT (Leung et al., 2011). In OCT-based studies where glaucoma disease progression was defined according to red-free fundus photographs, it has been demonstrated that analysis of both sectoral and mean RNFL thickness measurements is important to maximise detection of disease progression (Lee et al., 2009; Leung et al., 2010a). Using SD-OCT, RNFL thickness measurements in the inferior and inferior-temporal quadrants have been reported to be most predictive of glaucoma disease progression (Medeiros et al., 2009b; Leung et al., 2010b).

Clinically, the widely adopted OCT scan protocols play an essential role in glaucoma diagnosis and monitoring by allowing objective, quantitative structural measurements, and statistical classification by comparison to normative data (Kotowski et al., 2014; Fortune, 2019). However, they cannot reliably detect abnormal ONH features such as blood vessel alterations (Tanito et al., 2017), or optic disc haemorrhage suggestive of disease progression (Nitta et al., 2017), and therefore, should not replace clinical examination. Such OCT-derived data provide complementary information aimed to assist the clinician in diagnostic evaluation with respect to glaucoma disease. OCT-derived structural measures based on minimum distance mapping have been shown to enhance early glaucoma detection (Chauhan et al., 2013), and monitoring of structural changes (Gardiner et al., 2015), although without a commonly accepted reference measure of disease diagnosis and progression, the clinical applicability of these measures remains unknown. Even when standard automated perimetry is employed to monitor functional change in POAG, the rates of VF progression in glaucoma patients has been reported to be highly variable (Heijl et al., 2013b).

Furthermore, it is noteworthy that the prevalence of glaucoma, including its type and severity (Heijl, Bengtsson and Oskarsdottir, 2013a), varies between different geographic regions (Quigley and Broman, 2006), ethnicities (Kosoko-Lasaki et al., 2006), age (Bourne et al., 2016), and gender (Rudnicka et al., 2006). Additionally, since the appearance of the 'normal' ONH is largely variable (Jonas et al., 1988a; Lamparter et al., 2013), difficulties remain in the development of glaucoma diagnostic parameters with broad clinical utility. This is highlighted in discrepancies and subjectivity in glaucoma diagnosis, even among clinical experts (Rossetto et al., 2017; Hong et al., 2018).

Since glaucomatous optic neuropathy is highly variable in its development and advancement (Heijl et al., 2013b), OCT-derived parameters may falsely identify glaucoma onset and suggest disease progression. Therefore, decisions regarding clinical management of glaucoma should pivot on a combination of structural and functional measures, including clinical examination.

In summary, this study has determined that the regions of ONH parameters that best allowed discrimination of ONHs as a function of glaucoma disease stage were measurements performed primarily in the superior, inferior, IT, ST, and SN regions. ONH (prelamina depth

and thickness) and NFL (bNFL, MRW, MRA) parameters in these regions, including optic cup volume allow for the best ability for glaucoma detection among the OCT-based parameters evaluated in this study. Therefore, a combination of *in vivo* ONH and NFL parameters appear to hold potential to assist in glaucoma detection using OCT.

VI.7.1 Study limitations

A limitation in this study was vascular shadowing within the OCT image datasets. Due to this obscurity within the images, this resulted in an inability to record measurements of ONH parameters predominantly in the nasal side of the ONH. Due to the percentage of missing values within each variable, this resulted in 7 regional ONH parameters being excluded from PCA and LDA. Furthermore, in ONH parameters that were not excluded from PCA or LDA, several variables (n=28) contained missing data. To overcome missing values (i.e. to perform PCA and LDA), this resulted in data imputation via simple linear regression based on VF MD. Due to data imputation, this resulted in data that was 'not real' included in PCA and LDA and therefore represents a slight inaccuracy in the PCs and LDs that were generated following analysis. If vascular shadowing could be accurately removed from OCT image datasets this would gain more regional ONH structural information that could potentially differentiate ONHs as a function of glaucoma disease stage. Removal of OCT image shadowing are improved with algorithms such as adaptive compensation (Girard et al., 2011; Mari et al., 2013). However, these algorithms were found to be unsuitable for SD-OCT images acquired using the custom-built SD-OCT device that was used in this study.

Furthermore, due to OCT signal attenuation within the OCT datasets, on occasion it was not possible to visualise the anterior or posterior boundary of the LC. Therefore, this prohibited measurements of prelamina and LC thickness, and prelamina and LC volume. This resulted in a number of missing values for such parameters which were subsequently excluded from PCA and LDA. The use of a swept-source OCT device would allow better tissue penetration and therefore less signal attenuation; to allow clearer delineation of the anterior or posterior LC surfaces.

Finally, another limitation to this study was the sample size (n = 169 eyes). This study included 56 ONH variables in PCA and LDA. As proposed by Bellman (1957), the 'curse of

dimensionality' states that as the number of dimensions within the dataset increases (i.e. with more ONH variables included in PCA or LDA), to make meaningful separations of participant subsets, the number of observations within each group needs to increase exponentially.

To perform discriminant analysis, Wahl and Kronmal (1977) suggest it is desirable to have approximately five times as many observations as predictor variables. Additionally, at a minimum, it is reported that the smallest participant group size should exceed the number of predictor variables (Zavorka and Perrett, 2014). For a 'two-group' discriminant analysis, Congalton (1991) suggests a minimum sample size of 50 within each group, although also recommends that with a larger number of participant subsets this sample size should be increased to 75-100 observations per group. Therefore, in this study, since ONHs in the PG group (n=28), and in the MAG group (n=23) contained fewer observations than predictor variables (n=56), this may explain the overlap between participant groups according to glaucoma disease stage.

Future work would intend to increase the sample size included in this study, which may result in more adequate separation of participant groups according to disease stage; with aim to elucidate which ONH parameters allow the best differentiation of ONHs in glaucoma disease. This could allow identification of ONH biomarkers to enhance early detection of glaucoma onset or progression. Additionally, future work would include data for regional assessment of LC connective tissue alignment (i.e. LC coherence), as this has been shown to alter regionally within the full thickness of the LC in glaucoma disease, as described in Chapter 5 and *ex vivo* (Jones et al., 2015). These data were not included in PCA or LDA in this study as OCT image processing and LC coherence analysis has not yet been completed for the entire cohort of glaucoma and control participants included in this thesis.

VI.7.2 Conclusion

In conclusion, this study has demonstrated that a combination of regional ONH and NFL parameters, including optic cup volume are useful indicators for glaucoma detection, and the characterisation of ONHs according to glaucoma stage. Data analysed in this study suggests that prelamina depth and thickness, bNFL, MRW, MRA, and optic cup volume made a larger contribution to distinguish glaucomatous ONHs than pNFL and LC thickness. This suggests that

these *in vivo* quantitative ONH parameters could provide essential biomarkers that can be applied in both clinical diagnostic and research purposes for glaucoma disease.

VII. Chapter 7: Discussion

Glaucoma has been estimated to affect approximately 60 million people worldwide (Quigley and Broman, 2006; Quigley, 2011) and is the leading cause of irreversible blindness worldwide; resulting in bilateral blindness in more than 8 million people (Quigley and Broman, 2006; Quigley, 2011; Tham et al., 2014; Flaxman et al., 2017). Currently, clinical detection and definitive diagnosis of primary open angle glaucoma is based upon congruent damage to the ONH and loss of visual function and is often associated with raised intraocular pressure (Garway-Heath and Hitchings, 1998; Anderson, 2006; Keltner et al., 2006; Boland and Quigley, 2011; Jonas et al., 2017). Early detection of glaucomatous disease is difficult as ONH structural alterations related to axon parameters such as loss of the neuroretinal rim and enlargement of the optic cup (Quigley et al., 1982; Jonas et al., 1988c; Budde and Jonas, 1999) indicate that loss of RGC axons has already occurred. Furthermore, it is reported that 30% to 50% of RGCs may be affected before visual field defects are detected using standard automated perimetry (Quigley et al., 1981; Kerrigan-Baumrind et al., 2000; Harwerth et al., 2010).

Current glaucoma treatments aim to halt or slow disease progression (Heijl et al., 2002; Kass et al., 2002; Boland et al., 2013; Weinreb et al., 2014; Garway-Heath et al., 2015). Therefore, loss of vision that has occurred prior to the commencement of treatment is permanent. To preserve visual function and prevent further permanent vision loss, this signifies the importance of being able to detect and diagnose glaucoma as early as possible in order to initiate appropriate treatment and minimise ONH damage.

Since the LC is proposed as the site of RGC axon injury in glaucoma disease (Quigley and Addicks, 1981; Quigley et al., 1981), with LC morphological alterations (Quigley et al., 1983; Miller and Quigley, 1988; Tan et al., 2019) accompanying RGC dysfunction and/or death (McKinnon, 1997; Quigley, 1999; Kerrigan-Baumrind et al., 2000), and axon loss (Bowd et al., 2000; Medeiros et al., 2005b), this project aimed to determine *in vivo* ONH and axon-related parameters that have potential to act as biomarkers of disease. Early detection of glaucoma disease onset and/or an ability to monitor disease progression by identification of disease stage is critical for timely commencement of appropriate glaucoma treatment at its earliest stages.

For this reason, this thesis used EDI-OCT, in an *in vivo* cross-sectional study, to characterise ONH (i.e., ONH and NFL parameters) structural alterations at different disease stages (control [no ocular disease], preperimetric glaucoma [PG], early glaucoma [EG], and moderate-advanced glaucoma [MAG]) and as a function of visual field sensitivity. Axon-related parameters included bNFL, pNFL, MRW, MRA, prelamina thickness and prelamina volume. Additionally, ONH parameters, indicative of ONH structure, included prelamina depth, optic cup volume, LC depth, thickness, volume and coherence, as well as BMO diameter and surface area. This thesis study is novel as the first to investigate regional ONH structure as a function of glaucoma disease stage *in vivo*. Furthermore, this thesis study is the first of its kind to quantify 3D volumetric ONH parameter changes in glaucoma disease, and probe LC connective tissue structural alterations *in vivo* based on OCT-derived image analysis.

To elucidate which ONH parameters were the best indicators of glaucoma onset or risk of disease progression, the following specific objectives were undertaken to analyse ONH and axon-related indices as a function of glaucoma disease stage:

- Regional evaluation of ONH and NFL depth and thickness parameters (Chapter 3).
- Quantification of volumetric ONH parameters (Chapter 4).
- Analysis of regional LC coherence depth-wise through the ONH (Chapter 5).
- Statistical modelling of multivariate data to develop a combination of OCT-based parameters that best predicts ONH structural and/or NFL changes in early disease (Chapter 6).

Compared to control eyes, ONHs within the PG group displayed characteristic glaucomatous changes to the ONH, but without accompanying VF loss, whereas glaucomatous ONH changes were associated with VF loss in the EG and MAG groups. Below the results from each chapter are summarised according to changes observed between stages of glaucoma, in order of increasing severity of disease stage. In Table 7.1 and Figure 7.1, the changes observed between control and PG ONHs and axon parameters are shown. Optic cup volume was significantly different between controls and the PG group, consistent with a hallmark of glaucomatous optic neuropathy, the enlargement of the optic cup, concurrent with a

reduction of the NRR due to loss of RGC axons (Quigley and Green, 1979; Jonas et al., 1988c; Gardiner et al., 2011).

Control to preperimetric glaucoma
↑ prelamina depth
↓ prelamina thickness
↓ LC thickness
↓ bNFL, pNFL, MRW
↑ optic cup volume
↑ LC coherence in superior-temporal quadrant of mid-posterior LC

Control

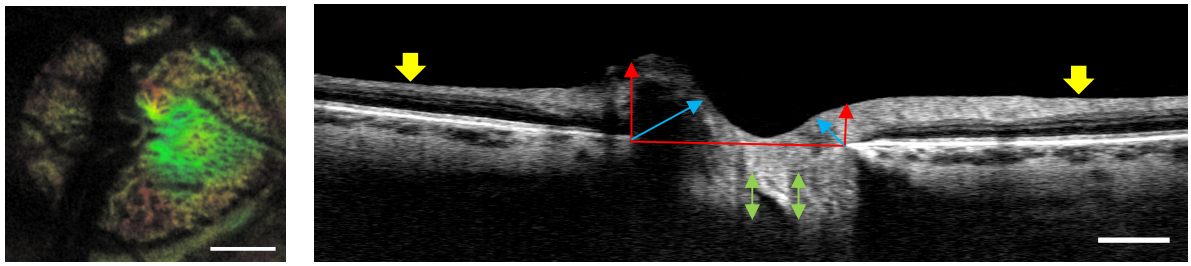

Preperimetric glaucoma

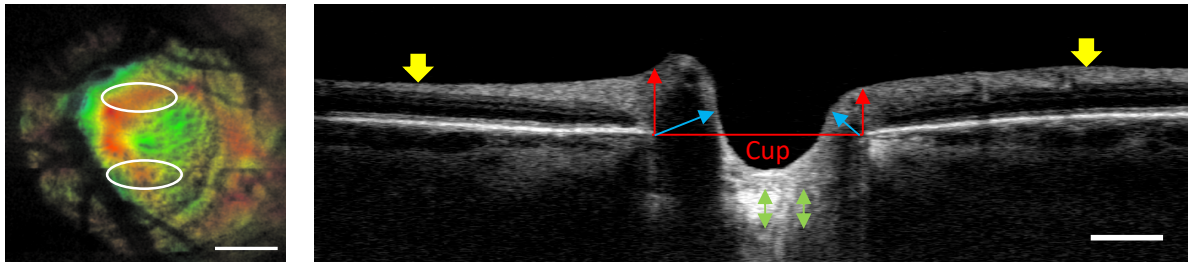

Figure 7.1: Summary of ONH and axon parameter differences between Control and PG ONHs; *Enface* OCT image slice through LC (left eyes) and OCT tomogram (IN-ST) indicate parameters: BMO (red line), bNFL (red arrows), pNFL (position of measurement denoted by yellow arrow heads), MRW (blue arrows), LC thickness (green arrows). Upper white oval indicates higher LC coherence in ST quadrant within the mid-posterior LC. Lower white oval suggests higher LC coherence in IT quadrant, although this was not significantly different. Scale bars = 500µm.

This study is the first to report on bNFL in glaucoma disease, and significant structural alterations to pNFL, MRW, and MRA according to glaucoma disease stage. In PG, there was also regional thinning of the NFL (bNFL and pNFL) and MRW, compared to controls. This supports previous OCT studies that showed NFL thickness to differentiate between healthy and glaucomatous eyes (Medeiros et al., 2005b; Leung et al., 2010b), and also had clinical potential in monitoring a decline in NFL thickness with glaucoma disease progression (Medeiros et al., 2009b; Leung et al., 2010a).

Control to PG	
RGC axon-related parameters	**ONH structural parameters**
• Decrease in prelamina thickness in all ONH regions, except nasal • Thinning of bNFL in inferior, temporal, and IT regions • Thinning of pNFL in superior region • Loss of neuroretinal rim: reduction of MRW in all regions, except nasal, temporal, and IT • No significant difference in MRA in any ONH region • No significant difference in prelamina volume	• Increase in prelamina depth in all ONH regions apart from central and temporal • Decrease in LC thickness in inferior, SN, and IN regions • Optic cup volume significantly larger in PG than controls • Increased LC coherence in ST quadrant in mid to posterior LC • No significant alteration in LC depth • No significant difference in LC volume • No significant difference in BMO diameter or surface area

Table 7.1: Summary of ONH and axon-related parameters changes/similarities between controls and preperimetric glaucoma. Red text indicates significant difference between glaucoma stages.

MRA did not significantly differ between PG and control ONHs in any region. As described, MRA adjusts for optic disc size; in that to encompass the same number of RGC axons, larger discs would display a thinner neuroretinal rim than smaller discs (Gardiner et al., 2014). In this thesis, participant inclusion criteria stipulated that mean spherical refractive error was within ± 6.00 D. Therefore, MRA may detect significant differences in ONHs outside of this refractive range, and potentially be a more suitable ONH parameter in participants with higher refractive errors for the detection of glaucoma onset or monitoring of disease progression.

In chapter 3, bNFL (inferior, temporal, and IT), and MRW (all regions except nasal, temporal, and IT) significantly differed between control and PG ONHs in more regions than pNFL (superior); suggesting that bNFL and MRW may be better parameters than pNFL for early glaucoma detection prior to vision loss. These findings were confirmed in chapter 6 where pNFL was considered to be less important than ONH parameters such as prelamina depth and thickness, bNFL, MRW, MRA, and optic cup volume. Therefore, even though pNFL is an established clinical measure used in glaucoma diagnosis and follow-up of disease progression (Medeiros et al., 2009b; Weinreb et al., 2014), data presented within this thesis suggests that RGC axon-related parameters measured within the ONH (such as bNFL and MRW) may be more appropriate biomarkers than pNFL for the earliest detection of glaucoma. This aligns

with that suggested by Gardiner et al. (2015) in that measures of MRW and MRA may be better for the early detection of glaucoma, whereas pNFL may be preferable for monitoring disease change over time (Chauhan et al., 2013; Gardiner et al., 2014).

In this study, ONHs in the PG group displayed significantly greater prelamina depth (relative to BMO) and thinner prelamina neural tissue compared to controls, see Figure 7.1. Since the prelamina, NFL, and NRR are comprised of RGC axons, this suggests that early glaucomatous changes (detected prior to VF loss) are as a consequence of RGC axon loss or compression of neural tissues. Since no VF loss was found with the PG group, these findings are consistent with observations that a substantial number of RGC axons can be lost before VF defects are detected (Quigley et al., 1982; Kerrigan-Baumrind et al., 2000).

Lamina cribrosa depth did not alter as a function of glaucoma stage in any ONH region, although the LC was significantly thinner in PG than controls in the inferior, IN, and SN regions. This corresponded to reports by Quigley et al. (1983) that compression of the LC occurred at an early stage in glaucoma, with backward bowing of the LC reported at later stages, indicative of LC compression as an early pathogenetic factor. The lack of LC depth change is consistent with Agoumi et al. (2011) who reported a thinned prelamina, but no change in posterior LC displacement following IOP elevation in human POAG and control eyes. LC thinning in PG, compared to controls, was found in the superior and inferior quadrants of the LC (see chapter 3), consistent with reports of increased susceptibility to damage due to these LC inferior regions containing larger pores and less connective tissue and glial cell structural elements, than the nasal-temporal regions (Quigley and Addicks, 1981; Radius and Gonzales, 1981; Quigley et al., 1983).

ONH and axon parameter differences between PG and EG ONHs are shown in Figure 7.2 and Table 7.2. Although parameters (chapter 6) such as prelamina depth and thickness, and optic cup volume were deemed to be appropriate measures for the characterisation of ONHs according to glaucoma disease stage and in early detection of glaucoma, no significant differences in these parameters were found between PG and EG ONHs in any region (Table 7.2). Therefore, this suggests that significant alterations in the anterior ONH occur in

glaucoma at a very early stage (i.e., between controls and PG), even before detection of vision loss and thereby prior to permanent vision loss.

Axon parameters, bNFL, pNFL, MRW, and MRA in all regions of the ONH, were negatively correlated with VF MD. Correspondingly, bNFL (superior, inferior, SN, and ST), pNFL (ST), MRW (inferior and ST), and MRA (inferior, nasal, IT, and ST) was significantly less in EG than PG (see Figure 7.2). Since significant differences between PG and EG were found in more regions for bNFL, MRW, and MRA than pNFL, this indicates that measurements of bNFL, MRW, and MRA are more appropriate parameters to suggest disease progression (i.e. from PG to EG) than pNFL. This aligns with data presented in chapter 6 where pNFL was considered a less important indicator than other parameters such as prelamina depth and thickness, bNFL, MRW, MRA, and optic cup volume.

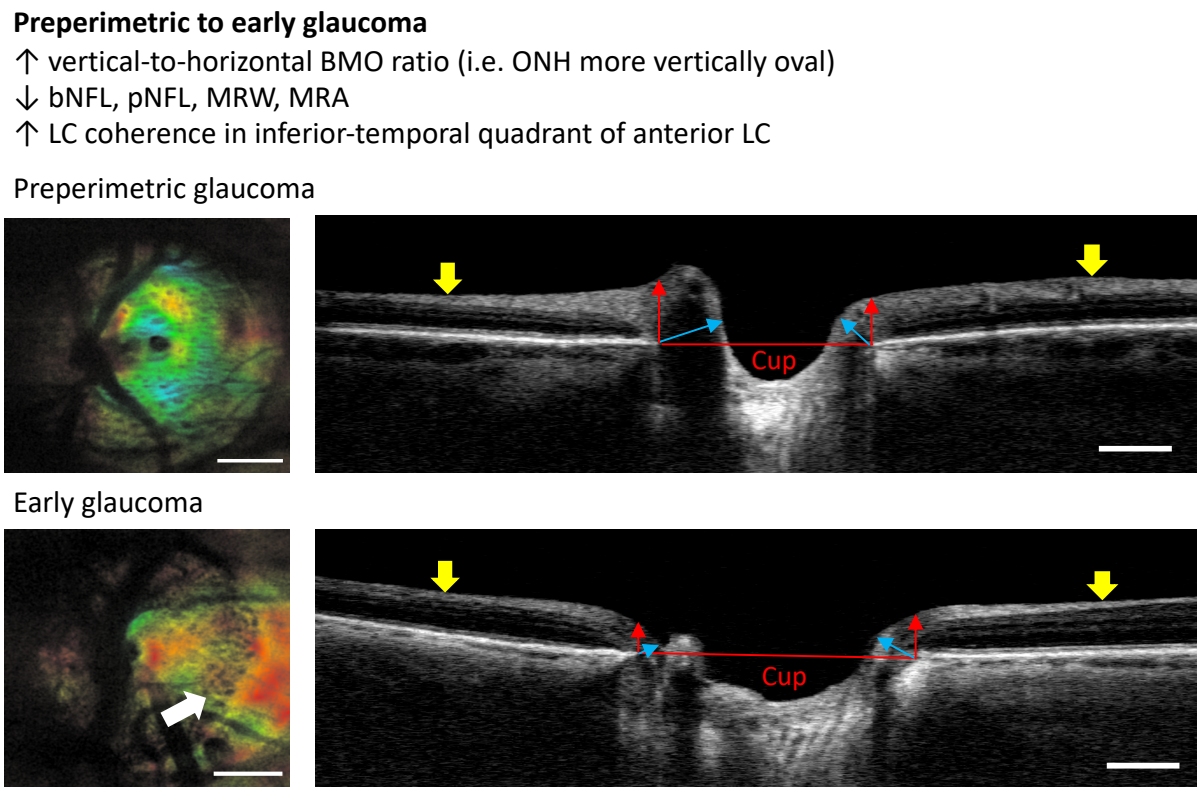

Figure 7.2: Summary of ONH and axon parameter differences between PG and EG ONHs; *Enface* OCT image slice through LC (left eyes) and OCT tomogram (IN-ST) indicate parameters: BMO (red line), bNFL (red arrows), pNFL (position of measurement denoted by yellow arrow heads), MRW (blue arrows). White arrowhead indicates higher LC coherence in IT quadrant of anterior LC. Scale bars = 500µm.

PG to EG	
RGC axon-related parameters	**ONH structural parameters**
• Thinning of bNFL in superior, inferior, SN, ST ONH regions • Thinning of pNFL in ST region • Loss of neuroretinal rim: reduction of MRW in inferior and ST regions • Reduction of MRA in inferior, nasal, IT, and ST regions • No significant difference in prelamina thickness in any ONH region • No significant difference in prelamina volume	• Increase in LC coherence in IT quadrant in anterior LC • Vertical to horizontal BMO diameter ratio larger in EG than PG, i.e. more vertically oval • No significant difference in prelamina depth in any ONH region • No significant difference in LC depth or thickness in any region • No significant difference in optic cup volume • No significant difference in LC volume • No significant difference in BMO surface area

Table 7.2: Summary of changes to ONH structure and axon-related parameters between preperimetric and early glaucoma. Red text indicates significant difference between glaucoma stages.

In chapter 5, *in vivo* analysis of LC microstructure identified an increase in LC coherence in EG compared to PG in the inferior-temporal quadrant of the anterior LC. This aligns with that found in the *ex vivo* LC, where Jones et al. (2015) reported increased LC coherence in early and advanced glaucomatous eyes in the inferior-temporal quadrant throughout the entire thickness of the LC compared to controls. However, not fully consistent with the *ex vivo* LC, as presented in chapter 5, LC coherence was increased in PG ONHs compared to controls in the superior region of the mid-posterior LC. Furthermore, as shown in chapter 5, LC coherence did not significantly differ between controls and EG or MAG groups in any region throughout the thickness of the LC. However, in the inferior-temporal quadrant of the anterior LC, EG and MAG ONHs displayed significantly higher LC coherence than that in the PG group. This indicated that at different stages of glaucoma disease, there are regional alterations in LC coherence that occur depth-wise through the LC. This suggests there are alterations to the LC connective tissue present in early glaucoma disease, which is consistent with that reported in human glaucoma (Hernandez et al., 1990; Hernandez et al., 2008) and monkey experimental glaucoma (Bellezza et al., 2003; Roberts et al., 2009; Roberts et al., 2010b). Alterations in LC connective tissue coherence found in this *in vivo* study would likely impact/reflect on the LC microarchitecture such as LC beam and pore parameters (Ivers et al.,

2011; Wang et al., 2013; Nadler et al., 2014). This implies that within the LC microstructure, there may be indicators to suggest glaucoma onset or progression. Thus, *in vivo* evaluation of the LC microarchitecture in more detail is intended for future work.

As shown above, BMO diameter did not significantly differ between control and PG ONHs, and additionally no differences were observed between PG and EG groups. However, in EG, the vertical-to-horizontal BMO ratio (which takes into account the ONH size) was significantly larger than in the PG group, i.e., the ONH became more vertically oval in EG compared to PG. This is consistent with Buteikiene et al. (2017) where in small optic discs (disc area <1.5mm^2), POAG ONHs were more vertically oval than control ONHs based on OCT-derived measures. Although, in medium (disc area between 1.5mm^2 and 2mm^2) and large (disc area >2mm^2) sized optic discs, optic disc shape did not significantly differ between POAG and controls. Jonas and Papastathopoulos (1996) reported that in highly myopic (> -8D refractive error) glaucomatous and non-glaucomatous eyes, optic disc shape was significantly more vertically oval than in glaucomatous and control eyes with refractive error less than -8D. However, in eyes with refractive error less than -8D, the control and glaucoma eyes did not significantly differ in the vertically oval optic disc shape. This difference to that found in this current study may be related to Jonas and Papastathopoulos (1996) including POAG, secondary OAG, and normal-tension glaucoma in their group of glaucoma participants; whereas this thesis study only included POAG participants. For instance, the normal-tension glaucoma participants may show less alteration to disc shape as their IOP is considered to be within normal range, since raised IOP in glaucoma has been reported to potentially exert stretch to the globe and may cause myopia (Perkins and Phelps, 1982). An explanation for the change in optic disc shape reported in this current study could be related to regional structural differences within the LC (Quigley and Addicks, 1981; Radius and Gonzales, 1981). Since the superior and inferior poles contain less connective tissue than the nasal-temporal LC, the superior and inferior regions (i.e., vertical ONH meridian) are perhaps weaker and more prone to stretch than the horizontal ONH meridian, and therefore resulting in an increase to ONH vertical ovality.

Differences observed in ONH and axon parameters between EG and MAG ONHs are summarised in Figure 7.3 and Table 7.3. The significant negative correlation of prelamina volume with loss of VF sensitivity observed was consistent with the smaller prelamina volume

in MAG, compared to the EG group. This aligns with chapter 6 data, whereby prelamina volume was considered less important than parameters such as prelamina depth and thickness, bNFL, MRW, and optic cup volume for early glaucoma detection, whereas prelamina volume identified differences at a later disease stage. For instance, in addition to prelamina volume; optic cup volume, prelamina depth and thickness, bNFL, pNFL, MRW, and MRA identified significant differences between EG and MAG (see Table 7.3 and Figure 7.3); indicating these parameters hold potential to detect disease progression. Therefore, as outlined in chapter 6, prelamina depth and thickness, bNFL, MRW, MRA, and optic cup volume were deemed the most appropriate parameters for early detection of glaucoma and characterisation of ONHs according to glaucoma disease stage.

Early to moderate-advanced glaucoma
↑ prelamina depth
↓ prelamina thickness
↓ bNFL, pNFL, MRW, MRA
↑ optic cup volume
↓ prelamina volume

Early glaucoma

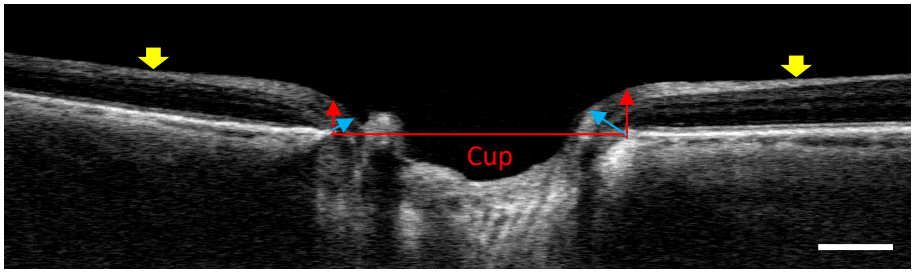

Moderate-advanced glaucoma

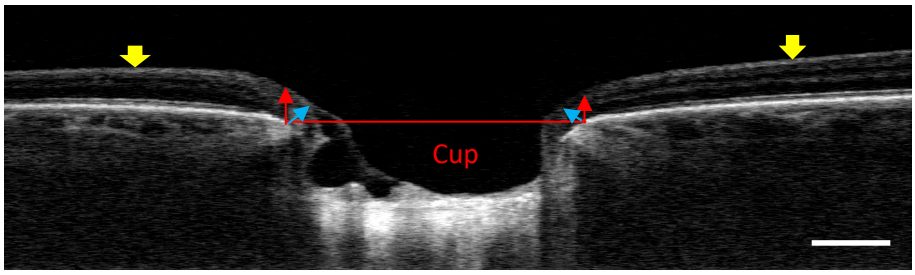

Figure 7.3: Summary of ONH and axon parameter differences between EG and MAG ONHs; OCT tomograms (IN-ST) indicate parameters: BMO (red line), bNFL (red arrows), pNFL (position of measurement denoted by yellow arrow heads), MRW (blue arrows). Scale bars = 500µm.

EG to MAG	
RGC axon-related parameters	**ONH structural parameters**
• Decrease in prelamina thickness in superior ONH region • Thinning of bNFL in all regions apart from temporal • Thinning of pNFL in inferior, temporal, IT and ST regions • Decrease in MRW in all regions apart from nasal and temporal • Decrease in MRA in superior and inferior ONH regions • Prelamina volume significantly less in MAG than EG	• Increase in prelamina depth in superior ONH region • Optic cup volume significantly larger in MAG than EG • Nasal-temporal BMO diameter significantly larger in MAG than EG • No significant difference in LC depth or thickness between MAG and EG in any ONH region (central LC thinner in MAG than PG) • No significant difference in LC volume • No significant difference in BMO surface area • No significant difference in LC coherence in any region, throughout full thickness of LC

Table 7.3: Summary of changes to ONH structure and axon-related parameters between early and moderate-advanced glaucoma. Red text indicates significant difference between glaucoma stages.

Anterior LC surface depth was found to significantly increase relative to BMO in all ONH regions with loss of VF function, although posterior LC surface depth did not significantly alter in any region with loss of VF sensitivity. This resulted in a significant decrease in LC volume and LC thickness in all regions with loss of visual function. Indeed, central LC thickness was significantly thinner in MAG than EG. Furthermore, LC depth did not significantly alter as a function of glaucoma stage in any ONH region, which contradicts previous reports of backward LC displacement in human glaucoma (Quigley et al., 1983; Tan et al., 2019) and monkey experimental glaucoma models (Yang et al., 2007b; Yang et al., 2011b) relative to BMO reference plane. In this study, an explanation for the lack of posterior LC migration may be that as the LC becomes stiffer with age (Albon et al., 1995; Albon et al., 2000b; Midgett et al., 2017), if glaucomatous eyes exhibited stiffer LCs (Zeimer and Ogura, 1989), then backward bowing of the LC would be less pronounced.

Since LC depth did not alter as a function of glaucoma disease stage these data were excluded from analyses performed within chapter 6. Additionally, LC volume and nasal measures of LC thickness were also excluded due to excessive missing observations caused by vascular

shadowing within the OCT image datasets. Due to this, LC depth, volume, and LC thickness in the nasal quadrant were considered less optimal for the characterisation of ONHs with respect to glaucoma disease. However, significant regional differences in LC thickness were identified in PG ONHs, prior to vision loss, and significant regional alteration in LC coherence was identified in early glaucoma stages (i.e., PG and EG); suggesting LC structural alterations are present in early disease. LC coherence data was not included in analyses performed in chapter 6 as at the time of analyses, the complete dataset for the entire cohort of participants was not available. Confirmation of such LC coherence alterations in early disease with an increased sample size is intended for future work.

Appropriate treatment and management of glaucoma disease is essential to maintain patient quality of life prior to decline of visual function (Hirooka et al., 2017). Therefore, detection of glaucoma onset using OCT may be of benefit in a primary care setting such as optometrists, as well as in a secondary care setting such as ophthalmologists to assist in clinical decision making.

Spectral domain OCT has allowed for segmentation and selective analysis of the inner retinal layers including the NFL, RGC layer, and inner plexiform layer, comprising the axons, cell bodies, and RGC dendrites respectively (Wang et al., 2009). Analysis performed on the segmented inner retinal layers has been shown to have improved glaucoma diagnostic ability than total macula thickness measures (Tan et al., 2009; Mori et al., 2010).

The most widely adopted OCT-based parameter in clinical assessment of glaucoma is evaluation of the peripapillary NFL (Sung et al., 2011; Bussel et al., 2014). However, OCT quantification of ONH parameters including NRR (Chauhan et al., 2013), cup-disc ratio and cup volume (Sung, Na and Lee, 2012; Fortune, 2019) have been shown to differentiate between healthy and glaucomatous eyes. Thus, the diagnostic accuracy of OCT-derived parameters has been shown to be improved when using a combination of OCT parameters providing structural information regarding the macula, NFL, and the ONH (Medeiros et al., 2005b; Mwanza et al., 2013), reviewed by (Grewal and Tanna, 2013; Mwanza et al., 2018).

However, using OCT with respect to glaucoma diagnosis, the Cochrane review (Michelessi et al., 2015) indicates that almost all studies in this field are case-control designed studies, which is known to overestimate accuracy (Mowatt et al., 2008). This leads to a high risk of bias as participants were not consecutively or randomly selected from a single, well-defined source population, but were identified as 'diseased' and 'non-diseased' *a priori* (Oddone et al., 2016). Ideally, participants included in OCT-based glaucoma diagnosis studies should be a consecutive series of patients with risk factors for glaucoma including a family history of glaucoma, or patients with mild ocular hypertension, who were screened by OCT to evaluate the requirement of referral to ophthalmologists (Oddone et al., 2016).

In glaucoma, it has been reported there is definite loss of RGC axons prior to reproducible VF defects, leading to ONH structural alterations (Quigley et al., 1982; Centofanti et al., 2005). Additionally, due to its asymptomatic nature, even among people with glaucoma, only approximately half of them are aware they have the disease in developed countries, and even fewer in low-middle income countries (Quigley, 2011). Since there is a dissociation between structure and function in glaucoma, and the fact that the disease is slowly progressive by nature, longer duration follow-up studies are needed to establish whether OCT-derived structural information can highlight predisposition to subsequent development of VF loss (Kotowski et al., 2014). Therefore, longitudinal predictions from OCT structural analysis may aid in early glaucoma diagnosis and improve disease prognosis.

Elevated IOP is considered the principal modifiable risk factor for POAG development and disease progression (Heijl et al., 2002; Davis et al., 2016). Current treatment methods for POAG involve lowering IOP via therapeutic or surgical methods that aims to slow/halt disease progression and preserve the patient's visual function (Weinreb et al., 2016; Schuster et al., 2020).

Following acute IOP elevation in human eyes, Agoumi et al. (2011) reported compression and backward displacement of prelamina tissues. Additionally, using monkey eyes with elevated IOP, Yang et al. (2011b) reported posterior migration of the LC. Furthermore, following IOP reduction in human eyes there has been shown to be thickening of prelamina tissues (Reis et al., 2012a), and anterior movement of the LC (Reis et al., 2012a; Lee et al., 2013a). Thus,

alterations in IOP play a role in ONH structure and influence ONH parameters. Therefore, parameters that influence IOP may act as confounders for *in vivo* quantification of ONH structure. A confounder is a variable whose presence affects both the dependent and independent variables under investigation so that the results do not reflect the actual relationship and may lead to spurious associations (Pourhoseingholi, Baghestani and Vahedi, 2012).

The prevalence of POAG is strongly age-related (Sommer et al., 1991b; Leske et al., 2008). However, there have been conflicting reports describing the association between increasing age and IOP, with some studies reporting an increase in IOP with age (Wu and Leske, 1997; Bonomi et al., 1998), and others reporting a decrease in IOP with age (Shiose, 1990). Alternatively, other studies report no significant association between age and IOP (Hirvela, Tuulonen and Laatikainen, 1994; Rochtchina, Mitchell and Wang, 2002). McLeod et al. (1990) reported that while IOP does not necessarily increase with age, IOP was positively correlated with a change in systolic blood pressure.

Topical glaucoma medications have been shown to be effective in lowering IOP and reducing VF deterioration (Crowston and Weinreb, 2005; Garway-Heath et al., 2015). Furthermore, the use of systemic beta-blockers and nitrates have been shown to be significantly associated with lower IOP (Khawaja et al., 2014), and may protect against development of glaucoma (Owen et al., 2010). Additionally, the use of statins has been associated with a significant reduction in the risk of POAG development (Leung et al., 2010c; Stein et al., 2012). De Castro et al. (2007) suggest that statin drugs may be associated with slowed progression of ONH parameters such as neuroretinal rim volume and RNFL thickness in longitudinal evaluation of glaucoma suspects. However, other studies do not indicate a preventive role of statins against glaucoma (Iskedjian et al., 2009; Owen et al., 2010). Participants with systemic hypertension or diabetes mellitus showed an increased risk of developing POAG compared to persons with neither of these conditions, whereas persons with hyperlipidaemia showed a decreased risk of glaucoma (Newman-Casey et al., 2011).

Therefore, there may be several extraneous confounding variables such as age, IOP, systemic disease and medications that could affect the development and progression of POAG and

hold influence over ONH structure. Therefore, these confounding factors should be taken into account when using ONH structural parameters as biomarkers to indicate glaucoma disease stage. Controlling for confounding variables (e.g., via use of regression models as performed in this thesis study) may have implications in the interpretation of ONH structure and management of glaucoma patients with comorbidity, which may provide insight into the pathophysiologic processes of glaucoma.

In summary, data analysed in this thesis study has determined that the optimal parameters that allow for the best indication of glaucoma onset and/or could be used to suggest disease progression, are parameters relating to the anterior ONH structure, such as prelamina depth and optic cup volume, and RGC axon-related parameters quantified within the ONH, such as prelamina thickness, bNFL, MRW, MRA. Findings from this thesis study suggest that *in vivo* ONH and axon-related parameters may provide clinically relevant quantitative features that could be used alongside the glaucoma risk stratification system, as developed by Shah et al. (2020 - in preparation). Such parameters could act to supplement clinical decision making by the indication of glaucoma participants at higher risk of disease development and vision loss.

VII.1 Limitations of study

Light cast upon structures causes shadowing, which, in OCT imaging is inevitable. Retinal vasculature and/or prelamina neural tissue can cause significant shadows within OCT images of the ONH (Lucy et al., 2015). The presence of shadows within the OCT image datasets was a limitation in this thesis study. Vascular or neural tissue shadowing prevented measurement of prelamina thickness and volume, and LC depth, thickness and volume. Additionally, in chapter 5, analysis of LC coherence was not possible in the nasal side of the ONH. Due to the proportion of missing observations caused by vascular or neural tissue shadowing this meant that parameters including measurements of nasal prelamina and LC thickness, and LC volume were excluded from multivariate analyses performed in chapter 6; therefore, influencing which ONH parameters were deemed optimal for the characterisation of ONHs according to glaucoma disease stage. Due to this drawback with OCT images, processing techniques have been developed such as algorithms to aid in the removal of vascular shadows and compensate for OCT signal attenuation. Additionally, a reduction in image noise overamplification can

improve contrast of deep ocular structures such as the LC and improve tissue boundaries (Girard et al., 2011; Mari et al., 2013; Girard et al., 2015). However, such algorithms have not yet been deemed optimal to improve visualisation of ONH structures in OCT image datasets acquired using the custom-built OCT device used in this thesis study.

In order to calculate prelamina thickness and volume, both the prelamina surface and anterior LC surface had to be visualised and demarcated. Similarly, calculation of LC thickness and volume relies upon visualisation of both anterior and posterior LC surfaces. On occasion, this was prevented by not only shadowing within the OCT images, but also OCT signal attenuation with increasing axial depth within the ONH. For example, in control participants with thicker prelamina tissue than glaucoma participants, this made visualisation of the anterior and particularly the posterior LC surface more difficult. Swept-source OCT may allow for improved tissue penetration and visualisation of the LC, thereby aiding in measurement of prelamina thickness and volume, and LC thickness and volume.

To allow greater image resolution, LC coherence data analysed in chapter 5 were acquired using 10° SD-OCT image datasets. This resulted in a scan width at the retina of approximately 3mm. Due to this narrow scan width, the 10° OCT image datasets were more prone to motion artefacts; as such, 4 OCT image datasets were excluded as a result of excessive eye movements. Currently, the research-based OCT device used in this thesis study does not incorporate an eye-tracking system. This technology could allow for less motion artefacts within the OCT images, and therefore fewer OCT images excluded, which is advantageous for data acquisition and analysis.

In this thesis study, the majority of glaucoma participants recruited in this study were in the EG group, with fewer participants in the PG and MAG groups. Therefore, since participant numbers were uneven amongst disease stage groups, the addition of participants to PG and MAG this may lead to more conclusive analyses as to which ONH features best indicate glaucoma onset at its earliest stages and potentially suggest disease progression. Additionally, there was a difference in age between the control and glaucoma participants, which may represent a flaw in analysis. However, to address this, using multiple linear regression models, where increasing age was found to have a significant effect on a given ONH parameter, age

was included in the regression model to take into consideration the difference in age between participant groups.

VII.2 Conclusion

This thesis was aimed at the characterisation of ONH structural and RGC axon-related parameters as a function of glaucoma disease stage in order to identify biomarkers that could be used to indicate glaucoma onset at its earliest stages (prior to permanent vision loss), and so such biomarkers could hold potential to suggest disease progression.

Multivariate analyses identified ONH structural alterations (such as increased prelamina depth and optic cup volume) and loss of RGC axons (i.e., thinner prelamina, bNFL, MRW, and MRA), as early indicators of glaucoma onset. Furthermore, regional LC thickness was significantly less in PG, and LC coherence altered depth-wise through the LC; in PG (superior region of mid-posterior LC) and EG (inferior-temporal region of anterior LC). This suggests there are significant LC structural alterations present in early glaucomatous disease which could further aid in glaucoma detection and potentially gain a better understanding of the glaucoma disease process.

VII.3 Future work

- Increase participant number for analysis of LC coherence to confirm the regional and depth-related changes in LC structure reported in early glaucoma ONHs. In Chapter 5, data was acquired using 10° OCT image datasets to allow for greater resolution of LC parameters, however, data acquisition was not possible in all OCT datasets due to motion artefacts due to small eye movements. Therefore, in future, the use of an eye tracking system during OCT image acquisition would counteract this difficulty and improve OCT image quality.

- Evaluate regional LC pore morphometry parameters in 10° *in vivo* ONH OCT datasets; with aim to determine potential biomarkers within the LC microarchitecture to indicate early glaucoma onset or suggest disease progression and gain a better understanding of LC microstructural changes that occur in glaucoma.

- Develop techniques to perform textural analysis as a surrogate to assess LC connective tissue and/or RGC axon-related changes at a resolution appropriate for OCT image analyses.

- The macula region of the retina contains the largest concentration of RGCs (Curcio and Allen, 1990). During the course of this thesis study, 20° SD-OCT scans centred on the macula were acquired from all participants included. Future work would involve retinal layer segmentation and thickness analysis based on these macula OCT image datasets. Inner retinal layer thicknesses will be used as a surrogate measure to evaluate RGC loss and potential retinal layer remodelling according to glaucoma disease stage.

- All OCT image analysis techniques described in this thesis would be vastly improved if accurate removal of vascular shadows from the OCT datasets could be achieved. Adaptive compensation algorithms have improved such image processing techniques (Girard et al., 2011; Mari et al., 2013; Girard et al., 2015), however, such algorithms have not yet allowed sufficient improvement to OCT images acquired with the custom-built OCT device used in this thesis. Future work would intend to adapt/develop image post-processing techniques to aid in OCT shadow removal and enhance visibility of ONH structures.

- Increase participant number for additional analysis of parameters such as LC thickness and volume as these were indicated to be important factors in glaucomatous optic neuropathy (Chapter 3 identified that LC thickness altered as function of disease stage). Additionally, Chapter 5 suggested that there was an alteration in LC coherence in early glaucoma disease, consistent with an *ex vivo* study of the LC (Jones et al., 2015).

- Acquire image datasets using a long-wavelength swept-source OCT system (now commercially available) to enable better penetration through the depth of the ONH and less signal attenuation. It is anticipated that this would allow for better image

quality and clearer delineation of the anterior and posterior LC surface boundaries. Therefore, this would enable measurement of prelamina thickness and volume, and LC thickness and volume in more participants, resulting in less missing observations within the ONH dataset.

- Multivariate analysis indicated that parameters such as prelamina depth and thickness, bNFL, MRW, MRA, and optic cup volume were optimal for the characterisation of ONHs according to glaucoma disease stage. However, this subset of parameters did not achieve full separation of participant groups (i.e. controls, PG, EG, and MAG). An increased number of participants in each stage of glaucoma (particularly PG and MAG) may achieve more adequate separation of participant groups; with aim to further refine which ONH parameters provide the best indication of glaucoma development or disease progression.

References

Abrams L S, Scott I U, Spaeth G L, Quigley H A, and Varma R (1994) Agreement among optometrists, ophthalmologists, and residents in evaluating the optic disc for glaucoma. *Ophthalmology* 101: 1662-1667.

Adhi M, and Duker J S (2013) Optical coherence tomography - current and future applications. *Current Opinion in Ophthalmology* 24: 213-221.

Agawa T, Miura M, Ikuno Y, Makita S, Fabritius T, Iwasaki T, Goto H et al. (2011) Choroidal thickness measurement in healthy Japanese subjects by three-dimensional high-penetration optical coherence tomography. *Graefes Archive for Clinical and Experimental Ophthalmology* 249: 1485-1492.

Agoumi Y, Sharpe G P, Hutchison D M, Nicolela M T, Artes P H, and Chauhan B C (2011) Laminar and Prelaminar Tissue Displacement During Intraocular Pressure Elevation in Glaucoma Patients and Healthy Controls. *Ophthalmology* 118: 52-59.

Agurto C, Barriga E S, Murray V, Nemeth S, Crammer R, Bauman W, Zamora G et al. (2011) Automatic Detection of Diabetic Retinopathy and Age-Related Macular Degeneration in Digital Fundus Images. *Investigative Ophthalmology & Visual Science* 52: 5862-5871.

Ahmed F, Chaudhary P, and Sharma S C (2001) Effects of increased intraocular pressure on rat retinal ganglion cells. *International Journal of Developmental Neuroscience* 19: 209-218.

Akagi T, Hangai M, Kimura Y, Ikeda H O, Nonaka A, Matsumoto A, Akiba M et al. (2013) Peripapillary Scleral Deformation and Retinal Nerve Fiber Damage in High Myopia Assessed With Swept-Source Optical Coherence Tomography. *American Journal of Ophthalmology* 155: 927-936.

Akagi T, Hangai M, Takayama K, Nonaka A, Ooto S, and Yoshimura N (2012) In Vivo Imaging of Lamina Cribrosa Pores by Adaptive Optics Scanning Laser Ophthalmoscopy. *Investigative Ophthalmology & Visual Science* 53: 4111-4119.

Akoglu H (2018) User's guide to correlation coefficients. *Turkish Journal of Emergency Medicine* 18: 91-93.

Al-Kandari N M, and Jolliffe I T (2005) Variable selection and interpretation in correlation principal components. *Environmetrics* 16: 659-672.

Albon J, Karwatowski W S S, Avery N, Easty D L, and Duance V C (1995) Changes in the collagenous matrix of the aging human lamina-cribrosa. *British Journal of Ophthalmology* 79: 368-375.

Albon J, Karwatowski W S S, Easty D L, Sims T J, and Duance V C (2000a) Age related changes in the non-collagenous components of the extracellular matrix of the human lamina cribrosa. *British Journal of Ophthalmology* 84: 311-317.

Albon J, Purslow P P, Karwatowski W S S, and Easty D L (2000b) Age related compliance of the lamina cribrosa in human eyes. *British Journal of Ophthalmology* 84: 318-323.

Almasieh M, Wilson A M, Morquette B, Vargas J L C, and Di Polo A (2012) The molecular basis of retinal ganglion cell death in glaucoma. *Progress in Retinal and Eye Research* 31: 152-181.

An G Z, Omodaka K, Tsuda S, Shiga Y, Takada N, Kikawa T, Nakazawa T et al. (2018) Comparison of Machine-Learning Classification Models for Glaucoma Management. *Journal of Healthcare Engineering* 2018.

Anderson D R (1969) Ultrastructure of human and monkey lamina cribrosa and optic nerve head. *Archives of Ophthalmology* 82: 800-&.

Anderson D R, Feuer W, and Schiffman J (2008) Normal-tension glaucoma. *Ophthalmology* 115: 590-591.

Anderson D R, and Hoyt W F (1969) Ultrastructure of intraorbital portion of human and monkey optic nerve. *Archives of Ophthalmology* 82: 506-530.

Anderson D R, Hoyt W F, and Hogan M J (1967) The fine structure of the astroglia in the human optic nerve and optic nerve head. *Trans Am Ophthalmol Soc* 65: 275-305.

Anderson R S (2006) The psychophysics of glaucoma: Improving the structure/function relationship. *Progress in Retinal and Eye Research* 25: 79-97.

Ang L P K, Aung T, Chua W H, Yip L W, and Chew P T K (2004) Visual field loss from primary angle closure glaucoma: A comparative study of symptomatic and asymptomatic disease. *Ophthalmology* 111: 1636-1640.

ANSI (2000) Safe use of lasers & safe use of optical fiber communications. *American National Standards Institute - Z136 Committee. Orlando Laser Institute America*: 168-173.

Anton A, Moreno-Montanes J, Blazquez F, Alvarez A, Martin B, and Molina B (2007) Usefulness of optical coherence tomography parameters of the optic disc and the retinal nerve fiber layer to differentiate glaucomatous, ocular hypertensive, and normal eyes. *Journal of Glaucoma* 16: 1-8.

Arintawati P, Sone T, Akita T, Tanaka J, and Kiuchi Y (2013) The Applicability of Ganglion Cell Complex Parameters Determined From SD-OCT Images to Detect Glaucomatous Eyes. *Journal of Glaucoma* 22: 713-718.

Arthur S N, Aldridge A J, De Leon-Ortega J, McGwin G, Xie A Y, and Girkin C A (2006) Agreement in assessing cup-to-disc ratio, measurement among stereoscopic optic nerve head photographs, HRT II, and stratus OCT. *Journal of Glaucoma* 15: 183-189.

Aung T, Friedman D S, Chew P T K, Ang L P, Gazzard G, Lai Y F, Yip L et al. (2004) Long-term outcomes in Asians after acute primary angle closure. *Ophthalmology* 111: 1464-1469.

Azuara-Blanco A, Katz L J, Spaeth G L, Vernon S A, Spencer F, and Lanzl I M (2003) Clinical agreement among glaucoma experts in the detection of glaucomatous changes of the optic disk using simultaneous stereoscopic photographs. *American Journal of Ophthalmology* 136: 949-950.

Babyak M A (2004) What you see may not be what you get: A brief, nontechnical introduction to overfitting in regression-type models. *Psychosomatic Medicine* 66: 411-421.

Balaratnasingam C, Morgan W H, Bass L, Matich G, Cringle S J, and Yu D Y (2007) Axonal transport and cytoskeletal changes in the laminar regions after elevated intraocular pressure. *Investigative Ophthalmology & Visual Science* 48: 3632-3644.

Barella K A, Costa V P, Vidotti V G, Silva F R, Dias M, and Gomi E S (2013) Glaucoma Diagnostic Accuracy of Machine Learning Classifiers Using Retinal Nerve Fiber Layer and Optic Nerve Data from SD-OCT. *Journal of Ophthalmology* 2013.

Barrancos C, Rebolleda G, Oblanca N, Cabarga C, and Munoz-Negrete F J (2014) Changes in lamina cribrosa and prelaminar tissue after deep sclerectomy. *Eye* 28: 58-65.

Bathija R, Zangwill L, Berry C, Sample P A, and Weinreb R N (1998) Detection of early glaucomatous structural damage with confocal scanning laser tomography. *Journal of Glaucoma* 7: 121-127.

Beck R W, Servais G E, and Hayreh S S (1987) Anterior ischemic optic neuropathy .IX. Cup-to-disk ratio and its role in pathogenesis. *Ophthalmology* 94: 1503-1508.

Belghith A, Bowd C, Medeiros F A, Hammel N, Yang Z Y, Weinreb R N, and Zangwill L M (2016a) Does the Location of Bruch's Membrane Opening Change Over Time? Longitudinal Analysis Using San Diego Automated Layer Segmentation Algorithm (SALSA). *Investigative Ophthalmology & Visual Science* 57: 675-682.

Belghith A, Medeiros F A, Bowd C, Liebmann J M, Girkin C A, Weinreb R N, and Zangwill L M (2016b) Structural change can be detected in advanced glaucoma eyes. *Investigative Ophthalmology & Visual Science* 57: 511-518.

Bellezza A J, Hart R T, and Burgoyne C F (2000) The optic nerve head as a biomechanical structure: Initial finite element modeling. *Investigative Ophthalmology & Visual Science* 41: 2991-3000.

Bellezza A J, Rintalan C J, Thompson H W, Downs J C, Hart R T, and Burgoyne C F (2003) Deformation of the lamina cribrosa and anterior scleral canal wall in early experimental glaucoma. *Investigative Ophthalmology & Visual Science* 44: 623-637.

Bellman R E (1957) Dynamic programming. *Princeton University Press*.

Bennett A G, Rudnicka A R, and Edgar D F (1994) Improvements on littmann method of determining the size of retinal features by fundus photography. *Graefes Archive for Clinical and Experimental Ophthalmology* 232: 361-367.

Bhandari A, Fontana L, Fitzke F W, and Hitchings R A (1997) Quantitative analysis of the lamina cribrosa in vivo using a scanning laser opthalmoscope. *Current Eye Research* 16: 1-8.

Birnbaum A, Johnstone I M, Nadler B, and Paul D (2013) Minimax bounds for sparse PCA with noisy high dimensional data. *Annals of Statistics* 41: 1055-1084.

Bland J M, and Altman D G (1986) Statistical Methods For Assessing Agreement Between Two Methods of Clinical Measurement. *Lancet* 1: 307-310.

Bland J M, and Altman D G (1996) Statistics notes: Measurement error proportional to the mean. *British Medical Journal* 313: 106-106.

Blumberg D M, De Moraes C G, Liebmann J M, Garg R, Chen C, Theventhiran A, and Hood D C (2016) Technology and the Glaucoma Suspect. *Investigative Ophthalmology & Visual Science* 57: OCT80-OCT85.

Boland M V, Ervin A M, Friedman D S, Jampel H D, Hawkins B S, Vollenweider D, Chelladurai Y et al. (2013) Comparative Effectiveness of Treatments for Open-Angle Glaucoma: A Systematic Review for the U.S. Preventive Services Task Force. *Annals of Internal Medicine* 158: 271-279.

Boland M V, and Quigley H A (2011) Evaluation of a combined index of optic nerve structure and function for glaucoma diagnosis. *Bmc Ophthalmology* 11.

Boland M V, Zhang L, Broman A T, Jampel H D, and Quigley H A (2008) Comparison of optic nerve head topography and visual field in eyes with open-angle and angle-closure glaucoma. *Ophthalmology* 115: 239-245.

Bonomi L, Marchini G, Marraffa M, Bernardi P, De Franco I, Perfetti S, Varotto A et al. (1998) Prevalence of glaucoma and intraocular pressure distribution in a defined population - The Egna-Neumarkt study. *Ophthalmology* 105: 209-215.

Boulton G, Rawlins M, Vallance P, and Walport M (2011) Science as a public enterprise: the case for open data. *Lancet* 377: 1633-1635.

Bourne R R A, Taylor H R, Flaxman S R, Keeffe J, Leasher J, Naidoo K, Pesudovs K et al. (2016) Number of People Blind or Visually Impaired by Glaucoma Worldwide and in World Regions 1990-2010: A Meta-Analysis. *Plos One* 11.

Bowd C, Weinreb R N, Williams J M, and Zangwill L M (2000) The retinal nerve fiber layer thickness in ocular hypertensive, normal, and glaucomatous eyes with optical coherence tomography. *Archives of Ophthalmology* 118: 22-26.

Bowling B, Chen S D M, and Salmon J F (2005) Outcomes of referrals by community optometrists to a hospital glaucoma service. *British Journal of Ophthalmology* 89: 1102-1104.

Breusegem C, Fieuws S, Stalmans I, and Zeyen T (2011) Agreement and Accuracy of Non-Expert Ophthalmologists in Assessing Glaucomatous Changes in Serial Stereo Optic Disc Photographs. *Ophthalmology* 118: 742-746.

Broman A T, Quigley H A, West S K, Katz J, Munoz B, Bandeen-Roche K, Tielsch J M et al. (2008) Estimating the rate of progressive visual field damage in those with open-angle glaucoma, from cross-sectional data. *Investigative Ophthalmology & Visual Science* 49: 66-76.

Brubaker R F (1991) Flow of aqueous-humor in humans - the friedenwald lecture. *Investigative Ophthalmology & Visual Science* 32: 3145-3166.

Budde W M, and Jonas J B (1999) Morphology of the optic disc in glaucoma. I. Primary open-angle glaucomas. *Klinische Monatsblatter Fur Augenheilkunde* 215: 211-220.

Budenz D L, Barton K, Whiteside-de Vos J, Schiffman J, Bandi J, Nolan W, Herndon L et al. (2013) Prevalence of Glaucoma in an Urban West African Population The Tema Eye Survey. *Jama Ophthalmology* 131: 651-658.

Budenz D L, Chang R T, Huang X R, Knighton R W, and Tielsch J M (2005) Reproducibility of retinal nerve fiber thickness measurements using the stratus OCT in normal and glaucomatous eyes. *Investigative Ophthalmology & Visual Science* 46: 2440-2443.

Budenz D L, Rhee P, Feuer W J, McSoley J, Johnson C A, and Anderson D R (2002) Comparison of glaucomatous visual field defects using standard full threshold and Swedish interactive threshold algorithms. *Archives of Ophthalmology* 120: 1136-1141.

Bunce C, and Wormald R (2008) Causes of blind certifications in England and Wales: April 1999 to March 2000. *Eye* 22: 905-911.

Bunce C, Xing W, and Wormald R (2010) Causes of blind and partial sight certifications in England and Wales: April 2007-March 2008. *Eye* 24: 1692-1699.

Burgansky-Eliash Z, Wollstein G, Chu T J, Ramsey J D, Glymour C, Noecker R J, Ishikawa H et al. (2005) Optical coherence tomography machine learning classifiers for glaucoma detection: A preliminary study. *Investigative Ophthalmology & Visual Science* 46: 4147-4152.

Burgoyne C F (2011) A biomechanical paradigm for axonal insult within the optic nerve head in aging and glaucoma. *Experimental Eye Research* 93: 120-132.

Burgoyne C F, and Downs J C (2008) Premise and prediction - How optic nerve head biomechanics underlies the susceptibility and clinical behavior of the aged optic nerve head. *Journal of Glaucoma* 17: 318-328.

Burgoyne C F, Downs J C, Bellezza A J, and Hart R T (2004) Three-dimensional reconstruction of normal and early glaucoma monkey optic nerve head connective tissues. *Investigative Ophthalmology & Visual Science* 45: 4388-4399.

Burgoyne C F, Downs J C, Bellezza A J, Suh J K F, and Hart R T (2005) The optic nerve head as a biomechanical structure: a new paradigm for understanding the role of IOP-related stress and strain in the pathophysiology of glaucomatous optic nerve head damage. *Progress in Retinal and Eye Research* 24: 39-73.

Burgoyne C F, Thompson H, Roberts V, Sigal I A, Downs J, and Yang H (2010) Deformation of the Early Glaucomatous Monkey Optic Nerve Head Connective Tissue Following Acute IOP Elevation Within 3-D Histomorphometric Reconstructions. *Investigative Ophthalmology & Visual Science* 51.

Burk R O W, Rohrschneider K, Noack H, and Volcker H E (1992) Are large optic nerve heads susceptible to glaucomatous damage at normal intraocular-pressure - a 3-dimensional study by laser scanning tomography. *Graefes Archive for Clinical and Experimental Ophthalmology* 230: 552-560.

Burlina P M, Joshi N, Pekala M, Pacheco K D, Freund D E, and Bressler N M (2017) Automated Grading of Age-Related Macular Degeneration From Color Fundus Images Using Deep Convolutional Neural Networks. *Jama Ophthalmology* 135: 1170-1176.

Bussel, II, Wollstein G, and Schuman J S (2014) OCT for glaucoma diagnosis, screening and detection of glaucoma progression. *British Journal of Ophthalmology* 98: 15-19.

Buteikiene D, Kybartaite-Ziliene A, Kriauciuniene L, Barzdziukas V, Januleviciene I, and Paunksnis A (2017) Morphometric parameters of the optic disc in normal and glaucomatous eyes based on time-domain optical coherence tomography image analysis. *Medicina-Lithuania* 53: 242-252.

Cadima J, and Jolliffe I (2009) On relationships between uncentred and column centred principal component analysis. *Pakistan Journal of Statistics* 25: 473-503.

Cadima J, and Jolliffe I T (1995) Loadings and correlations in the interpretation of principal components. *Journal of Applied Statistics* 22: 203-214.

Cadima J, and Jolliffe I T (1996) Size and shape-related principal component analysis. *Biometrics* 52: 710-716.

Caprioli J (1989) Correlation of visual function with optic-nerve and nerve-fiber layer structure in glaucoma. *Survey of Ophthalmology* 33: 319-330.

Caprioli J, and Miller J M (1987) Optic disk rim area is related to disk size in normal subjects. *Archives of Ophthalmology* 105: 1683-1685.

Caprioli J, Sears M, and Miller J M (1987) Patterns of early visual field loss in open angle glaucoma. *American Journal of Ophthalmology* 103: 512-517.

Cattell R B (1966) The Scree test for the number of factors. *Multivariate behavioral research* 1: 245-276.

Centofanti M, Zeyen T, Miglior S, and European Glaucoma Prevention S (2005) Results of the European Glaucoma Prevention Study. *Ophthalmology* 112: 366-375.

Chauhan B C, Drance S M, Douglas G R, and Johnson C A (1989) Visual field damage in normal-tension and high-tension glaucoma. *American Journal of Ophthalmology* 108: 636-642.

Chauhan B C, and Johnson C A (1999) Test-retest variability of frequency-doubling perimetry and conventional perimetry in glaucoma patients and normal subjects. *Investigative Ophthalmology & Visual Science* 40: 648-656.

Chauhan B C, O'Leary N, AlMobarak F A, Reis A S C, Yang H L, Sharpe G P, Hutchison D M et al. (2013) Enhanced Detection of Open-angle Glaucoma with an Anatomically Accurate Optical Coherence Tomography-Derived Neuroretinal Rim Parameter. *Ophthalmology* 120: 535-543.

Chi T, Ritch R, Stickler D, Pitman B, Tsai C, and Hsieh F Y (1989) Racial differences in optic nerve head parameters. *Archives of Ophthalmology* 107: 836-839.

Cho J W, Sung K R, Yun S C, Na J H, Lee Y, and Kook M S (2012) Progression detection in different stages of glaucoma: mean deviation versus visual field index. *Japanese Journal of Ophthalmology* 56: 128-133.

Choma M A, Sarunic M V, Yang C H, and Izatt J A (2003) Sensitivity advantage of swept source and Fourier domain optical coherence tomography. *Optics Express* 11: 2183-2189.

Chrysostomou V, Rezania F, Trounce I A, and Crowston J G (2013) Oxidative stress and mitochondrial dysfunction in glaucoma. *Current Opinion in Pharmacology* 13: 12-15.

Chung E, Demetriades A M, Christos P J, and Radcliffe N M (2015) Structural glaucomatous progression before and after occurrence of an optic disc haemorrhage. *British Journal of Ophthalmology* 99: 21-25.

Cohen J (1992) A power primer. *Psychological Bulletin* 112: 155-159.

Coleman A L (1999) Glaucoma. *Lancet* 354: 1803-1810.

Congalton R G (1991) A review of assessing the accuracy of classifications of remotely sensed data. *Remote Sensing of Environment* 37: 35-46.

Congdon N, Wang F, and Tielsch J M (1992) Issues in the epidemiology and population-based screening of primary angle-closure glaucoma. *Survey of Ophthalmology* 36: 411-423.

Crowston J G, and Weinreb R N (2005) Glaucoma medication and aqueous humor dynamics. *Current Opinion in Ophthalmology* 16: 94-100.

Cull G A, Reynaud J, Wang L, Cioffi G A, Burgoyne C F, and Fortune B (2012) Relationship between Orbital Optic Nerve Axon Counts and Retinal Nerve Fiber Layer Thickness Measured by Spectral Domain Optical Coherence Tomography. *Investigative Ophthalmology & Visual Science* 53: 7766-7773.

Curcio C A, and Allen K A (1990) Topography of ganglion-cells in human retina. *Journal of Comparative Neurology* 300: 5-25.

Daling J R, and Tamura H (1970) Use of orthogonal factors for selection of variables in a regression equation - illustration. *The Royal Statistical Society Series C-Applied Statistics* 19: 260-268.

Dandona L, Quigley H A, Brown A E, and Enger C (1990) Quantitative regional structure of the normal human lamina cribrosa - a racial comparison. *Archives of Ophthalmology* 108: 393-398.

Davis B M, Crawley L, Pahlitzsch M, Javaid F, and Cordeiro M F (2016) Glaucoma: the retina and beyond. *Acta Neuropathologica* 132: 807-826.

Day A C, Baio G, Gazzard G, Bunce C, Azuara-Blanco A, Munoz B, Friedman D S et al. (2012) The prevalence of primary angle closure glaucoma in European derived populations: a systematic review. *British Journal of Ophthalmology* 96: 1162-1167.

De Castro D K, Punjabi O S, Bostrom A G, Stamper R L, Lietman T M, Ray K, and Lin S C (2007) Effect of statin drugs and aspirin on progression in open-angle glaucoma suspects using confocal scanning laser ophthalmoscopy. *Clinical and Experimental Ophthalmology* 35: 506-513.

Deeks J J (2001) Systematic reviews in health care - Systematic reviews of evaluations of diagnostic and screening. *British Medical Journal* 323: 157-162.

DeLeon-Ortega J E, Arthur S N, McGwin G, Xie A Y, Monheit B E, and Girkin C A (2006) Discrimination between glaucomatous and nonglaucomatous eyes using quantitative imaging devices and subjective optic nerve head assessment. *Investigative Ophthalmology & Visual Science* 47: 3374-3380.

Devalla S K, Chin K S, Mari J M, Tun T A, Strouthidis N G, Aung T, Thiery A H et al. (2018a) A Deep Learning Approach to Digitally Stain Optical Coherence Tomography Images of the Optic Nerve Head. *Investigative Ophthalmology & Visual Science* 59: 63-74.

Devalla S K, Liang Z, Pham T H, Boote C, Strouthidis N G, Thiery A H, and Girard M J A (2020) Glaucoma management in the era of artificial intelligence. *British Journal of Ophthalmology* 104: 301-311.

Devalla S K, Renukanand P K, Sreedhar B K, Subramanian G, Zhang L, Perera S, Mari J M et al. (2018b) DRUNET: a dilated-residual U-Net deep learning network to segment optic nerve head tissues in optical coherence tomography images. *Biomedical Optics Express* 9: 3244-3265.

Dong Z M, Wollstein G, Wang B, and Schuman J S (2017) Adaptive optics optical coherence tomography in glaucoma. *Progress in Retinal and Eye Research* 57: 76-88.

Donoho D L, Maleki A, Shahram M, Rahman I U, and Stodden V (2009) Reproducible Research in Computational Harmonic Analysis. *Computing in Science & Engineering* 11: 8-18.

Downs J C (2015) Optic nerve head biomechanics in aging and disease. *Experimental Eye Research* 133: 19-29.

Downs J C, and Girkin C A (2017) Lamina cribrosa in glaucoma. *Current Opinion in Ophthalmology* 28: 113-119.

Downs J C, Roberts M D, and Burgoyne C F (2008) Mechanical environment of the optic nerve head in glaucoma. *Optometry and Vision Science* 85: 425-435.

Downs J C, Roberts M D, and Sigal I A (2011) Glaucomatous cupping of the lamina cribrosa: A review of the evidence for active progressive remodeling as a mechanism. *Experimental Eye Research* 93: 133-140.

Downs J C, Yang H L, Girkin C, Sakata L, Bellezza A, Thompson H, and Burgoyne C F (2007) Three-dimensional histomorphometry of the normal and early glaucomatous monkey optic nerve head: Neural canal and subarachnoid space architecture. *Investigative Ophthalmology & Visual Science* 48: 3195-3208.

Drance S, Anderson D R, Schulzer M, and Collaborative Normal-Tension G (2001) Risk factors for progression of visual field abnormalities in normal-tension glaucoma. *American Journal of Ophthalmology* 131: 699-708.

Drance S M (1989) Disk haemorrhages in the glaucomas. *Survey of Ophthalmology* 33: 331-337.

Drexler W (2004) Ultrahigh-resolution optical coherence tomography. *Journal of Biomedical Optics* 9: 47-74.

Drexler W, and Fujimoto J G (2008) State-of-the-art retinal optical coherence tomography. *Progress in Retinal and Eye Research* 27: 45-88.

Drexler W, Morgner U, Kartner F X, Pitris C, Boppart S A, Li X D, Ippen E P et al. (1999) In vivo ultrahigh-resolution optical coherence tomography. *Optics Letters* 24: 1221-1223.

Elkington A R, Inman C B E, Steart P V, and Weller R O (1990) The structure of the lamina-cribrosa of the human eye: an immunocytochemical and electron microscopical study. *Eye* 4: 42-57.

Esmaeelpour M, Povazay B, Hermann B, Hofer B, Kajic V, Kapoor K, Sheen N J L et al. (2010) Three-Dimensional 1060-nm OCT: Choroidal Thickness Maps in Normal Subjects and Improved Posterior Segment Visualization in Cataract Patients. *Investigative Ophthalmology & Visual Science* 51: 5260-5266.

Fallon M, Valero O, Pazos M, and Anton A (2017) Diagnostic accuracy of imaging devices in glaucoma: A meta-analysis. *Survey of Ophthalmology* 62: 446-461.

Fan S, Hejkal J J, Gulati V, Galata S, Camras C B, and Toris C B (2011) Aqueous Humor Dynamics During the Day and Night in Volunteers With Ocular Hypertension. *Archives of Ophthalmology* 129: 1162-1166.

Fang L Y, Cunefare D, Wang C, Guymer R H, Li S T, and Farsiu S (2017a) Automatic segmentation of nine retinal layer boundaries in OCT images of non-exudative AMD patients using deep learning and graph search. *Biomedical Optics Express* 8: 2732-2744.

Fang L Y, Wang C, Li S T, Yan J, Chen X D, and Rabbani H (2017b) Automatic classification of retinal three-dimensional optical coherence tomography images using principal component analysis network with composite kernels. *Journal of Biomedical Optics* 22.

Fang Y A, Pan Y Z, Li M, Qiao R H, and Cai Y (2010) Diagnostic capability of Fourier-Domain optical coherence tomography in early primary open angle glaucoma. *Chinese Medical Journal* 123: 2045-2050.

Faridi O S, Park S C, Kabadi R, Su D, De Moraes C G, Liebmann J M, and Ritch R (2014) Effect of Focal Lamina Cribrosa Defect on Glaucomatous Visual Field Progression. *Ophthalmology* 121: 1524-1530.

Fechtner R D, and Weinreb R N (1994) Mechanisms of optic-nerve damage in primary open-angle glaucoma. *Survey of Ophthalmology* 39: 23-42.

Fercher A F, Hitzenberger C K, Drexler W, Kamp G, and Sattmann H (1993) In-Vivo optical coherence tomography. *American Journal of Ophthalmology* 116: 113-115.

Flammer J, and Mozaffarieh M (2007) What is the present pathogenetic concept of glaucomatous optic neuropathy? *Survey of Ophthalmology* 52: S162-S173.

Flammer J, and Orgul S (1998) Optic nerve blood-flow abnormalities in glaucoma. *Progress in Retinal and Eye Research* 17: 267-289.

Flammer J, Orgul S, Costa V P, Orzalesi N, Krieglstein G K, Serra L M, Renard J P et al. (2002) The impact of ocular blood flow in glaucoma. *Progress in Retinal and Eye Research* 21: 359-393.

Flaxman S R, Bourne R R A, Resnikoff S, Ackland P, Braithwaite T, Cicinelli M V, Das A et al. (2017) Global causes of blindness and distance vision impairment 1990-2020: a systematic review and meta-analysis. *Lancet Global Health* 5: E1221-E1234.

Fleiss J L (1986) The Design and Analysis of Clinical Experiments. New York: Wiley.

Folio L S, Wollstein G, and Schuman J S (2012) Optical Coherence Tomography: Future Trends for Imaging in Glaucoma. *Optometry and Vision Science* 89: E554-E562.

Fontana L, Bhandari A, Fitzke F W, and Hitchings R A (1998) In vivo morphometry of the lamina cribrosa and its relation to visual field loss in glaucoma. *Current Eye Research* 17: 363-369.

Fortune B (2019) Optical coherence tomography evaluation of the optic nerve head neuro-retinal rim in glaucoma. *Clinical and Experimental Optometry* 102: 286-290.

Foster P J, Buhrmann R, Quigley H A, and Johnson G J (2002) The definition and classification of glaucoma in prevalence surveys. *British Journal of Ophthalmology* 86: 238-242.

Freddo T F (2001) Shifting the paradigm of the blood-aqueous barrier. *Experimental Eye Research* 73: 581-592.

Friedman D S, Wolfs R C W, O'Colmain B, Klein B E, Taylor H R, West S, Leske C et al. (2004) Prevalence of open-angle glaucoma among adults in the United States. *Archives of Ophthalmology* 122: 532-538.

Fujimoto J G, Pitris C, Boppart S A, and Brezinski M E (2000) Optical coherence tomography: An emerging technology for biomedical imaging and optical biopsy. *Neoplasia* 2: 9-25.

Fujita Y, Imagawa T, and Uehara M (2000) Comparative study of the lamina cribrosa and the pial septa in the vertebrate optic nerve and their relationship to the myelinated axons. *Tissue & Cell* 32: 293-301.

Furlanetto R L, Park S C, Damle U J, Sieminski S F, Kung Y T, Siegal N, Liebmann J M et al. (2013) Posterior Displacement of the Lamina Cribrosa in Glaucoma: In Vivo Interindividual and Intereye Comparisons. *Investigative Ophthalmology & Visual Science* 54: 4836-4842.

Furuyoshi N, Furuyoshi M, May C A, Hayreh S S, Alm A, and Lutjen-Drecoll E (2000) Vascular and glial changes in the retrolaminar optic nerve in glaucomatous monkey eyes. *Ophthalmologica* 214: 24-32.

Gaasterland D, Tanishima T, and Kuwabara T (1978) Axoplasmic flow during chronic experimental glaucoma .1. Light and electron-microscopic studies of monkey optic nerve head during development of glaucomatous cupping. *Investigative Ophthalmology & Visual Science* 17: 838-846.

Gabriele M L, Wollstein G, Ishikawa H, Xu J A, Kim J, Kagemann L, Folio L S et al. (2010) Three dimensional optical coherence tomography imaging: Advantages and advances. *Progress in Retinal and Eye Research* 29: 556-579.

Gandhi M, and Dubey S (2013) Evaluation of the Optic Nerve Head in Glaucoma. *J Curr Glaucoma Pract* 7: 106-114.

Gardiner S K, Boey P Y, Yang H L, Fortune B, Burgoyne C F, and Demirel S (2015) Structural Measurements for Monitoring Change in Glaucoma: Comparing Retinal Nerve Fiber Layer Thickness With Minimum Rim Width and Area. *Investigative Ophthalmology & Visual Science* 56: 6886-6891.

Gardiner S K, Johnson C A, and Demirel S (2011) Cup Size Predicts Subsequent Functional Change in Early Glaucoma. *Optometry and Vision Science* 88: 1470-1476.

Gardiner S K, Ren R J, Yang H L, Fortune B, Burgoyne C F, and Demirel S (2014) A Method to Estimate the Amount of Neuroretinal Rim Tissue in Glaucoma: Comparison With Current Methods for Measuring Rim Area. *American Journal of Ophthalmology* 157: 540-549.

Garway-Heath D F, Crabb D P, Bunce C, Lascaratos G, Amalfitano F, Anand N, Azuara-Blanco A et al. (2015) Latanoprost for open-angle glaucoma (UKGTS): a randomised, multicentre, placebo-controlled trial. *Lancet* 385: 1295-1304.

Garway-Heath D F, and Hitchings R A (1998) Quantitative evaluation of the optic nerve head in early glaucoma. *British Journal of Ophthalmology* 82: 352-361.

Garway-Heath D F, Ruben S T, Viswanathan A, and Hitchings R A (1998) Vertical cup/disc ratio in relation to optic disc size: its value in the assessment of the glaucoma suspect. *British Journal of Ophthalmology* 82: 1118-1124.

Garway-Heath D F, Wollstein G, and Hitchings R A (1997) Aging changes of the optic nerve head in relation to open angle glaucoma. *British Journal of Ophthalmology* 81: 840-845.

Gasser P, and Flammer J (1991) Blood-cell velocity in the nailfold capillaries of patients with normal-tension and high-tension glaucoma. *American Journal of Ophthalmology* 111: 585-588.

Gezelter J D (2015) Open Source and Open Data Should Be Standard Practices. *Journal of Physical Chemistry Letters* 6: 1168-1169.

Giovannini A, Amato G, and Mariotti C (2002) The macular thickness and volume in glaucoma: an analysis in normal and glaucomatous eyes using OCT. *Acta Ophthalmologica Scandinavica* 80: 34-36.

Girard M J A, Strouthidis N G, Ethier C R, and Mari J M (2011) Shadow Removal and Contrast Enhancement in Optical Coherence Tomography Images of the Human Optic Nerve Head. *Investigative Ophthalmology & Visual Science* 52: 7738-7748.

Girard M J A, Tun T A, Husain R, Acharyya S, Haaland B A, Wei X, Mari J M et al. (2015) Lamina Cribrosa Visibility Using Optical Coherence Tomography: Comparison of Devices and Effects of Image Enhancement Techniques. *Investigative Ophthalmology & Visual Science* 56: 865-874.

Girkin C A, Fazio M A, Yang H L, Reynaud J, Burgoyne C F, Smith B, Wang L et al. (2017) Variation in the Three-Dimensional Histomorphometry of the Normal Human Optic Nerve Head With Age and Race: Lamina Cribrosa and Peripapillary Scleral Thickness and Position. *Investigative Ophthalmology & Visual Science* 58: 3759-3769.

Girkin C A, McGwin G, McNeal S F, and DeLeon-Ortega J (2003) Racial differences in the association between optic disc topography and early glaucoma. *Investigative Ophthalmology & Visual Science* 44: 3382-3387.

Golubnitschaja O, and Flammer J (2007) What are the biomarkers for glaucoma? *Survey of Ophthalmology* 52: S155-S161.

Gordon M O, Beiser J A, Brandt J D, Heuer D K, Higginbotham E J, Johnson C A, Keltner J L et al. (2002) The Ocular Hypertension Treatment Study - Baseline factors that predict the onset of primary open-angle glaucoma. *Archives of Ophthalmology* 120: 714-720.

Green S B (1991) How many subjects does it take to do a regression analysis. *Multivariate behavioral research* 26: 499-510.

Grewal D S, and Tanna A P (2013) Diagnosis of glaucoma and detection of glaucoma progression using spectral domain optical coherence tomography. *Current Opinion in Ophthalmology* 24: 150-161.

Guadagnoli E, and Velicer W F (1988) Relation of sample size to the stability of component patterns. *Psychological Bulletin* 103: 265-275.

Gulshan V, Peng L, Coram M, Stumpe M C, Wu D, Narayanaswamy A, Venugopalan S et al. (2016) Development and Validation of a Deep Learning Algorithm for Detection of Diabetic Retinopathy in Retinal Fundus Photographs. *Jama-Journal of the American Medical Association* 316: 2402-2410.

Hagiwara Y, Koh J E W, Tan J H, Bhandary S V, Laude A, Ciaccio E J, Tong L et al. (2018) Computer-aided diagnosis of glaucoma using fundus images: A review. *Computer Methods and Programs in Biomedicine* 165: 1-12.

Hale G M, and Querry M R (1973) Optical-constants of water in 200-nm to 200-mum wavelength region. *Applied Optics* 12: 555-563.

Halupka K J, Antony B J, Lee M H, Lucy K A, Rai R S, Ishikawa H, Wollstein G et al. (2018) Retinal optical coherence tomography image enhancement via deep learning. *Biomedical Optics Express* 9: 6205-6221.

Hammer M, Roggan A, Schweitzer D, and Muller G (1995) Optical properties of ocular fundus tissues - an in-vitro study using the double-integrating-sphere technique and inverse monte-carlo simulation. *Physics in Medicine and Biology* 40: 963-978.

Han I C, and Jaffe G J (2009) Comparison of Spectral- and Time-Domain Optical Coherence Tomography for Retinal Thickness Measurements in Healthy and Diseased Eyes. *American Journal of Ophthalmology* 147: 847-858.

Harwerth R S, and Quigley H A (2006) Visual field defects and retinal ganglion cell losses in patients with glaucoma. *Archives of Ophthalmology* 124: 853-859.

Harwerth R S, Wheat J L, Fredette M J, and Anderson D R (2010) Linking structure and function in glaucoma. *Progress in Retinal and Eye Research* 29: 249-271.

Harwerth R S, Wheat J L, and Rangaswamy N V (2008) Age-related losses of retinal ganglion cells and axons. *Investigative Ophthalmology & Visual Science* 49: 4437-4443.

Hayreh S S (1969) Blood supply of optic nerve head and its role in optic atrophy, glaucoma, and oedema of optic disc. *British Journal of Ophthalmology* 53: 721-748.

Hayreh S S (1972) Optic disc changes in glaucoma. *British Journal of Ophthalmology* 56: 175-185.

Hayreh S S (2001) Blood flow in the optic nerve head and factors that may influence it. *Progress in Retinal and Eye Research* 20: 595-624.

Hee M R, Izatt J A, Swanson E A, Huang D, Schuman J S, Lin C P, Puliafito C A et al. (1995) Optical coherence tomography of the human retina. *Archives of Ophthalmology* 113: 325-332.

Heijl A, Bengtsson B, and Oskarsdottir S E (2013a) Prevalence and Severity of Undetected Manifest Glaucoma Results from the Early Manifest Glaucoma Trial Screening. *Ophthalmology* 120: 1541-1545.

Heijl A, Buchholz P, Norrgren G, and Bengtsson B (2013b) Rates of visual field progression in clinical glaucoma care. *Acta Ophthalmologica* 91: 406-412.

Heijl A, Leske M C, Bengtsson B, Hyman L, Hussein M, and Early Manifest Glaucoma Trial G (2002) Reduction of intraocular pressure and glaucoma progression - Results from the early manifest glaucoma trial. *Archives of Ophthalmology* 120: 1268-1279.

Heijl A, Lindgren A, and Lindgren G (1989) Test-retest variability in glaucomatous visual fields. *American Journal of Ophthalmology* 108: 130-135.

Heijl A, Lindgren G, and Olsson J (1989) The effect of perimetric experience in normal subjects. *Archives of Ophthalmology* 107: 81-86.

Henderer J D (2006) Disc damage likelihood scale. *British Journal of Ophthalmology* 90: 395-396.

Hermann M M, Theofylaktopoulos I, Bangard N, Jonescu-Cuypers C, Coburger S, and Diestelhorst M (2004) Optic nerve head morphometry in healthy adults using confocal laser scanning tomography. *British Journal of Ophthalmology* 88: 761-765.

Hernandez M R (1992) Ultrastructural immunocytochemical analysis of elastin in the human lamina cribrosa - changes in elastic fibers in primary open angle glaucoma. *Investigative Ophthalmology & Visual Science* 33: 2891-2903.

Hernandez M R (2000) The optic nerve head in glaucoma: Role of astrocytes in tissue remodeling. *Progress in Retinal and Eye Research* 19: 297-321.

Hernandez M R, Andrzejewska W M, and Neufeld A H (1990) Changes in the extracellular-matrix of the human optic-nerve head in primary open-angle glaucoma. *American Journal of Ophthalmology* 109: 180-188.

Hernandez M R, Igoe F, and Neufeld A H (1986) Extracellular matrix of the human optic nerve head. *American Journal of Ophthalmology* 102: 139-148.

Hernandez M R, Igoe F, and Neufeld A H (1988) Cell culture of the human lamina cribrosa. *Investigative Ophthalmology & Visual Science* 29: 78-89.

Hernandez M R, Luo X X, Andrzejewska W, and Neufeld A H (1989) Age-related-changes in the extracellular-matrix of the human optic-nerve head. *American Journal of Ophthalmology* 107: 476-484.

Hernandez M R, Miao H X, and Lukas T (2008) Astrocytes in glaucomatous optic neuropathy. *Glaucoma: an Open Window to Neurodegeneration and Neuroprotection* 173: 353-373.

Hernandez M R, and Pena J D O (1997) The optic nerve head in glaucomatous optic neuropathy. *Archives of Ophthalmology* 115: 389-395.

Herndon L W, Weizer J S, and Stinnett S S (2004) Central corneal thickness as a risk factor for advanced glaucoma damage. *Archives of Ophthalmology* 122: 17-21.

Hirooka K, Nitta E, Ukegawa K, and Tsujikawa A (2017) Vision-related quality of life following glaucoma filtration surgery. *Bmc Ophthalmology* 17.

Hirvela H, Tuulonen A, and Laatikainen L (1994) Intraocular pressure and prevalence of glaucoma in elderly people in Finland - a population-based study. *International Ophthalmology* 18: 299-307.

Hitzenberger C K, Trost P, Lo P W, and Zhou Q Y (2003) Three-dimensional imaging of the human retina by high-speed optical coherence tomography. *Optics Express* 11: 2753-2761.

Hogan M J, Alvarado J A, and Weddell J E (1971) Histology of the human eye: an atlas and textbook. *Philadelphia, USA: WB Saunders*.

Hong S W, Koenigsman H, Ren R J, Yang H L, Gardiner S K, Reynaud J, Kinast R M et al. (2018) Glaucoma Specialist Optic Disc Margin, Rim Margin, and Rim Width Discordance in Glaucoma and Glaucoma Suspect Eyes. *American Journal of Ophthalmology* 192: 65-76.

Huang D, Swanson E A, Lin C P, Schuman J S, Stinson W G, Chang W, Hee M R et al. (1991) Optical coherence tomography. *Science* 254: 1178-1181.

Huang M L, and Chen H Y (2005) Development and comparison of automated classifiers for glaucoma diagnosis using stratus optical coherence tomography. *Investigative Ophthalmology & Visual Science* 46: 4121-4129.

Hurvich C M, and Tsai C L (1990) The impact of model selection on inference in linear regression. *American Statistician* 44: 214-217.

Huston P, Edge V L, and Bernier E (2019) Reaping the benefits of Open Data in public health. *Canada Communicable Disease Report* 45: 252-256.

Hwang Y H, and Kim Y Y (2012) Glaucoma Diagnostic Ability of Quadrant and Clock-Hour Neuroretinal Rim Assessment Using Cirrus HD Optical Coherence Tomography. *Investigative Ophthalmology & Visual Science* 53: 2226-2234.

ICNIRP (2000) Revision of guidelines on limits of exposure to laser radiation of wavelengths between 400nm and 1.4um. *Health Physics* 79: 431-440.

Iester M, Courtright P, and Mikelberg F S (1999) The confocal laser scanning discriminant analysis formula and measures of visual field. *Acta Ophthalmologica Scandinavica* 77: 64-66.

Iester M, Jonas J B, Mardin C Y, and Budde W M (2000) Discriminant analysis models for early detection of glaucomatous optic disc changes. *British Journal of Ophthalmology* 84: 464-468.

Iester M, Mardin C Y, Budde W M, Junemann A G, Hayler J K, and Jonas J B (2002) Discriminant analysis formulas of optic nerve head parameters measured by confocal scanning laser tomography. *Journal of Glaucoma* 11: 97-104.

Iester M, Mikelberg F S, Swindale N V, and Drance S M (1997a) ROC analysis of Heidelberg Retina Tomograph optic disc shape measures in glaucoma. *Canadian Journal of Ophthalmology-Journal Canadien D Ophtalmologie* 32: 382-388.

Iester M, Perdicchi A, Capris E, Siniscalco A, Calabria G, and Recupero S M (2008) Comparison Between Discriminant Analysis Models and "Glaucoma Probability Score" for the Detection of Glaucomatous Optic Nerve Head Changes. *Journal of Glaucoma* 17: 535-540.

Iester M, Swindale N V, and Mikelberg F S (1997b) Sector-based analysis of optic nerve head shape parameters and visual field indices in healthy and glaucomatous eyes. *Journal of Glaucoma* 6: 371-376.

Inoue R, Hangai M, Kotera Y, Nakanishi H, Mori S, Morishita S, and Yoshimura N (2009) Three-dimensional high-speed optical coherence tomography imaging of lamina cribrosa in glaucoma. *Ophthalmology* 116: 214-222.

Ioannidis J P A (2005) Why most published research findings are false. *Plos Medicine* 2: 696-701.

Iskedjian M, Walker J H, Desjardins O, Robin A L, Covert D W, Bergamini M V W, and Einarson T R (2009) Effect of selected antihypertensives, antidiabetics, statins and diuretics on adjunctive medical treatment of glaucoma: A population based study. *Current Medical Research and Opinion* 25: 1879-1888.

Ivers K M, Li C H, Patel N, Sredar N, Luo X D, Queener H, Harwerth R S et al. (2011) Reproducibility of Measuring Lamina Cribrosa Pore Geometry in Human and Nonhuman Primates with In Vivo Adaptive Optics Imaging. *Investigative Ophthalmology & Visual Science* 52: 5473-5480.

Izatt J A, and Choma M A (2008) Theory of optical coherence tomography. In: Drexler, W. and Fujimoto, J. G. (eds) Optical Coherence Tomography. *Biological and Medical Physics, Biomedical Engineering*: 47-72.

Izatt J A, Hee M R, Swanson E A, Lin C P, Huang D, Schuman J S, Puliafito C A et al. (1994) Micrometer-scale resolution imaging of the anterior eye in-vivo with optical coherence tomography. *Archives of Ophthalmology* 112: 1584-1589.

Jampel H D, Friedman D, Quigley H, Vitale S, Miller R, Knezevich F, and Ding Y L (2009) Agreement Among Glaucoma Specialists in Assessing Progressive Disc Changes From Photographs in Open-Angle Glaucoma Patients. *American Journal of Ophthalmology* 147: 39-44.

Jeoung J W, and Park K H (2010) Comparison of Cirrus OCT and Stratus OCT on the Ability to Detect Localized Retinal Nerve Fiber Layer Defects in Preperimetric Glaucoma. *Investigative Ophthalmology & Visual Science* 51: 938-945.

Jirarattanasopa P, Ooto S, Tsujikawa A, Yamashiro K, Hangai M, Hirata M, Matsumoto A et al. (2012) Assessment of Macular Choroidal Thickness by Optical Coherence Tomography and Angiographic Changes in Central Serous Chorioretinopathy. *Ophthalmology* 119: 1666-1678.

Johnson C A, Adams A J, and Lewis R A (1989) Evidence for a neural basis of age-related visual field loss in normal observers. *Investigative Ophthalmology & Visual Science* 30: 2056-2064.

Johnson M (2006) 'What controls aqueous humour outflow resistance?'. *Experimental Eye Research* 82: 545-557.

Johnstone I M, and Lu A Y (2009) On Consistency and Sparsity for Principal Components Analysis in High Dimensions. *Journal of the American Statistical Association* 104: 682-693.

Jolliffe I T (1972) Variables in a Principal Component Analysis. 1: Artificial Data. *Journal of the Royal Statistical Society* 21: 160-173.

Jolliffe I T (1973) Discarding variables in a Principal Component Analysis. 2: Real Data. *The Royal Statistical Society Series C-Applied Statistics* 22: 21-31.

Jolliffe I T, and Cadima J (2016) Principal component analysis: a review and recent developments. *Philosophical Transactions of the Royal Society a-Mathematical Physical and Engineering Sciences* 374.

Jolliffe I T, Morgan B J T, and Young P J (1996) A simulation study of the use of principal components in linear discriminant analysis. *Journal of Statistical Computation and Simulation* 55: 353-366.

Jonas J B, Aung T, Bourne R R, Bron A M, Ritch R, and Panda-Jonas S (2017) Glaucoma. *Lancet* 390: 2183-2193.

Jonas J B, Berenshtein E, and Holbach L (2003) Anatomic relationship between lamina cribrosa, intraocular space, and cerebrospinal fluid space. *Investigative Ophthalmology & Visual Science* 44: 5189-5195.

Jonas J B, Fernandez M C, and Naumann G O H (1991) Correlation of the optic disk size to glaucoma susceptibility. *Ophthalmology* 98: 675-680.

Jonas J B, Fernandez M C, and Sturmer J (1993) Pattern of glaucomatous neuroretinal rim loss. *Ophthalmology* 100: 63-68.

Jonas J B, Gusek G C, Guggenmoosholzmann I, and Naumann G O H (1988a) Variability of the real dimensions of normal human optic disks. *Graefes Archive for Clinical and Experimental Ophthalmology* 226: 332-336.

Jonas J B, Gusek G C, and Naumann G O (1988b) Optic disc, cup and neuroretinal rim size, configuration and correlations in normal eyes. *Investigative Ophthalmology & Visual Science* 29: 1151-1158.

Jonas J B, Gusek G C, and Naumann G O H (1988c) Optic disc morphometry in chronic primary open-angle glaucoma.1. Morphometric intrapapillary characteristics. *Graefes Archive for Clinical and Experimental Ophthalmology* 226: 522-530.

Jonas J B, Hayreh S S, and Tao Y (2009) Central Corneal Thickness and Thickness of the Lamina Cribrosa and Peripapillary Sclera in Monkeys. *Archives of Ophthalmology* 127: 1395-1396.

Jonas J B, and Holbach L (2005) Central corneal thickness and thickness of the lamina cribrosa in human eyes. *Investigative Ophthalmology & Visual Science* 46: 1275-1279.

Jonas J B, Jonas R A, Jonas S B, and Panda-Jonas S (2012) Lamina cribrosa thickness correlated with peripapillary sclera thickness. *Acta Ophthalmologica* 90: e248-e250.

Jonas J B, Mullerbergh J A, Schlotzerschrehardt U M, and Naumann G O H (1990) Histomorphometry of the human optic nerve. *Investigative Ophthalmology & Visual Science* 31: 736-744.

Jonas J B, and Papastathopoulos K I (1996) Optic disc shape in glaucoma. *Graefes Archive for Clinical and Experimental Ophthalmology* 234: 167-173.

Jonas J B, Schmidt A M, Mullerbergh J A, Schlotzerschrehardt U M, and Naumann G O H (1992) Human optic-nerve fiber count and optic disk size. *Investigative Ophthalmology & Visual Science* 33: 2012-2018.

Jonas J B, Stroux A, Velten I, Juenemann A, Martus P, and Budde W M (2005) Central corneal thickness correlated with glaucoma damage and rate of progression. *Investigative Ophthalmology & Visual Science* 46: 1269-1274.

Jonas J B, and Xu L (2014) Histological changes of high axial myopia. *Eye* 28: 113-117.

Jones H J, Girard M J, White N, Fautsch M P, Morgan J E, Ethier C R, and Albon J (2015) Quantitative analysis of three-dimensional fibrillar collagen microstructure within the normal, aged and glaucomatous human optic nerve head. *Journal of the Royal Society Interface* 12.

Jung Y H, Park H Y L, Jung K I, and Park C K (2015) Comparison of Prelaminar Thickness between Primary Open Angle Glaucoma and Normal Tension Glaucoma Patients. *Plos One* 10.

Kaiser H F (1960) The application of electronic computers to factor analysis. *Educational and Psychological Measurement* 20: 141-151.

Kaiser H J, Schoetzau A, Stumpfig D, and Flammer J (1997) Blood-flow velocities of the extraocular vessels in patients with high-tension and normal-tension primary open-angle glaucoma. *American Journal of Ophthalmology* 123: 320-327.

Kansal V, Armstrong J J, Pintwala R, and Hutnik C (2018) Optical coherence tomography for glaucoma diagnosis: An evidence based meta-analysis. *Plos One* 13.

Karaskiewicz J, Penkala K, Mularczyk M, and Lubinski W (2017) Evaluation of retinal ganglion cell function after intraocular pressure reduction measured by pattern electroretinogram in patients with primary open-angle glaucoma. *Documenta Ophthalmologica* 134: 89-97.

Kass M A, Heuer D K, Higginbotham E J, Johnson C A, Keltner J L, Miller J P, Parrish R K et al. (2002) The Ocular Hypertension Treatment Study - A randomized trial determines that topical ocular hypotensive medication delays or prevents the onset of primary open-angle glaucoma. *Archives of Ophthalmology* 120: 701-713.

Keltner J L, Johnson C A, Anderson D R, Levine R A, Fan J J, Cello K E, Quigley H A et al. (2006) The association between glaucomatous visual fields and optic features in the ocular treatment study nerve head hypertension. *Ophthalmology* 113: 1603-1612.

Keltner J L, Johnson C A, Quigg J M, Cello K E, Kass M A, Gordon M O, and Ocular Hypertension Treatment S (2000) Confirmation of visual field abnormalities in the ocular hypertension treatment study. *Archives of Ophthalmology* 118: 1187-1194.

Kendell K R, Quigley H A, Kerrigan L A, Pease M E, and Quigley E N (1995) Primary open angle glaucoma is not associated with photoreceptor loss. *Investigative Ophthalmology & Visual Science* 36: 200-205.

Kergoat H, Kergoat M J, Justino L, and Lovasik J V (2001) Age-related topographical changes in the normal human optic nerve head measured by scanning laser tomography. *Optometry and Vision Science* 78: 431-435.

Kerrigan L A, Zack D J, Quigley H A, Smith S D, and Pease M E (1997) TUNEL-positive ganglion cells in human primary open-angle glaucoma. *Archives of Ophthalmology* 115: 1031-1035.

Kerrigan-Baumrind L A, Quigley H A, Pease M E, Kerrigan D F, and Mitchell R S (2000) Number of ganglion cells in glaucoma eyes compared with threshold visual field tests in the same persons. *Investigative Ophthalmology & Visual Science* 41: 741-748.

Khaw P T, Shah P, and Elkington A R (2004) ABC of eyes - Glaucoma - 1: Diagnosis. *British Medical Journal* 328: 97-99.

Khawaja A P, Chan M P Y, Broadway D C, Garway-Heath D F, Luben R, Yip J L Y, Hayat S et al. (2014) Systemic Medication and Intraocular Pressure in a British Population The EPIC-Norfolk Eye Study. *Ophthalmology* 121: 1501-1507.

Kim D W, Jeoung J W, Kim Y W, Girard M J A, Mari J M, Kim Y K, Park K H et al. (2016) Prelamina and Lamina Cribrosa in Glaucoma Patients With Unilateral Visual Field Loss. *Investigative Ophthalmology & Visual Science* 57: 1662-1670.

Kim J A, Kim T W, Lee E J, Girard M J A, and Mari J M (2020) Comparison of Lamina Cribrosa Morphology in Eyes with Ocular Hypertension and Normal-Tension Glaucoma. *Investigative Ophthalmology & Visual Science* 61.

Kim S, Sung K R, Lee J R, and Lee K S (2013a) Evaluation of Lamina Cribrosa in Pseudoexfoliation Syndrome Using Spectral-Domain Optical Coherence Tomography Enhanced Depth Imaging. *Ophthalmology* 120: 1798-1803.

Kim S J, Cho K J, and Oh S (2017) Development of machine learning models for diagnosis of glaucoma. *Plos One* 12.

Kim T W, Kagemann L, Girard M J A, Strouthidis N G, Sung K R, Leung C K, Schuman J S et al. (2013b) Imaging of the Lamina Cribrosa in Glaucoma: Perspectives of Pathogenesis and Clinical Applications. *Current Eye Research* 38: 903-909.

King A, Azuara-Blanco A, and Tuulonen A (2013) Glaucoma. *British Medical Journal* 346.

Kirwan R P, Fenerty C H, Crean J, Wordinger R J, Clark A F, and O'Brien C J (2005) Influence of cyclical mechanical strain on extracellular matrix gene expression in human lamina cribrosa cells in vitro. *Molecular Vision* 11: 798-810.

Kiumehr S, Park S C, Dorairaj S, Teng C C, Tello C, Liebmann J M, and Ritch R (2012) In Vivo Evaluation of Focal Lamina Cribrosa Defects in Glaucoma. *Archives of Ophthalmology* 130: 552-559.

Klein B E K, Klein R, Sponsel W E, Franke T, Cantor L B, Martone J, and Menage M J (1992) Prevalence of glaucoma - the beaver-dam eye study. *Ophthalmology* 99: 1499-1504.

Kokotas H, Kroupis C, Chiras D, Grigoriadou M, Lamnissou K, Petersen M B, and Kitsos G (2012) Biomarkers in primary open angle glaucoma. *Clinical Chemistry and Laboratory Medicine* 50: 2107-2119.

Koo T K, and Li M Y (2016) A Guideline of Selecting and Reporting Intraclass Correlation Coefficients for Reliability Research. *Journal of Chiropractic Medicine* 15: 155-163.

Kosoko-Lasaki O, Gong G, Haynatzki G, and Wilson M R (2006) Race, ethnicity and prevalence of primary open-angle glaucoma. *Journal of the National Medical Association* 98: 1626-1629.

Kotecha A, Izadi S, and Jeffery G (2006) Age-related changes in the thickness of the human lamina cribrosa. *British Journal of Ophthalmology* 90: 1531-1534.

Kotecha A, Spratt A, Bunce C, Garway-Heath D F, Khaw P T, Viswanathan A, and MoreFlow Study G (2009) Optic Disc and Visual Field Changes after Trabeculectomy. *Investigative Ophthalmology & Visual Science* 50: 4693-4699.

Kotowski J, Folio L S, Wollstein G, Ishikawa H, Ling Y, Bilonick R A, Kagemann L et al. (2012) Glaucoma discrimination of segmented cirrus spectral domain optical coherence tomography (SD-OCT) macular scans. *British Journal of Ophthalmology* 96: 1420-1425.

Kotowski J, Wollstein G, Ishikawa H, and Schuman J S (2014) Imaging of the optic nerve and retinal nerve fiber layer: An essential part of glaucoma diagnosis and monitoring. *Survey of Ophthalmology* 59: 458-467.

Krzyzanowska-Berkowska P, Melinska A, Helemejko I, and Iskander D R (2018) Evaluating displacement of lamina cribrosa following glaucoma surgery. *Graefes Archive for Clinical and Experimental Ophthalmology* 256: 791-800.

Kuang T M, Zhang C W, Zangwill L M, Weinreb R N, and Medeiros F A (2015) Estimating Lead Time Gained by Optical Coherence Tomography in Detecting Glaucoma before Development of Visual Field Defects. *Ophthalmology* 122: 2002-2009.

Kumar K (2017) Principal Component Analysis: Most Favourite Tool in Chemometrics. *Resonance-Journal of Science Education* 22: 747-759.

Kwun Y, Han J C, and Kee C (2015) Comparison of Lamina Cribrosa Thickness in Normal Tension Glaucoma Patients With Unilateral Visual Field Defect. *American Journal of Ophthalmology* 159: 512-518.

Lalezary M, Medeiros F A, Weinreb R N, Bowd C, Sample P A, Tavares I M, Tafreshi A et al. (2006) Baseline optical coherence tomography predicts the development of glaucomatous change in glaucoma suspects. *American Journal of Ophthalmology* 142: 576-582.

Lamparter J, Russell R A, Zhu H G, Asaoka R, Yamashita T, Ho T, and Garway-Heath D F (2013) The Influence of Intersubject Variability in Ocular Anatomical Variables on the Mapping of Retinal Locations to the Retinal Nerve Fiber Layer and Optic Nerve Head. *Investigative Ophthalmology & Visual Science* 54: 6074-6082.

Larros J M, Moreno-Montanes J, Martinez-de-la-Casa J M, Polo V, Velazquez-Villoria A, Berrozpe C, and Garcia-Granero M (2015) A Diagnostic Calculator for Detecting Glaucoma on the Basis of Retinal Nerve Fiber Layer, Optic Disc, and Retinal Ganglion Cell Analysis by Optical Coherence Tomography. *Investigative Ophthalmology & Visual Science* 56: 6788-6795.

Lee D, Lee W, Lee Y, and Pawitan Y (2010a) Super-sparse principal component analyses for high-throughput genomic data. *Bmc Bioinformatics* 11.

Lee E J, Kim T W, Park K H, Seong M, Kim H, and Kim D M (2009) Ability of Stratus OCT to Detect Progressive Retinal Nerve Fiber Layer Atrophy in Glaucoma. *Investigative Ophthalmology & Visual Science* 50: 662-668.

Lee E J, Kim T W, and Weinreb R N (2012) Reversal of Lamina Cribrosa Displacement and Thickness after Trabeculectomy in Glaucoma. *Ophthalmology* 119.

Lee E J, Kim T W, Weinreb R N, and Kim H (2013a) Reversal of Lamina Cribrosa Displacement after Intraocular Pressure Reduction in Open-Angle Glaucoma. *Ophthalmology* 120: 553-559.

Lee E J, Kim T W, Weinreb R N, Park K H, Kim S H, and Kim D M (2011) Visualization of the Lamina Cribrosa Using Enhanced Depth Imaging Spectral-Domain Optical Coherence Tomography. *American Journal of Ophthalmology* 152: 87-95.

Lee E J, Kim T W, Weinreb R N, Suh M H, and Kim H (2013b) Lamina cribrosa thickness is not correlated with central corneal thickness or axial length in healthy eyes. *Graefes Archive for Clinical and Experimental Ophthalmology* 251: 847-854.

Lee J R, Jeoung J W, Choi J, Choi J Y, Park K H, and Kim Y D (2010b) Structure-Function Relationships in Normal and Glaucomatous Eyes Determined by Time- and Spectral-Domain Optical Coherence Tomography. *Investigative Ophthalmology & Visual Science* 51: 6424-6430.

Lee K Y C, Tomidokoro A, Sakata R, Konno S, Mayama C, Saito H, Hayashi K et al. (2010c) Cross-sectional Anatomic Configurations of Peripapillary Atrophy Evaluated with Spectral Domain-Optical Coherence Tomography. *Investigative Ophthalmology & Visual Science* 51: 666-671.

Lee S H, Kim T W, Lee E J, Girard M J A, and Mari J M (2017) Diagnostic Power of Lamina Cribrosa Depth and Curvature in Glaucoma. *Investigative Ophthalmology & Visual Science* 58.

Lehman B M, Berntsen D A, Bailey M D, and Zadnik K (2009) Validation of Optical Coherence Tomography-Based Crystalline Lens Thickness Measurements in Children. *Optometry and Vision Science* 86: 181-187.

Leite M T, Sakata L M, and Medeiros F A (2011) Managing glaucoma in developing countries. *Arquivos Brasileiros De Oftalmologia* 74: 83-84.

Leitgeb R, Hitzenberger C K, and Fercher A F (2003) Performance of fourier domain vs. time domain optical coherence tomography. *Optics Express* 11: 889-894.

Leitgeb R A, Drexler W, Unterhuber A, Hermann B, Bajraszewski T, Le T, Stingl A et al. (2004) Ultrahigh resolution Fourier domain optical coherence tomography. *Optics Express* 12: 2156-2165.

Leske M C, Heijl A, Hussein M, Bengtsson B, Hyman L, Komaroff E, and Early Manifest Glaucoma Trial G (2003) Factors for glaucoma progression and the effect of treatment - The Early Manifest Glaucoma Trial. *Archives of Ophthalmology* 121: 48-56.

Leske M C, Wu S Y, Hennis A, Honkanen R, Nemesure B, and Grp B E S (2008) Risk factors for incident open-angle glaucoma. *Ophthalmology* 115: 85-93.

Leung C K S, Chan W M, Yung W H, Ng A C K, Woo J, Tsang M K, and Tse R K K (2005) Comparison of macular and peripapillary measurements for the detection of glaucoma - An optical coherence tomography study. *Ophthalmology* 112: 391-400.

Leung C K S, Cheung C Y L, Lin D S, Pang C P, Lam D S C, and Weinreb R N (2008) Longitudinal Variability of Optic Disc and Retinal Nerve Fiber Layer Measurements. *Investigative Ophthalmology & Visual Science* 49: 4886-4892.

Leung C K S, Cheung C Y L, Weinreb R N, Qiu K L, Liu S, Li H T, Xu G H et al. (2010a) Evaluation of Retinal Nerve Fiber Layer Progression in Glaucoma: A Study on Optical Coherence Tomography Guided Progression Analysis. *Investigative Ophthalmology & Visual Science* 51: 217-222.

Leung C K S, Chiu V, Weinreb R N, Liu S, Ye C, Yu M, Cheung C Y L et al. (2011) Evaluation of Retinal Nerve Fiber Layer Progression in Glaucoma A Comparison between Spectral-Domain and Time-Domain Optical Coherence Tomography. *Ophthalmology* 118: 1558-1562.

Leung C K S, Lam S, Weinreb R N, Liu S, Ye C, Liu L, He J et al. (2010b) Retinal Nerve Fiber Layer Imaging with Spectral-Domain Optical Coherence Tomography Analysis of the Retinal Nerve Fiber Layer Map for Glaucoma Detection. *Ophthalmology* 117: 1684-1691.

Leung C K S, Yu M, Weinreb R N, Ye C, Liu S, Lai G, and Lam D S C (2012) Retinal Nerve Fiber Layer Imaging with Spectral-Domain Optical Coherence Tomography: A Prospective Analysis of Age-Related Loss. *Ophthalmology* 119: 731-737.

Leung D Y L, Li F C H, Kwong Y Y Y, Tham C C Y, Chi S C C, and Lam D S C (2010c) Simvastatin and Disease Stabilization in Normal Tension Glaucoma: A Cohort Study. *Ophthalmology* 117: 471-476.

Li S F, Wang X Z, Li S N, Wu G W, and Wang N L (2010) Evaluation of optic nerve head and retinal nerve fiber layer in early and advance glaucoma using frequency-domain optical coherence tomography. *Graefes Archive for Clinical and Experimental Ophthalmology* 248: 429-434.

Li X D, Gold H, Weissman N, Pitris C, Saunders K, Ghanti R, Fujimoto J et al. (2000) In vivo intravascular imaging with OCT: Comparison with ultrasound.*Biomedical Topical Meetings, Technical Digest*. Vol. 38. pp. 32-34.

Li Z X, He Y F, Keel S, Meng W, Chang R T, and He M G (2018) Efficacy of a Deep Learning System for Detecting Glaucomatous Optic Neuropathy Based on Color Fundus Photographs. *Ophthalmology* 125: 1199-1206.

Lichter P R (1976) Variability of expert observers in evaluating the optic disc. *Trans Am Ophthalmol Soc*: 532-572.

Linden C, and Alm A (1999) Prostaglandin analogues in the treatment of glaucoma. *Drugs & Aging* 14: 387-398.

Lisboa R, Paranhos A, Weinreb R N, Zangwill L M, Leite M T, and Medeiros F A (2013) Comparison of Different Spectral Domain OCT Scanning Protocols for Diagnosing Preperimetric Glaucoma. *Investigative Ophthalmology & Visual Science* 54: 3417-3425.

Litjens G, Kooi T, Bejnordi B E, Setio A A A, Ciompi F, Ghafoorian M, van der Laak J et al. (2017) A survey on deep learning in medical image analysis. *Medical Image Analysis* 42: 60-88.

Littmann H (1982) Determination of the real size of an object on the fundus of the living eye. *Klinische Monatsblatter Fur Augenheilkunde* 180: 286-289.

Liu H, Fan S, Gulati V, Camras L J, Zhan G L, Ghate D, Camras C B et al. (2011) Aqueous Humor Dynamics During the Day and Night in Healthy Mature Volunteers. *Archives of Ophthalmology* 129: 269-275.

Lopes F S, Matsubara I, Almeida I, Dorairaj S K, Vessani R M, Paranhos A, and Prata T S (2019) Structure-function relationships in glaucoma using enhanced depth imaging optical coherence tomography-derived parameters: a cross-sectional observational study. *Bmc Ophthalmology* 19.

Lucy K A, Wang B, Ishikawa H, Bilonick R A, Ling Y, Grulkowski I, Liu J J et al. (2015) Pre-laminar tissue thickness measurably affects the visualization of the lamina cribrosa (LC). *Investigative Ophthalmology & Visual Science* 56.

Maetschke S, Antony B, Ishikawa H, Wollstein G, Schuman J, and Garnavi R (2019) A feature agnostic approach for glaucoma detection in OCT volumes. *Plos One* 14.

Mari J M, Strouthidis N G, Park S C, and Girard M J A (2013) Enhancement of Lamina Cribrosa Visibility in Optical Coherence Tomography Images Using Adaptive Compensation. *Investigative Ophthalmology & Visual Science* 54: 2238-2247.

McKean-Cowdin R, Wang Y, Wu J, Azen S P, Varma R, and Los Angeles Latino Eye Study G (2008) Impact of visual field loss on health-related quality of life in glaucoma - The Los Angeles Latino Eye Study. *Ophthalmology* 115: 941-948.

McKinnon S J (1997) Glaucoma, apoptosis, and neuroprotection. *Curr Opin Ophthalmol* 8: 28-37.

McLeod S D, West S K, Quigley H A, and Fozard J L (1990) A longitudinal study of the relationship between intraocular and blood pressures. *Investigative Ophthalmology & Visual Science* 31: 2361-2366.

Medeiros F A, Alencar L M, Zangwill L M, Bowd C, Sample P A, and Weinreb R N (2009a) Prediction of Functional Loss in Glaucoma From Progressive Optic Disc Damage. *Archives of Ophthalmology* 127: 1250-1256.

Medeiros F A, Lisboa R, Weinreb R N, Liebmann J M, Girkin C, and Zangwill L M (2013) Retinal Ganglion Cell Count Estimates Associated with Early Development of Visual Field Defects in Glaucoma. *Ophthalmology* 120: 736-744.

Medeiros F A, Vizzeri G, Zangwill L M, Alencar L M, Sample P A, and Weinreb R N (2008) Comparison of retinal nerve fiber layer and optic disc imaging for diagnosing glaucoma in patients suspected of having the disease. *Ophthalmology* 115: 1340-1346.

Medeiros F A, Zangwill L M, Alencar L M, Bowd C, Sample P A, Susanna R, and Weinreb R N (2009b) Detection of Glaucoma Progression with Stratus OCT Retinal Nerve Fiber Layer, Optic Nerve Head, and Macular Thickness Measurements. *Investigative Ophthalmology & Visual Science* 50: 5741-5748.

Medeiros F A, Zangwill L M, Bowd C, Sample P A, and Weinreb R N (2005a) Use of progressive glaucomatous optic disk change as the reference standard for evaluation of diagnostic tests in glaucoma. *American Journal of Ophthalmology* 139: 1010-1018.

Medeiros F A, Zangwill L M, Bowd C, Vessani R M, Susanna R, and Weinreb R N (2005b) Evaluation of retinal nerve fiber layer, optic nerve head, and macular thickness measurements for glaucoma detection using optical coherence tomography. *American Journal of Ophthalmology* 139: 44-55.

Michelessi M, Lucenteforte E, Oddone F, Brazzelli M, Parravano M, Franchi S, Ng S M et al. (2015) Optic nerve head and fibre layer imaging for diagnosing glaucoma. *Cochrane Database of Systematic Reviews*.

Midgett D E, Pease M E, Jefferys J L, Patel M, Franck C, Quigley H A, and Nguyen T D (2017) The pressure-induced deformation response of the human lamina cribrosa: Analysis of regional variations. *Acta Biomaterialia* 53: 123-139.

Miller K M, and Quigley H A (1988) The clinical appearance of the lamina cribrosa as a function of the extent of glaucomatous optic nerve damage. *Ophthalmology* 95: 135-138.

Mills R P, Budenz D L, Lee P P, Noecker R J, Walt J G, Siegartel L R, Evans S J et al. (2006) Categorizing the stage of glaucoma from pre-diagnosis to end-stage disease. *American Journal of Ophthalmology* 141: 24-30.

Minckler D S (1981) Optic-nerve damage in glaucoma. Obstruction to axoplasmic flow. *Survey of Ophthalmology* 26: 128-136.

Minckler D S, Bunt A H, and Johanson G W (1977) Orthograde and retrograde axoplasmic-transport during acute ocular hypertension in monkey. *Investigative Ophthalmology & Visual Science* 16: 426-441.

Molloy J C (2011) The Open Knowledge Foundation: Open Data Means Better Science. *Plos Biology* 9.

Moore S, and Thanos S (1996) Differential increases in rat retinal ganglion cell size with various methods of optic nerve lesion. *Neuroscience Letters* 207: 117-120.

Morgan J E (1994) Selective cell-death in glaucoma - does it really occur. *British Journal of Ophthalmology* 78: 875-879.

Morgan J E (2002) Retinal ganglion cell shrinkage in glaucoma. *Journal of Glaucoma* 11: 365-370.

Morgan J E, Uchida H, and Caprioli J (2000) Retinal ganglion cell death in experimental glaucoma. *British Journal of Ophthalmology* 84: 303-310.

Morgan R W, and Drance S M (1975) Chronic open-angle glaucoma and ocular hypertension - epidemiological study. *British Journal of Ophthalmology* 59: 211-215.

Mori S, Hangai M, Sakamoto A, and Yoshimura N (2010) Spectral-domain Optical Coherence Tomography Measurement of Macular Volume for Diagnosing Glaucoma. *Journal of Glaucoma* 19: 528-534.

Morrison J C, Dormanpease M E, Dunkelberger G R, and Quigley H A (1990) Optic nerve head extracellular-matrix in primary optic atrophy and experimental glaucoma. *Archives of Ophthalmology* 108: 1020-1024.

Mowatt G, Burr J M, Cook J A, Siddiqui M A R, Ramsay C, Fraser C, Azuara-Blanco A et al. (2008) Screening Tests for Detecting Open-Angle Glaucoma: Systematic Review and Meta-analysis. *Investigative Ophthalmology & Visual Science* 49: 5373-5385.

Mumcuoglu T, Wollstein G, Wojtkowski M, Kagemann L, Ishikawa H, Gabriele M L, Srinivasan V et al. (2008) Improved visualization of glaucomatous retinal damage using high-speed ultrahigh-resolution optical coherence tomography. *Ophthalmology* 115: 782-789.

Murtagh P, Greene G, and O'Brien C (2020) Current applications of machine learning in the screening and diagnosis of glaucoma: a systematic review and Meta-analysis. *International Journal of Ophthalmology* 13: 149-162.

Musch D C, Gillespie B W, Lichter P R, Niziol L M, Janz N K, and Investigators C S (2009) Visual Field Progression in the Collaborative Initial Glaucoma Treatment Study The Impact of Treatment and Other Baseline Factors. *Ophthalmology* 116: 200-207.

Mwanza J C, Chang R T, Budenz D L, Durbin M K, Gendy M G, Shi W, and Feuer W J (2010) Reproducibility of Peripapillary Retinal Nerve Fiber Layer Thickness and Optic Nerve Head Parameters Measured with Cirrus HD-OCT in Glaucomatous Eyes. *Investigative Ophthalmology & Visual Science* 51: 5724-5730.

Mwanza J C, Oakley J D, Budenz D L, Anderson D R, and Cirrus Optical Coherence T (2011a) Ability of Cirrus HD-OCT Optic Nerve Head Parameters to Discriminate Normal from Glaucomatous Eyes. *Ophthalmology* 118: 241-U234.

Mwanza J C, Oakley J D, Budenz D L, Chang R T, Knight O J, and Feuer W J (2011b) Macular Ganglion Cell-Inner Plexiform Layer: Automated Detection and Thickness Reproducibility with

Spectral Domain-Optical Coherence Tomography in Glaucoma. *Investigative Ophthalmology & Visual Science* 52: 8323-8329.

Mwanza J C, Warren J L, and Budenz D L (2018) Utility of combining spectral domain optical coherence tomography structural parameters for the diagnosis of early Glaucoma: a mini-review. *Eye and Vision* 5.

Mwanza J C, Warren J L, Budenz D L, and Ganglion Cell Anal Study G (2013) Combining Spectral Domain Optical Coherence Tomography Structural Parameters for the Diagnosis of Glaucoma With Early Visual Field Loss. *Investigative Ophthalmology & Visual Science* 54: 8393-8400.

Myers J S, Fudemberg S J, and Lee D (2018) Evolution of optic nerve photography for glaucoma screening: a review. *Clinical and Experimental Ophthalmology* 46: 169-176.

Myint J, Edgar D F, Kotecha A, Murdoch I E, and Lawrenson J G (2011) A national survey of diagnostic tests reported by UK community optometrists for the detection of chronic open angle glaucoma. *Ophthalmic and Physiological Optics* 31: 353-359.

Na J H, Sung K R, Lee J R, Lee K S, Baek S, Kim H K, and Sohn Y H (2013) Detection of Glaucomatous Progression by Spectral-Domain Optical Coherence Tomography. *Ophthalmology* 120: 1388-1395.

Nadler Z, Wang B, Schuman J S, Ferguson R D, Patel A, Hammer D X, Bilonick R A et al. (2014) In Vivo Three-Dimensional Characterization of the Healthy Human Lamina Cribrosa With Adaptive Optics Spectral-Domain Optical Coherence Tomography. *Investigative Ophthalmology & Visual Science* 55: 6459-6466.

Naz A S, Qamar A, Ul Haque S, Zaman Y, and Faheem F (2020) Association of lamina cribrosa morphometry with retinal nerve fiber layer loss and visual field defects in primary open angle glaucoma. *Pakistan Journal of Medical Sciences* 36: 521-525.

Nduaguba C, Ugurlu S, and Caprioli J (1998) Acquired pits of the optic nerve in glaucoma: Prevalence and associated visual field loss. *Acta Ophthalmologica Scandinavica* 76: 273-277.

Newman-Casey P A, Talwar N, Nan B, Musch D C, and Stein J D (2011) The Relationship Between Components of Metabolic Syndrome and Open-Angle Glaucoma. *Ophthalmology* 118: 1318-1326.

NICE (2017) National Institute for Health and Care Excellence. *NG81 Glaucoma*.

Nitta K, Wajima R, Tachibana G, Inoue S, Ohigashi T, Otsuka N, Kurashima H et al. (2017) Prediction of Visual Field Progression in Patients with Primary Open-Angle Glaucoma, Mainly Including Normal Tension Glaucoma. *Scientific Reports* 7.

Nuyen B, Mansouri K, and Weinreb R (2012) Imaging of the Lamina Cribrosa using Swept-Source Optical Coherence Tomography. *J Curr Glaucoma Pract* 6: 113-119.

Oddone F, Centofanti M, Tanga L, Parravano M, Michelessi M, Schiavone M, Villani C M et al. (2011) Influence of Disc Size on Optic Nerve Head versus Retinal Nerve Fiber Layer Assessment for Diagnosing Glaucoma. *Ophthalmology* 118: 1340-1347.

Oddone F, Lucenteforte E, Michelessi M, Rizzo S, Donati S, Parravano M, and Virgili G (2016) Macular versus Retinal Nerve Fiber Layer Parameters for Diagnosing Manifest Glaucoma A Systematic Review of Diagnostic Accuracy Studies. *Ophthalmology* 123: 939-949.

Ogden T E, Duggan J, Danley K, Wilcox M, and Minckler D S (1988) Morphometry of nerve fiber bundle pores in the optic nerve head of the human. *Experimental Eye Research* 46: 559-568.

Oh J Y, and Park K H (2004) Analysis of optic disc change using the Heidelberg Retina Tomograph in an acquired pit of the optic nerve. *Ophthalmic Surgery Lasers & Imaging* 35: 325-327.

Ohnell H, Heijl A, Brenner L, Anderson H, and Bengtsson B (2016) Structural and Functional Progression in the Early Manifest Glaucoma Trial. *Ophthalmology* 123: 1173-1180.

Oliveira C, Harizman N, Girkin C A, Xie A, Tello C, Liebmann J M, and Ritch R (2007) Axial length and optic disc size in normal eyes. *British Journal of Ophthalmology* 91: 37-39.

Omodaka K, Horii T, Takahashi S, Kikawa T, Matsumoto A, Shiga Y, Maruyama K et al. (2015) 3D Evaluation of the Lamina Cribrosa with Swept-Source Optical Coherence Tomography in Normal Tension Glaucoma. *Plos One* 10.

Osborne N N, and del Olmo-Aguado S (2013) Maintenance of retinal ganglion cell mitochondrial functions as a neuroprotective strategy in glaucoma. *Current Opinion in Pharmacology* 13: 16-22.

Osborne N N, Melena J, Chidlow G, and Wood J P M (2001) A hypothesis to explain ganglion cell death caused by vascular insults at the optic nerve head: possible implication for the treatment of glaucoma. *British Journal of Ophthalmology* 85: 1252-1259.

Osborne N N, Ugarte M, Chao M, Childlow G, Bae J H, Wood J P M, and Nash M S (1999) Neuroprotection in relation to retinal ischemia and relevance to glaucoma. *Survey of Ophthalmology* 43: S102-S128.

Owen C G, Carey I M, Shah S, de Wilde S, Wormald R, Whincup P H, and Cook D G (2010) Hypotensive Medication, Statins, and the Risk of Glaucoma. *Investigative Ophthalmology & Visual Science* 51: 3524-3530.

Oyama T, Abe H, and Ushiki T (2006) The connective tissue and glial framework in the optic nerve head of the normal human eye: light and scanning electron microscopic studies. *Archives of Histology and Cytology* 69: 341-356.

Parikh R S, Parikh S, Sekhar G C, Kumar R S, Prabakaran S, Babu J G, and Thomas R (2007) Diagnostic capability of optical coherence tomography (Stratus OCT 3) in early glaucoma. *Ophthalmology* 114: 2238-2243.

Park H Y L, Jeon S H, and Park C K (2012a) Enhanced Depth Imaging Detects Lamina Cribrosa Thickness Differences in Normal Tension Glaucoma and Primary Open-Angle Glaucoma. *Ophthalmology* 119: 10-20.

Park S C, Brumm J, Furlanetto R L, Netto C, Liu Y Y, Tello C, Liebmann J M et al. (2015) Lamina Cribrosa Depth in Different Stages of Glaucoma. *Investigative Ophthalmology & Visual Science* 56: 2059-2064.

Park S C, De Moraes C G V, Teng C C, Tello C, Liebmann J M, and Ritch R (2012b) Enhanced Depth Imaging Optical Coherence Tomography of Deep Optic Nerve Complex Structures in Glaucoma. *Ophthalmology* 119: 3-9.

Park S C, Kiumehr S, Teng C C, Tello C, Liehmann J M, and Ritch R (2012c) Horizontal Central Ridge of the Lamina Cribrosa and Regional Differences in Laminar Insertion in Healthy Subjects. *Investigative Ophthalmology & Visual Science* 53: 1610-1616.

Parrish R K, Feuer W J, Schiffman J C, Lichter P R, Musch D C, and Group C O D S (2009) Five-year Follow-up Optic Disc Findings of the Collaborative Initial Glaucoma Treatment Study. *American Journal of Ophthalmology* 147: 717-724.

Parrish R K, Schiffman J C, Feuer W J, Anderson D R, Budenz D L, Wells-Albornoz M, Vandenbroucke R et al. (2005) Test-retest reproducibility of optic disk deterioration detected from stereophotographs by masked graders. *American Journal of Ophthalmology* 140: 762-764.

Patel N B, Lim M, Gajjar A, Evans K B, and Harwerth R S (2014a) Age-Associated Changes in the Retinal Nerve Fiber Layer and Optic Nerve Head. *Investigative Ophthalmology & Visual Science* 55: 5134-5143.

Patel N B, Sullivan-Mee M, and Harwerth R S (2014b) The Relationship Between Retinal Nerve Fiber Layer Thickness and Optic Nerve Head Neuroretinal Rim Tissue in Glaucoma. *Investigative Ophthalmology & Visual Science* 55.

Patino C M, McKean-Cowdin R, Azen S P, Allison J C, Choudhury F, Varma R, and Los Angeles Latino Eye Study G (2010) Central and Peripheral Visual Impairment and the Risk of Falls and Falls with Injury. *Ophthalmology* 117: 199-U125.

Pavlidis M, Stupp T, Naskar R, Cengiz C, and Thanos S (2003) Retinal ganglion cells resistant to advanced glaucoma: A postmortem study of human retinas with the carbocyanine dye DiI. *Investigative Ophthalmology & Visual Science* 44: 5196-5205.

Pederson J E A, D.R. (1980) The mode of progressive disc cupping in ocular hypertension and glaucoma. *Archives of Ophthalmology* 98: 490-495.

Pena J D O, Netland P A, Vidal I, Dorr D A, Rasky A, and Hernandez M R (1998) Elastosis of the lamina cribrosa in glaucomatous optic neuropathy. *Experimental Eye Research* 67: 517-524.

Perkins E S, and Phelps C D (1982) Open angle glaucoma, ocular hypertension, low-tension glaucoma, and refraction. *Archives of Ophthalmology* 100: 1464-1467.

Phene S, Dunn R C, Hammel N, Liu Y, Krause J, Kitade N, Schaekermann M et al. (2019) Deep Learning and Glaucoma Specialists The Relative Importance of Optic Disc Features to Predict Glaucoma Referral in Fundus Photographs. *Ophthalmology* 126: 1627-1639.

Pieroth L, Schuman J S, Hertzmark E, Hee M R, Wilkins J R, Coker J, Mattox C et al. (1999) Evaluation of focal defects of the nerve fiber layer using optical coherence tomography. *Ophthalmology* 106: 570-579.

Pointer J S (1997) The diurnal variation of intraocular pressure in non-glaucomatous subjects: Relevance in a clinical context. *Ophthalmic and Physiological Optics* 17: 456-465.

Pourhoseingholi M A, Baghestani A R, and Vahedi M (2012) How to control confounding effects by statistical analysis. *Gastroenterology and Hepatology from Bed to Bench* 5: 79-83.

Povazay B, Bizheva K, Hermann B, Unterhuber A, Sattmann H, Fercher A F, Drexler W et al. (2003) Enhanced visualization of choroidal vessels using ultrahigh resolution ophthalmic OCT at 1050 nm. *Optics Express* 11: 1980-1986.

Povazay B, Hermann B, Unterhuber A, Hofer B, Sattmann H, Zeiler F, Morgan J E et al. (2007a) Three-dimensional optical coherence tomography at 1050 nm versus 800 nm in retinal pathologies: enhanced performance and choroidal penetration in cataract patients. *Journal of Biomedical Optics* 12: 1-7.

Povazay B, Hofer B, Hermann B, Unterhuber A, Morgan J E, Glittenberg C, Binder S et al. (2007b) Minimum distance mapping using three-dimensional optical coherence tomography for glaucoma diagnosis. *Journal of Biomedical Optics* 12.

Povazay B, Hofer B, Torti C, Hermann B, Tumlinson A R, Esmaeelpour M, Egan C A et al. (2009) Impact of enhanced resolution, speed and penetration on three-dimensional retinal optical coherence tomography. *Optics Express* 17: 4134-4150.

Prata T S, Lopes F S, Prado V G, Almeida I, Matsubara I, Dorairaj S, Furlanetto R L et al. (2017) In vivo analysis of glaucoma-related features within the optic nerve head using enhanced depth imaging optical coherence tomography. *Plos One* 12.

Prinz F, Schlange T, and Asadullah K (2011) Believe it or not: how much can we rely on published data on potential drug targets? *Nature Reviews Drug Discovery* 10: 712-712.

Prünte C O, S.; Flammer, J. (1998) Abnormalities of microcirculation in glaucoma: facts and hints. *Current Opinion in Ophthalmology* 9: 50-55.

Puliafito C A, Hee M R, Lin C P, Reichel E, Schuman J S, Duker J S, Izatt J A et al. (1995) Imaging of macular diseases with optical coherence tomography. *Ophthalmology* 102: 217-229.

Quigley H A (1987) Reappraisal of the mechanisms of glaucomatous optic nerve damage. *Eye* 1: 318-322.

Quigley H A (1993) Medical progress - open-angle glaucoma. *New England Journal of Medicine* 328: 1097-1106.

Quigley H A (1999) Neuronal death in glaucoma. *Progress in Retinal and Eye Research* 18: 39-57.

Quigley H A (2011) Glaucoma. *Lancet* 377: 1367-1377.

Quigley H A, and Addicks E M (1981) Regional differences in the structure of the lamina cribrosa and their relation to glaucomatous optic-nerve damage. *Archives of Ophthalmology* 99: 137-143.

Quigley H A, Addicks E M, and Green W R (1982) Optic nerve damage in human glaucoma. III. Quantitative correlation of nerve fiber loss and visual field defect in glaucoma, ischemic neuropathy, papilledema, and toxic neuropathy. *Archives of Ophthalmology* 100: 135-146.

Quigley H A, Addicks E M, Green W R, and Maumenee A E (1981) Optic-nerve damage in human glaucoma 2. The site of injury and susceptibility to damage. *Archives of Ophthalmology* 99: 635-649.

Quigley H A, and Anderson D R (1976) Dynamics and location of axonal-transport blockade by acute intraocular-pressure elevation in primate optic-nerve. *Investigative Ophthalmology* 15: 606-616.

Quigley H A, and Broman A T (2006) The number of people with glaucoma worldwide in 2010 and 2020. *British Journal of Ophthalmology* 90: 262-267.

Quigley H A, Brown A, and Dormanpease M E (1991a) Alterations in elastin of the optic nerve head in human and experimental glaucoma. *British Journal of Ophthalmology* 75: 552-557.

Quigley H A, Brown A E, Morrison J D, and Drance S M (1990) The Size and Shape of the Optic Disc in Normal Human Eyes. *Archives of Ophthalmology* 108: 51-57.

Quigley H A, Dorman-Pease M E, and Brown A E (1991b) Quantitative study of collagen and elastin of the optic nerve head and sclera in human and experimental monkey glaucoma. *Current Eye Research* 10: 877-888.

Quigley H A, Dunkelberger G R, and Green W R (1988) Chronic human glaucoma causing selectively greater loss of large optic-nerve fibers. *Ophthalmology* 95: 357-363.

Quigley H A, Dunkelberger G R, and Green W R (1989) Retinal ganglion-cell atrophy correlated with automated perimetry in human eyes with glaucoma. *American Journal of Ophthalmology* 107: 453-464.

Quigley H A, and Green W R (1979) The histology of human glaucoma cupping and optic-nerve damage - clinicopathologic correlation in 21 eyes. *Ophthalmology* 86: 1803-1830.

Quigley H A, Hohman R M, Addicks E M, Massof R W, and Green W R (1983) Morphologic changes in the lamina cribrosa correlated with neural loss in open-angle glaucoma. *American Journal of Ophthalmology* 95: 673-691.

Quigley H A, Katz J, Derick R J, Gilbert D, and Sommer A (1992) An evaluation of optic disk and nerve-fiber layer examinations in monitoring progression of early glaucoma damage. *Ophthalmology* 99: 19-28.

Quigley H A, McKinnon S J, Zack D J, Pease M E, Kerrigan-Baumrind L A, Kerrigan D F, and Mitchell R S (2000) Retrograde axonal transport of BDNF in retinal ganglion cells is blocked by acute IOP elevation in rats. *Investigative Ophthalmology & Visual Science* 41: 3460-3466.

Quigley H A, Sanchez R M, Dunkelberger G R, Lhernault N L, and Baginski T A (1987) Chronic glaucoma selectively damages large optic-nerve fibers. *Investigative Ophthalmology & Visual Science* 28: 913-920.

Radius R L (1981) Regional specificity in anatomy at the lamina cribrosa. *Arch Ophthalmol* 99: 478-480.

Radius R L (1983) Pressure-induced fast axonal transport abnormalities and the anatomy at the lamina cribrosa in primate eyes. *Investigative Ophthalmology & Visual Science* 24: 343-346.

Radius R L (1987) Anatomy of the optic nerve head and glaucomatous optic neuropathy. *Survey of Ophthalmology* 32: 35-44.

Radius R L, and Gonzales M (1981) Anatomy of the lamina cribrosa in human eyes. *Archives of Ophthalmology* 99: 2159-2162.

Rahman F, Zekite A, Bunce C, Jayaram H, and Flanagan D (2020) Recent trends in vision impairment certifications in England and Wales. *Eye* 34: 1271-1278.

Ran A R, Tham C C, Chan P C, Cheng C Y, Tham Y C, Rim T H, and Cheung C Y (2021) Deep learning in glaucoma with optical coherence tomography: a review. *Eye* 35: 188-201.

Reis A S C, O'Leary N, Stanfield M J, Shuba L M, Nicolela M T, and Chauhan B C (2012a) Laminar Displacement and Prelaminar Tissue Thickness Change after Glaucoma Surgery Imaged with Optical Coherence Tomography. *Investigative Ophthalmology & Visual Science* 53: 5819-5826.

Reis A S C, O'Leary N, Yang H L, Sharpe G P, Nicolela M T, Burgoyne C F, and Chauhan B C (2012b) Influence of Clinically Invisible, but Optical Coherence Tomography Detected, Optic Disc Margin Anatomy on Neuroretinal Rim Evaluation. *Investigative Ophthalmology & Visual Science* 53: 1852-1860.

Reis A S C, Sharpe G P, Yang H L, Nicolela M T, Burgoyne C F, and Chauhan B C (2012c) Optic Disc Margin Anatomy in Patients with Glaucoma and Normal Controls with Spectral Domain Optical Coherence Tomography. *Ophthalmology* 119: 738-747.

Ren R J, Li B, Gao F, Li L Q, Xu X L, Wang N L, and Jonas J B (2010) Central corneal thickness, lamina cribrosa and peripapillary scleral histomorphometry in non-glaucomatous chinese eyes. *Graefes Archive for Clinical and Experimental Ophthalmology* 248: 1579-1585.

Ren R J, Wang N L, Li B, Li L Q, Gao F, Xu X L, and Jonas J B (2009) Lamina Cribrosa and Peripapillary Sclera Histomorphometry in Normal and Advanced Glaucomatous Chinese Eyes with Various Axial Length. *Investigative Ophthalmology & Visual Science* 50: 2175-2184.

Resnikoff S, Pascolini D, Etya'ale D, Kocur I, Pararajasegaram R, Pokharel G P, and Mariotti S P (2004) Global data on visual impairment in the year 2002. *Bulletin of the World Health Organization* 82: 844-851.

Reus N J, Lemij H G, Garway-Heath D F, Airaksinen P J, Anton A, Bron A M, Faschinger C et al. (2010) Clinical Assessment of Stereoscopic Optic Disc Photographs for Glaucoma: The European Optic Disc Assessment Trial. *Ophthalmology* 117: 717-723.

Rhodes L A, Huisingh C, Johnstone J, Fazio M, Smith B, Clark M, Downs J C et al. (2014) Variation of Laminar Depth in Normal Eyes With Age and Race. *Investigative Ophthalmology & Visual Science* 55: 8123-8133.

Roberts M D, Grau V, Grimm J, Reynaud J, Bellezza A J, Burgoyne C F, and Downs J C (2009) Remodeling of the Connective Tissue Microarchitecture of the Lamina Cribrosa in Early Experimental Glaucoma. *Investigative Ophthalmology & Visual Science* 50: 681-690.

Roberts M D, Liang Y, Sigal I A, Grimm J, Reynaud J, Bellezza A, Burgoyne C F et al. (2010a) Correlation between Local Stress and Strain and Lamina Cribrosa Connective Tissue Volume Fraction in Normal Monkey Eyes. *Investigative Ophthalmology & Visual Science* 51: 295-307.

Roberts M D, Sigal I A, Liang Y, Burgoyne C F, and Downs J C (2010b) Changes in the Biomechanical Response of the Optic Nerve Head in Early Experimental Glaucoma. *Investigative Ophthalmology & Visual Science* 51: 5675-5684.

Rochtchina E, Mitchell P, and Wang J J (2002) Relationship between age and intraocular pressure: The Blue Mountains Eye Study. *Clinical and Experimental Ophthalmology* 30: 173-175.

Rossetto J D, Melo L A S, Campos M S, and Tavares I M (2017) Agreement on the evaluation of glaucomatous optic nerve head findings by ophthalmology residents and a glaucoma specialist. *Clinical Ophthalmology* 11: 1281-1284.

Rotchford A P, Kirwan J F, Muller M A, Johnson G J, and Roux P (2003) Temba glaucoma study: A population-based cross-sectional survey in urban South Africa. *Ophthalmology* 110: 376-382.

Rousseau V, and Sabel B A (2001) Restoration of vision IV: role of compensatory soma swelling of surviving retinal ganglion cells in recovery of vision after optic nerve crush. *Restorative Neurology and Neuroscience* 18: 177-189.

Roy A G, Conjeti S, Karri S P K, Sheet D, Katouzian A, Wachinger C, and Navab N (2017) ReLayNet: retinal layer and fluid segmentation of macular optical coherence tomography using fully convolutional networks. *Biomedical Optics Express* 8: 3627-3642.

Rudnicka A R, Mt-Isa S, Owen C G, Cook D G, and Ashby D (2006) Variations in primary open-angle glaucoma prevalence by age, gender, and race: A Bayesian meta-analysis. *Investigative Ophthalmology & Visual Science* 47: 4254-4261.

Sakamoto A, Hangai M, Nukada M, Nakanishi H, Mori S, Kotera Y, Inoue R et al. (2010) Three-Dimensional Imaging of the Macular Retinal Nerve Fiber Layer in Glaucoma with Spectral-Domain Optical Coherence Tomography. *Investigative Ophthalmology & Visual Science* 51: 5062-5070.

Sakata L M, DeLeon-Ortega J, Sakata V, and Girkin C A (2009) Optical coherence tomography of the retina and optic nerve - a review. *Clinical and Experimental Ophthalmology* 37: 90-99.

Sarunic M V, Asrani S, and Izatt J A (2008) Imaging the ocular anterior segment with real-time, full-range Fourier-Domain optical coherence tomography. *Archives of Ophthalmology* 126: 537-542.

Saw S M, Gazzard G, Shih-Yen E C, and Chua W H (2005) Myopia and associated pathological complications. *Ophthalmic and Physiological Optics* 25: 381-391.

Schaffer C (1993) Selecting a classification method by cross validation. *Machine Learning* 13: 135-143.

Scheffer J (2002) Dealing with missing data. *Research Letters in the Information and Mathematical Sciences* 3: 153-160.

Schmitt J M (1999) Optical coherence tomography (OCT): A review. *Ieee Journal of Selected Topics in Quantum Electronics* 5: 1205-1215.

Schulzer M, Alward W L, Feldman F, Cashwell L F, Wilensky J, Geijssen H C, Greeve E et al. (1998) Comparison of glaucomatous progression between untreated patients with normal-

tension glaucoma and patients with therapeutically reduced intraocular pressures. *American Journal of Ophthalmology* 126: 487-497.

Schuman J S (2008) Spectral Domain Optical Coherence Tomography for Glaucoma (An AOS Thesis). *Trans Am Ophthalmol Soc* 106: 426-458.

Schuman J S (2012) Detection and Diagnosis of Glaucoma: Ocular Imaging. *Investigative Ophthalmology & Visual Science* 53: 2488-2490.

Schuman J S, Hee M R, Arya A V, Pedut-Kloizman T, Puliafito C A, Fujimoto J G, and Swanson E A (1995a) Optical coherence tomography: a new tool for glaucoma diagnosis. *Current Opinion in Ophthalmology* 6: 89-95.

Schuman J S, Hee M R, Puliafito C A, Wong C, Pedutkloizman T, Lin C P, Hertzmark E et al. (1995b) Quantification of nerve-fiber layer thickness in normal and glaucomatous eyes using optical coherence tomography - a pilot-study. *Archives of Ophthalmology* 113: 586-596.

Schuman J S, PedutKloizman T, Hertzmark E, Hee M R, Wilkins J R, Coker J G, Puliafito C A et al. (1996) Reproducibility of nerve fiber layer thickness measurements using optical coherence tomography. *Ophthalmology* 103: 1889-1898.

Schuster A K, Erb C, Hoffmann E M, Dietlein T, and Pfeiffer N (2020) The Diagnosis and Treatment of Glaucoma. *Deutsches Arzteblatt International* 117: 225-234.

Schwartz J T (1976) Methodologic differences and measurement of cup-disc ratio - epidemiologic assessment. *Archives of Ophthalmology* 94: 1101-1105.

Seo J H, Kim T W, and Weinreb R N (2014) Lamina Cribrosa Depth in Healthy Eyes. *Investigative Ophthalmology & Visual Science* 55: 1241-1250.

Shah P, Masood I, Sii F, Lee G, Kirwan J F, and Dulku S (2020 - in preparation) Glauc-Strat-Fast: Development and implementation of a real-world glaucoma risk stratification tool.

Sharma P, Sample P A, Zangwill L M, and Schuman J S (2008) Diagnostic Tools for Glaucoma Detection and Management. *Survey of Ophthalmology* 53: S17-S32.

Shiose Y (1984) The aging effect on intraocular-pressure in an apparently normal population. *Archives of Ophthalmology* 102: 883-887.

Shiose Y (1990) Intraocular pressure - new perspectives. *Survey of Ophthalmology* 34: 413-435.

Shoji T, Sato H, Ishida M, Takeuchi M, and Chihara E (2011) Assessment of Glaucomatous Changes in Subjects with High Myopia Using Spectral Domain Optical Coherence Tomography. *Investigative Ophthalmology & Visual Science* 52: 1098-1102.

Shrout P E, and Fleiss J L (1979) Intraclass Correlations - Uses In Assessing Rater Reliability. *Psychological Bulletin* 86: 420-428.

Sigal I A, Flanagan J G, Tertinegg I, and Ethier C R (2010) 3D morphometry of the human optic nerve head. *Experimental Eye Research* 90: 70-80.

Sihota R, Sony P, Gupta V, Dada T, and Singh R (2005) Comparing glaucomatous optic neuropathy in primary open angle and chronic primary angle closure glaucoma eyes by optical coherence tomography. *Ophthalmic and Physiological Optics* 25: 408-415.

Smith G (2018) Step away from stepwise. *Journal of Big Data* 5: 1-12.

Sommer A, Katz J, Quigley H A, Miller N R, Robin A L, Richter R C, and Witt K A (1991a) Clinically detectable nerve fiber atrophy precedes the onset of glaucomatous field loss. *Archives of Ophthalmology* 109: 77-83.

Sommer A, Tielsch J M, Katz J, Quigley H A, Gottsch J D, Javitt J, and Singh K (1991b) Relationship between intraocular-pressure and primary open angle glaucoma among white and black-americans - the baltimore eye survey. *Archives of Ophthalmology* 109: 1090-1095.

Spaeth G L, Henderer J, Liu C, Kesen M, Altangerel A, Bayer A, Katz J et al. (2002) The disc damage likelihood scale: reproducibility of a new method of estimating the amount of optic nerve damage caused by glaucoma. *Trans Am Ophthalmol Soc* 100: 181-186.

Spaeth G L, Lopes J F, Junk A K, Grigorian A P, and Henderer J (2006) Systems for staging the amount of optic nerve damage in glaucoma: A critical review and new material. *Survey of Ophthalmology* 51: 293-315.

Spaide R F, Koizumi H, and Pozonni M C (2008) Enhanced depth imaging spectral-domain optical coherence tomography. *American Journal of Ophthalmology* 146: 496-500.

Srinivasan V J, Wojtkowski M, Fujimoto J G, and Duker J S (2006) In vivo measurement of retinal physiology with high-speed ultrahigh-resolution optical coherence tomography. *Optics Letters* 31: 2308-2310.

Stein J D, Newman-Casey P A, Talwar N, Nan B, Richards J E, and Musch D C (2012) The Relationship Between Statin Use and Open-Angle Glaucoma. *Ophthalmology* 119: 2074-2081.

Stodden V (2009) The Legal Framework for Reproducible Scientific Research Licensing and Copyright. *Computing in Science & Engineering* 11: 35-40.

Strasak A M, Zaman Q, Pfeiffer K P, Gobel G, and Ulmer H (2007) Statistical errors in medical research - a review of common pitfalls. *Swiss Medical Weekly* 137: 44-49.

Strouthidis N G, Grimm J, Williams G A, Cull G A, Wilson D J, and Burgoyne C F (2010) A Comparison of Optic Nerve Head Morphology Viewed by Spectral Domain Optical Coherence

Tomography and by Serial Histology. *Investigative Ophthalmology & Visual Science* 51: 1464-1474.

Stroux A, Martus P, Budde W, Horn F, Junemann A, Korth M, and Jonas J B (2003) Sequential classification in glaucoma diagnosis. *Graefes Archive for Clinical and Experimental Ophthalmology* 241: 277-283.

Sull A C, Vuong L N, Price L L, Srinivasan V J, Gorczynska I, Fujimoto J G, Schuman J S et al. (2010) Comparison of spectral/fourier domain optical coherence tomography instruments for assessment of normal macular thickness. *Retina-the Journal of Retinal and Vitreous Diseases* 30: 235-245.

Sull A C, Vuong L N, Srinivasan V, Witkin A J, Wojtkowski M, Fujimoto J G, and Duker J S (2008) The evolution of spectral-domain optical coherence tomography. *Retina Today* 6: 39-44.

Sung K R, Kim J S, Wollstein G, Folio L, Kook M S, and Schuman J S (2011) Imaging of the retinal nerve fibre layer with spectral domain optical coherence tomography for glaucoma diagnosis. *British Journal of Ophthalmology* 95: 909-914.

Sung K R, Na J H, and Lee Y (2012) Glaucoma Diagnostic Capabilities of Optic Nerve Head Parameters as Determined by Cirrus HD Optical Coherence Tomography. *Journal of Glaucoma* 21: 498-504.

Susanna R (1983) The lamina cribrosa and visual field defects in open angle glaucoma. *Canadian Journal of Ophthalmology* 18: 124-126.

Swanson E A, Izatt J A, Hee M R, Huang D, Lin C P, Schuman J S, Puliafito C A et al. (1993) In-Vivo retinal imaging by optical coherence tomography. *Optics Letters* 18: 1864-1866.

Syam P P, Mavrikakis I, and Liu C (2005) Importance of early morning intraocular pressure recording for measurement of diurnal variation of intraocular pressure. *British Journal of Ophthalmology* 89: 926-927.

Takayama K, Hangai M, Kimura Y, Morooka S, Nukada M, Akagi T, Ikeda H O et al. (2013) Three-Dimensional Imaging of Lamina Cribrosa Defects in Glaucoma Using Swept-Source Optical Coherence Tomography. *Investigative Ophthalmology & Visual Science* 54: 4798-4807.

Tan J C H, Garway-Heath D F, and Hitchings R A (2003) Variability across the optic nerve head in scanning laser tomography. *British Journal of Ophthalmology* 87: 557-559.

Tan N Y Q, Tham Y C, Thakku G, Wang X F, Baskaran M, Tan M C L, Mari J M et al. (2019) Changes in the Anterior Lamina Cribrosa Morphology with Glaucoma Severity. *Scientific Reports* 9.

Tan O, Chopra V, Lu A T H, Schuman J S, Ishikawa H, Wollstein G, Varma R et al. (2009) Detection of Macular Ganglion Cell Loss in Glaucoma by Fourier-Domain Optical Coherence Tomography. *Ophthalmology* 116: 2305-2314.

Tanito M, Nitta K, Katai M, Kitaoka Y, Yokoyama Y, Omodaka K, and Nakazawa T (2017) Differentiation of glaucomatous optic discs with different appearances using optic disc topography parameters: The Glaucoma Stereo Analysis Study. *Plos One* 12.

Tarabishy A B, Alexandrou T J, and Traboulsi E I (2007) Syndrome of myelinated retinal nerve fibers, myopia, and amblyopial: A review. *Survey of Ophthalmology* 52: 588-596.

Tatham A J, Weinreb R N, Zangwill L M, Liebmann J M, Girkin C A, and Medeiros F A (2013) The Relationship Between Cup-to-Disc Ratio and Estimated Number of Retinal Ganglion Cells. *Investigative Ophthalmology & Visual Science* 54: 3205-3214.

Tearney G J, Bouma B E, Boppart S A, Golubovic B, Swanson E A, and Fujimoto J G (1996) Rapid acquisition of in vivo biological images by use of optical coherence tomography. *Optics Letters* 21: 1408-1410.

Terry L, Cassels N, Lu K, Acton J H, Margrain T H, North R V, Fergusson J et al. (2016) Automated Retinal Layer Segmentation Using Spectral Domain Optical Coherence Tomography: Evaluation of Inter-Session Repeatability and Agreement between Devices. *Plos One* 11: 1-15.

Tezel G, Trinkaus K, and Wax M B (2004) Alterations in the morphology of lamina cribrosa pores in glaucomatous eyes. *British Journal of Ophthalmology* 88: 251-256.

Thakku S G, Tham Y C, Baskaran M, Mari J M, Strouthidis N G, Aung T, Cheng C Y et al. (2015) A Global Shape Index to Characterize Anterior Lamina Cribrosa Morphology and Its Determinants in Healthy Indian Eyes. *Investigative Ophthalmology & Visual Science* 56: 3604-3614.

Tham Y C, Li X, Wong T Y, Quigley H A, Aung T, and Cheng C Y (2014) Global Prevalence of Glaucoma and Projections of Glaucoma Burden through 2040 A Systematic Review and Meta-Analysis. *Ophthalmology* 121: 2081-2090.

Thevenaz P, Ruttimann U E, and Unser M (1998) A pyramid approach to subpixel registration based on intensity. *Ieee Transactions on Image Processing* 7: 27-41.

Thompson A C, Jammal A A, and Medeiros F A (2019) A Deep Learning Algorithm to Quantify Neuroretinal Rim Loss From Optic Disc Photographs. *American Journal of Ophthalmology* 201: 9-18.

Thompson B (1995) Stepwise regression and stepwise discriminant analysis need not apply here: a guidelines editorial. *Educational and Psychological Measurement* 55: 525-534.

Thylefors B, and Negrel A D (1994) The global impact of glaucoma. *Bulletin of the World Health Organization* 72: 323-326.

Tian H J, Li L, and Song F (2017) Study on the deformations of the lamina cribrosa during glaucoma. *Acta Biomaterialia* 55: 340-348.

Tielsch J M, Katz J, Singh K, Quigley H A, Gottsch J D, Javitt J, and Sommer A (1991) A population-based evaluation of glaucoma screening - The Baltimore Eye Survey. *American Journal of Epidemiology* 134: 1102-1110.

Ting D S W, Cheung C Y L, Lim G, Tan G S W, Quang N D, Gan A, Hamzah H et al. (2017) Development and Validation of a Deep Learning System for Diabetic Retinopathy and Related Eye Diseases Using Retinal Images From Multiethnic Populations With Diabetes. *Jama-Journal of the American Medical Association* 318: 2211-2223.

Traber G L, Weber K P, Sabah M, Keane P A, and Plant G T (2017) Enhanced Depth Imaging Optical Coherence Tomography of Optic Nerve Head Drusen A Comparison of Cases with and without Visual Field Loss. *Ophthalmology* 124: 66-73.

Tun T A, Thakku S G, Png O, Baskaran M, Htoon H M, Sharma S, Nongpiur M E et al. (2016) Shape Changes of the Anterior Lamina Cribrosa in Normal, Ocular Hypertensive, and Glaucomatous Eyes Following Acute Intraocular Pressure Elevation. *Investigative Ophthalmology & Visual Science* 57: 4869-4877.

Tuulonen A, and Airaksinen P J (1992) Optic disc size in exfoliative, primary open angle, and low-tension glaucoma. *Archives of Ophthalmology* 110: 211-213.

Uchida H, Brigatti L, and Caprioli J (1996) Detection of structural damage from glaucoma with confocal laser image analysis. *Investigative Ophthalmology & Visual Science* 37: 2393-2401.

Ugurlu S, Weitzman M, Nduaguba C, and Caprioli J (1998) Acquired pit of the optic nerve: A risk factor for progression of glaucoma. *American Journal of Ophthalmology* 125: 457-464.

Unterhuber A, Povazay B, Hermann B, Sattmann H, Chavez-Pirson A, and Drexler W (2005) In vivo retinal optical coherence tomography at 1040 nm - enhanced penetration into the choroid. *Optics Express* 13: 3252-3258.

Unterlauft J D, Theilig T, Hasan S, Bohm M R, and Rauscher F (2020) Analysis of Glaucomatous Changes of the Macula Using Optical Coherence Tomography. *Klinische Monatsblatter Fur Augenheilkunde* 237: 185-191.

Van Veldhuisen P C, Ederer F, Gaasterland D E, Sullivan E K, Beck A, Prum B E, Cyrlin M N et al. (2000) The advanced glaucoma intervention study (AGIS): 7. The relationship between control of intraocular pressure and visual field deterioration. *American Journal of Ophthalmology* 130: 429-440.

VanVoorhis C R W, and Morgan B (2007) Understaing power and rules of thumb for determining sample sizes. *Tutorials in Quantitative Methods for Psychology* 3: 43-50.

Varela H J, and Hernandez M R (1997) Astrocyte responses in human optic nerve head with primary open-angle glaucoma. *Journal of Glaucoma* 6: 303-313.

Varma R, Quigley H A, and Pease M E (1992a) Changes in optic disk characteristics and the number of nerve-fibers in experimental glaucoma. *American Journal of Ophthalmology* 114: 554-559.

Varma R, Steinmann W C, and Scott I U (1992b) Expert agreement in evaluating the optic disk for glaucoma. *Ophthalmology* 99: 215-221.

Varma R, Tielsch J M, Quigley H A, Hilton S C, Katz J, Spaeth G L, and Sommer A (1994) Race-related, age-related, gender-related, and refractive error-related differences in the normal optic disc. *Archives of Ophthalmology* 112: 1068-1076.

Vrabec F (1976) Glaucomatous cupping of human optic disc - neurohistologic study. *Albrecht Von Graefes Archiv Fur Klinische Und Experimentelle Ophthalmologie* 198: 223-234.

Wahl P W, and Kronmal R A (1977) Discriminant functions when covariances are unequal and sample sizes are moderate. *Biometrics* 33: 479-484.

Wallace D M, and O'Brien C J (2016) The role of lamina cribrosa cells in optic nerve head fibrosis in glaucoma. *Experimental Eye Research* 142: 102-109.

Walport M, and Brest P (2011) Sharing research data to improve public health. *Lancet* 377: 537-539.

Walter S, and Tiemeier H (2009) Variable selection: current practice in epidemiological studies. *European Journal of Epidemiology* 24: 733-736.

Wang B, Lucy K A, Schuman J S, Ishikawa H, Bilonick R A, Sigal I A, Kagemann L et al. (2017) Location of the Central Retinal Vessel Trunk in the Laminar and Prelaminar Tissue of Healthy and Glaucomatous Eyes. *Scientific Reports* 7.

Wang B, Lucy K A, Schuman J S, Sigal I A, Bilonick R A, Lu C, Liu J et al. (2018) Tortuous Pore Path Through the Glaucomatous Lamina Cribrosa. *Scientific Reports* 8.

Wang B, Nevins J E, Nadler Z, Wollstein G, Ishikawa H, Bilonick R A, Kagemann L et al. (2013) In Vivo Lamina Cribrosa Micro-Architecture in Healthy and Glaucomatous Eyes as Assessed by Optical Coherence Tomography. *Investigative Ophthalmology & Visual Science* 54: 8270-8274.

Wang J, Wang Z, Li F, Qu G X, Qiao Y, Lv H R, and Zhang X L (2019) Joint retina segmentation and classification for early glaucoma diagnosis. *Biomedical Optics Express* 10: 2639-2656.

Wang M, Hood D C, Cho J S, Ghadiali Q, De Moraes G V, Zhang X, Ritch R et al. (2009) Measurement of Local Retinal Ganglion Cell Layer Thickness in Patients With Glaucoma Using Frequency-Domain Optical Coherence Tomography. *Archives of Ophthalmology* 127: 875-881.

Wang Y X, Xu L A, Yang H, and Jonas J B (2010) Prevalence of Glaucoma in North China: The Beijing Eye Study. *American Journal of Ophthalmology* 150: 917-924.

Weber A J, Kaufman P L, and Hubbard W C (1998) Morphology of single ganglion cells in the glaucomatous primate retina. *Investigative Ophthalmology & Visual Science* 39: 2304-2320.

Weinreb R N, Aung T, and Medeiros F A (2014) The Pathophysiology and Treatment of Glaucoma A Review. *Jama-Journal of the American Medical Association* 311: 1901-1911.

Weinreb R N, and Khaw P T (2004) Primary open-angle glaucoma. *Lancet* 363: 1711-1720.

Weinreb R N, Leung C K S, Crowston J G, Medeiros F A, Friedman D S, Wiggs J L, and Martin K R (2016) Primary open-angle glaucoma. *Nature Reviews Disease Primers* 2.

Weinreb R N, Zangwill L, Berry C C, Bathija R, and Sample P A (1998) Detection of glaucoma with scanning laser polarimetry. *Archives of Ophthalmology* 116: 1583-1589.

Weisman R L, Asseff C F, Phelps C D, Podos S M, and Becker B (1973) Vertical elongation of the optic cup in glaucoma. *Transactions American Academy of Ophthalmology and Otolaryngology* 77: 157-163.

West S K, Rubin G S, Broman A T, Munoz B, Bandeen-Roche K, Turano K, and Team S E E P (2002) How does visual impairment affect performance on tasks of everyday life? The SEE Project. *Archives of Ophthalmology* 120: 774-780.

Whittingham M J, Stephens P A, Bradbury R B, and Freckleton R P (2006) Why do we still use stepwise modelling in ecology and behaviour? *Journal of Animal Ecology* 75: 1182-1189.

Wilkinson M D, Dumontier M, Aalbersberg I J, Appleton G, Axton M, Baak A, Blomberg N et al. (2016) The FAIR Guiding Principles for scientific data management and stewardship. *Scientific Data* 3.

Winkler M, Jester B, Nien-Shy C, Massei S, Minckler D S, Jester J V, and Brown D J (2010) High resolution three-dimensional reconstruction of the collagenous matrix of the human optic nerve head. *Brain Research Bulletin* 81: 339-348.

Wojtkowski M, Bajraszewski T, Gorczynska I, Targowski P, Kowalczyk A, Wasilewski W, and Radzewicz C (2004) Ophthalmic imaging by spectral optical coherence tomography. *American Journal of Ophthalmology* 138: 412-419.

Wojtkowski M, Leitgeb R, Kowalczyk A, Bajraszewski T, and Fercher A F (2002) In vivo human retinal imaging by Fourier domain optical coherence tomography. *Journal of Biomedical Optics* 7: 457-463.

Wojtkowski M, Srinivasan V, Fujimoto J G, Ko T, Schuman J S, Kowalczyk A, and Duker J S (2005) Three-dimensional retinal imaging with high-speed ultrahigh-resolution optical coherence tomography. *Ophthalmology* 112: 1734-1746.

Wollstein G, Kagemann L, Bilonick R A, Ishikawa H, Folio L S, Gabriele M L, Ungar A K et al. (2012) Retinal nerve fibre layer and visual function loss in glaucoma: the tipping point. *British Journal of Ophthalmology* 96: 47-52.

Wollstein G, Schuman J S, Price L L, Aydin A, Beaton S A, Stark P C, Fujimoto J G et al. (2004) Optical coherence tomography (OCT) macular and peripapillary retinal nerve fiber layer measurements and automated visual fields. *American Journal of Ophthalmology* 138: 218-225.

Wood A, Binns A, Margrain T, Drexler W, Povazay B, Esmaeelpour M, and Sheen N (2011) Retinal and Choroidal Thickness in Early Age-Related Macular Degeneration. *American Journal of Ophthalmology* 152: 1030-1038.

Wu S Y, and Leske M C (1997) Associations with intraocular pressure in the Barbados Eye Study. *Archives of Ophthalmology* 115: 1572-1576.

Wu Z H, Xu G H, Weinreb R N, Yu M, and Leung C K S (2015) Optic Nerve Head Deformation in Glaucoma A Prospective Analysis of Optic Nerve Head Surface and Lamina Cribrosa Surface Displacement. *Ophthalmology* 122: 1317-1329.

Yan D B, Coloma F M, Metheetrairut A, Trope G E, Heathcote J G, and Ethier C R (1994) Deformation of the lamina cribrosa by elevated intraocular pressure. *British Journal of Ophthalmology* 78: 643-648.

Yang H L, Downs J C, Bellezza A, Thompson H, and Burgoyne C F (2007a) 3-D histomorphometry of the normal and early glaucomatous monkey optic nerve head: Prelaminar neural tissues and cupping. *Investigative Ophthalmology & Visual Science* 48: 5068-5084.

Yang H L, Downs J C, Girkin C, Sakata L, Bellezza A, Thompson H, and Burgoyne C F (2007b) 3-D histomorphometry of the normal and early glaucomatous monkey optic nerve head: Lamina cribrosa and peripapillary scleral position and thickness. *Investigative Ophthalmology & Visual Science* 48: 4597-4607.

Yang H L, Luo H M, Hardin C, Wang Y X, Jeoung J W, Albert C, Vianna J R et al. (2020) Optical Coherence Tomography Structural Abnormality Detection in Glaucoma Using Topographically Correspondent Rim and Retinal Nerve Fiber Layer Criteria. *American Journal of Ophthalmology* 213: 203-216.

Yang H L, Thompson H, Roberts M D, Sigal I A, Downs J C, and Burgoyne C F (2011a) Deformation of the Early Glaucomatous Monkey Optic Nerve Head Connective Tissue after Acute IOP Elevation in 3-D Histomorphometric Reconstructions. *Investigative Ophthalmology & Visual Science* 52: 345-363.

Yang H L, Williams G, Downs J C, Sigal I A, Roberts M D, Thompson H, and Burgoyne C F (2011b) Posterior (Outward) Migration of the Lamina Cribrosa and Early Cupping in Monkey Experimental Glaucoma. *Investigative Ophthalmology & Visual Science* 52: 7109-7121.

Ye C, Yu M, and Leung C K S (2016) Impact of segmentation errors and retinal blood vessels on retinal nerve fibre layer measurements using spectral-domain optical coherence tomography. *Acta Ophthalmologica* 94: E211-E219.

Ye H, and Hernandez M R (1995) 2 subpopulations of astrocytes type-1 in human optic-nerve heads. *Investigative Ophthalmology & Visual Science* 36: S964-S964.

Yeoh J, Rahman W, Chen F, Hooper C, Patel P, Tufail A, Webster A R et al. (2010) Choroidal imaging in inherited retinal disease using the technique of enhanced depth imaging optical coherence tomography. *Graefes Archive for Clinical and Experimental Ophthalmology* 248: 1719-1728.

Yoshikawa M, Akagi T, Hangai M, Ohashi-Ikeda H, Takayama K, Morooka S, Kimura Y et al. (2014) Alterations in the Neural and Connective Tissue Components of Glaucomatous Cupping After Glaucoma Surgery Using Swept-Source Optical Coherence Tomography. *Investigative Ophthalmology & Visual Science* 55: 477-484.

You J Y, Park S C, Su D, Teng C C, Liebmann J M, and Ritch R (2013) Focal Lamina Cribrosa Defects Associated With Glaucomatous Rim Thinning and Acquired Pits. *Jama Ophthalmology* 131: 314-320.

Yu M, Lin C, Weinreb R N, Lai G, Chiu V, and Leung C K S (2016) Risk of Visual Field Progression in Glaucoma Patients with Progressive Retinal Nerve Fiber Layer Thinning A 5-Year Prospective Study. *Ophthalmology* 123: 1201-1210.

Zavorka S, and Perrett J J (2014) Minimum Sample Size Considerations for Two-Group Linear and Quadratic Discriminant Analysis with Rare Populations. *Communications in Statistics-Simulation and Computation* 43: 1726-1739.

Zawadzki R J, Cense B, Zhang Y, Choi S S, Miller D T, and Werner J S (2008) Ultrahigh-resolution optical coherence tomography with monochromatic and chromatic aberration correction. *Optics Express* 16: 8126-8143.

Zeimer R, Asrani S, Zou S Z, Quigley H, and Jampel H (1998) Quantitative detection of glaucomatous damage at the posterior pole by retinal thickness mapping - A pilot study. *Ophthalmology* 105: 224-231.

Zeimer R C, and Ogura Y (1989) The relation between glaucomatous damage and optic nerve head mechanical compliance. *Archives of Ophthalmology* 107: 1232-1234.

Zhang C W, Tatham A J, Weinreb R N, Zangwill L M, Yang Z Y, Zhang J Z, and Medeiros F A (2014) Relationship between Ganglion Cell Layer Thickness and Estimated Retinal Ganglion Cell Counts in the Glaucomatous Macula. *Ophthalmology* 121: 2371-2379.

Zhang Q, Xu L, Wei W B, Wang Y X, and Jonas J B (2019) Size and Shape of Bruch's Membrane Opening in Relationship to Axial Length, Gamma Zone, and Macular Bruch's Membrane Defects. *Investigative Ophthalmology & Visual Science* 60: 2591-2598.

Zhang X B, Dastiridou A, Francis B A, Tan O, Varma R, Greenfield D S, Schuman J S et al. (2016) Baseline Fourier-Domain Optical Coherence Tomography Structural Risk Factors for Visual Field Progression in the Advanced Imaging for Glaucoma Study. *American Journal of Ophthalmology* 172: 94-103.

Appendix I

Example of 3D mean filter with specified pixel radii and respective line plot profiles is given in Figure II.1.

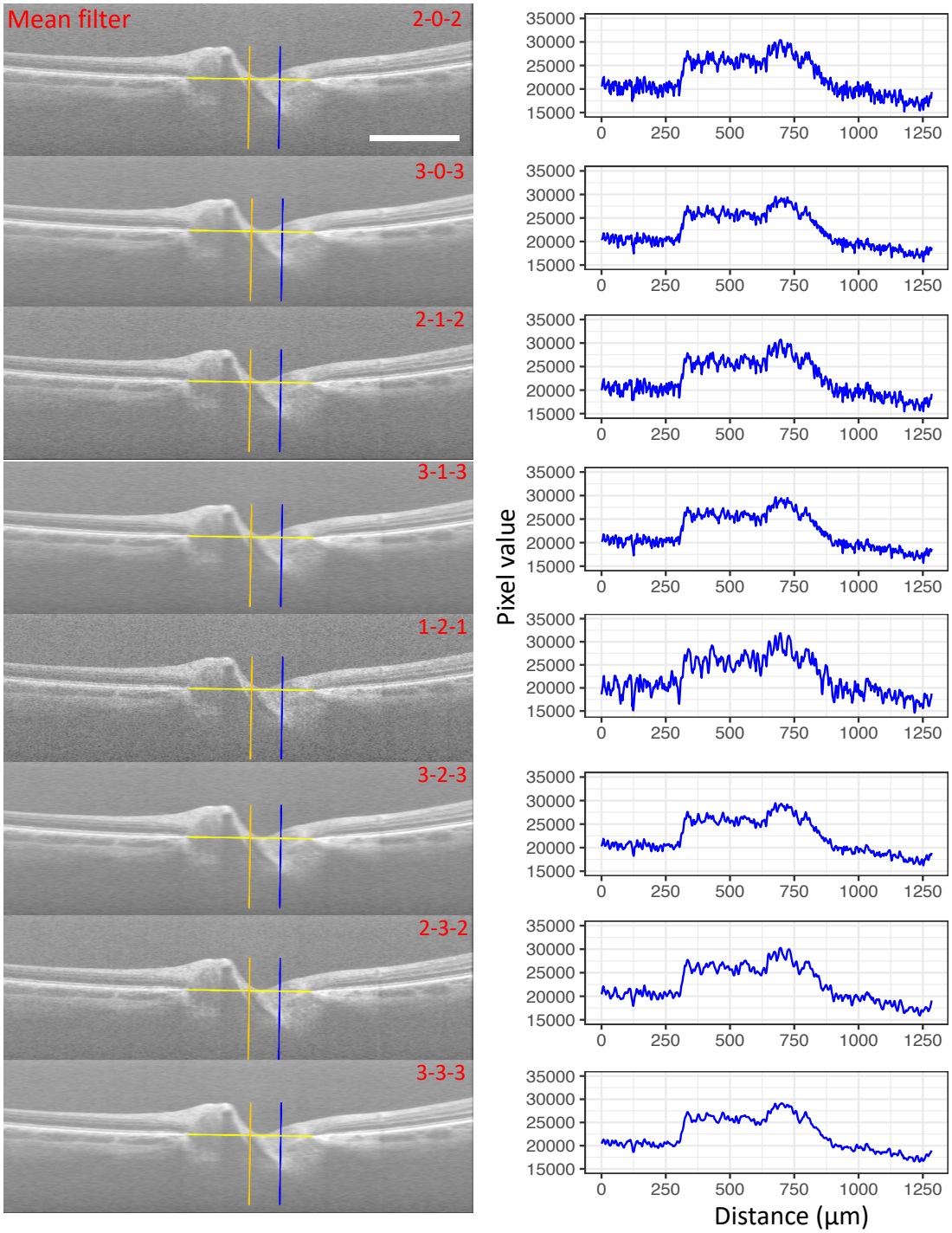

Figure II.1: Nasal-temporal ONH b-scan following 3D mean filter of varying pixel radii, with graphical representation of intensity line plot profile. Pixel radii displayed within OCT image in x-z-y directions respectively. BMO marked in yellow, ONH centre marked in orange, blue line represents position of intensity profile plot. Scale bar = 1mm.

Example of 3D median filter with specified pixel radii and respective line plot profiles is given in Figure II.2.

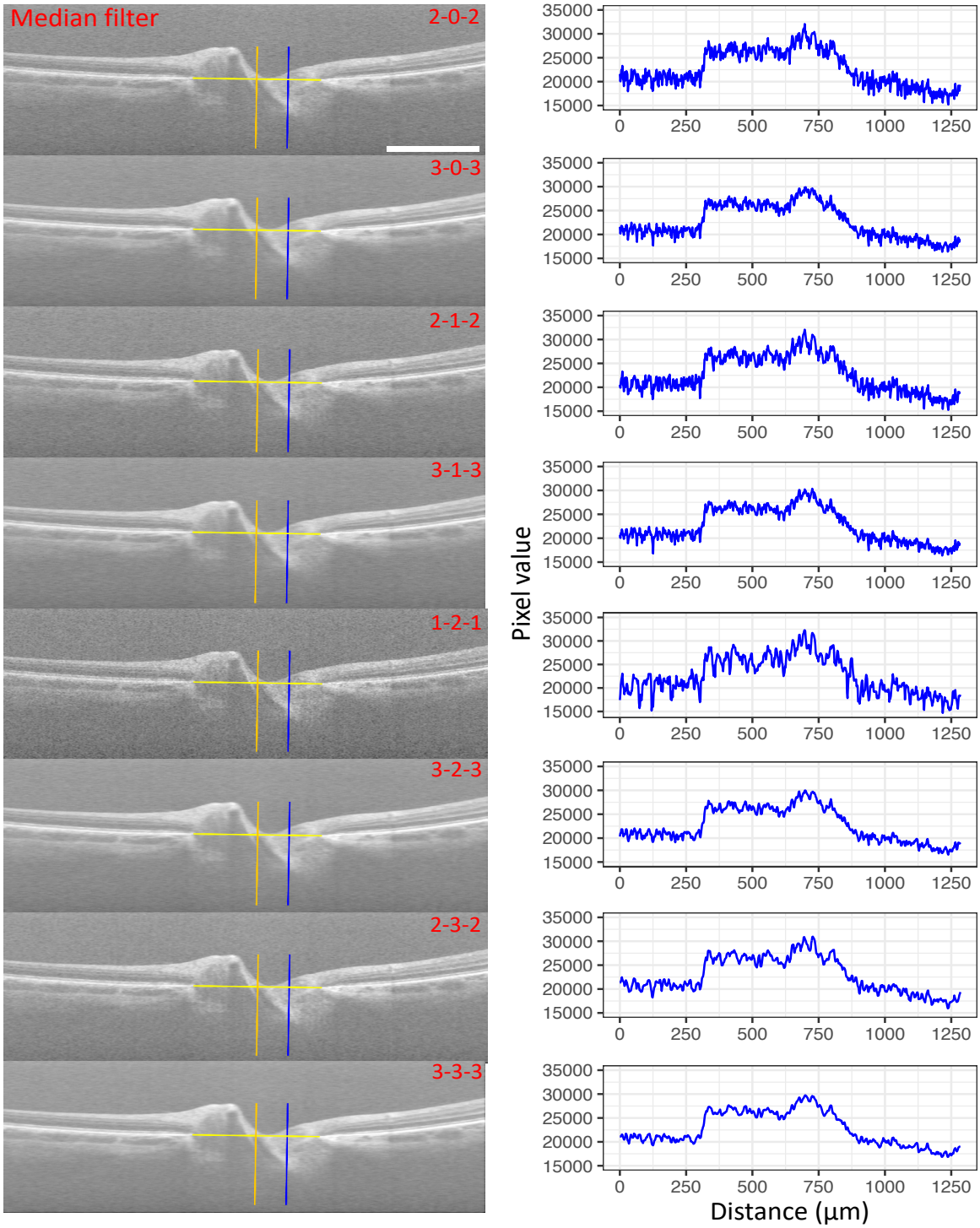

Figure II.2: Nasal-temporal ONH b-scan following 3D median filter of varying pixel radii, with graphical representation of intensity line plot profile. Pixel radii displayed within OCT image in x-z-y directions respectively. BMO marked in yellow, ONH centre marked in orange, blue line represents position of intensity profile plot. Scale bar = 1mm.

Appendix II

Table III.1 presents Bruch's membrane opening diameter in four ONH orientations measured as a function of glaucoma disease stage.

BMO (μm)	**C**	**PG**	**EG**	**MAG**
	Mean ± Standard Deviation			
S – I	1544.77 ± 142.06	1633.37 ± 192.56	1610.98 ± 181.99	1629.29 ± 190.48
N – T	1461.87 ± 115.48	1609.08 ± 237.82	1493.19 ± 233.53	1561.88 ± 231.03
SN – IT	1520.38 ± 142.56	1652.12 ± 202.18	1572.07 ± 243.02	1600.43 ± 206.43
ST – IN	1493.55 ± 133.27	1606.55 ± 192.70	1551.00 ± 212.25	1566.68 ± 214.18
V:H ratio	1.06 ± 0.09	1.01 ± 0.10	1.09 ± 0.11	1.05 ± 0.09
	Median and Interquartile Range			
S – I	1530.88 1462.62 - 1621.74	1600.99 1512.30 - 1777.50	1580.33 1467.62 - 1740.81	1611.39 1510.84 - 1724.38
N – T	1436.98 1389.14 – 1514.25	1580.68 1493.76 - 1735.79	1495.99 1298.71 - 1625.90	1551.73 1487.72 - 1619.25
SN – IT	1518.18 1426.53 - 1598.77	1629.77 1504.74 - 1755.90	1551.49 1401.41 - 1657.92	1581.24 1515.08 - 1689.91
ST – IN	1487.14 1406.58 - 1547.22	1604.05 1478.00 - 1693.09	1558.66 1399.18 - 1690.28	1560.10 1488.24 - 1629.71
V:H ratio	1.06 1.00 – 1.10	1.03 0.95 – 1.08	1.08 1.02 – 1.15	1.05 1.01 – 1.09

Table III.1: Bruch's membrane opening as a function of glaucoma disease stage. Presented as mean and standard deviation, and median and interquartile range.

Table III.2 presents regional measures of prelamina depth and thickness as a function of glaucoma disease stage.

ONH Parameter	Region	C	PG	EG	MAG
		Mean ± Standard Deviation			
Prelamina depth (μm)	Centre	115.78 ± 193.13	251.74 ± 124.08	248.45 ± 158.95	293.19 ± 180.06
	Superior	-40.11 ± 249.33	215.71 ± 211.30	238.87 ± 201.49	333.21 ± 200.69
	Inferior	-115.05 ± 197.85	72.15 ± 229.94	145.42 ± 212.08	269.24 ± 168.91
	Nasal	-197.71 ± 191.77	36.73 ± 221.74	-21.43 ± 245.64	132.45 ± 276.60
	Temporal	15.66 ± 203.05	150.70 ± 169.97	156.99 ± 155.90	211.56 ± 173.20
	SN	-113.06 ± 197.60	127.07 ± 236.26	138.80 ± 229.19	221.06 ± 268.02
	IT	-47.07 ± 177.11	90.89 ± 178.52	145.79 ± 167.62	217.16 ± 175.88
	ST	-39.32 ± 199.96	196.36 ± 186.34	219.15 ± 180.38	293.05 ± 189.46
	IN	-150.93 ± 236.02	57.37 ± 241.46	45.16 ± 254.85	145.36 ± 264.34
Prelamina thickness (μm)	Centre	251.98 ± 161.20	134.52 ± 64.95	137.37 ± 82.71	127.08 ± 75.78
	Superior	405.81 ± 224.67	200.56 ± 126.24	175.90 ± 123.38	127.83 ± 105.55
	Inferior	477.48 ± 173.66	328.26 ± 193.12	247.88 ± 158.69	151.78 ± 87.69
	Nasal	487.81 ± 210.59	321.53 ± 210.49	338.22 ± 215.88	273.25 ± 183.73
	Temporal	325.01 ± 163.99	216.82 ± 115.17	202.36 ± 105.85	166.49 ± 116.28
	SN	457.41 ± 192.53	277.80 ± 196.87	254.81 ± 173.21	181.74 ± 119.65
	IT	395.25 ± 154.05	280.77 ± 124.38	222.05 ± 116.12	158.36 ± 81.46
	ST	392.35 ± 178.39	201.71 ± 128.76	179.25 ± 114.96	129.43 ± 88.83
	IN	534.29 ± 188.17	257.30 ± 128.10	317.19 ± 197.11	255.82 ± 193.77

Table III.2: Regional measures of prelamina depth and thickness presented as mean and standard deviation for each stage of glaucoma.

Inter-group differences for regional measures of prelamina depth and thickness, and *P* values adjusted for multiple comparisons are shown in Table III.3.

ONH Parameter	Region	Multiple Comparisons: Adjusted *P* values					
		C-PG	C-EG	C-MAG	PG-EG	PG-MAG	EG-MAG
Prelamina depth	Centre	0.099	0.008	0.005	0.718	0.426	0.876
	Superior	0.003	<0.001	<0.001	0.381	<0.001	0.011
	Inferior	0.009	<0.001	<0.001	0.228	0.003	0.102
	Nasal	0.033	0.029	<0.001	0.983	0.489	0.178
	Temporal	0.095	0.010	0.004	0.899	0.477	0.741
	SN	0.010	<0.001	<0.001	0.635	0.277	0.778
	IT	0.002	<0.001	<0.001	0.453	0.080	0.517
	ST	<0.001	<0.001	<0.001	0.801	0.074	0.196
	IN	0.002	<0.001	<0.001	0.994	0.796	0.540
Prelamina thickness	Centre	<0.001	<0.001	<0.001	0.987	0.869	0.940
	Superior	<0.001	<0.001	<0.001	0.531	0.005	0.038
	Inferior	0.003	<0.001	<0.001	0.331	0.004	0.070
	Nasal	0.093	0.014	0.001	0.999	0.564	0.485
	Temporal	<0.001	<0.001	<0.001	0.962	0.432	0.560
	SN	0.006	<0.001	<0.001	0.992	0.555	0.565
	IT	<0.001	<0.001	<0.001	0.554	0.037	0.231
	ST	<0.001	<0.001	<0.001	0.890	0.156	0.287
	IN	<0.001	<0.001	<0.001	0.333	0.953	0.678

Table III.3: Inter-group differences for regional prelamina depth and thickness as a function of glaucoma disease stage. Red text indicates significant difference between groups at $p < 0.05$.

Table III.4 presents regional measurements of lamina cribrosa depth and thickness as a function of glaucoma disease stage.

ONH Parameter	Region	C	PG	EG	MAG
		Mean ± Standard Deviation			
Anterior lamina cribrosa depth (μm)	Centre	367.76 ± 89.52	384.56 ± 102.32	392.38 ± 110.77	417.78 ± 154.82
	Superior	387.15 ± 85.61	450.44 ± 97.56	431.82 ± 111.73	461.04 ± 164.23
	Inferior	366.65 ± 88.31	395.50 ± 106.13	405.48 ± 107.31	421.02 ± 133.83
	Nasal	344.91 ± 82.36	399.99 ± 91.40	378.61 ± 112.36	420.31 ± 140.49
	Temporal	345.69 ± 87.01	367.52 ± 106.12	362.32 ± 94.52	380.42 ± 138.14
	SN	369.05 ± 81.20	428.11 ± 105.03	408.87 ± 103.21	464.64 ± 161.01
	IT	352.48 ± 83.99	371.66 ± 110.85	367.31 ± 107.88	375.51 ± 129.87
	ST	359.01 ± 92.53	402.69 ± 107.61	406.32 ± 100.48	422.48 ± 152.48
	IN	368.44 ± 77.37	391.75 ± 102.41	389.39 ± 129.33	415.43 ± 121.39
Posterior lamina cribrosa depth (μm)	Centre	596.69 ± 107.57	600.75 ± 106.86	590.72 ± 108.98	595.97 ± 154.42
	Superior	616.31 ± 113.30	638.26 ± 119.73	608.32 ± 114.43	625.67 ± 171.62
	Inferior	591.36 ± 109.82	597.45 ± 120.64	584.86 ± 128.51	588.53 ± 144.23
	Nasal	579.89 ± 115.73	596.58 ± 112.77	576.55 ± 104.18	643.12 ± 138.29
	Temporal	579.56 ± 115.79	585.40 ± 113.24	560.19 ± 103.65	551.21 ± 151.14
	SN	592.54 ± 109.33	628.16 ± 121.37	590.20 ± 117.46	627.82 ± 162.88
	IT	579.33 ± 104.66	578.42 ± 127.95	560.80 ± 103.45	534.30 ± 129.06
	ST	590.34 ± 95.72	596.36 ± 114.34	590.57 ± 100.81	582.62 ± 157.56
	IN	576.99 ± 141.55	595.90 ± 99.24	576.41 ± 146.78	591.10 ± 139.65
Lamina cribrosa thickness (μm)	Centre	232.81 ± 37.24	214.34 ± 28.61	197.07 ± 40.10	175.69 ± 28.98
	Superior	224.27 ± 47.02	189.15 ± 43.95	178.07 ± 45.86	164.63 ± 37.28
	Inferior	230.82 ± 51.44	200.16 ± 37.18	186.97 ± 46.47	167.51 ± 33.50
	Nasal	225.29 ± 58.85	219.71 ± 37.21	194.80 ± 47.75	178.17 ± 48.79
	Temporal	234.53 ± 46.98	214.42 ± 45.59	200.85 ± 50.49	170.78 ± 48.62
	SN	222.57 ± 35.56	179.33 ± 53.40	179.57 ± 41.94	152.32 ± 22.02
	IT	227.09 ± 36.87	196.27 ± 40.26	194.37 ± 43.78	163.97 ± 21.75
	ST	225.60 ± 44.63	193.29 ± 35.25	184.89 ± 37.35	165.48 ± 29.02
	IN	221.38 ± 43.49	190.29 ± 29.35	185.75 ± 46.83	165.11 ± 29.51

Table III.4: Mean and standard deviation of regional lamina cribrosa depth and thickness for each stage of glaucoma.

Inter-group differences for regional measures of LC depth and thickness, and *P* values adjusted for multiple comparisons are shown in Table III.5.

ONH Parameter	Region	Multiple Comparisons: Adjusted *P* values					
		C-PG	C-EG	C-MAG	PG-EG	PG-MAG	EG-MAG
Anterior lamina cribrosa depth	Centre	0.998	0.695	0.656	0.296	0.315	0.994
	Superior	0.616	0.713	0.466	0.980	0.985	0.842
	Inferior	0.783	0.238	0.360	0.440	0.694	0.994
	Nasal	0.312	0.626	0.289	0.804	1.000	0.763
	Temporal	0.988	0.989	0.998	0.702	0.875	0.997
	SN	0.917	0.582	0.168	0.902	0.259	0.443
	IT	0.987	0.611	0.940	0.513	0.984	0.754
	ST	0.959	0.759	0.555	0.909	0.659	0.898
	IN	0.999	0.991	0.998	0.961	0.990	0.998
Posterior lamina cribrosa depth	Centre	0.796	0.998	0.985	0.542	0.830	0.985
	Superior	0.999	0.984	1.000	0.987	0.997	0.922
	Inferior	0.935	0.963	0.999	0.996	0.928	0.953
	Nasal	0.989	0.998	0.469	0.996	0.621	0.293
	Temporal	0.703	0.835	0.387	0.954	0.863	0.443
	SN	0.979	0.999	0.958	0.974	0.655	0.768
	IT	0.626	0.999	0.647	0.100	0.999	0.068
	ST	0.926	0.999	0.989	0.790	0.972	0.969
	IN	0.966	0.862	0.993	0.986	0.996	0.938
Lamina cribrosa thickness	Centre	0.919	0.035	0.003	0.199	0.013	0.337
	Superior	0.069	0.010	0.022	0.995	0.944	0.973
	Inferior	0.005	<0.001	<0.001	0.883	0.144	0.265
	Nasal	0.998	0.599	0.272	0.813	0.413	0.745
	Temporal	0.767	0.130	0.009	0.661	0.067	0.270
	SN	0.026	0.041	0.003	0.875	0.845	0.252
	IT	0.454	0.334	0.012	0.999	0.254	0.089
	ST	0.181	0.015	0.001	0.894	0.156	0.295
	IN	0.048	0.052	<0.001	0.985	0.290	0.092

Table III.5: Tukey post-hoc comparisons of lamina cribrosa depth and thickness as a function of glaucoma disease stage for each ONH region. Red text indicates significant difference between groups at $p < 0.05$.

Table III.6 presents regional measurements of nerve fibre layer thickness (border and peripapillary) as a function of glaucoma disease stage.

ONH Parameter	Region	C	PG	EG	MAG
		Mean ± Standard Deviation			
bNFL thickness (μm)	Superior	355.49 ± 56.07	320.53 ± 95.83	275.01 ± 66.47	196.41 ± 77.32
	Inferior	354.52 ± 56.52	303.90 ± 80.57	252.82 ± 72.92	191.46 ± 70.20
	Nasal	294.90 ± 64.96	261.48 ± 65.99	227.52 ± 64.63	183.77 ± 91.58
	Temporal	242.14 ± 66.09	212.07 ± 56.34	186.23 ± 39.49	165.61 ± 41.11
	SN	336.97 ± 57.40	313.75 ± 88.08	260.69 ± 73.55	206.74 ± 74.83
	IT	275.72 ± 54.81	234.30 ± 51.53	205.54 ± 54.87	152.69 ± 54.96
	ST	307.33 ± 54.22	280.25 ± 61.91	217.59 ± 48.88	177.47 ± 64.98
	IN	349.20 ± 65.80	310.21 ± 68.25	276.02 ± 76.54	225.58 ± 81.93
pNFL thickness (μm)	Superior	116.50 ± 23.14	88.20 ± 28.61	80.86 ± 24.47	73.59 ± 25.67
	Inferior	113.63 ± 23.58	100.21 ± 22.82	91.07 ± 22.49	74.47 ± 29.50
	Nasal	55.92 ± 11.76	52.98 ± 10.51	48.55 ± 15.03	39.17 ± 18.84
	Temporal	55.54 ± 13.61	55.51 ± 14.58	46.62 ± 11.80	38.29 ± 10.90
	SN	97.58 ± 16.41	95.53 ± 21.33	81.58 ± 26.89	74.19 ± 34.78
	IT	84.32 ± 16.42	82.41 ± 27.02	68.30 ± 26.43	50.04 ± 16.90
	ST	97.23 ± 23.82	94.26 ± 22.51	74.61 ± 21.84	58.82 ± 24.09
	IN	94.51 ± 22.33	84.64 ± 19.65	72.86 ± 21.70	61.80 ± 19.06

Table III.6: Mean and standard deviation of regional border and peripapillary NFL for each stage of glaucoma.

Inter-group differences for regional measures of bNFL and pNFL, and *P* values adjusted for multiple comparisons are shown in Table III.7.

ONH Parameter	Region	Multiple Comparisons: Adjusted *P* values					
		C-PG	C-EG	C-MAG	PG-EG	PG-MAG	EG-MAG
bNFL thickness	Superior	0.408	<0.001	<0.001	0.035	<0.001	<0.001
	Inferior	0.014	<0.001	<0.001	<0.001	<0.001	0.002
	Nasal	0.169	<0.001	<0.001	0.106	<0.001	0.023
	Temporal	0.017	<0.001	<0.001	0.206	0.023	0.464
	SN	0.939	<0.001	<0.001	0.003	<0.001	0.007
	IT	0.021	<0.001	<0.001	0.174	<0.001	<0.001
	ST	0.224	<0.001	<0.001	<0.001	<0.001	0.004
	IN	0.174	<0.001	<0.001	0.323	0.002	0.044
pNFL thickness	Superior	0.009	<0.001	<0.001	0.653	0.419	0.899
	Inferior	0.083	<0.001	<0.001	0.494	<0.001	0.008
	Nasal	0.887	0.319	0.009	0.839	0.059	0.140
	Temporal	0.810	0.002	<0.001	0.100	<0.001	0.016
	SN	0.983	0.136	0.008	0.100	0.006	0.353
	IT	0.999	0.467	<0.001	0.457	<0.001	0.003
	ST	0.944	0.006	<0.001	0.038	<0.001	0.007
	IN	0.167	<0.001	<0.001	0.113	0.002	0.183

Table III.7: Tukey post-hoc comparisons of border and peripapillary NFL thickness as a function of glaucoma disease stage for each ONH region. Red text indicates significant difference between groups at $p < 0.05$.

Table III.8 presents regional measures of minimum rim width and area as a function of glaucoma disease stage.

ONH Parameter	Region	C	PG	EG	MAG
		Mean ± Standard Deviation			
Minimum rim width (μm)	Superior	328.44 ± 66.58	262.63 ± 90.27	231.71 ± 83.98	160.71 ± 95.02
	Inferior	344.58 ± 76.65	276.82 ± 88.42	221.62 ± 81.81	152.54 ± 61.56
	Nasal	296.89 ± 76.47	252.76 ± 79.58	213.85 ± 78.95	166.78 ± 91.99
	Temporal	203.99 ± 56.76	176.80 ± 50.47	155.65 ± 48.52	130.42 ± 52.50
	SN	333.74 ± 66.07	257.87 ± 81.18	235.34 ± 78.18	175.72 ± 85.18
	IT	240.95 ± 55.45	210.13 ± 63.08	168.96 ± 57.30	121.13 ± 59.14
	ST	275.03 ± 65.90	229.68 ± 59.34	176.90 ± 64.25	131.76 ± 54.85
	IN	349.49 ± 81.43	294.08 ± 76.55	262.49 ± 89.07	198.70 ± 87.67
Minimum rim area (mm^2)	Superior	0.17 ± 0.04	0.15 ± 0.07	0.13 ± 0.05	0.09 ± 0.05
	Inferior	0.18 ± 0.04	0.16 ± 0.06	0.12 ± 0.05	0.09 ± 0.04
	Nasal	0.15 ± 0.04	0.14 ± 0.08	0.11 ± 0.04	0.08 ± 0.04
	Temporal	0.10 ± 0.03	0.10 ± 0.04	0.08 ± 0.04	0.07 ± 0.04
	SN	0.17 ± 0.04	0.14 ± 0.06	0.12 ± 0.05	0.09 ± 0.05
	IT	0.12 ± 0.04	0.12 ± 0.06	0.09 ± 0.04	0.07 ± 0.04
	ST	0.13 ± 0.03	0.12 ± 0.04	0.09 ± 0.04	0.07 ± 0.03
	IN	0.17 ± 0.05	0.16 ± 0.06	0.13 ± 0.05	0.10 ± 0.05

Table III.8: Mean and standard deviation of regional minimum rim width and area for each stage of glaucoma.

Inter-group differences for regional measures of minimum rim width and area, and *P* values adjusted for multiple comparisons are shown in Table III.9.

ONH Parameter	Region	Multiple Comparisons: Adjusted *P* values					
		C-PG	C-EG	C-MAG	PG-EG	PG-MAG	EG-MAG
Minimum rim width	Superior	0.028	<0.001	<0.001	0.612	<0.001	0.002
	Inferior	0.015	<0.001	<0.001	0.013	<0.001	0.005
	Nasal	0.260	<0.001	<0.001	0.093	0.007	0.392
	Temporal	0.090	0.007	<0.001	0.801	0.190	0.447
	SN	0.011	<0.001	<0.001	0.817	0.013	0.029
	IT	0.155	<0.001	<0.001	0.061	<0.001	0.002
	ST	0.014	<0.001	<0.001	0.034	<0.001	0.008
	IN	0.024	<0.001	<0.001	0.225	<0.001	0.019
Minimum rim area	Superior	0.632	0.060	<0.001	0.713	0.002	0.009
	Inferior	0.669	<0.001	<0.001	0.017	<0.001	0.043
	Nasal	0.994	0.058	0.033	0.041	0.023	0.873
	Temporal	0.896	0.101	0.181	0.318	0.450	1.000
	SN	0.179	0.002	<0.001	0.354	0.010	0.150
	IT	0.999	0.093	0.002	0.030	<0.001	0.098
	ST	0.940	0.001	<0.001	0.019	<0.001	0.062
	IN	0.638	<0.001	<0.001	0.053	<0.001	0.072

Table III.9: Tukey post-hoc comparisons of minimum rim width and area as a function of glaucoma disease stage for each ONH region. Red text indicates significant difference between groups at $p < 0.05$.

Appendix III

Table V.1 presents regional LC coherence for each stage of glaucoma disease with increased axial depth.

ONH Depth OCT Slice	Region	Coherence: Mean ± Standard Deviation			
		Control	PG	EG	MAG
1	SST	0.15 ± 0.07	0.14 ± 0.10	0.16 ± 0.07	0.20 ± 0.10
	ST	0.11 ± 0.05	0.13 ± 0.06	0.14 ± 0.10	0.16 ± 0.08
	TST	0.12 ± 0.06	0.12 ± 0.07	0.12 ± 0.08	0.10 ± 0.08
	TIT	0.12 ± 0.06	0.10 ± 0.06	0.14 ± 0.09	0.17 ± 0.10
	IT	0.13 ± 0.06	0.10 ± 0.05	0.15 ± 0.09	0.17 ± 0.11
	IIT	0.15 ± 0.06	0.15 ± 0.07	0.15 ± 0.10	0.17 ± 0.09
2	SST	0.13 ± 0.06	0.13 + 0.04	0.16 ± 0.08	0.20 ± 0.11
	ST	0.12 ± 0.06	0.12 ± 0.06	0.14 ± 0.11	0.18 ± 0.10
	TST	0.14 ± 0.06	0.12 ± 0.07	0.14 ± 0.09	0.15 ± 0.09
	TIT	0.15 ± 0.09	0.13 ± 0.08	0.16 ± 0.09	0.17 ± 0.14
	IT	0.16 ± 0.08	0.12 ± 0.06	0.18 ± 0.09	0.20 ± 0.15
	IIT	0.16 ± 0.07	0.17 ± 0.09	0.18 ± 0.11	0.19 ± 0.15
3	SST	0.15 ± 0.08	0.13 ± 0.04	0.17 ± 0.07	0.16 ± 0.03
	ST	0.12 ± 0.07	0.13 ± 0.06	0.14 ± 0.10	0.16 ± 0.09
	TST	0.13 ± 0.08	0.15 ± 0.07	0.13 ± 0.07	0.16 ± 0.11
	TIT	0.17 ± 0.09	0.14 ± 0.08	0.15 ± 0.08	0.19 ± 0.12
	IT	0.16 ± 0.09	0.12 ± 0.08	0.17 ± 0.09	0.22 ± 0.15
	IIT	0.16 ± 0.08	0.17 ± 0.10	0.18 ± 0.10	0.23 ± 0.17
4	SST	0.09 ± 0.04	0.21 ± 0.12	0.19 ± 0.06	0.12 ± 0.06
	ST	0.12 ± 0.08	0.15 ± 0.08	0.15 ± 0.08	0.14 ± 0.09
	TST	0.13 ± 0.09	0.15 ± 0.07	0.14 ± 0.06	0.14 ± 0.10
	TIT	0.17 ± 0.09	0.16 ± 0.09	0.15 ± 0.08	0.19 ± 0.12
	IT	0.17 ± 0.08	0.13 ± 0.09	0.17 ± 0.08	0.20 ± 0.14
	IIT	0.17 ± 0.09	0.17 ± 0.10	0.17 ± 0.10	0.18 ± 0.16
5	SST	0.11 ± 0.04	0.22 ± 0.09	0.19 ± 0.07	0.15 ± 0.06
	ST	0.12 ± 0.07	0.16 ± 0.09	0.15 ± 0.07	0.15 ± 0.07
	TST	0.13 ± 0.09	0.14 ± 0.06	0.14 ± 0.06	0.13 ± 0.07
	TIT	0.16 ± 0.10	0.16 ± 0.08	0.15 ± 0.08	0.16 ± 0.09
	IT	0.17 ± 0.09	0.14 ± 0.07	0.16 ± 0.08	0.17 ± 0.10
	IIT	0.17 ± 0.10	0.18 ± 0.08	0.17 ± 0.09	0.18 ± 0.13
6	SST	0.16 ± 0.07	0.25 ± 0.08	0.23 ± 0.08	0.25 ± ------
	ST	0.11 ± 0.06	0.18 ± 0.08	0.15 ± 0.08	0.16 ± 0.07
	TST	0.13 ± 0.10	0.16 ± 0.07	0.16 ± 0.07	0.13 ± 0.05
	TIT	0.16 ± 0.10	0.18 ± 0.11	0.15 ± 0.10	0.21 ± 0.09
	IT	0.17 ± 0.10	0.15 ± 0.05	0.17 ± 0.09	0.22 ± 0.08
	IIT	0.18 ± 0.10	0.19 ± 0.10	0.15 ± 0.08	0.27 ± 0.09

Table V.1: Regional measures of lamina cribrosa coherence as a function of glaucoma stage with increased axial depth through the LC (OCT slices 1 to 6). Dash indicates insufficient data for that region due to vascular shadowing within the OCT dataset. PG = preperimetric glaucoma, EG = early glaucoma, MAG = moderate-advanced glaucoma, S = superior, I = inferior, T = temporal.

OCT Slice 1 Coherence	Dx (*p*-value)	Age (years)	AxL (mm)	MS (D)	ACD (mm)	CCT (µm)	IOP (mmHg)
SST	C: <0.001	-0.0005 ± 0.003	-0.004 ± 0.03	0.001 ± 0.01	0.05 ± 0.03	0.00008 ± $5.6e^{-4}$	0.0002 ± 0.007
t value	PG: 0.822	-0.15	-0.16	0.09	1.78	0.15	0.04
p value	EG: 0.926	0.877	0.873	0.923	0.090	0.881	0.972
	MAG: 0.258						
ST	C: <0.001	0.00005 ± 0.002	0.02 ± 0.01	0.01 ± 0.007	0.02 ± 0.01	-0.0002 ± 0.0003	0.002 ± 0.005
t value	PG: 0.494	0.03	1.67	1.60	1.22	-0.69	0.34
p value	EG: 0.283	0.973	0.104	0.119	0.231	0.494	0.735
	MAG: 0.102						
TST	C: 0.090	-0.0004 ± 0.001	0.0006 ± 0.01	0.004 ± 0.005	0.02 ± 0.01	-0.0002 ± 0.0002	0.0005 ± 0.003
t value	PG: 0.701	-0.37	0.06	0.80	2.28	-0.84	0.16
p value	EG: 0.659	0.709	0.951	0.429	0.026	0.399	0.875
	MAG: 0.121						
TIT	C: <0.001	-0.0007 ± 0.001	0.0005 ± 0.01	-0.0004 ± 0.006	0.02 ± 0.01	-0.0001 ± 0.0002	-0.004 ± 0.004
t value	PG: 0.636	-0.53	0.05	-0.08	1.73	-0.62	-0.90
p value	EG: 0.298	0.601	0.963	0.939	0.088	0.536	0.373
	MAG: 0.058						
IT	C: <0.001	-0.0007 ± 0.001	0.01 ± 0.01	0.001 ± 0.006	0.02 ± 0.01	-0.0003 ± 0.0003	-0.004 ± 0.004
t value	PG: 0.496	-0.55	1.02	0.22	1.33	-1.18	-1.10
p value	EG: 0.304	0.586	0.313	0.824	0.188	0.239	0.276
	MAG: 0.079						
IIT	C: <0.001	0.0001 ± 0.001	0.01 ± 0.01	0.002 ± 0.008	0.02 ± 0.01	-0.0002 ± 0.0003	-0.004 ± 0.004
t value	PG: 0.961	-0.09	0.97	0.25	1.25	-0.91	-0.96
p value	EG: 0.913	0.931	0.340	0.804	0.219	0.370	0.342
	MAG: 0.441						

Table V.2: Independent variables included in linear mixed-effects regression model for each ONH region for OCT slice 1. Presented as effect size ± standard error (i.e. how much LC coherence changes per one-unit change in the independent variable), also the t-value and *p*-value. Red text indicates the independent variable had a significant effect at $p < 0.05$. OCT = optical coherence tomography, Dx = stage of glaucoma, AxL = axial length, MS = mean sphere refractive error, ACD = anterior chamber depth, CCT = central corneal thickness, IOP = intraocular pressure, S = superior, I = inferior, T = temporal.

OCT Slice 2 Coherence	Dx (*p*-value)	Age (years)	AxL (mm)	MS (D)	ACD (mm)	CCT (µm)	IOP (mmHg)
SST	C: <0.001	0.004 ± 0.003	-0.01 ± 0.02	-0.01 ± 0.01	0.02 ± 0.03	-0.0006 ± 0.0005	-0.0001 ± 0.007
t value	PG: 0.923	1.21	-0.51	-0.70	0.86	-1.21	-0.02
p value	EG: 0.525	0.242	0.615	0.491	0.402	0.242	0.986
	MAG: 0.033						
ST	C: 0.055	0.001 ± 0.001	0.03 ± 0.01	0.005 ± 0.007	0.0007 ± 0.02	-0.0002 ± 0.0004	-0.0009 ± 0.005
t value	PG: 0.526	0.96	2.41	0.70	0.05	-0.65	-0.16
p value	EG: 0.766	0.342	0.021	0.492	0.963	0.519	0.870
	MAG: 0.323						
TST	C: <0.001	0.0002 ± 0.001	0.008 ± 0.01	-0.0004 ± 0.006	0.01 ± 0.01	-0.0002 ± 0.0002	-0.006 ± 0.004
t value	PG: 0.371	0.16	0.71	-0.08	0.80	-0.90	-1.48
p value	EG: 0.896	0.872	0.479	0.936	0.425	0.370	0.146
	MAG: 0.662						
TIT	C: <0.001	0.0002 ± 0.002	-0.01 ± 0.02	-0.006 ± 0.008	0.03 ± 0.02	-0.0002 ± 0.0003	-0.009 ± 0.004
t value	PG: 0.327	0.16	-0.70	-0.77	1.93	-0.45	-1.89
p value	EG: 0.437	0.876	0.490	0.445	0.057	0.656	0.064
	MAG: 0.802						
IT	C: <0.001	0.001 ± 0.002	0.005 ± 0.02	-0.001 ± 0.008	0.03 ± 0.02	-0.0001 ± 0.0004	-0.005 ± 0.005
t value	PG: 0.108	0.56	0.32	-0.15	1.72	-0.28	-1.03
p value	EG: 0.402	0.573	0.752	0.883	0.089	0.780	0.306
	MAG: 0.192						
IIT	C: 0.867	-0.0007 ± 0.002	0.02 ± 0.02	0.005 ± 0.009	0.06 ± 0.01	-0.0003 ± 0.0003	-0.009 ± 0.005
t value	PG: 0.982	-0.38	1.34	0.53	3.78	-1.10	-1.71
p value	EG: 0.484	0.706	0.189	0.598	<0.001	0.281	0.096
	MAG: 0.886						

Table V.3: Independent variables included in linear mixed-effects regression model for each ONH region for OCT slice 2. Presented as effect size ± standard error (i.e. how much LC coherence changes per one-unit change in the independent variable), also the t-value and *p*-value. Red text indicates the independent variable had a significant effect at $p < 0.05$. OCT = optical coherence tomography, Dx = stage of glaucoma, AxL = axial length, MS = mean sphere refractive error, ACD = anterior chamber depth, CCT = central corneal thickness, IOP = intraocular pressure, S = superior, I = inferior, T = temporal.

OCT Slice 3 Coherence	Dx (*p*-value)	Age (years)	AxL (mm)	MS (D)	ACD (mm)	CCT (µm)	IOP (mmHg)
SST	C: <0.001	0.006 ± 0.003	-0.006 ± 0.02	-0.008 ± 0.01	-0.04 ± 0.02	-0.0006 ± 0.0004	-0.0002 ± 0.006
t value	PG: 0.567	2.05	-0.26	-0.75	-1.78	-0.14	-0.04
p value	EG: 0.682	0.055	0.799	0.466	0.093	0.890	0.972
	MAG: 0.749						
ST	C: <0.001	0.001 ± 0.002	0.03 ± 0.02	0.01 ± 0.008	-0.007 ± 0.02	-0.0002 ± 0.0004	-0.002 ± 0.005
t value	PG: 0.948	0.66	1.22	1.40	-0.40	-0.03	-0.43
p value	EG: 0.442	0.503	0.319	0.170	0.694	0.974	0.673
	MAG: 0.180						
TST	C: <0.001	0.0005 ± 0.001	-0.009 ± 0.01	-0.005 ± 0.005	0.007 ± 0.01	0.0001 ± 0.0003	-0.004 ± 0.004
t value	PG: 0.532	0.43	-0.86	-0.90	0.61	0.05	1.12
p value	EG: 0.848	0.669	0.392	0.374	0.542	0.962	0.319
	MAG: 0.208						
TIT	C: 0.119	-0.0005 ± 0.002	-0.002 ± 0.01	-0.003 ± 0.008	0.04 ± 0.01	-0.0004 ± 0.0003	-0.008 ± 0.005
t value	PG: 0.102	-0.33	-0.14	-0.43	2.77	-1.32	1.62
p value	EG: 0.231	0.740	0.891	0.665	0.007	0.193	0.114
	MAG: 0.806						
IT	C: <0.001	-0.0002 ± 0.002	0.0002 ± 0.02	0.003 ± 0.008	0.04 ± 0.01	-0.0005 ± 0.0004	-0.007 ± 0.005
t value	PG: 0.101	-0.09	0.01	0.32	1.78	-1.32	-1.43
p value	EG: 0.641	0.926	0.992	0.751	0.105	0.193	-.159
	MAG: 0.101						
IIT	C: 0.119	0.0002 ± 0.002	0.008 ± 0.02	0.001 ± 0.01	0.06 ± 0.02	-0.0006 ± 0.0004	-0.01 ± 0.006
t value	PG: 0.102	0.10	0.43	0.12	3.43	-1.65	-1.88
p value	EG: 0.231	0.920	0.664	0.907	0.001	0.106	0.067
	MAG: 0.806						

Table V.4: Independent variables included in linear mixed-effects regression model for each ONH region for OCT slice 3. Presented as effect size ± standard error (i.e. how much LC coherence changes per one-unit change in the independent variable), also the t-value and *p*-value. Red text indicates the independent variable had a significant effect at $p < 0.05$. OCT = optical coherence tomography, Dx = stage of glaucoma, AxL = axial length, MS = mean sphere refractive error, ACD = anterior chamber depth, CCT = central corneal thickness, IOP = intraocular pressure, S = superior, I = inferior, T = temporal.

OCT Slice 4 Coherence	Dx (*p*-value)	Age (years)	AxL (mm)	MS (D)	ACD (mm)	CCT (µm)	IOP (mmHg)
SST	C: 0.054	0.004 ± 0.002	-0.03 ± 0.01	-0.004 ± 0.009	-0.003 ± 0.02	0.0001 ± 0.0003	0.007 ± 0.004
t value	PG: <0.001	2.63	-3.07	-0.40	-0.19	0.34	1.84
p value	EG: 0.074	0.016	0.006	0.691	0.853	0.741	0.083
	MAG: 0.617						
ST	C: <0.001	-0.0006 ± 0.002	0.02 ± 0.02	0.008 ± 0.007	0.003 ± 0.02	-0.0002 ± 0.0004	-0.005 ± 0.005
t value	PG: 0.550	-0.32	1.01	1.12	0.19	-0.57	-0.93
p value	EG: 0.237	0.753	0.320	0.271	0.854	0.572	0.358
	MAG: 0.545						
TST	C: <0.001	0.0001 ± 0.001	-0.01 ± 0.01	-0.006 ± 0.006	0.001 ± 0.01	-0.0002 ± 0.0003	-0.005 ± 0.004
t value	PG: 0.379	0.09	-1.17	-0.95	0.11	-0.65	-1.25
p value	EG: 0.713	0.932	0.249	0.345	0.911	0.517	0.218
	MAG: 0.652						
TIT	C: 0.188	0.002 ± 0.002	-0.01 ± 0.02	-0.006 ± 0.008	0.04 ± 0.01	-0.0009 ± 0.0003	-0.006 ± 0.005
t value	PG: 0.298	-1.44	-0.80	-0.76	2.82	-0.24	-1.28
p value	EG: 0.384	0.156	0.425	0.448	0.006	0.814	0.814
	MAG: 0.935						
IT	C: 0.225	-0.001 ± 0.001	-0.002 ± 0.02	0.0008 ± 0.008	0.04 ± 0.01	-0.0001 ± 0.0004	-0.005 ± 0.005
t value	PG: 0.258	-0.60	-0.17	0.09	2.92	-0.36	-0.94
p value	EG: 0.407	0.544	0.864	0.921	0.005	0.723	0.351
	MAG: 0.736						
IIT	C: 0.731	0.0006 ± 0.002	-0.003 ± 0.02	0.003 ± 0.01	0.07 ± 0.02	-0.0002 ± 0.0004	-0.009 ± 0.006
t value	PG: 0.968	0.03	-0.15	0.25	4.03	-0.62	-1.43
p value	EG: 0.189	0.974	0.880	0.806	<0.001	0.543	0.163
	MAG: 0.933						

Table V.5: Independent variables included in linear mixed-effects regression model for each ONH region for OCT slice 4. Presented as effect size ± standard error (i.e. how much LC coherence changes per one-unit change in the independent variable), also the t-value and *p*-value. Red text indicates the independent variable had a significant effect at $p < 0.05$. OCT = optical coherence tomography, Dx = stage of glaucoma, AxL = axial length, MS = mean sphere refractive error, ACD = anterior chamber depth, CCT = central corneal thickness, IOP = intraocular pressure, S = superior, I = inferior, T = temporal.

OCT Slice 5 Coherence	Dx (*p*-value)	Age (years)	AxL (mm)	MS (D)	ACD (mm)	CCT (µm)	IOP (mmHg)
SST	C: 0.069	0.005 ± 0.002	0.005 ± 0.02	-0.004 ± 0.01	-0.02 ± 0.03	-0.0005 ± 0.0004	0.008 ± 0.005
t value	PG: 0.004	2.84	0.25	-0.38	-0.75	-1.30	1.65
p value	EG: 0.624	0.010	0.806	0.713	0.467	0.215	0.127
	MAG: 0.961						
ST	C: 0.017	0.0003 ± 0.001	0.04 ± 0.01	0.02 ± 0.006	0.02 ± 0.02	-0.0003 ± 0.0003	0.0003 ± 0.004
t value	PG: 0.526	0.21	2.89	3.08	1.25	-0.84	0.06
p value	EG: 0.307	0.837	0.007	0.005	0.221	0.405	0.952
	MAG: 0.315						
TST	C: <0.001	-0.0008 ± 0.001	0.009 ± 0.01	0.005 ± 0.007	0.01 ± 0.01	-0.0004 ± 0.0003	0.0008 ± 0.004
t value	PG: 0.822	-0.55	0.67	0.69	0.86	-1.21	0.18
p value	EG: 0.755	0.582	0.501	0.493	0.394	0.231	0.852
	MAG: 0.734						
TIT	C: <0.001	-0.001 ± 0.001	0.005 ± 0.02	0.007 ± 0.008	0.02 ± 0.02	-0.0004 ± 0.0003	-0.009 ± 0.005
t value	PG: 0.958	-0.94	0.30	0.83	1.31	-1.12	-1.90
p value	EG: 0.944	0.351	0.768	0.410	0.196	0.269	0.062
	MAG: 0.651						
IT	C: <0.001	-0.003 ± 0.002	0.01 ± 0.01	0.01 ± 0.007	0.03 ± 0.01	-0.0002 ± 0.0003	-0.008 ± 0.004
t value	PG: 0.291	-1.81	0.78	1.58	1.97	-0.76	-1.97
p value	EG: 0.819	0.075	0.439	0.118	0.052	0.451	0.055
	MAG: 0.968						
IIT	C: <0.001	-0.004 ± 0.002	0.02 ± 0.02	0.01 ± 0.007	0.04 ± 0.02	-0.0004 ± 0.0004	-0.008 ± 0.006
t value	PG: 0.534	-1.63	0.79	1.65	1.91	-1.03	-1.34
p value	EG: 0.522	0.112	0.434	0.105	0.064	0.311	0.188
	MAG: 0.447						

Table V.6: Independent variables included in linear mixed-effects regression model for each ONH region for OCT slice 5. Presented as effect size ± standard error (i.e. how much LC coherence changes per one-unit change in the independent variable), also the t-value and *p*-value. Red text indicates the independent variable had a significant effect at $p < 0.05$. OCT = optical coherence tomography, Dx = stage of glaucoma, AxL = axial length, MS = mean sphere refractive error, ACD = anterior chamber depth, CCT = central corneal thickness, IOP = intraocular pressure, S = superior, I = inferior, T = temporal.

OCT Slice 6 Coherence	Dx (*p*-value)	Age (years)	AxL (mm)	MS (D)	ACD (mm)	CCT (µm)	IOP (mmHg)
SST	-	-	-	-	-	-	-
t value							
p value							
ST	C: <0.001	0.0006 ± 0.002	0.03 ± 0.02	0.009 ± 0.006	0.03 ± 0.02	0.0003 ± 0.0004	0.004 ± 0.006
t value	PG: 0.184	0.27	1.64	1.63	1.53	0.81	0.67
p value	EG: 0.346	0.792	0.114	0.115	0.139	0.424	0.507
	MAG: 0.325						
TST	C: <0.001	0.0007 ± 0.002	0.02 ± 0.02	0.002 ± 0.009	0.0004 ± 0.02	-0.0005 ± 0.0004	0.003 ± 0.006
t value	PG: 0.343	0.37	0.89	0.20	0.02	-1.15	0.48
p value	EG: 0.333	0.712	0.377	0.845	0.983	0.255	0.634
	MAG: 0.844						
TIT	C: <0.001	-0.002 ± 0.003	0.03 ± 0.02	0.01 ± 0.01	-0.002 ± 0.02	-0.0008 ± 0.0005	-0.006 ± 0.007
t value	PG: 0.546	-0.85	1.19	0.80	-0.07	-1.69	-0.81
p value	EG: 0.806	0.400	0.241	0.428	0.942	0.097	0.423
	MAG: 0.737						
IT	C: <0.001	-0.004 ± 0.002	0.02 ± 0.02	0.02 ± 0.01	0.01 ± 0.02	-0.0007 ± 0.0004	-0.009 ± 0.006
t value	PG: 0.754	-1.77	1.23	1.61	0.71	-1.55	-1.47
p value	EG: 0.921	0.086	0.231	0.119	0.481	0.132	0.156
	MAG: 0.293						
IIT	C: <0.001	-0.004 ± 0.003	0.04 ± 0.03	0.009 ± 0.009	0.03 ± 0.03	-0.0006 ± 0.0005	0.004 ± 0.008
t value	PG: 0.558	-1.32	1.69	0.98	0.97	-1.02	0.53
p value	EG: 0.499	0.201	0.104	0.337	0.344	0.316	0.602
	MAG: 0.120						

Table V.7: Independent variables included in linear mixed-effects regression model for each ONH region for OCT slice 6. Presented as effect size ± standard error (i.e. how much LC coherence changes per one-unit change in the independent variable), also the t-value and *p*-value. Red text indicates the independent variable had a significant effect at $p < 0.05$. OCT = optical coherence tomography, Dx = stage of glaucoma, AxL = axial length, MS = mean sphere refractive error, ACD = anterior chamber depth, CCT = central corneal thickness, IOP = intraocular pressure, S = superior, I = inferior, T = temporal. Dash (-) indicates insufficient data for that region due to vascular shadowing within the OCT dataset.

ONH OCT Slice	Region	Pearson's r	*P*-value
1	SST	0.29	0.118
	ST	0.15	0.211
	TST	-0.11	0.262
	TIT	0.25	0.009
	IT	0.22	0.029
	IIT	0.03	0.769
2	SST	0.30	0.101
	ST	0.23	0.063
	TST	0.10	0.319
	TIT	0.18	0.063
	IT	0.23	0.023
	IIT	0.05	0.685
3	SST	0.08	0.679
	ST	0.19	0.117
	TST	0.08	0.444
	TIT	0.19	0.053
	IT	0.24	0.018
	IIT	0.16	0.176
4	SST	-0.03	0.872
	ST	0.02	0.871
	TST	-0.01	0.912
	TIT	0.20	0.051
	IT	0.24	0.021
	IIT	0.07	0.584
5	SST	0.01	0.953
	ST	0.07	0.597
	TST	0.04	0.681
	TIT	0.08	0.442
	IT	0.10	0.387
	IIT	0.07	0.592
6	SST	0.36	0.249
	ST	0.09	0.614
	TST	0.03	0.850
	TIT	0.21	0.120
	IT	0.25	0.071
	IIT	0.28	0.102

Table V.8: Association between regional depth-related LC coherence and VF MD. Red text indicates significant correlation at $p < 0.05$.

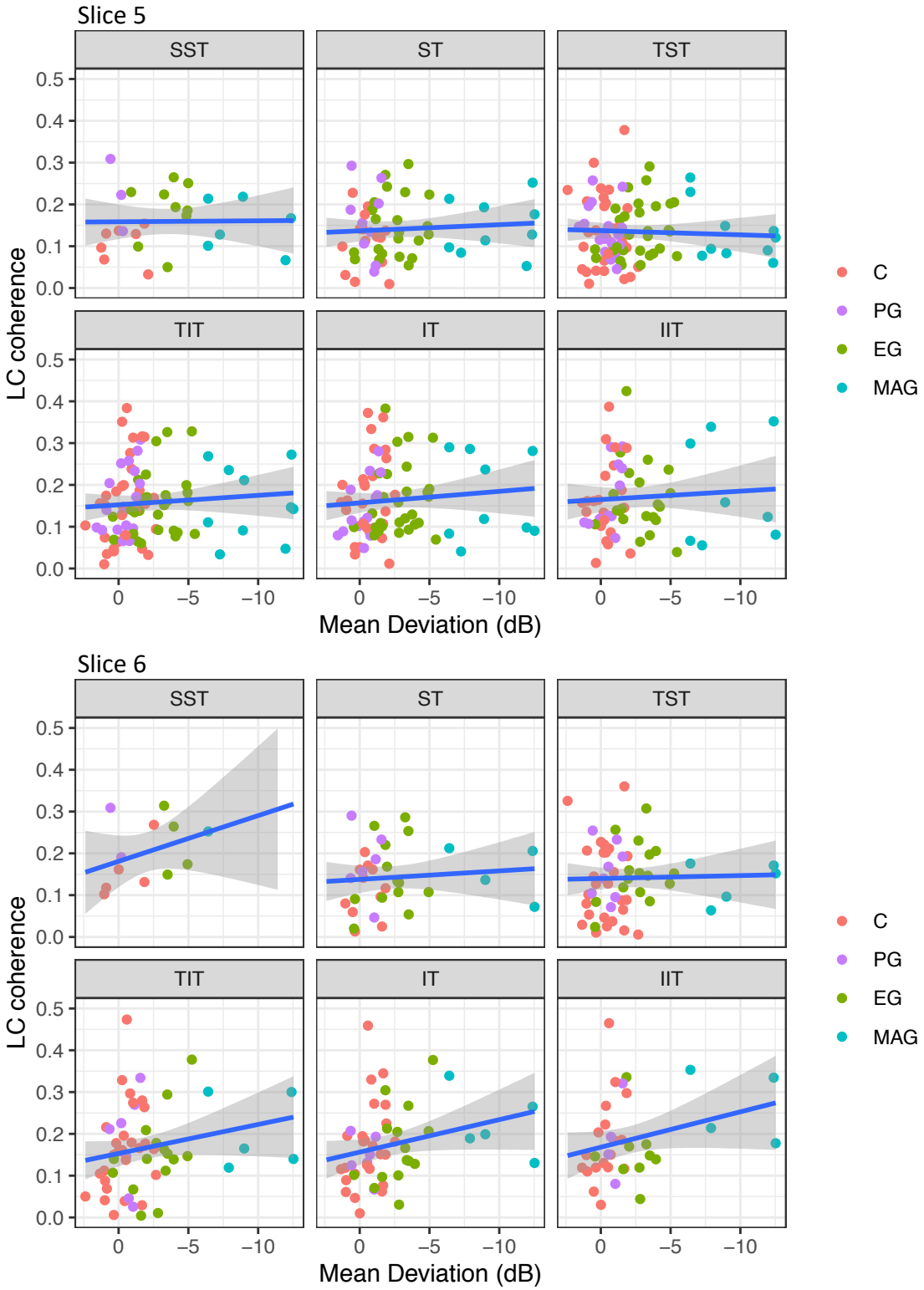

Figure V.1: Regional LC coherence as a function of VF MD for OCT slices 5 and 6. S = superior, I = inferior, T = temporal. Blue line indicates regression line and grey shading represents 95% confidence intervals. Region SST contains relatively fewer observations due to vascular shadowing in this region within OCT image datasets.

Group	OCT Slice	Regional differences in LC coherence for each stage of glaucoma: Adjusted *P*-values														
		SST-ST	SST-TST	SST-TIT	SST-IT	SST-IIT	ST-TST	ST-TIT	ST-IT	ST-IIT	TST-TIT	TST-IT	TST-IIT	TIT-IT	TIT-IIT	IT-IIT
Control	1	0.352	0.539	0.448	0.757	0.999	0.990	0.998	0.917	0.217	0.999	0.996	0.313	0.977	0.197	0.609
	2	0.890	0.998	1.000	1.000	0.996	0.942	0.766	0.539	0.362	0.994	0.916	0.738	0.997	0.945	0.997
	3	0.392	0.546	0.989	0.952	0.902	0.994	0.395	0.614	0.829	0.500	0.781	0.954	0.998	0.979	0.999
	4	0.981	0.999	0.645	0.840	0.874	0.732	0.034	0.110	0.171	0.280	0.644	0.757	0.993	0.995	1.000
	5	0.886	1.000	0.982	0.903	0.993	0.707	0.138	0.046	0.253	0.748	0.398	0.894	0.992	1.000	0.987
	6	0.122	0.523	0.949	0.982	0.997	0.684	0.103	0.058	0.052	0.628	0.443	0.386	0.999	0.990	0.999
PG	1	1.000	0.998	0.914	0.955	0.999	0.989	0.629	0.799	0.987	0.861	0.999	0.722	0.999	0.178	0.332
	2	0.911	0.682	0.961	0.855	1.000	0.982	0.999	0.999	0.788	0.815	0.996	0.226	0.988	0.841	0.549
	3	1.000	0.999	1.000	0.999	0.986	0.999	1.000	0.992	0.938	1.000	0.911	0.966	0.945	0.945	0.574
	4	0.865	0.943	0.977	0.845	0.999	0.997	0.976	1.000	0.803	0.999	0.992	0.901	0.945	0.978	0.669
	5	0.473	0.262	0.818	0.499	0.892	0.996	0.930	1.000	0.922	0.453	0.974	0.508	0.916	1.000	0.906
	6	0.754	0.686	0.980	0.730	1.000	1.000	0.932	1.000	0.699	0.839	1.000	0.542	0.897	0.975	0.619
EG	1	0.887	0.518	0.890	0.984	0.999	0.962	1.000	0.991	0.905	0.935	0.640	0.385	0.992	0.901	0.995
	2	0.792	0.647	0.999	1.000	0.935	0.999	0.774	0.371	0.051	0.511	0.154	0.012	0.985	0.503	0.862
	3	0.362	0.171	0.871	0.998	0.992	0.997	0.824	0.248	0.014	0.443	0.050	0.001	0.913	0.198	0.736
	4	0.227	0.140	0.599	0.721	0.995	0.999	0.928	0.816	0.233	0.783	0.603	0.101	0.999	0.722	0.849
	5	0.181	0.089	0.476	0.518	0.957	0.999	0.953	0.928	0.362	0.772	0.712	0.146	1.000	0.821	0.852
	6	0.172	0.294	0.196	0.369	0.494	0.995	1.000	0.978	0.977	0.999	0.999	0.999	0.992	0.990	1.000
MAG	1	0.674	0.001	0.836	0.844	1.000	0.023	0.999	0.999	0.721	0.006	0.008	0.001	1.000	0.869	0.871
	2	0.936	0.251	0.680	0.976	0.999	0.626	0.985	0.999	0.994	0.939	0.477	0.430	0.946	0.876	0.999
	3	1.000	0.999	0.999	0.893	0.755	0.996	0.999	0.841	0.700	0.965	0.535	0.419	0.940	0.823	0.998
	4	1.000	0.999	0.939	0.900	0.949	0.999	0.790	0.705	0.863	0.584	0.492	0.716	1.000	1.000	1.000
	5	0.995	0.826	0.998	1.000	0.999	0.970	1.000	0.997	0.926	0.941	0.800	0.513	0.999	0.945	0.995
	6	0.966	0.884	0.962	0.779	0.269	0.996	0.127	0.028	0.002	0.036	0.007	<0.001	0.934	0.169	0.546

Table V.9: Regional differences in LC coherence for each stage of glaucoma with increased axial depth. Red text indicates significant difference between regions at $p < 0.05$.

Appendix IV

Table VI.1 presents linear regressions equations used to perform data imputation for each of the 28 variables which contained missing observations.

ONH variable	Linear regression equation
Inferior-Temporal LC thickness	Y = 217.91 + 4.85 x MD
Superior LC thickness	Y = 205.47 + 3.81 x MD
Temporal LC thickness	Y = 227.35 + 4.67 x MD
Inferior LC thickness	Y = 214.99 + 3.93 x MD
Superior-Temporal LC thickness	Y = 210.57 + 4.32 x MD
Inferior-Temporal pNFL	Y = 81.23 + 2.67 x MD
Inferior-Nasal pNFL	Y = 87.27 + 2.44 x MD
Nasal pNFL	Y = 54.69 + 1.36 x MD
Inferior pNFL	Y = 107.02 + 3.23 x MD
Superior-Nasal pNFL	Y = 93.50 + 1.81 x MD
Superior prelamina thickness	Y = 295.25 + 16.06 x MD
Prelamina volume	Y = 0.562 + 0.011 x MD
Inferior prelamina thickness	Y = 382.01 + 20.51 x MD
Temporal prelamina thickness	Y = 267.18 + 8.94 x MD
Superior-Temporal prelamina thickness	Y = 290.67 + 14.89 x MD
Lamina cribrosa central thickness	Y = 222.74 + 4.14 x MD
Inferior-Temporal prelamina thickness	Y = 325.42 + 15.24 x MD
Temporal pNFL	Y = 53.47 + 1.39 x MD
Superior-Temporal pNFL	Y = 91.68 + 3.52 x MD
Superior-Temporal bNFL	Y = 277.52 + 9.88 x MD
Superior pNFL	Y = 101.28 + 2.65 x MD
Superior-Nasal prelamina depth	Y = 9.01 – 21.29 x MD
Superior-Nasal bNFL	Y = 312.48 + 10.32 x MD
Prelamina central thickness	Y = 190.45 + 5.13 x MD
Inferior-Temporal prelamina depth	Y = 31.73 – 17.73 x MD
Inferior-Temporal bNFL	Y = 249.40 + 8.49 x MD
Inferior-Nasal prelamina depth	Y = -59.35 – 21.12 x MD
Cup volume	Y = 0.088 – 0.017 x MD

Table VI.1: Linear regression equation used for data imputation for each of the 28 variables containing missing values. Where Y is the variable name. MD = Mean Deviation.

Regional ONH parameter	Region	Pearson's correlation coefficient									
		PC 1		PC 2		PC 3		PC 4		PC 5	
		r	*P*-value	r	*P*-value	r	*P*-value	r	*P*-value	r	*P*-value
Prelamina depth	Centre	0.66	<0.001	-0.58	<0.001	-0.04	0.595	-0.08	0.305	0.20	0.011
	Superior	0.78	<0.001	-0.45	<0.001	-0.02	0.826	-0.03	0.682	-0.07	0.344
	Inferior	0.81	<0.001	-0.28	<0.001	-0.07	0.387	-0.11	0.137	0.08	0.321
	Nasal	0.65	<0.001	-0.43	<0.001	-0.25	0.001	0.10	0.210	0.19	0.012
	Temporal	0.70	<0.001	-0.48	<0.001	0.03	0.707	-0.28	<0.001	0.12	0.131
	SN	0.72	<0.001	-0.49	<0.001	-0.08	0.328	0.05	0.496	0.04	0.637
	IT	0.80	<0.001	-0.34	<0.001	0.01	0.909	-0.25	0.001	0.12	0.112
	ST	0.80	<0.001	-0.43	<0.001	-0.02	0.812	-0.13	0.081	0.01	0.913
	IN	0.67	<0.001	-0.34	<0.001	-0.17	0.023	-0.09	0.236	0.20	0.008
Prelamina thickness	Centre	-0.61	<0.001	0.41	<0.001	0.07	0.360	0.14	0.069	0.13	0.092
	Superior	-0.69	<0.001	0.28	<0.001	0.04	0.639	0.05	0.518	0.28	<0.001
	Inferior	-0.76	<0.001	0.08	0.307	0.07	0.344	0.13	0.093	0.16	0.032
	Nasal	Excluded from PCA									
	Temporal	-0.66	<0.001	0.33	<0.001	0.03	0.662	0.35	<0.001	0.19	0.014
	SN	Excluded from PCA									
	IT	-0.81	<0.001	0.17	0.027	-0.001	0.986	0.27	<0.001	0.18	0.020
	ST	-0.74	<0.001	0.28	<0.001	0.03	0.673	0.18	0.020	0.26	<0.001
	IN	Excluded from PCA									

Table VI.2: Pearson's correlation between regional measures of prelamina depth and thickness, and the first 5 PCs. Red text indicates a strong association at $r \geq 0.70$ and $P < 0.05$.

Regional ONH parameter	Region	Pearson's correlation coefficient									
		PC 1		PC 2		PC 3		PC 4		PC 5	
		r	*P*-value	r	*P*-value	r	*P*-value	r	*P*-value	r	*P*-value
LC thickness	Centre	-0.52	<0.001	-0.47	<0.001	0.51	<0.001	0.19	0.013	-0.18	0.017
	Superior	-0.49	<0.001	-0.43	<0.001	0.53	<0.001	0.20	0.008	-0.07	0.369
	Inferior	-0.46	<0.001	-0.50	<0.001	0.56	<0.001	0.07	0.374	-0.05	0.520
	Nasal	Excluded from PCA									
	Temporal	-0.43	<0.001	-0.50	<0.001	0.56	<0.001	0.18	0.020	-0.10	0.184
	SN	Excluded from PCA									
	IT	-0.50	<0.001	-0.41	<0.001	0.56	<0.001	0.16	0.044	-0.08	0.312
	ST	-0.56	<0.001	-0.45	<0.001	0.48	<0.001	0.13	0.094	-0.08	0.282
	IN	Excluded from PCA									
Volumetric ONH parameter											
Optic cup volume		0.71	<0.001	-0.37	<0.001	-0.29	<0.001	-0.09	0.265	0.15	0.058
Prelamina volume		-0.25	<0.001	-0.53	<0.001	-0.12	0.122	0.21	0.005	0.16	0.043
LC volume		Excluded from PCA									
BMO surface area		0.18	0.020	-0.50	<0.001	-0.57	<0.001	0.29	<0.001	-0.36	<0.001

Table VI.3: Pearson's correlation between regional measures of LC thickness, and volumetric measures of optic cup and prelamina volume, and BMO surface area, and the first 5 PCs. Red text indicates a strong association at $r \geq 0.70$ and $P < 0.05$.

Regional ONH parameter	Region	Pearson's correlation coefficient									
		PC 1		PC 2		PC 3		PC 4		PC 5	
		r	*P*-value	r	*P*-value	r	*P*-value	r	*P*-value	r	*P*-value
bNFL	Superior	-0.77	<0.001	-0.10	0.192	0.05	0.534	-0.40	<0.001	0.27	<0.001
	Inferior	-0.80	<0.001	-0.09	0.235	-0.04	0.615	-0.24	0.002	0.15	0.056
	Nasal	-0.74	<0.001	-0.01	0.898	0.03	0.743	-0.33	<0.001	-0.21	0.005
	Temporal	-0.56	<0.001	-0.09	0.246	-0.15	0.048	0.20	0.009	0.37	<0.001
	SN	-0.74	<0.001	-0.06	0.437	0.14	0.065	-0.44	<0.001	0.01	0.927
	IT	-0.74	<0.001	-0.21	0.005	-0.24	0.002	0.11	0.149	0.30	<0.001
	ST	-0.75	<0.001	-0.19	0.013	-0.05	0.560	-0.08	0.320	0.35	<0.001
	IN	-0.72	<0.001	-0.03	0.743	0.10	0.203	-0.29	<0.001	-0.23	0.003
pNFL	Superior	-0.52	<0.001	-0.14	0.061	0.05	0.533	-0.22	0.004	0.04	0.604
	Inferior	-0.58	<0.001	-0.24	0.002	-0.01	0.938	-0.22	0.004	-0.004	0.960
	Nasal	-0.42	<0.001	-0.24	0.002	0.06	0.466	-0.07	0.386	0.03	0.684
	Temporal	-0.51	<0.001	-0.30	<0.001	0.17	0.026	0.17	0.029	0.06	0.472
	SN	-0.33	<0.001	-0.39	<0.001	0.02	0.816	-0.33	<0.001	-0.08	0.274
	IT	-0.47	<0.001	-0.40	<0.001	-0.14	0.069	0.23	0.003	0.01	0.858
	ST	-0.66	<0.001	-0.33	<0.001	-0.02	0.769	0.02	0.798	0.05	0.506
	IN	-0.54	<0.001	-0.29	<0.001	0.04	0.577	-0.04	0.628	0.12	0.120

Table VI.4: Pearson's correlation between regional measures of border and peripapillary NFL, and the first 5 PCs. Red text indicates a strong association at $r \geq 0.70$ and $P < 0.05$.

Regional ONH parameter	Region	Pearson's correlation coefficient									
		PC 1		PC 2		PC 3		PC 4		PC 5	
		r	*P*-value	r	*P*-value	r	*P*-value	r	*P*-value	r	*P*-value
MRW	Superior	-0.80	<0.001	0.01	0.912	-0.09	0.231	-0.26	<0.001	0.25	0.001
	Inferior	-0.83	<0.001	-0.07	0.384	-0.10	0.201	-0.19	0.012	0.17	0.032
	Nasal	-0.79	<0.001	0.15	0.058	-0.02	0.777	-0.18	0.020	-0.28	<0.001
	Temporal	-0.74	<0.001	0.01	0.895	-0.24	0.002	0.26	<0.001	0.04	0.589
	SN	-0.83	<0.001	0.16	0.037	0.03	0.653	-0.20	0.009	-0.09	0.242
	IT	-0.82	<0.001	-0.20	0.008	-0.29	<0.001	0.05	0.555	0.06	0.455
	ST	-0.85	<0.001	-0.15	0.058	-0.13	0.093	0.02	0.814	0.20	0.009
	IN	-0.80	<0.001	0.12	0.136	0.06	0.472	-0.19	0.015	-0.29	<0.001
MRA	Superior	-0.61	<0.001	-0.19	0.013	-0.30	<0.001	-0.27	<0.001	0.12	0.125
	Inferior	-0.69	<0.001	-0.21	0.007	-0.33	<0.001	-0.19	0.016	0.06	0.452
	Nasal	-0.65	<0.001	-0.06	0.405	-0.36	<0.001	-0.01	0.877	-0.48	<0.001
	Temporal	-0.50	<0.001	-0.19	0.014	-0.51	<0.001	0.38	<0.001	-0.24	0.002
	SN	-0.71	<0.001	-0.004	0.957	-0.28	<0.001	-0.06	0.469	-0.24	0.002
	IT	-0.62	<0.001	-0.36	<0.001	-0.52	<0.001	0.15	0.058	-0.13	0.097
	ST	-0.69	<0.001	-0.38	<0.001	-0.33	<0.001	0.11	0.147	-0.001	0.985
	IN	-0.68	<0.001	-0.14	0.073	-0.19	0.012	-0.09	0.271	-0.44	<0.001

Table VI.5: Pearson's correlation between regional measures of minimum rim width and area, and the first 5 PCs. Red text indicates a strong association at $r \geq 0.70$ and $P < 0.05$.

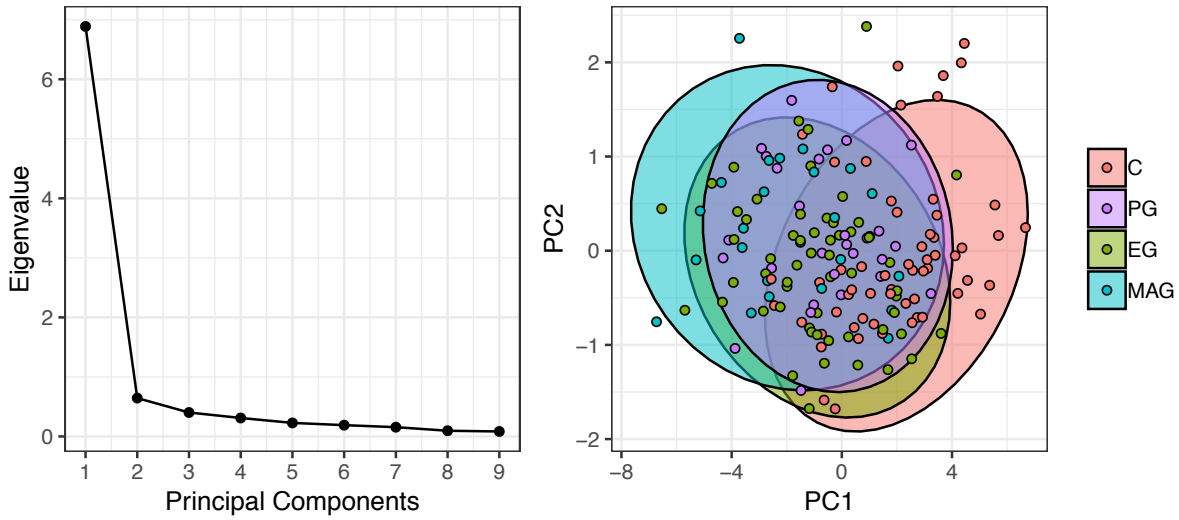

Figure VI.1: Scree-plot (left) and PCs 1 and 2 for prelamina depth as a function of glaucoma disease stage (right). Oval polygons represent 95% confidence intervals.

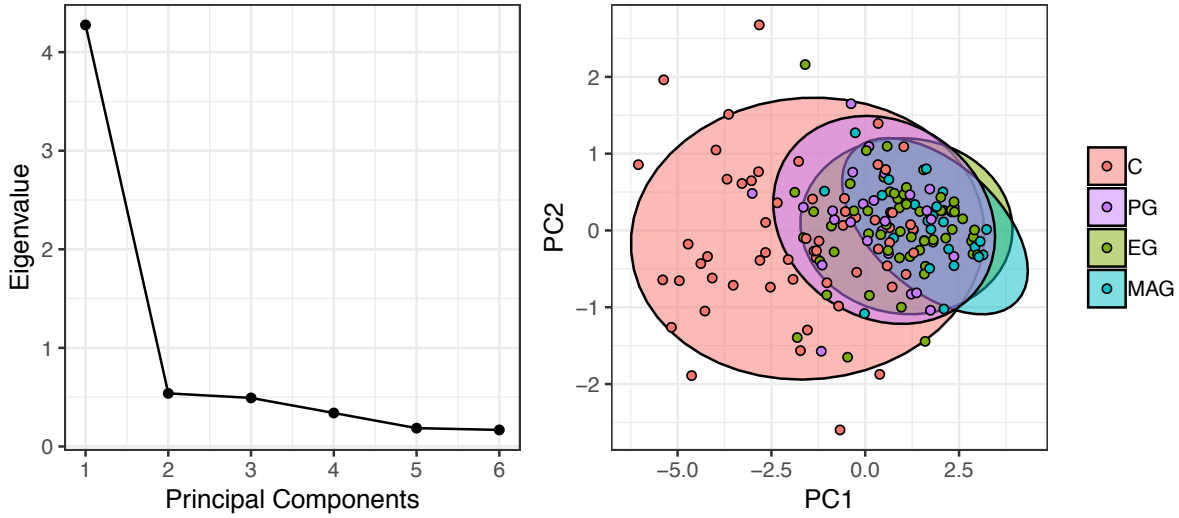

Figure VI.2: Scree-plot (left) and PCs 1 and 2 for prelamina thickness as a function of glaucoma disease stage (right). Oval polygons represent 95% confidence intervals.

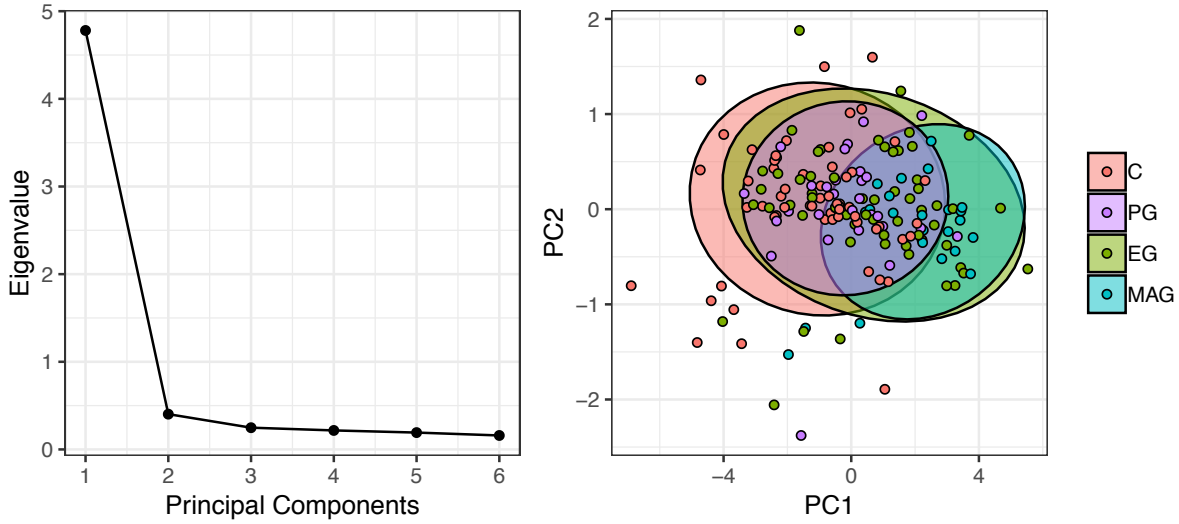

Figure VI.3: Scree-plot (left) and PCs 1 and 2 for lamina cribrosa thickness as a function of glaucoma disease stage (right). Oval polygons represent 95% confidence intervals.

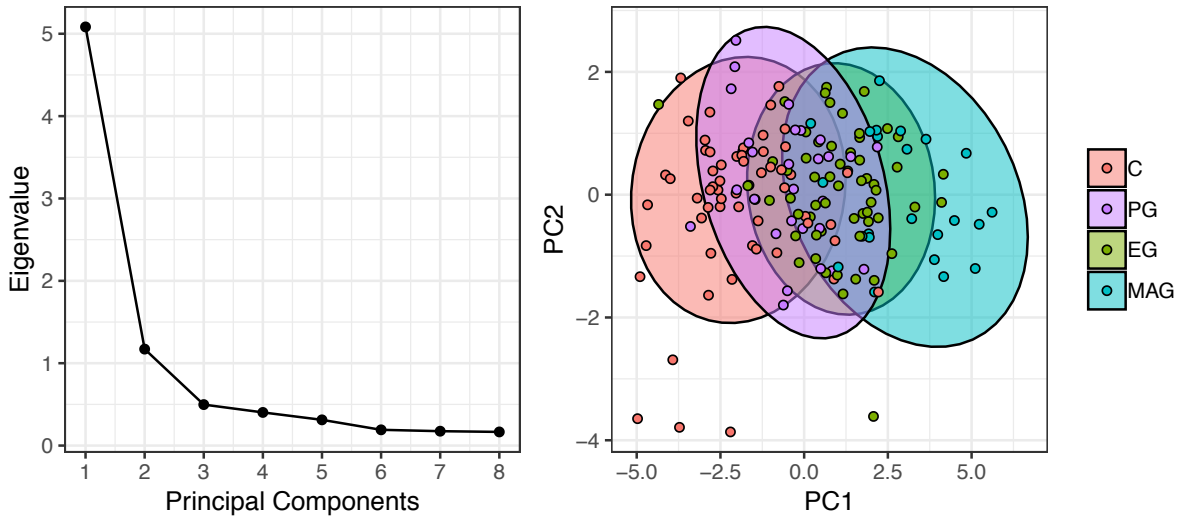

Figure VI.4: Scree-plot (left) and PCs 1 and 2 for border nerve fibre layer thickness as a function of glaucoma disease stage (right). Oval polygons represent 95% confidence intervals.

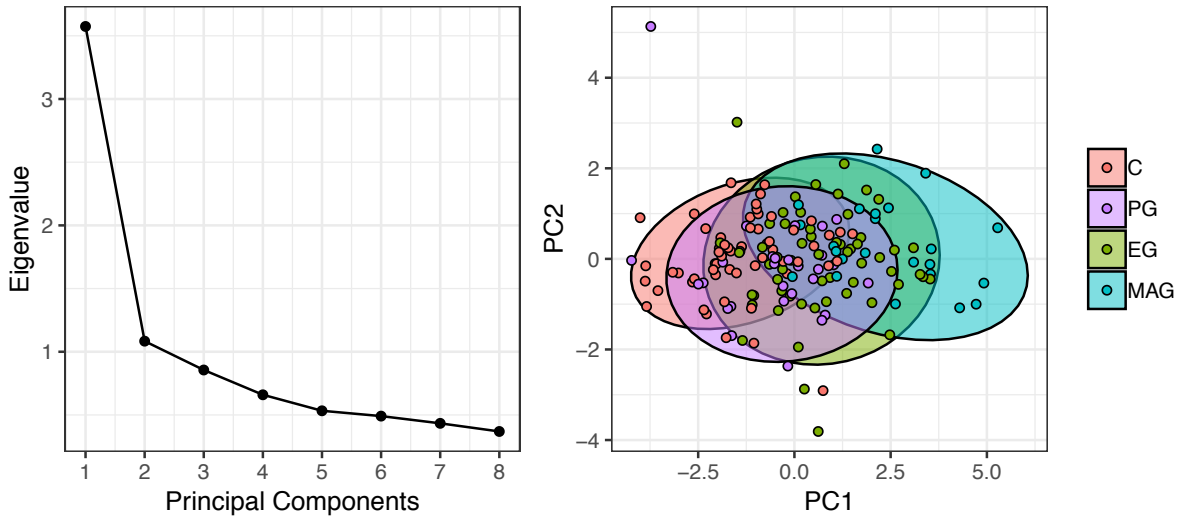

Figure VI.5: Scree-plot (left) and PCs 1 and 2 for peripapillary nerve fibre layer thickness as a function of glaucoma disease stage (right). Oval polygons represent 95% confidence intervals.

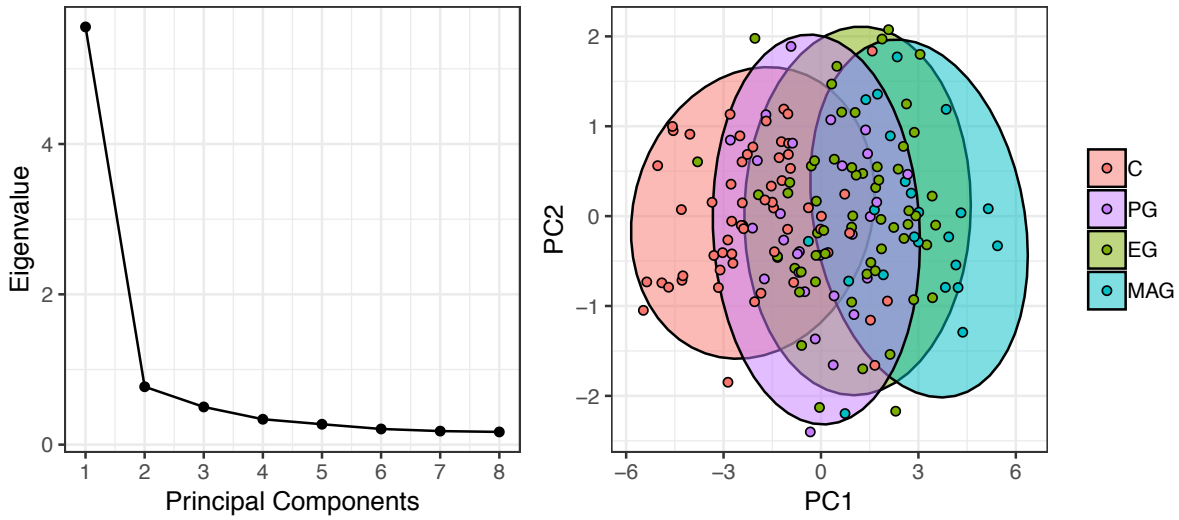

Figure VI.6: Scree-plot (left) and PCs 1 and 2 for minimum rim width as a function of glaucoma disease stage (right). Oval polygons represent 95% confidence intervals.

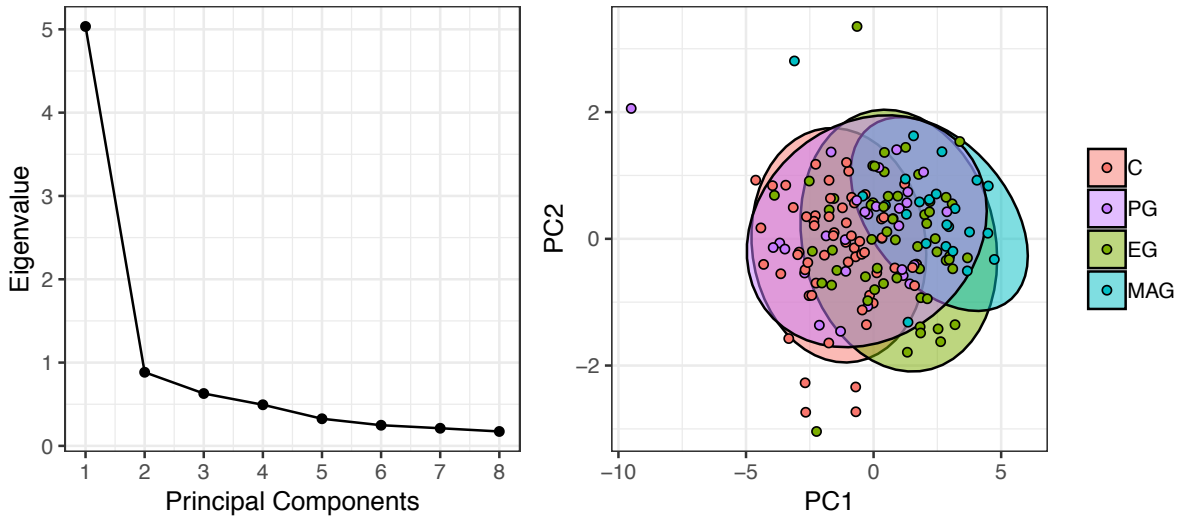

Figure VI.7: Scree-plot (left) and PCs 1 and 2 for minimum rim area as a function of glaucoma disease stage (right). Oval polygons represent 95% confidence intervals.

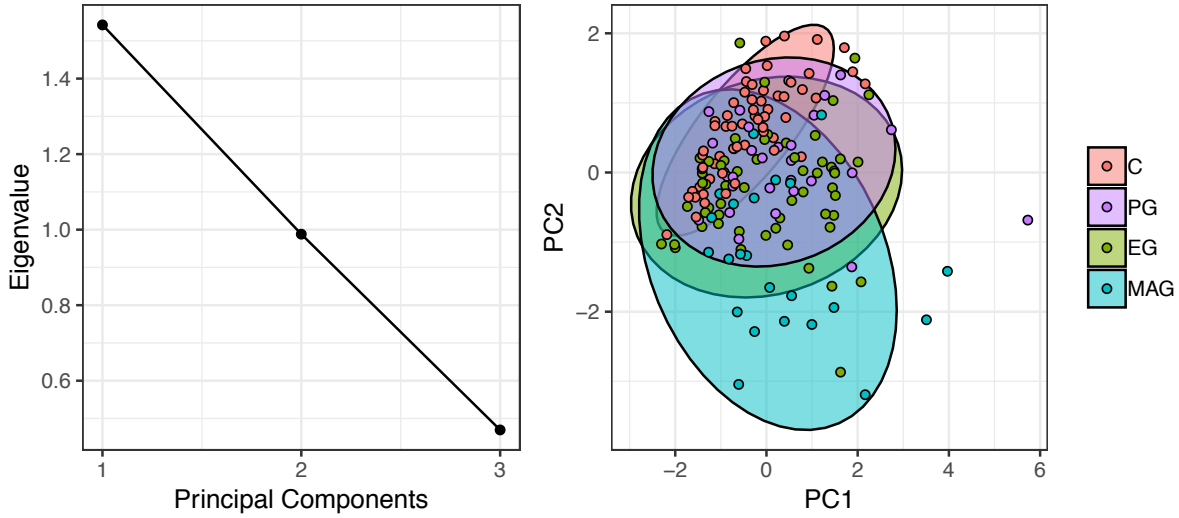

Figure VI.8: Scree-plot (left) and PCs 1 and 2 for 3D ONH parameters as a function of glaucoma disease stage (right). Oval polygons represent 95% confidence intervals. ONH parameters included optic cup and prelamina volume, and BMO surface area.

Appendix V

Copyright permit for Figure 1.1:

This Agreement between Mr. Ryan Bartlett ("You") and American Medical Association ("American Medical Association") consists of your license details and the terms and conditions provided by American Medical Association and Copyright Clearance Centre.

License Number	4885930911933
License date	Aug 11, 2020
Licensed Content Publisher	American Medical Association
Licensed Content Publication	JAMA Ophthalmology
Licensed Content Title	Ultrastructure of Intraorbital Portion of Human and Monkey Optic Nerve
Licensed Content Author	Anderson, Douglas R.; Hoyt, William F.
Licensed Content Date	Oct 1, 1969
Licensed Content Volume	82
Licensed Content Issue	4
Volume number	82
Issue number	4
Type of Use	Dissertation/Thesis
Requestor type	Student
Reusing this material for promotional purposes	No
Format	Print and Electronic
Portion	Figures/Tables/Images
Number of figures/tables/images	1
List of figures/tables/images	Schematic drawing of optic nerve
Will you be translating?	No
Circulation/distribution	10
Distributing to	Europe
Order reference number	4885930911933
Title	Ryan Bartlett
Institution name	Cardiff University

Copyright permit for Figure 1.2 (a):

This Agreement between Mr. Ryan Bartlett ("You") and Elsevier ("Elsevier") consists of your license details and the terms and conditions provided by Elsevier and Copyright Clearance Centre.

License Number	4885940275634
License date	Aug 11, 2020
Licensed Content Publisher	Elsevier
Licensed Content Publication	The Lancet
Licensed Content Title	Glaucoma
Licensed Content Author	Harry A Quigley
Licensed Content Date	16–22 April 2011
Licensed Content Volume	377
Licensed Content Issue	9774
Licensed Content Pages	11
Start Page	1367
End Page	1377
Type of Use	Thesis/Dissertation
Portion	Figures/Tables/Illustrations
Number of figures/tables/illustrations	2
Format	Print and Electronic
Are you the author of this Elsevier article?	No
Will you be translating?	No
Title	Ryan Bartlett
Institution name	Cardiff University

Copyright permit for Figure 1.2 (b):

This Agreement between Mr. Ryan Bartlett ("You") and American Medical Association ("American Medical Association") consists of your license details and the terms and conditions provided by American Medical Association and Copyright Clearance Centre.

License Number	4885950450465
License date	Aug 11, 2020
Licensed Content Publisher	American Medical Association
Licensed Content Publication	JAMA Ophthalmology
Licensed Content Title	Regional Differences in the Structure of the Lamina Cribrosa and Their Relation to Glaucomatous Optic Nerve Damage
Licensed Content Author	Quigley, Harry A.; Addicks, Earl M.
Licensed Content Date	Jan 1, 1981
Licensed Content Volume	99
Licensed Content Issue	1
Volume number	99
Issue number	1
Type of Use	Dissertation/Thesis
Requestor type	Student
Reusing this material for promotional purposes	No
Format	Print and Electronic
Portion	Figures/Tables/Images
Number of figures/tables/images	2
List of figures/tables/images	Figure 3
Will you be translating?	No
Circulation/distribution	10
Distributing to	Europe
Order reference number	4885950450465
Title	Ryan Bartlett
Institution name	Cardiff University

Copyright permit for Figure 1.3:

This Agreement between Mr. Ryan Bartlett ("You") and Elsevier ("Elsevier") consists of your license details and the terms and conditions provided by Elsevier and Copyright Clearance Centre.

License Number	4885940275634
License date	Aug 11, 2020
Licensed Content Publisher	Elsevier
Licensed Content Publication	The Lancet
Licensed Content Title	Glaucoma
Licensed Content Author	Harry A Quigley
Licensed Content Date	16–22 April 2011
Licensed Content Volume	377
Licensed Content Issue	9774
Licensed Content Pages	11
Start Page	1367
End Page	1377
Type of Use	Thesis/Dissertation
Portion	Figures/Tables/Illustrations
Number of figures/tables/illustrations	2
Format	Print and Electronic
Are you the author of this Elsevier article?	No
Will you be translating?	No
Title	Ryan Bartlett
Institution name	Cardiff University

Copyright permit for Figure 1.4:

This Agreement between Mr. Ryan Bartlett ("You") and American Medical Association ("American Medical Association") consists of your license details and the terms and conditions provided by American Medical Association and Copyright Clearance Centre.

License Number	4885950901674
License date	Aug 11, 2020
Licensed Content Publisher	American Medical Association
Licensed Content Publication	JAMA
Licensed Content Title	The Pathophysiology and Treatment of Glaucoma: A Review
Licensed Content Author	Weinreb, Robert N.; Aung, Tin
Licensed Content Date	May 14, 2014
Licensed Content Volume	311
Licensed Content Issue	18
Volume number	311
Issue number	18
Type of Use	Dissertation/Thesis
Requestor type	Student
Reusing this material for promotional purposes	No
Format	Print and Electronic
Portion	Figures/Tables/Images
Number of figures/tables/images	2
List of figures/tables/images	Figures 1 and 2
Will you be translating?	No
Circulation/distribution	10
Distributing to	Europe
Order reference number	4885950901674
Title	Ryan Bartlett
Institution name	Cardiff University

Copyright permit for Figure 1.5:

This Agreement between Mr. Ryan Bartlett ("You") and American Medical Association ("American Medical Association") consists of your license details and the terms and conditions provided by American Medical Association and Copyright Clearance Centre.

License Number	4885950901674
License date	Aug 11, 2020
Licensed Content Publisher	American Medical Association
Licensed Content Publication	JAMA
Licensed Content Title	The Pathophysiology and Treatment of Glaucoma: A Review
Licensed Content Author	Weinreb, Robert N.; Aung, Tin
Licensed Content Date	May 14, 2014
Licensed Content Volume	311
Licensed Content Issue	18
Volume number	311
Issue number	18
Type of Use	Dissertation/Thesis
Requestor type	Student
Reusing this material for promotional purposes	No
Format	Print and Electronic
Portion	Figures/Tables/Images
Number of figures/tables/images	2
List of figures/tables/images	Figures 1 and 2
Will you be translating?	No
Circulation/distribution	10
Distributing to	Europe
Order reference number	4885950901674
Title	Ryan Bartlett
Institution name	Cardiff University

Copyright permit for Figure 1.6:

This Agreement between Mr. Ryan Bartlett ("You") and American Medical Association ("American Medical Association") consists of your license details and the terms and conditions provided by American Medical Association and Copyright Clearance Centre.

License Number	4916001368486
License date	Sep 25, 2020
Licensed Content Publisher	American Medical Association
Licensed Content Publication	JAMA
Licensed Content Title	The Pathophysiology and Treatment of Glaucoma: A Review
Licensed Content Author	Weinreb, Robert N.; Aung, Tin
Licensed Content Date	May 14, 2014
Licensed Content Volume	311
Licensed Content Issue	18
Volume number	311
Issue number	18
Type of Use	Dissertation/Thesis
Requestor type	Student
Reusing this material for promotional purposes	No
Format	Print and Electronic
Portion	Figures/Tables/Images
Number of figures/tables/images	2
List of figures/tables/images	Figures 3 and 4
Will you be translating?	No
Circulation/distribution	10
Distributing to	Europe
Order reference number	4916001368486
Title	Ryan Bartlett
Institution name	Cardiff University

Copyright permit for Figure 1.7:

This Agreement between Mr. Ryan Bartlett ("You") and Elsevier ("Elsevier") consists of your license details and the terms and conditions provided by Elsevier and Copyright Clearance Centre.

License Number	4885960031811
License date	Aug 11, 2020
Licensed Content Publisher	Elsevier
Licensed Content Publication	Experimental Eye Research
Licensed Content Title	Glaucomatous cupping of the lamina cribrosa: A review of the evidence for active progressive remodelling as a mechanism
Licensed Content Author	J. Crawford Downs, Michael D. Roberts, Ian A. Sigal
Licensed Content Date	Aug 1, 2011
Licensed Content Volume	93
Licensed Content Issue	2
Licensed Content Pages	8
Start Page	133
End Page	140
Type of Use	Thesis/Dissertation
Portion	Figures/Tables/Illustrations
Number of figures/tables/illustrations	3
Format	Print and Electronic
Are you the author of this Elsevier article?	No
Will you be translating?	No
Title	Ryan Bartlett
Institution name	Cardiff University

Copyright permit for Figure 1.8:

This Agreement between Mr. Ryan Bartlett ("You") and Elsevier ("Elsevier") consists of your license details and the terms and conditions provided by Elsevier and Copyright Clearance Centre.

License Number	4885960031811
License date	Aug 11, 2020
Licensed Content Publisher	Elsevier
Licensed Content Publication	Experimental Eye Research
Licensed Content Title	Glaucomatous cupping of the lamina cribrosa: A review of the evidence for active progressive remodelling as a mechanism
Licensed Content Author	J. Crawford Downs, Michael D. Roberts, Ian A. Sigal
Licensed Content Date	Aug 1, 2011
Licensed Content Volume	93
Licensed Content Issue	2
Licensed Content Pages	8
Start Page	133
End Page	140
Type of Use	Thesis/Dissertation
Portion	Figures/Tables/Illustrations
Number of figures/tables/illustrations	3
Format	Print and Electronic
Are you the author of this Elsevier article?	No
Will you be translating?	No
Title	Ryan Bartlett
Institution name	Cardiff University

Copyright permit for Figure 1.9:

This Agreement between Mr. Ryan Bartlett ("You") and Springer Nature ("Springer Nature") consists of your license details and the terms and conditions provided by Springer Nature and Copyright Clearance Centre.

License Number	4894120805593
License date	Aug 22, 2020
Licensed Content Publisher	Springer Nature
Licensed Content Publication	Springer eBook
Licensed Content Title	Theory of Optical Coherence Tomography
Licensed Content Author	J. A. Izatt, M. A. Choma
Licensed Content Date	Jan 1, 2008
Type of Use	Thesis/Dissertation
Requestor type	University/Academic
Format	Print and Electronic
Portion	Figures/Tables/Illustrations
Number of figures/tables/illustrations	5
Will you be translating?	No
Circulation/distribution	1 - 29
Author of this Springer Nature content	No
Title	Ryan Bartlett
Institution name	Cardiff University

Copyright permit for Figure 1.10:

This Agreement between Mr. Ryan Bartlett ("You") and John Wiley and Sons ("John Wiley and Sons") consists of your license details and the terms and conditions provided by John Wiley and Sons and Copyright Clearance Centre.

License Number	4885991416726
License date	Aug 11, 2020
Licensed Content Publisher	John Wiley and Sons
Licensed Content Publication	Clinical & Experimental Ophthalmology
Licensed Content Title	Imaging of the lamina cribrosa and its role in glaucoma: a review
Licensed Content Author	Nicholas YQ Tan, Victor Koh, Michaël JA Girard, et al
Licensed Content Date	Jan 10, 2018
Licensed Content Volume	46
Licensed Content Issue	2
Licensed Content Pages	12
Type of use	Dissertation/Thesis
Requestor type	University/Academic
Format	Print and electronic
Portion	Figure/Table
Number of figures/tables	2
Will you be translating?	No
Title	Ryan Bartlett
Institution name	Cardiff University